الجمهورية الجزائرية الديمقراطية الشعبية

People's Democratic Republic of Algeria

وزارة التعليم العالي والبحث العلمي

Ministry of Higher Education and Scientific Research

MOHAMED KHIDER UNIVERSITY OF BISKRA
FACULTY OF SCIENCE AND TECHNOLOGY
DEPARTMENT OF INDUSTRIAL CHEMISTRY
Reference: .....



جامعة محمد خيضر-بسكرة
كلية العلوم والتكنولوجيا
قسم الكيمياء الصناعية
المرجع: .....

A thesis submitted in fulfillment of the requirements for the degree of:

LMD Doctorate

Specialty: Chemical Engineering

Valorization of agricultural wastes in the production of carbon-based materials: Application for the removal of pollutants from water

---

Presented by:

Mazen Saleh Farhan Al-Hazeef

Publicly on: 14/06/2026

In front of the jury composed of

Prof. Abdelkrim Merzougui	**Professor**	**President**	**University of Biskra**
Prof. Amel Aidi	**Professor**	**Supervisor**	**University of Biskra**
Prof. Lynda Hecini	**Research Director**	**Co-Supervisor**	**CRSTRA-Biskra**
Prof. Chahinez Fares	**Professor**	**Examiner**	**University of Chlef**
Dr. Hanane Rehali	**Associate Professor**	**Examiner**	**University of Biskra**

Academic Year: 2025/2026

Copyright Page

* * * * * *

© 2026 Biskra University

All Rights Reserved.

University of Biskra

Academic Year: 2025/2026

Declaration of Copyright and Data Protection

No part of this doctoral thesis may be reproduced, stored in a retrieval system, or transmitted in any form or by any means—electronic, mechanical, photocopying, recording, or otherwise—without the prior, explicit written permission of the **author** and/or **Biskra University**.

This thesis encompasses both previously published research and unpublished, proprietary data. Therefore, the following strict conditions apply to the consultation and use of this document:

1. Published Work: Portions of this research have been previously published as original research articles in peer-reviewed journals. The copyright for those specifically formatted articles may be subject to agreements established with the respective publishers. Full academic citations for these published works are appropriately referenced within the body of this thesis.

2. Unpublished Data: This document contains original, unreleased data, methodologies, and findings. **It is strictly forbidden to extract, utilize, reproduce, distribute, or publish any data, figures, or unpublished results contained herein under any circumstances.** Any unauthorized use of this data constitutes a breach of copyright and academic integrity.

Requests for permission to reference or utilize any unpublished material must be directed to the **author** and/or **Biskra University** in writing.

Contact Information:

mazen.saleh@univ-biskra.dz; mazen.saleh100@gmail.com.

Acknowledgements

* * * * * *

First and foremost, I would like to express my profound gratitude to Almighty Allah for granting me the strength, health, and patience to complete this doctoral research.

My deepest appreciation and profound respect go to my primary supervisor, **Pr. Amel Aidi**. I am incredibly grateful for her continuous guidance, invaluable mentorship, and immense scientific knowledge throughout my Ph.D. journey. Her encouragement and critical insights were instrumental in shaping this research and overcoming the various experimental challenges.

I am equally deeply indebted to my co-supervisor, **Pr. Lynda Hecini**, for her continuous support, expert advice, and the time she dedicated to reviewing my work. Her contributions and access to the resources at CRSTRA-Biskra significantly enriched the quality of this thesis.

I would like to extend my sincere thanks to the President of the jury, **Pr. Abdelkrim Merzougui**, for doing me the honor of presiding over my defense committee. I also warmly thank the other esteemed members of the examination jury, **Pr. Chahinez Fares** and **Dr. Hanene Rehali**, for graciously accepting to review my dissertation and for their constructive feedback.

I gratefully acknowledge the **Faculty of Science and Technology at Mohamed Khider University of Biskra** for providing the academic environment and laboratory facilities necessary to conduct my experimental work on carbon-based materials and agricultural waste valorization.

A special word of thanks goes to the soil laboratory engineer and staff at CRSTRA, particularly **Mr. Tarek Othmane**, for their technical assistance during the experimental work.

Finally, no words can adequately express my gratitude to my beloved family. To my parents, whose unconditional love, endless prayers, and sacrifices have been the foundation of my success. Thank you for always believing in me.

Dedication

* * * * *

Every challenging work requires self-effort as well as the guidance of elders, especially those who are very close to our hearts.

I dedicate this thesis to my beloved parents, whose endless love, countless sacrifices, and continuous prayers have been my greatest source of strength and inspiration. Thank you for instilling in me the value of education and for believing in me even when I doubted myself.

To my dear brothers and sisters, for their unwavering support, encouragement, and for always being by my side.

To all my family and friends who have supported me throughout this journey.

To those not mentioned here, thank you for your unwavering emotional support and for standing by my side during the most demanding times of this Ph.D. journey.

This achievement is as much yours as it is mine.

Mazen Saleh Farhan Al-Hazeef

Abstract

* * * * *

Water contamination by synthetic dyes, phenols, and pesticides necessitates sustainable remediation materials. To address this requirement, Date Palm Spikelets were valorized into a novel zinc oxide-modified activated carbon composite (ZnO@DPS-AC) via simultaneous $ZnCl_2$ activation and pyrolysis at 600°C. Characterization confirmed nanometric ZnO particles (33.07 nm) embedded within a graphitic matrix exhibiting a specific surface area of 1028.63 m^2/g, a total pore volume of 0.555 cm^3/g, and a point of zero charge of 6.67. Batch adsorption studies achieved high maximum capacities of 274 mg/g for Methyl Orange (MO), 170 mg/g for Catechol (CAT), and 291.38 mg/g for Acetamiprid (ACE). Thermodynamic and mechanistic analyses revealed distinct energetic profiles. The adsorption of MO and CAT was endothermic (ΔH° = 77.45 and 42.27 to 110.16 kJ/mol, respectively), driven by electrostatic attraction, hydrogen bonding, π-π interactions, pore-filling, and inner-sphere surface complexation. Conversely, ACE adsorption was exothermic (ΔH° = -31.18 kJ/mol)—furthermore, *pH*-independent, operating efficiently at ambient temperatures entirely via non-electrostatic physical forces. For process optimization, Artificial Neural Networks coupled with Genetic Algorithms consistently identified superior global optima compared to Response Surface Methodology across diverse computational architectures. Continuous fixed-bed column studies further demonstrated dynamic ACE capacities of up to 348.55 mg/g. Mathematical evaluation established the equivalence of the classical breakthrough models (Yoon-Nelson, Thomas, and Adams-Bohart) and confirmed the dual-rate Chu-Hashim model as the optimal predictive framework (R^2 = 0.969-0.999). Ultimately, ZnO@DPS-AC provides a cost-effective, structurally robust, and versatile platform for advanced multi-class wastewater remediation.

Keywords: Agricultural waste valorization; Activated carbon; Adsorption; Zinc oxide; Methyl Orange; Catechol; Acetamiprid; Response Surface Methodology; Artificial Neural Networks; Genetic Algorithm; Breakthrough curve modeling.

Résumé

* * * * *

La contamination de l'eau par les colorants synthétiques, les phénols et les pesticides nécessite des matériaux de remédiation durables. Pour répondre à cette exigence, des épillets de palmier dattier ont été valorisés en un nouveau composite de charbon actif modifié à l'oxyde de zinc via une activation simultanée au $ZnCl_2$ et une pyrolyse à 600°C. La caractérisation a confirmé la présence de particules nanométriques de ZnO (33.07 nm) intégrées au sein d'une matrice graphitique présentant une surface spécifique de 1028.63 m^2/g, un volume poreux total de 0.555 cm^3/g et un point de charge nulle de 6.67. Les études d'adsorption en mode discontinu ont atteint des capacités maximales élevées de 274 mg/g pour le méthyl orange (MO), 170 mg/g pour le catéchol (CAT) et 291.38 mg/g pour l'acétamipride (ACE). Les analyses thermodynamiques et mécanistiques ont révélé des profils énergétiques distincts. L'adsorption du MO et du CAT était endothermique (ΔH° = 77.45 et 42.27 à 110.16 kJ/mol, respectivement), régie par l'attraction électrostatique, les liaisons hydrogène, les interactions π-π, le remplissage des pores et la complexation de surface en sphère interne. Inversement, l'adsorption de l'ACE était exothermique (ΔH° = -31.18 kJ/mol) et indépendante du *pH*, fonctionnant efficacement à des températures ambiantes entièrement via des forces physiques non électrostatiques. Pour l'optimisation du processus, les réseaux de neurones artificiels couplés aux algorithmes génétiques ont systématiquement identifié des optimums globaux supérieurs par rapport à la méthodologie des surfaces de réponse à travers diverses architectures informatiques. Des études continues sur colonne à lit fixe ont en outre démontré des capacités dynamiques pour l'ACE atteignant 348.55 mg/g. L'évaluation mathématique a établi l'équivalence des modèles classiques de courbe de percée (Yoon-Nelson, Thomas et Adams-Bohart) tout en confirmant le modèle à double vitesse de Chu-Hashim comme le cadre prédictif optimal (R^2 = 0.969 à 0.999). En fin de compte, le ZnO@DPS-AC constitue une plateforme rentable, structurellement robuste et polyvalente pour la remédiation avancée des eaux usées à classes multiples.

Mots-clés : Valorisation des déchets agricoles ; Charbon actif ; Adsorption ; Oxyde de zinc ; Méthyl orange ; Catéchol ; Acétamipride ; Méthodologie des surfaces de réponse ; Réseaux de neurones artificiels ; Algorithme génétique ; Modélisation des courbes de percée.

الملخص

* * * * *

يتطلب تلوث المياه بالأصباغ الاصطناعية والفينولات والمبيدات الحشرية استخدام مواد معالجة مستدامة. واستجابةً لهذا المطلب، تم استغلال سنابل النخيل في تصنيع مركب جديد من الكربون المنشط المعدل بأكسيد الزنك (ZnO@DPS-AC) من خلال عملية مزدوجة تتمثل في تنشيط الكربون باستخدام كلوريد الزنك ($ZnCl_2$) والانحلال الحراري عند درجة حرارة 600 درجة مئوية. وأكدت عملية التوصيف وجود جزيئات أكسيد الزنك نانومترية (33.07 نانومتر) مدمجة في مصفوفة جرافيتية تظهر مساحة سطح محددة تبلغ 1028.63 م^2/جم، وحجم مسام إجمالي يبلغ 0.555 سم^3/جم، ونقطة شحنة صفرية تبلغ 6.67. حققت دراسات الامتصاص الدفعي سعات قصوى عالية بلغت 274 مجم/جم لميثيل البرتقالي (MO)، و170 مجم/جم للكاتيكول (CAT)، و291.38 مجم/جم للأسيتاميبريد (ACE). كشفت التحليلات الديناميكية الحرارية والميكانيكية عن ملامح طاقية مميزة. كان امتصاص الميثيل البرتقالي والكاتيكول امتصاصًا ماصًا للحرارة (ΔH° = 77.45 و42.27 إلى 110.16 كيلوجول/مول، على التوالي)، مدفوعًا بالجاذبية الكهروستاتيكية، والروابط الهيدروجينية، والتفاعلات π-π، وملء المسام، والتعقيد السطحي للكرة الداخلية. وعلى العكس من ذلك، كان امتصاص ACE طاردًا للحرارة (ΔH° = -31.18 كيلوجول/مول) — علاوة على ذلك، فهو مستقل عن درجة الحموضة، ويعمل بكفاءة في درجات الحرارة المحيطة بالكامل عبر قوى فيزيائية غير كهروستاتيكية. من أجل تحسين العملية، حددت الشبكات العصبية الاصطناعية المقترنة بالخوارزميات الجينية باستمرار أفضل الحلول المثلى الشاملة مقارنة بمنهجية سطح الاستجابة عبر بنى حسابية متنوعة. وأظهرت الدراسات المستمرة على أعمدة الطبقة الثابتة قدرات ديناميكية لـ ACE تصل إلى 348.55 مجم/جم. أثبتت الدراسة الحسابية التكافؤ بين نماذج الاختراق الكلاسيكية (يون-نيلسون، وتوماس، وآدامز-بوهارت)، وأكدت أن نموذج تشو-هاشم CHu-Hashim ثنائي المعدل هو الإطار التنبئي الأمثل (R^2 = 0.969-0.999). وفي النهاية، يوفر ZnO@DPS-AC منصة فعالة من حيث التكلفة وقوية من الناحية الهيكلية ومتعددة الاستخدامات لمعالجة مياه الصرف الصحي المتعددة الفئات على مستوى متقدم.

الكلمات المفتاحية :تثمين النفايات الزراعية؛ الكربون المنشط؛ الامتزاز ؛ أكسيد الزنك؛ الميثيل البرتقالي؛ الكاتيكول؛ الأسيتاميبريد؛ منهجية سطح الاستجابة؛ الشبكات العصبية الاصطناعية؛ الخوارزميات الجينية؛ نمذجة منحنى الاختراق.

Table of Contents

* * * * *

Contents

Copyright Page ..... **i**

Acknowledgements ..... **i**

Dedication ..... **ii**

Abstract ..... **iii**

Résumé ..... **iv**

الملخص ..... **v**

Table of Contents ..... **vi**

List of Figures ..... **xvii**

List of Tables ..... **xxiii**

List of Symbols and Abbreviations ..... **xxvi**

General Introduction **1**

Chapter I: Literature Review: Water Pollution and Advanced Remediation Strategies **5**

I.1 Introduction 5

I.2 Water pollution and pollutants of interest 5

I.3 Methyl orange 6

I.3.1 Structure and physicochemical properties 6

I.3.2 Industrial synthesis 7

I.3.3 Commercial and scientific applications 8

I.4 Catechol 10

I.4.1 Structure and properties 10

I.4.2 Industrial production 11

I.4.3 Natural and anthropogenic environmental sources 11

I.4.4 Industrial applications 12

I.4.5 Toxicity to humans and the environment 13

I.4.6 Toxicity and environmental fate 14

I.5 Acetamiprid 15
I.5.1 Structure and properties 15
I.5.2 Agricultural deployment 15
I.5.3 Mode of action 16
I.5.4 Mammalian toxicology and human safety profile 16
I.5.5 Ecotoxicological profile 17
I.5.6 Environmental fate, mobility, and persistence profiles 17
I.6 Remediation strategies MO, CAT, and ACE 18
I.6.1 Methyl orange remediation 19
I.6.2 Catechol remediation 23
I.6.3 Acetamiprid remediation 26
I.7 Comparative summary between MO, CAT, and ACE 28
I.8 Conclusion 29
Chapter II: Theoretical Principles of Adsorption, Process Modeling and Optimization 30
II.1 Introduction 30
II.2 Principles of adsorption 30
II.2.1 Definitions and concepts 31
II.2.2 Mechanics of mass transport in porous adsorbents 34
II.2.3 Factors affecting adsorption 35
II.2.4 Adsorption equilibrium (isotherms) 38
II.2.5 Adsorption kinetics 40
II.2.6 Adsorption thermodynamics 44
II.3 Activated carbon 46
II.3.1 Definition 46
II.3.2 Microcrystalline structure of activated carbon 46
II.3.3 Properties of AC 49
II.3.4 Precursors for AC production 49
II.3.5 Activation methods 51
II.4 Response surface methodology in adsorption studies 53
II.4.1 Principles of RSM 54
II.4.2 Common RSM designs 55
II.4.3 Statistical validation and model adequacy 57

II.4.4 Multi-response optimization and verification 57
II.4.5 Advantages of response surface methodology 58
II.5 Artificial neural networks in adsorption modeling 59
II.5.1 Architecture of artificial neural networks 59
II.5.2 Fundamental components: neurons, weights, and biases 61
II.5.3 Activation functions 61
II.5.4 Network training and optimization algorithms 63
II.5.5 Comparative analysis of RSM and ANN in adsorption modeling 64
II.6 Genetic algorithm and ANN-GA hybridization 65
II.6.1 ANN-GA synergy 66
II.6.2 Fundamental genetic operators 66
II.6.3 Termination and convergence 67
II.7 Continuous flow (column) adsorption studies 67
II.7.1 Anatomy and dynamics of the breakthrough curve 67
II.7.2 Factors affecting performance 69
II.7.3 Kinetic models of column adsorption 69
II.8 Conclusion 71
Chapter III: Materials and Experimental Methodology 72
III.1 Introduction 72
III.2 Target pollutants 72
III.3 Chemical reagents for synthesis and modification 72
III.4 Precursor material 73
III.5 Synthesis and modification protocols 73
III.5.1 Pre-treatment of DPS 73
III.5.2 Preparation of DPS-Biochar 74
III.5.3 Synthesis of zinc oxide-modified activated carbon 74
III.5.4 Surface oxidation of ZnO@DPS-AC composite 75
III.6 Physicochemical characterization techniques 76
III.6.1 Thermogravimetric analysis and derivative thermogravimetry 76
III.6.2 Proximate analysis 76
III.6.3 Point of zero charge 78
III.6.4 Scanning electron microscopy coupled with dispersive X-ray spectroscopy 78

III.6.5 Fourier transform infrared spectroscopy 78
III.6.6 X-ray diffraction 79
III.6.7 Raman spectroscopy 79
III.6.8 Surface area and porosity analysis 79
III.7 Analytical methods for pollutant quantification 82
III.7.1 Stock solutions 82
III.7.2 Determination of maximum absorption and calibration curves 82
III.8 Batch adsorption experiments 83
III.8.1 Single-factor Optimization 84
III.8.2 Separation and measurement 84
III.8.3 Calculation of adsorption capacity and efficiency 84
III.9 Adsorbent reusability and regeneration studies 85
III.10 Adsorption isotherm and kinetic studies 85
III.11 Statistical validation and goodness-of-fit 86
III.12 Thermodynamic study 87
III.13 Process optimization via response surface methodology 88
III.13.1 Software 88
III.13.2 Experimental design matrix 88
III.13.3 Mathematical modeling and response analysis 89
III.13.4 Statistical validation 90
III.13.5 Multi-objective optimization and desirability function 91
III.14 Artificial neural network modeling 91
III.14.1 Data preprocessing and normalization 92
III.14.2 Dynamic architecture generation 92
III.14.3 Training algorithms and hyperparameter tuning 93
III.14.4 Robustness via cross-validation and ensemble learning 93
III.14.5 Model selection and performance evaluation 93
III.15 Multi-objective optimization using genetic algorithm 94
III.15.1 Algorithm architecture and island mode 94
III.15.2 Genetic operators and selection 94
III.15.3 Hyperparameter optimization via grid search 94
III.15.4 Diversity and local search enhancement 95

III.15.5 Convergence criteria and Pareto refinement 95
III.16 Fixed-bed column adsorption studies 96
III.16.1 Experimental configuration and apparatus 96
III.16.2 Kinetic modeling of column adsorption 97
III.16.3 Operational design and parameters 97
III.16.4 Evaluation of column performance 98
III.16.5 Model fitting and performance evaluation 99
III.17 Conclusion 100
Chapter IV: Synthesis and Physicochemical Characterization of the ZnO@DPS-AC 102
IV.1 Introduction 102
IV.2 TGA and DTG analysis of DPS 102
IV.2.1 Multi-stage thermal degradation 103
IV.2.2 Differential analysis 103
IV.3 Proximate analysis 105
IV.3.1 Analysis of inorganic and volatile components 105
IV.3.2 Yield and structural density 105
IV.4 Point of zero charge 106
IV.5 Scanning electron microscopy coupled with energy-dispersive X-ray spectroscopy 106
IV.5.1 Impact of $ZnCl_2$ on the porosity and surface chemistry of DPS 107
IV.5.2 Integrated SEM-EDX analysis of adsorbed pollutants 107
IV.5.3 Structural evolution and adsorptive performance 108
IV.6 Surface functional group analysis 108
IV.6.1 Characterization of raw DPS and DPS-Biochar 110
IV.6.2 Role of $ZnCl_2$ in ZnO@DPS-AC functionalization 110
IV.6.3 Surface functional group evolution post-adsorption 111
IV.7 Structural characterization via X-ray diffraction 111
IV.7.1 Evolution of the carbon matrix and ZnO synthesis 112
IV.7.2 Phase identification and crystallite size in ZnO@DPS–AC 112
IV.7.3 Structural stability post-adsorption 112
IV.8 Raman spectroscopy 114
IV.8.1 First-order Raman scattering 114
IV.8.2 Second-order scattering 115

IV.8.3 Spectral evolution of ZnO@DPS–AC–CAT 116
IV.8.4 Analysis of the zinc oxide phase 116
IV.9 Textural properties 117
IV.9.1 Nitrogen physisorption isotherms and pore architecture 117
IV.9.2 Textural evolution following chemical activation 118
IV.9.3 Post-adsorption textural modifications and mechanistic insights 120
IV.9.4 Characteristic adsorption energy and surface heterogeneity 121
IV.10 Conclusion 121
Chapter V: Batch Adsorption of Methyl Orange onto ZnO@DPS-AC: Modeling, Optimization, and Mechanisms 123
V.1 Introduction 123
V.2 Effect of operational parameters on MO adsorption 124
V.2.1 Effect of adsorbent dosage 124
V.2.2 Effect of initial solution pH 125
V.2.3 Effect of ionic strength 127
V.2.4 Effect of contact time 128
V.2.5 Effect of initial dye concentration 130
V.3 Kinetic modeling and mass transfer mechanisms 131
V.4 Isotherm modeling and equilibrium studies 134
V.5 Comparative assessment of adsorbent performance 136
V.6 Thermodynamic analysis 138
V.7 Desorption, regeneration, and cyclic reusability 142
V.8 Optimization via response surface methodology 143
V.8.1 Experimental design and model development 143
V.8.2 Model selection and statistical validation 145
V.8.3 ANOVA analysis and significance of model terms 147
V.8.4 Development of predictive regression equations 150
V.8.5 Two-Dimensional interaction analysis 153
V.8.6 Three-Dimensional response surface topologies 156
V.8.7 Multi-objective optimization of process parameters 161
V.8.8 Experimental validation 163
V.9 Modeling of MO adsorption via artificial neural network 163

V.9.1 Model development and hyperparameter optimization 163
V.9.2 Best model architecture and training convergence 164
V.9.3 Predictive accuracy and residual analysis 167
V.9.4 Cross-validation and model robustness 168
V.9.5 Mechanistic insights via sensitivity analysis 168
V.10 Optimization of methyl orange adsorption via genetic algorithm 170
V.10.1 Optimization framework and parameter selection for MO 170
V.10.2 Convergence and optimization dynamics of the MO system 171
V.10.3 Pareto front analysis for the MO adsorption 171
V.10.4 Optimal adsorption conditions for MO adsorption 172
V.10.5 Experimental validation 174
V.11 Mechanistic insights into methyl orange adsorption 174
V.11.1 Electrostatic interactions 175
V.11.2 Hydrogen bonding 176
V.11.3 Physical pore filling 176
V.11.4 π–π stacking interactions 176
V.11.5 Chemisorption and Surface Complexation 177
V.11.6 n–π Interactions 178
V.12 Conclusion 178
Chapter VI: Batch Adsorption of Catechol onto ZnO@DPS-AC: Modeling, Optimization, and Mechanisms 181
VI.1 Introduction 181
VI.2 Effect of operational parameters 181
VI.2.1 Effect of adsorbent dosage 181
VI.2.2 Effect of initial solution pH 183
VI.2.3 Effect of ionic strength 185
VI.2.4 Effect of contact time 187
VI.2.5 Effect of initial CAT concentration 189
VI.3 Kinetic modeling and mass transfer mechanisms 190
VI.4 Isotherm modeling and equilibrium studies 192
VI.4.1 Performance of multi–parameter isotherms 192
VI.4.2 Evaluation of adsorption capacity and temperature effects 193

VI.4.3 Interpretation of the Freundlich exponent (*n*) 195
VI.5 Comparative assessment of adsorbent performance 195
VI.6 Thermodynamic analysis 195
VI.6.1 Thermodynamic consistency and temperature effects 196
VI.6.2 Comparison of linear and nonlinear data treatment 197
VI.6.3 Analysis of thermodynamic parameters 198
VI.6.4 Justification of the Sips model thermodynamic anomaly 198
VI.6.5 Mechanistic classification 199
VI.7 Desorption, regeneration, and cyclic reusability 199
VI.7.1 Performance over multiple cycles 199
VI.7.2 Evaluation of regeneration reagents 200
VI.7.3 Post–regeneration efficiency and mechanistic insights 201
VI.8 Optimization via response surface methodology 202
VI.8.1 Experimental design and model development 202
VI.8.2 Model selection and statistical validation 204
VI.8.3 ANOVA and significance of model terms 205
VI.8.4 Development of predictive regression equations 208
VI.8.5 Two–Dimensional interaction analysis 209
VI.8.6 Three–Dimensional response surfaces for adsorption capacity 213
VI.8.7 Three–Dimensional response surfaces for removal percentage 214
VI.8.8 Multi-objective optimization of process parameters 217
VI.8.9 Experimental validation 218
VI.9 Modeling of CAT adsorption via artificial neural network 219
VI.9.1 Model development and hyperparameter optimization 219
VI.9.2 Best model architecture and training convergence 220
VI.9.3 Predictive accuracy and residual analysis 223
VI.9.4 Cross-validation and model robustness 224
VI.9.5 Mechanistic insights via sensitivity analysis 224
VI.10 Optimization of catechol batch adsorption via genetic algorithm 225
VI.10.1 Optimization framework and parameter selection for CAT 225
VI.10.2 Convergence and optimization dynamics of the CAT system 227
VI.10.3 Pareto front analysis for the CAT adsorption 229

VI.10.4 Optimal adsorption conditions for CAT adsorption 230
VI.10.5 Experimental validation 231
VI.11 Mechanistic insights into catechol adsorption 231
VI.11.1 Pore-filling mechanism 232
VI.11.2 Hydrogen bonding 232
VI.11.3 Inner-sphere surface complexation 233
VI.11.4 π–π electron-donor-acceptor interactions 234
VI.11.5 Role of electrostatic interactions 236
VI.1 Conclusion 236
Chapter VII: Batch Adsorption of Acetamiprid onto ZnO@DPS-AC: Modeling, Optimization, and Mechanisms 238
VII.1 Introduction 238
VII.2 Effect of operational parameters 238
VII.2.1 Effect of adsorbent mass 238
VII.2.2 Effect of initial solution *pH* 240
VII.2.3 Effect of ionic strength 242
VII.2.4 Effect of contact time 243
VII.2.5 Effect of initial ACE concentration 244
VII.3 Kinetic modeling and mass transfer mechanisms 246
VII.4 Isotherm modeling and equilibrium studies 247
VII.5 Comparative assessment of adsorbent performance 250
VII.6 Thermodynamic analysis 251
VII.7 Desorption, regeneration, and cyclic reusability 254
VII.8 Optimization via response surface methodology 256
VII.8.1 Model development and selection 256
VII.8.2 Statistical validation and goodness-of-fit observation 257
VII.8.3 ANOVA analysis and significance of model terms 259
VII.8.4 Development of regression equations 262
VII.8.5 Two-Dimensional interaction analysis 264
VII.8.6 Three-dimensional response surface topologies 267
VII.8.7 Multi-objective optimization of process parameters 269
VII.8.8 Experimental validation 272

VII.9 Modeling of ACE adsorption via artificial neural network 272
VII.9.1 Model development and hyperparameter optimization 272
VII.9.2 Best model architecture and training convergence 273
VII.9.3 Predictive accuracy and residual analysis 274
VII.9.4 Cross-validation and model robustness 276
VII.9.5 Mechanistic insights via sensitivity analysis 277
VII.10 Optimization of acetamiprid adsorption via genetic algorithm 278
VII.10.1 Optimization framework and parameter selection for ACE 279
VII.10.2 Convergence and optimization dynamics of the ACE system 280
VII.10.3 Pareto front analysis for the ACE adsorption 281
VII.10.4 Optimal adsorption conditions for ACE adsorption 282
VII.10.5 Experimental validation 283
VII.11 Mechanistic insights into acetamiprid adsorption 283
VII.11.1 Pore-filling mechanism 283
VII.11.2 Hydrogen bonding 284
VII.11.3 π–π electron donor-acceptor interactions 285
VII.11.4 Thermodynamic exclusion of surface complexation 285
VII.12 Conclusion 286
Chapter VIII: Column Adsorption Studies of Methyl Orange, Catechol, and Acetamiprid onto ZnO@DPS-AC 289
VIII.1 Introduction 289
VIII.2 Mathematical models for breakthrough curve analysis 290
VIII.2.1 Classical logistic models and their mathematical equivalence 291
VIII.2.2 Logarithmic modified models 292
VIII.2.3 Chu-Hashim model 294
VIII.3 Dynamic adsorption of Methyl Orange 295
VIII.3.1 Breakthrough curve behavior and column performance metrics 295
VIII.3.2 Breakthrough curve modeling and model comparison 298
VIII.4 Dynamic adsorption of Catechol 302
VIII.4.1 Breakthrough curve behavior and column performance metrics 302
VIII.4.2 Breakthrough curve modeling and model comparison 305
VIII.5 Dynamic adsorption of Acetamiprid 308

VIII.5.1 Breakthrough curve behavior and column performance metrics 308
VIII.5.2 Breakthrough curve modeling and model comparison..... 312
VIII.6 Comparative analysis across pollutants..... 314
VIII.7 Conclusion..... 318
General Conclusion 320
Recommendations and perspective..... 323
Appendix 325
References 341
List of Publications and Communications 372

List of Figures

* * * * *

Figure I.1 Chemical structure of MO, CAT, and ACE 6

Figure I.2 Structural transformation of MO 7

Figure I.3 Classification of wastewater treatment technologies based on physical, chemical, and biological principles (El-Azazy et al., 2020) 19

Figure II.1 Basic concepts of adsorption (Worch, 2012) 32

Figure II.2 Schematic representation of the four stages of mass transfer during the adsorption process (Wang et al., 2020) 34

Figure II.3 Schematic of graphite and activated carbon structures (Adapted from (Bandosz, 2006; Sayed et al., 2019; Yap et al., 2023)) 48

Figure II.4 Schematic representation of the internal pore architecture and the various surface functional groups associated with activated carbon (Berillo & Ermukhambetova, 2024; Sultana et al., 2022) 49

Figure II.5 Artificial neural network architecture, components and training framework for adsorption process 60

Figure II.6 Evolution of the breakthrough curve profile over time in a continuous fixed-bed adsorption system 68

Figure III.1 Schematic illustration of ZnO@DPS-AC composite synthesis 75

Figure III.2 Determination of λ_{max} of: (**a**) MO, (**b**) CAT, and (**c**) ACE 83

Figure III.3 Calibration curves of: (**a**) MO, (**b**) CAT, and (**c**) ACE 83

Figure III.4 Schematic representation of the ANN modeling process 92

Figure III.5 Schematic of the GA optimization loop 96

Figure III.6 Experimental setup of dynamic adsorption of target pollutants 98

Figure IV.1 Thermal decomposition profile of raw DPS under an inert atmosphere: **(a)** TGA profile; **(b)** DTG profile; and **(c)** DSC profile 104

Figure IV.2 pH_{pzc} of ZnO@DPS-AC 106

Figure IV.3 SEM micrographs (at dual magnifications) and corresponding EDX elemental profiles of the synthesized materials: (**a**) DPS-Biochar derived from DPS; (**b**) ZnO@DPS-AC composite after $ZnCl_2$ activation and pyrolysis; and the ZnO@DPS-AC adsorbent after the adsorption of (**c**) MO, (**d**) CAT, and (**e**) ACE 109

Figure IV.4 FTIR spectra of (**a**) raw DPS waste, (**b**) DPS-Biochar, (**c**) ZnO@DPS–AC, and the composite after the adsorption of (**d**) MO, (**e**) CAT, and (**f**) ACE. 111

Figure IV.5 XRD patterns illustrating the structural evolution and stability of the adsorbents: (**a**) DPS-Biochar, (**b**) DPS–Zn (pre-pyrolysis), (**c**) identified reflections correspond to the hexagonal wurtzite phase of ZnO (JCPDS card no. 98–006–512), (**d**) ZnO@DPS–AC, and the composite following the adsorption of (**e**) MO, (**f**) CAT, and (**g**) ACE 113

Figure IV.6 Raman spectra of DPS-Biochar, ZnO@DPS-AC, and the composite post-adsorption of MO, CAT, and ACE 114

Figure IV.7 N_2 adsorption-desorption of: (**a**) ZnO@DPS-AC, (**b**) ZnO@DPS-AC-MO, (**c**) ZnO@DPS-AC-ACE, (**d**) ZnO@DPS-AC-CAT, and (**e**) DPS-Biochar 118

Figure IV.8 PSD of: (**a**) ZnO@DPS-AC, (**b**) ZnO@DPS-AC-MO, (**c**) ZnO@DPS-AC-ACE, (**d**) ZnO@DPS-AC-CAT, and (**e**) DPS-Biochar 119

Figure V.1 Influence of operating parameters on the removal of MO by ZnO@DPS-AC: (**a**) adsorbent mass, (**b**) point of zero charge of the composite, (**c**) initial solution *pH*, and (**d**) ionic strength 125

Figure V.2 (**a**) Effect of contact time at different initial concentrations, (**b**) effect of initial MO concentration on adsorption capacity, (**c**) non-linear plot of Vermeulen model, and (**d**) non-linear regression equilibrium isotherm for MO adsorption onto ZnO@DPS-AC 128

Figure V.3 van 't Hoff thermodynamic plots for the adsorption of MO onto ZnO@DPS-AC comparing (**a-f**) linear regression and (**g-l**) non-linear regression forms 140

Figure V.4 Reusability and cyclic regeneration efficiency of the composite over three cycles 143

Figure V.5 Two-dimensional interaction plots derived from the RSM-CCD model demonstrating the effects of paired operational variables on MO adsorption capacity 155

Figure V.6 Two-dimensional interaction plots derived from the RSM-CCD model demonstrating the effects of paired operational variables on MO removal percentage 156

Figure V.7 Three-dimensional response surface plots illustrating the interactive effects of operational parameters on the MO adsorption capacity of the ZnO@DPS-AC composite (part 1) 157

Figure V.8 Three-dimensional response surface plots illustrating the interactive effects of operational parameters on the MO adsorption capacity of the ZnO@DPS-AC composite (part 2) 157

Figure V.9 Three-dimensional response surface plots illustrating the interactive effects of operational parameters on the MO removal percentage of the ZnO@DPS-AC composite (Part 1) 160

Figure V.10 Three-dimensional response surface plots illustrating the interactive effects of operational parameters on the MO removal percentage of the ZnO@DPS-AC composite (Part 2) 160

Figure V.11 Effect of the number of hidden layer neurons on the mean squared error (MSE) and coefficient of determination (R^2) during hyperparameter optimization for the MO adsorption model 164

Figure V.12 Evaluation of the optimized ANN architecture for MO adsorption: (**a**) schematic representation of the network topology; (**b**) learning curve demonstrating training convergence across cross-validation folds; and scatter plots comparing ANN-predicted values against actual experimental data for (**c**) equilibrium adsorption capacity and (**d**) removal percentage 165

Figure V.13 Residual analysis of the optimized ensemble model for MO adsorption: (**a**) residuals versus predicted values and (**b**) residual probability distribution for adsorption capacity; (**c**) residuals versus predicted values and (**d**) residual probability distribution for removal percentage 167

Figure V.14 Cross-validation performance charts detailing the fold-by-fold validation metrics for MO adsorption: (**a**) R^2 for adsorption capacity, (**b**) R^2 for removal percentage, (**c**) mean squared error (MSE) for adsorption capacity, and (**d**) MSE for removal percentage 168

Figure V.15 Comprehensive performance evaluation of the optimized ANN configuration: (**a**) MSE convergence versus epoch during the training, validation, and testing phases; (**b**) regression plots for data subsets; (**c**) error histogram across all data partitions; and (**d**) mechanistic sensitivity analysis via the Garson algorithm evaluating the relative importance of independent input variables 169

Figure V.16 Comprehensive evaluation of Genetic Algorithm (GA) grid search parameters for MO adsorption: (**a**) hypervolume heatmaps across varying population sizes, crossover rates, and mutation rates, and (**b**) ranking of the 27 evaluated configurations based on their overall composite scores 171

Figure V.17 Evolutionary dynamics of the multi-objective optimization for MO adsorption: (**a**) progression of the best and average values for adsorption capacity and removal efficiency, (**b**) hypervolume progression, (**c**) final Pareto front highlighting representative optimal solutions, and (**d**) population diversity across generations 172

Figure V.18 Progression of key multi-objective optimization metrics over generations during MO adsorption: (**a**) Pareto front size, (**b**) generation-to-generation improvements, (**c**) spacing metric, and (**d**) spread metric 173

Figure V.19 Schematic illustration of the proposed physicochemical mechanisms for the adsorption of methyl orange onto the hierarchical ZnO@DPS-AC composite 175

Figure V.20 Performance comparison between standard ZnO@DPS-AC and oxidized ZnO@DPS-AC for MO removal 177

Figure VI.1 (**a**) Effect of adsorbent dosage on CAT adsorption capacity and removal percentage, (**b**) Distribution of CAT protonation states as a function of solution pH, (**c**) UV-Vis absorption spectra of the CAT solution recorded at varying *pH* values (*pH* 2–12), and (**d**) Effect of initial solution pH on the adsorption efficiency of CAT onto the ZnO@DPS-AC composite 183

Figure VI.2 Effect of operational parameters on CAT adsorption onto ZnO@DPS-AC: (**a**) Ionic strength, (**b**) Contact time, and (**c**) Initial concentration. (**d**) Adsorption isotherms of CAT evaluated at different temperatures (30, 35, and 45 °C) 188

Figure VI.3 van't Hoff plots for the thermodynamic evaluation of CAT adsorption onto ZnO@DPS-AC using (**a–d**) linear and (**e–h**) non-linear regression forms across tested isotherm models 197

Figure VI.4 Recycling and regeneration performance of ZnO@DPS-AC over three consecutive adsorption-desorption cycles 201

Figure VI.5 Two-dimensional interaction plots derived from the RSM-CCD model demonstrating the effects of paired operational variables on CAT adsorption capacity 210

Figure VI.6 Two-dimensional interaction plots derived from the RSM-CCD model demonstrating the effects of paired operational variables on CAT removal percentage 212

Figure VI.7 Three-dimensional response surface plots illustrating the interactive effects of operational parameters on the CAT adsorption capacity of the ZnO@DPS-AC composite 215

Figure VI.8 Three-dimensional response surface plots illustrating the interactive effects of operational parameters on the CAT removal percentage of the ZnO@DPS-AC composite 216

Figure VI.9 Effect of the number of hidden layer neurons on the mean squared error (MSE) and coefficient of determination (R^2) during hyperparameter optimization for the CAT adsorption model 219

Figure VI.10 Evaluation of the optimized ANN architecture for CAT adsorption: (**a**) schematic representation of the network topology; (**b**) learning curve demonstrating training convergence across cross-validation folds; and scatter plots comparing ANN-predicted values against actual experimental data for (**c**) equilibrium adsorption capacity and (**d**) removal percentage 221

Figure VI.11 Residual analysis of the optimized ensemble model for CAT adsorption: (**a**) residuals versus predicted values and (**b**) residual probability distribution for adsorption capacity; (**c**) residuals versus predicted values and (**d**) residual probability distribution for removal percentage 223

Figure VI.12 Cross-validation performance charts detailing the fold-by-fold validation metrics for CAT adsorption: (**a**) R^2 for adsorption capacity, (**b**) R^2 for removal percentage, (**c**) mean squared error (MSE) for adsorption capacity, and (**d**) MSE for removal percentage 225

Figure VI.13 Comprehensive performance evaluation of the optimized ANN configuration: (**a**) MSE convergence versus epoch during the training, validation, and testing phases; (**b**) regression plots for data subsets; (**c**) error histogram across all data partitions; and (**d**) mechanistic sensitivity analysis via the Garson algorithm evaluating the relative importance of independent input variables 226

Figure VI.14 Comprehensive evaluation of Genetic Algorithm grid search parameters for CAT adsorption: (**a**) hypervolume heatmaps across varying population sizes, crossover rates, and mutation rates, and (**b**) ranking of the 27 evaluated configurations based on their overall composite scores 227

Figure VI.15 Evolutionary dynamics of the multi-objective optimization for CAT adsorption: (**a**) progression of the best and average values for adsorption capacity and removal efficiency, (**b**) hypervolume progression, (**c**) final Pareto front highlighting representative optimal solutions, and (**d**) population diversity across generations 228

Figure VI.16 Progression of key multi-objective optimization metrics over generations during catechol adsorption: (**a**) Pareto front size, (**b**) generation-to-generation improvements, (**c**) spacing metric, and (**d**) spread metric 229

Figure VI.17 Schematic illustration of the proposed physicochemical mechanisms for the adsorption of catechol onto the hierarchical ZnO@DPS-AC composite 232

Figure VI.18 Comparison of equilibrium adsorption capacity between pristine ZnO@DPS-AC and oxidized ZnO@DPS-AC 235

Figure VII.1 Influence of operating parameters on ACE adsorption onto ZnO@DPS-AC: (**a**) effect of adsorbent mass, (**b**) effect of initial solution pH, (**c**) effect of ionic strength, and (**d**) effect of contact time 240

Figure VII.2 (**a**) Effect of initial concentration on the specific uptake of ACE at different temperatures, and (**b**) equilibrium adsorption isotherms for ACE onto ZnO@DPS-AC. 245

Figure VII.3 Linear (**a-d**) and non-linear (**e-h**) van 't Hoff plots for the thermodynamic evaluation of ACE adsorption onto ZnO@DPS-AC. 253

Figure VII.4 Cyclic reusability and ethanol regeneration of the ZnO@DPS-AC composite 255

Figure VII.5 Two-dimensional interaction plots illustrating the combined effects of operating parameters on the ACE adsorption capacity 265

Figure VII.6 Two-dimensional interaction plots illustrating the combined effects of operating

parameters on the ACE removal 266

Figure VII.7 Three-dimensional response surface plots demonstrating the interactive effects of operating parameters on the ACE adsorption capacity 268

Figure VII.8 Three-dimensional response surface plots demonstrating the interactive effects of operating parameters on the ACE removal percentage 270

Figure VII.9 Effect of the number of hidden layer neurons on the mean squared error (MSE) and coefficient of determination (R^2) during hyperparameter optimization for the ACE adsorption model 273

Figure VII.10 Evaluation of the optimized ANN architecture for ACE adsorption: (**a**) schematic representation of the network topology; (**b**) learning curve demonstrating training convergence across cross-validation folds; and scatter plots comparing ANN-predicted values against actual experimental data for (**c**) equilibrium adsorption capacity and (**d**) removal percentage 274

Figure VII.11 Residual analysis of the optimized ensemble model for ACE adsorption: (**a**) residuals versus predicted values and (**b**) residual probability distribution for adsorption capacity; (**c**) residuals versus predicted values and (**d**) residual probability distribution for removal percentage 276

Figure VII.12 Cross-validation performance charts detailing the fold-by-fold validation metrics for ACE adsorption: (**a**) R^2 for adsorption capacity, (**b**) R^2 for removal percentage, (**c**) mean squared error (MSE) for adsorption capacity, and (**d**) MSE for removal percentage 277

Figure VII.13 Comprehensive performance evaluation of the optimized ANN configuration: (**a**) MSE convergence versus epoch during the training, validation, and testing phases; (**b**) regression plots for data subsets; (**c**) error histogram across all data partitions; and (**d**) mechanistic sensitivity analysis via the Garson algorithm evaluating the relative importance of independent input variables 278

Figure VII.14 Comprehensive evaluation of Genetic Algorithm (GA) grid search parameters for ACE adsorption: (**a**) hypervolume heatmaps across varying population sizes, crossover rates, and mutation rates, and (**b**) ranking of the 27 evaluated configurations based on their overall composite scores 279

Figure VII.15 Evolutionary dynamics of the multi-objective optimization for ACE adsorption: (**a**) progression of the best and average values for adsorption capacity and removal efficiency, (**b**) hypervolume progression, (**c**) final Pareto front highlighting representative optimal solutions, and (**d**) population diversity across generations 280

Figure VII.16 Progression of key multi-objective optimization metrics over generations during ACE adsorption: (**a**) Pareto front size, (**b**) generation-to-generation improvements, (**c**) spacing metric, and (**d**) spread metric 281

Figure VII.17 Performance comparison between the pristine ZnO@DPS-AC and oxidized ZnO@DPS-AC composites 284

Figure VII.18 Schematic illustration of the proposed physicochemical mechanisms for the adsorption of ACE onto the ZnO@DPS-AC composite 286

Figure VIII.1 Experimental breakthrough curves for MO adsorption onto ZnO@DPS-AC, illustrating the effects of (**a**) adsorbent bed mass, (**b**) volumetric flow rate, and (**c**) initial concentration 296

Figure VIII.2 Experimental breakthrough curves for CAT adsorption onto ZnO@DPS-AC, illustrating the effects of (**a**) adsorbent bed mass, (**b**) volumetric flow rate, and (**c**) initial concentration 303

Figure VIII.3 Experimental breakthrough curves for the agrochemical ACE adsorption onto ZnO@DPS-AC, illustrating the effects of (**a**) adsorbent bed mass, (**b**) volumetric flow rate, and (**c**) initial concentration 310

List of Tables

* * * * *

Table I.1 Detailed physicochemical properties of MO (Information, 2004; Iwuozor et al., 2021; Sunthar et al., 2023) 7

Table I.2 Physicochemical properties of CAT (Information, 2025a)..... 10

Table I.3 Physicochemical properties of ACE (Agency, 2023; Authority, 2016; Information, 2025b; Zuščíková et al., 2023) 15

Table I.4 Comparative toxicological and environmental profile 28

Table II.1 Comparative analysis of physisorption and chemisorption..... 33

Table II.2 Comparative analysis of CCD and BBD designs for adsorption optimization 57

Table II.3 Strategic comparison of RSM and ANN in the context of adsorption research (Desalegn et al., 2024; Mourabet, 2014; Shanmugaprakash & Sivakumar, 2013) 65

Table III.1 Experimental ranges for the OFAT optimization of adsorption parameters 84

Table III.2 Experimental factors and levels for the RSM optimization of MO, CAT, and ACE removal..... 89

Table III.3 Experimental design matrix for fixed-bed column studies..... 97

Table IV.1 Properties of the prepared ZnO@DPS-AC composite..... 105

Table IV.2 Raman spectroscopic parameters including D-band and G-band positions, and the calculated intensity ratios (I_D/I_G) for DPS-Biochar, ZnO@DPS-AC, and the composite after adsorption of MO, CAT, and ACE 115

Table IV.3 Textural and structural parameters of the DPS-Biochar, ZnO@DPS-AC, and the spent adsorbents following the uptake of MO, CAT, and ACE 118

Table V.1 Kinetic modeling parameters for the adsorption of MO onto ZnO@DPS-AC at initial concentrations of 150 mg/L and 200 mg/L 133

Table V.2 Adsorption isotherms parameters for MO removal onto ZnO@DPS-AC composite 135

Table V.3 Comparison of the maximum monolayer adsorption capacity of ZnO@DPS-AC for MO with other adsorbents reported in the literature..... 137

Table V.4 Comparison of thermodynamic parameters (ΔG°, ΔH°, ΔS) for MO adsorption, derived from linear and non-linear regression of various isotherm models..... 141

Table V.5 Sequential model sum of squares and adequacy metrics for the adsorption capacity response surface model 144

Table V.6 Sequential model sum of squares and adequacy metrics for the removal percentage response surface model 146

Table V.7 ANOVA analysis for the quadratic response surface model corresponding to adsorption capacity..... 148

Table V.8 ANOVA analysis for the quadratic response surface model corresponding to removal percentage..... 149

Table V.9 Optimization results by RSM for MO adsorption 161

Table V.10 Summary of the top 10 ANN configurations evaluated during the systematic grid search for MO adsorption 166

Table V.11 Optimal batch adsorption conditions derived from the Genetic Algorithm for three representative Pareto solutions for MO: maximum capacity, maximum removal rate, and the compromise solution 174

Table VI.1 Kinetic model parameters for the adsorption of CAT onto ZnO@DPS–AC..... 192

Table VI.2 Isotherm model parameters for the adsorption of CAT onto the ZnO@DPS–AC composite at varying temperatures (30, 35, and 45 °C) 193

Table VI.3 Comparison of maximum monolayer adsorption capacities of CAT onto various adsorbents reported in the literature 196

Table VI.4 Thermodynamic parameters (ΔG°, ΔH°, ΔS°) for the adsorption of CAT onto ZnO@DPS-AC calculated via linear and non-linear van't Hoff equations 198

Table VI.5 Sequential model sum of squares and model summary statistics for CAT adsorption capacity..... 202

Table VI.6 Sequential model sum of squares and model summary statistics for CAT removal percentage..... 203

Table VI.7 ANOVA analysis for the quadratic response surface model evaluating CAT adsorption capacity..... 206

Table VI.8 ANOVA analysis for the quadratic response surface model evaluating CAT removal percentage..... 207

Table VI.9 RSM desirability optimization scenarios for CAT adsorption onto ZnO@DPS-AC ... 217

Table VI.10 Summary of the top 10 ANN configurations evaluated during the systematic grid search for CAT adsorption 222

Table VI.11 Optimal batch adsorption conditions derived from the Genetic Algorithm for three representative Pareto solutions for CAT: maximum capacity, maximum removal rate, and the compromise solution 230

Table VII.1 Kinetic model parameters and statistical error functions for the adsorption of ACE onto ZnO@DPS-AC..... 247

Table VII.2 Adsorption isotherm model parameters for ACE removal using the ZnO@DPS-AC composite 249

Table VII.3 Comparison of the maximum adsorption capacity of ZnO@DPS-AC for ACE with other reported adsorbents in the literature..... 250

Table VII.4 Thermodynamic parameters of ACE adsorption onto ZnO@DPS-AC..... 254

Table VII.5 Fit statistics and adequacy evaluation of the mathematical models for ACE adsorption capacity..... 257

Table VII.6 Fit statistics and adequacy evaluation of the mathematical models for ACE removal percentage..... 258

Table VII.7 ANOVA analysis for the quadratic model describing ACE adsorption capacity 260

Table VII.8 ANOVA analysis for the quadratic model describing ACE removal percentage 261

Table VII.9 Desirability function optimization scenarios for ACE adsorption 271

Table VII.10 Summary of the top 10 ANN configurations evaluated during the systematic grid search for ACE adsorption 275

Table VII.11 Optimal batch adsorption conditions derived from the Genetic Algorithm for three representative Pareto solutions for ACE: maximum capacity, maximum removal rate, and the compromise solution 282

Table VIII.1 Mathematical equivalence of the Y-N, Th, and A-B models demonstrated on the MO Experiment 1 dataset (C_0 = 100 mg/L, Q_v = 3 mL/min, m = 125 mg) 292

Table VIII.2 Summary of experimental conditions and breakthrough performance metrics for dynamic adsorption of MO. Experiment 3 (shaded) serves as the shared reference condition across all three variable groups 298

Table VIII.3 Fitted kinetic parameters of Y-N, log Y-N, and C-H models for all seven MO breakthrough experiments 300

Table VIII.4 Comparison of experimental and model-predicted breakthrough and exhaustion parameters for MO 301

Table VIII.5 Summary of experimental conditions and breakthrough performance metrics for dynamic adsorption of CAT 305

Table VIII.6 Fitted parameters of the Th, log-Th, and C-H models for all seven CAT breakthrough experiments 307

Table VIII.7 Comparison of experimental and model-predicted breakthrough and exhaustion parameters for CAT 308

Table VIII.8 Summary of experimental conditions and breakthrough performance metrics for dynamic adsorption of ACE 311

Table VIII.9 Fitted parameters of the A-B, log A-B, and C-H models for all seven ACE breakthrough experiments 314

Table VIII.10 Comparison of experimental and model-predicted breakthrough and exhaustion parameters for ACE 315

Table VIII.11 Comparative summary of dynamic adsorption performance and model results for MO, CAT, and ACE at the shared reference condition 317

List of Symbols and Abbreviations

* * * * *

Symbol	Meaning	Unit
[C°]	Standard State Concentration (1 M)	mol/L
•O_2^-	Superoxide Anions	–
•OH	Hydroxyl Radicals	–
1/n	Heterogeneity Factor	–
2D	Two-Dimensional	–
2FI	Two-Factor Interaction	–
3D	Three-Dimensional	–
A-B	Adams-Bohart Model	–
AC	Activated Carbon	–
ACE	Acetamiprid	–
ACGIH	American Conference of Governmental Industrial Hygienists	–
Adj-R^2	Adjusted Coefficient of Determination	–
A_m	Cross-Sectional Area of Nitrogen Molecule (0.162)	nm^2/molecule
ANN	Artificial Neural Network	–
ANOVA	Analysis of Variance	–
AOPs	Advanced Oxidation Processes	–
AP	Adequate Precision	–
AW	Akaike Weight	%
b	ANN Bias	–
BBD	Box-Behnken Design	–
BDD	Boron-Doped Diamond	–
BET	Brunauer-Emmett-Teller	–
BJH	Barrett-Joyner-Halenda	–
BP	Backpropagation	–
BR	Bayesian Regularization Algorithm	–
C_0	Initial Adsorbate Concentration	mg/L
CAC	Commercial Activated Carbon	–
CAT	Catechol	–
C_{BET}	BET Constant Related to The Energy of Adsorption	–
CCD	Central Composite Design	–
C_e	Equilibrium Adsorbate Concentration	mg/L
CF	Coagulation-Flocculation	–

C_{IPD}	Constant Mathematically Related to the Thickness of the Hydrodynamic Boundary Layer	–
CNS	Central Nervous System	–
COD	Chemical Oxygen Demand	–
AIC_c	Corrected Akaike Information Criterion	–
CR	Crossover Rate	–
C_t	Adsorbate Concentration at Time t	mg/L
CV	Coefficient of Variation	%
D	Average Crystallite Size	nm
DFA	Desirability Function Approach	–
d_i	Dimensionless Desirability Scale	–
DOE	Design of Experiments	–
D_{opt}	Overall Global Desirability	–
DPP	Differential Pulse Polarography	–
DPS	Date Palm Spikelets	–
DPW	Date Palm Waste	–
D_s	Diffusion Coefficient	m^2/s
DSA	–Dimensionally Stable Anode	–
DSC	Differential Scanning Calorimetry	–
DTG	Derivative Thermogravimetric	–
E	Mean Free Energy of Adsorption	kJ/mol
E_0	Characteristic Adsorption Energy	kJ/mol
EANN	Ensemble Artificial Neural Network	–
EAOPs	Electrochemical Advanced Oxidation Processes	–
EBCT	Empty Bed Contact Times	–
EC	Electrocoagulation	–
EDS	Energy Dispersive X-Ray Spectroscopy	–
FTIR	Fourier Transform Infrared Spectroscopy	–
F-value	Fisher's Variance Ratio	–
FWHM	Full Width at Half Maximum	°
GA	Genetic Algorithm	–
GAC	Granular Activated Carbons	–
GAPPC	Granular Activated Pomegranate Peel Carbon	–
GO	Graphene Oxide	–
GPR	Gaussian Process Regression	–
H^+	Hydronium Ions	–
IARC	International Agency for Research on Cancer	–
IUPAC	International Union of Pure and Applied Chemistry	–
k	Dimensionless Shape Factor	–
k_1	Specific PFO Rate Constant	min^{-1} or h^{-1}
k_2	PSO Rate Constant	g/mg.min

k_{AB}	Kinetic Constant of the Adams-Bohart Model	L/mg·min
K_D	Distribution Coefficient	L/g
K_{Eq}°	Standard Thermodynamic Equilibrium Constant	–
K_F	Freundlich Constant	$(mg/g)/(L/mg)^{1/n}$
K_g	Isotherm Constant, such as the Langmuir, Sips, or Liu Constants	L/mg
k_{IPD}	Intra-Particle Diffusion Rate Constant	$mg/g.min^{0.5}$
K_L	Langmuir Equilibrium Constant	L/mg
K_{Model}	Best-Fit Isotherm Constant	–
K_{oc}	Organic Carbon Partition Coefficient	–
k_{Th}	Thomas Kinetic Rate Constant	L/min.mg
k_{YN}	Kinetic Rate Constant of Yoon-Nelson	min^{-1}
L_0	Average Pore Diameter	nm
LDF	Linear Driving Force	–
LDH	Layered Double Hydroxide	–
LM	Levenberg-Marquardt Algorithm	–
LoF	Lack-Of-Fit	–
m	Adsorbent Mass	mg
MGO	Magnetic Graphene Oxide	–
MO	Methyl Orange	–
MOFs	Metal-Organic Frameworks	–
MOGA	Multi-Objective Genetic Algorithm	–
MR	Mutation Rate	–
MSE	Mean Squared Error	–
M_{total}	Total Mass of the Adsorbate Introduced into the Fixed-Bed System	mg
MTZ	Mass Transfer Zone	–
M_w	Molecular Weight	g/mol
MWCNTs	Multi-Walled Carbon Nanotubes	–
N_0	Volumetric Saturation Capacity of N_2	mg/L
N_A	Avogadro's Number (6.022 ×1023)	molecule/mol
nAChR	Nicotinic Acetylcholine Receptor	–
NSGA-II	Non-Dominated Sorting Genetic Algorithm II	–
OFAT	One-Factor-at-a-Time	–
OH^-	Hydroxide Ions	–
P	Population Size	–
PFO	Pseudo-First-Order Model	–
pH_{PZC}	Point Of Zero Charge	–
pKa	Dissociation Constant	–

PSO	Pseudo-Second-Order	–
PVA	Polyvinyl Alcohol	–
p-value	Probability Value	–
PVC	Polyvinyl Chloride	–
q_0	Dynamic Equilibrium Adsorption Capacity of the Bed	mg/g
q_e	Equilibrium Adsorption Capacity (mg/g)	–
q_m	Predicted Langmuir Maximum Monolayer Adsorption Capacity	mg/g
q_t	Adsorption Capacity at Time t	mg/g
q_{total}	Total Column Adsorption Capacity	mg/g
R	Removal Efficiency or Removal Percentage	%
R^2	Coefficient of Determination	–
Red-χ^2	Reduced Chi-Squared	–
R_L	Separation Factor	–
RMSE	Residual Root Mean Square Error	–
ROS	Reactive Oxygen Species	–
r_p	Average Particle Radius	cm
RSM	Response Surface Methodology	–
S_{BET}	BET Specific Surface Area	m^2/g
SD	Standard Deviation	–
SEM	Scanning Electron Microscope	–
S_{ext}	External Surface Area	m^2/g
$S_{Langmuir}$	Langmuir Surface Area	m^2/g
S_{micro}	Micropore Surface Area	m^2/g
t_b	Breakthrough Point	min
t_e	Exhaustion Point	min
TGA	Thermogravimetric Analysis	–
Th	Thomas Model	–
trainbr	Bayesian Regularization Algorithm	–
trainlm	Levenberg-Marquardt Algorithm	–
$t_{thickness}$	Statistical Thickness	Å
t_{total}	Total Flow Time	min
U_0	Superficial Velocity	cm/min
US-EPA	United States Environmental Protection Agency	–
V	Volume of the Solution	L
V_{ads}	Volume of Gas Adsorbed at Pressure P	cm^3 STP/g
V_{eff}	Total Volume of Effluent Treated by the Column	–
V_m	Volume of Gas Required to Form a Complete Monolayer	cm^3 STP/g
V_{meso}	Mesopore Volume	cm^3 /g

$\mathbf{V_{micro}}$	Micropore Volume	cm^3 /g
$\mathbf{V_{Total}}$	Total pore Volume	cm^3 /g
$\mathbf{V_m^{mol}}$	Molar Volume of N_2 (22414)	cm^3 STP/mol
w	ANN Weight	–
$\mathbf{X_{opt}}$	Optimal Conditions	–
XRD	X-Ray Diffraction	–
Y-N	Yoon-Nelson Model	–
Z	Bed Mass	mg
α	Axial Distance	–
$\mathbf{\alpha_e}$	Initial Adsorption Rate of the Elovich Model	mg/g.min
$\mathbf{\beta_e}$	Desorption Constant	g/mg
$\mathbf{\beta_w}$	Full Width at Half Maximum	°
γ	Activity Coefficient	–
ΔG	Gibbs Energy Change	kJ/mol
ΔG°	Standard Gibbs Energy Change	kJ/mol
ΔH°	Standard Enthalpy Change	kJ/mol
ΔS°	Standard Entropy Change	kJ/mol
η	Learning Rate	–
θ	Bragg Angle	°
λ	X-Ray Wavelength	nm
$\mathbf{\lambda_{max}}$	Wavelength of Maximum Absorption	nm

General Introduction

* * * * *

Water is a fundamental resource for sustaining life and enabling socioeconomic development (Seow et al., 2022). However, rapid industrialization, uncontrolled urbanization, and intensive agricultural practices have severely degraded global water quality (Alam et al., 2022). The continuous release of complex, toxic, and recalcitrant effluents into aquatic environments poses a serious threat to ecological stability and public health (Sultana et al., 2022). Among these contaminants, synthetic dyes (Methyl Orange, MO), phenolic compounds (Catechol, CAT), and agricultural pesticides (Acetamiprid, ACE) require immediate scientific intervention. Their high toxicity, resistance to biodegradation, and potential carcinogenic or mutagenic effects make them hazardous even at trace concentrations (Tcheka et al., 2024; Q. Wang et al., 2023).

Conventional wastewater treatment methods, such as coagulation-flocculation (Hecini et al., 2022; Liu et al., 2022), membrane filtration (Marrot et al., 2006; Souhıla, 2024), and biological degradation (Thao et al., 2013; Yadav et al., 2021), have historically been used to mitigate these hazards. However, these approaches frequently exhibit significant technical and economic limitations, including prohibitive operational costs, high energy demands, incomplete pollutant mineralization, and the generation of toxic secondary sludge (Alomar et al., 2023; Sultana et al., 2022). Consequently, adsorption has emerged as a highly efficient and economically viable alternative for wastewater remediation. Its design simplicity, operational flexibility, high removal capacity, and avoidance of harmful by-products make it exceptionally well-suited for industrial applications (Iwuozor et al., 2021). Although commercial activated carbon serves as the benchmark adsorbent due to its high surface area and well-developed porosity, its widespread use faces a major material bottleneck: reliance on expensive, non-renewable fossil precursors (e.g., coal and peat) and energy-intensive activation processes (Rattanapan et al., 2017; Sultana et al., 2022). This economic constraint has catalyzed a shift toward circular economy principles and green chemistry, specifically targeting the valorization of abundant, low-cost, and renewable agricultural wastes (Al-Ghouti & Da'ana, 2020; El Ouadrhiri et al., 2021).

In Algeria, particularly in the Biskra region, extensive date palm cultivation generates large quantities of lignocellulosic biomass waste, notably Date Palm Spikelets (DPS). Repurposing this agricultural residue into advanced carbon-based materials simultaneously provides cost-effective water purification and resolves severe solid waste management challenges associated with agricultural by-

products (El Ouadrhiri et al., 2021). The use of DPS as a carbon precursor remains an underdeveloped area of research. A review of existing scientific literature reveals only two prior investigations using this specific biomass: one involving microwave-assisted modification (Emami & Azizian, 2014) and another utilizing phosphoric acid activation (Djaber et al., 2025). Because pristine or conventionally activated biomass-derived carbons typically demonstrate limited adsorption capacities and poor selectivity for complex, multi-class pollutants, the simultaneous chemical activation and targeted functionalization of DPS with metallic particles represents a highly promising, unexplored frontier in materials science. Specifically, incorporating Zinc Oxide (ZnO) introduces new active binding sites, enhances surface reactivity, and yields a synergistic composite material (ZnO@DPS-AC) with superior adsorptive performance.

Transitioning from laboratory-scale synthesis to practical environmental application demands rigorous process optimization. The complex, non-linear interactions among operational parameters (solution pH, initial adsorbate concentration, adsorbent dosage, contact time, and temperature) necessitate advanced computational modeling. Conventional optimization heavily relies on Response Surface Methodology (RSM); however, its built-in desirability function typically uses derivative-based search algorithms (Dean et al., 2015; Marinković, 2021). In multi-variable adsorption systems, this approach frequently converges on local optima, failing to identify the true global maximum response (Montgomery & Runger, 2018; Montgomery et al., 2009). This limitation becomes pronounced when the underlying response surface is highly nonlinear or inadequately represented by simple second-order models, as standard RSM captures quadratic approximations rather than complex nonlinearities across the full design space (Karri et al., 2018; Montgomery & Runger, 2018).

To bypass this mathematical constraint and ensure identification of the absolute global optimum for the ZnO@DPS-AC composite, an advanced evolutionary machine-learning framework was implemented. A Genetic Algorithm (GA) was utilized to explore the entire parameter space simultaneously, effectively avoiding local optima. To enable this extensive search, an Artificial Neural Network (ANN) was trained as a rapid, continuous surrogate fitness function, allowing the GA to efficiently evaluate thousands of simulated conditions. Additionally, this work includes a methodological evaluation of the data density required for robust ANN training in such systems. To model MO and CAT, validated quadratic RSM equations were used to augment the data, providing the ANN with a dense topological map. Conversely, the ANN model for ACE was trained entirely on the original, non-augmented experimental matrix derived from the Design of Experiments (DoE).

Comparing these architectures validates the adaptability of the ANN-GA framework across varying degrees of data availability, demonstrating its robustness in managing complex multiclass pollutant remediation.

Despite extensive research on conventional biochars, engineering a highly functionalized ZnO@DPS-AC composite for the targeted removal of dyes, phenols, and pesticides remains unexplored. Furthermore, integrating a comparative ANN-GA machine-learning framework to overcome the limitations of classical RSM and applying it to continuous fixed-bed column systems represents a significant advancement in chemical and environmental engineering.

In this context, the primary aim of this doctoral research is to synthesize, characterize, and apply a novel, high-performance carbon-based composite (ZnO@DPS-AC) derived from local, underutilized agricultural waste for advanced water remediation. To achieve this overarching goal, the specific objectives are as follows:

- **Synthesis and functionalization:** Develop an optimized protocol for preparing Activated Carbon (AC) from DPS with simultaneous Zinc Oxide functionalization through chemical activation.
- **Physicochemical characterization:** Analyze the morphological, structural, and chemical properties of the ZnO@DPS-AC composite using advanced analytical techniques (TGA, SEM-EDX, FTIR, XRD, Raman, and BET analysis).
- **Batch adsorption studies:** Evaluate the adsorptive efficiency of the composite against three distinct pollutant classes (Methyl Orange, Catechol, and Acetamiprid) through comprehensive kinetic, isotherm, and thermodynamic assessments.
- **Advanced computational optimization:** Systematically compare machine-learning data architectures and utilize an ANN-GA framework to bypass gradient-based statistical limitations, determining absolute optimal operational conditions.
- **Continuous system application:** Investigate the dynamic adsorption behavior of the composite in a continuous fixed-bed column setup to bridge laboratory theory with real-world industrial applicability.
- **Regeneration and reusability:** Assess the structural stability, cyclic reusability, and economic viability of the ZnO@DPS-AC composite across multiple adsorption-desorption cycles.

To systematically address these objectives, the manuscript is organized as follows:

- **Chapter I** presents a literature review on water pollution, detailing the environmental impacts of the targeted contaminants and exploring current wastewater remediation technologies, with an emphasis on the extreme novelty of DPS as a precursor.
- **Chapter II** outlines the theoretical principles governing adsorption, the physical chemistry of activated carbon, and the mathematical foundations of the applied modeling techniques (Isotherms, Kinetics, Thermodynamics, RSM, ANN, and GA).
- **Chapter III** details the materials, experimental protocols, and analytical methods used for the synthesis, characterization, and application of the ZnO@DPS-AC composite in batch and continuous modes.
- **Chapter IV** discusses the physicochemical and structural characterization results of the synthesized adsorbent.
- **Chapters V, VI, and VII** analyze the batch adsorption studies for Methyl Orange, Catechol, and Acetamiprid, respectively. These chapters examine comparative machine-learning architectures (augmented versus purely experimental data), predictive accuracy of models, and mechanistic insights into pollutant uptake.
- **Chapter VIII** transitions to dynamic studies, presenting breakthrough curve analysis and mathematical modeling of the continuous fixed-bed column adsorption for the three pollutants.
- Finally, a **General Conclusion** synthesizes the major experimental and computational findings and offers specific recommendations for future investigations in environmental engineering and advanced materials science.

Chapter I: Literature Review: Water Pollution and Advanced Remediation Strategies

* * * * *

I.1 Introduction

The persistent discharge of synthetic chemicals into aquatic ecosystems poses a severe environmental challenge. Rapid global industrialization and intensive agricultural practices generate substantial effluent volumes laden with recalcitrant organic pollutants. Even at trace concentrations, these contaminants present distinct toxicological and bioaccumulative hazards to both human health and ecological stability.

This chapter systematically reviews the specific aqueous pollutants targeted for remediation: MO, CAT, and ACE to establish the context for the experimental work. The subsequent sections detail their physicochemical properties, industrial synthesis pathways, environmental fate, and corresponding toxicological profiles.

Additionally, this chapter critically evaluates the efficacy of current advanced remediation strategies. By assessing the operational advantages and inherent technical limitations of established and emerging treatment frameworks (including biological degradation, membrane filtration, Advanced Oxidation Processes (AOPs), and physical adsorption), this review constructs the scientific rationale for the current investigation. Ultimately, this evaluation underscores the need to engineer high-performance, low-cost carbonaceous adsorbents as a sustainable solution for the advanced decontamination of complex wastewater matrices.

I.2 Water pollution and pollutants of interest

Rapid industrial expansion, population growth, and intensive agricultural practices have severely degraded global freshwater resources. Aquatic contamination has evolved from a localized issue into a systemic crisis threatening ecological stability, food security, and public health. Among the diverse contaminants entering aquatic ecosystems, organic pollutants (specifically synthetic dyes, phenolic compounds, and pesticide residues) present an exceptional challenge. Their environmental recalcitrance, bioaccumulative tendencies, and distinct toxicity at trace concentrations make remediation exceedingly difficult. This section systematically reviews three targeted aqueous pollutants: methyl orange (an anionic azo dye), catechol (a phenolic derivative), and acetamiprid (a neonicotinoid insecticide). The subsequent analysis defines their physicochemical properties,

environmental fate, and the technical limitations of existing treatment technologies. The molecular structures of these three contaminants are illustrated in **Figure I.1**.

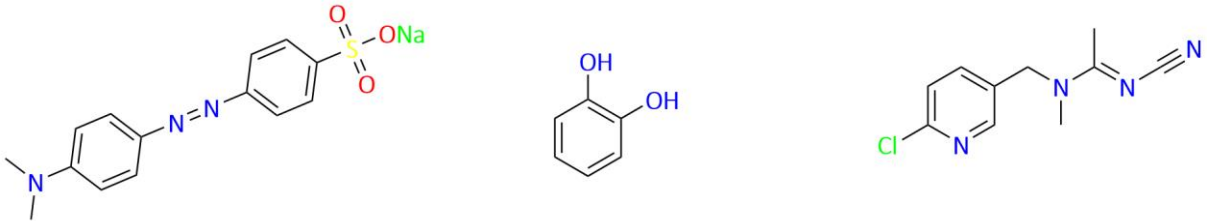

Methyl Orange Catechol Acetamiprid

Figure I.1 Chemical structure of MO, CAT, and ACE

I.3 Methyl orange

I.3.1 Structure and physicochemical properties

MO is a synthetic organic compound classified as an azo dye. Its chemical structure features an azo linkage (–N=N–) bridging two substituted aromatic rings. This configuration creates a conjugated π–electron system that governs the chromophoric properties of the molecule (Zollinger, 2003). The molecule contains a sulfanilic acid moiety coupled to N, N-dimethylaniline. A sulfonate group ($–SO_3^-$) attached to one phenyl ring provides high aqueous solubility and defines the molecule's anionic character, fundamentally distinguishing it from cationic and neutral dyes (Miller, 2010). The opposing phenyl ring contains a dimethylamino group that functions as an electron donor (Abbou et al., 2023).

The colorimetric behavior of MO depends on a protonation-deprotonation equilibrium that dictates its optical response in aqueous environments. Functioning as a weak acid with a Dissociation Constant (*pKa*) of approximately 3.47 at 25 °C, the dye displays specific spectral characteristics based on the solution *pH* (Iwuozor et al., 2021). In neutral and alkaline conditions, MO exists primarily in a deprotonated azo form (**Figure I.2**). This state exhibits extensive conjugation across the azo linkage and a strong absorption band near 464 nm, resulting in a yellow-orange coloration. Conversely, acidic conditions induce protonation of the azo nitrogen, forming a resonance-stabilized azonium ion. This structural modification alters the electronic transitions within the π-conjugated system, displacing the absorption maximum to longer wavelengths and generating a red color (Arif, 2025; Z. Liu et al., 2021; Pires et al., 2012; Simão & Cerdeira, 2016). This pH-dependent transformation enables its widespread use in the laboratory as an indicator, particularly for titrations of strong acids with weak bases, where

the equivalence point falls within the acidic range (Souhıla, 2024).

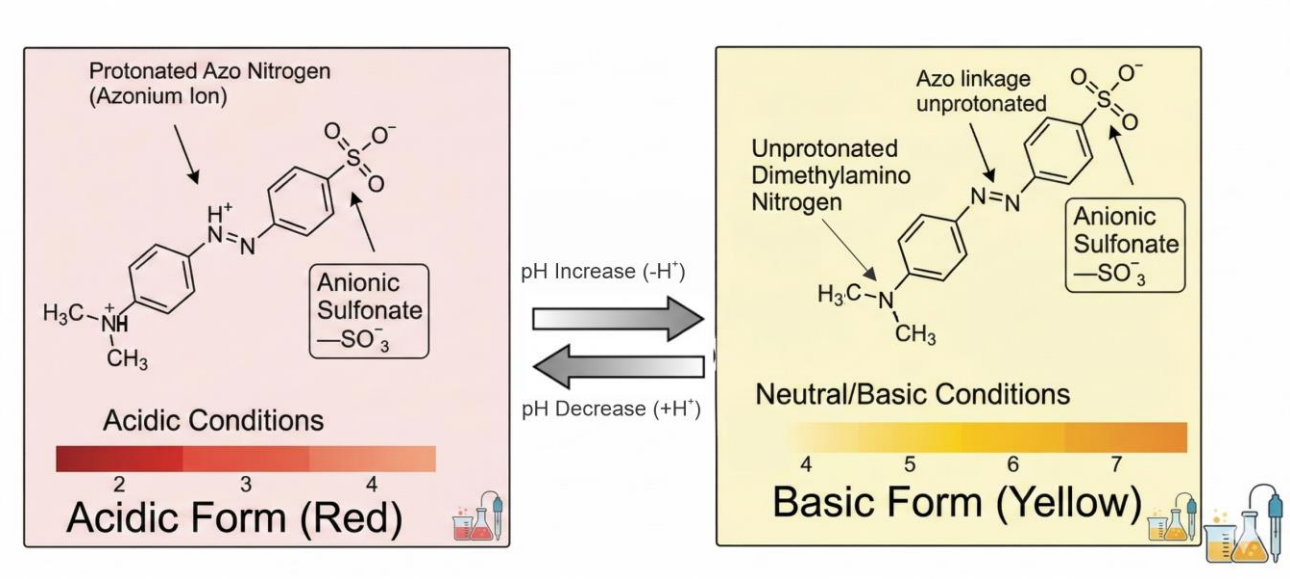

Figure I.2 Structural transformation of MO

The physical stability of MO significantly contributes to its environmental persistence. This compound appears as an orange-yellow powder at ambient temperatures and exhibits a high melting point exceeding 300 °C, often undergoing thermal decomposition before melting (Information, 2004). Aqueous solubility approaches 5 g/L due to the hydrophilic sodium sulfonate motif, yet the dye remains practically insoluble in nonpolar solvents such as diethyl ether (Sunthar et al., 2023). The detailed physicochemical parameters of MO are summarized in **Table I.1**.

I.3.2 Industrial synthesis

The industrial synthesis of MO relies on a sequential, two-step diazotization and coupling process. The reaction is initiated by treating sulfanilic acid with sodium nitrite and a mineral acid (typically hydrochloric acid) at low temperature to generate a highly reactive, unstable diazonium salt. This intermediate is immediately coupled with N, N-dimethylaniline in a weakly acidic to neutral aqueous medium. The coupling proceeds via electrophilic aromatic substitution at the para position, successfully establishing the defining azo linkage. The resultant product is isolated as a sodium salt by adding sodium chloride to induce salting-out, followed by standard filtration and thermal drying to yield the commercial orange powder (Astolfi & Mayville, 2003; Simão & Cerdeira, 2016).

Table I.1 Detailed physicochemical properties of MO (Information, 2004; Iwuozor et al., 2021;

Sunthar et al., 2023)

Property	Value	Scientific context
IUPAC Name	Sodium 4-[[4-(dimethylamino)phenyl]diazenyl]benzenesulfonate	Standard nomenclature
CAS Registry Number	547-58-0	Global identifier for regulatory tracking
Molecular Formula	$C_{14}H_{14}N_3NaO_3S$	Reflects the sodium salt form typically used
Molecular Weight	327.33 g/mol	Determines diffusion coefficients and molarity calculations
Appearance	Orange/Yellow Powder	Solid phase morphology
Solubility (Water)	~5 g/L (20 °C)	High enough to create concentrated dye baths
Solubility (Ethanol)	Soluble	Allows for use in organic solvent matrices
pKa	3.47 (at 25 °C)	Critical parameter for the indicator function
Absorption Maximum	464 nm	In a neutral/basic aqueous solution
Density	1.28 g/cm³	Relative to water

I.3.3 Commercial and scientific applications

The functional utility of MO extends across large-scale industrial manufacturing and high-precision analytical chemistry.

I.3.3.1 Textile and dyeing industries

Commercially designated as C.I. Acid Orange 52, MO functions as a standard acid dye. It exhibits a high chemical affinity for protein-derived fibers (including wool and silk) and synthetic polyamides (such as nylon). The physical dyeing mechanism relies heavily on ionic interactions between the anionic sulfonate moiety of the dye molecule and the protonated cationic amino groups along the target fiber's polymer chain. Although advanced alternative dyes are widely available, methyl orange remains industrially relevant due to its robust colorimetric intensity and overall economic efficiency (Fastuca, 2018; Yahia et al., 2012).

I.3.3.2 Analytical chemistry (Titrimetry)

Within scientific research, the compound is primarily utilized as a highly sensitive *pH* indicator. Because its characteristic color transition occurs within a strictly acidic domain (*pH* 3.1 to 4.4), it is the preferred indicator for titrations involving strong acids and weak bases (for example, the neutralization of hydrochloric acid with ammonia). At the equivalence point, the reaction yields a salt that hydrolyzes to form a slightly acidic solution, which aligns perfectly with the functional transition

range of methyl orange. Conversely, indicators such as phenolphthalein prove ineffective in this context because their transition intervals lie exclusively within the alkaline range.

I.3.3.3 Environmental tracer

Due to its high aqueous solubility and its precise detectability by UV-Vis spectroscopy, MO serves as an effective model aqueous pollutant. Environmental engineering studies frequently utilize this dye to rigorously evaluate the performance of novel photocatalysts, advanced adsorbents, and membrane filtration systems (He et al., 2011).

I.3.3.4 Human health toxicity and safety profile

MO presents specific human health hazards through ingestion, dermal contact, and inhalation of dust. The compound is classified as *acutely toxic if swallowed* (Hazard Statement H301), demonstrating a high acute oral toxicity in murine models (rat LD50 of approximately 60 mg/kg). Acute exposure commonly induces ocular and epidermal irritation, whereas the inhalation of airborne particulates frequently precipitates respiratory distress (Azami et al., 2012; Gong et al., 2013). This respiratory risk is particularly severe in poorly ventilated industrial environments. Furthermore, repeated or high-level exposure may generate systemic health complications. Available safety documentation indicates positive mutagenicity signals in microbial screening assays (utilizing bacterial or yeast cultures). Although definitive human carcinogenicity data remain limited, these microbiological results strongly suggest genotoxic potential and warrant rigorous evaluation. Consequently, laboratory and industrial handling must strictly adhere to chemical hygiene protocols. Personnel must utilize appropriate personal protective equipment (including nitrile gloves and chemical splash goggles) to minimize dust generation and prevent direct exposure.

I.3.3.5 Environmental concerns

The discharge of methyl orange is highly problematic for aquatic ecosystems. The chemical stability of its aromatic mono-azo structure dictates significant persistence under standard aerobic conditions, rendering conventional biological wastewater treatment highly ineffective and facilitating extensive transport in receiving waters (Ramath et al., 2023; Shah et al., 2021). Even at trace concentrations, the dye produces intense coloration, increasing light attenuation in the water bodies. This optical interference severely suppresses photosynthesis in primary producers, subsequently reducing overall ecosystem productivity (Bassam et al., 2024; Tcheka et al., 2024). The resulting ecological stress propagates through aquatic food webs, often decreasing dissolved oxygen availability and severely

impacting fish and invertebrate populations (Haque et al., 2024; Tcheka et al., 2024).

Furthermore, while the molecule resists aerobic breakdown, anaerobic environments induce reductive transformation. This specific degradation pathway cleaves the azo linkage, producing toxic aromatic amines (specifically sulfanilic acid and N, N-dimethyl-p-phenylenediamine). The scientific literature consistently highlights these secondary metabolites as severe toxicological hazards requiring extensive risk assessment prior to environmental discharge (Arif, 2025; Feng et al., 2012; Yu et al., 2017).

I.4 Catechol

I.4.1 Structure and properties

CAT is commonly designated as pyrocatechol. It is a reactive phenolic compound distinguished by two hydroxyl groups occupying the ortho positions of a central benzene ring. This specific structural adjacency is chemically significant. It facilitates intramolecular hydrogen bonding, which dictates the compound's volatility and extensive aqueous solubility (exceeding 450 g/L). Furthermore, this ortho-configuration allows the molecule to function effectively as a bidentate ligand for the chelation of transition metal ions (Information, 2025a). Functioning as a weak acid with a *pKa* of approximately 9.45, CAT remains predominantly protonated at neutral *pH*. In alkaline environments, it readily deprotonates to generate reactive catecholate anions (Information, 2025a; Kamarehie et al., 2024). In its pure solid phase, CAT forms white to light tan crystals. However, the compound is highly susceptible to auto-oxidation. Upon exposure to ambient oxygen and photon irradiation, it oxidizes, yielding reactive quinone intermediates and complex polymeric aggregates that manifest macroscopically as a brown discoloration (Jarabak et al., 1998; Pillar-Little & Guzman, 2017). This fundamental redox activity dictates both its broad industrial utility and its mechanisms of environmental toxicity. The specific physicochemical parameters of CAT are detailed in **Table I.2**.

Table I.2 Physicochemical properties of CAT (Information, 2025a)

Property	Value	Scientific context
Common Synonyms	Pyrocatechol	Standard industrial nomenclature
IUPAC Name	Benzene-1,2-diol	Standard nomenclature
CAS Registry Number	120–80–9	Identifier
Molecular Formula	$C_6H_6O_2$	Phenolic derivative

Molecular Weight	110.11 g/mol	Low molecular weight facilitates absorption
Melting Point	100 - 105 °C	Solid at room temperature
Boiling Point	245.5 °C	Sublimes at atmospheric pressure
Vapor Pressure	10 mmHg at 118 °C	Moderate volatility when heated
Water Solubility	461 g/L (25 °C)	Extremely soluble (hydrophilic)
Log Kow	0.88	Low lipophilicity; low bioaccumulation
Flash Point	127 °C (261 °F)	Combustible solid

I.4.2 Industrial production

Contemporary industrial synthesis of CAT primarily relies on catalyzed hydroxylation of phenol. This direct oxidation process utilizes hydrogen peroxide (H_2O_2) in the presence of acidic or transition metal catalysts (Huang et al., 2011). The reaction pathway yields a characteristic binary mixture of CAT (1,2-dihydroxybenzene) and its para-isomer, hydroquinone (1,4-dihydroxybenzene). These resulting isomers are subsequently isolated through precise fractional distillation based on their differing boiling points (Matsuura et al., 1974). Historically, CAT was produced by destructive distillation of coal tar or by energy-intensive alkaline hydrolysis of 2-chlorophenol (Draths & Frost, 1993). Modern manufacturing exclusively favors the phenol-peroxide route due to its high scalability and the operational ability to control isomer ratios through careful thermodynamic and catalytic regulation. To reduce reliance on petroleum feedstocks, emerging chemical engineering research is investigating sustainable, bio-based synthesis routes that utilize renewable precursors such as lignin and glucose (Arreola-Najera et al., 2025; Balderas-Hernández et al., 2014).

I.4.3 Natural and anthropogenic environmental sources

I.4.3.1 Combustion and pyrolysis

CAT is generated extensively during the thermal decomposition of lignin and other lignocellulosic biomass. Analytical studies consistently identify the compound as a major constituent of wood smoke, as well as tobacco and cannabis combustion aerosols. Consequently, it persists as a ubiquitous atmospheric and aqueous pollutant in geographic regions experiencing widespread wildfires or heavy anthropogenic biomass burning (Morash et al., 2022).

I.4.3.2 Industrial effluents

CAT is frequently detected in wastewater from pulp and paper mills as a byproduct of lignin

degradation. It is also a prevalent contaminant in effluents discharged from textile manufacturing facilities and oil refineries. The compound's high aqueous solubility facilitates its rapid transport from these industrial point sources directly into vulnerable aquatic ecosystems (Morash et al., 2022; Schweigert et al., 2001).

I.4.3.3 Natural occurrence

Beyond anthropogenic sources, CAT occurs naturally as a secondary metabolite in various fruits and vegetables (such as onions and apples). In specific botanical systems, it functions naturally as a defense mechanism against pathogens (Information, 2025a).

I.4.4 Industrial applications

Due to its versatile chemical reactivity and specific structural properties, CAT holds substantial value across multiple industrial sectors (Babić et al., 2021; Cancer, 1999; Im & Jeon, 2016; International Agency for Research on, 1999; James, 1946; Morash et al., 2022; Prakash et al., 2010; Saha et al., 2013; Suresh et al., 2012b; W. Wang et al., 2023).

I.4.4.1 Pesticide synthesis

A significant portion of global CAT production is allocated to the synthesis of carbamate insecticides. It serves as a direct precursor to propoxur and carbofuran, which are widely used in agricultural pest management. To produce these bioactive agents, the CAT moiety undergoes specific chemical modifications, frequently via etherification.

I.4.4.2 Flavor and fragrance

CAT is the foundational starting material for the commercial production of vanillin (4-hydroxy-3-methoxybenzaldehyde) and ethyl vanillin. Through a controlled methylation process utilizing guaiacol as an intermediate, CAT is transformed into this globally prevalent flavoring compound.

I.4.4.3 Pharmaceutical precursor

In the pharmaceutical sector, CAT is integral to the synthesis of L-DOPA (a primary therapeutic agent for Parkinson's disease) and various adrenaline-derived medications. These applications directly leverage its structural homology to endogenous catecholamines.

I.4.4.4 Specialty chemicals

The compound exhibits diverse utility in specialized chemical formulations:

- Photography: historically, CAT functioned as a photographic developing agent owing to its capacity to reduce silver halides.
- Polymerization inhibition: Its strong antioxidant properties enable it to efficiently scavenge free radicals, thereby stabilizing reactive monomers during prolonged storage and transport.
- Inks and Dyes: It is a critical formulation component in specialty inks and industrial fur dyes.

I.4.5 Toxicity to humans and the environment

CAT presents a highly complex toxicological profile characterized by acute systemic toxicity, genotoxic potential, and targeted cytotoxicity toward pigment-producing cells.

I.4.5.1 Human and mammalian toxicity

In mammalian models, CAT demonstrates significant acute toxicity following ingestion or dermal exposure. Reported oral LD50 values are approximately 300 mg/kg in mice and 210 mg/kg in guinea pigs. The clinical presentation of acute poisoning closely resembles general phenol intoxication. Symptoms include Central Nervous System (CNS) depression, muscular convulsions, and respiratory failure, accompanied by the excretion of darkened urine caused by quinone metabolites. Furthermore, CAT is a severe localized irritant that can inflict permanent ocular damage and induce allergic contact dermatitis upon dermal exposure (Information, 2025a; Morash et al., 2022).

Chronic exposure has prompted strict regulatory classification. The International Agency for Research on Cancer (IARC) categorizes catechol as a Group 2B carcinogen (possibly carcinogenic to humans) (Cancer, 1999). Similarly, the American Conference of Governmental Industrial Hygienists (ACGIH classifies it as an A3 confirmed animal carcinogen. Mechanistically, this oncogenic potential is driven by co-carcinogenic activity and bioactivation into o-benzoquinone. This electrophilic intermediate covalently binds to cellular DNA and proteins. Concurrently, the molecule's continuous redox cycling generates Reactive Oxygen Species (ROS, including superoxide anions and hydroxyl radicals, which collectively induce severe oxidative DNA strand breaks (Bolton et al., 2000; Morash et al., 2022; Schweigert et al., 2001).

I.4.5.2 Specific toxicity to melanocytes

CAT exhibits distinct, highly targeted cytotoxicity toward pigment systems, preferentially damaging melanocytes via tyrosinase-dependent pathways. In this suicide-substrate mechanism, tyrosinase (an enzyme expressed in melanocytes) oxidizes CAT to highly reactive o-quinones. These intermediates aggressively deplete intracellular glutathione (GSH) and covalently alter thiol-bearing proteins,

culminating in melanocyte dysfunction and apoptosis. Experimental exposure in zebrafish models suppresses the transcription of critical melanogenic regulators (such as mitfa, mc1r, and tyr). This suppression manifests macroscopically as reduced melanocyte dendricity and generalized depigmentation. These findings contextualize the severe safety concerns surrounding the historical use of CAT derivatives in skin-whitening cosmetics (Morash et al., 2022).

I.4.5.3 Environmental impact

When discharged at elevated concentrations, CAT exerts immediate adverse effects on ecological systems. In aquatic environments, the compound is acutely toxic to critical indicator species, including Daphnia magna and teleost fish (such as rainbow trout and zebrafish). The mechanisms underlying this acute aquatic toxicity are consistently linked to severe respiratory inhibition and acute oxidative stress pathways (Schweigert et al., 2001).

I.4.6 Toxicity and environmental fate

Environmental regulatory bodies, including the United States Environmental Protection Agency (US-EPA), classify CAT as a high-priority pollutant owing to its severe toxicity and profound ecological risks. The compound is readily absorbed through the epidermis, ocular tissues, and gastrointestinal tract. This rapid absorption precipitates systemic toxicity clinically manifested as central nervous system depression, methemoglobinemia, and renal tubular necrosis. Mechanistically, this toxicity is driven by the molecule's inherent redox activity. CAT readily undergoes auto-oxidation to form o-benzoquinone, a process that concurrently generates superoxide anion radicals and other ROS. These highly reactive intermediates subsequently induce severe oxidative stress and irreversible DNA damage (Information, 2025a; Kamarehie et al., 2024; Schweigert et al., 2001).

Furthermore, the IARC has formally designated CAT as a Group 2B carcinogen (possibly carcinogenic to humans). This classification is supported by empirical evidence demonstrating its capacity to induce glandular stomach adenocarcinomas in rodent models (Cancer, 1999). In aquatic ecosystems, CAT exhibits greater acute toxicity than phenol. Its lethality varies significantly across different aquatic organisms, mandating rigorous, highly efficient wastewater treatment protocols prior to environmental discharge (Schweigert et al., 2001).

I.5 Acetamiprid

I.5.1 Structure and properties

ACE is a prominent neonicotinoid insecticide, classified as a second-generation compound. While first-generation neonicotinoids (such as imidacloprid) possess a nitroimine (=N-NO_2) functional group, ACE is structurally defined by a cyanoimine (N-CN) pharmacophore. This structural distinction is chemically highly significant. The cyano group fundamentally dictates the molecule's polarity, metabolic stability, and specific receptor affinity. Structurally, ACE incorporates a chloropyridinyl moiety similar to imidacloprid but lacks an imidazolidine ring, resulting in a more flexible, open-chain acetamidine configuration (Sun et al., 2024).

Table I.3 Physicochemical properties of ACE (Agency, 2023; Authority, 2016; Information, 2025b; Zuščíková et al., 2023)

Property	Value	Scientific context
IUPAC Name	N–[(6-chloro– 3–pyridinyl)methyl]–N'–cyano-N-methylethanimidamide	Standard nomenclature
CAS Registry Number	160430–64–8	Identifier
Trade Names	Assail, Chipco, Mospilan, Pristine	Commercial formulations
Molecular Formula	$C_{10}H_{11}ClN_4$	Chlorinated organic
Molecular Weight	222.67 g/mol	Moderate size allows translocation
Water Solubility	2950 – 4250 mg/L (25 °C)	Very high for an insecticide; systemic
Log Pow	0.80	Low bioaccumulation potential
Vapor Pressure	$<10^{-8}$ – 7.5×10^{-10} mmHg (25 °C)	Non-volatile
Soil Adsorption (K_{oc})	157 – 298 L/kg	Moderately mobile in soil
pKa	0.7	Very weak base

In its pure physical state, ACE presents as a white, odorless crystalline solid. It exhibits a relatively high aqueous solubility compared to conventional insecticides. This specific hydrophilic property is engineered to facilitate rapid systemic uptake by target plants, while concurrently increasing the compound's potential for groundwater leaching. The specific physicochemical parameters governing its behavior are summarized in **Table I.3**.

I.5.2 Agricultural deployment

Agrochemical formulations utilize ACE strictly as a systemic insecticide. It is designed for rapid

absorption by plant tissues via soil drenching, seed coating, or direct foliar application. Following absorption, the active compound is translocated through the xylem network, providing durable, internal protection against sap-feeding insects (Wallace, 2014; Zuščíková et al., 2023). Its bioactivity spectrum is highly targeted toward hemipteran species (including aphids, whiteflies, and planthoppers), thysanopterans (thrips), and specific lepidopterans. Consequently, it functions as a foundational tool within Integrated Pest Management (IPM) frameworks for high-value agricultural commodities such as leafy vegetables, citrus, pome fruits, viticulture, and cotton (Bass et al., 2015; Eren & Gurkan, 2018; Sun et al., 2024). Additionally, ACE has extensive targeted use in commercial cherry production, serving as the primary chemical control against the cherry fruit fly to prevent catastrophic yield losses (Tamaš et al., 2025).

I.5.3 Mode of action

The insecticidal mechanism of ACE involves its function as a selective agonist of the nicotinic acetylcholine receptor (nAChR) within the insect central nervous system. Upon binding to the post-synaptic nAChR, ACE resists hydrolysis by acetylcholinesterase (unlike the endogenous neurotransmitter acetylcholine). This resistance leads to persistent stimulation of ion channels. Continuous activation facilitates a prolonged influx of sodium ions (Na^+), leading to hyperexcitation, convulsions, paralysis, and ultimately insect mortality. Significantly, the presence of a cyanoimine functional group confers a high binding affinity for insect nAChRs while maintaining a low affinity for vertebrate subtypes. This structural specificity provides a substantial mammalian safety margin relative to older organophosphate insecticides (Andrew & Samuels, 2024; Cartereau et al., 2018; Costas-Ferreira & Faro, 2021; Products & Residues, 2013; Sun et al., 2024; Taillebois et al., 2024; Zhang et al., 2024).

I.5.4 Mammalian toxicology and human safety profile

ACE generally exhibits a comparatively favorable acute toxicity profile in mammalian systems compared with earlier generations of insecticides. Acute oral toxicity assessments in murine models reveal LD50 values that fluctuate significantly based on formulation and biological sex, ranging from approximately 146 mg/kg to exceeding 1000 mg/kg. Based on available oncogenicity data, regulatory bodies such as the US-EPA have classified the parent compound as not likely to be carcinogenic to humans, underscoring its safety margin in standard acute exposure scenarios (Agency, 2020).

Despite this relatively benign acute profile, contemporary research increasingly focuses on the

potential risks associated with chronic exposure and metabolic byproducts. The primary metabolites, including IM-2-1 and IC-0 (6-chloronicotinic acid), have demonstrated developmental toxicity in aquatic models. For instance, medaka fish embryos exposed to IC-0 exhibited significant mortality and teratogenic abnormalities. These findings suggest that degradation products may pose distinct developmental hazards (Sun et al., 2024). Furthermore, mechanistic studies in vertebrate models indicate that high-dose exposure to ACE can induce systemic oxidative stress, precipitating lipid peroxidation and subsequent DNA damage. This oxidative mechanism is corroborated by genotoxicity assays reporting micronuclei formation and chromosomal aberrations in bone marrow cells. Additional emerging evidence points to reproductive toxicity characterized by compromised sperm quality in rodent models (Zhang et al., 2024; Zuščíková et al., 2023).

I.5.5 Ecotoxicological profile

ACE is often characterized as having a more favorable safety profile for pollinators than nitro-substituted neonicotinoids, such as imidacloprid. The oral median lethal dose (LD50) for honeybees (Apis mellifera) is reported to be approximately 14.5 µg/bee, a value significantly higher than the nanogram-level toxicity thresholds observed for neonicotinoids. However, this perceived safety is highly nuanced. Commercial formulations often exhibit greater toxicity than the pure active ingredient, likely due to synergistic interactions with surfactants and adjuvants. Moreover, there is growing concern regarding sublethal impacts. Evidence suggests that even non-lethal exposure can compromise colony viability by impairing critical navigation and foraging behaviors (Sun et al., 2024; Zhao et al., 2024).

Conversely, ACE poses acute risks to aquatic ecosystems, demonstrating high toxicity toward aquatic invertebrates. Orders such as Ephemeroptera (mayflies), Trichoptera (caddisflies), and Diptera (midges) are particularly sensitive to neonicotinoid exposure. Runoff-mediated contamination of surface waters can precipitate the collapse of these invertebrate populations, which serve as foundational components of the aquatic food web. Such disruptions can trigger trophic cascades, ultimately reducing food availability for higher trophic levels, including fish and avian species. This ecological phenomenon has become a primary driver for heightened regulatory scrutiny (Agency, 2023).

I.5.6 Environmental fate, mobility, and persistence profiles

ACE exhibits moderate mobility within soil matrices, a characteristic dictated by its relatively low

Organic Carbon Partition Coefficient (K_{oc} values ranging from 157 to 298). This physicochemical trait significantly elevates the risk of groundwater leaching, particularly within highly permeable soils. Localized redox conditions strongly govern the environmental persistence of this compound. Under aerobic soil conditions, ACE degrades rapidly, with typical half-lives (DT50) of 1-8 days. However, this period can extend up to 420 days in specific aqueous environments, such as those maintained at pH 9 (Agency, 2023; Authority, 2016; Lewis et al., 2016). In aquatic systems, the parent compound degrades into secondary metabolites (specifically N-desmethylacetamiprid and 6-chloronicotinic acid), which exhibit divergent toxicological profiles and persistence behaviors compared with the primary molecule (Authority, 2016; Guzsvány et al., 2009; Sun et al., 2024).

A critical environmental liability arises from ACE's exceptional stability under anaerobic conditions. In oxygen-depleted zones (such as deep subsurface soils and anaerobic benthic sediments), the suppression of microbial degradation pathways severely inhibits breakdown. This inhibition results in significantly extended half-lives of approximately 477 to 585 days (Agency, 2023). This differential persistence ensures that if ACE infiltrates anaerobic domains, it effectively becomes a long-term legacy pollutant. Such recalcitrance poses a persistent threat to groundwater quality and benthic ecological stability.

I.6 Remediation strategies of MO, CAT, and ACE

The escalating global crisis of aquatic contamination, propelled by rapid industrial expansion, strictly demands the continuous optimization of advanced wastewater treatment technologies. Modern industrial effluents are increasingly complex. They are heavily laden with recalcitrant organic compounds that frequently overwhelm and bypass conventional physical and biological treatment frameworks (**Figure I.3**). Consequently, the complete remediation of MO, CAT, and ACE requires the deployment of highly engineered systems. Current methodologies encompass a broad spectrum of advanced techniques, including adsorption onto porous carbonaceous matrices, AOPs (primarily photocatalysis and Fenton-derived reactions), membrane filtration, and highly targeted enzymatic degradation.

These diverse technologies exhibit substantial variance regarding absolute removal efficiency, degree of total mineralization, operational cost, and system complexity. To circumvent the inherent technical limitations of any single approach, contemporary environmental engineering often integrates these methods (such as coupled adsorption-photocatalysis systems) to achieve synergistic decontamination.

The fundamental mechanisms, advantages, and operational constraints of these advanced technologies are detailed in the subsequent subsections, with a comprehensive comparative analysis provided in **0**.

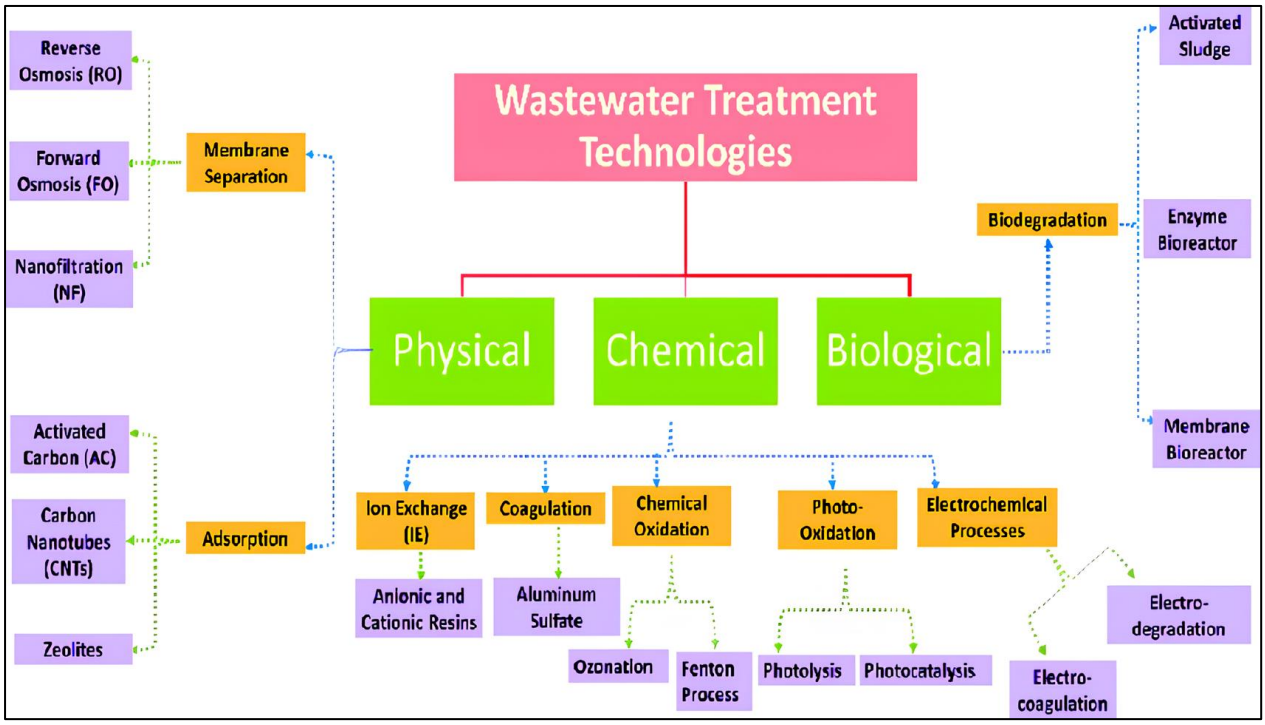

Figure I.3 Classification of wastewater treatment technologies based on physical, chemical, and biological principles (El-Azazy et al., 2020)

I.6.1 Methyl orange remediation

I.6.1.1 Physical technologies

Physical remediation methods, notably adsorption and membrane filtration, remain dominant technologies for dye removal. These approaches offer distinct operational simplicity, enable extensive adsorbent regeneration, and avoid the formation of secondary chemical sludge. The specific surface area, pore-size distribution, and surface chemistry of the applied material fundamentally govern the macroscopic efficacy of physical adsorption.

a) Metal-organic frameworks and nanocomposites

Metal-Organic Frameworks (MOFs) provide ultra-high specific surface areas and highly tunable internal pore architectures. However, their inherent powder morphology frequently introduces operational difficulties regarding continuous phase separation and recovery. Recent material engineering efforts focus on composite structures that safely integrate MOFs within robust macroscopic support matrices. The UiO-66-NH_2/GO@PVA nanocomposite exemplifies this

advanced design strategy. This material structurally combines the high porosity of a zirconium-based MOF (UiO-66-NH_2) with the mechanical stability of Polyvinyl Alcohol (PVA) and the highly conductive, planar geometry of Graphene Oxide (GO). Experimental analyses indicate that this composite achieves 99.6% removal efficiency of methyl orange within 60 min (Van Thang et al., 2025). By comparison, alternative MOF-based composites, such as Ni-doped ZIF-67 (Nazir et al., 2023) and GO/MIL-101(Fe) (Z. Liu et al., 2021), demonstrate maximum adsorption capacities of 151.74 mg/g and 186.20 mg/g, respectively. These metrics definitively position the UiO-66-NH_2/GO@PVA matrix as a highly effective physical adsorbent for anionic dyes.

b) Engineered clay-polymer membrane filtration

Although engineered nanomaterials exhibit exceptional adsorption capacities, their synthesis costs are frequently prohibitive. Modified natural minerals provide a highly cost-effective alternative. Integrating bentonite clay into Polyvinyl Chloride (PVC) membranes produces a hybrid filtration-adsorption system capable of simultaneous physical separation and chemical retention. Research utilizing natural bentonite incorporated into PVC matrices indicates that the membrane's overall retention capacity scales directly with the bentonite weight fraction. Functioning as a montmorillonite clay, bentonite features a layered silicate structure that swells predictably in aqueous environments, effectively expanding the available surface area for targeted ion exchange (Souhıla, 2024).

c) Activated carbon

Commercial Activated Carbon (CAC) functions as the industrial benchmark for evaluating novel porous adsorbents. While effective for MO removal, CAC often exhibits lower absolute adsorption capacities than functionalized MOFs. The elevated production costs and non-renewable origins of CAC have stimulated intensive research into low-cost, sustainable alternatives synthesized from biological precursors. Activated carbons derived from diverse agricultural residues, including coconut shells (Kamdod & Kumar, 2022), pinewood (De Smedt et al., 2024), and spent coffee grounds (Martínez et al., 2023), exhibit comparable or superior adsorptive performance. This efficacy is driven by their extensive surface areas, hierarchical pore networks, and diverse oxygen-containing surface functional groups. Utilizing biomass-derived carbons significantly reduces production costs and mitigates environmental impacts, offering a highly scalable solution for decontaminating dye-laden industrial effluents.

I.6.1.2 Advanced oxidation processes

In wastewater matrices where simple phase transfer (concentrating pollutants onto a solid support) is

insufficient, or where subsequent disposal of chemical sludge poses logistical challenges, AOPs offer a distinct advantage. These mechanisms facilitate total mineralization, completely degrading complex organic contaminants into carbon dioxide, water, and simple mineral salts.

a) Heterogeneous photocatalysis

Photocatalytic degradation employs semiconductor materials that, upon irradiation with photons with energy exceeding their bandgap, generate reactive electron-hole pairs (e^-/h^+). These charge carriers initiate rapid redox sequences, yielding highly oxidative Hydroxyl Radicals (•OH) and Superoxide Anions ($•O_2^-$). The synergistic combination of titanium dioxide (TiO_2) and zinc oxide (ZnO) has been extensively studied to suppress rapid electron-hole recombination, a phenomenon typically observed in single-component photocatalysts. Among the investigated formulations, a composite photocatalyst with an optimized ZnO: TiO_2 mass ratio of 0.131:1 achieved a peak degradation efficiency of 98.6%. The heterojunction established between the two metal oxides promotes efficient spatial charge separation, extending the half-life of photogenerated reactive oxygen species and significantly enhancing overall catalytic activity. Furthermore, this degradation efficiency is highly pH-dependent. Performance peaks at 93.9% under near-neutral conditions (*pH* 6.7) but drops substantially to 57.7% at *pH* 8, highlighting the semiconductor interface's extreme sensitivity to protonation states and localized surface charges (Dai et al., 2025). Subsequent enhancements have been achieved through selective transition metal doping and supporting matrices. For example, silver-doped TiO_2 achieved 95% degradation under identical experimental conditions where pure TiO_2 reached only 50% (Cheng et al., 2016). Similarly, lignin-derived carbon-supported ZnO composites achieved 96.9% dye degradation within 30 min, confirming the high viability of biomass-supported photocatalytic frameworks (Tang et al., 2024).

b) Coupled adsorption-photocatalysis systems

Hybrid configurations actively exploit the synergistic effect of rapid physical removal and continuous chemical degradation. In the absence of photon irradiation, TiO_2-based composites function as static adsorbents, effectively removing approximately 94% of aqueous methyl orange. Upon exposure to ultraviolet light, the physically adsorbed dye molecules undergo rapid mineralization, regenerating active surface sites in situ. This integrated approach demonstrates notable efficacy in complex binary mixtures containing both organic dyes and heavy metals. For instance, in effluents containing trace amounts of cadmium ions, the system achieved simultaneous removal efficiencies exceeding 90% for both the target dye and the dissolved metal (Rashed et al., 2017).

c) Fenton and Fenton-like oxidation

Classical Fenton oxidation relies on the catalytic reaction between aqueous ferrous iron (Fe^{2+}) and H_2O_2 to generate dense concentrations of •OH. Recent process optimization models utilizing Gaussian Process Regression (GPR), corroborated by experimental validation, identified the ideal parameters for MO mineralization. Operating at pH 3.5 with an [Fe^{2+}] of 25 mg/L and [H_2O_2] / [MO] molar ratio, the system achieved a 99% reduction in Chemical Oxygen Demand (COD) within 90 min. However, the industrial scalability of classical Fenton treatment is heavily constrained by its strict requirement for highly acidic environments (pH 3.0 to 3.5). This necessitates expensive continuous *pH* adjustment and generates large volumes of secondary iron sludge requiring specialized disposal protocols (Ouazene et al., 2025). To bypass these inherent limitations, alternative catalytic pathways have been engineered. Systems utilizing FeMnMg-Layered Double Hydroxide (LDH) to activate peroxymonosulfate exhibit broad pH tolerance, achieving 98% degradation of Orange II (a structural analog of methyl orange) at a neutral *pH* of 7.0 (Yajie Wang et al., 2024).

I.6.1.3 Bacterial degradation

Biological remediation is widely considered highly sustainable; however, its application is severely limited by the acute toxicity of azo dyes to standard activated sludge microorganisms. Contemporary environmental microbiology research focuses heavily on isolating extremophilic bacterial strains capable of enzymatically cleaving the highly stable azo linkage under specific physical conditions. A specialized strain of Pseudomonas aeruginosa, successfully isolated from raw textile wastewater, exhibits the distinct biochemical capacity to mineralize MO rather than merely fully decolorize the solution. This degradation relies on a highly regulated, sequential enzymatic cascade. Initially, azoreductase enzymes cleave the nitrogen double bond under microaerophilic conditions, yielding intermediate aromatic amines. These potentially toxic secondary metabolites are immediately oxidized and mineralized into benign end products by accompanying laccase and peroxidase enzymes. Achieving optimal kinetic efficiency requires strict maintenance of neutral pH conditions (7.0) and operating temperatures between 37 and 38 °C. The biological system also demands an external carbon co-substrate to continuously regenerate the essential electron carriers required for the initial reductive cleavage of the azo bond (Khan et al., 2022).

I.6.2 Catechol remediation

CAT presents a distinct remediation challenge. Although the compound is less chemically stable than azo dyes, its toxicity to microorganisms and its tendency to polymerize into dark, insoluble pigments

complicate conventional biological treatment. Consequently, research diverges into highly specific enzymatic treatments and broad-spectrum AOPs.

I.6.2.1 Physical methods

Adsorption remains particularly valuable for recovering phenolic compounds from wastewater for potential reuse rather than targeting their destruction.

a) Carbon-based adsorbent

Biochar, CAC, and biomass-derived AC are widely explored as porous adsorbents for the removal of CAT from aqueous media. Biochars produced from lignocellulosic residues, when tailored by high-temperature pyrolysis or chemical activation, develop significant micro-mesoporosity and diverse surface functionalities. These engineered properties enable rapid CAT uptake, primarily driven by van der Waals interactions and pore filling. High sorption affinities are consistently reported for biochars prepared at elevated temperatures from diverse biomass sources (Kasozi et al., 2010).

Granular and powdered CAC frameworks, traditionally used for phenolic wastewater treatment, predominantly remove CAT via π–π interactions between aromatic rings and graphitic domains. This mechanism is further stabilized by hydrogen bonding to oxygenated surface groups. Accordingly, these materials serve as standard benchmarks in batch adsorption studies evaluating CAT and related phenols (Kamarehie et al., 2024; Suresh et al., 2011b). More recently, activated carbons prepared from agricultural and industrial wastes (including CAT distillation residues and various lignocellulosic precursors) have achieved high specific surface areas and excellent CAT removal efficiencies. These characteristics highlight their viability as low-cost, sustainable alternatives to CAC for the advanced treatment of phenolic effluents (Borah, 2020; Q. Liu et al., 2021).

b) Magnetic Graphene Oxide

Graphene-based materials facilitate highly specific interactions with aromatic rings. Magnetic Graphene Oxide (MGO) demonstrates a distinct affinity for CAT, achieving an adsorption capacity of 104.5 mg/g. Under identical experimental conditions, this value is approximately six times higher than the capacity observed for phenol (18.4 mg/g). This significant enhancement is attributed to the second hydroxyl group on the CAT ring, which provides an additional hydrogen-bonding site for interaction with abundant oxygen-containing functional groups on the graphene oxide surface (such as epoxy, hydroxyl, and carboxyl groups). Consequently, these multiple binding sites facilitate stronger adsorbate-adsorbent interactions (Wu et al., 2024).

I.6.2.2 Chemical methods

a) Coagulation-Flocculation

Chemical Coagulation-Flocculation (CF) utilizing aluminum sulfate ($Al_2(SO_4)_3$) relies on the destabilization of colloidal suspensions and specific interactions between the metal coagulant and organic ligands. The ionic strength of the aqueous matrix heavily influences process efficiency. While CAT removal is relatively low (approximately 26.7%) in distilled water, it improves drastically to 64.7% in mineralized environments supplemented with calcium salts ($CaCl_2$) at pH 7. This performance enhancement is attributed to the formation of calcium-Catecholate complexes that bridge with aluminum hydroxides, improving overall floc size and settleability. Mechanistically, the process is governed by ligand exchange and surface complexation on $Al(OH)_3$ flocs. Optimal removal shifts toward pH 9, where CAT oxidizes to quinones that readily complex with aluminum species (Hecini et al., 2022). Although the generation of significant chemical sludge remains a persistent drawback, the low operational cost positions this method as a viable option for primary treatment.

b) Electrocoagulation

Electrocoagulation (EC) functions by generating coagulants in situ via the anodic dissolution of sacrificial iron electrodes, releasing metal ions that destabilize contaminants. The integration of EC with magnetic Granular Activated Pomegranate Peel Carbon (magnetic GAPPC) demonstrated a marked synergistic enhancement, with performance following the hierarchy EC-magnetic GAPPC > EC > magnetic GAPPC. Under optimal conditions (pH 6-8, a current density of 0.5 A/m^2, and a contact time of 30 min), this hybrid system achieved a maximum removal efficiency of 88%. Mechanistic analysis suggests that CAT degradation proceeds via the formation of benzoquinone as a primary intermediate, which eventually yields simple aliphatic acids (such as formic and acetic acids) and Fe-bonded complexes as semi-final oxidation products. Economically, the hybrid process is viable. It exhibits an estimated operational cost below $0.80/m^3$ and an energy consumption of 3.5 kWh/m^3, while generating a relatively low sludge volume of 220 mg/L (0.3 kg/m^3) (Mofrad et al., 2025).

c) Chemical and heterogeneous oxidation

Chemical oxidation becomes indispensable when pollutant concentrations exceed the functional thresholds for enzymatic stability or biological tolerance. Among these methods, ozonation exploits the high redox potential of ozone (O_3) to cleave aromatic structures. The absolute efficacy of this process is heavily dependent on *pH* conditions. The reaction is significantly more effective in the

alkaline range (*pH* 11.8–13.6), where ozone decomposes to generate non-selective •OH radicals that rapidly attack CAT. In contrast, acidic conditions favor a slower, more selective direct electrophilic attack by molecular ozone. While the degradation of the parent compound is rapid, complete mineralization remains challenging, as evidenced by a maximum COD reduction of only 53% observed at *pH* 11.8 (Parisheva & Demirev, 2001). Furthermore, studies on the heterogeneous oxidation of CAT in atmospheric aerosols indicate that reactive ozone uptake at the air-solid interface is maximized at 90% relative humidity. This observation highlights the broader environmental relevance of these oxidation pathways beyond conventional water treatment (Pillar-Little et al., 2015).

I.6.2.3 Biological degradation

Enzymatic treatment utilizes isolated enzymes to catalyze the oxidation of phenolic compounds. This targeted approach avoids the extreme pressures and temperatures required for thermochemical oxidation and minimizes the consumption of harsh synthetic reagents.

a) Peroxidase systems

Peroxidases catalyze the oxidation of phenolic substrates using hydrogen peroxide as a terminal electron acceptor. Recent investigations have evaluated Arugula Peroxidase as a cost-effective biocatalyst for pollutant remediation. AP demonstrates high efficacy, achieving near-complete elimination (95%) of CAT within 3 hours. The degradation follows pseudo-first-order kinetics with a specific rate constant of $2.8 \pm 0.2 \times 10^{-2}$ min^{-1}. The enzyme exhibits favorable Michaelis-Menten parameters, reporting a Michaelis constant (K_m) of 0.109 mM and a maximum velocity (V_{max}) of 0.0162 mmol/min. These kinetics indicate high substrate affinity, although comparative studies reveal an even greater affinity for resorcinol. AP functions optimally at pH 5.7 and 40 °C. The acidic pH optimum is essential for maintaining the appropriate protonation state of the active site histidine residues required for the catalytic cycle. While the enzyme retains activity across a broad temperature range (10 to 70 °C), it exhibits maximum long-term stability when stored at 4 °C. The ability to operate effectively at mild temperatures (40 °C) offers a distinct engineering advantage over thermal incineration, significantly reducing process energy consumption (Saleh et al., 2025).

b) Laccase-mediated oxidation

Laccases are multicopper oxidases that utilize molecular oxygen (O_2) rather than hydrogen peroxide to oxidize phenols. This mechanism offers a cleaner remediation pathway by reducing the system's dependence on stoichiometric chemical oxidants. While free laccase typically exhibits maximum activity at *pH* 8.0, immobilization on solid supports (such as magnetic nanoparticles) shifts the optimal

pH range toward more acidic conditions (pH 5-6) and considerably broadens the operational window (Yadav et al., 2021). Degradation efficiency can be enhanced by adding redox mediators such as vanillin or 2,2'-azino-bis(3-ethylbenzothiazoline-6-sulfonic acid) (ABTS). Specifically, the laccase-vanillin system enhances catalytic performance by overcoming steric hindrances that otherwise impede enzyme-substrate docking (Gałązka et al., 2023). A distinct physical advantage of laccase-mediated treatment is the induced mechanism of oxidative polymerization. This pathway converts toxic CAT monomers into insoluble poly(CAT), which can then be precipitated and removed via simple mechanical filtration. Subsequent thermal analysis confirms this structural transformation, revealing distinct thermal degradation profiles for the synthesized polymer compared to the initial monomer. This confirmation validates the overall efficacy of the polymerization pathway for phenolic remediation (Su et al., 2018).

I.6.3 Acetamiprid remediation

ACE presents a formidable challenge for complete mineralization due to its chemically stable chloropyridinyl structure. Technologies targeting ACE removal must provide sufficient energy to cleave the highly recalcitrant pyridine ring. Consequently, advanced electrochemical or photocatalytic methods are frequently required.

I.6.3.1 Adsorption by carbon-based adsorbent

The adsorptive removal of ACE exhibits significant performance disparities between engineered carbons and low-cost biochars. These differences are largely determined by the materials' textural properties and surface chemistry. Sludge-based activated carbons prepared via chemical activation with zinc chloride ($ZnCl_2$) demonstrate substantial adsorption capacities, reported up to 128.9 mg/g. This high capacity is directly attributed to their extensive microporosity and large surface area, which effectively trap the target pollutant (Sanz-Santos et al., 2021).

In contrast, biochar derived from eucalyptus wood chips shows markedly lower efficacy (4.87–5 mg/g). This discrepancy is primarily attributed to steric hindrance. The bulky aromatic entity of the ACE molecule requires specific pore dimensions and complementary functional groups to facilitate π–π interactions. While these features are abundant in optimized activated carbons, they are sparse in raw biochars, where the large adsorbate molecules can block pores and prevent multilayer adsorption. Despite these capacity differences, equilibrium data for both materials generally fit the Langmuir isotherm model, indicating that monolayer coverage remains the primary adsorption mechanism

(Srikhaow et al., 2022). Additionally, Multi-Walled Carbon Nanotubes (MWCNTs) offer intermediate performance (76.92 mg/g) characterized by rapid kinetics. This rapid uptake is due to the nanotube's highly accessible outer surface (Abualnaja et al., 2021).

I.6.3.2 Electrochemical advanced oxidation processes

Electrochemical advanced oxidation processes (EAOPs) utilize electrolytic cells to generate highly reactive oxidants in situ. The nature of the anode material heavily dictates the overall efficiency of these systems. The Boron-Doped Diamond (BDD) anode is widely recognized as the benchmark material for electrochemical incineration. Its wide potential window and high oxygen evolution overpotential strongly favor the generation of quasi-free hydroxyl radicals (BDD(•OH)) loosely adsorbed on the electrode surface.

Comparative studies at low pollutant concentrations (30 mg/L) indicate that both BDD and Dimensionally Stable Anode (DSA, TiO_2-RuO_2-IrO_2) exhibit the capability to degrade ACE. However, DSA performance is kinetically limited and requires elevated current densities (such as 90 mA/cm^2) and extended reaction times (up to 180 min) to achieve complete removal. As the ACE concentration increases to 300 mg/L, the superiority of BDD becomes far more pronounced. At this concentration, BDD achieves up to 71.4% COD removal at 90 mA/cm^2, whereas DSA shows minimal improvement in mineralization (Nunes de Morais et al., 2023). Lead dioxide (PbO_2) anodes represent an alternative with promising performance, attaining 96.8% degradation efficiency at lower concentrations (10 mg/L) within 90 min [(Kaludjerović et al., 2025).

The degradation pathway primarily involves anodic oxidation, in which non-selective •OH radicals attack the pyridine ring and the acyclic chain. Differential Pulse Polarography (DPP) studies confirm this mechanism, indicating first-order kinetics that scale with increasing current density (Kashid, 2025). Although BDD provides enhanced mineralization efficiency, its high energy consumption remains a practical limitation. Therefore, optimizing the applied current density is essential to balance diffusion-controlled oxidation with parasitic oxygen evolution.

I.6.3.3 Heterogeneous photocatalysis

Photocatalysis offers a solar-driven alternative to electrochemical methods. Graphitic Carbon Nitride (g-C_3N_4) has emerged as an effective metal-free semiconductor due to its strong visible-light responsiveness. When coupled with titanium dioxide (TiO_2), it forms a highly efficient heterojunction that significantly suppresses electron-hole recombination. This specific composite typically operates

via a Type-II or Z-scheme mechanism. This configuration facilitates the migration of photogenerated electrons to the conduction band of the lower-potential component to form $\bullet O_2^-$, while holes accumulate in the valence band to generate •OH (Kobkeatthawin et al., 2022; Pham et al., 2021).

The chemical degradation pathway proceeds via a stepwise oxidation, involving cleavage of the pyridine ring and the nitrile group. This reaction yields simpler intermediates such as 6-chloronicotinic acid, acetaldehyde, and formic acid (Guzsvány et al., 2009). Furthermore, the TiO_2/g-C_3N_4 composite exhibits excellent structural stability, maintaining robust catalytic performance across multiple recycling loops.

I.7 Comparative summary between MO, CAT, and ACE

The preceding analysis of MO, CAT, and ACE demonstrates that despite their disparate industrial origins and commercial applications, each compound presents severe environmental management challenges driven by chemical stability and complex biological interactions. **Table I.4** summarizes the specific toxicological hazards and environmental profiles associated with these three target pollutants.

Table I.4 Comparative toxicological and environmental profile

Feature	MO	CAT	ACE
Chemical Class	Azo Dye (Anionic)	Phenolic Intermediate	Neonicotinoid (Cyanoimine)
Primary Use	pH Indicator, Textile Dye	Pesticide Precursor, Flavoring	Crop Insecticide
Acute Mammalian Toxicity	High (Rat LD50 ~60 mg/kg)	Moderate (Rat LD50 ~300 mg/kg)	Low (Rat LD50 >140 mg/kg)
Specific Toxicity Target	DNA (via aromatic amines)	Melanocytes (via Tyrosinase)	nAChR (Neurotoxicity)
Key Environmental Hazard	Light Attenuation in water; Recalcitrance	Aquatic Toxicity; Microbial inhibition	Groundwater Leaching; Anaerobic persistence
Critical Management Issue	Treatment of azo-effluents	Control of dermal/inhalation exposure	Protection of aquatic invertebrates

I.8 Conclusion

This chapter provides a comprehensive review of the severe environmental and human health challenges associated with the continuous discharge of complex organic pollutants. The analysis

specifically focuses on MO, CAT, and ACE. An in-depth evaluation of their physicochemical properties, toxicological profiles, and environmental persistence demonstrates that these contaminants are highly recalcitrant to conventional biological and primary wastewater treatment methodologies.

A critical assessment of advanced remediation strategies, ranging from AOPs and membrane filtration to biological degradation, reveals that each technology possesses inherent operational and economic limitations. AOPs and membrane systems often exhibit high energy consumption, complex operational requirements, and the formation of toxic secondary by-products. Consequently, adsorption remains the most viable, efficient, and economically sustainable technology for the advanced treatment of these effluents.

In particular, the transition toward utilizing low-cost, renewable lignocellulosic biomass (including agricultural residues) for the synthesis of activated carbon effectively addresses dual objectives in solid waste management and water purification. Furthermore, current literature indicates that functionalizing these carbonaceous matrices with metal oxides, such as ZnO, can synergistically enhance their chemical affinity, catalytic potential, and overall adsorption capacity for multi-class pollutants.

Having established the environmental necessity and the technological advantages of functionalized carbon-based adsorbents, it is essential to understand the physicochemical laws and mathematical models governing their performance. Therefore, the subsequent chapter delineates the theoretical principles of adsorption, the structural chemistry of activated carbon, and the advanced modeling frameworks required to optimize these complex remediation systems.

Chapter II: Theoretical Principles of Adsorption, Process Modeling and Optimization

* * * * *

II.1 Introduction

The preceding chapter established the environmental context and the imperative to remediate pollutants such as dyes, phenols, and pesticides. Building on that foundation, the successful design and optimization of an effective treatment system require a rigorous understanding of the governing physical, chemical, and mathematical principles. Consequently, this chapter delineates the theoretical framework underlying the experimental methodologies and analytical models used throughout this research.

The analysis begins with a systematic examination of adsorption principles. It elucidates the fundamental mechanics of adsorbate-adsorbent interactions, mass transport in porous matrices, and the physicochemical parameters that govern process efficiency. Furthermore, the text provides a comprehensive overview of the mathematical modeling of adsorption systems. This overview explicitly covers the formulation of equilibrium isotherms, the derivation of kinetic rate equations, and the calculation of standard thermodynamic parameters.

Subsequently, the discussion addresses the structural chemistry and microcrystalline properties of activated carbon. This section highlights the transition from conventional fossil-based precursors to the sustainable use of abundant lignocellulosic agricultural residues.

Beyond fundamental physical chemistry, the latter half of the chapter introduces advanced statistical and computational modeling frameworks required for process optimization. It details the theoretical basis of RSM for optimizing multivariate systems. Additionally, it outlines the architecture of an ANN coupled with a GA for high-fidelity predictive modeling and offers a critical comparison of their respective technical advantages.

Finally, the chapter examines the fluid dynamics of continuous-flow adsorption systems. It presents the mathematical models used to predict breakthrough curves in fixed-bed columns, thereby bridging the gap between batch-scale theoretical kinetics and practical industrial applications.

II.2 Principles of adsorption

Adsorption is a cornerstone of surface science and interface engineering. It underpins critical

applications ranging from environmental remediation and water treatment to heterogeneous catalysis and gas separation. Fundamentally, adsorption is a mass transfer operation. It involves the accumulation of molecular species at the interface between two phases, typically a solid (the adsorbent) and a fluid (the adsorbate) (Patra & Narayanasamy, 2022). Unlike absorption, which is a volumetric process in which a substance permeates the bulk of another phase, adsorption remains strictly a surface phenomenon. The thermodynamic imperative drives this process to reduce interfacial energy.

The atoms on the surface of a solid lattice exist in a state of unsaturation. Unlike bulk atoms surrounded by nearest neighbors with balanced interatomic forces, surface atoms exhibit residual attractive forces perpendicular to the surface plane. These unbalanced valencies generate high surface energy. Consequently, they create a thermodynamic driving force that attracts and retains molecular species from the adjacent fluid phase to satisfy these forces and lower the system's total free energy (Bansal & Goyal, 2005; Faust & Aly, 2013; Marsh & Rodriguez-Reinonso, 2006; Tewari, 1981; Tien, 1994). This section provides a comprehensive theoretical examination of the principles governing adsorption. It details fundamental definitions, factors influencing the process, equilibrium isotherm modeling, kinetic dynamics, and thermodynamic analysis.

II.2.1 Definitions and concepts

Establishing a rigorous academic framework for adsorption studies requires a clear delineation of primary components and interaction mechanisms. The terminology utilized here strictly aligns with the recommendations of the International Union of Pure and Applied Chemistry (IUPAC). The foundational concepts of adsorption are visually represented in **Figure II.1**.

II.2.1.1 Adsorbate and adsorbent

The adsorbate is the molecular species that undergoes accumulation at the interface. In wastewater treatment, this typically refers to the targeted pollutant (e.g., heavy metal ions, synthetic dyes, or pharmaceutical compounds) removed from the aqueous phase. Conversely, the adsorbent is the solid substrate providing the active surface area for this accumulation (Machado, 2015). The efficacy of an adsorbent depends heavily on its specific surface area and internal pore structure. These physical characteristics dictate the overall accessibility of active sites to the adsorbate molecules. The reverse process, where adsorbed species are released back into the bulk fluid phase, is termed desorption. Understanding desorption is essential for evaluating the regeneration potential and long-term

reusability of engineered adsorbent materials (Worch, 2012). The interaction between adsorbate and adsorbent is formally classified into two distinct categories based on the nature and magnitude of the forces involved: physisorption (physical adsorption) and chemisorption (chemical adsorption).

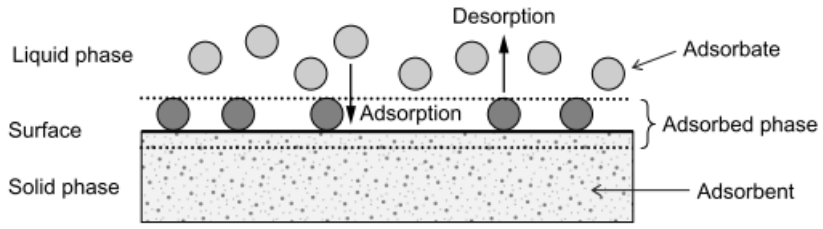

Figure II.1 Basic concepts of adsorption (Worch, 2012)

II.2.1.2 Physisorption

Physisorption involves the formation of non-specific, weak intermolecular bonds between the adsorbate and the adsorbent surface. These interactions are primarily governed by van der Waals forces, encompassing London dispersion forces and dipole-dipole interactions (Bhuyan & Ahmaruzzaman, 2023; Tran et al., 2016). Because these attractive forces are ubiquitous, physisorption can theoretically occur in any solid-fluid system under favorable temperature and pressure conditions. Thermodynamically, physisorption is an exothermic process. However, the heat of adsorption (ΔH_{ads}) remains relatively low, typically falling between 20 and 40 kJ/mol. This magnitude closely mirrors the enthalpy of condensation, reflecting the strictly physical nature of the interfacial bonding.

A defining feature of physisorption is its high reversibility. Because the energy barrier to desorption is low, simply increasing the system temperature or reducing the adsorbate partial pressure readily facilitates molecular release (Tran et al., 2016). Structurally, physisorption is not confined to monolayer coverage. Once an initial molecular layer coats the surface, subsequent layers can accumulate via adsorbate-adsorbate interactions, leading to multilayer adsorption. This phenomenon becomes particularly dominant in systems featuring high adsorbate concentrations, where the adsorbed phase behaves much like a condensed liquid film. Furthermore, physisorption requires negligible activation energy (E_a). The process proceeds rapidly, and equilibrium is achieved quickly, limited predominantly by the adsorbate's diffusion rate to the solid surface (Alharbi et al., 2022; Rouquerol et al., 2013).

II.2.1.3 Chemisorption

Chemisorption entails the formation of strong, specific chemical bonds between the adsorbate molecules and localized active sites on the adsorbent matrix (Bhuyan & Ahmaruzzaman, 2023). These bonds may be covalent, ionic, or metallic (Pirilä, 2015). Unlike physisorption, chemisorption exhibits strict chemical specificity. It occurs only when the adsorbate and the adsorbent possess complementary functional groups that can react. A common example is the complexation of a heavy metal ion with a carboxyl moiety on a biochar surface (Marsh & Rodriguez-Reinonso, 2006).

The enthalpy of adsorption for chemisorption is substantially higher than that observed in physisorption, typically ranging from 80 to 400 kJ/mol. This elevated energy release serves as a definitive indicator of true chemical bond formation. Given the strength of these coordinate or covalent bonds, chemisorption is generally considered irreversible under standard ambient conditions. Reversing the process to regenerate the surface often demands significant energy input, such as intense thermal treatment or aggressive chemical elution (Tran et al., 2016).

Table II.1 Comparative analysis of physisorption and chemisorption

Characteristic	Physisorption (physical adsorption)	Chemisorption (chemical adsorption)
Nature of Forces	Weak van der Waals forces (London dispersion forces, dipole-dipole interactions).	Strong chemical bonds (covalent, ionic, metallic).
Specificity	Non-specific; occurs on any surface under favorable conditions.	Highly specific; requires complementary functional groups.
Heat of Adsorption (ΔH)	Low (20–40 kJ/mol); comparable to the heat of condensation.	High (80–400 kJ/mol); comparable to the heat of reaction.
Reversibility	Generally reversible; desorption occurs via heating or pressure reduction.	Generally irreversible; requires high energy or chemical reagents to reverse.
Temperature Effect	Exothermic; adsorption decreases as temperature increases.	Exothermic, but activated; rate may increase with T; equilibrium capacity decreases.
Activation Energy	Negligible; rapid equilibrium.	Appreciable; activated complex formation required.
Molecular Layering	Multilayer adsorption is possible (BET type).	Restricted to Monolayer adsorption (Langmuir type).

A major structural constraint of chemisorption is its absolute restriction to monolayer coverage. Once the specific active sites on the surface react with the adsorbate, no further chemical bonding can occur

at those sites, precluding multilayer formation via this mechanism. Additionally, chemisorption is an activated process requiring a measurable activation energy to overcome the reaction barrier. Consequently, while physisorption capacities universally decrease with increasing temperature, the chemisorption rate may initially increase with temperature as the system surpasses the activation energy threshold (E_a) (Tran et al., 2016). The fundamental distinctions between these two mechanisms are summarized in **Table II.1**.

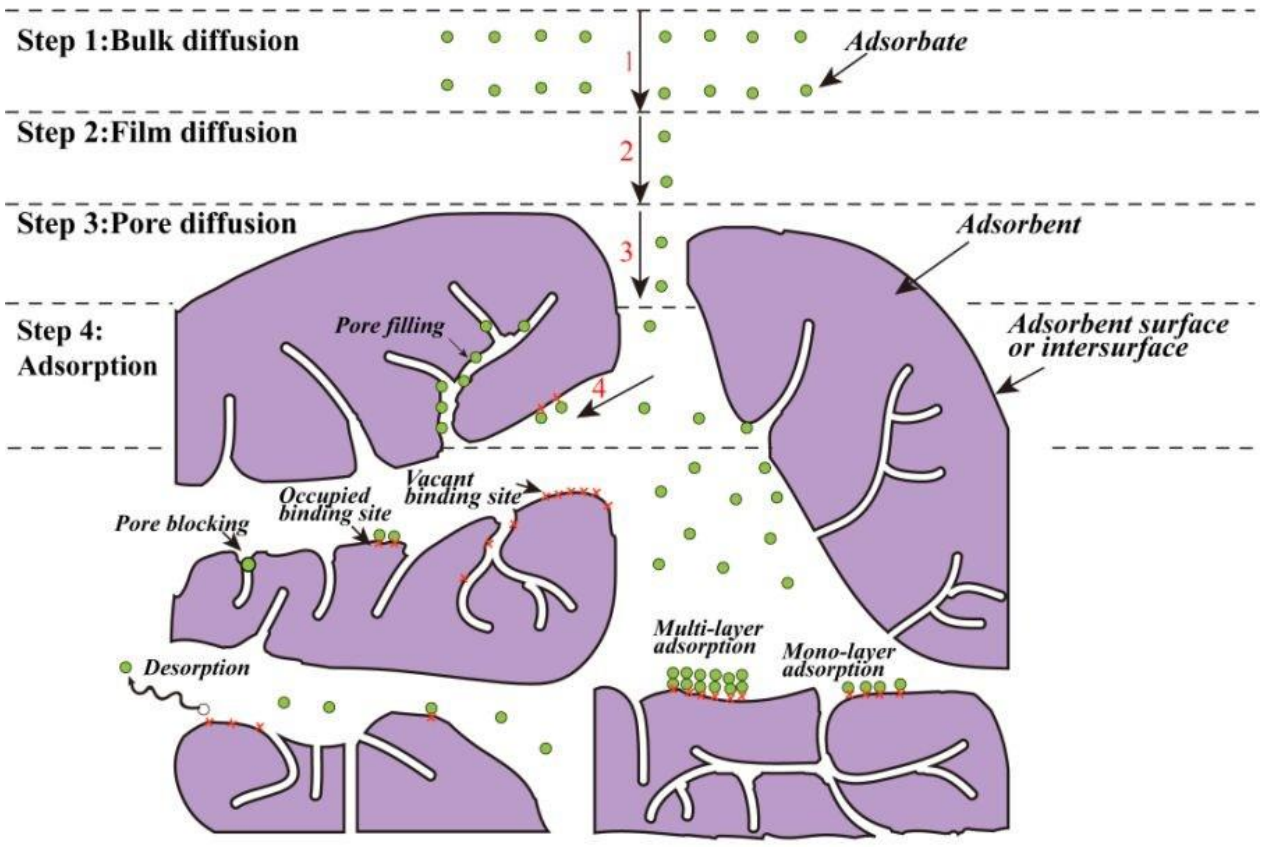

Figure II.2 Schematic representation of the four stages of mass transfer during the adsorption process (Wang et al., 2020)

II.2.2 Mechanics of mass transport in porous adsorbents

The transport of an adsorbate from the bulk solution to the internal surface of a porous adsorbent follows a well-defined four-stage sequence originally proposed by (Tran, You, Hosseini-Bandegharaei, et al., 2017; Weber Jr, 1984). The process begins with bulk transport, in which the adsorbate moves rapidly through the fluid phase. This is immediately followed by external film diffusion across the hydrodynamic boundary layer to the particle's exterior surface. The third and most critical phase is intraparticle diffusion. During this stage, molecules penetrate the internal porous

network via pore-volume or surface diffusion pathways. Finally, adsorptive attachment occurs at the active binding sites. Because bulk transport and surface attachment typically occur at high velocities, the overall adsorption rate is generally controlled by mass-transfer resistances associated with either film or intraparticle diffusion. This sequential mechanism is visually represented in **Figure II.2**.

II.2.3 Factors affecting adsorption

The adsorption process is a dynamic interaction governed by multiple physicochemical parameters. A rigorous understanding of these operational factors is essential for optimizing experimental conditions and interpreting subsequent kinetic and equilibrium data.

II.2.3.1 Effect of solution pH and point of zero charge

In liquid-phase adsorption, particularly for ionic species such as heavy metals and ionizable organic dyes, solution *pH* is the primary controlling parameter. The *pH* dictates the overall adsorption efficiency through two simultaneous, interacting mechanisms: the structural speciation of the adsorbate and the adsorbent surface charge.

The surface charge of an adsorbent matrix is characterized by the Point of Zero Charge (pH_{PZC}). This is the *pH* at which the net surface charge density equals zero. This parameter is fundamental for predicting electrostatic interactions within the system (Al-Maliky et al., 2021; Dvoynenko et al., 2021; Faizal et al., 2023).

- Behavior at $pH < pH_{PZC}$

Under acidic conditions, the concentration of Hydrogen Ions (H^+) in the solution is high. This abundance leads to the protonation of surface functional groups (for example, $–NH_2 + H^+ \rightarrow –NH^{3+}$, $–OH + H^+ \rightarrow –OH^{2+}$). Consequently, the adsorbent surface acquires a net positive charge. This condition electrostatically repels cationic adsorbates (such as Cd^{2+}, Pb^{2+}, or Methylene Blue) but highly favors the adsorption of anionic species (such as $Cr_2O_7^{2-}$ or MO) due to strong coulombic attraction.

- Behavior at $pH > pH_{PZC}$

In alkaline environments, the concentration of Hydroxide Ions ($OH^–$) increases. This induces the deprotonation of surface groups (for example, $–COOH \rightarrow –COO^– + H^+$). The surface subsequently develops a net negative charge. This state favors the adsorption of cationic species via electrostatic attraction while simultaneously repelling anionic adsorbates.

Concurrently, the solution *pH* governs the chemical speciation of the adsorbate (Al-Hazeef et al., 2024). For example, Chromium (VI) exists primarily as $HCrO^{4-}$ at low *pH* and transitions to CrO_4^{2-} at high *pH*. Similarly, complex organics such as tetracycline can exist as cations, zwitterions, or anions depending on their specific *pKa* values (Christl et al., 2016; Huang et al., 2021; Krishnani et al., 2013; Zhang et al., 2014). Therefore, the optimal adsorption *pH* occurs where the electrostatic attraction between the dominant adsorbate species and the highly charged adsorbent surface is maximized.

Furthermore, extreme *pH* conditions introduce secondary limiting factors. At very low *pH*, the high concentration of H^+ ions often directly competes with cationic adsorbates for available binding sites, significantly reducing removal efficiency. Conversely, at very high *pH*, heavy metal ions tend to precipitate out of solution as insoluble hydroxides ($M(OH)_2$). This shifts the primary removal mechanism from true surface adsorption to macroscopic chemical precipitation (Krishnani et al., 2013).

II.2.3.2 Effect of temperature

Temperature functions as a fundamental thermodynamic determinant in the adsorption process. It concurrently influences equilibrium capacity and kinetic rates.

- Exothermic processes

In physical adsorption (Tcheka et al., 2024) and specific chemisorption processes (Ladadok et al., 2018; Ren, 2011) exhibiting a negative Standard Enthalpy Change(ΔH°), an increase in temperature shifts the equilibrium backward. This behavior strictly follows Le Chatelier's principle (Gabelman, 2017). Consequently, the adsorption capacity decreases at higher temperatures. Physically, this reduction is attributed to the elevated thermal kinetic energy of the adsorbed molecules. This increased energy provides the necessary momentum for the molecules to overcome attractive forces and desorb from the surface vibrational wells.

- Endothermic processes

Conversely, processes characterized by a positive ΔH° exhibit an increase in adsorption capacity with increasing temperature. This phenomenon frequently occurs in chemisorption systems that require a high activation energy. It is also prevalent in porous adsorbents where applied heat induces structural swelling. Furthermore, elevated thermal energy increases the diffusion rate of large adsorbate molecules into internal microporous networks.

- Viscosity and diffusion

Beyond shifting equilibrium states, temperature profoundly affects mass transfer mechanisms. Elevated temperatures reduce solvent viscosity, thereby increasing the diffusion coefficient of the targeted adsorbate. This enhanced mobility accelerates molecular transport across the external hydrodynamic boundary layer and deeper into the internal pore matrix. Ultimately, this accelerated transport significantly shortens the time required for the system to achieve equilibrium ("Factors Affecting the Adsorption of Some Ionic Dyes on the Surface of Modify CaO from Eggshell," 2019).

II.2.3.3 Initial adsorbate concentration

The Initial Adsorbate Concentration (C_0) serves as the primary thermodynamic driving force necessary to overcome mass transfer resistances at the solid-liquid interface. Increasing C_0 inherently intensifies the concentration gradient. This intensification enhances the mass transfer driving force, ultimately yielding a higher equilibrium loading capacity (q_e).

Despite the rise in unit capacity, the overall Removal Efficiency (R %) generally declines at elevated concentrations due to progressive surface saturation. In highly dilute solutions, active binding sites are present in vast stoichiometric excess relative to the adsorbate, facilitating near-complete removal. As the initial concentration increases, the fixed finite number of available binding sites becomes saturated. This limitation prevents further uptake and results in a substantially lower percentage of the total adsorbate being removed from the aqueous phase (Rápó & Tonk, 2021).

II.2.3.4 Adsorbent dosage

The mass of adsorbent introduced into the system constitutes a highly critical operational parameter. It directly dictates the absolute number of active sites available for molecular binding. Increasing the adsorbent dosage typically improves the overall pollutant removal efficiency. This enhancement is a direct consequence of providing an expanded specific surface area and a greater abundance of accessible functional groups.

However, the q_e frequently exhibits a contradictory trend, demonstrating a marked decrease as adsorbent dosage increases. This specific behavior is commonly defined as the solid concentration effect. It primarily results from particle agglomeration occurring at high solid-to-liquid loadings. This aggregation physically obscures active sites and reduces the effective surface area available for interaction. Furthermore, agglomeration induces particle overlap, which significantly extends the intraparticle diffusion path length. These combined physical restrictions limit the overall adsorption efficiency per unit mass (Rápó & Tonk, 2021; Tcheka et al., 2024).

II.2.3.5 Ionic strength

Industrial and natural wastewaters invariably contain background electrolytes (such as NaCl and $CaCl_2$). These dissolved salts introduce variations in ionic strength that heavily influence both adsorption kinetics and equilibrium states. The impact of ionic strength remains highly complex and is typically governed by three competing physical mechanisms (Al-Hazeef et al., 2024; Hu et al., 2013; Tran, You, & Chao, 2017; Wang et al., 2021).

First, elevated ionic strength compresses the electrical double layer surrounding the adsorbent particle. This physical phenomenon is recognized as electrostatic screening. In processes driven primarily by electrostatic attraction (for example, cationic heavy-metal removal on a negatively charged carbon matrix), this screening significantly reduces the effective surface potential. The weakened coulombic attraction consequently reduces the overall adsorption capacity.

Second, an excess of background ions initiates competitive adsorption. In processes reliant on ion exchange, background cations (such as Na^+ or K^+) and anions (such as Cl^- or SO_4^{2-}) compete directly with the target adsorbate for occupancy at specific active binding sites.

Third, high salinity can induce a salting-out effect, which primarily impacts hydrophobic organic adsorbates. Elevated salt concentrations suppress the aqueous solubility of these organic molecules. This suppression induces thermodynamic instability in the fluid phase, driving the hydrophobic species toward the solid-liquid interface. In these systems, an increase in ionic strength often enhances macroscopic adsorption performance.

II.2.4 Adsorption equilibrium (isotherms)

The adsorption isotherm constitutes the most fundamental mathematical relationship for the characterization and design of solid-liquid interface systems. It describes the equilibrium distribution of the adsorbate between the solid phase (q_e, mg/g) and the bulk fluid phase (C_e, mg/L) at a constant temperature. Rigorous mathematical modeling of this equilibrium data yields critical insights into the macroscopic adsorption capacity, the energetic distribution of active binding sites (homogeneous versus heterogeneous), and the specific physical chemistry of the adsorbate-adsorbent interactions.

II.2.4.1 Langmuir isotherm

Originally formulated for gas-solid systems, the Langmuir model remains the principal theoretical framework for liquid-phase adsorption. The model postulates that adsorption involves monolayer coverage on a structurally homogeneous surface (Chen, 2015). It relies on four key mechanistic

assumptions (Tran, You, Hosseini-Bandegharaei, et al., 2017). First, adsorption is limited to a discrete monolayer; once a specific active site is occupied, no subsequent molecular accumulation can occur at those coordinates. Second, the solid surface is assumed to be energetically homogeneous, meaning all sites possess identical binding affinities. Third, the model precludes any lateral intermolecular interactions between adjacent adsorbed molecules. Finally, the adsorption process is inherently reversible.

The mathematical expression of the Langmuir equation (Al-Ghouti & Da'ana, 2020) is:

$$q_e = \frac{q_m K_L C_e}{1 + K_L C_e} \qquad \textbf{Eq. II.1}$$

Where q_e denotes the equilibrium adsorption capacity (mg/g), q_m represents the Theoretical Maximum Monolayer Capacity (mg/g), and K_L is the Langmuir equilibrium constant related to site affinity and the free energy of adsorption (L/mg).

The defining physical characteristic of the Langmuir isotherm is its prediction of an absolute saturation limit (q_m) at elevated concentrations. Process feasibility within this framework is frequently evaluated using a dimensionless Separation Factor (R_L), defined as:

$$R_L = \frac{1}{1 + K_L C_0} \qquad \textbf{Eq. II.2}$$

Where C_0 represents the initial adsorbate concentration, the magnitude of R_L dictates the isotherm profile: $R_L > 1$ indicates unfavorable adsorption; $R_L = 1$ reflects linear (Henry's Law) behavior; $0 <$ RL < 1 signifies highly favorable adsorption; and $R_L = 0$ denotes an irreversible process.

II.2.4.2 Freundlich isotherm

The Freundlich model provides an empirical equation for describing multilayer adsorption on highly heterogeneous surfaces. In contrast to the Langmuir theory, it explicitly rejects the assumption of energetic surface homogeneity. The model postulates that the adsorbent surface features a diverse distribution of active sites with varying adsorption energies (Murphy et al., 2023). High-affinity sites are initially occupied, and the heat of adsorption subsequently decays exponentially as surface coverage increases.

The Freundlich equation (Tran, You, Hosseini-Bandegharaei, et al., 2017) is mathematically expressed as:

$$q_e = K_F C_e^{1/n} \quad \textbf{Eq. II.3}$$

Where K_F (mg/g)/(L/mg)$^{1/n}$ is the Freundlich Constant indicative of relative adsorption capacity, and the exponent $1/n$ acts as a Heterogeneity Factor. Specifically, $1/n > 1$ indicates an unfavorable process, $1/n = 1$ represents linear adsorption, and $0 < 1/n < 1$ denotes a favorable interaction.

A major structural limitation of the Freundlich equation is its failure to predict a finite saturation limit. The model theoretically assumes that unit capacity (q_e) increases indefinitely with rising residual concentration (C_e). This assumption introduces significant predictive error at extremely high adsorbate concentrations.

II.2.4.3 Advanced adsorption isotherms

Beyond the classical Langmuir and Freundlich paradigms, advanced multi-parameter isotherm models provide a deeper analytical resolution for systems exhibiting complex multilayer phenomena and energetic heterogeneity. The **Dubinin-Radushkevich (D-R)** model applies specifically to porous architectures. It calculates the Mean Free Energy of Adsorption (E, kJ/mol) to distinguish mathematically between physical and chemical adsorption mechanisms.

To bridge the operational gap between ideal and non-ideal behaviors, hybrid three-parameter equations (such as the **Redlich-Peterson** and **Sips** models) were engineered. These formulations combine elements of both the Langmuir and the Freundlich theories to address inaccuracies at extreme concentrations. They successfully converge to Henry's law behavior at low concentrations and establish defined saturation limits at high concentrations.

Furthermore, models such as the **Khan** and **Toth** equations provide refined mathematical descriptions for highly heterogeneous matrices. The Toth equation proves specifically advantageous for characterizing quasi-Gaussian energy distributions across solid interfaces. Finally, the **Liu** isotherm integrates the Langmuir framework with a discrete distribution of equilibrium constants. This specific synthesis provides a highly robust fit for solid-liquid systems in which the active functional groups exhibit a broad continuum of binding energies. A more detailed mathematical formulation of these advanced models is provided in the **Appendix. B**.

II.2.5 Adsorption kinetics

Kinetic modeling is indispensable for the design of adsorption columns and batch reactors. It dictates the solute uptake rate and establishes the residence time required to complete the treatment process.

The kinetics of adsorption define the dependence of the macroscopic adsorption rate on both the initial adsorbate concentration and the physical nature of the solid surface. Furthermore, rigorous kinetic analysis isolates the primary rate-limiting step, distinguishing explicitly between mass-transfer and chemical reaction control.

Adsorption kinetics characterize the time-dependent progression of the molecular accumulation process. The mathematical formulation describes the relationship between the adsorbate capacity per unit weight of adsorbent (q_t, mg/g) and the specific contact time (t) necessary to achieve equilibrium (Kostoglou & Karapantsios, 2022; Revellame et al., 2020; Sangoremi, 2025). Mathematical modeling of these dynamic data yields fundamental physical insights into the primary rate-controlling mechanisms, including external film mass transfer and intraparticle diffusion. Consequently, accurate kinetic evaluation remains strictly required for the design, scale-up, and operational optimization of industrial adsorption systems.

This section provides a comprehensive review of the theoretical frameworks, governing equations, and physical limitations of the most widely used adsorption kinetic models. The subsequent discussion evaluates the Pseudo-First-Order (PFO), Pseudo-Second-Order (PSO), Elovich, and Weber-Morris models. This analysis synthesizes critical reviews and physicochemical interpretations established by Wang and Guo (2020), Zhang (2019), and Tran, You, Hosseini-Bandegharaei, et al. (2017).

II.2.5.1 Pseudo-First Order model

The PSO model, initially proposed by Lagergren (1898), remains one of the most common mathematical frameworks utilized to describe adsorption rates within liquid-solid systems.

The model assumes that the rate of change in solute uptake is directly proportional to the difference between the equilibrium adsorption capacity and the transient capacity observed at any specific time. It maintains theoretical consistency with the Linear Driving Force (LDF) model strictly when the associated adsorption isotherm exhibits linear behavior.

The kinetic equation is expressed as:

$$q_t = q_e(1 - exp^{(-k_1 t)}) \qquad \textbf{Eq. II.4}$$

Where q_t denotes the transient adsorption capacity at time t (mg/g), q_e represents the equilibrium adsorption capacity (mg/g), and k_1 is the specific PFO rate constant (min^{-1} or h^{-1}).

Regarding physical applicability, the model generally achieves high accuracy at high initial adsorbate

concentrations. It also effectively describes the initial rapid stages of the adsorption process or systems in which the adsorbent has a limited number of active binding sites. However, the PFO model frequently fails to capture kinetic data over the entire operational time range. It typically exhibits high predictive accuracy solely during the initial 20 to 30 min of solid-liquid contact.

II.2.5.2 Pseudo-Second Order (PSO) model

The PSO model was initially proposed by Blanchard et al. (1984) and later popularized by Ho et al. (1996) for dye adsorption.

Theory and Assumptions:

It is frequently assumed that the adsorption rate is controlled by chemisorption involving valency forces through the sharing or exchange of electrons between the adsorbent and adsorbate. However, this conclusion is often drawn purely from model fitting rather than analytical evidence.

The PSO model was originally formulated by Blanchard et al. (1984) and subsequently popularized by Ho et al. (1996) for the specific evaluation of dye adsorption. A common theoretical assumption holds that chemisorption mechanisms strictly control the overall adsorption rate. These mechanisms involve strong valency forces driven by the exchange or sharing of electrons between the solid matrix and the adsorbate. However, this specific chemical conclusion is often derived purely from high statistical correlation during mathematical fitting rather than definitive analytical or spectroscopic evidence.

The PSO equation is mathematically expressed as:

$$q_t = \frac{{q_e}^2 k_2 t}{1 + q_e K_2 t} \qquad \textbf{Eq. II.5}$$

Where k_2 denotes the PSO rate constant (g/mg.min).

The PSO model typically provides a superior statistical fit when initial solute concentrations are low. It is particularly applicable during the final stages of the mass transfer process as the system approaches equilibrium, or in environments where the adsorbent matrix provides an abundant supply of active binding sites. A significant analytical limitation is the tendency for linear PSO plots to yield artificially high R^2 values ($R^2 > 0.99$). This statistical artifact can be misleading and does not inherently validate the underlying physical mechanism of the proposed chemisorption system.

II.2.5.3 Elovich model

Originally proposed by Roginsky and Zeldovich (1934), the Elovich model is extensively utilized to characterize the specific kinetics of chemisorption on highly heterogeneous solid surfaces.

The fundamental theoretical assumption postulates that the available adsorption sites are energetically heterogeneous. Furthermore, it assumes that the activation energy required for subsequent molecular adsorption increases linearly with the mass of the targeted adsorbate on the surface.

The Elovich equation is formulated as:

$$q_t = \frac{1}{\beta_e} \ln (1 + \alpha_e \beta t) \qquad \textbf{Eq. II.6}$$

Herein, α_e represents the initial adsorption rate (mg/g.min), and β_e functions as a desorption constant mathematically related to both the extent of surface coverage and the activation energy profile (g/mg).

This equation is highly useful for systems dominated by chemisorption, particularly in gas-solid interactions and specific liquid-solid interfaces. A major limitation is its strictly empirical nature, which often lacks an exact physical meaning across diverse liquid-solid systems. Furthermore, the common simplified linear adaptation inherently assumes that $\alpha_e * \beta_e * t$ is significantly greater than 1, an assumption that frequently introduces substantial mathematical error during early interaction intervals.

II.2.5.4 Weber-Morris intraparticle diffusion model

The Weber-Morris model is an essential analytical tool for isolating the primary rate-controlling step in complex adsorption matrices. It specifically evaluates whether molecular diffusion within the internal pores dictates the overall kinetic velocity.

The theoretical framework recognizes that adsorption into porous materials requires multiple distinct steps. These include bulk fluid transport, external film diffusion, intraparticle (pore) diffusion, and final physical or chemical attachment to active sites. The Weber-Morris model mathematically isolates the internal diffusion step (Weber Jr & Morris, 1963).

The characteristic equation is:

$$q_t = k_{IPD} \sqrt{t} + C_{IPD} \qquad \textbf{Eq. II.7}$$

Where k_{IPD} is the specific intraparticle diffusion rate constant (mg/g.min$^{0.5}$). The intercept C_{IPD}

provides a constant mathematically related to the thickness of the hydrodynamic boundary layer. A larger calculated C_{IPD} value indicates a more pronounced boundary-layer effect.

This model is systematically applied to distinguish between external film diffusion and intraparticle diffusion. A fundamental physical limitation dictates that for intraparticle diffusion to be identified as the sole rate-limiting step, the linear plot of q_t versus $t^{0.5}$ must strictly pass through the origin (C_{IPD} = 0). The presence of multiple linear segments in this plot clearly indicates that the mass transfer process is controlled sequentially by more than one distinct physical mechanism.

II.2.6 Adsorption thermodynamics

Adsorption thermodynamics offers a macroscopic perspective on the energetic transitions, process feasibility, and the fundamental nature of interactions at the solid-liquid interface. Evaluating the energy balance as an adsorbate moves from the bulk solution to the adsorbent surface enables researchers to characterize the driving forces and the degree of molecular disorder. Characterizing these systems relies strictly on the determination of three standard thermodynamic parameters: the standard Gibbs energy change (ΔG°), the ΔH°, and the standard entropy change (ΔS°).

This section provides a critical synthesis of the theoretical and mathematical frameworks governing adsorption thermodynamics. To ensure a rigorous physical interpretation and avoid common methodological pitfalls identified in the literature, this discussion incorporates the critical reviews and corrections established by recent analytical studies (Hai, 2017; Lima et al., 2020; Lima et al., 2019; Shahwan, 2021; Tran et al., 2021; Tran et al., 2016; Tran, You, Hosseini-Bandegharaei, et al., 2017).

II.2.6.1 Thermodynamic equilibrium constant

A significant portion of the existing literature on adsorption contains fundamental inconsistencies regarding the derivation of the thermodynamic equilibrium constant (K_{Eq}°). A prevalent mistake involves the direct use of the distribution coefficient ($K_D = q_e/C_e$, measured in L/g) as a dimensionless equilibrium constant. As highlighted by Tran (2022), this approach is mathematically invalid because K_D possesses physical dimensions. Taking the logarithm of a dimensional quantity in the van't Hoff equation is physically meaningless. This error inevitably leads to calculated values that vary arbitrarily depending on the chosen concentration units (e.g., L/mg versus mL/g).

The classic relationship is expressed as:

$$\Delta G^{\circ} = -RTlnK_{Eq}^{\circ} \quad \textbf{Eq. II.8}$$

Furthermore, many studies incorrectly calculate K_{Eq}° from a single experimental data point at each temperature. This simplification fails to account for the concentration dependence of the adsorption process. The K_D represents merely a single point on the isotherm rather than a true representation of the equilibrium state across the entire system.

To rectify these errors, the K_{Eq}° must be derived as a strictly dimensionless value. According to the rigorous framework proposed by Lima et al. (2019), K_{Eq}° should be calculated by converting the equilibrium constant derived from the best-fitted isotherm model (K_g, such as the Langmuir, Sips, or Liu constants).

The correct conversion formula is:

$$K_{Eq}^{\circ} = \frac{1000 \times K_g \times M_w \times [C^{\circ}]}{\gamma} \quad \textbf{Eq. II.9}$$

In this expression, the factor of 1000 converts the mass units of K_g (from L/mg to L/g). The term M_w represents the molecular weight of the adsorbate (g/mol), and C° indicates the unitary standard concentration (typically 1 mol/L as defined by IUPAC). The variable γ represents the activity coefficient. This coefficient is generally assumed to equal unity in the highly dilute solutions typical of water treatment studies. Utilizing this dimensionless constant ensures that the resulting ΔG° values remain thermodynamically consistent and entirely independent of the selected concentration units.

II.2.6.2 Re-evaluating Gibbs energy and spontaneity

Regarding the interpretation of Gibbs energy, academic standards have shifted away from the term Gibbs free energy in favor of ΔG°. The inclusion of the word free is now considered technically redundant. A common misconception in the literature is the use of ΔG° to define the absolute spontaneity of a reaction.

In strict thermodynamic terms, spontaneity is dictated by the Gibbs energy change (ΔG) under actual experimental conditions. Conversely, ΔG° refers exclusively to the system existing at standard states (1 mol/L). Therefore, a positive ΔG° strictly indicates that the equilibrium position favors the reactants under standard conditions. It does not preclude the adsorption process from being spontaneous under the actual experimental concentrations utilized in the laboratory.

II.2.6.3 van't Hoff analysis

The temperature dependence of K_{Eq}° allows for the determination of ΔH° and ΔS° via the van't Hoff equation. While the linear form of this equation (plotting ln K_{Eq}° versus $1/T$) is traditionally favored for its mathematical simplicity, recent critiques suggest it can introduce significant statistical bias.

The linear form is defined as:

$$lnK_{Eq}^{\circ} = -\frac{\Delta H^{\circ}}{R} \times \frac{1}{T} + \frac{\Delta S^{\circ}}{R} \qquad \textbf{Eq. II.10}$$

In this approach, ΔH° is derived from the slope, and ΔS° is calculated from the intercept. However, mathematical linearization often distorts the fundamental error structure of the experimental data.

To prevent this distortion, the nonlinear form is increasingly preferred:

$$K_{Eq}^{\circ} = exp\left(-\frac{\Delta H^{\circ}}{RT} + \frac{\Delta S^{\circ}}{R}\right) \qquad \textbf{Eq. II.11}$$

Contemporary studies strongly recommend utilizing nonlinear optimization to solve this specific equation directly. This advanced computational method preserves the integrity of experimental errors and yields a far more accurate estimate of the system's true energetic parameters.

II.3 Activated carbon

II.3.1 Definition

Activated carbon is a highly porous, amorphous carbonaceous material defined by an exceptionally large internal surface area and a complex network of microscopic pores. As a processed form of carbon with a high degree of microporosity, AC is traditionally produced by carbonizing and subsequently activating carbon-rich precursors (Dubey et al., 2020). This synthesis transforms the raw material into a powerful adsorbent capable of sequestering a wide range of pollutants from both liquid and gaseous phases. The overall efficacy of AC is typically quantified by its Specific Surface Area (S_{BET}). Standard materials display surface areas ranging from 957 (Shin et al., 2021) to 2100 (Masoumi & Dalai, 2020) m^2/g, while advanced engineered composites can exceed 3000 m^2/g (Gierak & Łazarska, 2017; Sen, 2017).

II.3.2 Microcrystalline structure of activated carbon

The fundamental structure of AC is best described as a disordered or rudimentary form of graphite

(Çeçen & Aktas, 2012; Worch, 2012). Ideal graphite consists of perfectly aligned, parallel layers of hexagonal carbon rings exhibiting sp^2 hybridization and maintained strictly by van der Waals forces (Bandosz, 2006), as shown in **Figure II.3**. Conversely, AC comprises a random, disorganized arrangement of microcrystalline graphitic platelets (Çeçen & Aktas, 2012; Worch, 2012). Covalent carbon-carbon bonds cross-link these platelets. This arrangement creates an imperfect matrix in which the internal layers are less ordered and exhibit a larger interlayer spacing (typically 0.34-0.35 nm) than the 0.335 nm characteristic of pure graphite (Bandosz, 2006; Bansal & Goyal, 2005).

The voids generated by this disordered stacking constitute the material's porosity. The IUPAC classifies these cavities into three distinct groups: micropores (diameter < 2 nm), mesopores (2 to 50 nm), and macropores (> 50 nm) (Sing, 1985; Thommes et al., 2015), as shown in **Figure II.4**. A defining feature of these microcrystallites is the presence of a delocalized π−electron system. This system readily facilitates non-covalent interactions with aromatic adsorbates via π-π stacking (Bansal & Goyal, 2005).

Furthermore, the breaking of molecular bonds at the edges of these aromatic sheets during carbonization generates edge carbon atoms featuring unsaturated valencies and unpaired electrons (Bansal & Goyal, 2005; Çeçen & Aktas, 2012). These resonance-stabilized radicals are highly reactive. Consequently, they readily bond with heteroatoms such as oxygen, hydrogen, nitrogen, and sulfur (Bansal & Goyal, 2005). This reactivity produces a diverse array of surface functional groups. Alongside the internal pore architecture, these functional groups directly dictate the absolute adsorption capacity and the chemical reactivity of the activated carbon toward specific targeted pollutants (Bansal & Goyal, 2005; Worch, 2012).

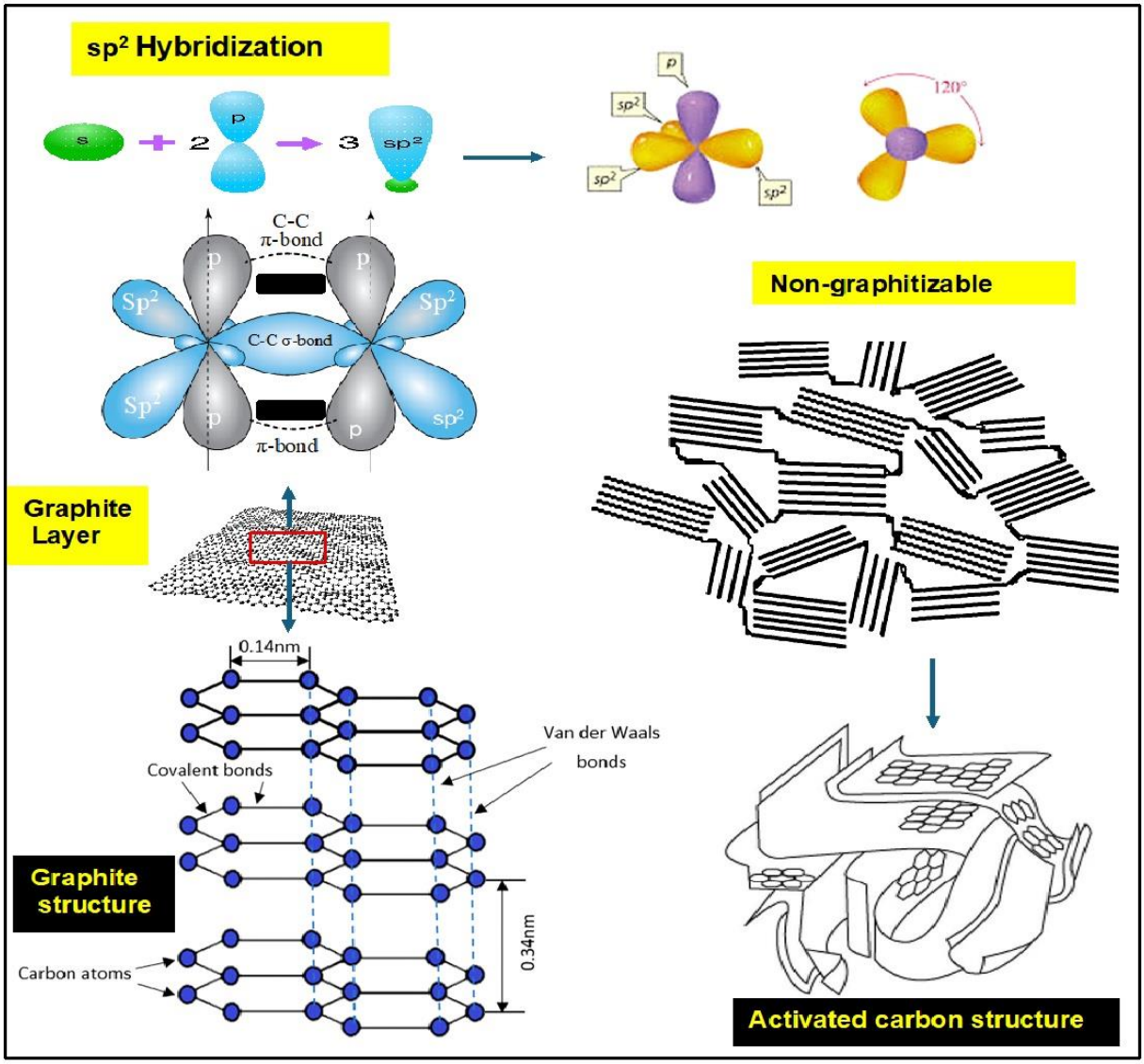

Figure II.3 Schematic of graphite and activated carbon structures (Adapted from (Bandosz, 2006; Sayed et al., 2019; Yap et al., 2023))

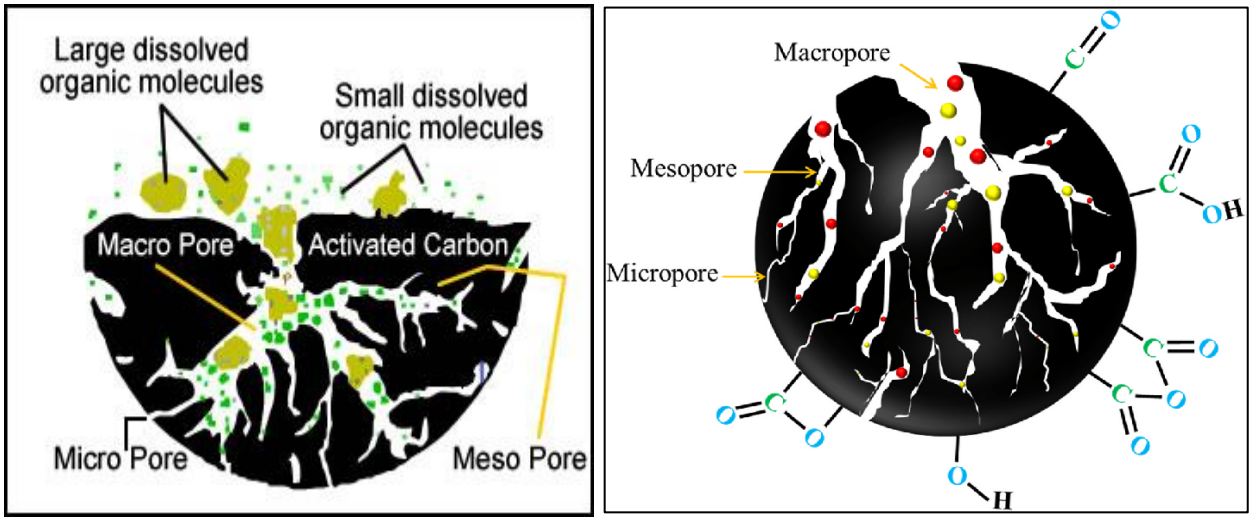

Figure II.4 Schematic representation of the internal pore architecture and the various surface functional groups associated with activated carbon (Berillo & Ermukhambetova, 2024; Sultana et al., 2022)

II.3.3 Properties of AC

Beyond physical porosity, the adsorption performance of AC is heavily governed by its surface chemistry. The carbon matrix is typically decorated with an array of oxygen-containing functional groups, including carboxyl, phenolic, and lactone moieties. These groups are predominantly introduced during the chemical activation phase (Bansal & Goyal, 2005; Kwiatkowski, 2011). They significantly influence both the overall surface charge (pH_{pzc}) and the material's relative hydrophobicity. This complex chemical environment enables diverse adsorption mechanisms, encompassing electrostatic attraction, π–π stacking, and hydrogen bonding. These mechanisms are strictly required for the effective adsorption of complex organic contaminants such as MO, CAT, and ACE.

II.3.4 Precursors for AC production

II.3.4.1 Conventional precursors

Historically, the commercial manufacturing of activated carbon relied heavily on fossil-based precursors. This specifically included various ranks of coal (such as bituminous, anthracite, and lignite) alongside peat (Haghbin & Niknam Shahrak, 2021; Martínez et al., 2023). These materials are traditionally favored for industrial-scale production due to their inherently high carbon density and rigid structural integrity. These characteristics reliably yield adsorbents featuring superior mechanical strength. The selection of a precursor depends not merely on its geographic availability, but also on

its capacity to be processed to meet the rigid specifications of targeted industrial applications.

Beyond fossil fuels, a restricted range of alternative resources has dominated the market. This includes wood, fruit stones, specific nutshells (particularly coconut shells), and certain synthetic organic polymers (Marsh & Rodriguez-Reinonso, 2006). Despite their proven effectiveness, conventional fossil-based precursors are under increasing scrutiny. They represent non-renewable resources characterized by escalating extraction costs and a severe environmental footprint. Consequently, research dictates a necessary shift toward identifying sustainable, low-cost alternatives that match the performance of these traditional materials without the associated ecological detriment.

II.3.4.2 Lignocellulosic and agro-industrial wastes

In the pursuit of sustainability and a circular economy, lignocellulosic biomass has emerged as a superior alternative precursor (Rattanapan et al., 2017). Agricultural residues such as pinewood (De Smedt et al., 2024), olive stones (Martínez et al., 2006), rice husks (Chang et al., 2023), walnut shells (Serafin et al., 2023), and wood sawdust (Sayed et al., 2024) are inherently renewable, abundant, and economically viable. Chemically, these materials exist as complex composites of cellulose, hemicellulose, and lignin. The natural fibrous structure of cellulose and the dense aromatic nature of lignin facilitate the extensive development of porous carbon networks upon activation. Because lignin constitutes the most thermally stable component, it contributes significantly to the final fixed carbon yield. Concurrently, the thermal decomposition of cellulose and hemicellulose generates the required internal pore volume (Chowdhury et al., 2013).

II.3.4.3 Date palm waste

Date palm trees (Phoenix dactylifera) are cultivated predominantly in arid zones, such as the Middle East and North Africa. Saudi Arabia alone hosts approximately 23 million trees, representing nearly 19% of the global population. This massive agricultural sector generates substantial volumes of lignocellulosic waste, including leaves, stems, and pits. An average tree produces 15-20 kg of residual biomass annually. Consequently, this high volume of waste represents an abundant, highly renewable precursor for the synthesis of activated carbon (Yahya et al., 2021).

Date Palm Waste (DPW) comprises fronds, rachis, fruit stalks, and seeds. These residues are strictly lignocellulosic, exhibiting a typical composition of 33 to 48% cellulose, 13 to 31% hemicellulose, and 33 to 48% lignin. Compared to other agricultural residues, DPW has a high volatile content and a relatively low ash fraction, making it an optimal precursor for carbonization (Nasser et al., 2016).

Conventionally, date palm waste is either diverted to landfills or burned openly in agricultural fields. These disposal methods generate significant environmental pollution and greenhouse gas emissions, while only a minor fraction is repurposed for animal feed. Therefore, its valorization into high-value activated carbon directly resolves two distinct environmental challenges: solid agricultural waste management and advanced water remediation.

II.3.5 Activation methods

The conversion of raw biomass into activated carbon proceeds through two primary pathways: physical activation and chemical activation.

II.3.5.1 Physical activation

Physical activation operates as a two-stage process. Initially, the precursor undergoes carbonization (pyrolysis) in an inert atmosphere (such as N_2) at elevated temperatures to produce a carbonaceous char. Subsequently, the char is activated using oxidizing gases, typically steam (H_2O) or carbon dioxide (CO_2), at high temperatures (Mergbi et al., 2023). These oxidizing agents selectively react with carbon atoms to generate the internal pore network (Rodríguez-Reinoso et al., 1995). The governing reactions are:

$$C + H_2O \xrightarrow{\Delta} CO + H_2O \qquad \textbf{Eq. II.12}$$

$$C + CO_2 \xrightarrow{\Delta} 2CO \qquad \textbf{Eq. II.13}$$

While physical activation represents a cleaner synthesis route by avoiding synthetic chemical agents, it inherently results in lower fixed carbon yields due to extensive burn-off. Furthermore, the process demands significantly higher thermodynamic energy input to sustain the necessary elevated activation temperatures.

II.3.5.2 Chemical activation

Chemical activation functions as a highly efficient, single-step procedure. The raw precursor is impregnated with a chemical dehydrating agent (such as H_3PO_4, $ZnCl_2$, KOH) and subsequently heat-treated at low to moderate temperatures. The chemical impregnant promotes extensive cross-linking, reduces tar formation, and lowers the required activation temperature. Consequently, this method reliably yields a higher final carbon mass and a significantly more developed microporous architecture than physical activation pathways (Seow et al., 2022).

II.3.5.3 Mechanism of $ZnCl_2$ activation

Zinc chloride ($ZnCl_2$) serves as a highly effective activating agent. It is widely favored for synthesizing carbons characterized by extreme microporosity and large specific surface areas. The activation process utilizing $ZnCl_2$ relies on a complex physicochemical mechanism that advances through several distinct phases. The specific efficacy of $ZnCl_2$ stems directly from its dual function as both a strong Lewis acid and a powerful dehydrating agent. This dual functionality fundamentally alters the standard thermal decomposition pathways of the lignocellulosic biomass.

a) Catalytic dehydration and aromatization

During the initial impregnation phase, aqueous $ZnCl_2$ penetrates the complex lignocellulosic matrix. It actively catalyzes the cleavage of glycosidic bonds within the cellulose structure and targets ether linkages within the lignin fraction. As the system temperature increases, the zinc salt accelerates the elimination of constituent hydrogen and oxygen atoms, releasing them primarily as water vapor (H_2O) and hydrogen gas (H_2). This induced dehydration effectively inhibits the formation of heavy tars. Instead, it promotes the rapid aromatization and cyclization of the carbon skeleton at exceptionally low temperatures. The generalized dehydration reaction is expressed as:

$$C_x(H_2O)_y(biomass) + ZnCl_2 \xrightarrow{\Delta} C(Char) + yH_2O \uparrow + Volatiles \qquad \textbf{Eq. II.14}$$

b) Intermediate formation and gaseous diffusion

Recent chemical engineering literature identifies a more sophisticated reaction pathway extending beyond simple pyrolytic dehydration. According to Ma (2017), the evolved water vapor reacts directly with the molten $ZnCl_2$ (which possesses a melting point of approximately 290 °C). This reaction yields an intermediate solid species, zinc oxide chloride hydrate ($Zn_2OCl_2.2H_2O$), which subsequently decomposes as the pyrolysis temperature escalates:

$$\left(C_xH_yO_z\right) + 2ZnCl_2 \xrightarrow{\Delta} \left(C_xH_{y-6}O_{z-3}\right) + Zn_2OCl_2.2H_2O + 2HCl \qquad \textbf{Eq. II.15}$$

$$Zn_2OCl_2.2H_2O \xrightarrow{\Delta} ZnO + ZnCl_{2(g)} + 2H_2O \qquad \textbf{Eq. II.16}$$

The vaporization of $ZnCl_2$ into the gaseous phase constitutes a critical structural step. As the gas diffuses outward through the dense carbonaceous matrix, it physically acts as a spatial template, generating an extensive internal surface area. This physical templating effectively prevents the macroscopic contraction of the carbon structure, permanently preserving the newly developed

porosity.

c) Template removal and porosity finalization

The crystalline ZnO particles generated during the intermediate decomposition stage remain firmly embedded within the carbon matrix. While retaining these particles is required to synthesize a functionalized ZnO@AC composite, standard non-functionalized carbon production employs a post-activation acidic wash (typically utilizing dilute HCl) to leach out the zinc species. Removing these solid metallic templates, combined with the structural voids left by the gaseous $ZnCl_2$, establishes the final highly porous network. This network is characterized by a high volume of micropores and small mesopores, which facilitate rapid adsorption of various organic pollutants, including MO, CAT, and ACE.

d) Comparison with other agents

Chemical activation with $ZnCl_2$ offers distinct structural advantages over alternative reagents. Phosphoric acid (H_3PO_4) typically promotes the formation of phosphate ester linkages, driving the development of significant mesoporosity. While mesoporosity is highly advantageous for capturing large macromolecules, $ZnCl_2$ preferentially generates narrow microporosity. This specific micro-architecture is geometrically ideal for trapping small to medium-sized adsorbates, such as specific pesticides and synthetic dyes (Haghbin & Niknam Shahrak, 2021; Lin et al., 2022). Furthermore, activation utilizing potassium hydroxide (KOH) initiates highly aggressive redox reactions that frequently obliterate the internal carbon structure to maximize surface area. In contrast, $ZnCl_2$ activation maintains superior structural integrity and consistently delivers higher overall carbon yields (Ma, 2017).

II.4 Response surface methodology in adsorption studies

The intricate dynamics of adsorption processes require sophisticated mathematical modeling for rigorous process optimization. This is particularly relevant when evaluating highly heterogeneous matrices, such as activated carbon, against complex organic adsorbates like MO, CAT, and ACE. Traditional optimization historically relied on the one-factor-at-a-time (OFAT) protocol. The OFAT method isolates a single independent operational variable (such as solution *pH*, adsorbent dosage, or temperature) and alters it while holding all other parameters strictly constant. Although this approach isolates the direct influence of a single variable, it systematically fails to capture the interactive effects among multiple factors (Isoda et al., 2014). For example, the influence of initial solution *pH* on an ionizable pesticide frequently depends on the applied thermal energy. A linear OFAT approach

inherently obscures this synergistic or antagonistic dependency. Furthermore, the OFAT technique suffers from significant operational inefficiencies. It frequently requires an exhaustive number of experimental iterations to identify a potential global optimum, yet it routinely terminates at local optima rather than achieving the true maximum efficiency.

To address these profound methodological deficiencies, modern environmental engineering heavily relies on RSM. RSM extends beyond a singular statistical test. It functions as a comprehensive, multivariate framework that mathematically integrates experimental design, polynomial regression modeling, and specific optimization algorithms. This synthesis effectively models the continuous relationship between a defined set of explanatory variables and one or multiple dependent responses. By fitting generalized polynomial equations to specific empirical data, RSM constructs a highly robust theoretical approximation of system behavior. This mathematical construct permits the precise calculation of optimal operational parameters designed to maximize pollutant removal percentages and/or absolute unit adsorption capacity. The subsequent theoretical formulations defining RSM, including the specific architectures of the Central Composite Design (CCD) and the Box-Behnken Design (BBD), are synthesized from established statistical literature (Montgomery, 2017; Montgomery et al., 2012; Montgomery & Runger, 2018; Montgomery et al., 2009; Myers, 2016).

II.4.1 Principles of RSM

The core theoretical principle of RSM assumes that a targeted response variable (Y) is a continuous function of the independent design variables (x_1, x_2, …, x_k). Within liquid-solid adsorption studies targeting MO, CAT, or ACE, these input variables correspond to primary physicochemical parameters. These parameters typically include the initial adsorbate concentration, adsorbent mass, aqueous solution *pH*, contact time, and system temperature.

This continuous mathematical relationship is frequently approximated using low-degree polynomial models. While first-order polynomials adequately facilitate initial screening experiments to isolate statistically significant factors, true optimization demands higher-order equations to accurately capture the spatial curvature of the multi-dimensional response surface. Consequently, the second-order (quadratic) polynomial model represents the standard formulation utilized across adsorption studies. Its structural flexibility accommodates non-linear dependencies and isolates definitive critical coordinates (including maxima, minima, and saddle points).

The generalized mathematical expression for a second-order regression model is defined as:

$$Y = \beta_0 + \sum_{i=1}^{k} \beta_i x_i + \sum_{i=1}^{k} \beta_{ii} x_i^2 + \sum_{i=1}^{k-1} \sum_{i=1}^{k} \beta_{ij} x_i x_j + \epsilon \qquad \textbf{Eq. II.17}$$

Where Y represents the predicted specific response (e.g., percentage removal efficiency or adsorption capacity), β_0 defines the equation intercept, and k indicates the total number of experimental factors evaluated. The linear coefficients (β_i) quantify the main effect of each parameter (x_i) in isolation. The quadratic coefficients (β_{ii}) determine the magnitude of surface curvature, enabling the mathematical model to identify precise peak performance regions rather than assuming linear continuity. The interaction coefficients (β_{ij}) strictly measure the synergistic or antagonistic interaction between the two factors (x_i and x_j). Finally, the term ε represents the random residual experimental error that remains unexplained by the defined model.

II.4.2 Common RSM designs

The structural integrity of any RSM approach depends explicitly on the selected experimental design matrix. This matrix dictates the geometric distribution of specific data points across the multidimensional experimental region. The CCD and BBD represent the two most ubiquitous second-order frameworks applied in porous carbon adsorption studies.

II.4.2.1 Central composite design

The CCD serves as a highly robust benchmark for response surface modeling, proving especially effective in systems possessing distinctly defined experimental boundary limits. The structural architecture of a CCD matrix relies on the direct superposition of three distinct data categories: factorial points, axial points, and central replicated points.

The factorial points (2^k) define a standard first-order foundational design, situated at the geometric vertices of an experimental hypercube (coded with values ±1). These points strictly govern the estimation of primary main effects and binary interactions. To capture systemic curvature and enable second-order modeling, axial points (or star points, $2k$) are introduced. These points project outward from the coordinate origin to a defined specific distance (α). The magnitude of α is mathematically critical. Setting $\alpha = (2^k)^{1/4}$ specifically achieves rotatability. Rotatability ensures that the predicted response variance remains uniform at any coordinate that is equidistant from the geometric center of the design space. Furthermore, incorporating multiple central-point replicates (n_c) is strictly required to quantify pure experimental error and to confirm overall model adequacy via an independent

curvature check.

A defining characteristic of the standard CCD is its requirement to evaluate every independent factor across five distinct, coded levels ($-\alpha$, -1, 0, +1, $+\alpha$). This structural approach guarantees an exceptionally high-resolution scan of the defined experimental domain. Consequently, it represents an optimal strategy for the rigorous optimization of diverse variables (such as *pH* and concentration gradients) requiring a broad evaluative spectrum.

II.4.2.2 Box-Behnken design

The BBD provides a highly efficient and structurally constrained alternative to the conventional CCD framework. Geometrically, the BBD excludes experimental testing at the absolute corners of the multi-dimensional hypercube. Instead, it positions designated data points precisely at the midpoints of the structural edges and directly at the design center. This distinct geometric configuration offers significant operational and chemical-safety advantages.

A primary strategic advantage of the BBD is its absolute restriction to exactly three parameter levels (typically coded as -1, 0, and +1). Compared to the rotatable CCD, which mandates five operational levels, the BBD provides substantial logistical simplicity. This simplicity becomes highly valuable when precise control of extreme boundary variables is mechanically difficult or when hardware constraints prevent the implementation of specific axial α limits.

Furthermore, the BBD inherently avoids extreme combinatorial conditions. By omitting experimental runs in which all independent factors operate simultaneously at their absolute maximum or minimum bounds, the BBD actively prevents evaluation in unstable or physically hazardous regions. At complex solid-liquid interfaces, simultaneous extreme conditions (e.g., high alkaline *pH* and maximum thermal input) often induce rapid degradation of delicate adsorbate molecules (e.g., ACE) or structural collapse within the carbon matrix. Excluding these extreme limits rigorously protects the integrity of the empirical data collected.

Finally, the BBD represents a highly cost-effective experimental strategy. For a standard three-factor optimization study, the BBD demands only 15 distinct runs, whereas a corresponding CCD requires 20. This experimental economy scales rapidly as the total number of evaluated variables increases. Therefore, the BBD remains a highly preferred framework for researchers seeking to minimize the use of specialized adsorbents and high-purity chemical reagents while maintaining the statistical robustness of the derived model.

Table II.2 Comparative analysis of CCD and BBD designs for adsorption optimization

Attribute	Central Composite Design	Box-Behnken Design
Geometric Structure	Vertices of hypercube, Axial points, and Center	Midpoints of edges and Center
Factor Levels	5 (-α, -1, 0, +1, + α)	3 (-1, 0, +1)
Corner Points	Included (Simultaneous extremes tested)	Excluded (Avoids simultaneous extremes)
Experimental Runs (k=3)	20 runs	15 runs
Statistical Power	High; excellent for boundary predictions	Moderate; excellent for the interior region
Rotatability	Achieved when $\alpha = (2^k)^{1/4}$	Always or nearly rotatable
Application Strategy	Comprehensive mapping and sequential modeling	Economic optimization within safe regions
Key Advantage	High resolution and prediction at boundaries	Resource efficiency and operational simplicity

II.4.3 Statistical validation and model adequacy

For polynomial models generated via RSM to be considered reliable for process prediction, they require rigorous statistical validation. This validation is typically executed through Analysis of Variance (ANOVA). The significance of the overall regression model, alongside its individual linear, quadratic, and interaction terms, is evaluated utilizing Fisher's variance ratio (*F-value*) and the corresponding probability value (*p-value*). A calculated model is generally deemed statistically significant when the *p-value* is less than 0.05, which establishes a 95% confidence level.

Furthermore, the Lack-of-Fit (LoF) test serves as a critical diagnostic tool. A non-significant LoF (*p-value*> 0.05) indicates that the proposed model successfully captures the empirical data's variance and that pure experimental error remains strictly minimal. Finally, model adequacy requires an assessment of the R^2 in relation to the R^2_{adj}. The proximity between these two statistical parameters confirms that the polynomial equation is not mathematically over-fitted and maintains high predictive power for subsequent experimental observations.

II.4.4 Multi-response optimization and verification

In adsorption studies targeting a single pollutant, process optimization often requires balancing competing operational objectives, such as q_e and R. This balance is achieved analytically via the Desirability Function approach (DFA). This mathematical technique transforms each estimated

response variable into a dimensionless desirability scale (di) bounded between 0 (completely undesirable) and 1 (ideal).

The overall global desirability (D_{opt}) is subsequently computed as the geometric mean of these individual desirability values. This allows identification of a single set of standardized operational conditions that simultaneously maximizes both q_e and R for the target adsorbate. The final stage of the RSM framework mandates direct experimental verification, in which the optimized parameter coordinates calculated by the theoretical model are rigorously tested in the laboratory. By calculating the percentage error between the experimental outcomes and the model-predicted values, the overall robustness of the derived model is confirmed. A typical deviation below 5% verifies the RSM framework's ability to map the complex multidimensional design space.

II.4.5 Advantages of response surface methodology

Implementing RSM over traditional univariate strategies provides significant technical advantages for optimizing complex adsorption interfaces. The primary structural merit of RSM is its high experimental parsimony and economic resource efficiency. By deploying specific design-of-experiments architectures, such as the BBD or the CCD, the total number of laboratory trials required is drastically reduced. This efficiency proves particularly valuable when evaluating custom-synthesized porous materials. It minimizes the exhaustive consumption of specialized adsorbents and high-purity chemical reagents while accelerating the experimental timeline without compromising statistical integrity.

Beyond simple logistical efficiency, RSM provides superior analytical resolution. It enables the strict mathematical quantification of interactive effects between independent variables. During remediation of diverse organic pollutants, the physical influence of a specific factor (e.g., aqueous pH) rarely operates independently of secondary factors (e.g., applied thermal energy or initial concentration gradients). RSM explicitly measures these synergistic or antagonistic interactions by deriving β_{ij}. This analytical capability provides a comprehensive mapping of the experimental domain that remains inherently invisible to linear OFAT methodologies.

Furthermore, RSM functions as a robust visualization and sensitivity tool. The underlying mathematical relationships are translated directly into three-dimensional response surface plots and associated two-dimensional contour maps. These topological representations facilitate an intuitive physical assessment of the system's sensitivity to specific parameter fluctuations. For example, the

precise curvature of the modeled surface dictates the operational robustness of the optimal region, while the elliptical geometry of the contour lines clarifies the exact strength of the binary-factor interactions.

Finally, the most distinctive engineering advantage of RSM lies in its ability to perform exact numerical optimization. By utilizing differential calculus to locate the specific stationary point on the response surface (where all partial derivatives of the polynomial equation equal zero), researchers can determine the exact operational conditions required to maximize pollutant removal. Integrating the mathematical Desirability Function further amplifies this capacity, enabling simultaneous performance optimization across mixed chemical environments. This specific integration ensures that the identified operational parameters represent a true global optimum, fully satisfying the competing equilibrium requirements of varied molecular species.

II.5 Artificial neural networks in adsorption modeling

Although RSM provides a structured optimization framework, its utility is ultimately constrained by the mathematical limitations of polynomial regression. Solid-liquid adsorption systems frequently exhibit pronounced non-linear behaviors. This nonlinearity is especially pronounced when using highly heterogeneous microporous matrices such as activated carbon. Consequently, the physical complexity of these systems readily exceeds the predictive capacity of standard second-order equations. ANNs provide a robust, data-driven alternative to overcome these specific modeling limitations. As universal approximators, ANNs mathematically map continuous nonlinear functions to arbitrary degrees of accuracy. They achieve this high-fidelity prediction independently of prior theoretical assumptions about the system's underlying structural mechanics (Shanmugaprakash & Sivakumar, 2013).

II.5.1 Architecture of artificial neural networks

The structural framework of an ANN comprises three interconnected tiers: the input layer, the hidden layers, and the output layer (**Figure II.5**). The input layer functions as the direct mathematical interface between the predictive algorithm and the experimental parameters (Nighojkar et al., 2023). In aqueous remediation studies targeting specific pollutants such as MO or CAT, these input neurons correspond directly to the independent operational variables. Standard variables include the initial adsorbate concentration, aqueous solution *pH*, adsorbent dosage mass, contact time, and system temperature. Each neuron quantifies a distinct parameter of the experimental design space and

transmits this numerical data forward to the subsequent computational layers.

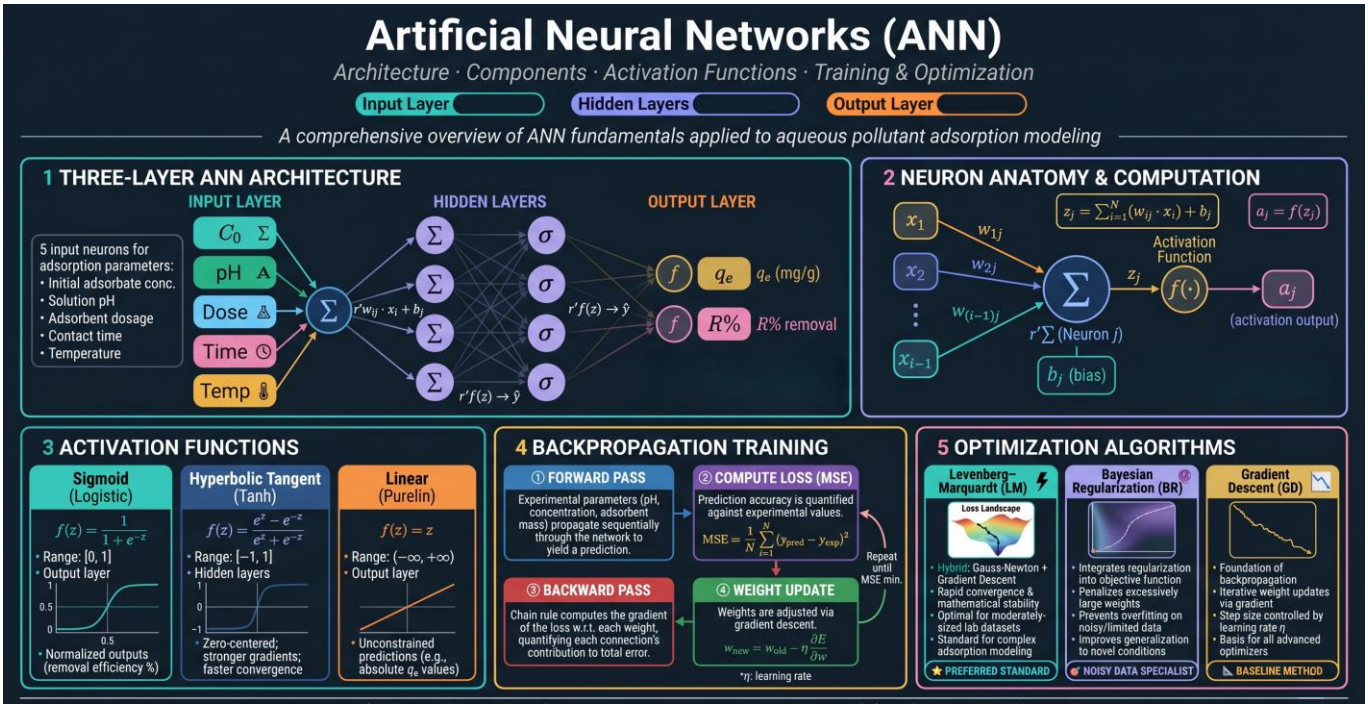

Figure II.5 Artificial neural network architecture, components and training framework for adsorption process

Primary computational processing occurs within the hidden layers. These intermediate structures mathematically map the complex non-linear relationships governing adsorption via a matrix of weighted interconnections and specialized activation functions. Optimizing the neuron count in these hidden layers is a fundamental step in hyperparameter tuning. Insufficient neurons typically lead to model underfitting, causing the algorithm to fail to capture the underlying mass transfer physics. Conversely, an excessive number of neurons often leads to overfitting. In an overfitted state, the network memorizes random statistical noise within the training data. This memorization severely compromises the model's predictive accuracy and generalization capacity when applied to novel experimental datasets (Ghaedi & Vafaei, 2017).

The output layer generates the final prediction from the processed signals. In environmental engineering applications, this terminal layer typically consists of a single or multiple neurons representing targeted dependent variables, such as equilibrium adsorption capacity and macroscopic removal efficiency (R %). By continuously comparing these predicted outputs against established experimental benchmarks, the network iteratively adjusts internal weights to minimize global computational error. This systematic refinement ultimately produces a robust predictive instrument

for process optimization (Ghaedi & Vafaei, 2017).

II.5.2 Fundamental components: neurons, weights, and biases

The primary computational unit of an ANN is the artificial neuron. The network's predictive capabilities are strictly determined by the mathematical strength of the interconnections linking its individual units. These connection strengths are defined numerically as weights (w). Each defined weight functions as a distinct scaling factor. It establishes the relative magnitude of a specific input signal as it propagates forward through the algorithmic structure.

To expand the mathematical flexibility of the model, a specific bias (b) term is structurally integrated into each neuron. This bias operates as a numerical threshold or offset. It permits the activation function to shift along the horizontal coordinate axis. This lateral shift remains mathematically essential. It allows the network to accurately map complex data patterns that do not naturally intersect the geometric origin, thereby significantly enhancing the model's absolute approximation capacity (Basheer & Hajmeer, 2000).

Mathematically, the data processing executed within a specific neuron (j) requires the systematic summation of all weighted inputs originating from the preceding layer, strictly followed by the addition of the designated bias term. The calculated net input (z_j) is formally expressed by the following equation (Bagheri et al., 2015):

$$z_j = \sum_{i=1}^{n} w_{ij} x_i + b_j \qquad \textbf{Eq. II.18}$$

Here, z_j represents the calculated net input to neuron j within the active layer. The variable x_i denotes the numerical input signal from neuron i in the preceding layer. The term w_{ij} denotes the specific weight applied to the connection between neuron i and neuron j, while bj denotes the assigned bias value.

An assigned activation function subsequently transforms this aggregated weighted sum. This function introduces the precise non-linearity required to approximate the highly complex, non-proportional physical relationships characteristic of organic pollutant adsorption.

II.5.3 Activation functions

To accurately model the complex dynamics of solid-liquid adsorption, the net signal entering a neuron

must be transformed by an activation function. The explicit purpose of this mathematical transformation is to introduce systemic non-linearity. Without it, the ANN functions merely as a conventional multi-linear regression tool. Consequently, the network becomes fundamentally incapable of mapping the intricate, synergistic dependencies among diverse operational parameters.

Selecting an appropriate activation function depends entirely on the functional requirements of the specific neural layer (Nighojkar et al., 2023). Advanced adsorption modeling predominantly implements three distinct mathematical functions: the linear function (purelin), the logistic sigmoid function (logsig), and the hyperbolic tangent function (tansig) (Cojocaru et al., 2021).

II.5.3.1 Sigmoid (Logistic) function

The logistic sigmoid function is mathematically defined by:

$$f(z) = \frac{1}{1 + exp^{-z}} \qquad \textbf{Eq. II.19}$$

This equation compresses continuous input data to a defined range, bounded by 0 and 1. Due to this absolute structural boundary, the sigmoid function is exceptionally effective for modeling normalized dependent variables, such as percentage removal efficiency (Ghaedi & Vafaei, 2017).

II.5.3.2 Hyperbolic Tangent (Tanh)

The hyperbolic tangent (tanh) function is mathematically expressed by:

$$f(z) = \frac{exp^{z} - exp^{-z}}{exp^{z} - exp^{-z}} \qquad \textbf{Eq. II.20}$$

This function maps incoming variables to a range of -1 to 1. As a strictly zero-centered mathematical function, it is highly preferred for deployment within hidden layers. It consistently generates stronger mathematical gradients. These robust gradients structurally facilitate significantly faster network convergence during the iterative training phase (Ghaedi & Vafaei, 2017).

II.5.3.3 Linear (purelin)

The pure linear function is defined simply by:

$$f(z) = z \qquad \textbf{Eq. II.21}$$

This activation mechanism transmits the raw input directly to the subsequent layer without imposing

any mathematical transformation. Environmental engineering models typically use this function solely in the final output stage. This specific placement allows the network to predict absolute physical metrics, such as q_e. Consequently, the final predictions remain unconstrained by the strict asymptotic limits that characterize sigmoid or hyperbolic tangent functions (Ghaedi & Vafaei, 2017).

II.5.4 Network training and optimization algorithms

The high predictive fidelity of an ANN is established entirely during the iterative training phase. In this procedural stage, the internal network weights and assigned biases are systematically adjusted to minimize the mathematical discrepancy between the model-predicted outputs and the established empirical targets. Within contemporary literature modeling the adsorption of complex organic pollutants, the Backpropagation (BP) algorithm remains the most universally applied training framework (Rumelhart et al., 1986; Werbos, 1974).

The standard backpropagation mechanism executes a highly cyclical, two-stage mathematical process. During the initial forward pass, designated experimental parameters (including solution pH, concentration gradients, and adsorbent mass) propagate sequentially through the network architecture. This sequential propagation yields a theoretical prediction for the targeted response. The absolute accuracy of this generated prediction is immediately quantified against the known experimental value utilizing a defined loss function (**Figure II.5**). The Mean Squared Error (MSE) is the most frequently deployed metric for this evaluation, mathematically expressed by:

$$MSE = \frac{1}{N}\sum_{i=1}^{N}\left(y_{pred} - y_{exp}\right)^2 \qquad \textbf{Eq. II.22}$$

Following this baseline evaluation, the algorithm initiates the backward pass. During this computational phase, the exact gradient of the loss function with respect to each weight is computed using the fundamental chain rule of calculus. This specific derivation precisely quantifies the proportional contribution of every distinct neural connection to the aggregate predictive error. To systematically reduce this total error, the network weights are iteratively modified according to the principles of gradient descent, defined formally by:

$$w_{new} = w_{old} - \eta\frac{\partial E}{\partial w} \qquad \textbf{Eq. II.23}$$

In this expression, the variable η represents the defined learning rate, and E is the loss function (*MSE*).

This designated hyperparameter strictly controls the absolute step size of the applied weight adjustments.

To maximize the computational efficiency of these specific weight updates, researchers frequently deploy highly specialized optimization algorithms. The Levenberg-Marquardt (LM) algorithm (Levenberg, 1944; Marquardt, 1963) currently serves as the analytical standard for complex adsorption modeling due to its highly efficient hybrid architecture. It successfully interpolates between the high precision of the Gauss-Newton algorithm and the robust stability of the standard gradient descent method. The LM approach is particularly distinguished by its rapid convergence velocity and mathematical stability. These traits render it highly optimal for processing the moderately sized datasets conventionally produced by batch-scale laboratory experiments (Huang et al., 2023).

As a mathematical alternative, Bayesian Regularization (BR) (MacKay, 1992) is frequently implemented when processing highly noisy empirical data or strictly limited sample matrices. By explicitly integrating a mathematical regularization term directly into the standard objective function, the BR algorithm actively penalizes the development of excessively large internal weights. This continuous penalization effectively prevents overfitting and significantly improves the model's generalization performance. Such generalization remains an absolute requirement for ensuring the trained network can reliably forecast removal efficiencies under novel operational conditions absent from the initial training matrix [(Ali et al., 2024).

II.5.5 Comparative analysis of RSM and ANN in adsorption modeling

Although RSM and ANN are robust empirical modeling techniques in environmental engineering, they operate on fundamentally different mathematical principles.

RSM is traditionally categorized as a white-box or gray-box modeling framework. This classification stems from the explicit mathematical transparency of the polynomial equations it derives. Within this structured framework, the calculated regression coefficients provide clear, isolable statistical interpretations. These coefficients permit researchers to quantitatively assess the exact physical influence of distinct operational parameters, such as thermal energy or surface *pH*, on the final response variable.

In sharp contrast, an ANN functions as a complex black-box model. Its internal weights and structural biases remain abstract, lacking direct physical or thermodynamic interpretations. Nevertheless, the network architecture's inherent capacity to map complex, multidimensional empirical data

consistently yields superior predictive accuracy.

The selection between these two methodologies is dictated strictly by the specific analytical objectives of the research. RSM persists as the optimal tool for general process optimization and initial factor screening. Its rigid mathematical structure allows the exact calculation of stationary points, including specific maxima and minima, by direct application of differential calculus. Conversely, ANN represents the superior analytical choice for the high-fidelity prediction and numerical simulation of non-linear chemical systems. Because the ANN framework lacks a closed-form mathematical equation that defines an absolute optimum, its practical application for process optimization requires coupling the network with advanced metaheuristic algorithms. Common integrations include GA (Pravina et al., 2023) or Particle Swarm Optimization (PSO) (Khiam et al., 2022). A comprehensive summary of the technical and strategic differences between these two methodologies is presented in **Table II.3**.

II.6 Genetic algorithm and ANN-GA hybridization

The GA is a stochastic, global optimization technique based on evolutionary computational principles (Katoch et al., 2021). Unlike traditional gradient-based optimization methods (such as those employed in RSM), GA explores the experimental design space through a population-based search (Pravina et al., 2023). This mechanism makes it exceptionally robust for resolving complex adsorption data matrices, where the relationships between variables are highly non-linear. Furthermore, the mathematical search space frequently contains multiple local optima that readily trap simpler, gradient-descent algorithms.

Table II.3 Strategic comparison of RSM and ANN in the context of adsorption research (Desalegn et al., 2024; Mourabet, 2014; Shanmugaprakash & Sivakumar, 2013)

Feature	Response Surface Methodology (RSM)	Artificial Neural Network (ANN)
Model Nature	Structured, Regression-based (Polynomial)	Unstructured, Data-driven (Black-box)
Primary Utility	Process Optimization & Factor Screening	Complex System Prediction & Simulation
Data Requirements	Small, structured datasets (DOE-based)	Larger datasets are required for training
Predictive Accuracy	Good ($R^2 \approx 0.90–0.98$)	Superior ($R^2 > 0.98$); captures high non-linearity

Optimization Method	Direct calculus (differentiation)	Iterative (requires Genetic Algorithms)
Interpretability	High (Coefficients indicate effect size)	Low (Weights are abstract)
Extrapolation	Poor (Polynomials diverge quickly)	Poor (Unreliable outside training domain)

II.6.1 ANN-GA synergy

Within an ANN-GA hybrid framework, these two methodologies fulfill distinct, complementary roles. The trained ANN functions as a black-box surrogate model, predicting the objective output for any given set of input parameters. However, it fundamentally lacks a built-in mathematical mechanism to identify the absolute optimal input conditions. Consequently, the GA serves as the overarching optimizer, utilizing the trained ANN directly as its fitness function (Moradmand et al., 2023). The GA executes rapid, iterative queries against the ANN to evaluate potential solutions. Through this continuous evaluation, the algorithm systematically shifts the parameter population toward the specific operational coordinates (pH, m, t, C_0, T) that yield maximum removal efficiency or equilibrium adsorption capacity.

II.6.2 Fundamental genetic operators

The mathematical progression of the solution space is governed by a cyclical computational process utilizing three primary operators (Greenstein et al., 2023).

II.6.2.1 Selection

This operator executes the probabilistic retention of optimal solutions. Parameter sets (individuals) with superior fitness values, corresponding to enhanced adsorption metrics, receive a higher probability of selection in the subsequent computational iteration. Common probabilistic techniques include stochastic uniform or roulette wheel selection. These specific methods ensure that high-performing solutions propagate while preserving sufficient algorithmic diversity from sub-optimal data points. This deliberate preservation explicitly prevents premature model convergence.

II.6.2.2 Crossover

Functioning as the primary search mechanism, the crossover operator systematically exchanges data segments between two parent arrays to generate novel parameter combinations. By mathematically merging high-performing vectors, the algorithm effectively probes unexplored regions of the

experimental design space. A defined crossover rate, typically bounded between 0.6 and 0.9, explicitly controls the frequency of this data exchange.

II.6.2.3 Mutation

To inhibit the data population from becoming excessively homogeneous, the mutation operator introduces random, low-probability numerical alterations to specific parameter values. This stochastic perturbation prevents stagnation in local optima. It allows the algorithm to jump to entirely distinct regions of the search space, thereby ensuring a rigorous global optimization.

II.6.3 Termination and convergence

The algorithm iteratively processes the data population until a predefined termination criterion is satisfied. This threshold is conventionally defined by a maximum number of iterations (generations) or a specific stall tolerance, at which the objective fitness value ceases to improve significantly across successive cycles (Greenstein et al., 2023). The terminal output is a globally optimized matrix of operational conditions. These derived parameters maximize the targeted sequestering of MO, CAT, or ACE. Consequently, this hybrid methodology delivers predictive precision that substantially exceeds that of traditional empirical modeling or standard RSM frameworks.

II.7 Continuous flow (column) adsorption studies

Although batch adsorption studies optimized via RSM and ANN provide essential equilibrium capacity and kinetic data, they are fundamentally restricted to steady-state conditions. Industrial applications of activated carbon for wastewater treatment (whether for dye removal or pesticide remediation) predominantly operate in continuous-flow, fixed-bed column configurations. In these dynamic systems, the adsorbate concentration functions depend on both time and bed depth. This creates a non-steady-state environment where mass transfer zones progress sequentially through the adsorbent bed. Consequently, evaluating continuous-flow performance remains a prerequisite for the industrial implementation of activated carbon in sequestering MO, CAT, and ACE.

II.7.1 Anatomy and dynamics of the breakthrough curve

In a fixed-bed adsorption study, the column's dynamic behavior determines the transition from batch-scale feasibility to continuous industrial application. This dynamic performance is mathematically and graphically represented by the breakthrough curve (**Figure II.6**). The curve plots the normalized effluent concentration (C_t/C_0) against time (t) or the total volume of treated effluent (V_{eff}) (Mon et al.,

2024).

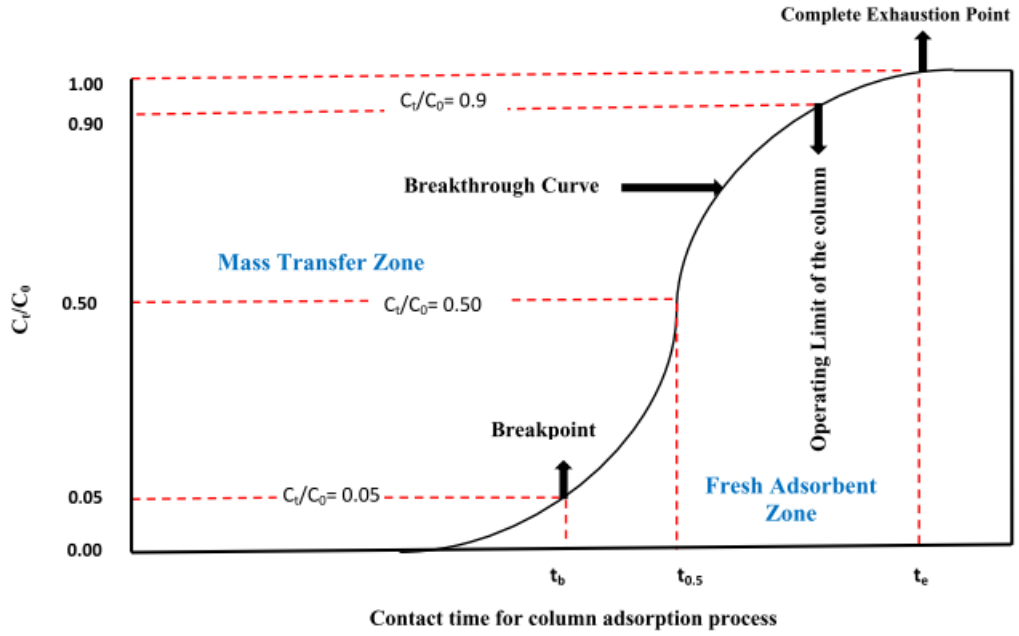

Figure II.6 Evolution of the breakthrough curve profile over time in a continuous fixed-bed adsorption system

An ideal breakthrough curve exhibits a definitive sigmoidal shape. This geometry represents the progression of the Mass Transfer Zone (MTZ) through the adsorbent matrix. During the initial operational phase, fresh activated carbon near the column inlet rapidly sequesters target pollutants, such as MO or CAT. This rapid adsorption keeps the MTZ entirely contained within the upper column limits, resulting in a negligible effluent concentration ($C_t \approx 0$) (Murphy et al., 2023).

As continuous operation proceeds, the uppermost bed layers reach saturation, forcing the MTZ to migrate downstream toward the outlet. The Breakthrough Point (t_b) occurs when the effluent concentration exceeds a predefined mathematical threshold. This threshold is frequently set at 5% of C_0 or is dictated directly by regulatory discharge limits. Identifying this exact temporal coordinate is critical in process engineering, as it formally signifies the conclusion of the effective service life for that specific operational cycle (Chowdhury et al., 2014).

The geometric profile of the curve between initial breakthrough and absolute saturation serves as a direct indicator of MTZ length and overall adsorption efficiency. A steep curve denotes a short MTZ. This profile indicates rapid adsorption kinetics and high bed utilization efficiency. Conversely, an elongated or shallow curve indicates slow internal diffusion and significant mass-transfer resistance. These physical limitations generate an extended MTZ, thereby reducing the operational efficiency of

the total carbon capacity.

Finally, the column reaches its practical operating limit as the bed approaches saturation (typically $C_t/C_0 \approx 0.90\text{-}0.95$). The complete Exhaustion Point (t_e) occurs when the adsorbent bed achieves full saturation ($C_t/C_0 \approx 1$), as depicted in **Figure II.6**. At this precise mathematical limit, the unit must be taken offline for physical regeneration or complete material replacement (Ahmed & Hameed, 2018; Aichour et al., 2019; Patel, 2019).

II.7.2 Factors affecting performance

In continuous-flow systems, adsorption efficiency depends entirely on the dynamic interactions between hydraulic conditions and mass-transfer resistances. Three primary operational parameters dictate fixed-bed performance: bed height, volumetric flow rate, and influent concentration (Mon et al., 2024). These specific variables strictly govern the geometric profile of the breakthrough curve and the total volume of treated effluent.

II.7.3 Kinetic models of column adsorption

Mathematical modeling of the breakthrough curve is essential for scaling empirical laboratory data into industrial column designs. These mathematical models quantify fundamental kinetic parameters and the bed's maximum dynamic adsorption capacity. Consequently, they enable the accurate prediction of column performance under highly variable operational conditions.

II.7.3.1 Thomas model

The Thomas model (Th) (Thomas, 1944) remains a primary mathematical framework for characterizing fixed-bed performance. This model is based on the Langmuir isotherm and a pseudo-second-order reversible reaction mechanism. Furthermore, it strictly postulates that axial dispersion within the column is mathematically negligible (Patel, 2019). The standard mathematical expression of the Thomas model is defined by:

$$\frac{C_t}{C_0} = \frac{1}{1 + exp\left[\left(\frac{k_{Th} \times q_0 \times m}{Q_v}\right) - k_{Th} \times C_0 \times t\right]} \qquad \textbf{Eq. II.24}$$

Here, k_{Th} (L/min.mg) represents the Thomas kinetic rate constant. The variable q_0 (mg/g) denotes the maximum solid-phase concentration or dynamic equilibrium adsorption capacity of the bed. The term m (g) specifies the total mass of the adsorbent bed, Q_v (L/min) defines the volumetric flow rate, C_0

(mg/L) is the influent adsorbate concentration, and t (min) is the operational time.

II.7.3.2 Yoon-Nelson model

The Yoon-Nelson model (Y-N) (Yoon & Nelson, 1984) offers a simplified theoretical approach. It requires no detailed information about the adsorbent or adsorbate's physical characteristics. This framework posits that the rate of decrease in the probability of adsorption for each molecule is directly proportional to the probability of its adsorption and subsequent breakthrough (Patel, 2019). The non-linear equation for this model is defined by:

$$\frac{C_t}{C_0} = \frac{1}{1 + exp\left(k_{YN} \times (\tau - t)\right)} \qquad \textbf{Eq. II.25}$$

Here, k_{YN} (min^{-1}) defines the kinetic rate constant, and τ (min) represents the exact operational time required to achieve 50% breakthrough. Consequently, researchers frequently use this mathematical model to accurately predict the column's operational half-life.

II.7.3.3 Adams-Bohart model

Rooted in surface reaction theory, the Adams-Bohart model (A-B) (Bohart & Adams, 1920) assumes the adsorption rate is proportional to both the residual capacity of the adsorbent bed and the bulk adsorbate concentration. Notably, this specific mathematical framework remains valid only for the initial portion of the breakthrough curve, typically bounded between $C_t/C_0 < 0.1$ and 0.5. The non-linear form of the Adams-Bohart model is formally expressed by (Chu, 2020a):

$$\frac{C_t}{C_0} = \frac{1}{1 + exp\left[\left(\frac{k_{BA} \times N_0 \times L}{u}\right) - k_{BA} \times C_0 \times t\right]} \qquad \textbf{Eq. II.26}$$

Where k_{AB} (L/mg·min) defines the kinetic constant, N_0 (mg/L) is the volumetric saturation capacity, U_0 (cm/min) is the superficial velocity, and L (cm) denotes the total bed depth. The U_0 is calculated by dividing the influent solution's volumetric flow rate by the column's cross-sectional area (Nazari et al., 2016).

It should be noted that the A-B, Thomas, and Y-N models are mathematically equivalent formulations of the same underlying logistic function, a fact with important consequences for model selection and explored in the context of the experimental results in **section VIII.2.1**.

II.8 Conclusion

This chapter established the fundamental theoretical and mathematical frameworks underpinning the experimental methodologies of this thesis. A rigorous examination of adsorption principles delineated the thermodynamic driving forces of mass transfer. It explicitly distinguished between physisorption and chemisorption mechanisms. Furthermore, it detailed the strict influence of operational parameters, including aqueous *pH*, system temperature, and ionic strength.

Subsequent sections explored the structural chemistry of activated carbon. This analysis highlighted the distinct advantages of chemical activation (specifically $ZnCl_2$) of lignocellulosic precursors. This targeted synthetic route engineers a highly porous, functionalized carbon matrix optimized for sequestering complex organic molecules. To accurately characterize these adsorbate-adsorbent interactions, the text systematically detailed the theoretical basis for kinetic modeling, equilibrium isotherms, and thermodynamic analysis. This comprehensive foundation ensures a mathematically robust approach to interpreting empirical data.

Beyond fundamental physical chemistry, this review addressed the inherent statistical limitations of traditional OFAT optimization within complex, multivariable systems. To resolve these limitations, advanced statistical and computational techniques were introduced. RSM was established as a rigorous tool for experimental design and parameter interaction analysis. Concurrently, ANN coupled with GA was presented as a superior computational method for nonlinear predictive modeling and global numerical optimization. Finally, a review of continuous fixed-bed column dynamics bridged the conceptual gap between batch-scale equilibrium theory and dynamic industrial application.

Chapter I previously established the macroscopic environmental context. This current chapter solidified the supporting theoretical and mathematical foundations. Consequently, Chapter III will directly apply these derived principles. It will detail the specific precursor materials, experimental protocols, and advanced analytical techniques utilized to synthesize and thoroughly evaluate the ZnO@DPS-AC composite.

Chapter III: Materials and Experimental Methodology

* * * * *

III.1 Introduction

The experimental framework detailed in this chapter addresses three primary objectives: the synthesis of activated carbon from DPW, the characterization of its physicochemical properties, and the evaluation of its adsorptive efficacy against water pollutants. To ensure data reproducibility and reliability, the methodology integrates standard chemical engineering operations with advanced statistical optimization and computational modeling.

The workflow is structured into four sequential phases. Phase I governs precursor preparation and the $ZnCl_2$ chemical activation process to tailor the adsorbent's textural properties. Phase II focuses on material characterization. Spectroscopic, microscopic, and thermal analyses are employed to elucidate the physical transformation mechanisms and surface functionalities of both the raw and activated materials. Phase III executes batch adsorption studies to extract equilibrium isotherms, kinetic parameters, and thermodynamic properties for three model pollutants: MO, CAT, and ACE. Finally, Phase IV implements RSM for empirical process optimization, alongside ANN modeling coupled with GA for predictive analytics. This concluding phase also incorporates continuous fixed-bed column studies to evaluate the industrial scalability of the synthesized adsorbent.

III.2 Target pollutants

Three model pollutants were selected to evaluate the versatility of the prepared carbon-based materials: MO, CAT, and ACE. MO ($C_{14}H_{14}N_3NaO_3S$, CAS: 547-58-0, M_w = 327.33 g/mol) served as a representative anionic azo dye typical of textile industry effluents. CAT ($C_6H_6O_2$, CAS: 120-80-9, M_w = 110.1 g/mol) was obtained from Sigma-Aldrich (analytical grade, >99% purity) to represent phenolic contaminants prevalent in pharmaceutical and petrochemical wastewaters. To assess the removal of agricultural pollutants, ACE ($C_{10}H_{11}ClN$, M_w = 222.67 g/mol) was sourced from a commercial insecticide formulation (Rustile, SARL Deachim) containing 20% active ingredient by weight.

III.3 Chemical reagents for synthesis and modification

The chemical activation of the agricultural precursor used $ZnCl_2$ from BIOCHEM Chemopharma. Solution *pH* adjustments required analytical-grade hydrochloric acid (HCl, Sigma-Aldrich) and

sodium hydroxide pellets (NaOH, BIOCHEM Chemopharma). The effect of ionic strength on the adsorption process was evaluated using sodium chloride (NaCl, Sigma-Aldrich). Additionally, hydrogen peroxide (H_2O_2, 30% v/v, Antiseptics Cherif) was acquired for surface modification and cleaning procedures. All chemicals were used as received without further purification. Deionized water was utilized extensively for all reagent preparations and for washing the synthesized materials to eliminate residual chemical activating agents.

III.4 Precursor material

DPS served as the precursor material for activated carbon production. This lignocellulosic biomass is an abundant agricultural residue produced during date (Phoenix dactylifera) harvesting. Raw DPS was collected from plantations in the Biskra region of southeastern Algeria. Utilizing this specific waste stream directly aligns with circular bioeconomy principles. The inherent chemical composition of DPS, characterized by high lignin and cellulose contents, provides an optimal foundation for developing microporous carbonaceous materials.

III.5 Synthesis and modification protocols

The adsorbent preparation followed a multi-stage protocol comprising precursor pretreatment, chemical impregnation, pyrolysis, and post-synthesis modification. Process parameters across all stages were strictly regulated to optimize the textural and surface chemical properties of the resulting composite.

III.5.1 Pre-treatment of DPS

DPS biomass was collected in a pre-dried state and manually sectioned to facilitate downstream processing. To eliminate surface contaminants (e.g., dust, soil, and field impurities), the material was washed extensively with tap water and then rinsed with deionized water to remove adventitious ions. The washed biomass was subsequently dried in a forced-convection oven at 105 °C for 48 h to a constant mass, ensuring complete moisture removal.

The desiccated material was initially crushed using a mortar grinder (Retsch RM 200) and subsequently pulverized in a high-speed mechanical grinder. To achieve a homogeneous particle size distribution, the resulting powder was fractionated using a standard mechanical shaker. The fraction passing through an 80-mesh screen ($0.90 <$ particle size < 0.180 mm) was isolated for the activation phase.

This specific particle size distribution was selected to maximize the impregnation efficiency of the chemical activating agent and promote uniform heat transfer during carbonization. Additionally, targeting this fraction mitigates the handling difficulties and mass-loss risks inherent to ultra-fine powders. The prepared precursor was stored in airtight polyethylene containers to prevent hygroscopic moisture reabsorption prior to synthesis.

III.5.2 Preparation of DPS-Biochar

An unmodified biochar was synthesized. Dried DPS powder was loaded into a ceramic crucible and positioned in the heating zone of a horizontal tubular furnace to establish a baseline for evaluating the enhancements imparted by ZnO modification. The material was carbonized in a single stage at 600 °C for 2 hours under an oxygen-limited atmosphere, with a heating rate of 10 °C/min. Post-pyrolysis, the carbonized residue was washed with 0.1 M HCl to solubilize acid-soluble ash and mineral constituents. Subsequent washing with deionized water was performed until the filtrate attained a neutral *pH*. The final product was oven-dried at 105 °C and designated as DPS-Biochar.

III.5.3 Synthesis of zinc oxide-modified activated carbon

The synthesis of the zinc oxide-modified activated carbon (ZnO@DPS-AC) employed a synchronized chemical activation and functionalization strategy adapted from Allalou et al. (2019). This protocol leverages $ZnCl_2$ as a dual-purpose agent. It acts as a potent dehydrating catalyst to promote the decomposition of the lignocellulosic precursor at reduced temperatures and as a precursor for the in situ formation of ZnO particles.

During the impregnation stage, 20 g of the sieved DPS precursor was blended with an equal mass of solid $ZnCl_2$ in a borosilicate beaker, yielding a 1:1 (w/w) precursor-to-activator ratio. Deionized water was added sparingly to generate a homogeneous slurry. This mixture was subjected to vigorous magnetic stirring at 65 °C for 4 hours. Elevated temperature reduces the viscosity of the medium and enhances the diffusion of Zn^{2+} ions into the biomass's porous architecture. Following impregnation, the slurry was dehydrated in a forced-convection oven at 105 °C for 24 h to yield a dry, reagent-loaded precursor.

The impregnated material underwent single-stage pyrolysis in a horizontal tubular furnace. The sample was heated to a terminal temperature of 600 °C at a ramp rate of 10 °C/min and held isothermally for 2h. During thermochemical conversion, the lignocellulosic framework carbonizes

into a rigid skeleton. Concurrently, $ZnCl_2$ induces dehydration and localized etching, thereby developing a high-surface-area microporous structure. A fraction of the zinc species simultaneously converts into ZnO particles, embedding directly within the nascent carbon matrix.

A sequential washing protocol was performed to eliminate residual $ZnCl_2$, soluble ash, and secondary reaction byproducts, ensuring composite purity and pore accessibility. The cooled pyrolyzed material was initially treated with 0.1 M HCl to neutralize basic impurities and extract labile zinc species. This step was followed by extensive washing with hot deionized water (≈ 80 °C) to remove residual salts. Final purification required rinsing with cold deionized water until the filtrate attained a neutral *pH* and exhibited no traces of chloride ions. The purified ZnO@DPS-AC was dried at 105 °C for 24 h and stored in a desiccator to preserve its physicochemical stability. All preparation steps of ZnO@DPS-AC are summarized in **Figure III.1**.

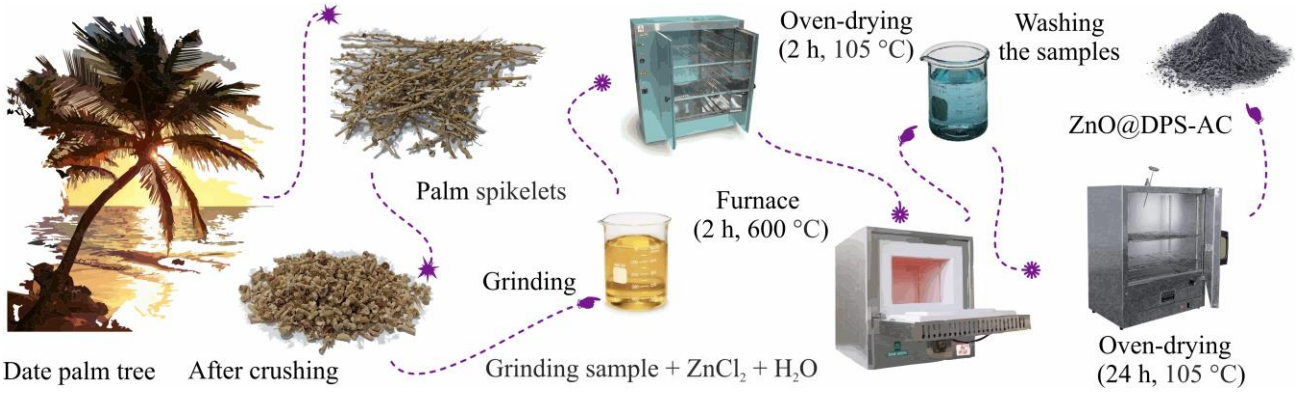

Figure III.1 Schematic illustration of ZnO@DPS-AC composite synthesis

III.5.4 Surface oxidation of ZnO@DPS-AC composite

In order to investigate the influence of oxygen-containing surface functional groups on the adsorption mechanism, specifically π-π and Lewis acid-base interactions, the ZnO@DPS-AC composite underwent a controlled oxidative treatment adapted from Tomul et al. (2021).

Exactly 1.0 g of the synthesized composite was dispersed in 100 mL of a 30% hydrogen peroxide (H_2O_2) solution. A mechanical stirrer maintained the suspension at 300 rpm and 30 °C for 6h. This mild oxidation introduces hydroxyl and carboxylic acid groups onto the carbon surface without compromising the composite's structural integrity. Post-oxidation, the mixture was cooled to ambient temperature and filtered through a 0.45 µm cellulose acetate membrane. The solid residue was washed with three 50 mL aliquots of deionized water to eliminate residual H_2O_2 and soluble byproducts. The washed solid was dried at 105 °C for 24 h. The resulting oxidized composite, designated as

ZnO@DPS-AC-Ox, was stored in a desiccator prior to adsorption testing.

III.6 Physicochemical characterization techniques

The physicochemical properties of the raw precursor and the engineered carbon composites were investigated through complementary characterization techniques. These analyses establish the material composition, structural framework, thermal stability, morphology, and surface chemistry. Each of these parameters directly dictates the overall adsorption performance.

III.6.1 Thermogravimetric analysis and derivative thermogravimetry

Thermogravimetric analysis (TGA) determined the thermal stability and compositional breakdown of the raw DPS. Approximately 12.5 mg of the dried sample was loaded into a crucible and analyzed using a simultaneous TGA-DSC instrument (SDT Q600, TA Instruments, New Castle, Delaware, USA). The thermal protocol applied a heating rate of 10 °C/min from 50 °C to 800 °C under a continuous nitrogen purge of 50 mL/min.

The instrument recorded the relative mass loss as a function of temperature. Concurrently, the derivative thermogravimetric (DTG) curve (dm/dT) was plotted to illustrate the rate of thermal degradation. The DTG profile isolates distinct thermal decomposition stages and precisely bounds the corresponding temperature regimes. Together, the TGA and DTG thermograms evaluate the structural stability of the precursor and isolate the discrete decomposition peaks for hemicellulose, cellulose, and lignin.

III.6.2 Proximate analysis

Proximate analysis was conducted to determine the carbonization yield, bulk density, total ash content, and moisture content of the activated carbon materials, both of which are critical indicators of adsorbent quality and performance.

III.6.2.1 Carbonization yield determination

Carbonization yield quantifies the mass fraction of solid residue retained after pyrolysis and serves as a primary indicator of process efficiency. The initial mass of the dried DPS precursor (m_1, g) was recorded prior to thermal treatment. A clean porcelain crucible was pre-weighed (m_2, g). Following pyrolysis and subsequent cooling to ambient temperature, the combined mass of the crucible and the carbonized product was determined (m_3, g). The carbonization yield was calculated utilizing **Eq. III.1**:

$$Yield\ (\%) = \frac{m_3 - m_2}{m_1} \times 100 \qquad \textbf{Eq. III.1}$$

III.6.2.2 Bulk density determination

Bulk density (or apparent density) defines the compactness and volumetric adsorption capacity of the synthesized material. This metric was adapted from procedures described by Ahmed and Dhedan (2012). The adsorbent was initially dried at 80 °C for 24 h to achieve a constant mass and eliminate residual moisture. A pre-weighed sample (m_{AC}, g) was transferred into a 10 mL graduated glass cylinder. The powder bed was consolidated by tapping the cylinder against a firm surface ten times, after which the final compacted volume (V_{AC}, mL) was recorded. Bulk density was calculated via **Eq. III.2**:

$$\rho\left(\frac{g}{mL}\right) = \frac{m_{AC}}{V_{AC}} \qquad \textbf{Eq. III.2}$$

III.6.2.3 Total ash content determination

Total ash content quantifies the inorganic mineral residue remaining after the complete oxidation of the carbon matrix. This analysis strictly adhered to the ASTM D2866-11 standard (Testing & Materials, 2011). A porcelain crucible was pre-ignited at 650 °C for 3 h, cooled in a desiccator, and weighed (m_0, g) to the nearest 0.1 mg. Approximately 1.0 g of dried activated carbon was transferred to the crucible, and the combined initial mass was recorded (m_1, g). The sample was subsequently calcined in a muffle furnace at 650 °C for 3 h to volatilize all carbonaceous matter completely. Upon cooling, the final mass of the crucible containing the ash residue was measured (m_2, g). Ash content was computed using **Eq. III.3**:

$$Ash(\%) = \frac{m_2 - m_0}{m_1 - m_0} \qquad \textbf{Eq. III.3}$$

III.6.2.4 Moisture content determination

Moisture content was evaluated via the standard oven-drying technique specified in ASTM D2867-17 (Testing & Materials, 2009). A clean glass weighing bottle with a matching stopper was pre-dried and weighed (m_0, g). A representative 1.0 g sample was introduced, and the combined initial mass was recorded (m_1, g). The open bottle was heated in a forced-air convection oven at 150 ± 5 °C for 3h. The bottle was subsequently capped, cooled in a desiccator, and reweighed to determine the final

mass (m_2, g). The mass fraction of moisture was calculated utilizing **Eq. III.4**:

$$M(\%) = \frac{m_1 - m_2}{m_1 - m_0} \qquad \textbf{Eq. III.4}$$

III.6.3 Point of zero charge

The surface charge characteristics of the ZnO@DPS-AC composite were evaluated by determining the pH_{PZC} via the pH drift method (Lopez-Ramon et al., 1999). A 0.1 M NaCl solution functioned as the inert background electrolyte. Aliquots of 50 mL were dispensed into a series of 250 mL Erlenmeyer flasks. The initial *pH* (pH_i) of each solution was adjusted to 2- 12 using 0.1 M HCl or 0.1 M NaOH. Exactly 50 mg of the adsorbent was introduced into each flask. The suspensions were sealed and agitated on a mechanical shaker for 24 h to ensure complete equilibration. After equilibrium, the final *pH* (pH_f) of the supernatant was measured with a calibrated digital *pH* meter. The *pH* differential ($\Delta pH = pH_i - pH_f$) was plotted against the initial *pH*. The pH_{PZC} corresponds to the x-intercept of this curve, where $\Delta pH = 0$.

III.6.4 Scanning electron microscopy coupled with dispersive X-ray spectroscopy

Surface morphology, porosity development, and topographical features of the adsorbents were visualized using a Prisma E Scanning Electron Microscope (SEM) (Thermo Fisher Scientific, Brno, Czech Republic). To prevent electron charging artifacts during high-resolution imaging, powder samples were affixed to aluminum stubs using double-sided conductive carbon tape. Elemental composition and spatial distribution were simultaneously mapped using an integrated UltraDry Energy Dispersive X-ray Spectroscopy (EDS) detector.

III.6.5 Fourier transform infrared spectroscopy

Fourier transform infrared (FTIR) spectroscopy identified and characterized the surface functional groups of the raw DPS, unmodified DPS-AC, ZnO@DPS-AC composite, and the pollutant-laden ZnO@DPS-AC post-adsorption. Spectra were recorded using a Shimadzu FTIR-8400S spectrophotometer (Shimadzu Corp., Kyoto, Japan). The analysis utilized the standard KBr pellet technique. Approximately 1.0 mg of pulverized sample was homogenized with 100 mg of spectroscopic-grade potassium bromide (KBr) and compressed into a transparent disc. Transmission spectra were acquired across a wavenumber range of 4000 to 400 cm^{-1} at a spectral resolution of 0.964 cm^{-1}.

III.6.6 X-ray diffraction

X-ray diffraction (XRD) determined the crystalline phases and structural ordering of the ZnO@DPS-AC composite. Data acquisition was performed on a Bruker D8 Advance diffractometer (Bruker AXS GmbH, Karlsruhe, Germany) equipped with a Cu Kα radiation source (λ = 1.5406 Å) operating at ambient temperature. Scans spanned an angular range (2θ) of 10° to 80°, utilizing a step size of 0.03° and a scan rate of 0.03°/s. High Score Plus software facilitated phase identification. The average crystallite size (*D*) of the ZnO particles was calculated via the Scherrer equation (**Eq. III.5**) (Scherrer, 1918):

$$D(nm) = \frac{k \times \lambda}{\beta_w \times cos\theta} \qquad \textbf{Eq. III.5}$$

Where k is the dimensionless shape factor (0.9), λ is the X-ray wavelength (0.15406 nm), β_w represents the full width at half maximum (FWHM) of the diffraction peak in radians, and θ is the Bragg angle.

III.6.7 Raman spectroscopy

Raman spectroscopy evaluated the graphitic quality of the carbon matrix and confirmed the integration of metal oxides. Measurements were performed using a Renishaw inVia Raman microscope (Renishaw plc, Wotton-under-Edge, UK) equipped with a 532 nm edge-laser excitation source operating at 10% power. A 50x objective lens focused the incident beam onto the sample surface. Scattered light was dispersed via an 1800 lines/mm diffraction grating and captured by a Centrus 0LL824 detector. To optimize the signal-to-noise ratio, spectra were acquired in continuous scan mode with an exposure time of 10 seconds and 20 accumulations. The analytical window spanned from 103 to 3804 cm^{-1}, centered at 1111 cm^{-1}.

III.6.8 Surface area and porosity analysis

The textural properties of the synthesized adsorbent, including specific surface area, pore volume, and pore size distribution, were determined via nitrogen (N_2) physisorption at -196.16 °C using a Micromeritics ASAP 2020 Plus (Version 2.00) surface area analyzer. Prior to measurement, the samples were degassed under vacuum at 150-200 °C for 8h to ensure the complete removal of pre-adsorbed moisture and volatile species from the surface and pore network.

III.6.8.1 Specific surface area determination

The S_{BET} was calculated from the nitrogen adsorption isotherm data using the Brunauer-Emmett-

Teller (BET) method (Brunauer et al., 1938). The BET equation, which describes the multilayer adsorption of gas molecules on a solid surface, is expressed in its linear form as **Eq. III.6**:

$$\frac{1}{V_{\text{ads}}\,(\,P_0\,/\,P\,-\,1\,)} = \frac{C\,-\,1}{V_m\,C}\left(\frac{P}{P_0}\right) + \frac{1}{V_m\,C_{BET}} \qquad \textbf{Eq. III.6}$$

Where V_{ads} is the volume of gas adsorbed at pressure P, P/P_0 is the relative pressure, V_m is the volume of gas required to form a complete monolayer cm^3 STP/g, and C_{BET} is the BET constant related to the energy of adsorption.

By plotting $(1/V_{ads})*(P_0/P - 1)$ against P_0/P over the relative pressure range of 0.05 to 0.30, the monolayer capacity (Vm) and the constant CBET were determined from the slope and y-intercept, respectively. The final S_{BET} was subsequently calculated utilizing **Eq. III.7**:

$$S_{\text{BET}} = \frac{V_m \cdot N_A \cdot A_m}{V_m^{\text{mol}}} \qquad \textbf{Eq. III.7}$$

Where N_A is Avogadro's number (6.022×10^{23} molecules/mol), A_m is the cross-sectional area of a nitrogen molecule (0.162 nm^2/molecule), and V_m^{mol} is the molar volume of N_2 (22414 cm^3/mol) at standard temperature and pressure (STP).

For comparative analysis, the Langmuir surface area ($S_{Langmuir}$) was evaluated by linearizing the Langmuir isotherm according to **Eq. III.8** (Tran et al., 2018):

$$\frac{P}{V_{\text{ads}}} = \frac{1}{V_m K} + \frac{P}{V_m} \qquad \textbf{Eq. III.8}$$

Where K represents the Langmuir constant, because the slope of this linear plot is equal to $1/V_m$, the Langmuir surface area can be derived using **Eq. III.9**:

$$S_{\text{Langmuir}} = \frac{V_m \cdot N_A \cdot A_m}{V_m^{\text{mol}}} \qquad \textbf{Eq. III.9}$$

III.6.8.2 Pore volume and pore size analysis

The V_p was estimated utilizing the Gurvich rule (Gurvich, 1915; Mason et al., 2014). This principle posits that at a relative pressure approaching saturation (typically $P/P_0 \approx 0.90–0.95$), all accessible pores are filled with condensed, liquid-like adsorbate. The adsorbed gas volume at standard temperature and pressure was converted to the equivalent liquid pore volume utilizing a conversion

factor (*CF*), as shown in **Eq. III.10**:

$$V_p(t) = V_{total(STP)} \times CF \quad \textbf{Eq. III.10}$$

This *CF* is fundamentally defined by **Eq. III.11**:

$$\text{Conversion Factor} = \frac{M_{w(L)}}{\rho_L \times V_m^{\text{mol}}} \quad \textbf{Eq. III.11}$$

Here, M_w is the molecular weight of the adsorbate (28.01 g/mol for N_2), and ρ_L is the liquid adsorbate density (0.808 g/cm^3 for N_2). The calculated *CF* is 0.0015466 cm^3 liquid/cm^3 STP.

The pore size distribution was determined from the desorption branch of the isotherm using the Faas Correction-Barrett-Joyner-Halenda (BJH) method (Barrett et al., 1951; Joyner et al., 1951). This approach provides reliable pore-size metrics by modeling capillary evaporation. Furthermore, the average pore width was calculated using **Eq. III.12**:

$$L_0(nm) = \frac{4 \times V_{BJH}}{A_{BJH}} \quad \textbf{Eq. III.12}$$

Here, V_{BJH} represents the cumulative pore volume in cm^3/g, and A_{BJH} is the cumulative pore area in m^2/g.

III.6.8.3 Microporosity and adsorption energy

The t-plot method, established by (De Boer et al., 1966), differentiated between micropore adsorption and external surface adsorption. The adsorbed volume was plotted against the statistical thickness ($t_{thickness}$ in Å) of the adsorbed layer. The t-values corresponding to each relative pressure (P/P_0) were calculated utilizing the standard Harkins-Jura equation (**Eq. III.13**) (Ngouallat et al., 2024):

$$t_{\text{thickness}} = \left[\frac{13.99}{0.034 - log\left(\frac{P}{P_0}\right)}\right]^{0.5} \quad \textbf{Eq. III.13}$$

From the resulting t-plot, the y-intercept of the linear regime yielded the micropore volume (V_{micro}), while the slope determined the external surface area (S_{ext}). The micropore surface area (S_{micro}) was subsequently derived by subtracting S_{ext} from the total BET surface area (S_{BET}). Finally, the characteristic adsorption energy (E_0) was estimated from the average pore diameter (L_0, nm) using the

empirical Stoeckli relationship (**Eq. III.16**) (Stoeckli et al., 1995):

$$V_{Micro} = \text{Intercept} \times \text{CF} \quad \textbf{Eq. III.14}$$

$$S_{ext} = Slope \times \frac{10^{-6}}{10^{-10}} \times \text{CF} \quad \textbf{Eq. III.15}$$

$$E_0 = \frac{10.8}{L_0} + 11.4 \quad \textbf{Eq. III.16}$$

III.7 Analytical methods for pollutant quantification

Accurate quantification of the target pollutant is required to evaluate adsorption efficiency. This study utilized UV-Visible (UV-Vis) spectrophotometry as the primary analytical technique.

III.7.1 Stock solutions

Stock solutions (1000 mg/L) of MO and CAT were prepared by dissolving 1000 mg of each solid precursor in 1000 mL of deionized water. For ACE, a 500 mg/L stock solution was formulated by dissolving a calculated mass of the commercial insecticide in deionized water, explicitly accounting for the 20% (w/w) active ingredient purity. To maintain chemical stability, MO solutions were stored in amber glass bottles to prevent photodegradation. CAT solutions were stored in the dark at 4 °C and used within 24 h to mitigate oxidative degradation. All working solutions for adsorption experiments were generated via the serial dilution of these primary stocks.

III.7.2 Determination of maximum absorption and calibration curves

Residual pollutant concentrations in the aqueous phase were quantified using a Hach DR6000 UV-vis spectrophotometer (Hach Company, Loveland, CO, USA). A standard MO solution was scanned across the UV-Vis spectrum (200 to 800 nm) to identify the wavelength of maximum absorption (λ_{max}). The result showed that the λ_{max} of the MO solution was at 464 nm (**Figure III.2(a)**). A calibration curve was constructed using standard solutions ranging from 0 to 60 mg/L (**Figure III.3(a)**). The natural *pH* of these solutions stabilized between 6.0 and 6.5, requiring no further adjustment.

Because CAT ionization is highly *pH*-dependent, its spectral behavior was evaluated over a broad *pH* range. Six 100 mg/L CAT sub-solutions were adjusted to *pH* values between 2 and 12, and each was scanned from 190 to 800 nm. Spectral data revealed a stable λ_{max} at 275 nm for solutions maintained

at *pH* 6 (**Figure III.2**(**b**)). Consequently, a CAT calibration curve was established for concentrations ranging from 0 to 130 mg/L at *pH* 7 (**Figure III.3**(**b**)).

The absorption spectrum of the ACE solution (derived from the Rustile formulation) was similarly scanned from 190 to 800 nm. The λ_{max} was identified at 245 nm (**Figure III.2**(**c**)). A corresponding calibration curve was generated for ACE concentrations ranging from 0 to 35 mg/L (**Figure III.3**(**c**)).

All three calibration curves exhibited high linearity, with coefficients of determination (R^2) exceeding 0.99. This confirms strict adherence to the Beer-Lambert law within the evaluated concentration ranges.

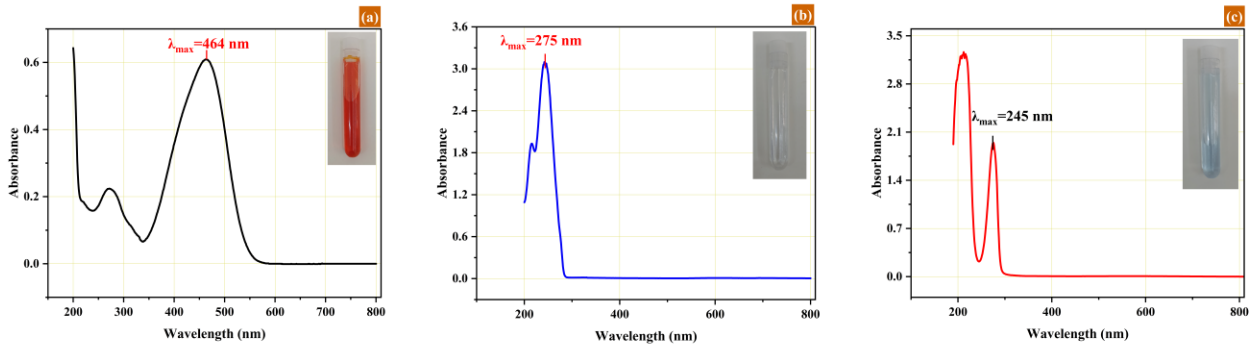

Figure III.2 Determination of λ_{max} of: (**a**) MO, (**b**) CAT, and (**c**) ACE

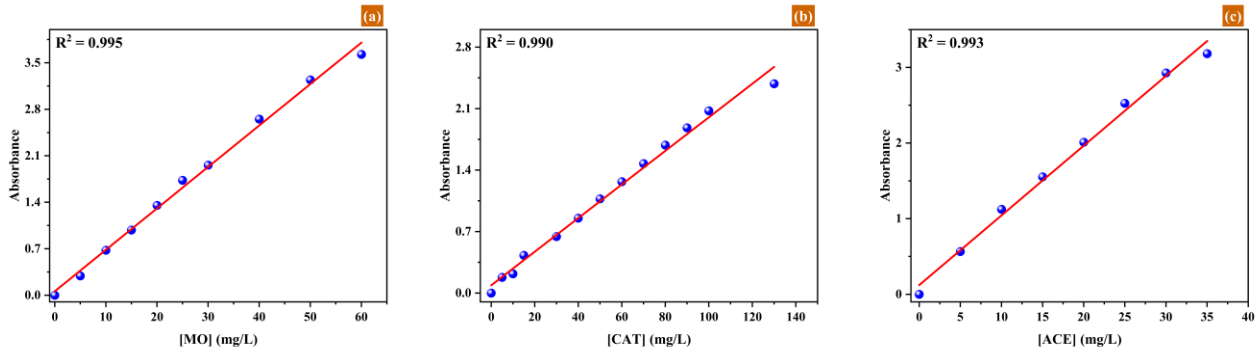

Figure III.3 Calibration curves of: (**a**) MO, (**b**) CAT, and (**c**) ACE

III.8 Batch adsorption experiments

Batch-mode adsorption experiments provided the primary data for the kinetic, equilibrium, and thermodynamic analyses. All trials were conducted in 250 mL Erlenmeyer flasks containing 50 mL of the respective pollutant solution. To eliminate external mass-transfer limitations, the flasks were agitated using a temperature-controlled magnetic stirrer at 300 rpm.

III.8.1 Single-factor Optimization

An OFAT approach was adopted to optimize the adsorption parameters systematically. The operational boundaries for initial solution *pH*, adsorbent dosage, initial pollutant concentration, contact time, temperature, and ionic strength were investigated as summarized in **Table III.1**.

Table III.1 Experimental ranges for the OFAT optimization of adsorption parameters

Parameter	MO	CAT	ACE	Unit / Condition
Adsorbent Dosage	15 – 100	15 – 100	15 – 200	mg/50 mL solution
Initial Concentration	50 – 500	25 – 200	50 – 400	mg/L
Contact Time	5 – 360	5 – 360	5 – 360	Minutes
Temperature	20, 30, 40	30, 35, 45	30, 40, 50	°C
Initial Solution *pH*	2 – 12	2 – 12	2 – 12	Adjusted via 0.1 M HCl or NaOH
Ionic Strength	0 – 1	0 – 1	0 – 1	M (using NaCl to simulate saline matrices)

III.8.2 Separation and measurement

Following the designated contact time, suspensions were passed through 0.45 µm cellulose acetate membrane filters or syringe filters to isolate the adsorbent particles. The residual aqueous pollutant concentration was quantified spectrophotometrically at the previously established λ_{max} for each compound. All experimental runs were performed in duplicate or triplicate. Results are reported as mean values, with error bars representing the standard deviation.

III.8.3 Calculation of adsorption capacity and efficiency

The adsorptive performance was evaluated through mass balance relationships. The repetitive definitions in the original draft were consolidated for clarity. The adsorption capacity at equilibrium (q_e, mg/g) and at any given time t (q_t, mg/g) were calculated using **Eq. III.17** and **Eq. III.18**, respectively:

$$q_e = \frac{(C_0 - C_e)V}{m} \qquad \textbf{Eq. III.17}$$

$$q_t = \frac{(C_0 - C_t)V}{m} \qquad \textbf{Eq. III.18}$$

The overall adsorption efficiency, or removal percentage, was determined via **Eq. III.19**:

$$R(\%) = \frac{C_0 - C_e}{C_0} \times 100$$ **Eq. III.19**

Where C_i, C_e, and C_t (mg/L) denote the pollutant concentrations initially, at equilibrium, and at time t, respectively; V (L) is the volume of the solution; and m (g) is the mass of the dry adsorbent.

III.9 Adsorbent reusability and regeneration studies

The practical applicability of the ZnO@DPS-AC composite was evaluated through sequential regeneration and reusability studies. Repeated adsorption and desorption cycles were executed until the target pollutant removal efficiency declined below 50%. Following each adsorption phase, the laden composite was collected and regenerated by immersion in a specific eluting agent. The desorbed material was subsequently washed with deionized water, dried at 105 °C for 24 h, and reintroduced into the subsequent adsorption cycle. The specific regeneration conditions for each pollutant were established as follows:

- **MO**: Adsorption utilized 360 mg of adsorbent in 600 mL of MO solution (100 or 200 mg/L). Desorption was achieved using 0.1 M NaOH at 50 °C for 4 h.
- **CAT**: Adsorption utilized 360 mg of adsorbent in 600 mL of CAT solution (50 or 100 mg/L). Desorption efficiency was evaluated using various agents (0.1 M HCl, 0.5 M NaOH, 0.1 M NaOH, and pure ethanol) at 27-50 °C for 4 h.
- **ACE**: Adsorption utilized 360 mg of adsorbent in 600 mL of ACE solution (100 or 200 mg/L). Desorption was achieved using pure ethanol at 27 °C for 4 h.

III.10 Adsorption isotherm and kinetic studies

Adsorption kinetics and equilibrium isotherms define the solute removal rate and elucidate the underlying interaction mechanisms between the adsorbates and the ZnO@DPS-AC composite. A comprehensive suite of mathematical models was applied to the experimental data to characterize this behavior. Kinetic analysis incorporated the PFO, PSO, Avrami, Elovich, and intra-particle diffusion models. Additionally, the Langmuir and the Freundlich isotherm models were utilized to evaluate the molecular distribution between the liquid and solid phases at equilibrium. Detailed mathematical formulations and their corresponding physical significance are documented in **sections II.2.4** and **II.2.5**, and in **Table Append. B.1**.

Kinetic experiments were conducted at ambient temperature to determine the precise equilibrium time

for each pollutant. Contact time was continuously monitored up to 270 min for CAT, 360 min for MO, and 300 min for ACE. Equilibrium studies quantified the combined influence of initial concentration and temperature across specific operational ranges. Initial concentrations spanned 25 to 200 mg/L for CAT (at 30, 35, and 45 °C), 50 to 500 mg/L for MO (at 20, 30, and 40 °C), and 50 to 400 mg/L for ACE (at 30, 40, and 50 °C).

To guarantee mathematical precision and statistical validity, all calculations were executed using a custom-developed MATLAB script. This included fitting all kinetic and isotherm data using non-linear regression. This computational tool also estimated the core thermodynamic parameters, specifically ΔG°, ΔH°, and ΔS°. These parameters collectively define the energetic favorability and spontaneity of the adsorption processes.

III.11 Statistical validation and goodness-of-fit

A robust statistical framework validated the reliability of the kinetic and isotherm models. To assess predictive accuracy across various mathematical models, multiple goodness-of-fit indicators were evaluated. These included the coefficient of determination (R^2, **Eq. III.20**), the adjusted coefficient of determination (*Adj*-R^2, **Eq. III.21**), the standard deviation (*SD*, **Eq. III.22**), and the reduced chi-squared statistic (*Red*-χ^2, **Eq. III.23**) (Al-Hazeef et al., 2024). Applying *Adj*-R^2 and *Red*-χ^2 is essential during non-linear regression. These specific parameters account for the degrees of freedom, effectively penalizing the model for additional variables and preventing the artificial inflation of fit quality. The fundamental statistical formulas are expressed as follows:

$$R^2 = 1 - \frac{\sum_{i=1}^{n}\left(q_{e,exp} - q_{e,cal}\right)^2}{\sum_{i=1}^{n}\left(q_{e,exp} - q_{e,mean}\right)^2} \quad \textbf{Eq. III.20}$$

$$R^2_{Adj} = 1 - (1 - R^2).\left(\frac{n-1}{n-p-1}\right) \quad \textbf{Eq. III.21}$$

$$SD = \sqrt{\left(\frac{1}{n-p}\right) \times \left[\sum_{i=1}^{n}\left(q_{e,exp} - q_{e,cal}\right)^2\right]} \quad \textbf{Eq. III.22}$$

$$Red_\chi^2 = \sum_{i=1}^{n}\frac{\left(q_{e,exp} - q_{e,cal}\right)^2}{n-p} \quad \textbf{Eq. III.23}$$

Additionally, the mean relative deviation modulus (E, %) quantified the average percentage error between the experimental observations and model predictions. The E value serves as a strict indicator of practical model applicability; values below 10% generally signify a highly acceptable fit for physical adsorption systems. This modulus is calculated using **Eq. III.24** (Praveen Kumar et al., 2006):

$$E(\%) = \frac{100}{n}\sum_{i=1}^{n}\left|\frac{q_{e,exp} - q_{e,cal}}{q_{e,exp}}\right| \qquad \textbf{Eq. III.24}$$

In these expressions, $q_{e,exp}$, and $q_{e,cal}$ represent the experimental and model-calculated adsorption capacities (mg/g), respectively. The variable n denotes the total number of experimental observations, and p refers to the number of parameters inherent to the specific model. High R^2 and $Adj\text{-}R^2$ values, coupled with minimized SD and $Red\text{-}\chi^2$ metrics, established the primary criteria for selecting the optimal models describing the adsorption of MO, CAT, and ACE onto the ZnO@DPS-AC composite.

III.12 Thermodynamic study

Consistent with the methodological rigor outlined in section **II.2.6**, the K_{Eq}° was not determined from isolated experimental points. Instead, a comprehensive evaluation integrated equilibrium isotherm data across three distinct temperatures for each pollutant. This multi-concentration approach ensures the calculated thermodynamic parameters accurately reflect system energetics across the entire functional adsorption range.

Following standard protocols, K_{Eq}° was derived by converting the best-fit isotherm constants (K_{Model}) extracted from the Langmuir, Sips, Liu, and Khan models into a dimensionless form. This transformation utilized the thermodynamic relationship defined in **Eq. III.25**:

$$K_{Eq}^{\circ} = \frac{1000 \times K_{Model} \times M_w \times [C^{\circ}]}{\gamma} \qquad \textbf{Eq. III.25}$$

Here, $[C^{\circ}]$ represents the standard state concentration (1 mol/L), M_w is the molecular weight of the specific adsorbate (MO, CAT, or ACE), and γ is the activity coefficient, which was assumed to be unity for the highly dilute aqueous solutions evaluated in this study. The ΔG° was subsequently calculated utilizing the fundamental thermodynamic relation (**Eq. II.8**).

To extract deeper insights into the driving forces of the adsorption process, ΔH° and ΔS° were

estimated using the van't Hoff equation (**Eq. II.10**). Linear and non-linear regression techniques were applied to the experimental data. By deploying both computational approaches, the consistency and reliability of the estimated ΔH° and ΔS° values were strictly cross-verified, ensuring a scientifically robust description of the spontaneity and thermal nature of the adsorbate-composite interactions.

III.13 Process optimization via response surface methodology

Preliminary batch adsorption studies elucidate the effects of individual parameters on pollutant removal but fail to capture potential synergistic or antagonistic interactions among variables. To address this limitation and isolate the precise conditions for maximum adsorptive performance, a systematic statistical optimization using RSM was employed. This approach integrates experimental design, mathematical modeling, and optimization algorithms to map the multidimensional relationship between independent operational variables and the resulting adsorptive responses.

III.13.1 Software

Experimental design generation, statistical analysis, and numerical optimization were executed using Design-Expert software (Version 13.0.5, Stat-Ease Inc., Minneapolis, MN, USA).

III.13.2 Experimental design matrix

The selection of independent variables and their operational ranges was based on the preliminary batch study data. To accommodate the specific parameter requirements for each pollutant, three distinct second-order experimental designs were implemented.

III.13.2.1 Methyl orange

A three-level BBD design evaluated five continuous factors: t, C_0, pH, T, and m. The design matrix comprised 46 experimental runs, including 6 central point replicates. The BBD framework was specifically selected to exclude extreme parameter combinations located at the vertices of the design space. Avoiding these vertices prevents experimental instability and mitigates non-linear behaviors that complicate predictive modeling.

III.13.2.2 Catechol

A rotatable CCD design optimized four factors: t, C_0, pH, and m. The axial distance (α) was established at 2.0 to ensure rotatability. This mathematical property guarantees that the variance of the predicted response remains constant at all points equidistant from the center of the design space.

The resulting matrix required 30 experimental runs, including 6 central points.

III.13.2.3 Acetamiprid

A Face-Centered CCD utilizing an α value of 1.0 evaluated four factors: t, C_0, m, and T. The face-centered geometry ensures that all experimental points remain strictly within the established physical limits of the operational conditions. Similar to the CAT matrix, this design consisted of 30 experimental runs with 6 central points.

Across all three systems, experimental runs were executed in a strictly randomized order to minimize the influence of unobserved systematic errors. No statistical blocking was applied to the design matrices. The independent variables and their corresponding coded levels (-1, 0, +1) are detailed in **Table III.2**.

Table III.2 Experimental factors and levels for the RSM optimization of MO, CAT, and ACE removal

Pollutant	Symbol	Factor	Unit	-α	-1	0	+1	+ α	Responses
MO						*(BBD)*			
	A	t	min	–	80	160	240	–	
	B	C_0	mg/L	–	100	250	400	–	
	C	pH	-	–	4	6	8	–	
	D	T	°C	–	25	35	45	–	
	E	m	mg	–	30	65	100	–	
CAT						*(Rotatable CCD)*			
	A	t	min	60	105	150	195	240	q_e and R
	B	C_0	mg/L	50	100	150	200	250	
	C	pH	-	2	4	6	8	10	
	D	m	mg	10	30	50	70	90	
ACE						*(Face-Centered CCD)*			
	A	t	min	–	30	105	180	–	
	B	C_0	mg/L	–	150	275	400	–	
	C	m	mg	–	30	65	100	–	
	D	T	°C	–	30	40	50	–	

III.13.3 Mathematical modeling and response analysis

To identify the mathematical function that best approximated the response surface, the experimental data were evaluated using a sequential model-sum-of-squares analysis. The data were fitted to linear, two-factor interaction (2FI), quadratic, and cubic models. Second-order (quadratic) polynomial equations were derived via multiple regression to express the target responses as continuous functions of the independent variables.

For each pollutant, two primary responses were monitored simultaneously: R (%) and q_e (mg/g). The experimental data were fitted to a quadratic (second-order) polynomial model to identify the critical points (maxima) and evaluate the curvature of the response surface. The general form of this regression model is defined by **Eq. II.17**.

III.13.4 Statistical validation and analysis of variance

To distinguish systematic effects from random experimental noise, the statistical adequacy of the selected models and the significance of the individual process variables were rigorously evaluated using Analysis of Variance. The complete mathematical formulations underlying this statistical validation are detailed in the **Appendix. C**.

The goodness-of-fit and predictive performance of the models were assessed using several stringent diagnostic metrics:

- **Significance testing**: The overall significance of the regression model and its individual terms was assessed using F and p-values, with a significance threshold of $\alpha = 0.05$ (95% confidence level). A comprehensive breakdown of Fisher's F-test framework, including hypothesis formulation and decision matrices, is provided in **Appendix. C.3**.
- **Lack-of-Fit (LoF) test**: The LoF test was used to detect systematic deviations between model predictions and experimental data by comparing residual error with pure error. A non-significant LoF ($p > 0.05$) was a strict prerequisite for model validity (see **Appendix. C.4** for the LoF F-test equation).
- **Goodness-of-Fit**: Fit quality was assessed using the coefficient of determination (R^2), the adjusted R^2, and the predicted R^2. A difference of less than 0.2 between the adjusted and predicted R^2 was set as a strict criterion to confirm predictive capability and to ensure against overfitting. The governing equations for these predictive capabilities are listed in **Appendix. C.3**.
- **Error and precision metrics**: The precision, consistency, and reproducibility of the experimental measurements were evaluated using the Coefficient of Variation (CV). Adequate Precision (AP) was used to assess the signal-to-noise ratio. An AP value greater than the standard threshold of 4 was required to confirm that the models had sufficient sensitivity to map the design space. The mathematical derivations for these error and precision metrics are provided in **Appendix. C.3**.

III.13.5 Multi-objective optimization and desirability function

The ultimate optimization objective was to isolate the operational parameters that simultaneously maximize both R and q_e for each of the three target pollutants. Multi-objective optimization was performed using the D_{opt} approach, following the procedure described in **section II.4.4**. Each response was transformed into a dimensionless desirability value scaling from 0 (completely undesirable) to 1 (ideal), and a global desirability metric was computed to identify the single optimal set of conditions (X_{opt}). Finally, validation experiments were executed in duplicate or triplicate under these predicted optimal conditions. Comparing these experimental results directly with the model predictions verified the physical reliability of the RSM framework used.

III.14 Artificial neural network modeling

To overcome the inherent limitations of polynomial-based models and provide a high-fidelity objective function for subsequent metaheuristic optimization, an ANN framework was constructed. Within this methodology, the ANN serves as a nonlinear mapping tool, directly correlating the input experimental variables (pH, m, C_0, t, and T) with the target responses (R and q_e).

Unlike standard RSM, which is restricted to second-order interactions, the ANN architecture captures complex, high-dimensional patterns without assuming a predefined mathematical relationship. This capability establishes the trained ANN as an ideal fitness function for the subsequent GA optimization stage. The complete computational framework was developed in MATLAB (R2021a). This modeling approach employed an automated optimization strategy to systematically identify the most robust predictive architecture for the complex adsorption dataset. The ANN flowchart is illustrated in **Figure III.4**.

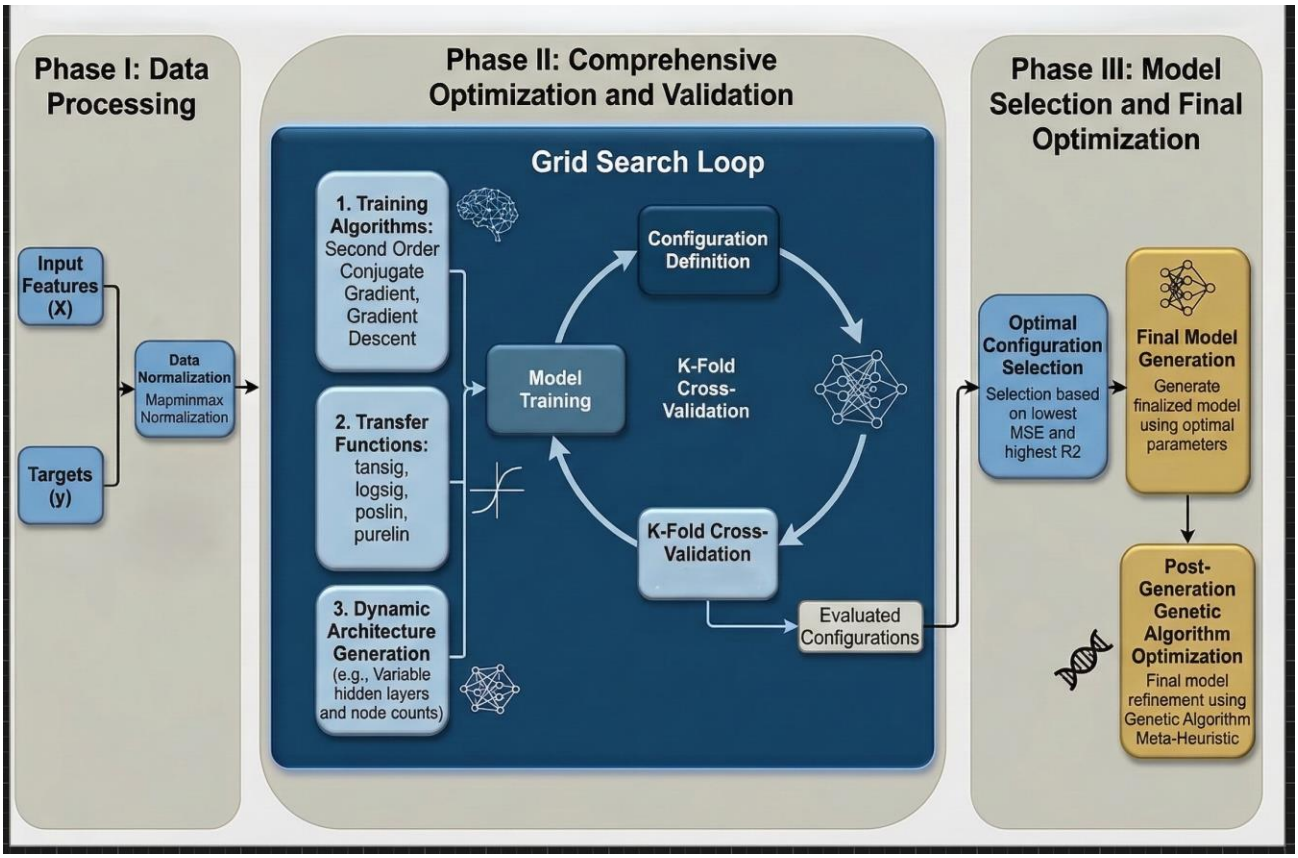

Figure III.4 Schematic representation of the ANN modeling process

III.14.1 Data preprocessing and normalization

To ensure efficient weight convergence and prevent neuron saturation within the hidden layers, all experimental datasets underwent rigorous normalization. Using the MATLAB mapminmax function, the inputs (x) and targets (y) were scaled to the strictly defined range [0.1, 0.9] according to **Eq. III.26**:

$$y = (y_{max} - y_{min}) \times \frac{x - x_{min}}{x_{max} - x_{min}} + y_{min} \qquad \textbf{Eq. III.26}$$

Here, x_{min} and x_{max} represent the minimum and maximum values of the raw input variables (e.g., contact time or solution *pH*), while y_{min} and y_{max} define the target normalization boundaries (0.1 and 0.9, respectively). This mathematical preprocessing guarantees that variables with disparate magnitudes and units exert proportional influence on the network learning trajectory.

III.14.2 Dynamic architecture generation

Rather than imposing a fixed, arbitrary architecture, the hidden layer configuration was dynamically generated based on inherent dataset complexity and sample size. The architectural search space

encompassed the following structural variations:

- **Single-layer configurations**: Evaluated networks containing 2 to 20 neurons to model fundamental functional relationships.
- **Transfer Functions**: Executed a systematic grid search across diverse activation function combinations. This specifically involved pairing the hyperbolic tangent sigmoid (tansig), log-sigmoid (logsig), and positive linear (poslin) functions in the hidden layers with a pure linear (purelin) activation function at the output layer.

III.14.3 Training algorithms and hyperparameter tuning

A systematic comparative analysis evaluated 8 distinct training algorithms to guarantee optimal convergence and network generalization. The evaluated algorithms included second-order numerical methods, specifically Levenberg-Marquardt (trainlm) and Bayesian Regularization (trainbr), alongside advanced gradient descent and conjugate gradient variants.

Algorithm-specific hyperparameters were strictly optimized utilizing a nested grid search protocol:

- **Regularization** (0 to 0.1): Integrated across all compatible algorithms to penalize excessively large weights and mitigate overfitting.
- **Update Parameters**: Tuned specific algorithmic variables, such as the initial update step (rp_{delta}) required for resilient backpropagation.

III.14.4 Robustness via cross-validation and ensemble learning

To eliminate the statistical variance associated with random weight initializations and strictly ensure predictive reliability, a k-fold cross-validation (k=3) strategy was implemented. Within each validation fold, an ensemble artificial neural network (EANN) comprising five independent networks was trained concurrently. The final model prediction was subsequently computed as the arithmetic mean of the individual ensemble member outputs.

III.14.5 Model selection and performance evaluation

The optimal network configuration was selected by minimizing the *MSE* and maximizing R^2 during the validation phase. The predictive performance of the final optimized ensemble was subsequently quantified using the R^2. This optimized ANN model served as the GA's direct objective fitness function to isolate the global optima of the physical adsorption parameters.

III.15 Multi-objective optimization using a genetic algorithm

To determine the absolute optimal adsorption conditions for MO, CAT, and ACE, a Multi-Objective Genetic Algorithm (MOGA) optimization approach was executed using customized code within the MATLAB environment. This approach simultaneously maximized two competing objectives: q_e and R. The previously trained ANN served as the core computational fitness-evaluation engine.

III.15.1 Algorithm architecture and island mode

The optimization framework used an island model architecture to maintain high population diversity and prevent premature convergence to local optima. The global population, determined via grid search, was evenly distributed across six independent islands. Within each of these sub-populations, the algorithm executes a continuous optimization loop of fitness evaluation (using the validated ANN model), selection, crossover, and mutation, as illustrated in **Figure III.5**. A ring topology migration mechanism exchanges the top-performing individuals between adjacent islands every 10 generations. This periodic migration effectively disseminates advantageous genetic information across the entire multidimensional search space.

III.15.2 Genetic operators and selection

The algorithm incorporated the fundamental principles of the Non-dominated Sorting Genetic Algorithm II (NSGA-II). The primary genetic operators included:

- **Selection**: Tournament selection identified parent chromosomes for the subsequent generation by evaluating their non-domination rank and crowding distance metrics.
- **Crossover**: Simulated binary crossover (SBX) recombines parent solutions using a crossover rate optimized via a systematic grid search.
- **Mutation**: Polynomial mutation introduced necessary genetic variation to maintain search-space exploration, operating at a mutation rate optimized via a systematic grid search.

III.15.3 Hyperparameter optimization via grid search

To ensure robust multi-objective optimization and prevent premature convergence, the fundamental GA hyperparameters were not fixed a priori. Instead, a systematic grid search was conducted prior to the final optimization run, encompassing 27 distinct configurations (a 3x3x3 design). The search space evaluated variations in population size (P), simulated binary crossover rates (CR), and polynomial mutation rates (MR). The performance of each configuration was quantitatively assessed using a

composite score that weighted five critical multi-objective performance indicators: hypervolume, Pareto front size, spacing uniformity, maximum spread, and convergence speed. The parameter configuration yielding the highest composite score was subsequently selected to generate the definitive Pareto-optimal front.

III.15.4 Diversity and local search enhancement

Two specialized modules were integrated to enhance the precision of the Pareto front:

- **Clustering analysis**: K-means clustering was executed periodically to analyze the spatial distribution of solutions. The clusters were subsequently adjusted to guarantee the exploration of underrepresented regions within the search space.
- **Local search**: An adaptive local search mechanism operated every 15 generations. This module utilized parallel search directions and a Pareto archive to strictly refine solutions in the immediate vicinity of the current front.

III.15.5 Convergence criteria and Pareto refinement

Algorithm progression was monitored using specific convergence metrics, including maximum generations, hypervolume improvement, Pareto front stability, and generalized spacing. The optimization terminated when the hypervolume improvement fell below 10^{-4} over a 100-generation window. Upon termination, the final Pareto solutions were denormalized using the inverse mapminmax function. This transformation reverted the variables to their original physical units for practical engineering interpretation.

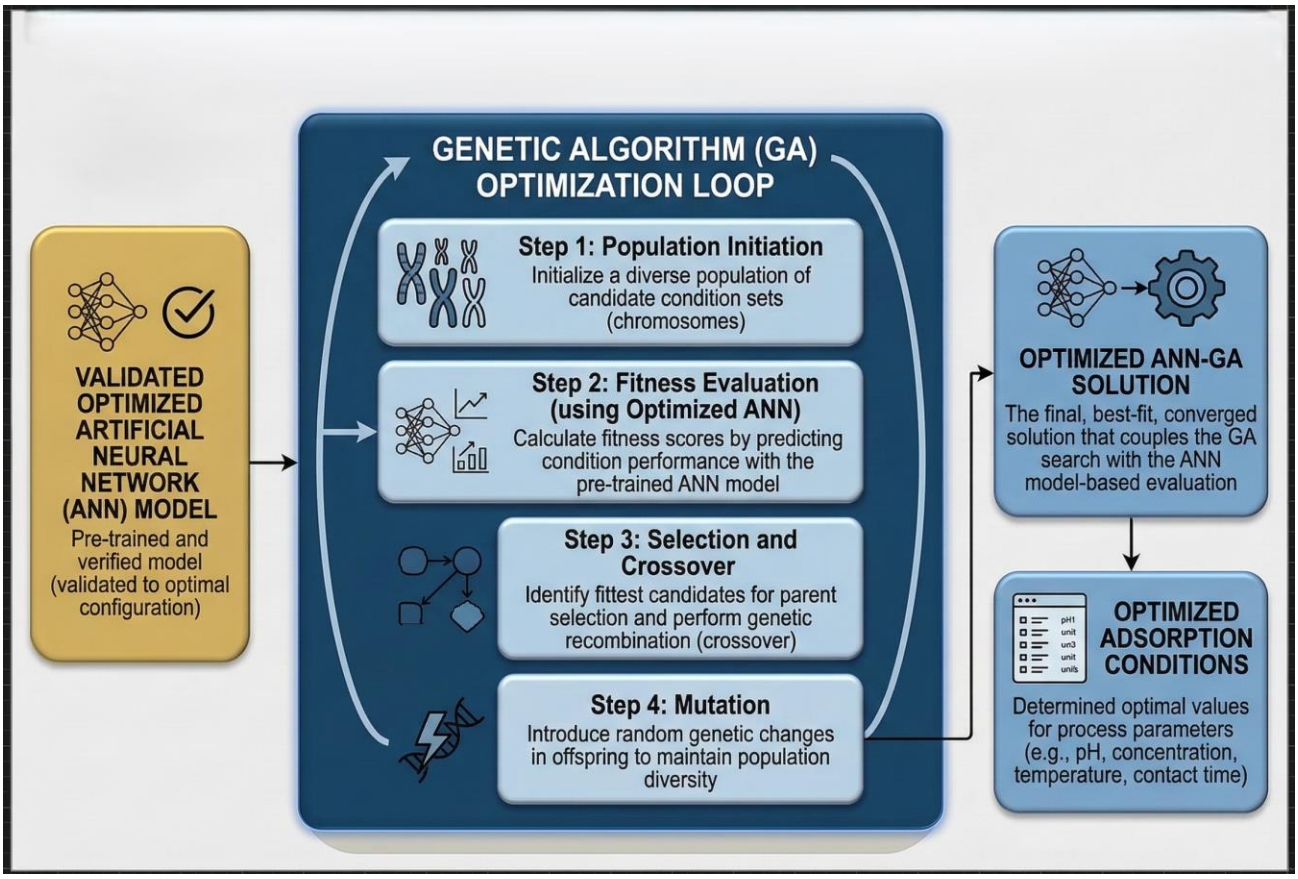

Figure III.5 Schematic of the GA optimization loop

III.16 Fixed-bed column adsorption studies

Fixed-bed column experiments evaluated the dynamic performance of the ZnO@DPS-AC composite under continuous flow conditions. This continuous-flow stage assesses the practical feasibility of the adsorbent in real-world wastewater treatment scenarios, where hydrodynamic parameters strictly govern the mass-transfer zone and breakthrough behavior.

III.16.1 Experimental configuration and apparatus

The experimental apparatus comprised a laboratory-scale glass column with an internal diameter of 1.0 cm and a total length of 5.0 cm. Specific masses of the ZnO@DPS-AC adsorbent (125, 250, and 500 mg) were packed into the column to establish varying bed depths. Cotton layers secured the top and bottom of the bed to ensure uniform liquid distribution and prevent adsorbent particle washout (**Figure III.6**).

The influent solution entered the column in downflow mode to minimize bed expansion and channeling. A high-precision peristaltic pump (Kamoer DIPump 550) maintained constant volumetric

flow rates. All dynamic experiments proceeded at ambient temperature. The initial influent *pH* was adjusted to the exact optimal value established during the prior batch optimization phase for each respective pollutant.

III.16.2 Kinetic modeling of column adsorption

Kinetic modeling of the continuous column adsorption utilized the mathematical frameworks initially detailed in **section II.2.5**. Mathematical modeling of the breakthrough curve translates empirical laboratory data into scalable industrial column designs. These models quantify fundamental kinetic parameters and the bed's maximum dynamic adsorption capacity, enabling accurate predictions of column performance under highly variable operational conditions.

III.16.3 Operational design and parameters

The dynamic behavior of the continuous system was investigated by varying three operational parameters: C_0, Q_v, and bed mass (Z). The complete experimental matrix governing the three target pollutants is detailed in **Table III.3**.

Table III.3 Experimental design matrix for fixed-bed column studies

Pollutant	Bed Weight (mg)	Flow Rate (mL/min)	C_0 (mg/L)
MO	125, 250, 500	3, 6, 9	200, 300, 400
CAT	125, 250, 500	3, 6, 9	100, 200, 300
ACE	125, 250, 500	3, 6, 9	100, 200, 300

Effluent aliquots were collected from the column outlet at predefined time intervals. The residual concentrations of MO, CAT, and ACE were quantified utilizing the spectrophotometric protocols detailed in the batch study section. Continuous flow experiments were terminated upon reaching bed exhaustion.

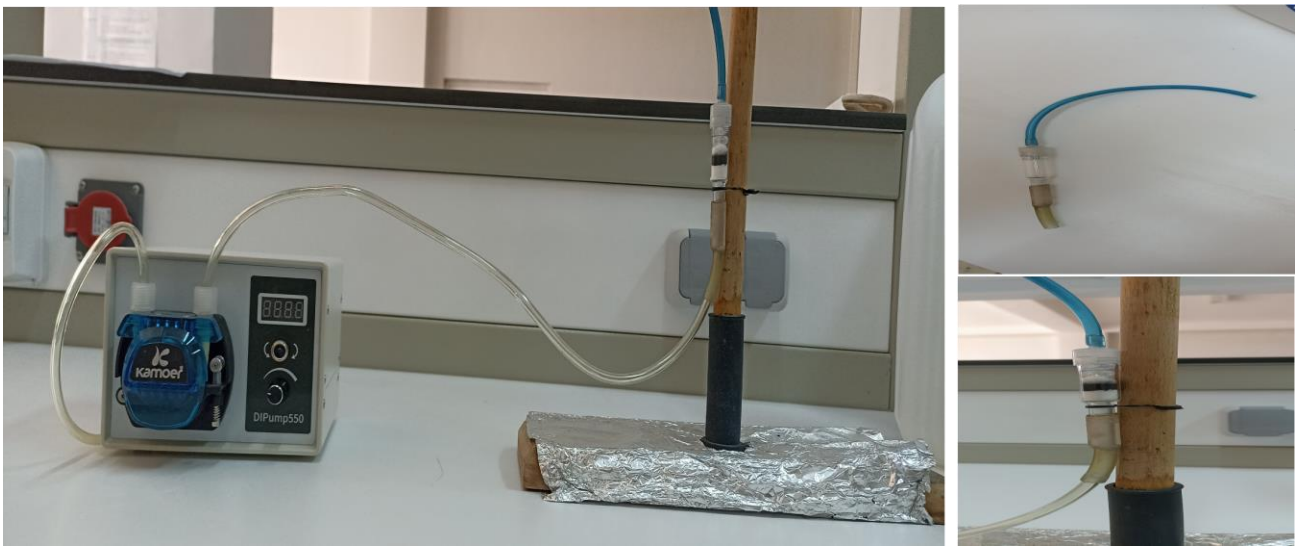

Figure III.6 Experimental setup of dynamic adsorption of target pollutants

III.16.4 Evaluation of column performance

Breakthrough curves characterized the dynamic performance of the fixed-bed column, which were generated as described in **section II.7.1**. To quantify the dynamic adsorption capacity and overall system efficiency strictly, the following fundamental mathematical parameters were computed (Aichour et al., 2019; Mon et al., 2024):

1. Total treated volume

The total volume of effluent treated by the column (V_{eff}, mL) is calculated via **Eq. III.27**:

$$V_{eff} = Q_v \times t_{total} \qquad \textbf{Eq. III.27}$$

Here, Q_v represents the volumetric flow rate (mL/min), and t_{total} denotes the total operation time (min) until exhaustion.

2. Total column adsorption capacity

The total mass of solute retained within the carbon bed (q_{total}, mg) is determined by integrating the area above the breakthrough curve (**Eq. III.28**):

$$q_{total} = \frac{Q_v}{1000}\int_0^t (C_0 - C_t)dt \qquad \textbf{Eq. III.28}$$

where C_0 and C_t (mg/L) correspond to the influent and effluent adsorbate concentrations, respectively.

3. Total influent mass

The total mass of the adsorbate introduced into the fixed-bed system (M_{total}, mg) is calculated using **Eq. III.29**:

$$M_{total} = \frac{C_0 \times Q_v \times t_{total}}{1000} \quad \textbf{Eq. III.29}$$

4. Total removal percentage R (%)

The overall dynamic efficiency of the column is defined as the ratio of the total adsorbed mass to the total influent mass (**Eq. III.30**):

$$R(\%) = \left(\frac{q_{total}}{M_{total}}\right) \times 100 \quad \textbf{Eq. III.30}$$

III.16.5 Model fitting and performance evaluation

The unknown parameters of the adsorption models were estimated by nonlinear least-squares regression in MATLAB. Nonlinear regression is preferred over linear regression because linearizing nonlinear equations alters their error distributions, violates fundamental statistical assumptions, and propagates errors, leading to inaccurate parameter estimates (Hu et al., 2019; Yu Wang et al., 2024).

To evaluate the validity of the models and determine the closeness of the experimental data to the calculated predicted values, a combination of statistical metrics was employed. The R^2 coefficient (R^2, **Eq. III.20**) is a widely used metric for assessing analytical accuracy and overall goodness-of-fit. The value indicates the proportion of variability explained by the model; values closer to unity (1) imply that the model highly accurately represents the experimental data (Yu Wang et al., 2024). However, relying exclusively on it can be misleading or inappropriate for evaluating nonlinear models (Apiratikul & Chu, 2021). The second metric is the residual root mean square error (*RMSE*, **Eq. III.31**). To supplement R^2, the *RMSE* (or relative *RMSE*) is used to measure the typical deviation of the experimental data points from the model's fitted curve. Unlike R^2, a lower *RMSE* indicates smaller error and a better fit (Apiratikul & Chu, 2021).

$$\mathrm{RMSE} = \sqrt{\frac{1}{z}\sum_{i=1}^{z}\left(C_{\mathrm{exp},i} - C_{\mathrm{cal},i}\right)^2} \quad \textbf{Eq. III.31}$$

When comparing multiple competing models with different numbers of adjustable parameters, using

only R^2 and *RMSE* is insufficient, as the fit will naturally favor the model with more parameters, leading to overfitting (Apiratikul & Chu, 2021). To overcome this, information-theoretic metrics such as the Corrected Akaike Information Criterion (AIC_c) and its derived Akaike Weight (AW) are utilized. It is calculated using the equations **Eq. III.32 -Eq. III.35**.

$$\mathrm{SSR} = \sum_{i=1}^{z} \left(C_{\mathrm{exp},i} - C_{\mathrm{cal},i}\right)^2 \qquad \textbf{Eq. III.32}$$

$$\mathrm{AIC} = z \ln\left(\frac{\mathrm{SSR}}{z}\right) + \frac{2z(p+1)}{z-p-2} \qquad \textbf{Eq. III.33}$$

$$\Delta_i = \mathrm{AIC}_i - \mathrm{AIC}_{\mathrm{m}} \qquad \textbf{Eq. III.34}$$

$$\mathrm{AW} = \frac{\exp(-0.5\Delta_i)}{\sum_{j=1}^{w} \exp(-0.5\Delta_j)} \times 100 \qquad \textbf{Eq. III.35}$$

In the provided equations, $C_{\mathrm{exp,i}}$ represents the experimental value for the *i*-th data point, while $C_{\mathrm{cal,i}}$ denotes the calculated or model-predicted value for that same point. The term $C_{\mathrm{exp,av}}$ denotes the average of all experimental values across the dataset, and z denotes the total number of data points analyzed. Furthermore, p signifies the number of parameters within the evaluated model. When assessing model selection criteria, AIC_i denotes the Akaike Information Criterion for the i-th model, and AICm denotes the minimum AIC across all candidate models, where w denotes the total number of candidate models.

The AIC_c imposes a strict penalty for model complexity (i.e., the number of parameters). Based on AIC_c scores, the AW is calculated to provide a direct estimate of the probability that a specific model is the absolute best among candidate models. The model exhibiting the highest *AW* percentage is selected as the statistically optimal model (Apiratikul & Chu, 2021; Chu & Hashim, 2023b, 2024b; Yu Wang et al., 2024).

III.17 Conclusion

This chapter detailed the experimental framework and analytical methodologies required to fulfill the core research objectives. The sequential methodology transitions from the sustainable synthesis of the novel adsorbent to its physicochemical characterization, concluding with its application and optimization in simulated water remediation scenarios.

The initial sections established the protocols for valorizing DPS into a high-performance

carbonaceous material. Simultaneous chemical activation and functionalization with $ZnCl_2$ yielded a highly porous, metal-oxide-embedded matrix (ZnO@DPS-AC). A comprehensive suite of characterization techniques validates this synthesis and elucidates the fundamental material properties. These techniques include TGA-DTG, SEM-EDX, FTIR, pH_{PZC}, XRD, Raman, and BET analysis.

Following material preparation, the methodology defined the batch adsorption protocols targeting three model pollutants: MO, CAT, and ACE. The experimental design systematically evaluated operational parameters (C_0, m, pH, t, ionic strength, and T) to facilitate precise kinetic, equilibrium, and thermodynamic modeling. Additionally, cyclic regeneration protocols evaluate the practical reusability and economic viability of the synthesized composite.

The methodology advances beyond traditional univariate analysis by integrating statistical and computational optimization techniques. RSM, executed via CCD and BBD, mathematically optimizes the multivariable adsorption processes. Furthermore, integrating ANN modeling with a GA provides high-fidelity predictive analytics and isolates global multi-objective optima. Finally, the configuration and mathematical evaluation of continuous fixed-bed column studies bridge the gap between batch-scale feasibility and dynamic, industrial-scale applicability.

With the materials, experimental procedures, and computational frameworks firmly established, the subsequent chapter presents and critically analyzes the empirical results. This analysis begins with the detailed physicochemical characterization of the raw precursor and the synthesized ZnO@DPS-AC composite.

Chapter IV: Synthesis and Physicochemical Characterization of the ZnO@DPS-AC

* * * * *

IV.1 Introduction

Developing highly effective adsorbents for environmental remediation requires a profound understanding of their physicochemical, morphological, and structural properties. The previous chapter detailed the experimental protocols for synthesizing a zinc oxide-modified activated carbon composite (ZnO@DPS-AC) from DPS, offering a sustainable and innovative approach to pollutant removal. Building on that foundation, this chapter provides a rigorous empirical validation of the synthesis process by comprehensively characterizing both the intermediate biochar and the final functionalized composite. Rather than merely observing the final product, this systematic evaluation is designed to elucidate the specific mechanisms of material formation, surface functionalization, and structural evolution.

To achieve this, a carefully selected suite of complementary analytical techniques was employed. TGA and DTG first evaluate the thermal decomposition profile of the raw biomass, which directly justifies the selected pyrolysis conditions. Subsequently, the structural and chemical transformations induced by simultaneous $ZnCl_2$ activation and pyrolysis are investigated. SEM-EDX characterizes the resulting surface topography, pore development, and elemental distribution, while FTIR spectroscopy, XRD, and Raman spectroscopy collectively probe the surface chemistry and structural ordering within the carbonaceous matrix. Together, these techniques confirm the successful incorporation of nanoscale ZnO particles into the graphitic carbon framework and identify the primary surface functional groups responsible for binding the target pollutant. Finally, BET analysis quantifies the specific surface area and pore-size distribution, which are the physical parameters that fundamentally dictate mass-transfer rates during adsorption. Ultimately, the structural and chemical characterization presented herein provides the critical mechanistic insights needed to interpret and justify the complex dynamic batch and continuous adsorption behaviors explored in subsequent chapters.

IV.2 TGA and DTG analysis of DPS

TGA coupled with DTG and Differential Scanning Calorimetry (DSC), evaluated the thermal degradation profile of DPS. These thermal analyses are essential for optimizing the pyrolysis parameters required to synthesize the activated carbon matrix. The resulting thermograms are

presented in **Figure IV.1**.

IV.2.1 Multi-stage thermal degradation

The thermal decomposition of DPS proceeds through three distinct stages. This progression reflects the complex structural breakdown of its lignocellulosic constituents (Bumajdad & Hasila, 2023; de Andrade et al., 2015; Kaya & Uzun, 2021):

- **Stage I**: Dehydration (50 °C to 113 °C): An initial, minor mass reduction occurs in this temperature range. This loss is primarily attributed to the evaporation of physically adsorbed moisture and the release of highly volatile organic molecules from the biomass surface.
- **Stage II**: Active Pyrolysis (183 °C to 488 °C): This temperature range corresponds to the primary degradation zone, where the majority of mass loss occurs. The stage involves the thermal devolatilization of hemicellulose and cellulose, accompanied by the initial fragmentation of lignin. Concurrently, oxygenated surface functionalities (such as lactones and carboxylic acids) decompose. This process typically yields CO_2 and CO as gaseous byproducts.
- **Stage III**: Carbonization and Stabilization (> 600 °C): Beyond 600 °C, the mass loss curve plateaus. This stabilization indicates the successful transformation of the raw biomass into a stable carbonaceous char. Reaching this thermal threshold ensures the near-complete volatilization of labile components while maximizing the final yield of the activated carbon framework.

IV.2.2 Differential analysis

The DTG profiles offer a highly resolved representation of the decomposition kinetics. Specifically, the data exhibit three characteristic thermal events corresponding to the primary biomass constituents (Kaya & Uzun, 2021; Tran et al., 2019):

- **Hemicellulose**: A visible shoulder at approximately 275 °C aligns with the established decomposition range of hemicellulose (210 °C to 325 °C). As an amorphous and heavily branched polymer, hemicellulose acts as the least thermally stable fraction.
- **Cellulose**: A sharp, intense peak centered at 330 °C indicates the rapid degradation of crystalline cellulose. This major transition typically occurs between 310 °C and 400 °C.
- **Lignin**: A broad, low-intensity tailing extends up to 465 °C and beyond, representing the gradual decomposition of lignin. The complex, highly cross-linked aromatic structure of lignin

dictates a wide range of degradation temperatures (160 °C to 900 °C). Consequently, lignin contributes significantly to the final char yield.

The DSC data (**Figure IV.1**(**c**)) correlate energetically with these structural transitions. Endothermic peaks during the first stage confirm the energy uptake required for moisture evaporation. In contrast, subsequent exothermic signals in the second stage correspond to the bond-breaking and molecular rearrangement events necessary to form the aromatized carbon matrix.

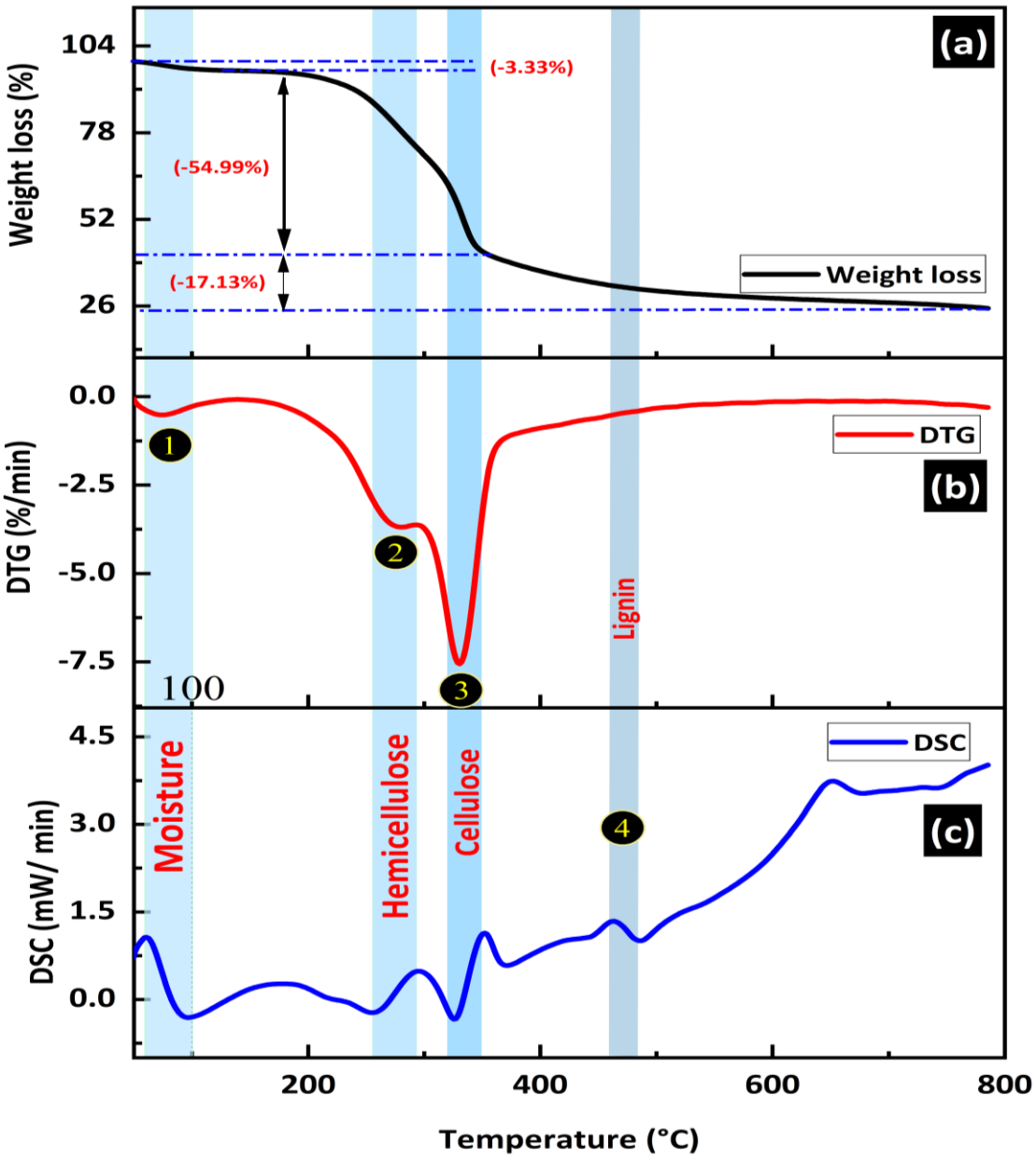

Figure IV.1 Thermal decomposition profile of raw DPS under an inert atmosphere: **(a)** TGA profile; **(b)** DTG profile; and **(c)** DSC profile

IV.3 Proximate analysis

Assessing the physicochemical properties of the synthesized ZnO@DPS-AC composite is necessary to evaluate its structural stability and viability for aquatic remediation. **Table IV.1** summarizes these fundamental characteristics.

IV.3.1 Analysis of inorganic and volatile components

The composite exhibited an ash content of 65.33%. This value significantly exceeds the standard baseline for typical biomass-derived activated carbons (usually <10%). Rather than indicating poor precursor quality, this elevated inorganic fraction directly quantifies the dense loading of ZnO within the carbon matrix, along with the inherent mineral matter retained from the DPS. These findings firmly corroborate the strong ZnO signals observed in both XRD and FTIR analyses.

Furthermore, the composite maintained a notably low moisture content of 2.42%. This confirms the thermal efficiency of the activation and drying protocols. As a result, the active pore network remains fully accessible for target pollutant capture, rather than being prematurely obstructed by adsorbed water molecules.

IV.3.2 Yield and structural density

The synthesis process achieved a carbonization yield of 42.11%, demonstrating a substantial conversion efficiency for chemically activated agricultural precursors. During pyrolysis, the $ZnCl_2$ activating agent functions as a potent dehydrant. It chemically suppresses tar formation and drives carbon fixation, effectively sustaining a high material yield even under aggressive thermal conditions.

Additionally, the final composite possesses a bulk density of 508.61 g/L, reflecting a highly consolidated structural framework. For large-scale environmental applications, this elevated bulk density is inherently advantageous. It maximizes the adsorbent mass that can be packed into a fixed-bed column, directly amplifying the volumetric treatment capacity and operational efficiency per continuous cycle.

Table IV.1 Properties of the prepared ZnO@DPS-AC composite

Property	ZnO@DPS-AC
Ash content (%)	65.33
Moisture Content (%)	2.42
Carbonization Yield (%)	42.11
Bulk density (g/L)	508.61

IV.4 Point of zero charge

The electrostatic properties and surface acid-base behavior of the ZnO@DPS-AC composite were characterized using pH_{pzc} analysis. As illustrated in **Figure IV.2**, the pH_{pzc} of the synthesized material is 6.67. This fundamental metric dictates the subsequent electrostatic interactions between the adsorbent surface and target aqueous pollutants.

At solution *pH* values below the pH_{pzc} ($pH < 6.67$), the composite surface undergoes protonation. The high proton concentration in the bulk solution yields a net positive charge on both the carbonaceous functional groups and the inherent ZnO active sites. Conversely, under conditions where $pH > 6.67$, surface deprotonation dominates, resulting in a net negative charge at the material interface.

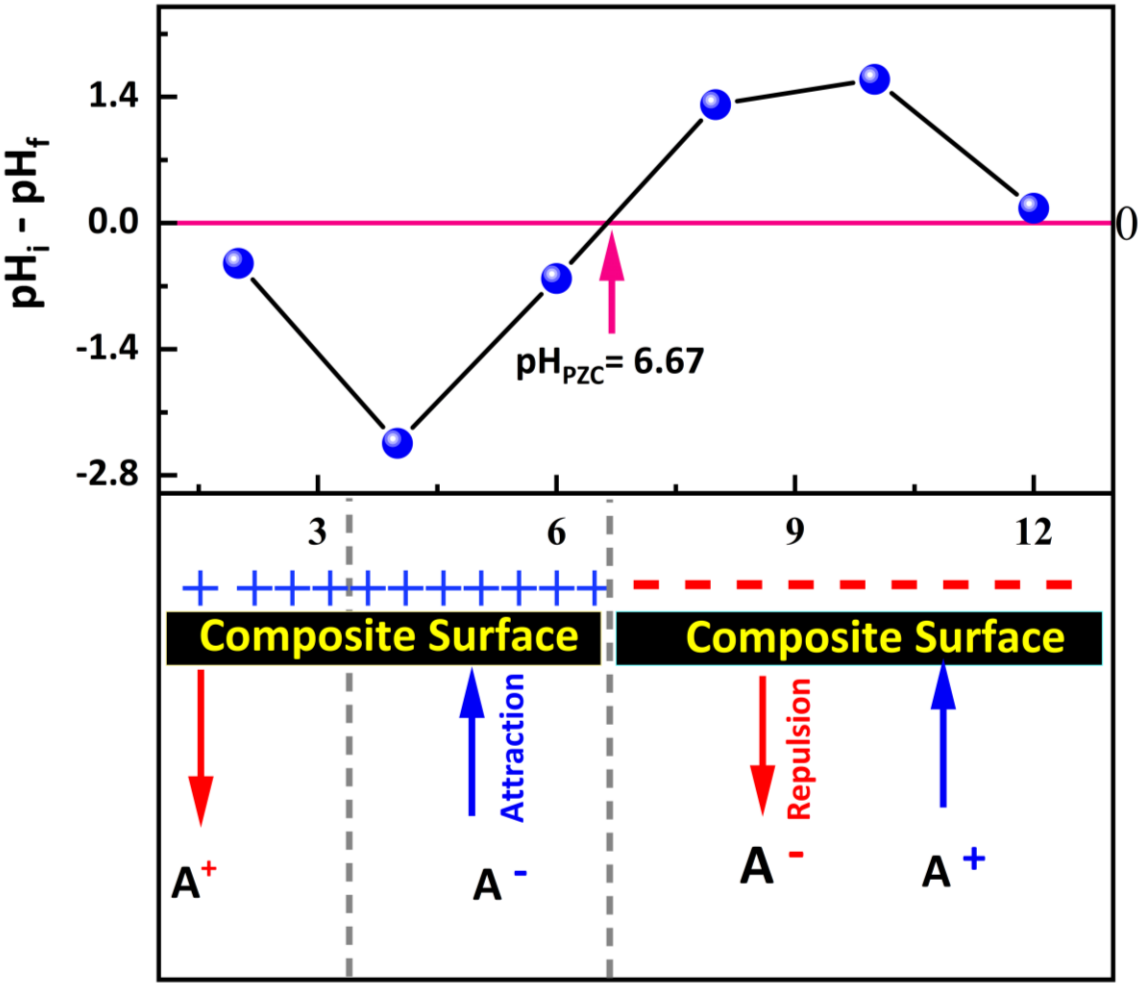

Figure IV.2 pH_{pzc} of ZnO@DPS-AC

IV.5 Scanning electron microscopy coupled with energy-dispersive X-ray spectroscopy

The physical and chemical transformation of raw DPS into a functionalized adsorbent, alongside its

subsequent pollutant removal performance, was evaluated using integrated SEM-EDX analysis. This combined approach directly correlates the evolution of structural porosity with localized chemical surface modifications.

IV.5.1 Impact of $ZnCl_2$ on the porosity and surface chemistry of DPS

The transition from inactivated DPS biochar to the ZnO@DPS-AC composite demonstrates the severe structural modifications induced by $ZnCl_2$ chemical activation. As depicted in **Figure IV.3(a)**, the initial biochar exhibits a relatively closed morphology. Smooth, rigid, fibrous surfaces and rudimentary vascular bundles are characteristic of lignocellulosic biomass. The corresponding EDX profile, dominated by carbon (73.04%) and oxygen (22.92%), confirms a standard carbonized matrix containing minor endogenous minerals (Mg, Si, Ca).

In contrast, the ZnO@DPS-AC composite (**Figure IV.3(b)**) displays a complete architectural shift toward a highly developed, honeycomb-like pore structure. During pyrolysis, $ZnCl_2$ acts as a strong dehydrating agent. It accelerates the thermal degradation of cellulose and hemicellulose and suppresses tar formation, ultimately generating the distinct macroporous and mesoporous cavities observed. Furthermore, EDX analysis confirms the successful integration of zinc (1.3%) into the carbon framework. These zinc species likely exist as ZnO clusters or particles. They serve as strategic active sites that enhance the overall adsorptive capacity through surface complexation.

IV.5.2 Integrated SEM-EDX analysis of adsorbed pollutants

The efficacy of the ZnO@DPS-AC composite in sequestering organic pollutants is substantiated by the visual and chemical transformations observed in the post-adsorption samples (**Figure IV.3 (c–e)**). Correlating morphological shifts with elemental fingerprints definitively confirms the successful loading of MO, CAT, and ACE onto the adsorbent surface.

- MO adsorption

Following MO adsorption, the SEM micrograph (**Figure IV.3 (c)**) reveals a distinct rounding of the previously sharp, well-defined pore edges characteristic of the pristine adsorbent. This morphological smoothing suggests the successful deposition of a molecular layer across the carbonaceous framework. Quantitative EDX analysis supports this observation by detecting a sulfur weight percentage of 0.78%. Because sulfur is a fundamental constituent of the sulfonic group ($–SO_3^-$) within the MO molecule (see **Figure I.1**), its detection provides conclusive evidence of dye adsorption. The

persistence of sulfur, alongside a zinc content of 1.64%, indicates that the MO molecules have effectively diffused into the macro- and mesoporous structures, occupying available active sites.

- CAT adsorption

The morphological evolution of the CAT-loaded sample (**Figure IV.3** (**d**)) features increased surface granularity relative to the pristine ZnO@DPS-AC. This roughened texture indicates the formation of a dense molecular layer of CAT across the adsorbent. Furthermore, EDX analysis shows a concurrent rise in zinc (2.59%) and sulfur (1.79%) content. This chemical signature suggests a synergistic interaction between the phenolic hydroxyl groups of CAT and the zinc-doped carbon matrix. The adsorption process likely involves a combination of hydrogen bonding and metal-ligand coordination. In this mechanism, the zinc centers act as Lewis acid sites, stabilizing the CAT molecules on the surface and thereby enhancing overall removal efficiency.

- ACE adsorption

The most pronounced structural transformation occurs following the adsorption of ACE (**Figure IV.3** (**e**)). The SEM image shows the deposition of bulky molecular aggregates that partially mask the composite's underlying honeycomb architecture. The EDX spectra provide rigorous evidence of successful loading, highlighting a significant increase in nitrogen (42.96%) and the emergence of chlorine (0.44%). Because the ACE molecule contains four nitrogen atoms and one chlorine atom (see **Section I.5.1** and **Figure I.1**), these elements serve as definitive chemical markers.

IV.5.3 Structural evolution and adsorptive performance

Integrated SEM-EDX analysis confirms a successful tripartite development process: (i) the pyrolytic conversion of dense DPS biomass into a highly porous carbonaceous matrix, (ii) the effective functionalization of the surface with zinc active sites, and (iii) the robust affinity of the resulting composite for chemically diverse pollutants. While pore-filling mechanisms and surface coating primarily characterize the removal of MO and CAT, the interaction with ACE is significantly more pronounced.

IV.6 Surface functional group analysis

FTIR spectroscopy was conducted to elucidate the surface chemistry of the materials and to identify the specific functional groups responsible for organic pollutant remediation. **Figure IV.4** illustrates the spectral evolution from the raw biomass precursor to the functionalized adsorbent, alongside the

subsequent post-adsorption states.

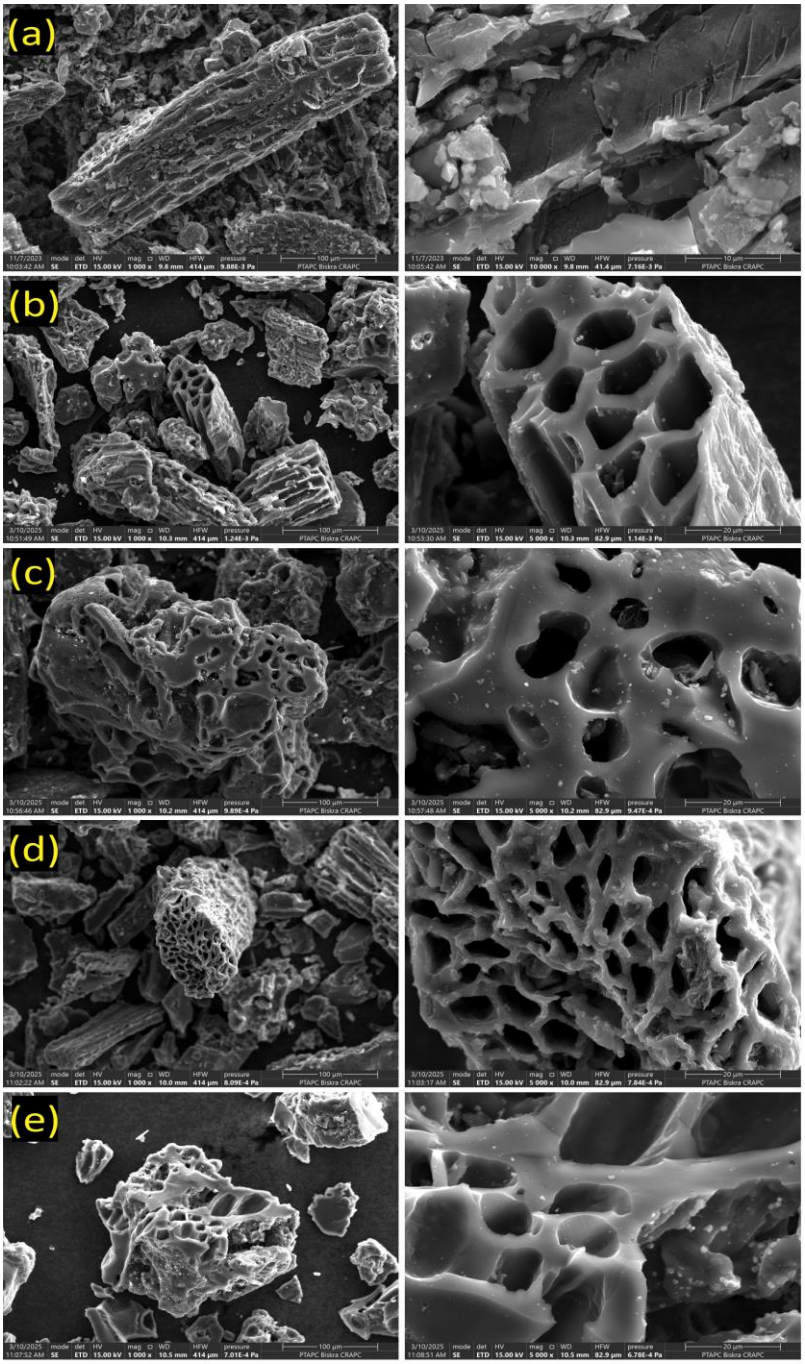

Element	Weight (%)
C	73.04
O	22.92
Mg	0.61
Si	0.56
S	0.76
K	1.02
Ca	1.09

Element	Weight (%)
C	77.11
O	21.24
S	0.36
Zn	1.3

Element	Weight (%)
C	77.62
O	19.96
S	0.78
Zn	1.64

Element	Weight (%)
C	77.24
O	18.38
S	1.79
Zn	2.59

Element	Weight (%)
C	35.94
O	12.6
S	2.39
Zn	5.67
N	42.96
Cl	0.44

Figure IV.3 SEM micrographs (at dual magnifications) and corresponding EDX elemental profiles of the synthesized materials: (**a**) DPS-Biochar derived from DPS; (**b**) ZnO@DPS-AC composite after $ZnCl_2$ activation and pyrolysis; and the ZnO@DPS-AC adsorbent after the adsorption of (**c**) MO, (**d**) CAT, and (**e**) ACE

IV.6.1 Characterization of raw DPS and DPS-Biochar

The spectrum of the raw DPS biomass exhibits a complex vibrational profile typical of lignocellulosic materials. A broad, intense band centered between 3000 and 3500 cm^{-1} is attributed to the stretching vibrations of hydroxyl (–OH) groups present in cellulose, hemicellulose, pectin, and lignin (Tcheka et al., 2024). Weak peaks located at 2930 and 2840 cm^{-1} correspond to the asymmetric and symmetric C–H stretching of aliphatic methylene groups (He et al., 2020). Within the carbonyl region (1740–1650 cm^{-1}), minor peaks and shoulders represent C=O stretching associated with hemicellulose or ester linkages (Azoulay et al., 2020; Rzig et al., 2021). A prominent band at 1624 cm^{-1} is assigned to C=C aromatic skeletal vibrations or the deformation of adsorbed water (Fu et al., 2009). The fingerprint region (1300 to 400 cm^{-1}) contains multiple signals related to C–O–C stretching and aromatic C–H out-of-plane bending (918 to 803 cm^{-1}) (Azoulay et al., 2020; El Hamdouni et al., 2022).

Upon carbonization to DPS-biochar, significant spectral transformations occurred. While the intensity of the –OH band increased, likely due to the concentration of recalcitrant phenolic structures, the aliphatic C–H peaks at 2930 and 2840 cm^{-1} diminished or completely disappeared. This indicates the extensive thermal degradation of alkyl chains. Furthermore, sharpening of the 1630 cm^{-1} band and increased peak definition in the 1600-400 cm^{-1} range suggest the formation of a highly stable, aromatized carbon framework during pyrolysis.

IV.6.2 Role of $ZnCl_2$ in ZnO@DPS-AC functionalization

The chemical activation process significantly altered the surface chemistry of the carbonaceous matrix. The transition to the ZnO@DPS-AC composite is characterized by a notable attenuation of the broad –OH band compared to the inactivated biochar. This reduction directly results from the dehydrating action of $ZnCl_2$. Acting as a Lewis acid catalyst, the activating agent promotes the removal of hydrogen and oxygen atoms as water vapor, thereby enriching the fixed carbon content (Yahya et al., 2015).

As Zn^{2+} ions coordinate with the glycosidic oxygen in cellulose and the ether or hydroxyl sites in lignin, they facilitate the catalytic cleavage of C–O–C and CH_2OH bonds (Santana et al., 2020). Importantly, the emergence of subtle vibrational modes in the low-frequency fingerprint region (below 500 cm^{-1}) corresponds to Zn–O stretching. This observation confirms the successful crystallization of ZnO nanoparticles within the porous carbon network. The overlap of these metal-

oxide vibrations with existing carbon skeletal peaks is a well-documented phenomenon in doped carbonaceous materials (Ahlawat et al., 2023).

IV.6.3 Surface functional group evolution post-adsorption

Following the adsorption of MO, CAT, and ACE, the most pronounced spectral change is the near-total disappearance of the broad -OH band (3000-3500 cm^{-1}). This attenuation provides rigorous evidence that surface hydroxyl groups, along with their associated zinc active sites, serve as primary binding sites for the target pollutants. The reduction in -OH intensity indicates that these groups become occupied through hydrogen bonding or dipole-dipole interactions with the pollutant functional groups, such as the sulfonic group in MO or the phenolic hydroxyl groups in CAT.

Additionally, significant intensity fluctuations emerged in the 500-400 cm^{-1} range post-adsorption. Because this region corresponds directly to metal-oxide (Zn-O) vibrations, these shifts confirm that the organic pollutants interact directly with the embedded ZnO nanoparticles.

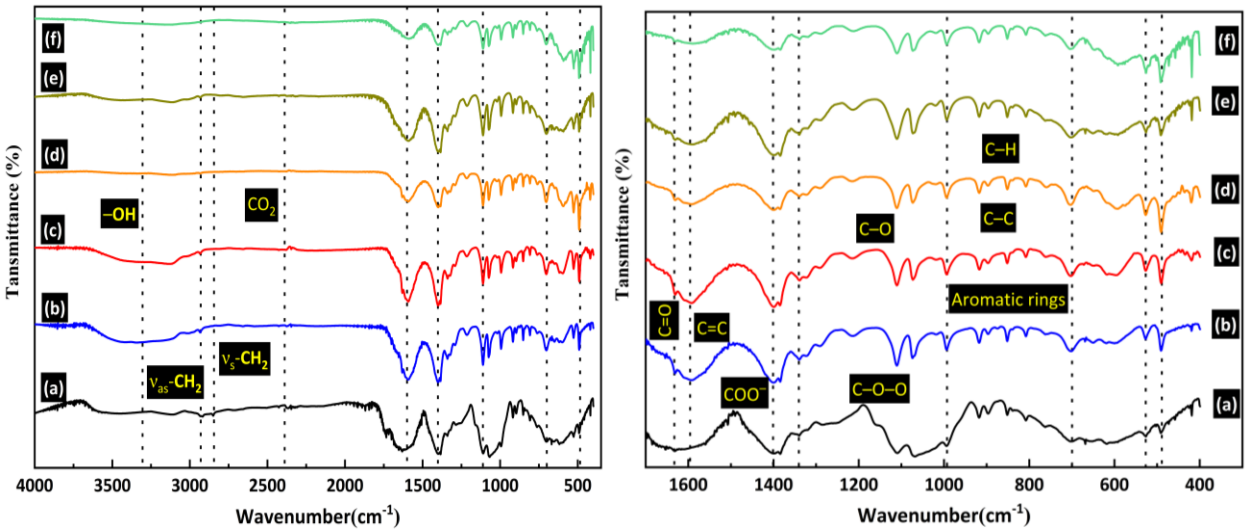

Figure IV.4 FTIR spectra of (**a**) raw DPS waste, (**b**) DPS-Biochar, (**c**) ZnO@DPS–AC, and the composite after the adsorption of (**d**) MO, (**e**) CAT, and (**f**) ACE.

IV.7 Structural characterization via X-ray diffraction

The crystalline structure and phase evolution of the materials, from the raw precursor to the post-adsorption composites, were investigated using XRD. The resulting diffractograms (**Figure IV.5**) provide definitive evidence regarding the carbonization process, the thermal synthesis of ZnO particles, and the structural stability of the adsorbent following pollutant removal.

IV.7.1 Evolution of the carbon matrix and ZnO synthesis

The XRD patterns for the DPS-biochar and the pre-pyrolysis DPS–Zn (zinc–impregnated) samples exhibit the characteristic profile of disordered carbonaceous materials. Specifically, two prominent broad reflections are observed at approximately $2\theta = 25°$ and 44°, corresponding to the (002) and (100) crystallographic planes of amorphous carbon, respectively. These broad bands signify a low degree of graphitization and a predominant turbostratic structure typical of lignocellulosic biomass derivatives.

Interestingly, the DPS-Zn sample (impregnated with $ZnCl_2$ but not yet pyrolyzed) shows no evidence of crystalline ZnO. This absence constitutes a definitive mechanistic observation. It confirms that the formation of the ZnO phase is not due to simple chemical impregnation but is explicitly triggered by thermal decomposition and redox reactions during pyrolysis. This observation aligns with the mechanism proposed in **Section II.3.5.3**, in which $ZnCl_2$ acts as a chemical activator that subsequently converts to stable ZnO species during high-temperature carbonization.

IV.7.2 Phase identification and crystallite size in ZnO@DPS–AC

Following pyrolysis, the ZnO@DPS–AC composite displays a distinct shift in its diffractogram (**Figure IV.5(d)**). The emergence of sharp, well-defined peaks confirms the transition from a purely amorphous state to a highly crystalline composite. The diffraction peaks located at the hkl planes of (010), (002), (011), (012), (110), (013), (020), (112), and (021) provide a precise match with the hexagonal wurtzite crystal system of ZnO (JCPDS card no. 98-006-512). This crystallographic verification conclusively proves the successful synthesis and embedding of ZnO particles within the porous carbon framework.

To further quantify the nature of the inorganic phase, the average crystallite size (D) was calculated using the Debye-Scherrer equation (**Eq. III.5**). Applying this equation to the most prominent ZnO reflections yielded an average crystallite size of 33.07 nm. This nanometric scale is highly advantageous for adsorption applications. It ensures a high surface-area-to-volume ratio, which provides more accessible active sites for target pollutant molecules at the solid-liquid interface.

IV.7.3 Structural stability post-adsorption

The structural integrity of the composite was evaluated by analyzing the XRD patterns of the adsorbent following the recovery of MO (ZnO@DPS–AC–MO), CAT (ZnO@DPS–AC–CAT), and

ACE (ZnO@DPS–AC–ACE). Post-adsorption, no new crystalline phases or significant peak shifts were detected. This indicates that the adsorption of these organic pollutants does not disrupt the fundamental lattice structure of the embedded ZnO particles.

However, a discernible reduction in peak intensities for the ZnO phase occurred across all post-adsorption samples. This phenomenon is typically attributed to the masking effect or X-ray attenuation caused by the successful loading of bulky organic molecules onto the surface and within the composite pores. As the target pollutants occupy the available active sites and coat the ZnO clusters, they physically attenuate the diffraction of incident X-rays from the underlying crystalline planes. This reduces the intensity of the diffraction signals without shifting their angular position. Ultimately, this crystallographic observation further corroborates the SEM–EDX data regarding the high loading capacity of the ZnO@DPS–AC platform.

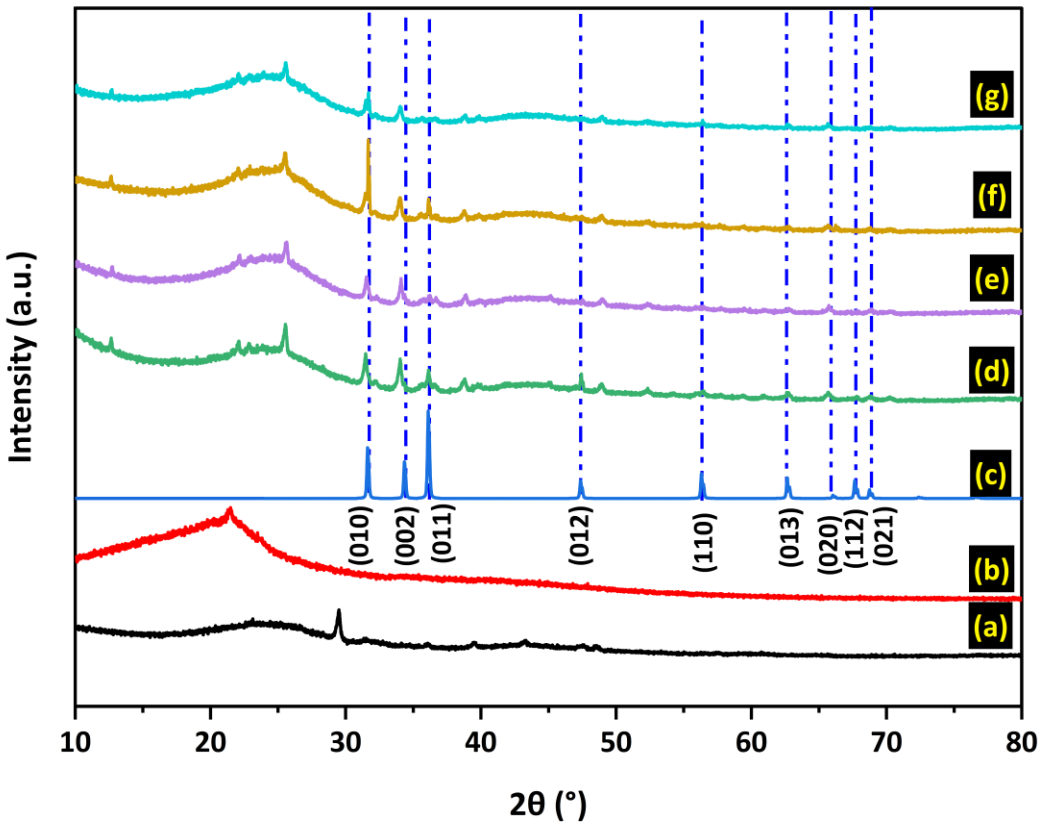

Figure IV.5 XRD patterns illustrating the structural evolution and stability of the adsorbents: (**a**) DPS-Biochar, (**b**) DPS–Zn (pre-pyrolysis), (**c**) identified reflections correspond to the hexagonal wurtzite phase of ZnO (JCPDS card no. 98–006–512), (**d**) ZnO@DPS–AC, and the composite following the adsorption of (**e**) MO, (**f**) CAT, and (**g**) ACE

IV.8 Raman spectroscopy

Raman spectroscopy served as a non-destructive analytical tool to evaluate the structural integrity, degree of graphitization, and phase composition of the synthesized materials. The resulting spectra feature distinct first-order and second-order vibrational modes and are illustrated in **Figure IV.6**. **Table IV.2** summarizes the corresponding band positions alongside the calculated intensity ratios (I_D/I_G).

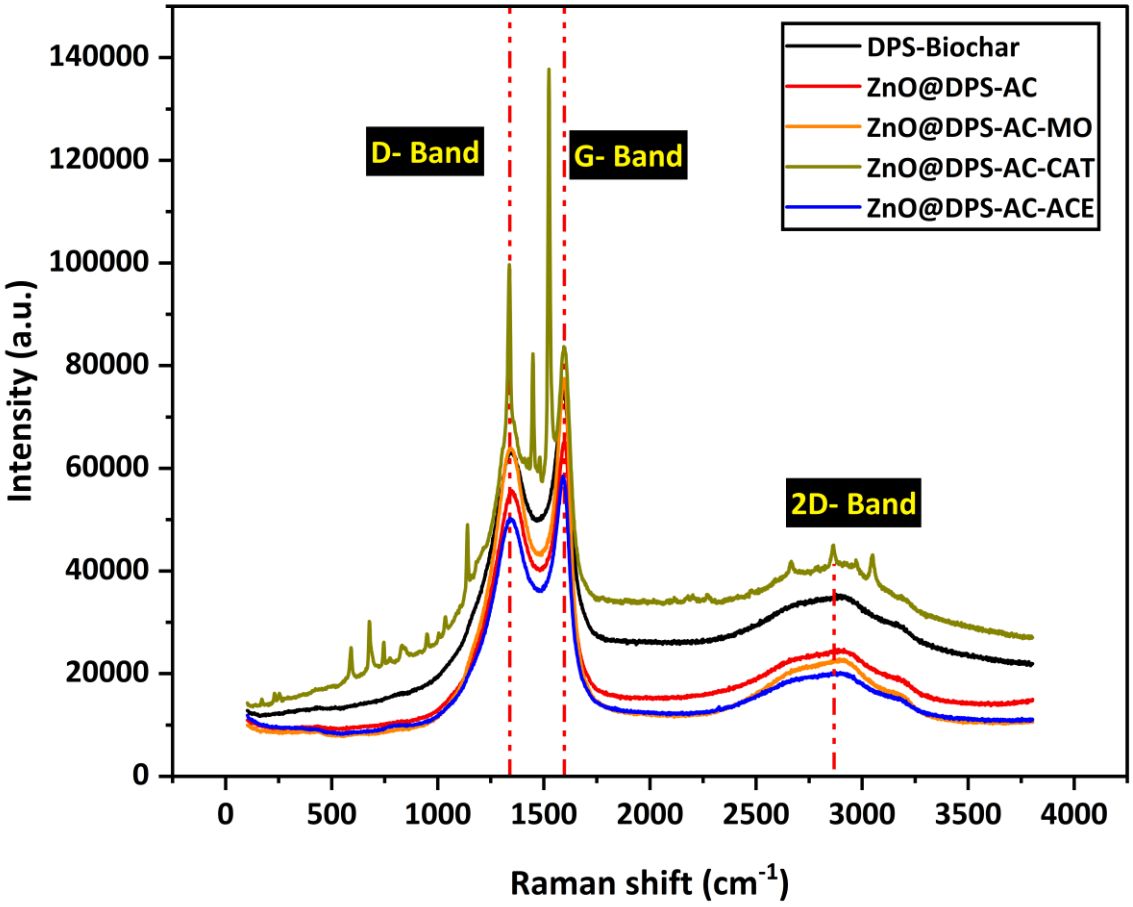

Figure IV.6 Raman spectra of DPS-Biochar, ZnO@DPS-AC, and the composite post-adsorption of MO, CAT, and ACE

IV.8.1 First-order Raman scattering

The first-order Raman region (1100 to 1700 cm^{-1}) for all samples is dominated by two prominent features: the D-band and the G-band.

- The D-band (~1342 cm^{-1}): This disorder-induced band arises from the A_{1g} breathing mode of

sp^3-hybridized carbon atoms. Its presence strictly depends on structural defects, such as vacancies, edge effects, or functional groups, that disrupt the hexagonal symmetry of the graphitic lattice.

- The G-band (~1595 cm^{-1}): This feature corresponds to the first-order E_{2g} stretching mode of sp^2-bonded carbon atoms within the hexagonal aromatic rings.

Table IV.2 Raman spectroscopic parameters including D-band and G-band positions, and the calculated intensity ratios (I_D/I_G) for DPS-Biochar, ZnO@DPS-AC, and the composite after adsorption of MO, CAT, and ACE

Material	D- Band(cm^{-1})	G-Band(cm^{-1})	I_D/I_G	2D-Band Profile
DPS-Biochar	1342	1595	0.837	Broad
ZnO@DPS-AC	1346	1595	1.047	Broad
ZnO@DPS-AC-MO	1342	1595	0.810	Broad
ZnO@DPS-AC-CAT	1338	1595	1.191	Sharp
ZnO@DPS-AC-ACE	1342	1590	0.851	Broad

The intensity ratio (I_D/I_G) provides a quantitative measure of structural disorder within the carbon matrix. For the DPS-biochar, this ratio was calculated at 0.837. Following chemical activation to form ZnO@DPS-AC, the I_D/I_G ratio increased significantly to 1.047. This rise demonstrates that the $ZnCl_2$ treatment successfully produced a highly porous, disordered carbon framework. The resulting matrix contains a higher density of sp^3 defect sites, which act as primary anchoring points for target pollutants. After the adsorption of MO and ACE, the intensity ratios decreased slightly to 0.810 and 0.851, respectively. This reduction suggests that the adsorbate molecules predominantly occupy these existing defect sites, subsequently attenuating the Raman signal associated with the underlying structural disorder.

IV.8.2 Second-order scattering

The 2D band (also called the G' band), located near 2850 $cm^{-}1$, corresponds to a second-order two-phonon resonance. Unlike the D-band, the 2D-band does not require structural defects for activation. Instead, it is highly sensitive to the stacking order and the number of layers within the carbon sheets.

In both the DPS-biochar and ZnO@DPS-AC samples, the 2D band appears notably broad and low in intensity. This spectral profile is characteristic of turbostratic carbon, where graphene-like domains are randomly oriented and lack long-range vertical stacking order. Consequently, this observation

establishes the amorphous nature of the date palm-derived carbon framework following pyrolysis and chemical activation.

IV.8.3 Spectral evolution of ZnO@DPS–AC–CAT

A distinct structural transformation occurred following the adsorption of ZnO@DPS–AC–CAT. Unlike the other targeted pollutants, CAT induced a clear transition from broad amorphous bands to sharp, highly resolved vibrational modes.

- 2D-band sharpening: The 2D–band transitioned from a broad hump to a sharp, intense peak. This morphological shift suggests a localized increase in structural regularity. The molecular ordering of CAT likely drives its deposition, forming a rigid, pseudo-crystalline layer on the adsorbent surface.
- Enhanced I_D/I_G ratio and emergent peaks: The CAT–loaded sample exhibited the highest I_D/I_G ratio (1.191). Additionally, new high-intensity peaks emerged at 1441 and 1524 cm^{-1}, accompanied by several satellite peaks within the fingerprint region. These distinct signals correspond to the vibrational modes of the newly formed CAT-zinc complex. The extreme sharpness of these peaks confirms that the CAT molecules are chemically anchored in a highly specific, rigid orientation. This configuration strongly implies bidentate coordination with the ZnO active sites, rather than non-specific random physisorption.

IV.8.4 Analysis of the zinc oxide phase

Despite the confirmed presence of elemental zinc through previous EDX and XRD analyses, the characteristic Raman-active modes of hexagonal wurtzite ZnO (typically documented at 99, 332, 439, and 584 cm^{-1} (Rungsawang et al., 2024)) were not prominently detected below 500 cm^{-1} in the ZnO@DPS–AC composite.

This signal attenuation is primarily due to fluorescence interference, an inherent limitation of the 532 nm excitation laser when analyzing biomass-derived carbon matrices. Although some literature reports successful ZnO peak detection using 532 nm excitation, the high scattering efficiency of the carbon D– and G–bands within this specific DPS–derived framework effectively overwhelms the weaker inorganic signals. This masking effect is further compounded by potential laser-induced fluorescence from recalcitrant biomass fragments.

For context, Zbair et al. (2018) successfully observed a Raman shift for ZnO in activated carbon

composites at 423 cm^{-1} using a 532 nm laser, a 100× objective lens, and a low laser power of 1.6 mW. Conversely, Albo Hay Allah and Alshamsi (2023) used a 785 nm laser to characterize similar ZnO@AC materials, yet their resulting spectra showed no discernible ZnO peaks below 500 cm^{-1}. These comparative observations verify that the Raman detectability of metallic oxides within carbonaceous composites remains highly sensitive to both the inherent properties of the precursor matrix and the specific operational parameters of the selected laser.

IV.9 Textural properties

IV.9.1 Nitrogen physisorption isotherms and pore architecture

The specific surface area and pore architecture of the synthesized materials govern their adsorptive capacities and mass transfer kinetics. Nitrogen physisorption analysis quantified the structural evolution induced by chemical activation and confirmed the post-adsorption pore-filling mechanisms. **Figure IV.7** presents the N_2 physisorption isotherms at 77 K for the DPS-Biochar, pristine ZnO@DPS-AC, and the pollutant-loaded samples. Based on the IUPAC classification (Thommes et al., 2015), the samples display a composite Type I(b)/Type II isotherm alongside a Type H4 hysteresis loop. The sharp increase in nitrogen uptake at low relative pressures ($P/P_0 < 0.1$) indicates substantial micropore filling. This behavior demonstrates the strong dehydrating and pore-drilling effects of the $ZnCl_2$ activating agent. A gradual upward slope at intermediate relative pressures precedes the closure of the H4 hysteresis loop near $P/P_0 = 0.4$. This structural signature confirms the presence of well-developed mesopores, which typically appear as slit-shaped pores between graphitic microcrystallites in the carbonized biomass. Furthermore, **Figure IV.8** shows that the pore widths fall within the mesopore range (2 to 50 nm), with maximum pore widths centered at 2.0 nm and 4.2 nm.

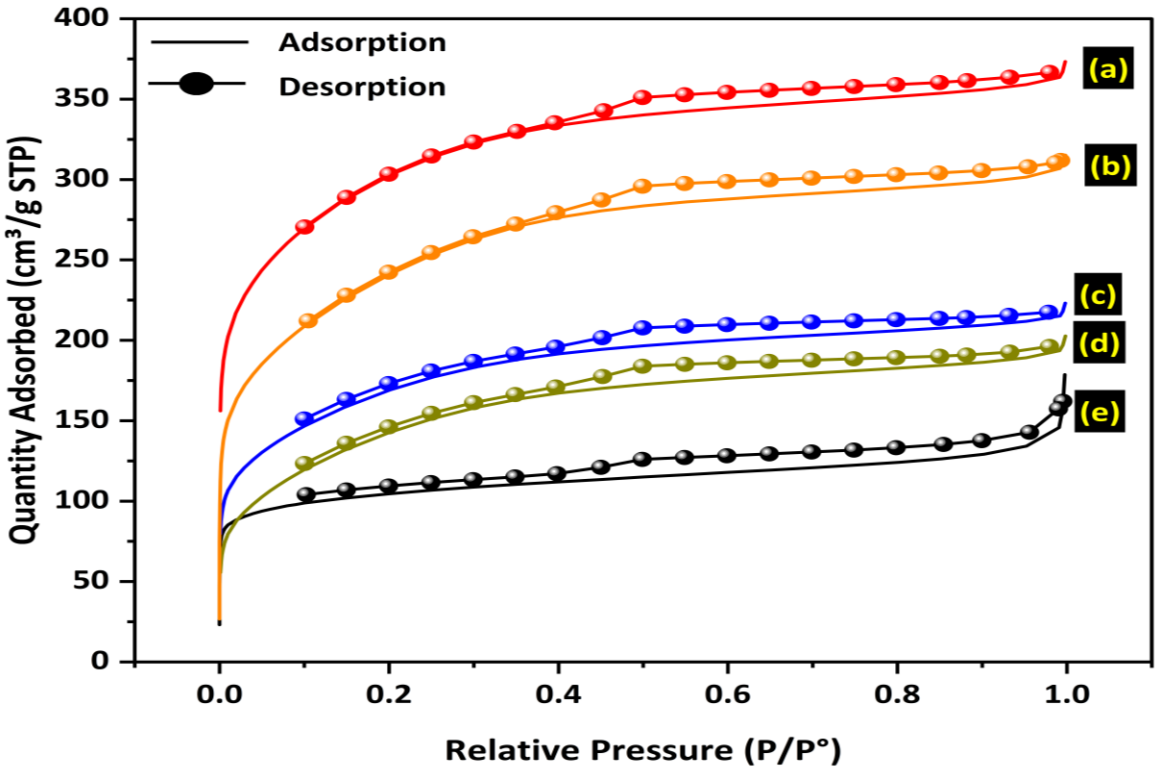

Figure IV.7 N_2 adsorption-desorption of: (**a**) ZnO@DPS-AC, (**b**) ZnO@DPS-AC-MO, (**c**) ZnO@DPS-AC-ACE, (**d**) ZnO@DPS-AC-CAT, and (**e**) DPS-Biochar

Table IV.3 Textural and structural parameters of the DPS-Biochar, ZnO@DPS-AC, and the spent adsorbents following the uptake of MO, CAT, and ACE

Properties	Unit	DPS-Biochar	ZnO@DPS–AC	ZnO@DPS–AC–MO	ZnO@DPS–AC–CAT	ZnO@DPS–AC-ACE
S_{BET}	m^2/g	345.53	1028.63	843.60	589.13	513.11
S_{Ext}	m^2/g	134.53	699.36	699.75	479.51	500.75
S_{Micro}	m^2/g	211.00	329.27	143.85	109.62	12.36
$S_{Longmuir}$	m^2/g	601.42	1585.85	1332.70	939.72	846.18
V_{Total}	cm^3/g	0.208	0.555	0.466	0.328	0.293
V_{Micro}	cm^3/g	0.103	0.159	0.065	0.050	0.000
V_{Meso}	cm^3/g	0.104	0.396	0.401	0.277	0.292
L_0	nm	5.86	2.78	2.75	2.81	2.84
E_0	kJ/mol	13.24	15.28	15.33	15.25	15.20

IV.9.2 Textural evolution following chemical activation

Table IV.3 summarizes the textural parameters. The DPS-Biochar sample possessed a moderate S_{BET} of 345.53 m^2/g and a V_{Total} of 0.208 cm^3/g. The chemical activation and thermal pyrolysis induced a profound structural transformation in the resulting ZnO@DPS-AC composite. The S_{BET} increased by

nearly 200% to 1028.63 m^2/g, accompanied by a Langmuir surface area expansion to 1585.85 m^2/g. The total pore volume expanded to 0.555 cm^3/g, showing high mesoporosity (0.396 cm^3/g) and a distinct microporous structure (0.159 cm^3/g).

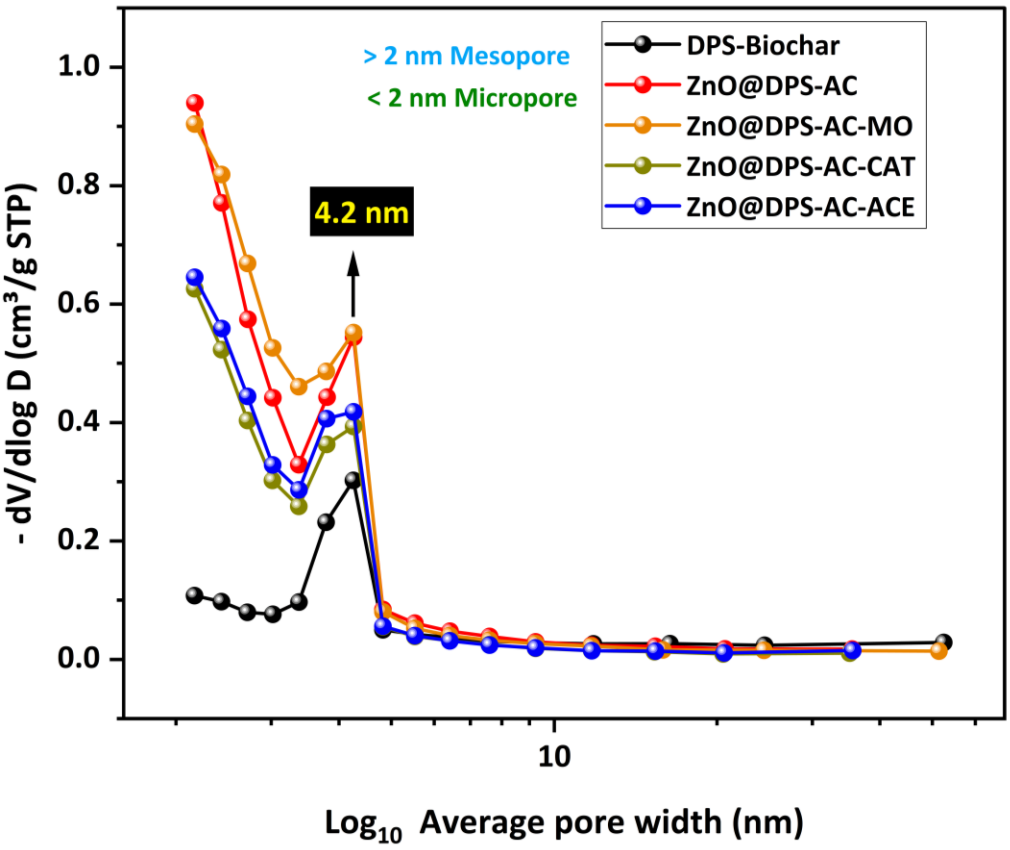

Figure IV.8 PSD of: (**a**) ZnO@DPS-AC, (**b**) ZnO@DPS-AC-MO, (**c**) ZnO@DPS-AC-ACE, (**d**) ZnO@DPS-AC-CAT, and (**e**) DPS-Biochar

The physicochemical mechanism driving this enhancement relies on the dual function of the zinc chloride activating agent. At elevated temperatures, it aggressively degrades the lignocellulosic framework and catalyzes carbon cross-linking. This creates a hierarchical network of micro- and mesopores while reducing the average pore diameter from 5.86 nm to 2.78 nm. This outcome contrasts sharply with recent literature. For example, Sayed et al. (2024) reported that incorporating ZnO into wood sawdust matrices severely reduced the specific surface area due to metal oxide nanoparticle agglomeration, which blocked pores. In contrast, the simultaneous activation and functionalization strategy utilized here avoided pore occlusion. This approach maintained a high initial surface area, allowing the ZnO active centers to remain highly dispersed without sacrificing essential void space.

IV.9.3 Post-adsorption textural modifications and mechanistic insights

The adsorption of MO, CAT, and ACE caused a precipitous decline in textural parameters across all samples. The ACE-loaded sample (ZnO@DPS-AC-ACE) exhibited an S_{BET} reduction of approximately 50% to 513.11 m^2/g, and the total pore volume halved to 0.293 cm^3/g. Measurable microporosity was eliminated (0.00 cm^3/g), while mesoporosity remained partially intact at 0.292 cm^3/g. This significant reduction in surface area and pore volume provides direct physical evidence for a pore-filling adsorption mechanism. Wang et al. (2016) similarly showed that diffusion and internal pore-filling dictate pesticide recovery in biochar matrices. Li et al. (2026) also confirmed that pore-filling acts as the primary physical adsorption mechanism for neonicotinoids on functionalized carbonaceous materials. This aligns with fundamental mass-transfer theories, in which organic adsorbates sequentially occupy the external surface area, mesopore channels, and, ultimately, the micropore volumes.

The differential reduction in microporosity versus mesoporosity provides deep mechanistic insights. The complete loss of measurable microporosity indicates that the bulky ACE molecules create severe steric hindrance upon entering the narrowest voids. These large pesticide molecules become wedged within the micropores or physically block their entrances, preventing further access of nitrogen gas during subsequent surface analysis. In contrast, the wider mesopores resist complete occlusion. They function as transport channels that remain partially open even after multi-layer adsorbate coverage forms.

The textural impact of ACE differs significantly from that of the smaller target pollutants. While MO and CAT adsorption reduced the surface area of the ZnO@DPS-AC composite, their post-adsorption matrices retained measurable microporosities of 0.065 cm^3/g and 0.050 cm^3/g, respectively. Smaller molecules, such as catechol, can penetrate deeply and pack efficiently within the micropores. The reduction of micropore volume to zero by ACE confirms that its adsorption is uniquely limited by size-exclusion and steric factors. Comparing these parameters with those of the zinc peroxide-based carbon composite synthesized by Kumar et al. (2025), the superior hierarchical architecture of the ZnO@DPS-AC matrix provides a distinct mass-transfer advantage. It prevents premature saturation, which is typically a limitation of microporous adsorbents.

Regarding MO, its molecular length of approximately 1.2 nm allowed it to migrate through mesoporous channels and block the microporous network. The porosity reduction was less severe for

CAT, aligning with its smaller molecular size. Its lower steric hindrance enabled denser packing within the ultramicropores without causing complete pore-mouth blockage. The overall post-adsorption porosity reduction confirms the pore-filling mechanism. This observation aligns with the findings of Tcheka et al. (2024) and De Smedt et al. (2024), who reported that organic pollutants diffuse into and occupy the internal hierarchical architecture of biochars.

IV.9.4 Characteristic adsorption energy and surface heterogeneity

The E_0 for the loaded composites remained consistent, ranging from 15.20 to 15.33 kJ/mol. According to Stoeckli et al. (2002), an E_0 value between 14 and 15 kJ/mol indicates either variable surface heterogeneity or the presence of super-micropores (1.5 to 2.5 nm). The average pore diameters and structural distributions confirm that the synthesized and laden composites exhibit a broad range of pores, with a strong concentration in the mesoporous range (2 to 50 nm) according to IUPAC classifications (Sing, 1985; Thommes et al., 2015).

IV.10 Conclusion

This chapter systematically evaluated the physicochemical, morphological, and structural evolution of the synthesized ZnO@DPS-AC composite, confirming the successful valorization of DPS into a high-performance, functionalized adsorbent. Thermal analysis (TGA/DTG) of the raw biomass elucidated the multi-stage degradation profile of its lignocellulosic constituents, thereby theoretically justifying the selection of 600 °C as the optimal pyrolysis temperature to ensure complete devolatilization and stable char formation. Following pyrolysis and $ZnCl_2$ activation, the material exhibited a robust carbonization yield and a uniquely high ash content. Rather than indicating poor precursor quality, these specific metrics provide powerful quantitative evidence of dense, uniform zinc loading effectively integrated within the stable carbon framework. The pH_{pzc} was determined to be 6.67, establishing the baseline for understanding the composite's pH-dependent electrostatic behavior in aqueous media.

The structural and morphological transformations were conclusively mapped using advanced spectroscopic and microscopic techniques. SEM-EDX analysis visually confirmed the dramatic transition from the dense, fibrous structure of the raw biomass to a highly developed, honeycomb-like macroporous and mesoporous architecture. Crucially, EDX mapping not only confirmed the uniform distribution of zinc active sites but also provided definitive evidence of successful pollutant capture by the emergence of distinct elemental markers (such as sulfur, nitrogen, and chlorine) in the post-

adsorption samples. Furthermore, surface chemistry elucidation via FTIR identified the critical role of oxygen-containing functional groups (specifically hydroxyls) and newly formed Zn–O bonds. These specific sites serve as primary anchoring sites, facilitating complexation and hydrogen bonding with target pollutants. Complementary structural analyses, including XRD and Raman spectroscopy, validated the presence of the crystalline hexagonal wurtzite phase of ZnO embedded within a partially graphitized, disordered carbon matrix. Finally, BET analysis confirmed the development of an extensive specific surface area and a hierarchical pore network, parameters that are fundamentally essential for overcoming mass transfer resistances during remediation.

This exhaustive characterization proves that the simultaneous chemical activation and metal-oxide functionalization engineered a highly porous, chemically reactive, and structurally robust composite. By effectively transforming an abundant agricultural waste product into a sophisticated, zinc-doped carbon matrix, this synthesis offers a highly viable and sustainable platform for complex water treatment applications. With the structural superiority and physical feasibility of the ZnO@DPS-AC material firmly established, the subsequent chapters will systematically evaluate its practical application in wastewater remediation, beginning with **Chapter V**, which investigates the dynamic batch adsorption, kinetic modeling, and RSM/ANN optimization for the removal of MO.

Chapter V: Batch Adsorption of Methyl Orange onto ZnO@DPS-AC: Modeling, Optimization, and Mechanisms

* * * * *

V.1 Introduction

The successful development of a high-performance adsorbent requires rigorous evaluation of its macroscopic adsorptive properties under controlled conditions. **Chapter IV** definitively established the physicochemical properties of the synthesized ZnO@DPS-AC composite, confirming the successful integration of nanometric zinc oxide within a highly porous, graphitic carbon matrix. Building directly upon this structural foundation, this chapter transitions from material characterization to practical environmental application by evaluating the batch adsorption of MO, a highly recalcitrant anionic azo dye.

Evaluating MO at this specific juncture is essential to validate the engineered surface chemistry of the composite, particularly its capacity to sequester complex organic molecules via combined physical and chemical mechanisms. To comprehensively assess this adsorptive efficiency, this chapter systematically investigates the influence of primary operational parameters, including adsorbent dosage, initial solution *pH*, ionic strength, contact time, and initial dye concentration.

The chapter's progression follows a rigid analytical framework. Initially, the dynamics of the solid-liquid interface are evaluated through rigorous kinetic and isotherm modeling, followed by a detailed thermodynamic analysis to assess the energetic favorability of the adsorption process. The economic viability of the ZnO@DPS-AC composite is subsequently tested through cyclic desorption and regeneration studies. To overcome the limitations of traditional univariate analysis, advanced computational methods are employed. The chapter compares the optimization of multivariable adsorption parameters using RSM against the high-fidelity predictive modeling capabilities of ANN coupled with GA. Finally, utilizing the derived empirical and statistical data, the chapter concludes by elucidating the specific physicochemical mechanisms governing the adsorption of MO onto the hierarchical composite surface.

V.2 Effect of operational parameters on MO adsorption

V.2.1 Effect of adsorbent dosage

Optimizing adsorbent dosage is essential to balance maximal contaminant removal with overall economic viability (Serban et al., 2023). The influence of the ZnO@DPS-AC composite dosage on MO removal was systematically evaluated. Increasing the composite mass from 15 mg to 65 mg substantially enhanced the MO removal efficiency from 33% to 98% (**Figure V.1(a)**). This trend aligns with the findings of Abbou et al. (2023), who reported that MO removal efficiency increased from approximately 10% to 99% as the modified clay dosage increased from 0.05 to 0.5 g. Ahlawat et al. (2023) reported similar results, demonstrating that MO *R*s using ZnO-based activated carbon composites increase significantly with increasing adsorbent dose. Furthermore, Bassam et al. (2024) confirmed that the retention q_e for MO correlates strongly with adsorbent mass until an equilibrium state is reached.

Physiochemically, this enhancement is driven by an expanded specific surface area and a proportionally higher density of vacant active sites available for MO-adsorbent interactions (Abbou et al., 2023). Higher dosages increase the collision probability between the anionic dye molecules and the composite surface. This dynamic facilitates greater uptake until the depletion of dye molecules in the solution induces a plateau (Ouedrhiri et al., 2022).

Despite the initial efficiency gains, experimental data indicated that *R* stabilized at or above 65 mg. This plateau, or marginal decline in relative q_e at higher doses, occurs because excessive adsorbent loading often leads to particle aggregation, as observed by Sorayyaei et al. (2021) and Pradhan et al. (2023). Such aggregation fundamentally reduces the effective surface area and lengthens the diffusion path, thereby impeding access to internal active sites (Sorayyaei et al., 2021). Consequently, to secure high removal efficiency while maintaining cost-effectiveness, a 30 mg dose of the ZnO@DPS-AC composite was selected for all subsequent batch experiments, aligning with the optimized dosing strategies reported by Bassam et al. (2024).

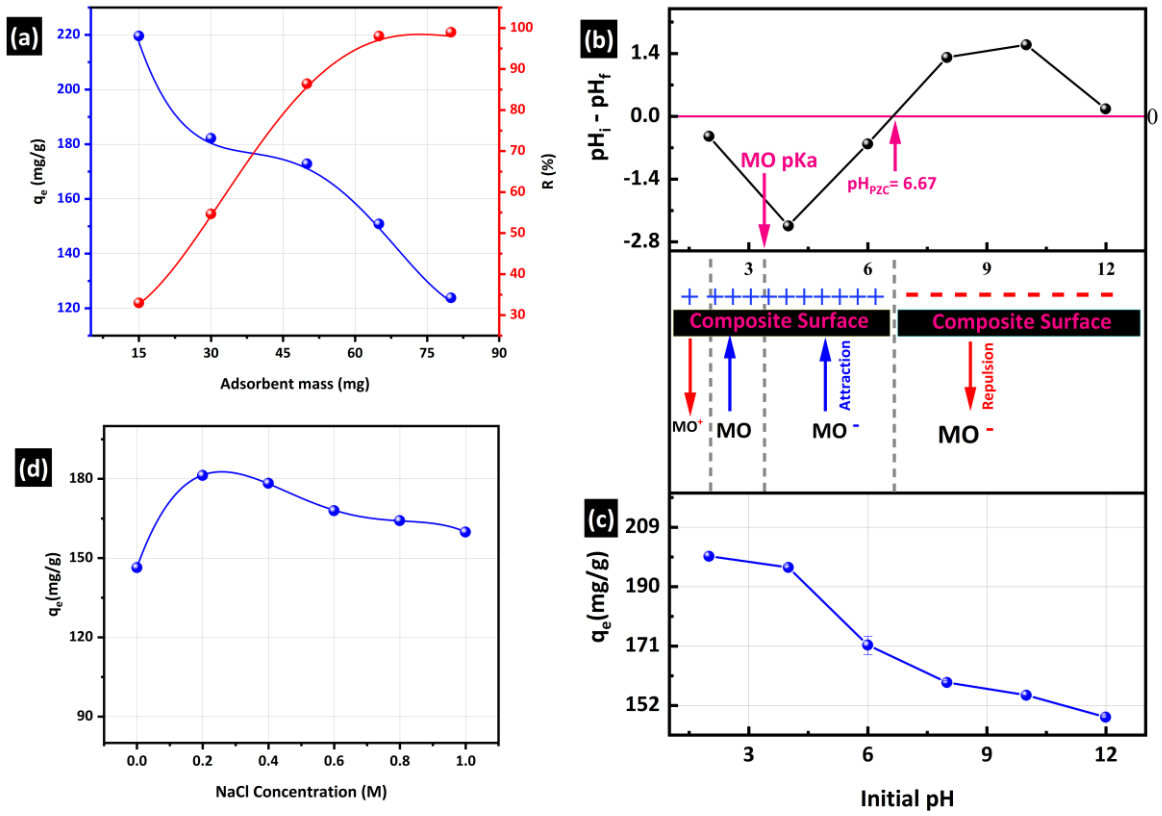

Figure V.1 Influence of operating parameters on the removal of MO by ZnO@DPS-AC: (**a**) adsorbent mass, (**b**) point of zero charge of the composite, (**c**) initial solution *pH*, and (**d**) ionic strength

V.2.2 Effect of initial solution pH

Solution *pH* is a fundamental parameter in adsorption systems, as it governs both the adsorbate's ionization state and the adsorbent's surface charge (Djezzar et al., 2024; Ramutshatsha-Makhwedzha et al., 2022). The impact of initial *pH* on MO sequestration by the ZnO@DPS-AC composite was evaluated across a range of 2.0 to 12.0. The maximum q_e reached 199.6 mg/g (corresponding to *R* of 99.8%) at *pH* 2.0, followed by a gradual decline to 148.14 mg/g (74.1% removal) as the *pH* was increased to 12.0.

This enhanced adsorption in acidic media aligns with De Smedt et al. (2024), who reported that MO adsorption onto activated carbon peaked at *pH* 2.0 and decreased as the solution became less acidic. Similar trends were established by Najibikhah and Rahbar-Kelishami (2024) and Sayed et

al. (2024), who recorded maximum MO uptake in highly acidic regimes for MXene and ZnO@AC composites, respectively. Furthermore, Zubair et al. (2020) noted that the adsorption of anionic MO onto date-palm-derived biochars is significantly favored under acidic conditions (*pH* 2-4).

The physicochemical mechanism driving this behavior is defined by the relationship between the dye's *pKa* and the adsorbent's *pH*pzc. The pH_{pzc} of 6.67 (**Figure V.1(b)** and **section IV.4**), determined via the *pH* drift method (**section III.6.3**), governs the surface charge behavior. Because MO has a *pKa* of 3.46, it predominantly exists as the active anion (MO–) at pH values above this threshold (Wei et al., 2023). Consequently, within the *pH* range of 3.46 to 6.67, strong electrostatic attraction occurs between the negatively charged sulfonate groups ($–SO_3^-$) of the dye and the protonated surface sites of the composite. At a highly acidic *pH* (2.0 to 3.46), MO exists in a neutral form (Aichour et al., 2022), yet it maintains favorable interactions with the highly positive surface via hydrogen bonding and persistent electrostatic forces, yielding the recorded maximum uptake at *pH* 2.0.

As the solution *pH* exceeds 6.67, the ZnO@DPS-AC surface undergoes deprotonation, acquiring a net negative charge. The subsequent decrease in adsorption efficiency is attributed to electrostatic repulsion between the anionic dye and the negatively charged adsorbent, exacerbated by competitive adsorption from abundant hydroxyl ions (OH^-) for the remaining active sites (Al-Hazeef et al., 2024).

Despite this repulsion, the composite maintained a commendable *R* of 74.1% at *pH* 12.0. This residual uptake indicates that, while electrostatic forces dominate the system, non-electrostatic mechanisms, such as pore-filling, π–π stacking interactions, and hydrophobic effects, also contribute significantly to sequestration. This hypothesis is consistent with the findings of Q. Wang et al. (2023), who observed substantial MO adsorption at *pH* 11.0, attributing the retention to active Van der Waals attractions and hydrogen bonding between surface hydroxyl groups and the electronegative heteroatoms (O, N, S) of the dye molecule.

Although absolute maximum efficiency occurred at *pH* 2.0, a standard operating *pH* of 6.0 was selected for all subsequent experimental stages. This parameter represents a strategic compromise between maintaining high *R* and ensuring environmental sustainability. Operating at near-neutral *pH* eliminates the need for large-scale acid consumption and prevents the downstream discharge

of highly acidic treated effluents, a rationale strongly supported by Martínez et al. (2023) for green water treatment methodologies.

V.2.3 Effect of ionic strength

Investigating the effect of ionic strength is critical for identifying the role of electrostatic interactions and evaluating adsorbent performance in hypersaline textile effluents (Wang et al., 2021). The q_e of the ZnO@DPS-AC composite for MO was evaluated across a NaCl concentration range of 0.2 to 1.0 M. The q_e initially increased from 146.35 mg/g to 181.30 mg/g (a 17.5% improvement in R) before experiencing a marginal decline (**Figure V.1(d)**). Notably, even at the maximum NaCl concentration of 1.0 M, the q_e remained superior to the baseline value recorded in the absence of salt.

This initial enhancement aligns with Al-Degs et al. (2008), who reported an increase in R of anionic reactive dyes upon salt addition. Physicochemically, this trend is driven by the aggregation or dimerization of dye molecules in solution. Elevated ionic strength intensifies intermolecular interactions, such as van der Waals and ion-dipole forces, compelling dye molecules to aggregate and thereby increasing their total sorption onto the composite surface. Furthermore, Hu et al. (2013) demonstrated that higher ionic strength enhances hydrophobic attraction between the dye's organic functional groups and the adsorbent matrix, effectively offsetting competitive ionic effects.

The observed behavior reflects a complex interplay of competing mechanisms. Although high ionic strength typically suppresses electrostatic interactions by screening surface charges (Hu et al., 2013), the sustained high R in this system suggests that non-electrostatic forces (such as hydrophobic interactions and pore-filling) are the dominant drivers of MO sequestration. This phenomenon is consistent with the salting-out effect discussed by Samiey and Toosi (2010), wherein high salt concentrations reduce the aqueous solubility of hydrophobic solutes and drive them toward the solid adsorbent interface.

These results differ from those reported by Q. Wang et al. (2023), who observed a monotonic decrease in MO removal with increasing NaCl concentration, attributed to the competitive occupation of active sites by chloride ions. This differentiation in the ZnO@DPS-AC system is likely attributable to a higher density of hydrophobic surface sites or the unique mesoporous architecture of the biomass-derived carbon, which specifically facilitates the accommodation of

bulky dye aggregates. The slight decline observed at higher NaCl concentrations likely marks the threshold where the screening of electrostatic attractions and ionic competition for active sites begin to outweigh the benefits of dye aggregation. Nevertheless, the composite's ability to maintain an enhanced q_e at 1.0 M NaCl underscores its practical suitability for treating hypersaline industrial wastewater.

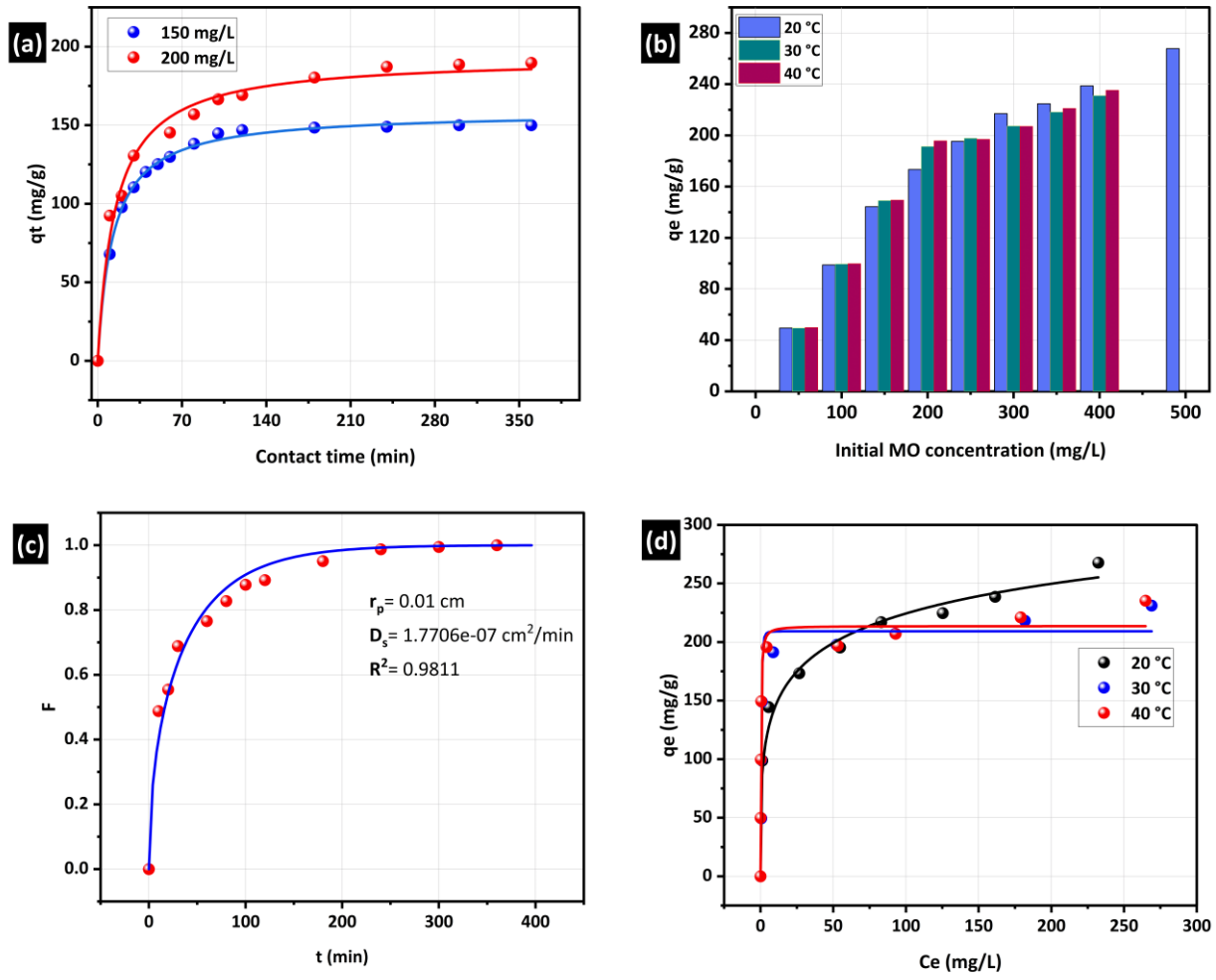

Figure V.2 (**a**) Effect of contact time at different initial concentrations, (**b**) effect of initial MO concentration on adsorption capacity, (**c**) non-linear plot of Vermeulen model, and (**d**) non-linear regression equilibrium isotherm for MO adsorption onto ZnO@DPS-AC

V.2.4 Effect of contact time

Determining the optimal contact time is essential for understanding adsorption dynamics and establishing the rate-controlling mechanisms required for kinetic modeling. The influence of

contact time on MO removal by the ZnO@DPS-AC composite was evaluated over 10-360 min at two initial concentrations (150 and 200 mg/L). A rapid initial uptake occurred within the first 10 minutes, achieving *R*s exceeding 45%. This corresponded to adsorption capacities of 68 mg/g and 92.5 mg/g at 150 and 200 mg/L, respectively (**Figure V.2(a)**). This accelerated initial rate aligns with the findings of Abbou et al. (2023), who reported that the majority of MO uptake (95.81%) onto modified clay occurred within the first 30 min. Sayed et al. (2024) and Pradhan et al. (2023) observed similar rapid kinetics, noting that equilibrium for MO removal using ZnO-based and magnetic carbon nanocomposites was largely approached within 60 min.

Physicochemically, this rapid initial stage is driven by a high density of vacant active sites and readily available functional groups on the composite's exterior surface, facilitating immediate electrostatic interactions with the anionic dye molecules. De Smedt et al. (2024) posited that high initial adsorption rates characterize mesoporous carbons, as exterior active sites are readily accessible and mass-transfer resistance is minimized during the early stages of contact.

Following this rapid phase, the adsorption rate transitioned to a gradual uptake period before reaching saturation. Equilibrium was established at approximately 120 min for the 150 mg/L concentration and between 180 and 240 min for the 200 mg/L concentration. At equilibrium, the system achieved *R*s of 100% (150 mg/g) and 94.85% (189.7 mg/g), respectively. This temporal progression is consistent with Q. Wang et al. (2023), who noted that MO saturation on carboxyl-functionalized chitosan was reached at 210 min. The prolonged time required to reach equilibrium at the higher concentration is corroborated by Zubair et al. (2020) and Najibikhah and Rahbar-Kelishami (2024). These studies suggest that as the initial concentration increases, competition for the remaining vacant sites intensifies, and the driving force of the concentration gradient progressively diminishes as the surface becomes saturated.

A multi-stage diffusion process explains the difference in equilibrium times (120 min versus 240 min). As exterior surface sites become populated, MO molecules must diffuse into the deeper mesoporous and microporous architecture of the biomass-derived carbon skeleton, encountering greater internal mass-transfer resistance. The ability of the ZnO@DPS-AC composite to achieve near-total removal at high concentrations within 240 min demonstrates exceptional kinetic efficiency compared to conventional biochars, which frequently require 360 to 720 min to reach similar saturation levels (Zubair et al., 2020).

V.2.5 Effect of initial dye concentration

The C_0 serves as a fundamental determinant of the adsorption process, providing the driving force to overcome mass-transfer resistance between the aqueous and solid phases. The influence of MO concentration was evaluated across a range of 50 to 500 mg/L (**Figure V.2(b)**). The q_e increased progressively with rising initial concentrations. Specifically, at lower concentrations (50-150 mg/L), the ZnO@DPS-AC composite exhibited an R of 96.2-99.0%. As the concentration was increased to the 200-500 mg/L range, a gradual increase in the total quantity adsorbed was observed, although the overall rate of removal began to decelerate.

This observed trend aligns with the research of Abbou et al. (2023), who reported that increasing MO concentration from 10 to 100 mg/L resulted in a significant increase in qe from 2.01 to 15.05 mg/g, after which qe stabilized due to active-site saturation. Similarly, Q. Wang et al. (2023) demonstrated that higher initial concentrations improved the availability of adsorption sites for magnetic chitosan composites, noting that a stronger concentration gradient facilitates the mass transfer of dye molecules to the adsorbent surface. Zubair et al. (2020) also confirmed that MO uptake onto date-palm-derived biochar increased from 48.90 mg/g to 193.89 mg/g as the concentration rose to 200 mg/L, indicating that the concentration difference was the primary driver of solid-phase loading.

Physiochemically, the increase in q_e is driven by the intensified concentration gradient, which acts as a powerful driving force to push MO molecules from the bulk solution into the hierarchical pore structure of the composite. At low initial concentrations, the ratio of available active sites to the total number of dye molecules is high, leading to near-total removal. However, as C_0 increases, these sites become occupied, and the competition for remaining vacancies intensifies. This dynamic leads to the observed plateau in R despite the ongoing increase in absolute q_e (Abbou et al., 2023; Q. Wang et al., 2023).

A significant comparison can be made with the findings of Tcheka et al. (2024), who utilized Hyphaene thebaica shells (HTBC) for MO removal. Their results revealed an L-type adsorption isotherm, characterized by a sharp plateau above 200 mg/L, suggesting that these surfaces reach effective saturation relatively early. In contrast, the ZnO@DPS-AC composite showed a gradual increase in uptake up to 500 mg/L at 20 ˚C. This differentiation suggests that the synthesized

composite possesses a more complex hierarchical pore architecture (likely a combination of the wood-derived activated carbon's mesopores and the additional active centers provided by the ZnO particles), which allows for sustained adsorption at high pollutant loadings where simpler biochars, such as those reported by Tcheka et al. (2024) and Sayed et al. (2024), might experience total site exhaustion.

The high R (96.2% to 99.0%) at 150 mg/L demonstrates that the ZnO@DPS-AC composite is significantly more potent than the materials studied by Abbou et al. (2023), whose modified clay reached a maximum q_e of only 15.58 mg/g. This suggests that the synergistic effect of the carbon skeleton and metal oxide impregnation provides a superior density of active sites, rendering the composite highly suitable for treating concentrated industrial dye effluents.

V.3 Kinetic modeling and mass transfer mechanisms

To elucidate the rate-controlling mechanisms and mass transfer characteristics governing MO removal onto the ZnO@DPS-AC composite, several kinetic models were evaluated using non-linear regression analysis. Experimental data were analyzed at two initial concentrations (150 and 200 mg/L), and model suitability was prioritized based on the highest $Adj\text{-}R^2$, the highest R^2, and the lowest $Red\text{-}\chi^2$ values. The Avrami model provided the most robust fit across both concentrations ($R^2 \geq 0.995$), followed closely by the PSO model (**Table V.1**).

Physicochemically, the superior fit of the Avrami model—particularly at the higher concentration (200 mg/L) where it outperformed the Elovich and PSO models—suggests a complex adsorption mechanism involving multiple stages or evolving surface conditions during the process. The calculated half-times ($t_{1/2}$) were exceptionally rapid, with values of less than 11 min at 150 mg/L and approximately 13 min at 200 mg/L. This rapid temporal progression aligns with Sayed et al. (2024) and Ahlawat et al. (2023), who reported similarly accelerated kinetics for MO removal utilizing ZnO-functionalized carbonaceous composites. The observed increase in $t_{1/2}$ with increasing initial concentration is attributed to intensified competition for available active sites as surface coverage increases, a phenomenon consistent with the theoretical analysis by Zhang (2019) regarding the dependence of adsorption rates on operating conditions.

The strong applicability of the PSO model (R^2 = 0.986 to 0.998) over the PFO model is significant for identifying the nature of the adsorbate-adsorbent interaction. This observation is corroborated

by Najibikhah and Rahbar-Kelishami (2024) and Abbou et al. (2023), who noted that MO adsorption onto modified MXenes and organoclays, respectively, is best described by PSO kinetics. As posited by Wang and Guo (2020), this trend indicates that the rate-limiting step is predominantly governed by chemisorption, involving valence forces through the sharing or exchange of electrons between the ZnO particles/activated carbon surface and the anionic MO molecules. Furthermore, the calculated equilibrium capacities ($q_{e,cal}$) for the PSO model (158.48 mg/g and 193.19 mg/g) closely matched the experimental values ($q_{e,exp}$), reinforcing the validity of a chemically controlled sequestration process.

To further investigate diffusion pathways, the Weber-Morris intra-particle diffusion (IPD) model and the Vermeulen approximation were applied. As detailed in **section II.2.5.4**, the IPD model was applied but showed a poor fit (R^2 = 0.053), confirming its limitations for systems dominated by multi-stage mass transfer, whereas the Vermeulen model (**Eq. V.1**) demonstrated excellent agreement with the experimental data ($R^2 \geq 0.981$), as illustrated in **Figure V.2(c)**. This differentiation is critical. The failure of the linear IPD model is attributed to its theoretical limitations, which typically limit it to approximating diffusion only for the initial 30% of fractional uptake. In contrast, the superior fit of the Vermeulen equation across the entire adsorption range ($0 \leq F \leq 1$) suggests that intra-particle diffusion is a significant, albeit not necessarily exclusive, rate-limiting step. This conclusion aligns with the mass transfer theory discussed by Chu et al. (2025), who argued that arbitrary data segmentation in IPD plots often yields physically meaningless results. In contrast, the Vermeulen model provides a more accurate estimation of the diffusion coefficient (D_s) using the full kinetic dataset.

$$F = \frac{q_t}{q_e} = \sqrt{1 - \exp\left(\frac{\pi^2 D_s t}{r_p^2}\right)} \qquad \textbf{Eq. V.1}$$

Where D_s is the surface diffusion coefficient in cm^2/min, r_p represents the average particle radius in cm, and t is the contact time in min.

A comparative analysis of the rate constants across concentrations revealed a consistent decline as the initial MO concentration increased. This trend is consistent with the observations of Tcheka et al. (2024) and Aichour et al. (2022). Their studies suggest that while higher initial concentrations provide a greater mass-transfer driving force, the resulting increase in surface coverage leads to

steric hindrance and increased electrostatic repulsion between adsorbate molecules, thereby reducing the apparent kinetic rate constants.

Table V.1 Kinetic modeling parameters for the adsorption of MO onto ZnO@DPS-AC at initial concentrations of 150 mg/L and 200 mg/L

Model	Unit	$[MO]_0$ = 150 mg/L	$[MO]_0$ = 200 mg/L
Experimental			
q_e	mg/g	150	189.7
$t_{0.5}$	min	<11	<14
PFO			
q_e	mg/g	145.384	175.681
k_1	L/min	0.050	0.048
$t_{0.5}$	min	13.878	14.37
R^2	–	0.982	0.942
Adj-R^2	–	0.979	0.930
Red-χ^2	–	0.362	1.712
PSO			
q_e	mg/g	158.484	193.198
k_2	g/mg.min	4.96E-04	3.52E-04
$t_{0.5}$	min	12.721	14.70
R^2	–	0.998	0.986
Adj-R^2	–	0.997	0.983
Red-χ^2	–	0.035	0.427
Avrami			
q_e	mg/g	150.000	189.700
k_{AV}	min^{-1}	0.050	3.97E-02
n_{AV}		0.686	0.528
$t_{0.5}$	min	11.690	12.58
R^2	–	0.999	0.995
Adj-R^2	–	0.999	0.994
Red-χ^2	–	0.021	0.135
Elovich			
α_e	mg/(g.min)	111.240	70.932
β_e	g/mg	0.046	0.034
R^2	–	0.961	0.992
Adj-R^2	–	0.954	0.991
Red-χ^2	–	0.644	0.173
Intra-Particle Diffusion			
k_{IPD}	mg/ [g. $min^{0.5}$]	11.288	13.142
R^2	–	0.053	0.440
Adj-R^2	–	-0.119	0.315
Red-χ^2	–	21.050	21.470

Vermeulen			
Slope	min^{-1}	0.025	0.0175
R^2	–	0.998	0.981
Adj-R^2	–	0.998	0.979
Red-χ^2	–	1.98E-04	0.003

V.4 Isotherm modeling and equilibrium studies

The distribution of MO molecules between the liquid and solid phases at equilibrium was evaluated to elucidate the surface properties and affinity of the ZnO@DPS-AC composite. Experimental data were obtained across an initial concentration range of 50 to 500 mg/L at 20 °C, 30 °C, and 40 °C. The resulting isotherms were classified as H-type, indicating a strong adsorption affinity between the composite surface and the anionic dye molecules (**Figure V.2(d)**).

This classification is validated by the findings of Tcheka et al. (2024), who categorized MO adsorption on Hyphaene thebaica-derived biochar as L-type, suggesting high affinity and monolayer formation. However, the H-type isotherm observed in this system indicates an even higher initial attraction. The synergistic effect of the wood-derived activated carbon skeleton and the embedded ZnO particles likely drives this enhanced affinity. According to Al-Ghouti and Da'ana (2020), H-type isotherms characterize systems in which the adsorbate exhibits such a high affinity that it is almost completely removed from dilute solutions.

A critical observation in this study is the temperature-dependent shift in model suitability. At 20 °C, the equilibrium data were best described by the Freundlich isotherm (R^2 = 0.981), whereas at 30 °C and 40 °C, the Langmuir model provided a superior fit (R^2 up to 0.94) (**Table V.2**).

Physicochemically, this transition suggests that at lower temperatures, the adsorption process is governed by a heterogeneous surface with potential multilayer coverage. This trend was similarly observed by Rattanapan et al. (2017) for coffee-ground-derived activated carbon. As the temperature increases to 30-40 °C, the system shifts toward monolayer adsorption on a homogeneous surface with energetically identical active sites. This transition is consistent with the findings of Sayed et al. (2024) and Ahlawat et al. (2023), who reported that MO adsorption onto ZnO-functionalized carbonaceous materials follows the Langmuir model, indicating that once an active site is occupied, no further adsorption occurs at that site.

Furthermore, multi-parameter models (Sips, Liu, and Langmuir-Freundlich) were utilized and

demonstrated nearly identical, robust fits (R^2 = 0.98 and $Adj\text{-}R^2$ = 0.97). The mathematical convergence of these models is explained by Al-Ghouti and Da'ana (2020), who noted that they function essentially as hybrids of the Langmuir and Freundlich theories. According to De Vargas Brião et al. (2023), this range of parameter values fits the equilibrium data well for a Type I isotherm. This specific behavior validates the shift toward Langmuir-like (Type I) curves at elevated temperatures, where the heterogeneity exponent approaching unity indicates a transition from a heterogeneous environment to a more homogeneous adsorption surface.

Table V.2 Adsorption isotherms parameters for MO removal onto ZnO@DPS-AC composite

		T=20 °C	T=30 °C	T=40 °
Model	**Unit**	**Value**	**Value**	**Value**
Experimental				
q_m	mg/g	267.67	231.065	235.28
Langmuir				
q_m	mg/g	226.792	214.773	215.171
K_L	L/mg	0.430	1.394	3.622
R^2	–	0.932	0.942	0.981
$Adj\text{-}R^2$	–	0.913	0.923	0.975
$Red\text{-}\chi^2$	–	3.427	4.076	0.826
Freundlich				
K_F	$(mg/g)/(mg/L)^n$	87.948	116.392	128.805
n	–	4.971	7.806	9.054
R^2	–	0.981	0.887	0.898
Adj R^2	–	0.975	0.850	0.864
$Red\text{-}\chi^2$	–	1.743	7.304	6.754
Sips				
q_{ms}	mg/g	463.535	209.230	213.640
K_s	$(mg/L)^{-ns}$	0.219	3.193	4.573
n_s	–	0.316	2.524	1.158
R^2	–	0.984	0.958	0.982
$Adj\text{-}R^2$	–	0.975	0.933	0.972
$Red\text{-}\chi^2$	–	1.544	3.590	0.783
Liu				
q_{mL}	mg/g	463.538	209.230	213.640
K_L	mg/L	122.036	0.631	0.269
n_L	–	0.316	2.524	1.158
R^2	–	0.984	0.958	0.982
$Adj\text{-}R^2$	–	0.975	0.933	0.972
$Red\text{-}\chi^2$	–	1.544	3.590	0.783
R-P				

K_{RP}	L/g	315.284	335.164	883.265
a_{RP}	$(mg/L)^{-g}$	2.827	1.725	4.454
g	–	0.848	0.978	0.981
R^2	–	0.990	0.945	0.984
$Adj\text{-}R^2$	–	0.985	0.911	0.975
$Red\text{-}\chi^2$	–	0.825	4.763	0.987
Khan				
q_{mK}	mg/g	93.701	188.583	190.064
b_K	L/mg	2.583s	1.746	4.578
a_K	–	0.843	0.974	0.979
R^2	–	0.991	0.945	0.984
$Adj\text{-}R^2$	–	0.987	0.912	0.975
$Red\text{-}\chi^2$	–	0.729	4.742	0.967
LF				
q_{mLF}	mg/g	463.570	209.230	213.640
K_{LF}	L/mg	0.008	1.584	3.715
n_{LF}	–	0.316	2.524	1.158
R^2	–	0.984	0.958	0.982
$Adj\text{-}R^2$	–	0.975	0.933	0.972
$Red\text{-}\chi^2$	–	1.544	3.590	0.783

V.5 Comparative assessment of adsorbent performance

To evaluate the efficacy of the synthesized ZnO@DPS-AC composite, its q_m for MO was compared with those of various adsorbents reported in the recent literature. Under the optimized conditions established in this study (C_0: 50-500 mg/L, *pH* 6.0, and 20 °C), the ZnO@DPS-AC composite exhibited a superior q_e of 226.81 mg/g.

As detailed in **Table V.3**, the performance of the ZnO@DPS-AC composite significantly exceeded that of several other metal-oxide/carbonaceous hybrids. Specifically, the q_m achieved in this work is markedly higher than the ZnO@AC composite derived from wood sawdust (44.5 mg/g) reported by Sayed et al. (2024) and the ZnO-NP@AC derived from commercial activated carbon (138.8 mg/g) investigated by Ahlawat et al. (2023). Physicochemically, this enhanced performance is likely driven by a synergistic effect between the hierarchical pore structure of the date palm spikelet-derived carbon and the high dispersion of ZnO particles. This combination provides a greater density of available active sites than the sawdust or commercial AC precursors used in those previous studies.

Furthermore, the ZnO@DPS-AC composite demonstrated superior q_m compared to raw or

chemically activated biochars. For instance, the q_m of 226.81 mg/g in this system exceeds that of Hyphaene thebaica biochar (HTBC) (195.15 mg/g) reported by Tcheka et al. (2024) and activated pine cone (APC) biochar (80.37 mg/g) reported by Kaya and Uzun (2021). A critical differentiation noted here is the solution *pH*. While the HTBC and APC biochars required highly acidic conditions (*pH* 2.0) to achieve their maximum uptake, the ZnO@DPS-AC composite maintains a higher q_m at a near-neutral *pH* of 6.0. This operational advantage suggests that incorporating ZnO particles effectively tunes the surface chemistry, enabling robust electrostatic attraction with the anionic MO dye even at elevated *pH*, where standard biochars typically exhibit reduced efficiency due to surface deprotonation.

Table V.3 Comparison of the maximum monolayer adsorption capacity of ZnO@DPS-AC for MO with other adsorbents reported in the literature

Adsorbent	**Adsorption Conditions**				$Q_{0(max)}$ **(mg/g)**	**Ref.**
	C_0 (mg/L)	m/V (g/L)	T(°C)	*pH*		
Hyphaene thebaica biochar (HTBC)	25–300	0.6	45	2	195.15	(Tcheka et al., 2024)
Commercial Activated Carbon (CAC)	5–100	0.1	25	3	129.3	(Serban et al., 2023)
Activated Pine Cone (APC) biochar	100–400	0.8	25	2	80.37	(Kaya & Uzun, 2021)
Wood Sawdust-derived composite (ZnO@AC)	10-200	1.2	20	3	44.5	(Sayed et al., 2024)
CAC-derived composite (ZnO-NP@AC) Orange Peel-derived composite (ZnO-NP@AC)	20-100	0.4	27	4	138.8 196.1	(Ahlawat et al., 2023)
SiO_2 Nano-particles	5-250	1.6	-	4	69.40	(Xin Zhang et al., 2023)
Date Palm Spikelets-derived composite (ZnO@DPS-AC)	50-500	1	20	6	226.81	**This work**

Although the ZnO@DPS-AC composite ranks among the high-performing adsorbents, its q_m

remains lower than that of highly specialized materials such as the protonated amine-modified hydrochar (PAMH) reported by Li et al. (2018), which reached 909.09 mg/g. This discrepancy is expected, as amine-modified systems possess a significantly higher density of specific nitrogenous functional groups that facilitate extremely strong ionic bonding with MO. Such a level of chemical modification fundamentally exceeds the standard metal-oxide impregnation utilized in this work.

Nevertheless, the ZnO@DPS-AC composite exhibits a q_m comparable to the orange peel-derived ZnO-NP@AC (196.1 mg/g) (Ahlawat et al., 2023). The slightly higher performance of the DPS-based composite (226.81 mg/g versus 196.1 mg/g) is attributed to the larger specific surface area and higher pore volume inherent in the spikelet-derived carbon skeleton. These results collectively validate that the ZnO@DPS-AC composite is a highly competitive and promising material for industrial wastewater remediation, offering a balanced profile of high q_m, rapid kinetics, and sustained effectiveness in non-extreme *pH* environments.

V.6 Thermodynamic analysis

The influence of solution temperature on the sequestration of MO onto ZnO@DPS-AC composites was evaluated to determine the underlying thermodynamic parameters governing the adsorption process. These parameters were calculated using the mathematical formulations detailed in **sections II.2.6** and **III.12**. Experimental data were analyzed at 293, 303, and 313 K using equilibrium constants ($K_{eq}°$) derived from the Langmuir, Sips, Liu, Khan, and Redlich-Peterson (R-P) models (**Figure V.3**).

The equilibrium constants for all models increased progressively with rising temperature. For example, the $K_{eq}°$ derived from the Langmuir model rose from 1.41×10^5 at 293 K 1.19×10^6 at 313 K, indicating that MO uptake is enhanced in a higher thermal environment (**Table V.4**). This temperature-dependent adsorption trend is validated by the findings of Ahlawat et al. (2023) and Sayed et al. (2024), who reported that MO removal using ZnO-based carbonaceous composites is favored at elevated temperatures. Physicochemically, this behavior is attributed to the increased mobility of the anionic dye molecules and the potential expansion of the internal pore structure of the biomass-derived activated carbon, facilitating deeper penetration of the adsorbate into the mesoporous channels. Furthermore, as suggested by Ouedrhiri et al. (2022), high temperatures can activate new binding sites on the composite surface, thereby increasing the total number of

effective collisions between the MO molecules and the ZnO active centers.

Thermodynamic parameters, including the ΔG°, ΔH°, and ΔS°, were calculated using both linear and nonlinear forms of the van't Hoff equation. Negative ΔG° values were obtained across all temperatures and models (ranging from approximately -19 to -37 kJ/mol), confirming that the adsorption of MO onto ZnO@DPS-AC is thermodynamically favorable. This result is consistent with the research of Machrouhi et al. (2023) and Bassam et al. (2024). The observation that ΔG° became more negative with increasing temperature indicates a stronger driving force for adsorption at elevated temperatures, a phenomenon validated by Sayed et al. (2024) for analogous magnetic carbon systems.

The standard change in ΔH° was positive across all models, corroborating the endothermic nature of the process. A critical distinction arises in the magnitude of ΔH°, depending on the fitting method and the specific model used. For the Langmuir, Sips, and Liu models, nonlinear fitting yielded ΔH° values ranging from 77.45 to 83.47 kJ/mol (**Table V.4**). According to the benchmarks established by Luo et al. (2016) and Aichour et al. (2022), and supporting literature (Chang & Thoman Jr, 2014; Xinyu Zhang et al., 2023), ΔH° values ≈80 kJ/mol are characteristic of chemisorption, whereas lower values typically suggest physisorption. Consequently, the high enthalpy values obtained from the Langmuir and Sips models suggest that MO uptake involves strong chemical interactions, such as covalent bonding or electron-sharing between the sulfonate groups of the dye and the ZnO particles (Sayed et al., 2024). However, the R-P model yielded a significantly lower ΔH° of 17.45 kJ/mol, indicating that the interaction is dominated by electrostatic attraction and mesoporous filling.

Methodological analysis revealed significant discrepancies between the linear and nonlinear van't Hoff fitting results. For instance, the Sips model yielded a linear ΔH° of 235.18 kJ/mol, compared with a nonlinear value of 83.47 kJ/mol. This observation is supported by Lima et al. (2020) and Tran et al. (2021), who argued that nonlinear regression provides more accurate estimations of thermodynamic parameters by avoiding the propagated errors and weight distortion inherent in the linearization of K_{eq}°.

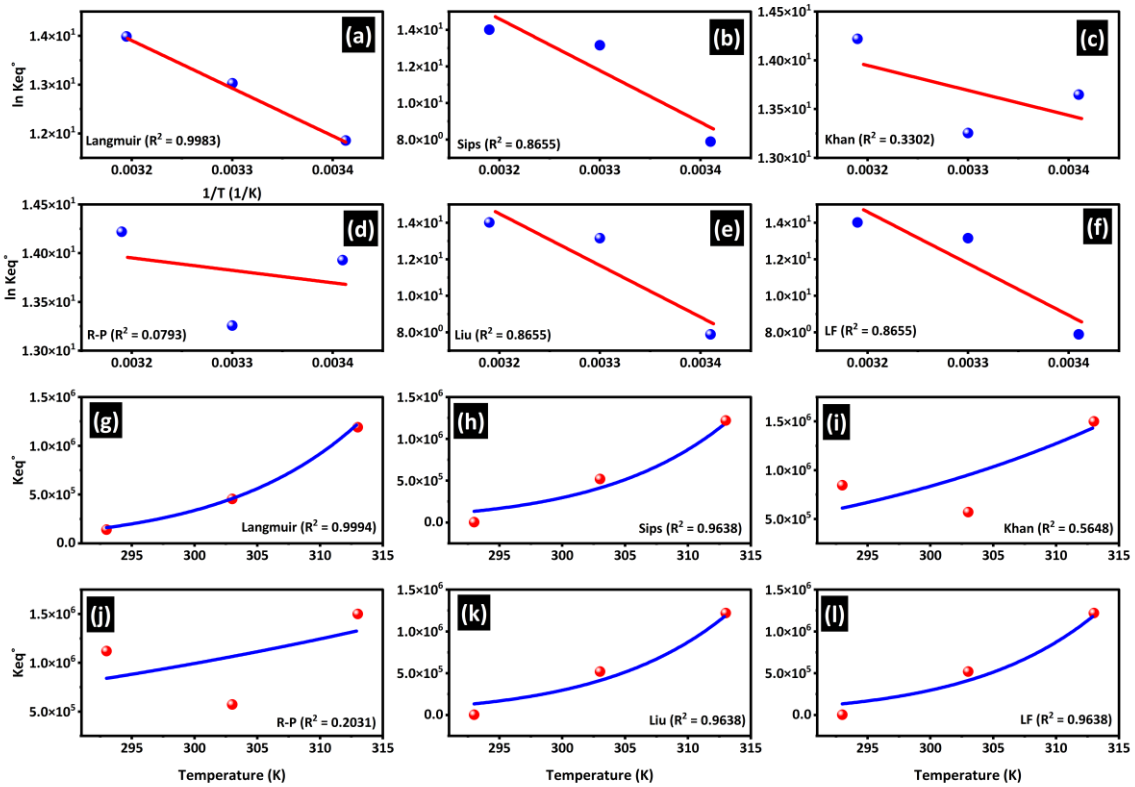

Figure V.3 van 't Hoff thermodynamic plots for the adsorption of MO onto ZnO@DPS-AC comparing (**a-f**) linear regression and (**g-l**) non-linear regression forms

Finally, the ΔS° was positive across all models, ranging from 0.17 to 0.38 kJ/mol K. This observation is validated by the research of Abbou et al. (2023), who noted that a positive ΔS° reflects increased randomness at the solid-liquid interface. This increase in disorder is likely driven by the release of previously adsorbed water molecules from the composite surface as the bulkier MO molecules displace them, a process that overcomes the loss of translational entropy of the dye itself.

Table V.4 Comparison of thermodynamic parameters (ΔG°, ΔH°, ΔS) for MO adsorption, derived from linear and non-linear regression of various isotherm models

		Linear Fitting			Non-Linear Fitting		
Model	***T* (K)**	**K_{eq}°**	**ΔG°(kJ/mol)**	**ΔH°(kJ/mol)**	**ΔS° (kJ/mol)**	**ΔG°(kJ/mol)**	**ΔH°(kJ/mol)**	**ΔS° (kJ/mol)**
Langmuir								
	293	1.41E+05	-28.894	81.364	0.376	-28.894	77.450	0.364
	303	4.56E+05	-32.843			-32.843		
	313	1.19E+06	-36.412			-36.412		
Sips								
	293	2.68E+03	-19.241	235.186	0.874	-19.241	83.476	0.383
	303	5.19E+05	-33.165			-33.165		
	313	1.22E+06	-36.478			-36.478		
Liu								
	293	2.68E+03	-19.243	235.154	0.873	-19.243	83.475	0.383
	303	5.19E+05	-33.165			-33.165		0.383
	313	1.22E+06	-36.478			-36.478		0.383
Khan								
	293	8.46E+05	-33.263	21.260	0.184	-33.263	32.588	0.222
	303	5.71E+05	-33.410			-33.410		
	313	1.50E+06	-37.022			-37.022		
R-P								
	293	1.12E+06	-33.939	10.624	0.150	-33.939	17.458	0.173
	303	5.72E+05	-33.411			-33.411		0.173
	313	1.50E+06	-37.026			-37.026		0.173
LF								
	293	2.68E+03	-19.240	235.205	0.874	-19.240	83.476	0.383
	303	5.19E+05	-33.165			-33.165		
	313	1.22E+06	-36.478			-36.478		

V.7 Desorption, regeneration, and cyclic reusability

A comprehensive evaluation of an adsorbent's reusability is essential for ensuring its economic viability and environmental sustainability in large-scale industrial applications. The reusability and regeneration potential of the ZnO@DPS-AC composite were evaluated over three consecutive cycles (**Figure V.4**). The composite exhibited significant initial q_e for MO; however, the *R* for the 200 mg/L initial dye concentration decreased from 88% to 39%, while the 100 mg/L concentration dropped from 99% to 53% over the three cycles.

This observed reduction in performance is validated by the findings of Abbou et al. (2023) and Blaisi et al. (2018), who reported that while modified clays and date palm ash-LDH composites are recyclable, they experience a progressive decline in *R* due to the gradual depletion of active adsorption sites and the irreversible binding of dye molecules. Physiochemically, this decline is driven by pore blocking and the occupation of active centers by residual dye aggregates that resist removal during simple washing steps, a phenomenon consistent with the observations of Wei et al. (2023) and Sayed et al. (2024) regarding carbonaceous adsorbents.

Following the third cycle, the laden ZnO@DPS-AC adsorbent was successfully regenerated using 0.1 M NaOH. The selection of an alkaline regenerant for an anionic dye system is consistent with the strategies employed by Aichour et al. (2022) and Q. Wang et al. (2023). The fundamental mechanism driving this approach relies on the high concentration of (OH^-) in the alkaline solution. These ions compete directly with the anionic MO molecules for active adsorption sites while simultaneously deprotonating the adsorbent surface. This deprotonation induces electrostatic repulsion, thereby facilitating efficient dye desorption. Post-regeneration, the composite demonstrated renewed effectiveness, achieving *R*s of approximately 77% at 200 mg/L and 71% at 100 mg/L.

The regeneration performance of the ZnO@DPS-AC composite compares favorably with other materials reported in the literature. For instance, the recovered efficiency of 71-77% following chemical regeneration is comparable to the 81% reported for magnetic Ni@C by Pradhan et al. (2023) and significantly outperforms the 33% reusability efficiency reported for standard ZnO@OP by Ahlawat, Ahlawat et al. (2023) after five cycles. Furthermore, the composite's ability to recover a substantial portion of its capacity with a standard 0.1 M NaOH solution underscores

its economic feasibility and stability. This aligns with the *memory effect* and structural robustness discussed by Grover et al. (2019) for advanced composite systems. These findings collectively demonstrate that the ZnO@DPS-AC composite is a cost-effective, durable, and recyclable adsorbent, highly suitable for the practical remediation of MO-laden industrial wastewater.

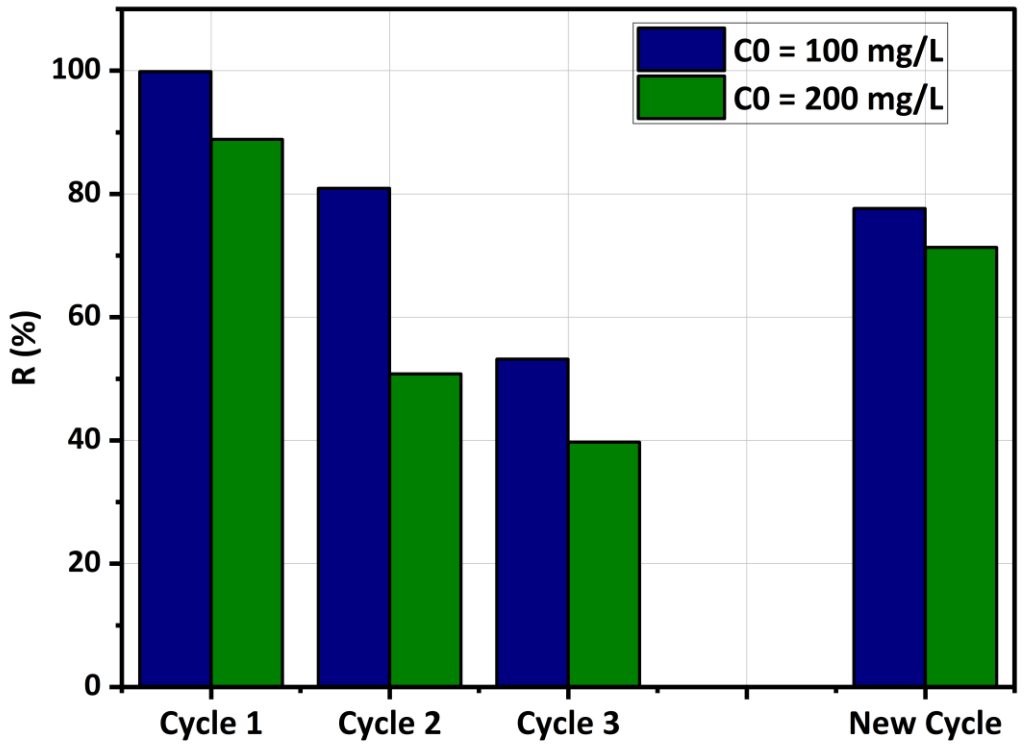

Figure V.4 Reusability and cyclic regeneration efficiency of the composite over three cycles

V.8 Optimization via response surface methodology

V.8.1 Experimental design and model development

To systematically interrogate the multidimensional design space governing the adsorption process, a five-factor BBD was employed. This RSM approach was selected to deconvolute the complex interactions between contact time (A), initial dye concentration (*B*), adsorbent dosage (*C*), solution *pH* (*D*), and temperature (*E*). Unlike OFAT methodologies, which often fail to detect synergistic effects among variables, the BBD enables rigorous quantification of linear, quadratic, and interactive effects with a significantly reduced number of experimental runs.

The corresponding design matrix comprised 46 discrete experimental runs. This configuration provided a robust dataset for modeling two critical response variables: q_e and R.

This methodological approach aligns with recent studies in adsorptive remediation. For example, Uddin and Baig (2019) used BBD to optimize MO removal using cobalt oxide nanoparticles, citing its efficiency for evaluating nonlinear relationships with fewer experiments than full factorial designs. Similarly, Abbou et al. (2023) successfully applied BBD to model the adsorption of MO dye onto clay-based composites. These established precedents further validate the utility of this statistical design for optimizing complex, multivariate adsorption systems.

Table V.5 Sequential model sum of squares and adequacy metrics for the adsorption capacity response surface model

Sequential model sum of squares							
Source	***SS***	***DF***	***MS***	***F-value***	***F-Table***	***p-value***	**Remarks**
Mean vs Total	1166.49	1	1166.49				
Linear vs Mean	5.86	5	1.17	35.37	2.45	< 0.0001	
2FI vs Linear	0.4055	10	0.0406	1.32	2.16	0.2635	
Quadratic vs 2FI	**0.8699**	**5**	**0.174**	**87.39**	**2.60**	**< 0.0001**	**Suggested**
Cubic vs Quadratic	0.0408	15	0.0027	3.04	2.85	0.0404	**Aliased**
Residual	0.0089	10	0.0009				
Total	1173.67	46	25.51				
Lack of Fit Test							
Source	***SS***	***DF***	***MS***	***F-value***	***F-Table***	***p-value***	**Remarks**
Linear	1.32	35	0.0378	70.99	4.48	< 0.0001	
2FI	0.9171	25	0.0367	68.91	4.52	< 0.0001	
Quadratic	**0.0471**	**20**	**0.0024**	**4.43**	**4.56**	**0.0531**	**Suggested**
Cubic	0.0063	5	0.0013	2.36	5.05	0.1839	**Aliased**
Pure Error	0.0027	5	0.0005				
Model summary statistics							
Source	***SD***	***R^2***	***Adj-R^2***	***Pre- R^2***	***PRESS***		
Linear	0.1820	0.8155	0.7925	0.7559	1.75		
2FI	0.1751	0.8720	0.8080	0.6962	2.18		
Quadratic	**0.0446**	**0.9931**	**0.9875**	**0.9732**	**0.1923**	**Suggested**	
Cubic	0.0299	0.9988	0.9944	0.9435	0.4058	**Aliased**	

V.8.2 Model selection and statistical validation

V.8.2.1 Sequential model selection

The experimental data were fitted to linear, two-factor interaction (2FI), quadratic, and cubic models to identify the mathematical function that best approximated the response surface. As detailed in **Table V.5** and **Table V.6**, the sequential model sum of squares analysis indicated that the quadratic model provided the most statistically significant improvement for both responses.

For the natural log-transformed q_e, the sequential model sum of squares indicated that the quadratic terms contributed significantly to the model fit. The calculated *F-value* of 87.39 vastly exceeded the critical *F-Table* value of 2.60 ($p < 0.0001$), whereas the 2FI terms did not provide significant improvement. A similar trend was observed for *R*, where the quadratic model yielded an F-value of 28.16, which is notably higher than the corresponding *F-Table* value of 2.60. This consistency aligns with the findings of Bassam et al. (2024), who optimized MO adsorption onto a Fe_2O_3/Mn_3O_4 magnetic nanocomposite and found that a quadratic polynomial was necessary to adequately capture the curvature of the response surface (*p-value* < 0.0001). Furthermore, the cubic model was aliased and offered no significant statistical improvement. This confirms that the quadratic polynomial was sufficient to capture the system behavior without overfitting.

V.8.2.2 Goodness-of-Fit statistics

V.8.2.3 Lack-of-Fit analysis

The signal-to-noise ratio was assessed using the adequate precision metric. The present study obtained values of 32.095 for q_e and 50.332 for *R*. These values substantially exceed the minimum threshold of 4, confirming that the model signals are sufficiently strong to map the design space. This finding mirrors the high precision ratios reported by Bhowmik et al. (2018) (ratio of 37.79) and Abbou et al. (2023) (ratio of 13.20), further validating the robustness of the experimental data.

The LoF test was used to detect systematic deviations between model predictions and experimental data. For q_e, the LoF *F-value* was 4.43. Crucially, this calculated value is strictly less than the critical *F-Table* value of 4.56. Because 4.43 < 4.56, the LoF is statistically non-significant at the 95% confidence level ($p = 0.0531$). This direct comparison to the theoretical F-distribution confirms that the quadratic model adequately fits the data and the residual variation is primarily due to pure error rather than model mismatch. While Sharifpour et al. (2019) reported a more

clearly non-significant LoF (*p-value* = 0.2958) for their MO removal model, the marginal value observed in this system (*p-value* = 0.0531) suggests possible minor curvature or experimental variability at mid-range concentrations. Nevertheless, it remains highly acceptable for optimization purposes. The *CV* was 3.98%, indicating high reproducibility of the experimental data. This is comparable to the low *CV* values (< 1%) reported in the optimization of hydrochar production by El Ouadrhiri et al. (2021).

Table V.6 Sequential model sum of squares and adequacy metrics for the removal percentage response surface model

Sequential model sum of squares							
Source	***SS***	***DF***	***MS***	***F-value***	***F-Table***	***p-value***	**Remarks**
Mean vs Total	3.255E+05	1	3.255E+05				
Linear vs Mean	12601.11	5	2520.22	28.13	2.45	< 0.0001	
2FI vs Linear	1355.12	10	135.51	1.82	2.16	0.0990	
Quadratic vs 2FI	**1892.21**	**5**	**378.44**	**28.16**	**2.60**	**< 0.0001**	**Suggested**
Cubic vs Quadratic	260.04	15	17.34	2.28	2.85	0.0952	**Aliased**
Residual	75.91	10	7.59				
Total	3.417E+05	46	7427.33				
Lack of Fit Test							
Source	***SS***	***DF***	***MS***	***F-value***	***F-Table***	***p-value***	**Remarks**
Linear	3558.90	35	101.68	20.86	4.48	0.0015	
2FI	2203.78	25	88.15	18.08	4.52	0.0022	
Quadratic	**311.58**	**20**	**15.58**	**3.20**	**4.56**	**0.1007**	**Suggested**
Cubic	51.53	5	10.31	2.11	5.05	0.2154	**Aliased**
Pure Error	24.38	5	4.88				
Model summary statistics							
Source	***SD***	***R^2***	***Adj-R^2***	***Pre-R^2***	***PRESS***		
Linear	9.46	0.7786	0.7509	0.7136	4635.12		
2FI	8.62	0.8623	0.7935	0.7135	4637.28		
Quadratic	**3.67**	**0.9792**	**0.9626**	**0.9208**	**1281.41**	**Suggested**	

Cubic	2.76	0.9953	0.9789	0.7940	3333.22	**Aliased**

V.8.3 ANOVA analysis and significance of model terms

The statistical adequacy of the polynomial equations and the significance of the individual process variables were rigorously evaluated using ANOVA analysis. This procedure partitions the total variation in the response data into parts associated with specific factors and interactions, thereby distinguishing systematic effects from experimental error.

V.8.3.1 Adsorption capacity model

The initial evaluation of the model for q_e suggested a quadratic fit. However, to satisfy the mathematical assumptions of constant variance and the normality of residuals, a natural logarithmic transformation ($\ln q_e$) was applied. As presented in **Table V.7**, the transformed model yielded an *F-value* of 179.17, confirming that the model is highly significant (*p-value* < 0.0001). The statistical significance of the specific operational terms is interpreted as follows.

Regarding the dominance of initial concentration (factor *B*), the ANOVA reveals that it is the most influential parameter, with an exceptionally high *F-value* of 2080.26. This statistical finding strongly corroborates the univariate batch experiment results discussed earlier in this chapter, which demonstrated that q_e increased progressively with rising initial concentrations (50 to 500 mg/L). As previously established, this is due to the higher concentration gradient, which serves as a driving force to overcome mass-transfer resistance.

Adsorbent dosage (factor *C*) emerged as the second most significant factor (*F-value* = 668.40). While the earlier batch studies indicated that increasing the dosage enhances total *R*, the ANOVA confirms that it also critically affects the unit q_e within the multivariate space. Physicochemically, this is attributed to alterations in the ratio of available active sites to adsorbate molecules.

Additionally, the temperature term (factor *E*) was highly significant (*F-value* = 51.66, *p-value* < 0.0001). This statistical validation of prior thermodynamic findings establishes that the adsorption process is endothermic ($\Delta H^\circ > 0$). The positive coefficient for factor E in the regression model confirms that elevated temperatures activate new binding sites and increase the kinetic mobility of MO molecules into the mesopores of the ZnO@DPS-AC composite.

Interestingly, the effect of *pH* (factor *D*) was found to be statistically insignificant (*p-value* =

0.7959) within the RSM study's specific design space. This finding contrasts directly with the isolated-batch studies, in which *pH* was a critical determinant (with maximum adsorption at *pH* 2.0). This discrepancy suggests that while *pH* is highly influential in isolation, its effect is heavily overshadowed by the massive influence of concentration and dosage when all parameters are varied simultaneously. Furthermore, because the RSM design range was centered near the selected operating *pH* of 6.0 (ranging from *pH* 4 to 8), the surface charge variations were naturally less drastic than those observed across the full *pH* 2 to 12 range tested in the univariate studies. Consequently, this narrower interval yielded a flatter response surface for this specific factor than for the more dominant variables.

Table V.7 ANOVA analysis for the quadratic response surface model corresponding to adsorption capacity

Source	*SS*	*DF*	*MS*	*F-value*	*p-value*	Significance
Model	7.13	20	0.3567	179.17	< 0.0001	Significant
A-Time	0.2834	1	0.2834	142.35	< 0.0001	Significant
B-Concentration	4.14	1	4.14	2080.26	< 0.0001	Significant
C-Dose	1.33	1	1.33	668.40	< 0.0001	Significant
D-pH	0.0001	1	0.0001	0.0684	0.7959	
E-Temperature	0.1029	1	0.1029	51.66	< 0.0001	Significant
AB	0.0608	1	0.0608	30.51	< 0.0001	Significant
AC	0.0686	1	0.0686	34.48	< 0.0001	Significant
AD	0.0013	1	0.0013	0.6280	0.4355	
AE	0.0174	1	0.0174	8.72	0.0067	Significant
BC	0.1838	1	0.1838	92.33	< 0.0001	Significant
BD	0.0030	1	0.0030	1.53	0.2283	
BE	0.0193	1	0.0193	9.68	0.0046	Significant
CD	0.0007	1	0.0007	0.3733	0.5467	
CE	0.0504	1	0.0504	25.32	< 0.0001	Significant
DE	0.0002	1	0.0002	0.0954	0.7599	
A^2	0.0723	1	0.0723	36.33	< 0.0001	Significant
B^2	0.8165	1	0.8165	410.10	< 0.0001	Significant
C^2	0.0212	1	0.0212	10.66	0.0032	Significant
D^2	0.0023	1	0.0023	1.18	0.2880	
E^2	0.0332	1	0.0332	16.69	0.0004	Significant
Residual	0.0498	25	0.0020			
Lack of Fit	0.0471	20	0.0024	4.43	0.0531	Not Significant

Pure Error	0.0027	5	0.0005
Cor Total	7.18	45	

Table V.8 ANOVA analysis for the quadratic response surface model corresponding to removal percentage

Source	*SS*	*DF*	*MS*	*F-value*	*p-value*	Significance
Model	15848.44	20	792.42	58.97	< 0.0001	Significant
A-Time	1416.39	1	1416.39	105.40	< 0.0001	Significant
B-Concentration	2921.81	1	2921.81	217.43	< 0.0001	Significant
C-Dose	7778.03	1	7778.03	578.80	< 0.0001	Significant
D-pH	2.95	1	2.95	0.2195	0.6434	Not Significant
E-Temperature	481.93	1	481.93	35.86	< 0.0001	Significant
AB	256.64	1	256.64	19.10	0.0002	Significant
AC	163.89	1	163.89	12.20	0.0018	Significant
AD	8.56	1	8.56	0.6371	0.4323	Not Significant
AE	76.95	1	76.95	5.73	0.0245	Significant
BC	581.59	1	581.59	43.28	< 0.0001	Significant
BD	16.15	1	16.15	1.20	0.2834	Not Significant
BE	103.84	1	103.84	7.73	0.0102	Significant
CD	3.36	1	3.36	0.2498	0.6216	Not Significant
CE	141.37	1	141.37	10.52	0.0033	Significant
DE	2.77	1	2.77	0.2060	0.6538	Not Significant
A^2	388.06	1	388.06	28.88	< 0.0001	Significant
B^2	295.47	1	295.47	21.99	< 0.0001	Significant
C^2	1737.94	1	1737.94	129.33	< 0.0001	Significant
D^2	50.23	1	50.23	3.74	0.0646	Not Significant
E^2	234.06	1	234.06	17.42	0.0003	
Residual	335.95	25	13.44			
Lack of Fit	311.58	20	15.58	3.20	0.1007	Not Significant
Pure Error	24.38	5	4.88			
Cor Total	16184.39	45				

V.8.3.2 Removal percentage model

The ANOVA results for *R* (**Table V.8**) yielded a model *F-value* of 58.97 (*p-value* < 0.0001). This indicates a distinct shift in factor importance compared to the previously discussed q_e model. Adsorbent dosage (factor C) emerged as the dominant parameter (F = 578.80). This statistical dominance aligns with the univariate batch observations, in which increasing the composite mass from 15 mg to 65 mg rapidly elevated *R* from 33% to 98% owing to the proliferation of available

surface-active sites. Furthermore, the analysis revealed significant interactive effects, most notably between initial dye concentration and adsorbent dosage (factor *BC*, *F-value* = 43.28).

A critical criterion for model acceptance is the LoF test, which compares the residual error to the pure error derived from replicated center points. As detailed in **Table V.7** and **Table V.8**, the LoF *F-value*s for q_e (4.43) and *R* (3.20) were both lower than their respective critical *F-Table* value of 4.56. Because the calculated variance ratios do not exceed the tabulated theoretical limits, their associated p-values strictly exceed 0.05. This confirms that the selected quadratic models adequately describe the functional relationship between the experimental factors and the target responses. The residual variation is largely attributed to random experimental noise rather than inherent model deficiency. Consequently, this statistical validation establishes that the developed polynomial models are robust predictors for optimizing the ZnO@DPS-AC adsorption system.

V.8.4 Development of predictive regression equations

To quantitatively describe the relationship between the five independent process variables and the overall adsorption performance, second-order polynomial equations were developed using multiple regression analysis. These mathematical models express the target responses as continuous functions of contact time (A), initial dye concentration (B), adsorbent dosage (C), solution *pH* (D), and temperature (E).

V.8.4.1 Actual factor equations

The empirical models, expressed in actual (uncoded) units, enable direct, practical prediction of system responses. The governing equation for q_e (mg/g) is presented as **Eq. V.2**, while the corresponding equation for *R* (%) is provided as **Eq. V.3**.

$$\begin{aligned}\ln(\text{Capacity}) = {} & 1.97746 + 0.008909(\text{Time}) + 0.003721(\text{Concentration}) \\ & + 0.006666(\text{Dose}) + 0.031810(\text{pH}) \\ & + 0.075744(\text{Temperature}) + 0.000010(\text{Time} \cdot \text{Concentration}) \\ & - 0.000047(\text{Time} \cdot \text{Dose}) + 0.000111(\text{Time} \cdot \text{pH}) \\ & - 0.000082(\text{Time} \cdot \text{Temperature}) \\ & + 0.000041(\text{Concentration} \cdot \text{Dose}) \\ & + 0.000092(\text{Concentration} \cdot \text{pH}) \\ & + 0.000046(\text{Concentration} \cdot \text{Temperature}) \\ & - 0.000195(\text{Dose} \cdot \text{pH}) - 0.000321(\text{Dose} \cdot \text{Temperature}) \\ & - 0.000345(\text{pH} \cdot \text{Temperature}) - 0.000014(\text{Time})^2 \\ & - 0.000014(\text{Concentration})^2 - 0.000040(\text{Dose})^2 \\ & - 0.004099(\text{pH})^2 - 0.000617(\text{Temperature})^2\end{aligned} \qquad \textbf{Eq. V.2}$$

$$\begin{aligned}\text{Removal} = {} & -130.08738 + 0.569763(\text{Time}) - 0.375949(\text{Concentration}) \\ & + 2.59210(\text{Dose}) + 6.15183(\text{pH}) + 5.55561(\text{Temperature}) \\ & + 0.000668(\text{Time} \cdot \text{Concentration}) - 0.002286(\text{Time} \cdot \text{Dose}) \\ & + 0.009144(\text{Time} \cdot \text{pH}) - 0.005483(\text{Time} \cdot \text{Temperature}) \\ & + 0.002297(\text{Concentration} \cdot \text{Dose}) \\ & + 0.006698(\text{Concentration} \cdot \text{pH}) \\ & + 0.003397(\text{Concentration} \cdot \text{Temperature}) \\ & - 0.013086(\text{Dose} \cdot \text{pH}) - 0.016986(\text{Dose} \cdot \text{Temperature}) \\ & - 0.041600(\text{pH} \cdot \text{Temperature}) - 0.001042(\text{Time})^2 \\ & - 0.000259(\text{Concentration})^2 - 0.011520(\text{Dose})^2 \\ & - 0.599786(\text{pH})^2 - 0.051787(\text{Temperature})^2\end{aligned} \qquad \textbf{Eq. V.3}$$

Because the q_e model was developed using a natural logarithmic transformation to stabilize variance, the predicted q_e must be back-transformed using the relationship $q_e = \exp(\ln q_e)$. Furthermore, to prevent severe extrapolation errors, these predictive equations must be applied strictly within the defined experimental design space.

V.8.4.2 Coded factor equations

The regression equations expressed in terms of coded factors (operational levels scaled from -1 to +1) are presented in **Eq. V.4** and **Eq. V.5**. These coded equations are critical for identifying the relative impact of the individual parameters by directly comparing the magnitude of their respective coefficients.

$$\begin{aligned}\ln(\text{Capacity}) = {} & +5.22 + 0.1331A + 0.5088B - 0.2884C - 0.0029D \\ & + 0.0802E + 0.1232AB - 0.1310AC + 0.0177AD - 0.0659AE \\ & + 0.2144BC + 0.0276BD + 0.0694BE - 0.0136CD \\ & - 0.1123CE - 0.0069DE - 0.0910A^2 - 0.3059B^2 - 0.0493C^2 \\ & - 0.0164D^2 - 0.0617E^2\end{aligned} \qquad \textbf{Eq. V.4}$$

$$\begin{aligned}\text{Removal} = {} & +96.00 + 9.41A - 13.51B + 22.05C - 0.4294D + 5.49E \\ & + 8.01AB - 6.40AC + 1.46AD - 4.39AE + 12.06BC + 2.01BD \\ & + 5.10BE - 0.9160CD - 5.95CE - 0.8320DE - 6.67A^2 \\ & - 5.82B^2 - 14.11C^2 - 2.40D^2 - 5.18E^2\end{aligned} \qquad \textbf{Eq. V.5}$$

The sign and magnitude of these coefficients provide quantitative insight into the adsorption mechanism of MO onto the ZnO@DPS-AC composite. In the q_e model (**Eq. V.4**), the linear coefficient for initial dye concentration (factor B) is positive and exhibits the highest overall magnitude (+0.5088). This indicates that increasing the MO concentration significantly enhances the q_e. This statistical finding quantitatively corroborates the concentration gradient and mass transfer mechanisms discussed comprehensively in **sections V.2.5** and **V.4**. Conversely, in the *R* model (**Eq. V.5**), the concentration term is negative (-13.51). This mathematically reflects the saturation of available active sites at higher dye loadings, which fundamentally reduces the overall percentage of dye removed despite the higher solid-phase unit loading.

Adsorbent dosage (factor C) shows an inverse relationship with both target responses. It serves as the most dominant positive parameter for *R* (+22.05 in **Eq. V.5**). However, it imparts a significant negative effect on q_e (-0.2884 in **Eq. V.4**). Physically, this confirms that while increasing the adsorbent mass provides a greater absolute number of active sites (elevating *R*), it simultaneously reduces the ratio of dye molecules to available active sites. This unsaturation dynamic lowers the amount of dye adsorbed per unit mass (q_e), a behavior strictly consistent with the findings of Uddin

and Baig (2019) for MO adsorption onto Co_3O_4 nanoparticles; it simultaneously reduces the ratio of dye molecules to available active sites.

The positive coefficient for temperature (factor *E*) in both predictive models (+0.0802 for q_e and +5.49 for *R*) statistically validates the endothermic nature of the sequestration process. This finding directly corroborates the thermodynamic analysis established earlier in **section V.6** ($\Delta H^\circ > 0$), confirming that elevated temperatures facilitate intra-particle diffusion and activate additional surface binding sites without requiring a repeated explanation of the heat of adsorption.

Regarding solution *pH* (factor *D*), the linear coefficient is comparatively small in both models (-0.0029 for q_e and -0.4294 for *R*). This implies that within the specific design space bounded by the RSM, *pH* exerted a less pronounced linear effect than concentration and dosage. However, the statistical significance of the quadratic term (D^2) in the prior ANOVA indicates a distinct curvature effect. The inherently negative sign of the linear coefficient suggests that increasing *pH* generally disfavors adsorption, which is consistent with the electrostatic repulsion mechanism between the anionic dye and the deprotonated composite surface, as detailed in the earlier batch studies.

V.8.5 Two-Dimensional interaction analysis

To visualize the synergistic and antagonistic effects between the independent variables, two-dimensional (2D) contour interaction plots were generated. These plots illustrate how the target response variables behave when two parameters vary simultaneously, while the remaining factors are held at their central experimental levels.

V.8.5.1 Interactive effects on adsorption capacity

The ANOVA analysis and corresponding regression coefficients (**Table V.7**) identified the interaction between initial concentration and adsorbent dosage (factor BC) as the most significant interactive term governing unit capacity. This was followed closely by the interaction between contact time and initial concentration (factor AB).

Figure V.5 illustrates the specific interaction between the initial MO concentration (factor *B*) and the adsorbent dosage (factor *C*), revealing a highly divergent trend. At elevated adsorbent dosages, the q_e exhibits only a marginal increase with increasing initial concentration. Conversely, at low adsorbent dosages, increasing the initial concentration results in a sharp, significant increase in q_e.

Physicochemically, this behavior is governed by the mass-transfer driving force. At low dosage, the ratio of adsorbate molecules to available active sites remains high. Increasing the concentration under these specific conditions significantly enhances the concentration gradient, compelling more MO molecules into the mesopores of the ZnO@DPS-AC composite per unit mass, thereby maximizing q_e. This observation aligns with Uddin and Baig (2019), who reported that, for Co3O4 nanoparticles, minimizing the adsorbent dose while simultaneously maximizing the initial dye concentration is a critical strategy for achieving high uptake capacity by reducing the fraction of unsaturated active sites.

Similarly, the interaction between contact time and concentration (factor *AB*) depicted in **Figure V.5** demonstrates that the slope of the time-dependency curve increases proportionately with concentration. At low initial MO concentrations, the contour curve is nearly horizontal, indicating that equilibrium is rapidly achieved through the immediate saturation of surface sites. Conversely, at high concentrations, the q_e continues to rise significantly over prolonged periods. This statistically corroborates the kinetic results previously discussed in **sections V.2.4 and V.3**, which established that the equilibrium time ranged from 120 to 240 min as the initial concentration increased. Elevated concentrations require longer contact times to allow MO molecules to effectively diffuse through the hydrodynamic boundary layer and penetrate the composite's deeper intra-particle pore architecture.

Regarding the interaction between solution *pH* and other parameters (such as factors *AD* and *AE*), the generated contour plots display parallel or near-parallel profiles (**Figure V.5**). This strict parallelism indicates a lack of significant parameter interaction. Specifically, the effect of contact time on capacity remains consistent across the *pH* levels within the bounded RSM design space. While the univariate batch studies detailed in **section V.2.2** confirmed that *pH* operates as a critical linear determinant affecting surface charge and electrostatic attraction, the RSM results comprehensively reveal that its specific influence within a multivariate system is predominantly additive rather than interactive.

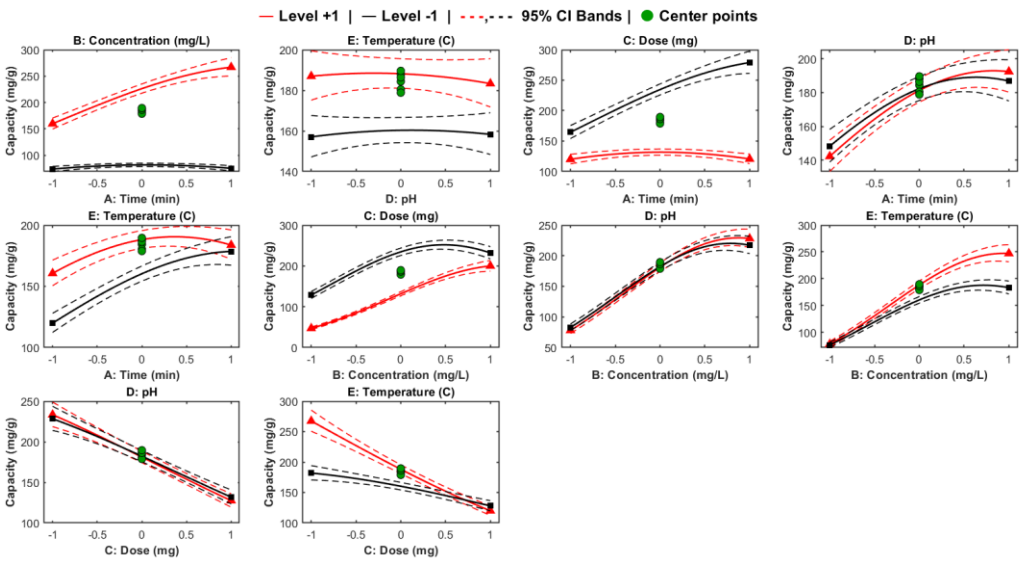

Figure V.5 Two-dimensional interaction plots derived from the RSM-CCD model demonstrating the effects of paired operational variables on MO adsorption capacity

V.8.5.2 Interactive effects on removal percentage

The interaction patterns for *R*, illustrated in **Figure V.6**, differ distinctly from those governing qe, particularly with respect to the influence of adsorbent dosage. The contour plot detailing the interaction between initial concentration and dosage (factor *BC*) displays a converging behavior. At elevated adsorbent dosages, the *R* remains consistently high (> 95%) regardless of the initial MO concentration. Conversely, at low adsorbent dosages, the *R* drops precipitously as the initial dye concentration increases. This demonstrates the buffering capacity inherent to high adsorbent dosing; a large mass of the ZnO@DPS-AC composite provides an abundance of surface functional groups and ZnO active centers sufficient to sequester high pollutant loads. At lower dosages, the limited number of available active sites quickly becomes saturated by high dye concentrations, leading to a stoichiometric breakthrough and a subsequently reduced *R*. This observation is consistent with the findings of Sharifpour et al. (2019) for Mn-doped CuO-AC, where an increased adsorbent mass provided the critical surface area necessary to maintain high *R* even at elevated pollutant concentrations.

Furthermore, the interaction plot evaluating contact time and dosage (factor AC) indicates that at low adsorbent dosages, extending the contact time significantly improves the overall *R*. In contrast, at high dosages, the sequestration process is so rapid that additional contact time exerts a negligible

effect on the final *R*. This statistically supports the rapid initial uptake mechanism previously established in **section V.2.4**. An abundance of exterior active sites at high dosages facilitates immediate bulk adsorption. Conversely, low-dosage systems rapidly become diffusion-controlled, necessitating extended contact durations to utilize internal mesoporous binding sites effectively.

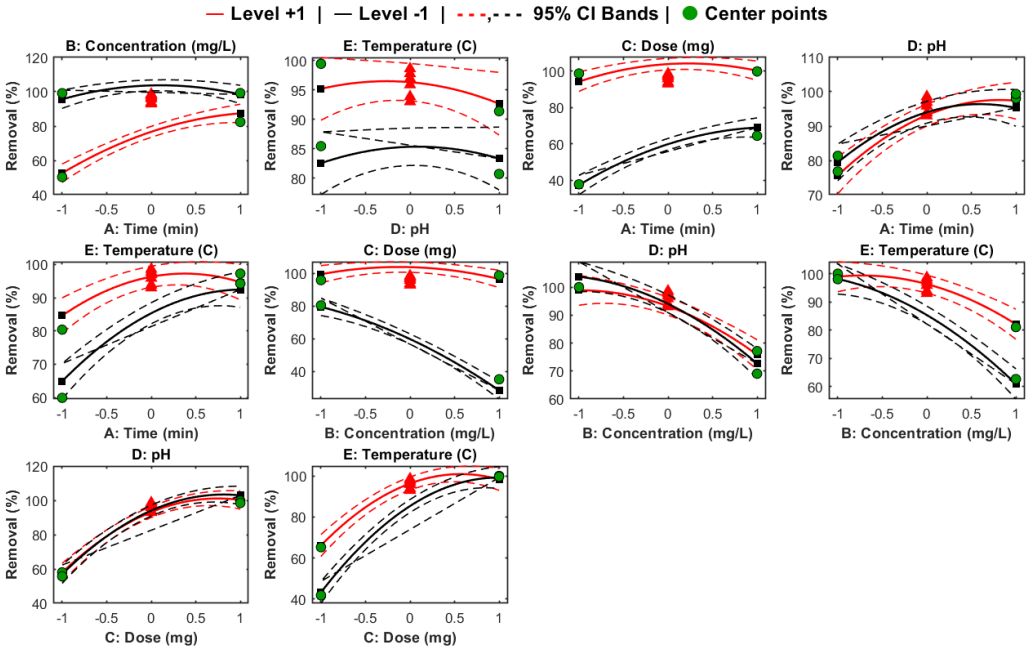

Figure V.6 Two-dimensional interaction plots derived from the RSM-CCD model demonstrating the effects of paired operational variables on MO removal percentage

V.8.6 Three-Dimensional response surface topologies

V.8.6.1 Three-Dimensional response surfaces for adsorption capacity

To graphically interpret the complex interactions among the independent variables governing q_e, three-dimensional (3D) response surface plots were generated (**Figure V.7** and **Figure V.8**). These visualizations of the regression equation facilitate the identification of optimal regions within the experimental design space where the unit q_e of the ZnO@DPS-AC composite is maximized.

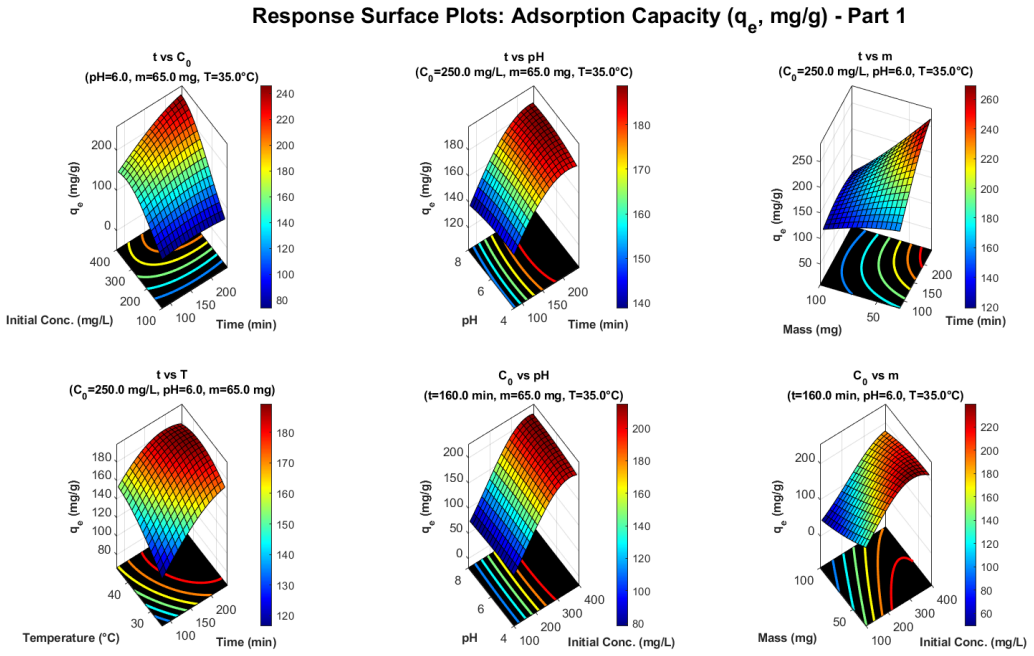

Figure V.7 Three-dimensional response surface plots illustrating the interactive effects of operational parameters on the MO adsorption capacity of the ZnO@DPS-AC composite (part 1)

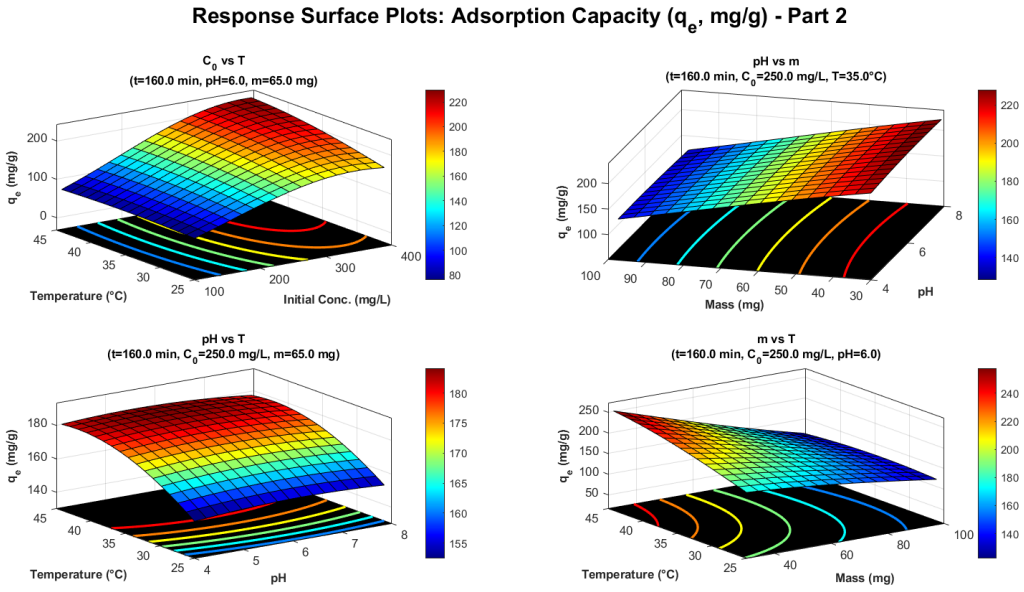

Figure V.8 Three-dimensional response surface plots illustrating the interactive effects of operational parameters on the MO adsorption capacity of the ZnO@DPS-AC composite (part 2)

The 3D response surface evaluating contact time and initial concentration exhibits a steep upward curvature, indicating a strong positive influence of both parameters on q_e. As depicted, q_e increases significantly with concurrent elevations in t and C_0. The effect of concentration is particularly pronounced, resulting in a steep slope across the response surface. This trend closely aligns with the kinetic and mass transfer mechanisms established during the batch studies **in sections V.2.4** and **V.2.5**. The required contact time allows the dye to overcome film and pore diffusion resistances, while a higher C_0 provides the steep concentration gradient required to drive MO molecules into the mesoporous network. This finding aligns with Uddin and Baig (2019), who used BBD to study cobalt oxide nanoparticles and reported that q_e is maximized at high initial concentrations due to increased collision frequency between dye molecules and active sites.

The 2D interaction plot of adsorbent mass versus temperature shows that q_e is maximized at low adsorbent mass and high temperature. Mathematically, q_e is defined by the inverse relationship (**Eq. III.17**); therefore, increasing m naturally lowers q_e. Physicochemically, this split-flux phenomenon occurs because higher dosages provide excess surface area, thereby decreasing the ratio of adsorbate molecules to active sites and leaving many binding centers unsaturated (Sharifpour et al., 2019). Additionally, the surface slopes gently upward toward higher temperatures, particularly at extended contact times. This positive correlation statistically validates the endothermic nature of the adsorption process ($\Delta H^\circ > 0$) determined in **section V.6**. As previously discussed, elevated temperatures increase the kinetic energy of the MO molecules and decrease solution viscosity, thereby enhancing the rate of intra-particle diffusion.

The response surface for initial concentration versus adsorbent mass displays a distinct contour twist, highlighting a critical operational trade-off. The peak q_e is located precisely at the coordinates corresponding to high C_0 and low mass. However, the plot indicates a slight decrease in q_e beyond 300 mg/L at low mass, suggesting a saturation threshold. To achieve maximum specific loading, the system must operate under conditions where the C_0 is highly abundant relative to the m, compelling the material to utilize its full saturation capacity. Conversely, combining high mass with low concentration yields the lowest q_e because the abundant active sites remain severely underutilized.

The 3D plots involving *pH* (t versus *pH* and C_0 versus *pH*) indicate that *pH* is less dominant in the multivariate design space than concentration and mass. The response surface is relatively flat,

exhibiting only a slight increase in q_e as *pH* rises from 4 to 8. This specific behavior contrasts with the univariate batch experiments, which identified *pH* 2.0 as the strict optimum for electrostatic attraction. The RSM results suggest that when multiple parameters are varied simultaneously, the strong driving force of the concentration gradient heavily overshadows pH-dependent electrostatic effects. Furthermore, the slight decrease observed in the high C_0 and low *pH* region suggests that extreme acidic conditions combined with high pollutant loads may induce dye aggregation or rapid surface saturation (issues that are inherently absent in dilute, single-factor experiments). This behavior confirms that the ZnO@DPS-AC composite remains highly effective across a broader *pH* range within complex, concentrated environments, corroborating the robust *R* observed at *pH* 12 in the batch studies.

V.8.6.2 Three-Dimensional response surfaces for removal percentage

While the analysis of q_e focuses on the sequestration efficiency of the solid material, the R serves as the critical parameter for assessing overall process efficiency and final effluent quality. The corresponding 3D response surface plots (**Figure V.9** and **Figure V.10**) reveal trends that are often the inverse of those observed for capacity, particularly with respect to the influence of adsorbent dosage and initial dye concentration.

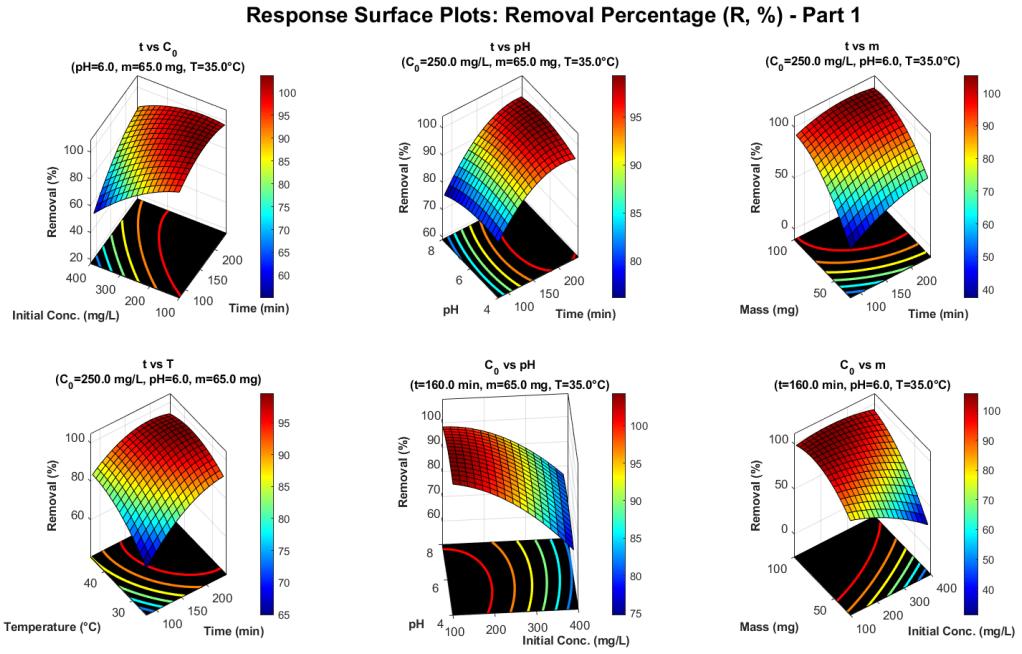

Figure V.9 Three-dimensional response surface plots illustrating the interactive effects of operational parameters on the MO removal percentage of the ZnO@DPS-AC composite (Part 1)

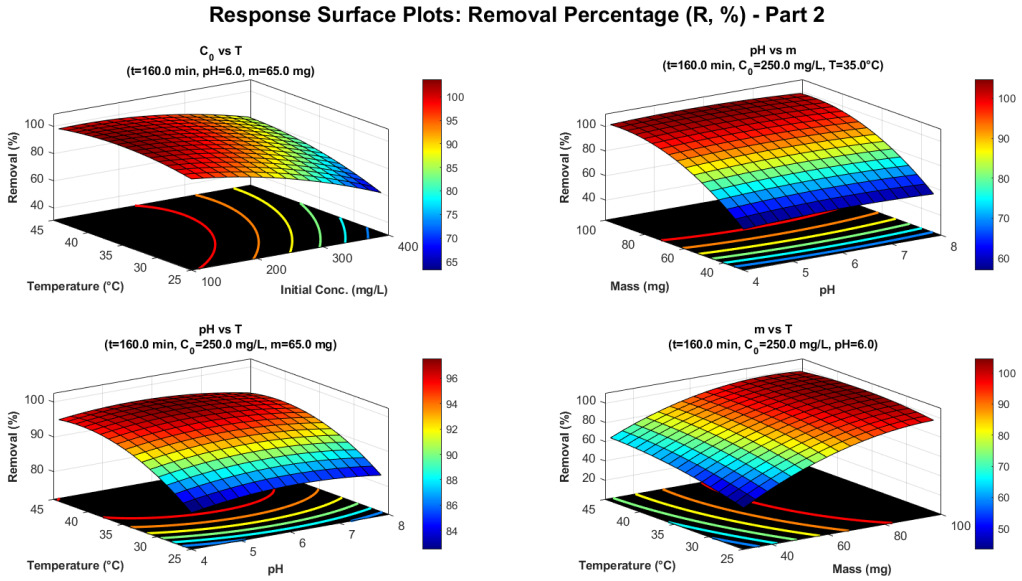

Figure V.10 Three-dimensional response surface plots illustrating the interactive effects of operational parameters on the MO removal percentage of the ZnO@DPS-AC composite (Part 2)

The interaction between m (factor C) and C_0 (factor B) generates a response surface resembling a twisted plane, which visually represents the physical phenomenon of adsorbent saturation (breakthrough). As illustrated in the 3D plot, the zone of maximal removal is located at the coordinates corresponding to high adsorbent dosage and low initial concentration. Conversely, the R drops precipitously to its minimum when the dosage is low and the concentration is high. This contour profile clearly illustrates the dynamic availability of active sites. Increasing the adsorbent dosage introduces a proliferation of surface functional groups and ZnO active centers into the system. At low C_0, these abundant sites readily sequester the available MO molecules, leading to near-total removal. However, at low dosages combined with high concentrations, the ratio of adsorbate molecules to active sites is excessively high. The limited number of binding centers is quickly overwhelmed, leading to rapid saturation and a high concentration of residual dye in the treated effluent. This specific behavior is consistent with the findings of Sharifpour et al. (2019) regarding the adsorption of dyes onto Mn-doped CuO-AC. They observed that while higher adsorbent masses ensure higher water purity (high R), they also result in lower unit capacity, thereby necessitating economic optimization of the trade-off. Similarly, Trifi et al. (2019) reported

that the *R* for azo dyes on orange peel-derived carbon increased rapidly with dosage due to the expanded surface area available for target binding.

The interaction plot for adsorbent mass and temperature confirms the thermodynamic nature of the system, demonstrating that *R* is maximized at high mass and high temperature. The surface exhibits a gradual upward slope with increasing temperature, a trend particularly evident at lower adsorbent dosages, where the system is not severely mass-transfer-limited. This positive correlation with temperature confirms the endothermic nature of the adsorption process ($\Delta H^{\circ}>0$), as previously determined in the thermodynamic analysis in **section V.6**. As established, elevated temperatures increase the kinetic energy of the MO molecules and reduce solution viscosity, thereby enhancing intra-particle diffusion into the mesoporous architecture of the ZnO@DPS-AC. Bessaha et al. (2023) reported similar behavior for MO adsorption on bentonite, where both q_e and *R* rose with temperature (from 25 °C to 55 °C), attributing this enhancement to the endothermic activation of surface sites and the increased kinetic mobility of the dye ions.

V.8.7 Multi-objective optimization of process parameters

Multi-objective optimization was performed using the Desirability Function approach (DFA), as formally described in **sections II.4.4** and **III.13.5**, targeting the simultaneous maximization of q_e and *R*. To determine the X_{opt} for the adsorptive remediation of MO, a numerical optimization was performed using the D_{opt}. Based on the economic and environmental objectives of large-scale wastewater treatment, three distinct scenarios were investigated, as summarized in **Table V.9**.

Table V.9 Optimization results by RSM for MO adsorption

Criterion	t (min)	C_0 (mg/L)	*m* (mg)	*pH*	*T* (°C)	Predicted q_e (mg/g)	Predicted *R* (%)	Desirability
Maximum Capacity	238.43	351.83	42.78	5.26	30.70	273.99	65.27	1.00
Maximum Removal	112.24	166.99	91.09	4.85	38.16	91.04	103.71	1.00
Multi-Objective	240.00	385.00	80.66	7.13	37.25	241.47	99.03	0.96

Scenario 1: maximizing adsorption capacity (Resource Efficiency)

When the optimization goal was strictly limited to maximizing q_e, the regression model predicted an optimal q_e of 273.99 mg/g. This was achieved at a low adsorbent dosage (42.78 mg) and a high initial concentration (351.8 mg/L), yielding a desirability score of 1.0 (D_{opt}). This result highlights the maximization of material efficiency. As previously established, operating at low dosages and high concentrations maximizes the ratio of adsorbate molecules to available surface sites, forcing saturation of the adsorbent per unit mass. The elevated concentration provides the steep concentration gradient needed to overcome mass-transfer resistance and drive MO into the internal mesopores. This trend is consistent with Uddin and Baig (2019), who optimized Co_3O_4 nanoparticles and found that maximizing qe required minimizing the adsorbent dose to prevent active-site unsaturation.

Scenario 2: maximizing removal percentage (Effluent Quality)

Conversely, when the objective was to maximize R, the model predicted complete dye removal (~100%) at a significantly higher m (91.09 mg) and a lower initial concentration (166.9 mg/L). This scenario represents the effluent purity objective. The high dosage ensures an absolute abundance of surface functional groups and active ZnO centers relative to the dye molecules. This surplus ensures the extraction of nearly every MO molecule from the solution, though it inherently results in lower uptake (q_e = 91.0 mg/g) due to site unsaturation. This physical trade-off aligns with (Sharifpour et al., 2019), who used CCD for Mn-doped CuO-AC. They reported that while high adsorbent masses ensure regulatory compliance with effluent purity requirements, they inherently compromise the economic utilization of the material's total q_e.

Scenario 3: multi-objective optimization (Industrial Balance)

A multi-objective scenario was designed to balance high q_e with high R, accurately reflecting realistic industrial operational constraints. The optimal conditions were identified as: contact time of 240 min, initial concentration of 385 mg/L, adsorbent dosage of 80.66 mg, *pH* of 7.15, and temperature of 37.2 °C. Under these unified conditions, the predicted q_e was 241.47 mg/g with a simultaneous R of 99.03% (D_{opt} = 0.958).

Physiochemically, the optimal *pH* of ~7.15 is highly significant. While the univariate batch studies (**section V.2.2**) indicated maximum attraction at *pH* 2.0 due to strong electrostatic interactions, the RSM modeling suggests that near-neutral conditions are completely sufficient for high performance within a multivariate system. This indicates that at high pollutant concentrations, non-

electrostatic forces (such as π-π stacking and hydrogen bonding) dominate the system, enabling effective treatment without the operational costs and environmental hazards associated with extreme acidification. This represents a significant practical advantage over materials such as the hydrochar studied by Tcheka et al. (2024), which strictly required a *pH* of 2.0 for optimal performance. Furthermore, the selection of 37.2 °C by the desirability function directly corroborates the endothermic nature ($\Delta H^{\circ} > 0$) established in the prior thermodynamic analysis, formally confirming that moderate heating enhances dye mobility and pore diffusion.

V.8.8 Experimental validation

To validate the predictive accuracy of the generated RSM models, confirmatory experiments were executed under the optimized conditions established for pilot-scale operation (C_0 = 240 mg/L, m = 80.0 mg, pH = 7.0, t = 240 min, and T = 37.0 °C). Under these specified parameters, the empirical results yielded a q_e of 225.43 mg/g and a simultaneous R of 94.46%. The relative error between the theoretical predictions and the experimental values was determined to be 4.8% for R, falling strictly within the acceptable statistical margin of error. This high degree of concordance confirms the validity, robustness, and reproducibility of the developed quadratic models for accurately predicting and optimizing methyl orange removal.

V.9 Modeling of MO adsorption via an artificial neural network

V.9.1 Model development and hyperparameter optimization

Developing a highly accurate ANN model requires systematic hyperparameter tuning to prevent underfitting and over-parameterization. Input and output data were normalized to [0.1, 0.9] using **Eq. III.26** (**section III.14.1**) prior to network training. The optimal topology was determined by iteratively adjusting the number of hidden-layer neurons and evaluating network performance. **Figure V.11** illustrates the effect of the hidden-layer neuron count on the *MSE* and R^2 during this optimization process for the MO adsorption model. Performance metrics clearly indicate that an architecture with 15 hidden neurons yielded the optimal balance, minimizing MSE while maximizing R^2.

To further refine the model, a systematic grid search was conducted to evaluate various training algorithms, transfer functions, and network sizes. **Table V.10** summarizes the top 10 ANN

configurations tested. The model utilizing the Scaled Conjugate Gradient (trainscg) algorithm, a Tansig hidden transfer function, and a Purelin output transfer function demonstrated superior performance. This optimal configuration (Algorithm 1) achieved a remarkably low mean *MSE* of 3.05E-04 (*SD* = 9.0E-06) and a high mean R^2 of 0.9942 (*SD* = 3.7E-04).

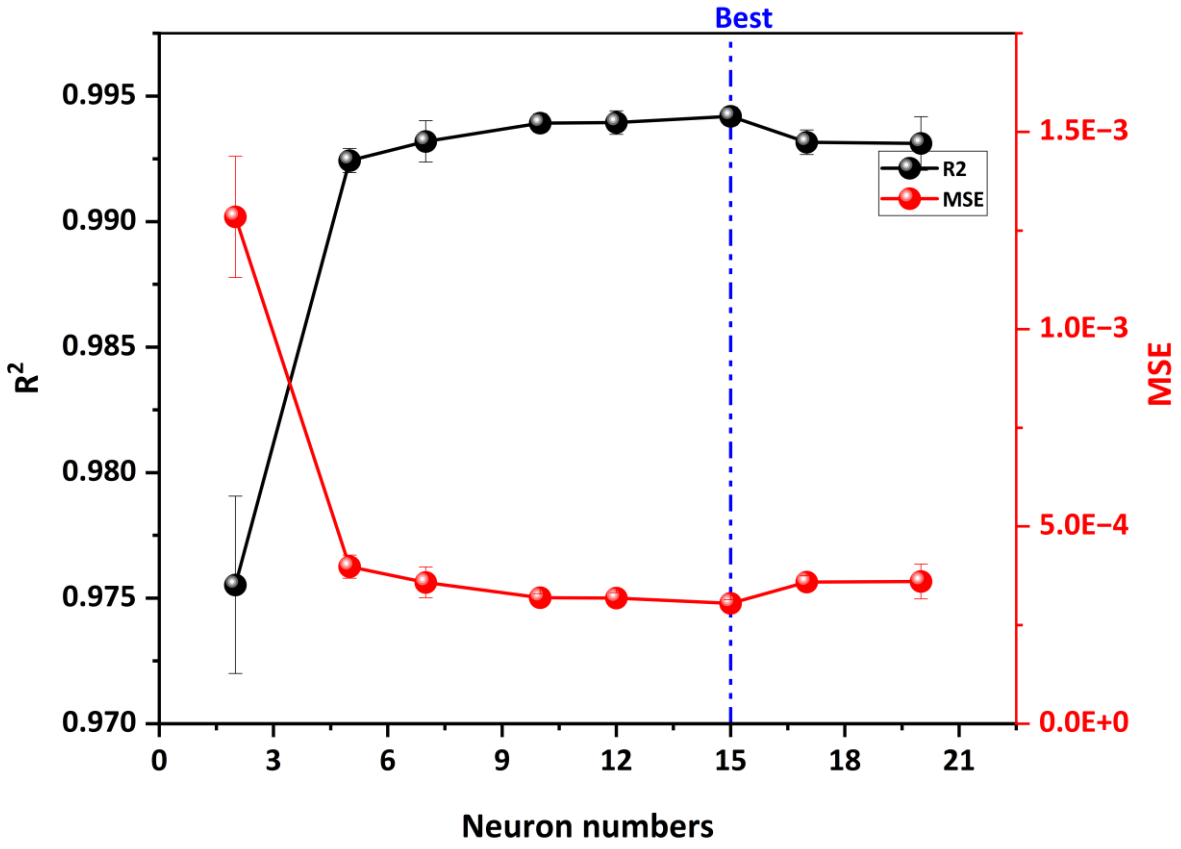

Figure V.11 Effect of the number of hidden layer neurons on the mean squared error (MSE) and coefficient of determination (R^2) during hyperparameter optimization for the MO adsorption model

V.9.2 Best model architecture and training convergence

Based on these optimization results, the final feed-forward multi-layer perceptron architecture was established. **Figure V.12(a)** provides a schematic representation of this optimized ANN topology. The network features an input layer with five independent variables (contact time, initial concentration, *pH*, adsorbent dose, and temperature), a single hidden layer of 15 neurons utilizing a hyperbolic tangent sigmoid (Tansig) activation function, and an output layer yielding two target

variables (equilibrium capacity and removal percentage) via a linear (Purelin) function. Training convergence across cross-validation folds was validated using the learning curve (**Figure V.12** (**b**)). The log MSE decreased rapidly before stabilizing, confirming that the network successfully mapped the input-output relationships without divergent behavior.

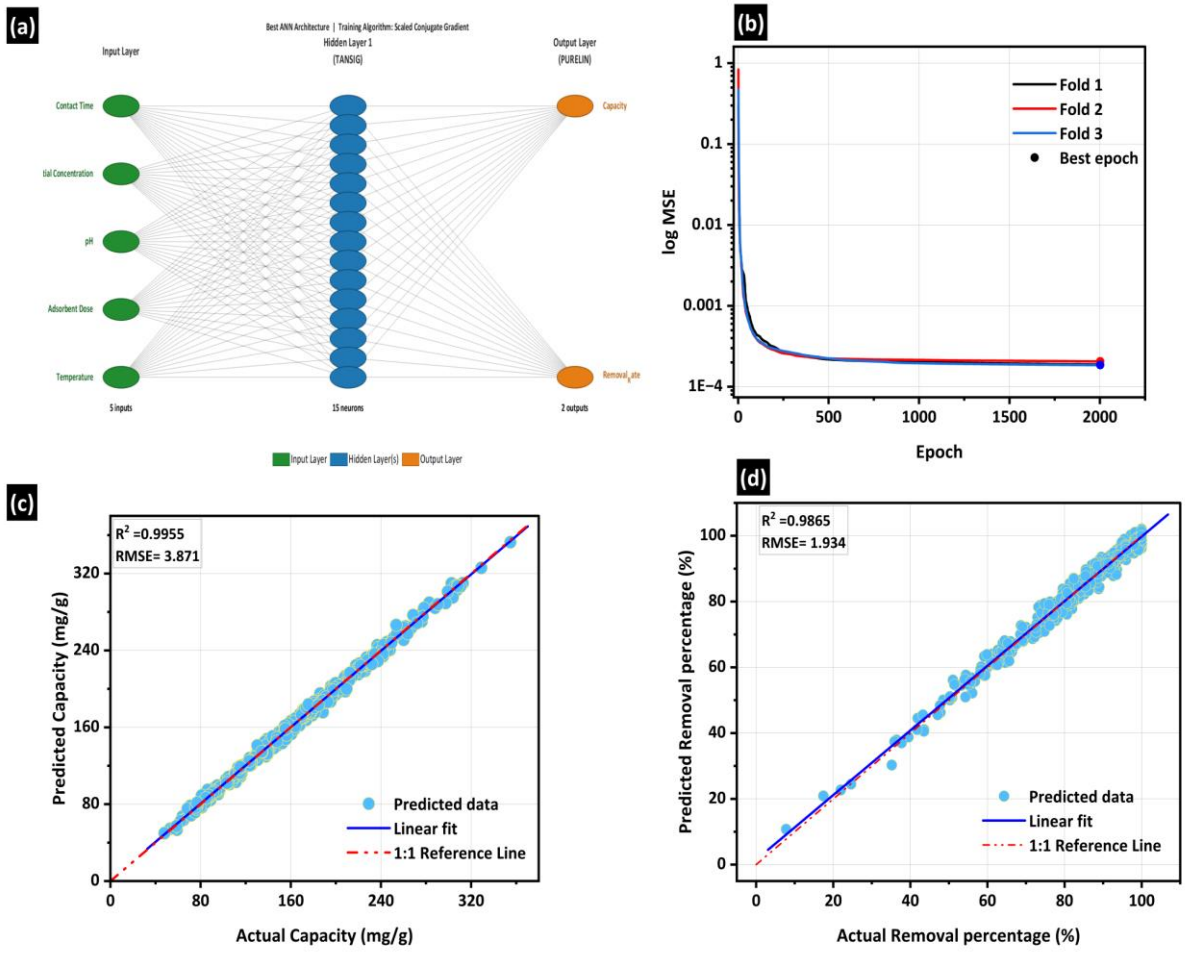

Figure V.12 Evaluation of the optimized ANN architecture for MO adsorption: (**a**) schematic representation of the network topology; (**b**) learning curve demonstrating training convergence across cross-validation folds; and scatter plots comparing ANN-predicted values against actual experimental data for (**c**) equilibrium adsorption capacity and (**d**) removal percentage

Table V.10 Summary of the top 10 ANN configurations evaluated during the systematic grid search for MO adsorption

N	Algorithm	Code	Neurons	Hidden TF.	Output TF.	Mean MSE	SD MSE	Mean R^2	SD R^2
1	Scaled Conjugate Gradient	trainscg	15	Tansig	Purelin	3.05E-04	9.0E-06	0.9942	3.7E-04
2	Conjugate Gradient with Polak-Ribiere	traincgp	12	Logsig	Purelin	3.10E-04	1.0E-05	0.9941	2.1E-04
3	Bayesian Regularization	trainbr	10	Tansig	Purelin	3.11E-04	2.6E-05	0.9941	9.3E-04
4	One-Step Secant	trainoss	15	Tansig	Purelin	3.11E-04	3.3E-05	0.9941	3.7E-04
5	Resilient Backpropagation	trainrp	20	Tansig	Purelin	3.12E-04	2.3E-05	0.9941	1.8E-04
6	Scaled Conjugate Gradient	trainscg	12	Logsig	Purelin	3.12E-04	1.7E-05	0.9940	7.5E-04
7	BFGS Quasi-Newton	trainbfg	10	Tansig	Purelin	3.13E-04	2.8E-05	0.9941	3.6E-04
8	Bayesian Regularization	trainbr	12	Logsig	Purelin	3.14E-04	3.5E-05	0.9940	7.8E-04
9	Levenberg-Marquardt	trainlm	10	Tansig	Purelin	3.14E-04	1.0E-05	0.9940	4.7E-04
10	Bayesian Regularization	trainbr	10	Logsig	Purelin	3.14E-04	1.6E-05	0.9940	6.3E-04

Note: TF = Transfer Function; SD = Standard Deviation; Code = MATLAB training algorithm function name.

V.9.3 Predictive accuracy and residual analysis

The generalization capability and predictive accuracy of the trained ANN were assessed by comparing predicted values against experimental data. Scatter plots for equilibrium adsorption capacity (**Figure V.12**(**c**)) and removal percentage (**Figure V.12**(**d**)) exhibit a tight distribution along the 1:1 reference line. Residual analysis was performed to validate the model's precision. **Figure V.13**(**a**) and **Figure V.13**(**b**) depict the residuals versus predicted values and the residual probability distribution for adsorption capacity, respectively. Similarly, **Figure V.13**(**c**) and **Figure V.13**(**d**) illustrate the corresponding plots for removal percentage. The residuals are randomly distributed around zero without discernible geometric patterns, and the probability histograms confirm a near-normal distribution of errors. This validates the absence of systemic bias in the model's predictive capabilities.

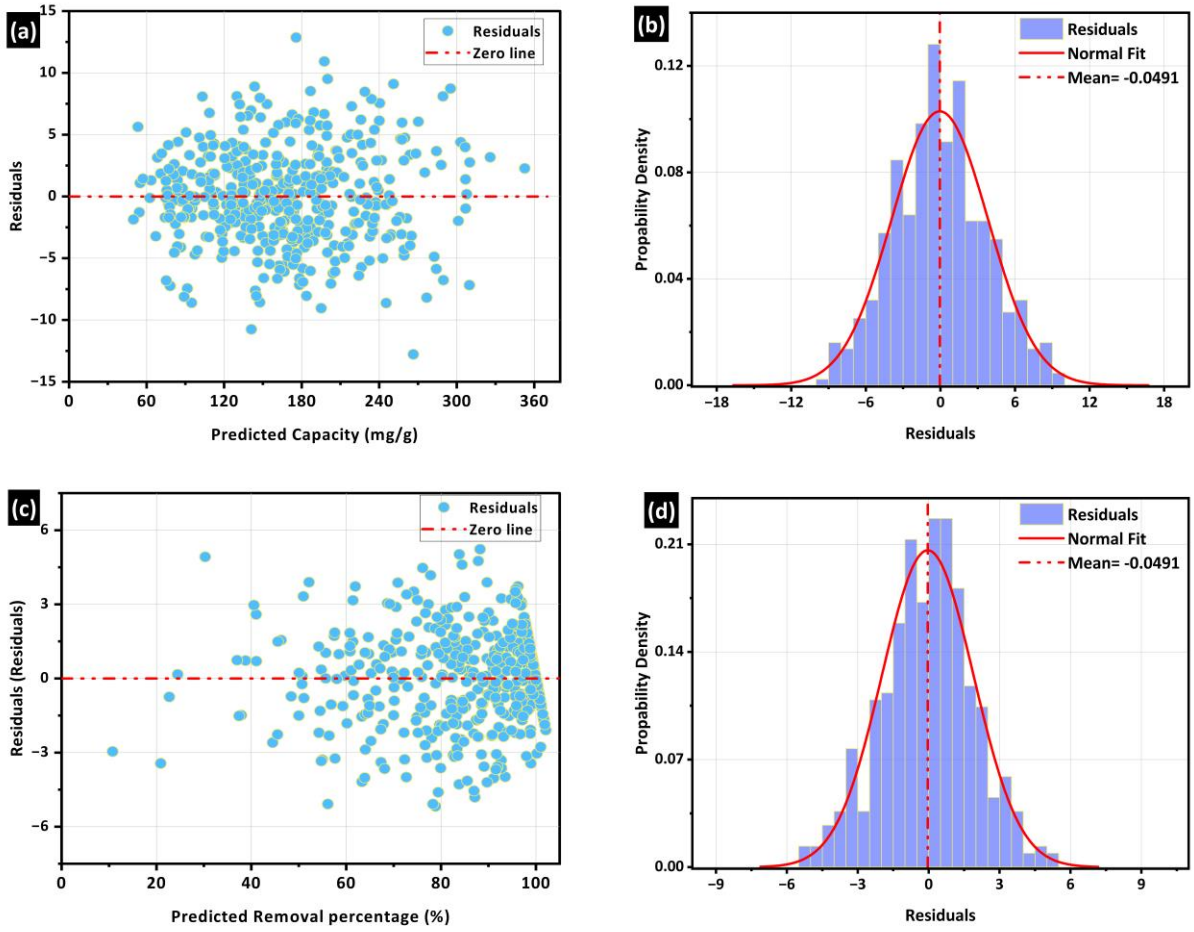

Figure V.13 Residual analysis of the optimized ensemble model for MO adsorption: (**a**) residuals versus predicted values and (**b**) residual probability distribution for adsorption capacity; (**c**) residuals versus predicted values and (**d**) residual probability distribution for removal percentage

V.9.4 Cross-validation and model robustness

K-fold cross-validation was implemented to ensure model robustness and prevent overfitting on the training dataset. **Figure V.14** presents the fold-by-fold validation metrics. These charts confirm highly consistent performance across all evaluated folds, demonstrated by stable R^2 values for both adsorption capacity (**Figure V.14(a)**) and removal percentage (**Figure V.14(b)**). Furthermore, the MSE for adsorption capacity (**Figure V.14(c)**) and removal percentage (**Figure V.14(d)**) remained consistently low across folds, substantiating the network's high reliability and robust predictive power on unseen data.

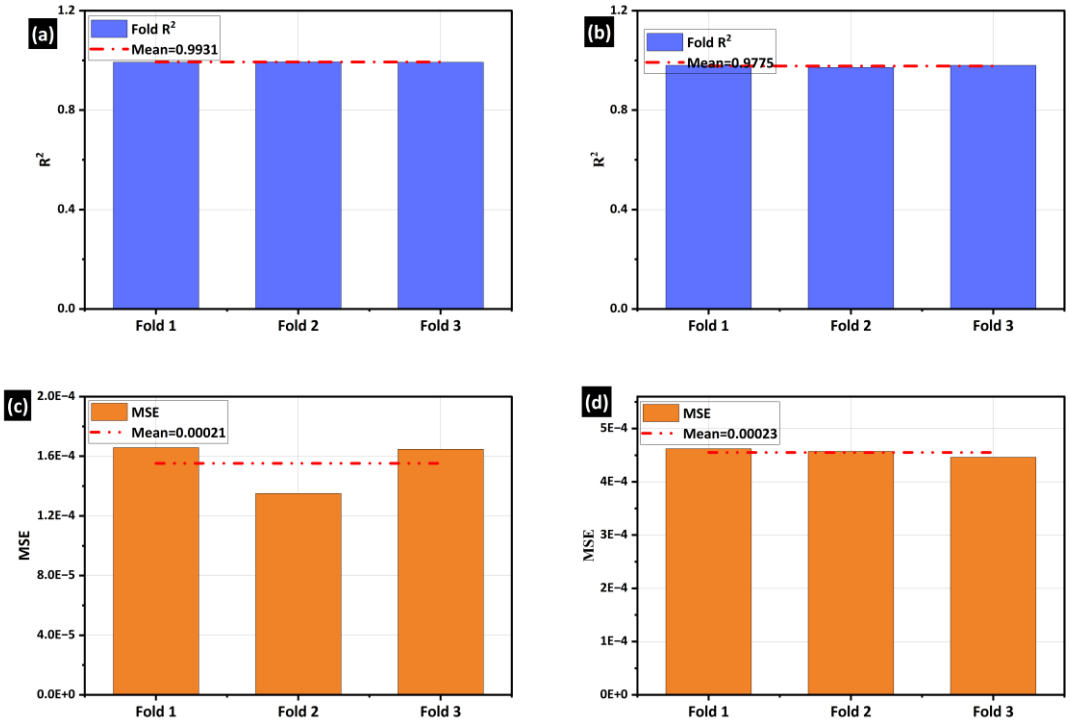

Figure V.14 Cross-validation performance charts detailing the fold-by-fold validation metrics for MO adsorption: (**a**) R^2 for adsorption capacity, (**b**) R^2 for removal percentage, (**c**) mean squared error (MSE) for adsorption capacity, and (**d**) MSE for removal percentage

V.9.5 Mechanistic insights via sensitivity analysis

A comprehensive performance evaluation of the optimized configuration further verified the integrity of the predictive framework. **Figure V.15(a)** displays the MSE convergence versus epoch during the

training, validation, and testing phases. The validation and test errors plateaued simultaneously, mitigating concerns about early overfitting. This stability is supported by excellent agreement in the regression plots for the data subsets (**Figure V.15(b)**) and a highly centralized error histogram across all data partitions (**Figure V.15(c)**).

Finally, to connect empirical black-box modeling with physical chemical phenomena, a mechanistic sensitivity analysis was conducted using the Garson algorithm to evaluate the relative importance of independent input variables (**Figure V.15(d)**). By partitioning the neural network connection weights, this analysis quantifies the proportional impact of operational parameters on adsorption capacity and removal efficiency. These computational findings offer critical insights into the rate-limiting steps and driving forces governing the MO adsorption mechanism onto the ZnO@DPs-AC surface.

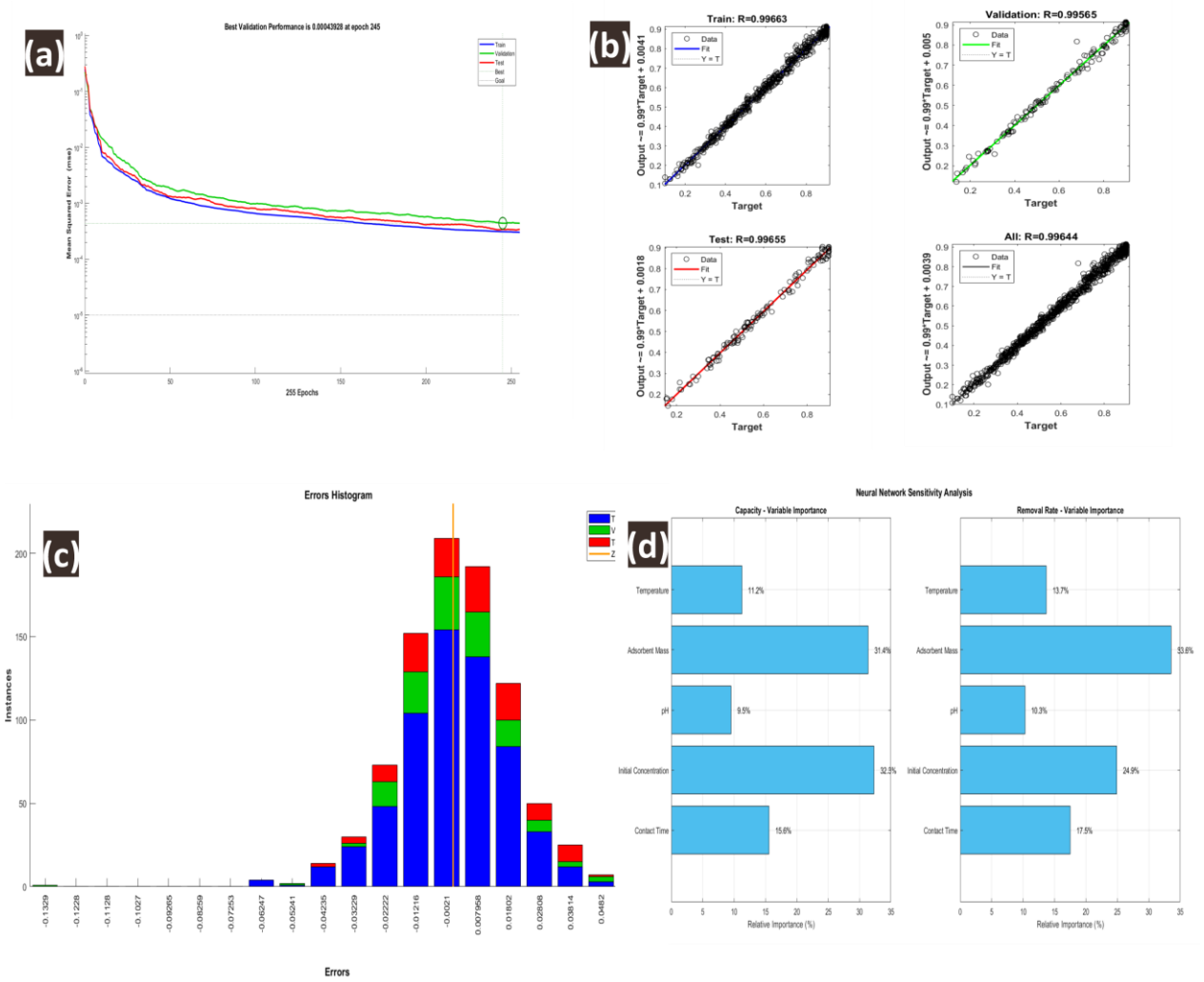

Figure V.15 Comprehensive performance evaluation of the optimized ANN configuration: (**a**) MSE

convergence versus epoch during the training, validation, and testing phases; (**b**) regression plots for data subsets; (**c**) error histogram across all data partitions; and (**d**) mechanistic sensitivity analysis via the Garson algorithm evaluating the relative importance of independent input variables

V.10 Optimization of methyl orange adsorption via genetic algorithm

This section employs a multi-objective GA to optimize the operational parameters governing the batch adsorption of MO onto the synthesized ZnO@DPS-AC composite. The computational optimization strategically addresses two inherently conflicting objectives: maximizing specific adsorption capacity and maximizing overall treatment system removal efficiency.

V.10.1 Optimization framework and parameter selection for MO

The computational efficacy of evolutionary algorithms depends heavily on precise hyperparameter tuning to balance global spatial exploration with local exploitation. To establish a rigorous mathematical framework, an exhaustive grid search evaluated 27 distinct combinations of population sizes, crossover rates, and mutation rates. The performance of each configuration was quantified and ranked using an overall composite score. This evaluation ensured that only the most efficient evolutionary parameters were deployed for the primary optimization runs. **Figure V.16** details these outcomes. Specifically, **Figure V.16**(**a**) presents hypervolume heatmaps illustrating the variance across the tested hyperparameters, while **Figure V.16**(**b**) ranks the configurations based on their composite scores.

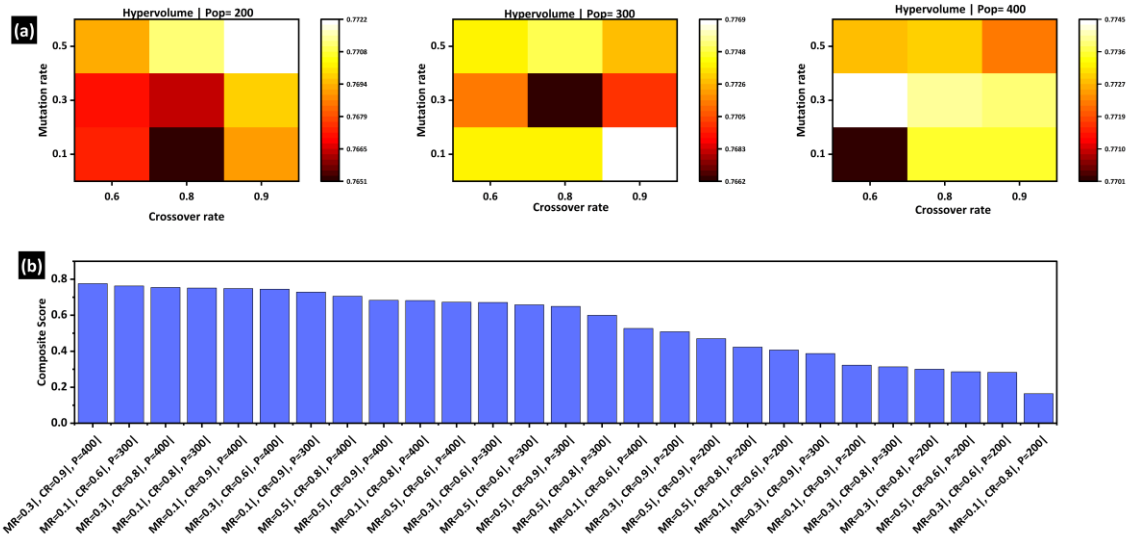

Figure V.16 Comprehensive evaluation of Genetic Algorithm (GA) grid search parameters for MO adsorption: (**a**) hypervolume heatmaps across varying population sizes, crossover rates, and mutation rates, and (**b**) ranking of the 27 evaluated configurations based on their overall composite scores

V.10.2 Convergence and optimization dynamics of the MO system

The evolutionary trajectory of the GA demonstrates its ability to efficiently map the multi-objective solution space of MO adsorption. As illustrated in **Figure V.17**(**a**), the algorithm yielded consistent improvements in both the best and average values for adsorption capacity and removal efficiency over successive generations. Convergence was confirmed by the rapid ascent and subsequent plateau of the hypervolume metric (**Figure V.17**(**b**)), indicating that the computational model successfully identified the global optimal boundaries.

Furthermore, the algorithm maintained high population diversity throughout the evolutionary process (**Figure V.17**(**d**)). This characteristic prevented premature convergence, enabling an exhaustive exploration of the physical boundary conditions governing the adsorption system. Secondary statistical indicators, including the generational expansion of the Pareto front size (**Figure V.18**(**a**)), periodic generation-to-generation improvements (**Figure V.18**(**b**)), spacing uniformity (**Figure V.18**(**c**)), and solution spread (**Figure V.18**(**d**)), further substantiate the mathematical robustness of the model. Together, these progression metrics verify the attainment of global optimization and the reliability of the derived trade-off configurations.

V.10.3 Pareto front analysis for the MO adsorption

Building upon the established convergence dynamics, the genetic algorithm resolved the true Pareto-optimal front for the MO adsorption system. Quantitative analysis of these frontier metrics provides critical insight into the quality and uniformity of the discovered optimal solutions. As depicted in **Figure V.17**(**c**), the final boundary explicitly maps the continuum of non-dominated solutions, mathematically illustrating the fundamental trade-offs between specific capacity and removal efficiency. This defined solution space serves as the requisite foundation for extracting targeted operational parameters.

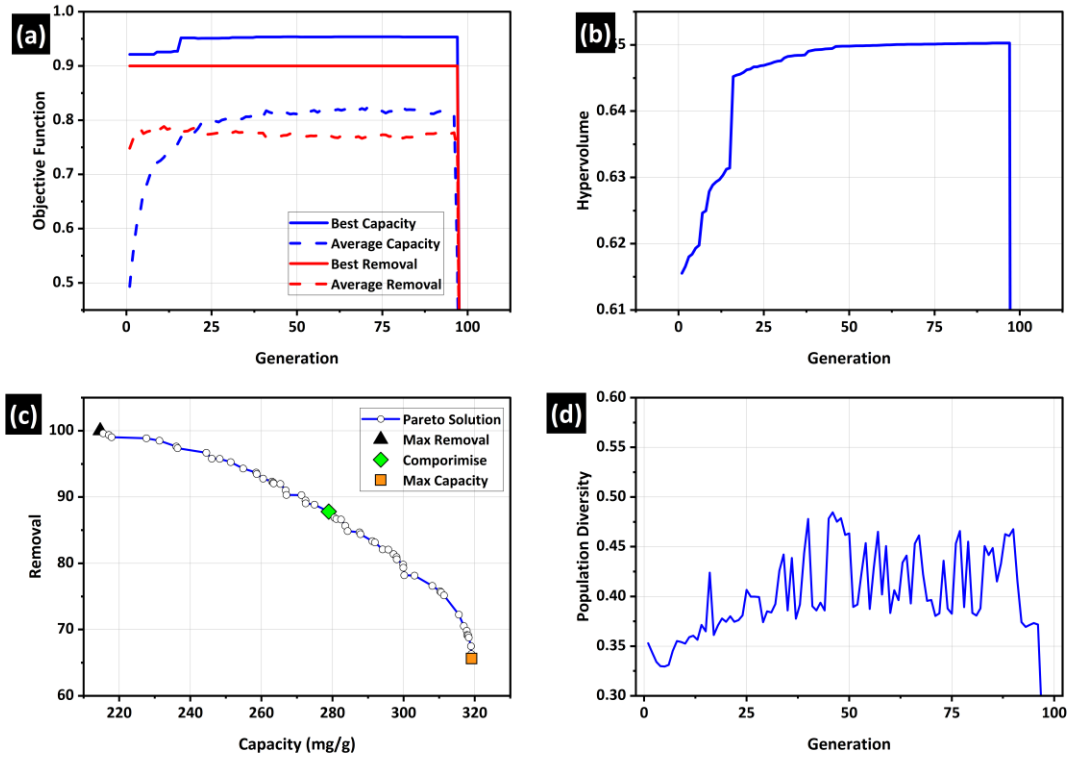

Figure V.17 Evolutionary dynamics of the multi-objective optimization for MO adsorption: (**a**) progression of the best and average values for adsorption capacity and removal efficiency, (**b**) hypervolume progression, (**c**) final Pareto front highlighting representative optimal solutions, and (**d**) population diversity across generations

V.10.4 Optimal adsorption conditions for MO adsorption

Three representative optimal solutions were extracted from the finalized Pareto front to guide practical engineering applications: maximizing adsorption capacity (Max q_e), maximizing removal efficiency (Max R), and establishing a mathematically balanced compromise. The specific operational configurations required to achieve these targets (contact time (t), initial concentration (C_0), pH, adsorbent mass (m), and temperature (T)) are detailed in **Table V.11**.

Maximum Capacity: Achieving a specific adsorption capacity of 319.10 mg/g requires a high initial MO concentration (387.36 mg/L) and a significantly reduced adsorbent mass (38.37 mg) at an elevated temperature (45.00 °C). However, operating under these mass-transfer-driven conditions inherently constrains the overall removal efficiency to 65.62%.

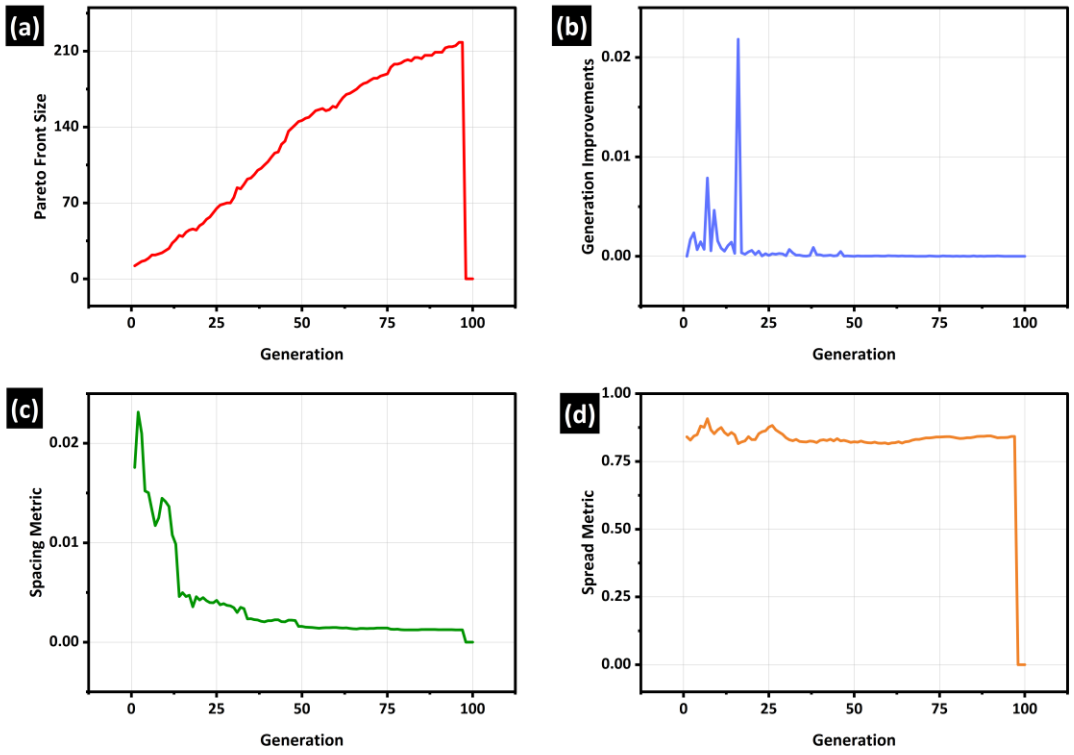

Figure V.18 Progression of key multi-objective optimization metrics over generations during MO adsorption: (**a**) Pareto front size, (**b**) generation-to-generation improvements, (**c**) spacing metric, and (**d**) spread metric

Maximum Removal: Conversely, achieving a 100% removal rate necessitates a comparatively high adsorbent dosage of 78.24 mg and an initial concentration of 335.88 mg/L. While this surplus of active sites ensures total pollutant sequestration, it proportionately reduces the specific unit capacity to 214.65 mg/g due to partial site unsaturation.

Compromise Solution: To align material efficiency with stringent effluent quality standards, the compromise formulation identifies a pragmatic operational midpoint. Using an intermediate adsorbent dosage of 61.09 mg and an initial concentration of 368.10 mg/L, this configuration yields an 87.80% removal rate and a robust capacity of 278.90 mg/g.

Table V.11 Optimal batch adsorption conditions derived from the Genetic Algorithm for three representative Pareto solutions for MO: maximum capacity, maximum removal rate, and the compromise solution

Solution Type	q_e (mg/g)	R (%)	t (min)	C_0 (mg/L)	*pH*	m (mg)	T(°C)
Max q_e	319.10	65.62	240.00	387.36	8.00	38.37	45.00
Max R	214.65	100	238.54	335.88	6.56	78.24	36.13
Compromise	278.90	87.80	240.00	368.10	7.04	61.09	42.29

V.10.5 Experimental validation

Empirical validation is required to confirm the predictive accuracy and physical validity of the computational model. Therefore, laboratory batch experiments mirroring the established compromise conditions were conducted. This procedure directly correlates the theoretical predictions derived from the genetic algorithm with the macroscopic adsorption behavior of the targeted pollutant. Under these specified parameters, the empirical results yielded an equilibrium adsorption capacity of 249.91 mg/g and a simultaneous removal efficiency of 84.05%. When compared with the theoretical predictions of the compromise solution (q_e = 278.90 mg/g and R = 87.80%), the relative errors were approximately 10.4% for capacity and 4.3% for removal percentage. These minor deviations fall strictly within the acceptable statistical margin of experimental and instrumental error. This high degree of concordance confirms the validity, robustness, and reproducibility of the multi-objective Genetic Algorithm for accurately mapping the complex design space and establishing reliable operational trade-offs for industrial methyl orange remediation.

V.11 Mechanistic insights into methyl orange adsorption

The adsorption of MO by the ZnO@DPS–AC composite is driven by a complex interplay between the material's structural architecture and surface chemistry. As established during physical characterization (**section IV.5.1**), the adsorbent exhibits a hierarchical, honeycomb-like micro- and mesoporous morphology (**Figure IV.3(b)**). This semi-graphitic framework yields an extensive S_{BET} of 1028.63 m^2/g (**section IV.9.2**, **Table IV.3**). Concurrently, the material retains a high ash content of 65.33% (**section IV.3.1**, **Table IV.1**), which quantitatively confirms the dense, uniform integration of ZnO nanoparticles throughout the carbon matrix.

Chemical evaluation further details a surface rich in oxygen-containing functional groups (predominantly hydroxyls) alongside embedded Zn–O active centers (**Figure IV.4**). Additionally, the

composite presents a pH_{pzc} of 6.67 (**section IV.4**, **Figure IV.2**). Together, these physical and chemical traits facilitate the high-affinity binding of anionic pollutants such as MO. Drawing upon empirical batch data, thermodynamic modeling, and spectroscopic analyses, the primary mechanisms governing this adsorption process are outlined below and comprehensively illustrated in **Figure V.19**.

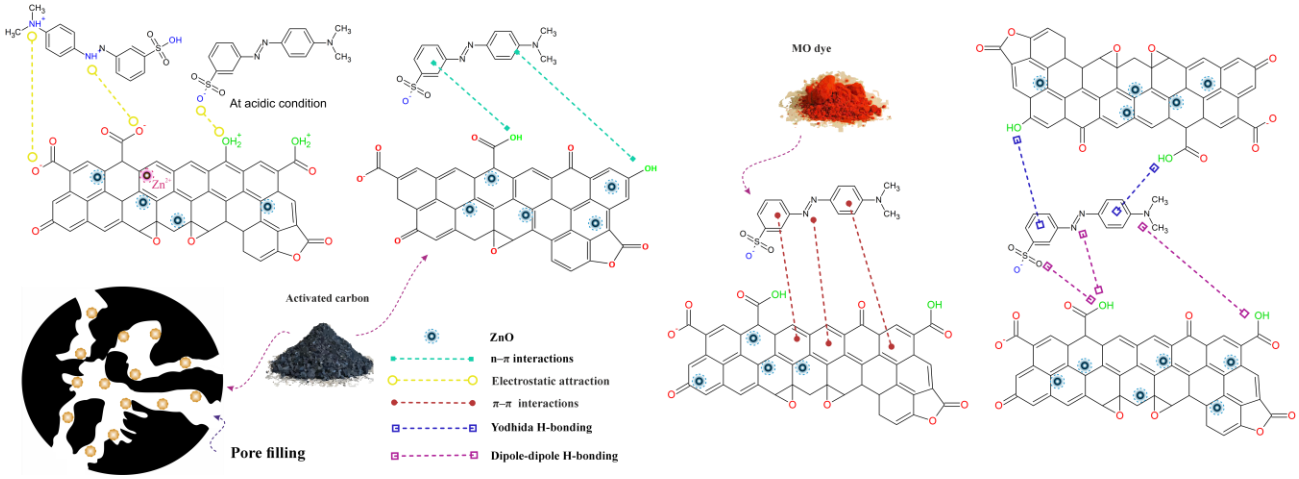

Figure V.19 Schematic illustration of the proposed physicochemical mechanisms for the adsorption of methyl orange onto the hierarchical ZnO@DPS-AC composite

V.11.1 Electrostatic interactions

The *pH*-dependent electrostatic attraction provides a primary driving force for MO adsorption. As previously established, the pH_{pzc} of the ZnO@DPS–AC composite is 6.67 (**section IV.2.4**). Because the *pKa* of MO is 3.46, the dye exists predominantly as the active anion (MO^-) in solutions above this pH. Consequently, the system yields the maximum equilibrium adsorption capacity in highly acidic media (*pH* 2.0-6.0). As established in **section V.2.2**, electrostatic attraction between the anionic sulfonate groups of MO and the protonated composite surface (below pH_{pzc} = 6.67) provides a necessary driving force for MO adsorption. However, variations in ionic strength produce statistically insignificant changes in the equilibrium capacity (**Figure V.1(d)**). This insensitivity implies that while electrostatic attraction facilitates initial binding, it does not strictly dominate the overall adsorption mechanism. Sayed et al. (2024) documented similar electrostatic phenomena for MO adsorption onto wood sawdust-derived ZnO@AC composites. As depicted in **Figure V.19**, this electrostatic attraction serves as a primary bridging force between the dye's anionic sulfonate groups and the protonated surface sites.

V.11.2 Hydrogen bonding

FTIR spectroscopy provides rigorous physical evidence for hydrogen bonding (**section IV.6.3**). Following the adsorption of MO, the broad hydroxyl (–OH) stretching band spanning 3000 to 3500 cm^{-1} on the ZnO@DPS–AC surface was nearly disappeared (**Figure IV.4**). This severe attenuation confirms that surface hydroxyl groups act as primary hydrogen bond donors, interacting robustly with the hydrogen bond acceptors (specifically the nitrogen, oxygen, and sulfur heteroatoms) inherent to the MO molecule. This system likely involves two distinct hydrogen-bonding modalities (Tran et al., 2020). The first is classical dipole-dipole H–bonding between the composite's hydroxyl groups and the oxygen and nitrogen atoms of the dye, a dynamic similarly reported for modified clays (Abbou et al., 2023) and biochar (Tcheka et al., 2024). The second modality is Yoshida H–bonding, characterized by the specific interaction between surface -OH groups and the extensive π–electron system of the MO aromatic rings. This mechanism was also reported by Sayed et al. (2024) for the adsorption of MO onto ZnO@AC composite derived from wood sawdust. This dual-modality hydrogen bonding—involving both classical dipole-dipole interactions and Yoshida H-bonding—is visually summarized in **Figure V.19**.

V.11.3 Physical pore filling

Nitrogen physisorption analyses conducted before and after MO uptake substantiate a prominent pore-filling mechanism (**section IV.9.3**). Following equilibrium adsorption, the specific surface area of the composite precipitously declines from 1028.63 m^2/g to 843.60 m^2/g(**Table IV.3**). Concurrently, the measurable micropore volume undergoes a strict reduction from 0.159 cm^3/g to 0.065 cm^3/g (**section IV.9**, **Figure IV.7**, **Figure IV.8**). This structural attenuation provides direct physical evidence that MO molecules diffuse deeply into the hierarchical carbon network and physically pack into the available mesoporous and microporous cavities. This physical entrapment aligns with the size-exclusion and intra–particle diffusion behaviors reported by Xin Zhang et al. (2023) for mesoporous silica nanoparticles.

V.11.4 π–π stacking interactions

As illustrated by the parallel molecular alignments in **Figure V.19**, strong non-covalent attractions arise between the π–electron system of the graphitic ZnO@DPS-AC framework and the aromatic rings or azo linkages (–N=N–) of the MO molecule (Tcheka et al., 2024). Spectroscopic analysis

corroborates this phenomenon, as evidenced by a reduction in the intensity of the aromatic C=C vibrational peak at 1593 cm^{-1} following equilibrium adsorption. To empirically validate this mechanism, the composite was subjected to controlled H_2O_2 oxidation (protocol detailed in **section III.5.4**) to reduce π-electron density and isolate the π-π interaction contribution. Consequently, the equilibrium adsorption capacity of the oxidized composite decreased significantly relative to the pristine material (**Figure V.20**). This measurable reduction formally confirms that π–π stacking contributes substantially to the overall adsorption process.

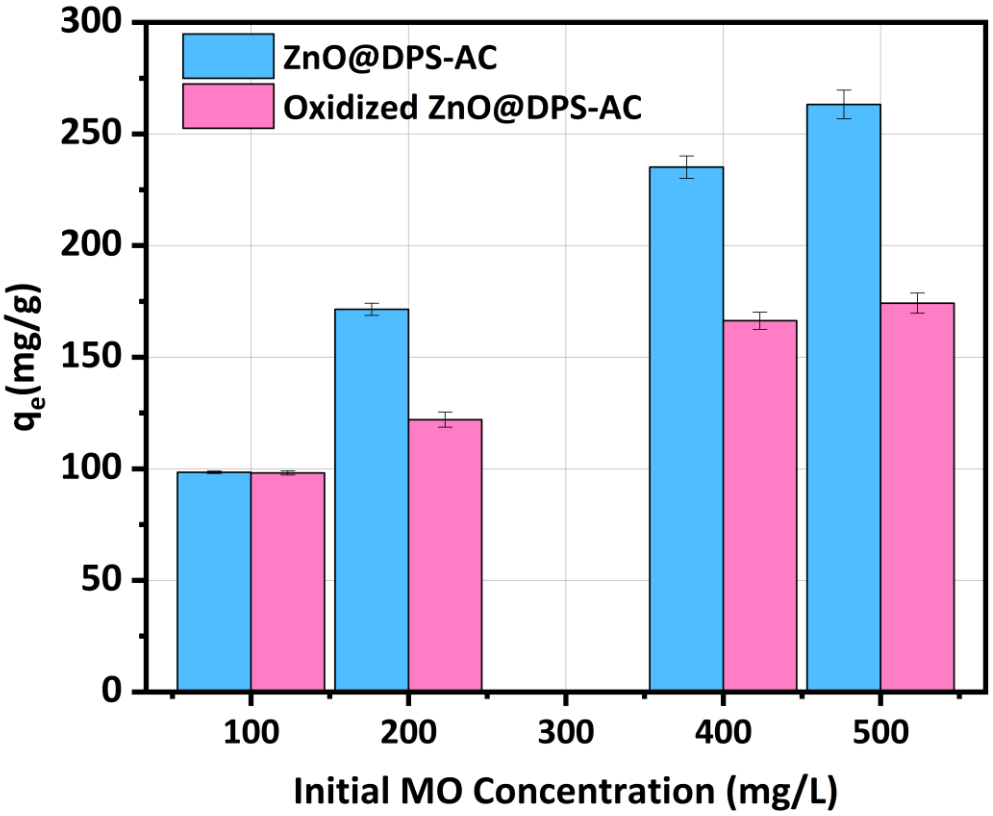

Figure V.20 Performance comparison between standard ZnO@DPS-AC and oxidized ZnO@DPS-AC for MO removal

V.11.5 Chemisorption and Surface Complexation

Both thermodynamic and spectroscopic evaluations rigorously establish the occurrence of surface complexation. As detailed in **section V.6**, the standard enthalpy changes ($\Delta H°$) derived from the Langmuir and Sips models strictly exceed 40 kJ/mol (**Table V.4**). Validated through non-linear van't

Hoff regression (**Figure V.3**), these thermodynamic parameters physically characterize the endothermic adsorption process as strong chemisorption. Spectroscopic analysis corroborates this thermodynamic classification. Following equilibrium adsorption, pronounced intensity fluctuations emerged in the 500 to 400 cm^{-1} FTIR fingerprint region, which corresponds directly to Zn–O vibrational modes (**Figure IV.4**). These spectral alterations provide physical evidence of direct metal-ligand coordination between the anionic sulfonate groups of the MO molecules and the embedded ZnO active centers. This chemical complexation aligns with the binding mechanisms outlined by Ahlawat et al. (2023), who established that direct covalent bonding between dye functional groups and metal-oxide centers yields highly stable, monolayer chemisorption.

V.11.6 n–π Interactions

Finally, n–π interactions are hypothesized to facilitate the overall adsorption, albeit to a lesser extent than primary hydrogen bonding. Spectroscopic evidence validates this secondary contribution; specifically, the attenuation of the C–O and C=O vibrational peaks post-adsorption is noticeably weaker than the near-elimination of the –OH band observed previously (**Figure IV.4**). Within this chemical dynamic, electron-rich heteroatoms on the ZnO@DPS–AC surface (such as carbonyl oxygens) function as n-electron donors. These surface sites interact directly with the electron-accepting π–electron system of the MO aromatic rings (Sayed et al., 2024; Tran et al., 2020). This specific interaction profile correlates with empirical findings reported for surfactant-modified clays (Abbou et al., 2023) and analogous zinc-doped activated carbons (Sayed et al., 2024). These n-π electron donor-acceptor exchanges are highlighted in **Figure V.19**, functioning alongside the primary chemical and electrostatic pathways to secure the dye molecule.

V.12 Conclusion

This chapter established the ZnO@DPS-AC composite as a highly effective, computationally optimized adsorbent for the remediation of MO. Empirical investigations demonstrated the material's robust performance across a diverse range of operational conditions. While the highest adsorption efficiency occurred at pH 2.0 (q_e = 199.6 mg/g), the composite maintained exceptional uptake at near-neutral pH 6.0. This resilience under milder conditions mitigates the environmental hazards and operational costs associated with extreme acidification. Furthermore, the system retained high capacity under hypersaline conditions. This stability indicates that MO adsorption is primarily

governed by non-electrostatic interactions, such as pore-filling and π-π stacking, facilitated by the hierarchical semi-graphitic architecture of the DPS precursor.

Kinetic and thermodynamic analyses further elucidated these macroscopic observations. The superior fit of the Avrami model ($R^2 \geq 0.995$) confirmed a multi-stage, evolving surface mechanism. Thermodynamic parameters ($\Delta G° < 0$, $\Delta H° \approx$ 77-83 kJ/mol, $\Delta S° > 0$) verified that the process is favorable, endothermic, and chemically driven. A temperature-dependent transition from heterogeneous Freundlich adsorption at 20 °C to Langmuir monolayer coverage at elevated temperatures yielded an equilibrium capacity of 226.81 mg/g. This performance significantly exceeds that of analogous ZnO-carbonaceous composites operating under comparable near-neutral conditions.

Multivariate optimization revealed the complex interdependencies of the adsorption system. While pH drove adsorption in univariate studies, initial concentration and adsorbent dosage dominated within the RSM design space. The RSM-BBD framework generated highly predictive quadratic models and identified a multi-objective optimum (q_e = 241.47 mg/g, R = 99.03%). However, the inherent limitation of gradient-based convergence toward local optima necessitated the deployment of an ANN coupled with a genetic algorithm (ANN-GA). By exploring the full non-linear parameter space, the ANN-GA resolved a true Pareto-optimal front and yielded a superior compromise solution (q_e = 278.90 mg/g, R = 87.80%). This substantial increase in validated capacity provides direct evidence that advanced machine learning frameworks are essential for optimizing complex adsorption systems.

The exceptional efficiency of the composite stems from the synergistic cooperation of five distinct physicochemical pathways: electrostatic attraction, dual-modality hydrogen bonding, physical pore-filling, π-π stacking, and surface complexation at embedded ZnO active centers. Cyclic stability studies confirmed the material's industrial viability, demonstrating 71-77% efficiency recovery following NaOH regeneration. A progressive decline in regeneration efficiency across cycles, likely due to irreversible pore blockage by dye aggregates, suggests that continuous-flow systems may behave differently from batch reactors. This specific limitation directly motivates the dynamic column investigations presented in **Chapter VIII**. Furthermore, this reduction could result from strong chemical bonds between the dye and the adsorbent.

Ultimately, these findings validate the valorization of DPS waste into a competitive, green adsorbent capable of treating concentrated dye effluents. Having established the operational, mechanistic, and

computational profile of the composite for a large ionizable dye, it is necessary to assess its versatility against a fundamentally different contaminant class. **Chapter VI** will evaluate the composite's performance against Catechol, a small, neutral, non-ionic phenolic compound. Because electrostatic attraction is absent in Catechol adsorption, the pore-filling and π-π mechanisms must operate without ionic driving forces. This shift represents a rigorous test of the material's underlying architecture and provides broader validation of its multi-class remediation potential.

Chapter VI: Batch Adsorption of Catechol onto ZnO@DPS-AC: Modeling, Optimization, and Mechanisms

* * * * *

VI.1 Introduction

The comprehensive characterization of the synthesized ZnO@DPS-AC composite requires evaluating its adsorptive versatility across structurally distinct chemical classes. While **Chapter V** established the optimal parameters and mechanisms for sequestering MO, this chapter transitions to the remediation of CAT, a highly reactive, low-molecular-weight phenolic intermediate. Evaluating CAT at this juncture is strictly necessary to determine how the engineered hierarchical carbon matrix and embedded zinc oxide active sites interact with smaller, hydroxyl-rich organic structures that rely on fundamentally different binding affinities.

To rigorously assess the adsorptive performance for CAT, this chapter systematically investigates the influence of primary operational parameters, including adsorbent dosage, initial solution *pH*, ionic strength, contact time, and initial pollutant concentration. The progression follows the established analytical framework. Initial empirical evaluations examine solid-liquid interface dynamics through kinetic and equilibrium isotherm modeling, followed by a robust thermodynamic analysis to ascertain the energetic nature of the interaction. Subsequently, the structural stability and practical reusability of the composite are tested through multiple desorption and regeneration cycles. Transitioning to advanced computational modeling, the chapter optimizes the multivariable adsorption process by comparing the response surface topologies generated via RSM methodology with the high-fidelity predictive capabilities of ANN integrated with GA. Finally, utilizing the derived empirical and statistical data, the chapter elucidates the precise physicochemical mechanisms (specifically pore-filling, hydrogen bonding, inner-sphere surface complexation, and π-π electron-donor-acceptor interactions) governing the sequestration of CAT onto the composite interface.

VI.2 Effect of operational parameters

VI.2.1 Effect of adsorbent dosage

The influence of adsorbent dosage on CAT removal was evaluated over the range of 15 to 75 mg, with the results depicted in **Figure VI.1(a)**. Throughout the tested range, R (%) and q_e (mg/g)

exhibited a clear reciprocal relationship. Specifically, the R (%) surged from 37.52% at a 15 mg dose to complete removal (100%) at a 75 mg dose of the ZnO@DPS–AC composite. Concurrently, the q_e values steadily declined as the adsorbent mass increased.

This observed phenomenon aligns strongly with recent literature on phenolic adsorption. Kamarehie et al. (2024) reported a substantial increase in CAT removal efficiency when the aluminum–coated activated carbon dosage was increased from 50 to 250 mg. Similarly, Vunain et al. (2018) documented a significant increase in CAT removal using sunflower seed hull-activated carbon as the dosage increased from 100 to 1200 mg. The inverse relationship between R and q_e was also validated by Mofrad et al. (2025), who found that while CAT removal increased to 77% at higher doses of magnetized pomegranate peel carbon, qe decreased concurrently.

From a physicochemical perspective, the progressive enhancement in R at higher dosages stems directly from the expanded total available surface area. As the mass of the ZnO@DPS–AC composite increases, the abundance of active binding sites and surface functional groups (such as the hydroxyl and carboxyl groups typical of activated carbons) scales proportionally (Vunain et al., 2018). This proliferation of sites increases the likelihood that CAT molecules will interact with the adsorbent surface via mechanisms such as π–π dispersion and Hydrogen bonding.

As previously established for MO in **section V.2.1**, the inverse relationship between adsorbent dosage and specific capacity is governed by site unsaturation and the split in mass flux phenomenon. This physical overlap of active sites effectively shields a portion of the reactive surface, thereby diminishing the available surface area for complexation (Vunain et al., 2018).

Notably, achieving 100% of R with a relatively modest dose of 75 mg indicates that the ZnO@DPS–AC composite features an exceptionally high density of reactive sites compared to conventional materials. For context, Kamarehie et al. (2024) required a substantially larger dose of 250 mg to achieve a comparable efficiency of 99.97%. This stark contrast demonstrates that impregnating ZnO nanoparticles onto the DPS–derived activated carbon matrix effectively amplifies surface reactivity. This enhanced performance is likely facilitated by the formation of strong inner–sphere complexes, in which CAT acts as a bridging ligand between the metallic centres.

Figure VI.1 (**a**) Effect of adsorbent dosage on CAT adsorption capacity and removal percentage, (**b**) Distribution of CAT protonation states as a function of solution pH, (**c**) UV-Vis absorption spectra of the CAT solution recorded at varying *pH* values (*pH* 2–12), and (**d**) Effect of initial solution pH on the adsorption efficiency of CAT onto the ZnO@DPS-AC composite

VI.2.2 Effect of initial solution pH

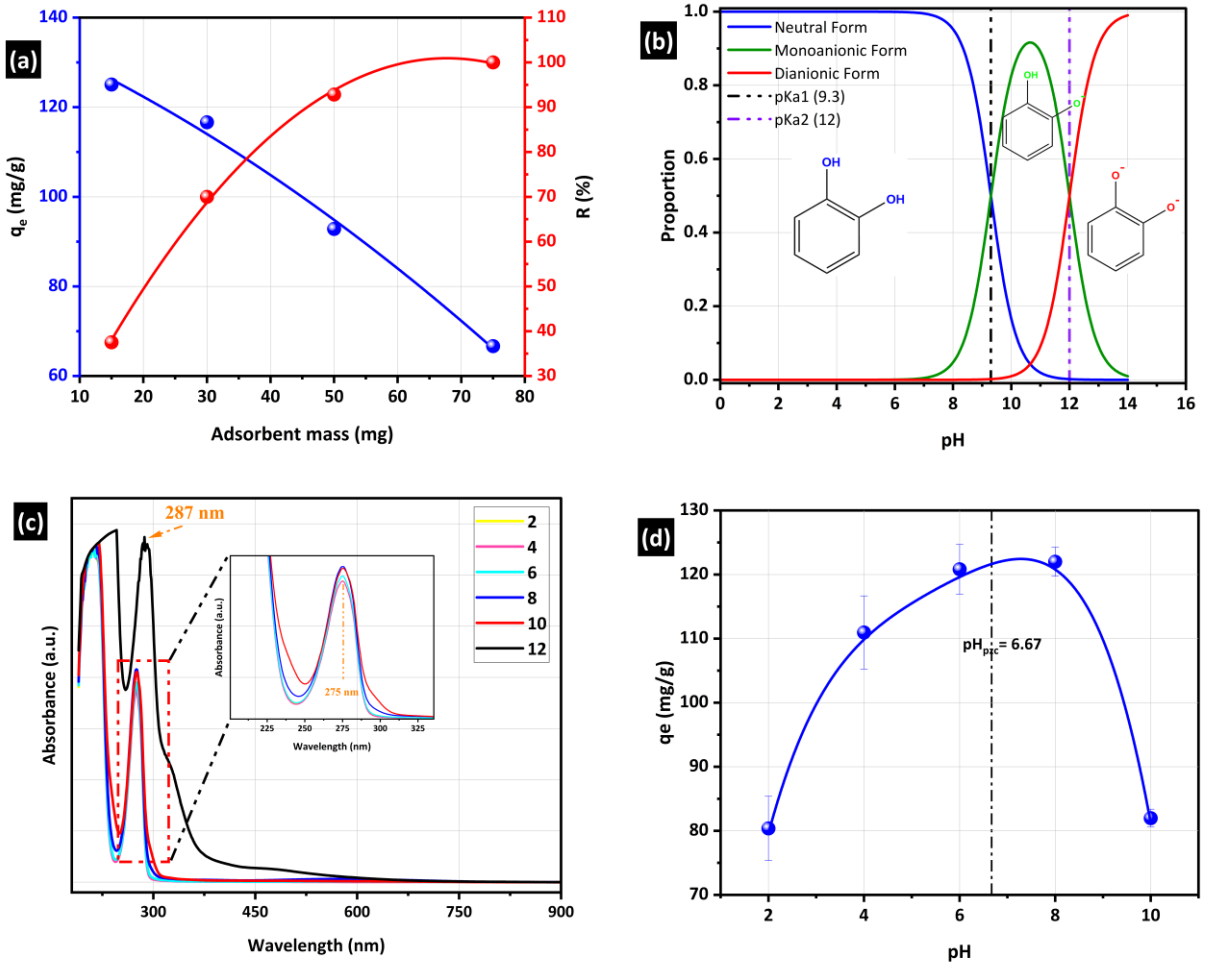

VI.2.2.1 CAT speciation and ionization characteristics

The adsorption behavior of CAT is intrinsically linked to its speciation, which is strictly governed by the solution *pH*. CAT functions as a Brønsted–Lowry diacid, capable of losing two protons at specific *pKa* values, typically reported as 9.3-9.48 (pKa_1) and 12-13 (pKa_2) (Gulley-Stahl et al., 2010; Kamarehie et al., 2024; Moreno-Piraján et al., 2012). Therefore, it exists as neutral forms at low *pH*, shifting to monoanionic and dianionic species with increasing *pH*, as illustrated in **Figure VI.1**(**b**). Experimental observations confirmed that below pKa_1, the adsorbate exists predominantly in its neutral molecular form (H_2CAT). As the *pH* approaches pKa_1, the formation of the

catecholate monoanion ($HCAT^-$) becomes significant (Finkelstein-Shapiro et al., 2016; Yang et al., 2012). This transition was visually supported by color changes in the solution and quantitatively confirmed by a distinct bathochromic shift in the UV–Vis spectra, with the maximum absorption wavelength (λmax) shifting from 275 nm to 287 nm at *pH* 12 (**Figure VI.1(c)**). This spectroscopic shift aligns with the findings of Kamarehie et al. (2024) and Abugazleh et al. (2020), who reported that deprotonation alters the aromatic ring's electronic structure, leading to increased peak intensity and a shift in the absorption maximum.

VI.2.2.2 Influence of *pH* on CAT adsorption

The influence of the initial *pH* on CAT removal by the ZnO@DPS–AC composite was evaluated over a pH range of 2-10 (Figure (**d**)). The q_e increased sharply from 76.83 mg/g at *pH* 2 to 110.95 mg/g at *pH* 4. This was followed by a progressive increase to a maximum of 122 mg/g at *pH* 8, after which it declined significantly to 81.9 mg/g at *pH* 10. Optimal adsorption occurred near the pH_{pzc} of the composite, which was determined to be 6.67 (**section IV.4**).

This behavior is well documented in the literature. Shen et al. (2019) similarly reported that maximum CAT adsorption on metal oxides occurs near the pH_{pzc} of the respective oxide, followed by a decrease as the alkalinity increases. Mofrad et al. (2025) observed an optimal pH range of 6 to 8 for CAT removal using magnetized activated pomegranate peel carbon, which closely aligns with the performance of the ZnO@DPS–AC composite. Additionally, Vunain et al. (2018) reported a peak CAT removal at *pH* 9 using sunflower seed hull-activated carbon, demonstrating a similar trend.

VI.2.2.3 Physicochemical mechanisms and surface interactions

The restricted q_e observed under highly acidic conditions (*pH* 2 to 4) is driven by competition between hydronium ions (H^+) and adsorbate molecules for active binding sites. At low *pH*, the surface of the ZnO@DPS–AC composite is heavily protonated, carrying a net positive charge ($pH < pH_{pzc}$), while CAT exists entirely in its neutral molecular form. As noted by Samiey and Toosi (2010), an excess of hydronium ions effectively blocks access to surface functional groups, thereby limiting pollutant uptake.

The optimal uptake observed at *pH* 8 results from a synergistic combination of π–π dispersion forces and dipole–dipole interactions. At near–neutral *pH*, the surface charge density of the

composite is minimized. This allows neutral CAT molecules to approach the surface without significant electrostatic hindrance. Vunain et al. (2018) attributed similar high removal rates to the prevalence of π–π and dipole–dipole interactions between the aromatic network of the carbon matrix and the phenylene ring of CAT. Furthermore, Hsu et al. (2025) suggested that at *pH* values below the *pKa* of phenolic contaminants, adsorption is primarily governed by hydrogen bonding and π–π stacking between the solute's hydroxyl groups and the composite's oxygen–containing functional groups, rather than electrostatic attraction.

Conversely, the sharp decline in *R* at *pH* values exceeding 8 is a direct consequence of electrostatic repulsion (Hsu et al., 2025). As the alkalinity increases toward *pH* 10, the surface of the ZnO@DPS–AC composite becomes increasingly electronegative ($pH > pH_{pzc}$). Simultaneously, a significant fraction of the CAT molecules deprotonates into negatively charged catecholate monoanions. Wu et al. (2024) and Ngwabebhoh and Yildiz (2019) documented that this concurrent increase in negative charge density on both the adsorbent surface and the solute generates strong electrostatic repulsive forces. This repulsion drastically reduces the effective collision frequency between the phases, thereby diminishing q_e.

A minor deviation is noted when comparing these results to the findings of Vunain et al. (2018), who achieved maximum CAT adsorption at *pH* 9. This variance is likely tied to the specific surface chemistry of their sunflower seed hull–derived carbon, which may stabilize surface complexes at higher alkalinity. For the ZnO@DPS–AC composite, the earlier onset of capacity decline beyond *pH* 8 is attributed to two factors. First, the experimental design did not evaluate performance specifically at *pH* 9, limiting a direct stepwise comparison. Second, the impregnation of ZnO nanoparticles likely accelerates the accumulation of surface negative charge compared to unmodified activated carbon, thereby triggering electrostatic repulsion at a lower *pH* threshold.

VI.2.3 Effect of ionic strength

The influence of ionic strength on the removal of CAT by the ZnO@DPS–AC composite was investigated over a NaCl concentration range of 0-1 M, as illustrated in **Figure VI.2** (**a**). Within the low–salinity regime (0 to 0.2 M NaCl), the q_e remained highly stable at approximately 121 mg/g. However, as the NaCl concentration exceeded 0.2 M, a progressive decline in q_e was recorded, ultimately reaching 110.7 mg/g at 1.0 M NaCl.

The stability of the q_e at low ionic strengths is thoroughly supported by existing literature. Yang et al. (2012) reported that CAT adsorption onto goethite remained unaffected by ionic strength variations from 0.01 to 0.1 M, a behavior attributed solely to the formation of inner–sphere complexes. Similarly, Gulley-Stahl et al. (2010) observed no discernible difference in CAT uptake across various metal oxides at low salinities. They established that inner–sphere complexes are generally insensitive to fluctuations in ionic strength, whereas outer–sphere complexes exhibit significant dependency due to their reliance on electrostatic forces. This initial insensitivity in the ZnO@DPS–AC system indicates that at lower molarities, the adsorption mechanism is dominated by strong specific chemical bonding that resists disruption by background Na^+ or Cl^- ions.

The subsequent decrease in q_e at elevated NaCl concentrations (0.2 to 1 M) aligns with established thermodynamic trends. Kamarehie et al. (2024) documented a similar reduction in pyrocatechol removal efficiency as background ion concentration increased, attributing the phenomenon to intensified electrostatic screening. Furthermore, Wu et al. (2024) noted that while moderate salinity can occasionally promote adsorption via double–layer compression, excessive ion concentrations inevitably depress q_e due to fierce site competition and electrostatic repulsion. From a physicochemical perspective, this high–salinity decline is driven by two concurrent mechanisms. First, the abundance of Na^+ or Cl^- ions screens the charged sites on the composite surface and compresses the electrical double layer, thereby suppressing electrostatic attraction between CAT molecules and the adsorbent (Hu et al., 2013). Second, as the NaCl concentration approaches 1 M, the dense inorganic ion population physically competes for available active sites, reducing the effective collision frequency of CAT molecules with the surface and inhibiting overall uptake.

A minor divergence is noted when comparing these findings with those of Al-Degs et al. (2008), who reported that increasing ionic strength could actively enhance the removal of certain organic dyes via salting–out effects or molecular aggregation. However, in the ZnO@DPS–AC system, the screening of functional groups and competitive ionic interference clearly outweigh any potential salting–out benefits at concentrations above 0.2 M. Nevertheless, the final q_e of 110.7 mg/g at 1 M NaCl represents merely a 9% reduction from the baseline capacity of 121 mg/g, demonstrating exceptional resilience under high–salinity conditions. This robust performance contrasts sharply with the Fe_3O_4 magnetic graphene oxide system evaluated by Wu et al. (2024), which suffered a drastic capacity collapse from approximately 110 mg/g to 18 mg/g under identical 1 M NaCl

conditions (an 84% reduction). The markedly superior ionic-strength tolerance of the ZnO@DPS–AC composite underscores the stable density of reactive sites generated by the ZnO impregnation, demonstrating that these functional groups remain accessible and chemically active even in severely saline environments.

VI.2.4 Effect of contact time

The influence of contact time on the removal of CAT by the ZnO@DPS–AC composite was evaluated over 10-270 min, as illustrated in **Figure VI.2(b)**. The experimental data revealed a distinct two–phase adsorption profile. An initial rapid uptake occurred within the first 30 min, during which the q_e reached 80.8 mg/g. A slower, progressive increase followed this until equilibrium was established at approximately 180 min. Consequently, a contact time of 240 min was used for all subsequent equilibrium studies to ensure complete saturation of the active binding sites. This rapid initial phase is a phenomenon frequently documented in the adsorption of phenolic compounds onto carbonaceous composites. Kamarehie et al. (2024) observed that pyrocatechol removal was notably fast within the first 20 min using aluminum–coated activated carbon, attributing this rapid kinetic response to the immediate availability of a high density of vacant surface sites.

Physicochemically, the transition from the rapid phase to the slower equilibrium phase is governed by site saturation and intraparticle diffusion. As contact time exceeds 30 min, the gradual depletion of available active sites reduces the overall adsorption rate. Vunain et al. (2018) explained that as the surface sites become occupied, repulsive forces emerge between the pre–adsorbed CAT molecules and those remaining in the bulk aqueous phase, thereby hindering further rapid uptake. Furthermore, the secondary slow phase indicates that CAT molecules must penetrate deeper into the internal micropore structure of the ZnO@DPS–AC composite. As noted by Suresh et al. (2011b), while film diffusion dominates the initial stage of adsorption, the rate–limiting step in the later stages typically involves intraparticle diffusion into the mesopores and micropores. This internal mass transfer inherently requires a significantly longer duration to achieve true thermodynamic equilibrium.

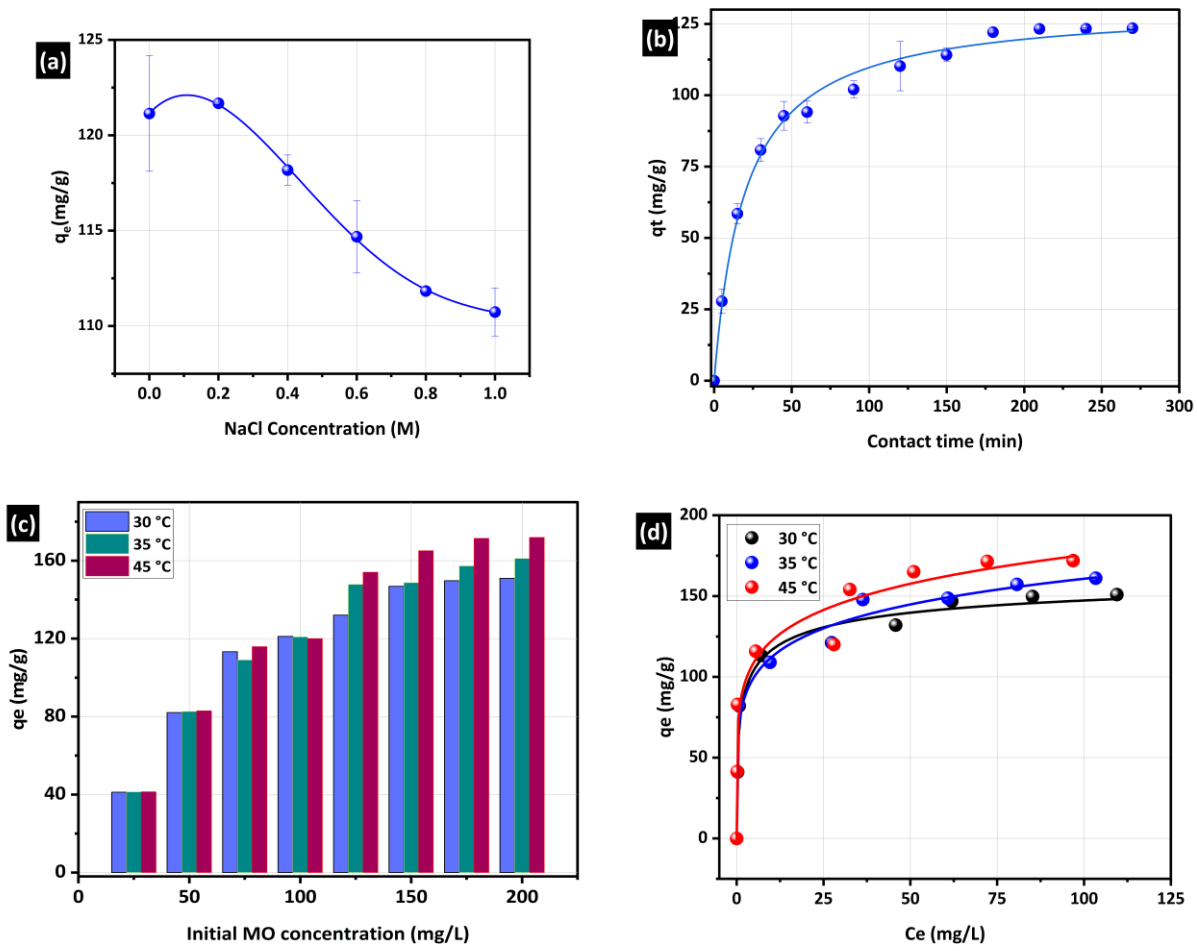

Figure VI.2 Effect of operational parameters on CAT adsorption onto ZnO@DPS-AC: (**a**) Ionic strength, (**b**) Contact time, and (**c**) Initial concentration. (**d**) Adsorption isotherms of CAT evaluated at different temperatures (30, 35, and 45 °C)

A notable distinction exists between the equilibrium time of the ZnO@DPS–AC composite and that of other adsorbent materials reported in the literature. Wu et al. (2024) reported an optimal equilibrium time of only 60 min for magnetic graphene oxide, and Mofrad et al. (2025) observed a similar 60 min threshold for magnetized pomegranate peel carbon. In contrast, the current composite's 180 min requirement is substantially longer. However, this equilibrium time remains considerably shorter than the 12 h required for conventional granular activated carbons (GAC) as reported by Suresh et al. (2011b). This accelerated kinetic performance relative to bare GAC is directly attributed to the synergistic effect of the metal oxide particles. As confirmed by Ponnusamy et al. (2019), the presence of ZnO clusters facilitates charge transfer from the oxygen p–orbitals of

CAT, effectively lowering the activation energy for surface complexation and accelerating the overall uptake rate. This intermediate kinetic behavior suggests that, while the ZnO particles effectively increase the density of reactive sites relative to unmodified GAC, the intricate pore network of the date palm spikelet–derived carbon maintains a diffusion–limited pathway. This complex internal structure necessitates a longer contact time than that required for simpler nanomaterials. Therefore, selecting 240 min as the standard operating parameter is scientifically justified to fully accommodate these complex mass transfer steps.

VI.2.5 Effect of initial CAT concentration

The influence of the initial CAT concentration on the R and q_e was investigated over a range of 25 to 200 mg/L at three distinct temperatures (**Figure VI.2(c)**). A rapid, near–complete removal of CAT was observed at lower initial concentrations (25-75 mg/L), yielding exceptionally high removal efficiencies of 96.2%-99.0%. As the initial concentration was systematically increased beyond 75 mg/L, the q_e values increased progressively, whereas the overall R declined proportionally. This equilibrium behavior is characteristic of an H–type isotherm, indicating a remarkably high affinity between the CAT molecules and the ZnO@DPS–AC composite surface.

The observed phenomenon—where q_e increases with initial concentration—is well established in the contemporary literature. Vunain et al. (2018) demonstrated that elevated initial CAT concentrations provide the necessary chemical potential to overcome mass transfer resistance between the bulk aqueous phase and the solid adsorbent surface, thereby driving higher localized uptake at equilibrium. Furthermore, the near–complete removal (up to 99%) achieved at lower concentrations is consistent with the findings of Kamarehie et al. (2024). They achieved 99.98% removal at an initial concentration of 20 mg/L, indicating that these dilute conditions are optimal for maximizing absolute phenolic recovery.

From a physicochemical perspective, the manifestation of an H–type isotherm signifies that the adsorbent possesses such a profound affinity for CAT that the solute is nearly entirely adsorbed, even under conditions of high dilution. According to the standard isotherm classification framework established by Giles et al. (1974), H–type curves are fundamentally associated with strong chemisorption or the formation of robust inner–sphere complexes. In the current system, the integration of ZnO nanoparticles likely enhances this surface affinity by facilitating the formation

of highly stable coordination complexes with catecholate ligands (Zhang et al., 2015). The subsequent continued increase in q_e at higher concentrations is driven by the steep concentration gradient. As the molecular density of CAT in the bulk solution increases, the statistical probability of effective collisions between the adsorbate molecules and the composite's available functional groups (such as localized hydroxyl and carboxyl sites) rises proportionally.

Conversely, the inevitable decline in R at concentrations above 75 mg/L is a direct consequence of active-site saturation. As noted by Kamarehie et al. (2024), for a fixed mass of adsorbent, the total number of active surface functional groups remains strictly finite. Therefore, as the initial concentration of CAT increases, the specific stoichiometric ratio of available binding sites to adsorbate molecules sharply decreases. This disparity leads to intense site competition and, consequently, a lower overall fraction of the pollutant being removed from the solution.

A highly significant observation in this study is the pronounced effect of temperature on the adsorption equilibrium. For any given initial CAT concentration, the experimental data showed an increase in q_e with increasing operational temperature, confirming the endothermic nature of the overall adsorption process. This thermal dependency aligns closely with the mechanisms described by Suresh et al. (2011a). They documented that elevated temperatures increase both the chemical potential and the kinetic mobility of phenolic molecules, providing the activation energy needed to penetrate deeper into the sterically restricted internal micropores of the carbon matrix. Ultimately, the distinct H–type isotherm profile recorded in this study represents a markedly superior adsorption performance compared to the standard, lower–affinity L–type isotherms reported for materials such as organophilic bentonite by Shakir et al. (2008). This stark contrast clearly underscores the powerful synergistic enhancement provided by ZnO impregnation of the DPS–derived activated carbon framework.

VI.3 Kinetic modeling and mass transfer mechanisms

The time–dependent removal of CAT by the ZnO@DPS–AC composite was evaluated via non–linear regression analysis using five distinct kinetic models: PFO, PSO, Avrami, Elovich, and Vermeulen. Statistical evaluation, grounded in $Adj–R^2$ and the $Red–\chi^2$, demonstrated that the PSO model provided the most accurate mathematical description of the experimental data ($Adj–R^2$ = 0.993; $Red–\chi^2$= 0.096). As detailed in **Table VI.1**, the model–calculated equilibrium capacity ($q_{e,cal}$

= 131.52 mg/g) and half–adsorption time ($t_{0.5,cal}$ = 19.88 min) exhibited excellent proximity to the experimentally observed values ($q_{e,exp}$ = 123.5 mg/g; $t_{0.5,exp}$ < 20 min), rigorously validating the suitability of the PSO model.

In the historical adsorption literature, a superior statistical fit to the PSO model has frequently been used as a definitive surrogate for concluding that a chemisorption mechanism is present, whereas the PFO model is typically associated with physisorption (Djezzar et al., 2024; Li et al., 2022; Sayed et al., 2024). However, as thoroughly documented by numerous contemporary scholars (Kumar, 2006; Lima et al., 2016; Tran, You, Hosseini-Bandegharaei, et al., 2017), the reliance on simple kinetic model fitting to definitively establish a binding mechanism is increasingly cautioned against. A scientifically rigorous determination of the adsorption mechanism must incorporate a comprehensive methodology that includes advanced analytical surface techniques (e.g., FTIR, XPS), empirical thermodynamic evaluations, and specific chemical knowledge of the localized adsorbate–adsorbent interfacial interactions.

The observed statistical preference for the PSO model over the PFO model can be fundamentally explained by the specific system conditions delineated by Wang and Guo (2020). They established that the PFO model is typically applicable to systems characterized by high initial adsorbate concentrations during the early contact stages, or to systems with a strictly limited number of active sites. Conversely, the PSO model strictly dominates during the final stages of adsorption or when the adsorbent features a stoichiometric abundance of active sites. In this study, the exceptionally high density of reactive sites generated by ZnO impregnation onto the date palm spikelet–derived carbon matrix facilitates sustained, high collision frequency between the phases, thereby strongly favoring the PSO kinetic pathway.

To further elucidate the physical mass transfer steps governing the uptake rate, the Vermeulen model was applied as a more mathematically robust alternative to the standard IPD equation (**Eq. II.7**). The experimental data exhibited a high degree of correlation with the Vermeulen model (*Adj–*R^2=0.991; *Red–*χ^2=0.0015). This strong mathematical fit confirms that intraparticle diffusion is a dominant, though not strictly exclusive, rate–limiting step in the transport of CAT into the internal pore network of the ZnO@DPS–AC composite.

Table VI.1 Kinetic model parameters for the adsorption of CAT onto ZnO@DPS–AC

Model	Unit	Value	Model	Unit	Value
Experimental			**Avrami**		
q_e	mg/g	123.5	q_e	mg/g	123.500
$t_{0.5}$	min	<20	k_{AV}	min^{-1}	0.032
PFO			n_{AV}	–	0.667
q_e	mg/g	117.274	$t_{0.5}$	min	17.886
k_1	L/min	0.037	R^2	–	0.993
$t_{0.5}$	min	18.758	$Adj–R^2$	–	0.992
R^2	–	0.970	$Red–\chi^2$	–	0.145
$Adj–R^2$	–	0.964	**Elovich**		
$Red–\chi^2$	–	0.771	α_e	mg/(g.min)	16.635
PSO			β_e	g/mg	0.040
q_e	mg/g	131.520	R^2	–	0.989
k_2	g/mg.min	3.8E-04	$Adj–R^2$	–	0.986
$t_{0.5}$	min	19.881	$Red–\chi^2$	–	0.319
R^2	–	0.994	**Vermeulen**		
$Adj–R^2$	–	0.993	*Slope*	min^{-1}	0.016
$Red–\chi^2$	–	0.096	R^2	–	0.992
			$Adj–R^2$	–	0.991
			$Red–\chi^2$	–	1.54E–03

VI.4 Isotherm modeling and equilibrium studies

The equilibrium distribution of CAT between the solid and liquid phases was rigorously evaluated using five isotherm models: Langmuir, Freundlich, Khan, Sips, and R–P. Statistical comparison (**Table VI.2**), based on Adj R^2 and $Red–\chi^2$, ranked the model suitability in the following descending order: Khan > R–P > Sips > Freundlich > Langmuir. Consequently, while all evaluated models provided reasonable mathematical descriptions of the experimental data, the three–parameter Khan model was identified as the most accurate for simulating the equilibrium adsorption of CAT onto the ZnO@DPS–AC composite.

VI.4.1 Performance of multi–parameter isotherms

The superior fit of three–parameter models (specifically the Khan, R–P, and Sips equations) over the traditional two–parameter frameworks (Langmuir and Freundlich) is directly attributed to their increased mathematical flexibility in describing surface heterogeneity. As noted by Al-Ghouti and Da'ana (2020), these multi–parameter models effectively circumvent the theoretical limitations of

the Freundlich model at high adsorbate concentrations and the Langmuir model on non–homogeneous surfaces. In this study, the Sips model was preferred over the Liu and Langmuir–Freundlich equations because these three formulations are mathematically equivalent and often yield identical parameter estimates when describing the same system. The strong correlation with the Khan model indicates that the ZnO@DPS–AC composite exhibits a hybrid adsorption characteristic. This behavior bridges the localized, monolayer binding associated with Langmuir theory and the heterogeneous energy distribution characteristic of the Freundlich model.

VI.4.2 Evaluation of adsorption capacity and temperature effects

The predicted Langmuir maximum monolayer adsorption capacity (q_m) was determined to range from 140 to 170 mg/g. This performance is significantly higher than the capacity of 0.042 mg/g reported by Kumar et al. (2017) for water hyacinth–derived activated carbon and the 84.66 mg/g documented by Kamarehie et al. (2024) for aluminum–coated oak wood activated carbon. However, it remains below the 271 mg/g achieved by Vunain et al. (2018) using sunflower seed hull carbon. The enhanced capacity of the current composite, relative to several literature benchmarks, is likely driven by the incorporation of metal oxide nanoparticles. These active phases provide specific reactive sites that facilitate inner–sphere complexation by forming bidentate or chelating structures (Heffner et al., 2022; Redfern et al., 2003).

A clear endothermic trend was observed, as both the q_e and the adsorption intensity increased with rising temperature (30 to 45 °C). This thermodynamic behavior is visually confirmed by the plot in **Figure VI.2(d)**, where the isotherms follow the strict order of T45 > T35 > T30 °C. This observation is in excellent agreement with Suresh et al. (2011a), who reported that an increase in thermal energy enhances the chemical potential and mobility of phenolic molecules. This additional energy enables the adsorbate to overcome physical barriers and penetrate deeper into the activated carbon matrix's internal micropores. This endothermicity is frequently attributed to the dehydration of CAT molecules in the aqueous phase. Specifically, the energy required to strip the hydration shells from the solute exceeds the exothermic energy released during surface binding, ultimately resulting in increased thermodynamic uptake at elevated temperatures (Suresh et al., 2011a; Suresh et al., 2012a).

Table VI.2 Isotherm model parameters for the adsorption of CAT onto the ZnO@DPS–AC

composite at varying temperatures (30, 35, and 45 °C)

Model	Unit	T=30 °C Value	T=35 °C Value	T=45 ° Value
Experimental				
q_m	mg/g	146.88	161.06	171.39
Langmuir				
q_m	mg/g	139.753	143.357	152.388
K_L	L/mg	1.569	2.546	3.846
R^2	–	0.961	0.924	0.898
$Adj–R^2$	–	0.948	0.898	0.864
$Red–\chi^2$	–	0.964	2.055	3.322
Freundlich				
K_F	$(mg/g)/(mg/L)^n$	73.863	75.618	83.227
$1/n$	–	0.159	0.166	0.162
R^2	–	0.968	0.971	0.954
Adj R^2	–	0.957	0.961	0.939
$Red–\chi^2$	–	1.434	1.461	2.230
Sips				
q_{ms}	mg/g	174.250	587.035	1156.931
K_s	$(mg/L)^{-ns}$	0.746	0.148	0.078
n_s	–	0.432	0.203	0.180
R^2	–	0.978	0.971	0.954
$Adj–R^2$	–	0.964	0.953	0.927
$Red–\chi^2$	–	1.064	1.675	2.598
R–P				
K_{RP}	L/g	397.678	1179.341	2307.698
a_{RP}	$(mg/L)^{-g}$	4.066	13.711	25.246
g	–	0.909	0.866	0.861
R^2	–	0.986	0.974	0.957
$Adj–R^2$	–	0.977	0.959	0.931
$Red–\chi^2$	–	0.628	1.341	2.378
Khan				
q_{mK}	mg/g	83.793	60.030	58.054
b_K	L/mg	4.151	14.156	26.769
a_K	–	0.905	0.866	0.862
R^2	–	0.987	0.975	0.957
$Adj–R^2$	–	0.979	0.960	0.932
$Red–\chi^2$	–	0.586	1.278	2.327

VI.4.3 Interpretation of the Freundlich exponent (1/*n*)

In the analysis of the Freundlich model, the exponent *n* in this study was found to fall within the strict range of 0 to 1. Significant variation exists in the literature regarding the physical interpretation of this parameter; certain researchers associate $1/n < 1$ with chemical processes and $1/n > 1$ with physical interactions. However, this study adopts the more rigorous clarification provided by Tran, You, Hosseini-Bandegharaei, et al. (2017). This framework establishes that the adsorption isotherm is linear when $n = 1$, highly favorable when $0 < 1/n < 1$, and unfavorable when $1/n > 1$. The observation of $1/n$ values strictly between 0 and 1 in the present study definitively confirms that the adsorption of CAT onto the ZnO@DPS–AC composite is a highly favorable thermodynamic process. This favorability perfectly aligns with the findings of Abugazleh et al. (2020), who noted that for titanium oxide and iron oxide substrates, the n values (or corresponding $1/n$ intensity parameters) remained within the favorable range. This mathematical condition indicates an exceptionally strong binding affinity between the aromatic rings of CAT and the adsorbent's surface functional groups.

The overall equilibrium profile, previously characterized as an H–type isotherm (**section VI.2.5**), physically demonstrates this high affinity. It suggests that $ZnCl_2$ impregnation effectively creates a composite surface with a high density of robust reactive centers that readily capture CAT molecules even at extremely low bulk concentrations.

VI.5 Comparative assessment of adsorbent performance

The q_m serves as a highly standardized metric for rigorously benchmarking the performance of the ZnO@DPS–AC composite against various alternative adsorbents reported in the literature. **Table VI.3** provides a comprehensive comparison of CAT uptake capacities across differing experimental conditions.

VI.6 Thermodynamic analysis

The influence of temperature on the removal of CAT by the ZnO@DPS–AC composite was investigated at 30 °C, 35 °C, and 45 °C to determine the fundamental thermodynamic parameters: $\Delta G°$, $\Delta H°$, and $\Delta S°$. These parameters were calculated using both linear and nonlinear forms of the van't Hoff equation, a rigorous methodology strongly advocated in recent scholarship to enhance

data reliability and minimize statistical errors.

Table VI.3 Comparison of maximum monolayer adsorption capacities of CAT onto various adsorbents reported in the literature

Adsorbent	Adsorption Conditions					q_m (mg/g)	Ref.
	t (min)	C_0 (mg/L)	*m*/*V* (g/L)	*T*(°C)	*p H*		
Sunflower seed hull AC (SSHAC)	50	25–200	2	30	9	270.22	(Vunain et al., 2018)
Chitosan@polyacrylamide@ZIF–8	–	10–100	–	–	–	165.30	(Hsu et al., 2025)
Magnetic Graphene Oxide (MGO)	60	–	0.256	25	–	179.00	(Wu et al., 2024)
Aluminum-coated Oak Wood AC	20	20-200	2	20	7	84.66	(Kamarehie et al., 2024)
Titanium Oxide	1440	-	10	27	7	108.87	(Abugazleh et al., 2020)
Date Palm Spikelets–derived composite (ZnO@DPS–AC)	240	25–200	1	30	6	139.75	**This work**

VI.6.1 Thermodynamic consistency and temperature effects

The results summarized in **Table VI.4** and **Figure VI.3** reveal that the equilibrium constants (K_{Model}) derived from the Langmuir, Khan, and R–P models increased with increasing temperature, definitively identifying adsorption as an endothermic process. This observed trend is consistently supported by Suresh et al. (2011a) and Vunain et al. (2018), who established that increased thermal energy enhances both the chemical potential and the kinetic mobility of CAT molecules. This additional energy enables the adsorbate to overcome internal mass-transfer resistance and penetrate deeper into the activated carbon matrix's micropores. Furthermore, higher temperatures facilitate the dehydration of the CAT molecules, because the energy required to strip the hydration shells is endothermic; thus, the overall thermodynamic process shows a net increase in uptake as the system temperature rises (Shahwan, 2021; Suresh et al., 2012a).

VI.6.2 Comparison of linear and nonlinear data treatment

A critical evaluation demonstrated that the signs of the estimated thermodynamic parameters remained consistent across the Langmuir, Khan, and R–P models, regardless of whether linear or nonlinear fitting was employed. However, significant discrepancies in magnitude were observed between the two fitting techniques for the Khan and R–P models, whereas the Langmuir model exhibited only minor mathematical differences. This outcome aligns tightly with the findings of Lima et al. (2020), who established that while linear and nonlinear methods typically yield identical algebraic signs, the nonlinear technique is statistically superior for accurately capturing the precise magnitude of enthalpy and entropy changes.

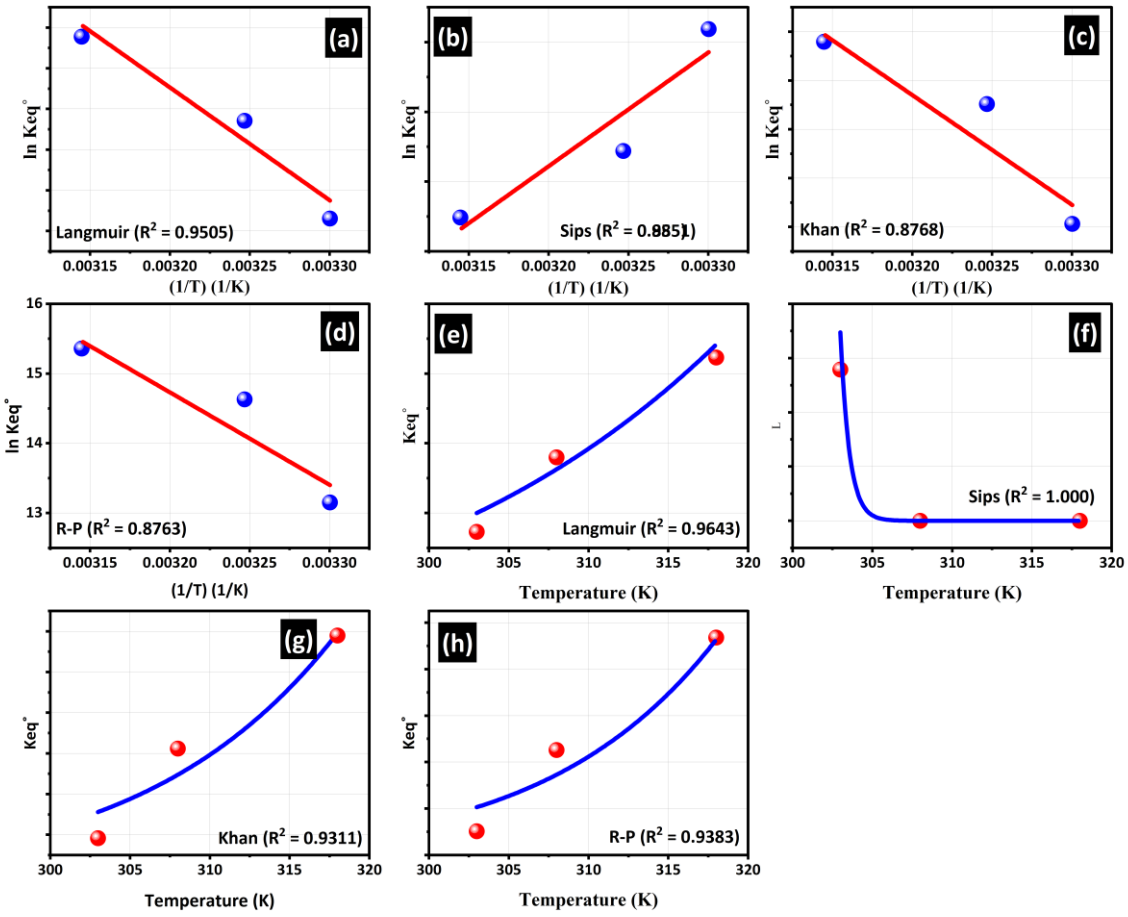

Figure VI.3 van't Hoff plots for the thermodynamic evaluation of CAT adsorption onto ZnO@DPS-AC using (**a–d**) linear and (**e–h**) non-linear regression forms across tested isotherm models

Table VI.4 Thermodynamic parameters (ΔG°, ΔH°, ΔS°) for the adsorption of CAT onto ZnO@DPS-AC calculated via linear and non-linear van't Hoff equations

				Linear Fitting			Non–Linear Fitting		
Model	***T* (K)**	K_{Model}	K_{eq}°	ΔG°	ΔH°	ΔS°	ΔG°	ΔH°	ΔS°
Langmuir									
	303	1.569	1.73E+05	-30.394	46.049	0.253	-30.394	42.271	0.241
	308	2.546	2.80E+05	-32.136			-32.136		
	318	3.846	4.23E+05	-34.270			-34.270		
Sips									
	303	0.507	5.58E+04	-27.546	-677.86	-2.160	-27.546	-1356.438	-4.384
	308	8.17E-05	9.00E+00	-5.628			-5.628		
	318	6.93E-07	7.63E-02	+6.807			+6.807		
Khan									
	303	4.151	4.57E+05	-32.847	93.336	0.418	-32.847	71.566	0.349
	308	14.156	1.56E+06	-36.532			-36.532		
	318	26.769	2.95E+06	-39.403			-39.403		
R–P									
	303	4.679	5.15E+05	-33.149	110.16	0.475	-33.1487	80.257	0.380
	308	20.549	2.26E+06	-37.487			-37.4868		
	318	42.470	4.68E+06	-40.624			-40.6235		

VI.6.3 Analysis of thermodynamic parameters

The calculated parameters revealed that the adsorption of CAT onto the ZnO@DPS–AC composite is thermodynamically favorable, as evidenced by negative ΔG° values across all applicable models (**Table VI.4**). The increasingly negative ΔG° values at elevated temperatures indicate enhanced thermodynamic favorability with increasing temperature. Positive ΔH° values (ranging from 42.27 to 110.16 kJ/mol) confirm the strongly endothermic nature of the adsorption process. Simultaneously, positive ΔS° values suggest increased randomness at the solid–solution interface. This increase in entropy is primarily due to the displacement and release of pre–adsorbed solvent (water) molecules from the ZnO@DPS–AC surface sites by the incoming CAT ligands.

VI.6.4 Justification of the Sips model thermodynamic anomaly

The Sips model presented a unique mathematical exception, wherein the calculated K_{eq}° decreased with temperature and the algebraic signs of the corresponding thermodynamic parameters inverted at high temperatures. This deviation is highly likely a mathematical artifact arising directly from the model's structural design. The Sips isotherm is a hybrid of the Langmuir and the Freundlich equations explicitly designed to describe surface heterogeneity (Al-Ghouti & Da'ana, 2020;

Murphy et al., 2023). Because the Sips formulation incorporates a heterogeneity exponent (n_s) that is inherently temperature–dependent, the regression can become mathematically unstable if the experimental data set does not span a sufficiently wide concentration gradient to fully saturate the heterogeneous sites. As noted by Richard et al. (2009), parameters for highly complex three–parameter equations, such as the Sips model, are often determined with less statistical precision than those of the simpler Langmuir model, which can occasionally render the derived thermodynamic values physically inconsistent.

VI.6.5 Mechanistic classification

In standard adsorption thermodynamics, the magnitude of $\Delta H°$ is frequently utilized to classify the binding interaction. Physisorption is typically associated with $\Delta H° <$ 40 kJ/mol, while chemisorption corresponds to $\Delta H° >$ 80 kJ/mol (Aichour et al., 2022; Luo et al., 2016). In the present study, the Langmuir–derived $\Delta H°$ (42.27 to 46.05 kJ/mol) and Khan/R–P–derived $\Delta H°$ (71.57 to 110.16 kJ/mol) values suggest a highly complex binding mechanism. The interfacial interaction is best described as a synergy between strong physical forces and weak chemisorption. The integration of ZnO nanoparticles facilitates the formation of inner–sphere complexes (chemisorption) through direct coordination with catecholate ligands, while the underlying ZnO@DPS–AC carbon matrix provides an extensive platform for π–π dispersion and hydrogen bonding (physisorption) (Gulley-Stahl et al., 2010; Yang et al., 2012). This hybrid nature is a hallmark of metal oxide–carbon composites, where initial surface binding is chemically driven, but the total volumetric uptake is heavily influenced by diffusion and physical transport mechanisms.

VI.7 Desorption, regeneration, and cyclic reusability

The reusability of an adsorbent is a critical parameter for determining its economic viability and environmental sustainability in large–scale industrial applications. The reusability and cyclic regeneration potential of the ZnO@DPS–AC composite for CAT removal were rigorously evaluated over three consecutive adsorption–desorption cycles, employing initial pollutant concentrations of 50 mg/L and 100 mg/L.

VI.7.1 Performance over multiple cycles

As illustrated in **Figure VI.4**, the removal efficiency of the ZnO@DPS–AC composite declined

progressively across three cycles when operated without intermediate chemical regeneration. At an initial CAT concentration of 50 mg/L, *R* dropped from a highly efficient 93.5% in the first cycle to 76.08% in the second, and finally declined to 56.44% in the third cycle. The progressive exhaustion of active binding sites was significantly accelerated at the higher initial concentration of 100 mg/L. Under these elevated loading conditions, the *R* plummeted from 67.07% in the first cycle to 26.97% in the second, and ultimately reached only 20.62% in the third.

This observed trend is fully consistent with findings across the relevant literature, which indicate that higher adsorbate concentrations lead to much faster saturation of the available surface–active sites. As noted by Kamarehie et al. (2024), as the sheer number of pre–adsorbed molecules on the adsorbent surface accumulates, localized repulsive forces are generated against incoming solute molecules. Consequently, the specific available surface area per unit mass of adsorbate drastically decreases. These operational data suggest that the ZnO@DPS–AC composite can maintain reasonable, practical performance for up to three sequential cycles at lower pollutant loadings before a dedicated regeneration step becomes strictly necessary.

VI.7.2 Evaluation of regeneration reagents

Chemical regeneration of the spent composite was attempted at ambient temperature using four distinct eluants: 0.1 M HCl, 0.5 M NaOH, 0.1 M NaOH, and pure ethanol. The experimental results demonstrated that both the acidic solution and the organic solvent were highly ineffective at desorbing the bound CAT. Conversely, the alkaline solutions recovered only relatively minor amounts of the adsorbed pollutant.

The distinct superiority of alkaline eluants over acidic or neutral solvents for the desorption of phenolic compounds is well supported by several preceding studies. Suresh et al. (2011a) established that NaOH was a significantly more effective eluent than either HCl or pure water for desorbing CAT and resorcinol from activated carbon matrices. They attributed this enhanced desorption directly to the chemically induced ionization of the phenolic compounds at high *pH* levels; this deprotonation sharply increases their aqueous solubility and thermodynamically facilitates their release from the carbon surface. Similarly, Hsu et al. (2025) successfully regenerated CS–PAA–ZIF–8 composites using 0.1 M NaOH over five consecutive cycles, reporting only minor progressive losses in q_e.

VI.7.3 Post–regeneration efficiency and mechanistic insights

Following the chemical desorption treatment using NaOH, a new complete adsorption cycle was executed. This post–regeneration cycle yielded a compromised *R* of only 36.0% for the 50 mg/L solution and 21.55% for the 100 mg/L solution. These recovered values are substantially lower than the original first–cycle capacities, indicating unequivocally that the ambient chemical regeneration process using NaOH was only marginally successful in fully vacating the previously occupied active sites.

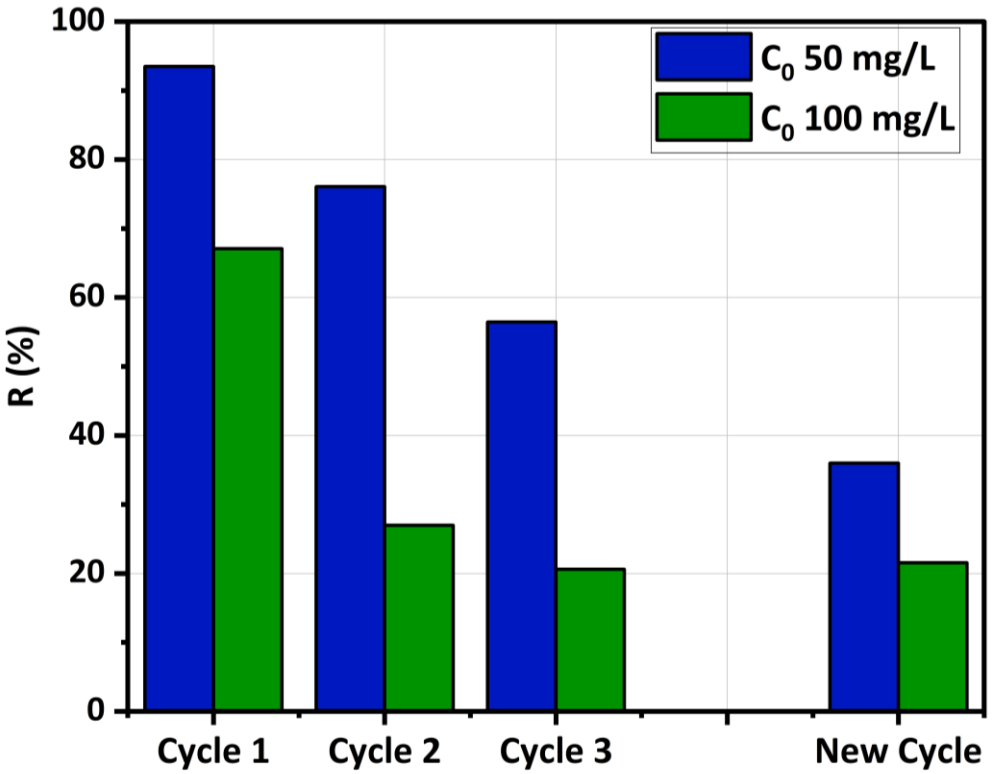

Figure VI.4 Recycling and regeneration performance of ZnO@DPS-AC over three consecutive adsorption-desorption cycles

The highly limited success of this chemical regeneration protocol strongly suggests the pervasive presence of robust chemisorption, specifically the formation of stable inner–sphere complexes between the catecholate ligands and the embedded ZnO nanoparticles. Ponnusamy et al. (2019) demonstrated that the coordinate covalent bonding between the oxygen p–orbitals of CAT and the d–orbitals of the Zn metallic centers is exceptionally strong. This potent electronic interaction likely explains why simple ambient solvent or mild alkaline washing fails to fully disrupt the

complex and restore the composite to its initial virgin capacity.

While certain pristine agricultural carbons, such as those derived entirely from sunflower seed hulls (Vunain et al., 2018), can maintain high cyclic reusability over five cycles using simple ethanol desorption, the specific kinetic behavior of the ZnO@DPS–AC composite suggests a fundamentally different binding paradigm. The metallic active sites engineered into this composite clearly form much more thermodynamically stable complexes, which will likely require high–energy thermal regeneration. Suresh et al. (2011a) noted that thermal desorption at elevated temperatures (e.g., 623 K) was far more effective than solvent–based desorption for deeply spent granular activated carbons, as the applied thermal energy provides the necessary thermodynamic force to break the robust chemisorptive bonds that chemical reagents cannot disrupt. These current findings definitively highlight that while the ZnO@DPS–AC composite is practically reusable for several unregenerated cycles, future process development must explicitly focus on optimizing rigorous regeneration protocols, potentially prioritizing integrated thermal treatments or highly advanced, multi–stage solvent techniques.

VI.8 Optimization via response surface methodology

VI.8.1 Experimental design and model development

A CCD was employed to deeply optimize the adsorption process and investigate the interactive effects of four critical operational parameters: contact time (60 to 240 min), initial CAT concentration (50 to 250 mg/L), solution *pH* (2 to 10), and adsorbent dosage (10 to 90 mg). The experimental matrix comprised 30 independent runs. This included 16 factorial points, 8 axial points, and 6 center points explicitly dedicated to assessing experimental reproducibility and quantifying pure error.

Two response variables were simultaneously evaluated: q_e (mg/g) and R (%). The experimental data were mathematically fitted to various polynomial models. Subsequent statistical evaluations, incorporating sequential F–tests, LoF tests, and goodness–of–fit metrics, definitively identified the quadratic model as the optimal fit for both responses (**Table VI.5** and **Table VI.6**).

Table VI.5 Sequential model sum of squares and model summary statistics for CAT adsorption capacity

Sequential model sum of squares							
Source	***SS***	***DF***	***MS***	***F–value***	***F-Table***	***p–value***	**Remarks**
Mean vs Total	2.952E+05	1	2.952E+05				
Linear vs Mean	14082.15	4	3520.54	30.07	2.76	< 0.0001	
2FI vs Linear	150.80	6	25.13	0.172	2.63	0.9812	
Quadratic vs 2FI	**2543.12**	**4**	**635.78**	**40.85**	**3.06**	**< 0.0001**	**Suggested**
Cubic vs Quadratic	114.60	8	14.32	0.844	3.73	0.5953	**Aliased**
Residual	118.84	7	16.98				
Total	3.122E+05	30	10406.66				
Lack of Fit Test							
Source	***SS***	***DF***	***MS***	***F–value***	***F-Table***	***p–value***	**Remarks**
Linear	2902.90	20	145.14	29.67	4.56	0.0007	
2FI	2752.10	14	196.58	40.19	4.64	0.0003	
Quadratic	**208.98**	**10**	**20.90**	**4.27**	**4.74**	**0.0613**	**Suggested**
Cubic	94.38	2	47.19	9.65	5.79	0.0192	**Aliased**
Pure Error	24.46	5	4.89				
Model summary statistics							
Source	***SD***	***R^2***	***Adj–R^2***	***Pre–R^2***	***PRESS***		
Linear	10.82	0.8279	0.8004	0.7337	4529.23		
2FI	12.09	0.8368	0.7509	0.7270	4644.14		
Quadratic	**3.94**	**0.9863**	**0.9735**	**0.9272**	**1238.94**	**Suggested**	
Cubic	4.12	0.9930	0.9711	0.1989	13625.92	**Aliased**	

Table VI.6 Sequential model sum of squares and model summary statistics for CAT removal percentage

Sequential model sum of squares							
Source	***SS***	***DF***	***MS***	***F–value***	***F–Table***	***p–value***	**Remarks**
Mean vs Total	7.147E+06	1	7.147E+06				
Linear vs Mean	1.228E+06	4	3.070E+05	53.38	2.76	< 0.0001	
2FI vs Linear	16017.16	6	2669.53	0.3970	2.63	0.8717	
Quadratic vs 2FI	**1.207E+05**	**4**	**30178.19**	**64.29**	**3.06**	**< 0.0001**	**Suggested**

Cubic vs Quadratic	3740.17	8	467.52	0.9916	3.73	0.5111	**Aliased**
Residual	3300.51	7	471.50				
Total	8.519E+06	30	2.840E+05				
Lack of Fit Test							
Source	***SS***	***DF***	***MS***	***F–value***	***F–Table***	***p–value***	**Remarks**
Linear	1.425E+05	20	7126.26	28.61	4.56	0.0007	
2FI	1.265E+05	14	9036.28	36.28	4.64	0.0004	
Quadratic	**5795.20**	**10**	**579.52**	**2.33**	**4.74**	**0.1819**	**Suggested**
Cubic	2055.02	2	1027.51	4.12	5.79	0.0875	**Aliased**
Pure Error	1245.49	5	249.10				
Model summary statistics							
Source	***SD***	***R^2***	***Adj–R^2***	***Pre–R^2***		***PRESS***	
Linear	75.83	0.8952	0.8784	0.8369		2.237E+05	
2FI	82.00	0.9069	0.8578	0.8483		2.081E+05	
Quadratic	**21.67**	**0.9949**	**0.9901**	**0.9744**		**35173.82**	**Suggested**
Cubic	21.71	0.9976	0.9900	0.7829		2.977E+05	**Aliased**

VI.8.2 Model selection and statistical validation

VI.8.2.1 Sequential model selection

The sequential model sum of squares analysis (**Table VI.5)** revealed that the quadratic model provided a statistically significant improvement over both the linear and 2FI models for both target responses. For the q_e, the quadratic terms contributed an additional sum of squares of 2543.12 with an exceptionally high calculated *F-value* of 40.85 (*p-value* < 0.0001). Similarly, for the removal response (evaluated after a power transformation where $\lambda = 1.47$), the quadratic model exhibited vastly superior performance with an *F-value* of 64.29 (*p-value* < 0.0001). In both cases, these calculated *F-values* vastly exceed their corresponding critical F-table thresholds, unequivocally validating the selection of the quadratic polynomials.

While a cubic model was also tested, it was mathematically aliased and demonstrated no significant improvement over the quadratic model (*p–value* = 0.5953 for capacity; *p–value* = 0.5111 for *R*). This confirms that the quadratic polynomial adequately captures the complex system behavior without artificially overfitting the data.

VI.8.2.2 Goodness–of–Fit statistics

VI.8.2.3 Lack of Fit analysis

The LoF test is an essential diagnostic for evaluating whether a selected empirical model adequately captures the experimental observations. For the capacity model, the LoF *F-value* was calculated at 4.27 (*p-value* = 0.0613). Crucially, this value remains strictly below the critical *F-table* value of 4.74 for 10 and 5 degrees of freedom. Therefore, the lack of fit does not cross the statistical significance threshold of α = 0.05. While this *p-value* of 6.13% indicates minor systematic deviations that warrant cautious interpretation, the *F-table* comparison confirms the model's structural validity. In contrast, the removal model demonstrated a distinctly non-significant LoF with an *F-value* of 2.33, which is well below the 4.74 critical limit (*p-value* = 0.1819), confirming excellent model adequacy. This higher *p–value* mathematically proves that the formulated quadratic polynomial effectively captures all systematic variance, meaning that any residual deviations are attributable strictly to random experimental error.

VI.8.3 ANOVA and significance of model terms

VI.8.3.1 Adsorption capacity model

The ANOVA analysis (**Table VI.7** and **Table VI.8**) revealed that the overall quadratic model is highly significant, exhibiting an *F–value* of 77.00 (*p–value*< 0.0001). This calculated variance ratio is nearly 32 times greater than the critical *F-table* value of 2.42, confirming that the probability of this magnitude of variance occurring by chance is less than 0.01%. Individual term analysis identified the initial concentration (*B*), adsorbent dosage (*D*), and contact time (*A*) as the dominant linear main effects, yielding *F–values* of 534.38, 327.01, and 43.46, respectively (all *p–values* < 0.0001). Notably, the initial solution *pH* (*C*) exhibited no significant linear effect (*F–value* = 0.0316, *p–value* = 0.8613), indicating that its physical influence upon the system manifests primarily through quadratic curvatures rather than direct linear scaling.

Among the two–factor interaction terms, only the contact time-initial concentration pairing (*AB*) achieved statistical significance (*F–value* = 5.78, *p–value* = 0.0296). This specific mathematical interaction demonstrates that the kinetic effect of contact time on overall capacity is heavily concentration–dependent. At elevated initial pollutant loadings, extended contact times yield substantially greater marginal improvements in q_e, as the chemical potential driving internal mass transfer remains elevated throughout the entire adsorption duration.

Furthermore, the quadratic terms for all four independent variables demonstrated high statistical significance: A^2 (*F–value* = 8.40, p = 0.0110), B^2 (*F–value*= 8.81, *p–value* = 0.0096), C^2 (*F–value* = 103.59, *p–value* < 0.0001), and D^2 (*F–value* = 22.32, *p–value*= 0.0003). The exceptionally high *F–value* associated with C^2 mathematically validates that the initial *pH* exerts a highly pronounced non–linear influence on the system. This statistical finding perfectly corroborates the physical bell–shaped pH dependence curve established in the earlier single–factor batch studies (section VI.2.2), where maximum pollutant uptake consistently occurred near the composite's point of zero charge (pH_{pzc} = 6.67).

Table VI.7 ANOVA analysis for the quadratic response surface model evaluating CAT adsorption capacity

Source	*SS*	*DF*	*MS*	*F–value*	*p–value*	Significance
Model	16776.06	14	1198.29	77.00	< 0.0001	Significant
A–Contact Time	676.36	1	676.36	43.46	< 0.0001	Significant
B–Initial Concentration	8316.22	1	8316.22	534.38	< 0.0001	Significant
C–*pH*	0.4920	1	0.4920	0.0316	0.8613	
D–Adsorbent dose	5089.07	1	5089.07	327.01	< 0.0001	Significant
AB	89.92	1	89.92	5.78	0.0296	Significant
AC	19.57	1	19.57	1.26	0.2797	
AD	31.86	1	31.86	2.05	0.1730	
BC	0.0036	1	0.0036	0.0002	0.9880	
BD	2.74	1	2.74	0.1763	0.6805	
CD	6.70	1	6.70	0.4303	0.5218	
A^2	130.76	1	130.76	8.40	0.0110	Significant
B^2	137.06	1	137.06	8.81	0.0096	Significant
C^2	1612.17	1	1612.17	103.59	< 0.0001	Significant
D^2	347.30	1	347.30	22.32	0.0003	Significant
Residual	233.44	15	15.56			
Lack of Fit	208.98	10	20.90	4.27	0.0613	Not Significant
Pure Error	24.46	5	4.89			
Cor Total	17009.50	29				

VI.8.3.2 Removal percentage model

The ANOVA analysis for the transformed *R* model yielded an even higher overall *F–value* of 207.66 (*p–value* < 0.0001). Because 207.66 vastly exceeds the critical *F-table* limit of 2.42, it indicates the strong statistical dependence of this target response on the investigated experimental factors. The hierarchy of statistical significance followed a distinct mathematical pattern, in which the *D* variable heavily dominated the model (*F–value* = 1848.29), followed by *B* (*F–value* =

709.47) and A (*F–value* = 58.11). The exceptionally high *F–value* assigned to the dosage parameter physically reflects the direct stoichiometric relationship between the available mass of the active solid phase and the total fraction of pollutant successfully removed from the aqueous solution.

Table VI.8 ANOVA analysis for the quadratic response surface model evaluating CAT removal percentage

Source	*SS*	*DF*	*MS*	*F–value*	*p–value*	Significance
Model	1.365E+06	14	97469.06	207.66	< 0.0001	Significant
A–Contact Time	27276.40	1	27276.40	58.11	< 0.0001	Significant
B–Initial Concentration	3.330E+05	1	3.330E+05	709.47	< 0.0001	Significant
C–*pH*	0.2632	1	0.2632	0.0006	0.9814	
D–Adsorbent dose	8.675E+05	1	8.675E+05	1848.29	< 0.0001	Significant
AB	234.09	1	234.09	0.4987	0.4909	
AC	349.45	1	349.45	0.7445	0.4018	
AD	803.44	1	803.44	1.71	0.2105	
BC	10.54	1	10.54	0.0225	0.8829	
BD	14468.84	1	14468.84	30.83	< 0.0001	Significant
CD	150.80	1	150.80	0.3213	0.5792	
A^2	5932.27	1	5932.27	12.64	0.0029	
B^2	24434.31	1	24434.31	52.06	< 0.0001	Significant
C^2	72753.04	1	72753.04	155.00	< 0.0001	Significant
D^2	756.79	1	756.79	1.61	0.2235	
Residual	7040.68	15	469.38			
Lack of Fit	5795.20	10	579.52	2.33	0.1819	Not Significant
Pure Error	1245.49	5	249.10			
Cor Total	1.372E+06	29				

A notable divergence from the capacity model is the high statistical significance of the two–factor interaction between the initial concentration and the adsorbent dosage (*BD*, *F–value* = 30.83, *p–value* < 0.0001). This specific interaction mathematically reveals that the initial pollutant loading strongly modulates the physical effectiveness of increasing the adsorbent dosage. Under low–concentration conditions, systematic increases in dosage yield rapidly diminishing returns as the available binding sites become severely unsaturated. Conversely, at elevated initial concentrations, the addition of adsorbent mass provides proportionally greater improvements in the overall *R*.

The quadratic terms A^2, B^2, and C^2 all achieved high statistical significance (*F–value* = 12.64, 52.06, and 155.00, respectively). However, the quadratic dosage term (D^2) was found to be statistically non–significant (*F–value*=1.61, *p–value* = 0.2235). This lack of quadratic significance

mathematically suggests that the absolute R scales approximately linearly with the applied adsorbent mass within the tested experimental boundaries, without exhibiting pronounced response curvature.

VI.8.4 Development of predictive regression equations

VI.8.4.1 Actual factor equations

The formulated quadratic models, when expressed in actual (uncoded) physical units, enable direct predictive modeling of the operational system. For q_e, the empirical regression is defined as:

$$q_e = 15.13 - 0.211A + 0.504B + 25.75C - 1.22D + 0.00105AB - 0.0123AC - 0.00157AD - 0.000151BC - 0.000414BD - 0.0162CD + 0.00108A^2 - 0.000894B^2 - 1.92C^2 + 0.00890D^2 \quad \textbf{Eq. VI.1}$$

For the R, the power–transformed regression model ($R^{1.47}$) is defined as:

$$R^{1.47} = -5.75 - 1.77A - 4.64B + 167.30C + 14.61D + 0.00170AB - 0.0519AC + 0.00787AD - 0.00812BC - 0.0301BD - 0.0768CD + 0.00726A^2 + 0.0119B^2 - 12.88C^2 - 0.0131D^2 \quad \textbf{Eq. VI.2}$$

It must be noted that the calculated R requires a distinct mathematical back–transformation to return to the standard R, necessitated by the transformation factor (λ= 1.47) applied during statistical optimization:

$$R = (R^{1.47})^{\frac{1}{1.47}} \quad \textbf{Eq. VI.3}$$

These empirical equations must be applied strictly within the defined boundaries of the experimental design space to avoid severe extrapolation errors systematically. Furthermore, the negative mathematical coefficients associated with specific linear terms (for instance, the –0.211 coefficient for contact time in the capacity model) do not inherently indicate antagonistic physical effects. Instead, they strictly reflect the mathematical balance of linear and quadratic variable contributions across the evaluated multidimensional space.

VI.8.4.2 Coded factor equations

By converting the physical variables into standardized, dimensionless coded factors (scaling from -1 to +1), the quadratic regression models facilitate a direct, normalized evaluation of parametric influence. For q_e, the coded regression is derived as:

$$q_e = 102.52 + 5.31A + 18.61B + 0.14C - 14.56D + 2.37AB - 1.11AC - 1.41AD - 0.015BC - 0.41BD - 0.65CD + 2.18A^2 - 2.24B^2 - 7.67C^2 + 3.56D^2 \quad \textbf{Eq. VI.4}$$

For the *R*, the corresponding coded regression is:

$$R^{1.47} = 488.11 + 33.73A - 117.70B - 0.33C + 190.08D + 3.83AB - 4.67AC + 7.09AD - 0.81BC - 30.09BD - 3.0`7CD + 14.50A^2 + 29.43B^2 - 50.76C^2 - 5.18D^2 \quad \textbf{Eq. VI.5}$$

These coded polynomial equations permit a direct statistical comparison of individual factor importance strictly through the evaluation of absolute coefficient magnitudes. For the q_e response, the magnitudes of the primary coefficients rank in the following order: *B* (18.61) > *D* (14.56) > C^2 (7.67) > *A* (5.31). This mathematical ranking rigorously confirms that the initial pollutant loading gradient and available mass act as the dominant driving forces for absolute surface uptake.

Conversely, for the *R* response, the statistical hierarchy shifts distinctly: *D* (190.08) > *B* (117.70) > the quadratic C^2 (50.76) > *A* (33.73). This pronounced shift explicitly highlights the overwhelming parametric influence of the applied adsorbent dosage on achieving high macroscopic clean–up efficiencies.

VI.8.5 Two–Dimensional interaction analysis

VI.8.5.1 Interactive effects on adsorption capacity

The two–dimensional interaction plots (**Figure VI.5**) provide a clear visual assessment of the coupled and independent parametric effects governing the overall operational process. Consistent with the statistical evaluation of the regression coefficients (**Table VI.7**), the graphical analysis confirms that the interaction between *AB* constitutes the sole dominant interactive effect influencing q_e. All other parameter pairings exhibit strictly independent physical behavior.

The statistical significance of the interaction between contact time and initial concentration (*p–value* = 0.0296) is visually evident from the distinct divergence of the plotted response contours. Under low–concentration conditions (100 mg/L), q_e increases only marginally (from 92 to 100 mg/g) as the contact time extends from 105 to 195 min. However, at an elevated initial concentration (200 mg/L), the absolute capacity increases substantially from 100 to 120 mg/g over the same operational time interval.

This spatial divergence definitely signifies a concentration–driven internal mass transfer mechanism. High initial pollutant loadings establish and maintain a steep concentration gradient between the bulk aqueous solution and the solid adsorbent surface throughout the treatment cycle. This sustained gradient provides the continuous chemical potential required to drive prolonged intraparticle diffusion. Conversely, at low initial concentrations, the mass transfer driving force diminishes rapidly as the system approaches thermodynamic equilibrium, rendering extended contact times physically and mathematically less productive. From a practical engineering standpoint, this confirms that high–strength industrial wastewaters logically justify longer hydraulic retention times, whereas dilute effluent streams achieve near–maximum saturation capacity quite rapidly.

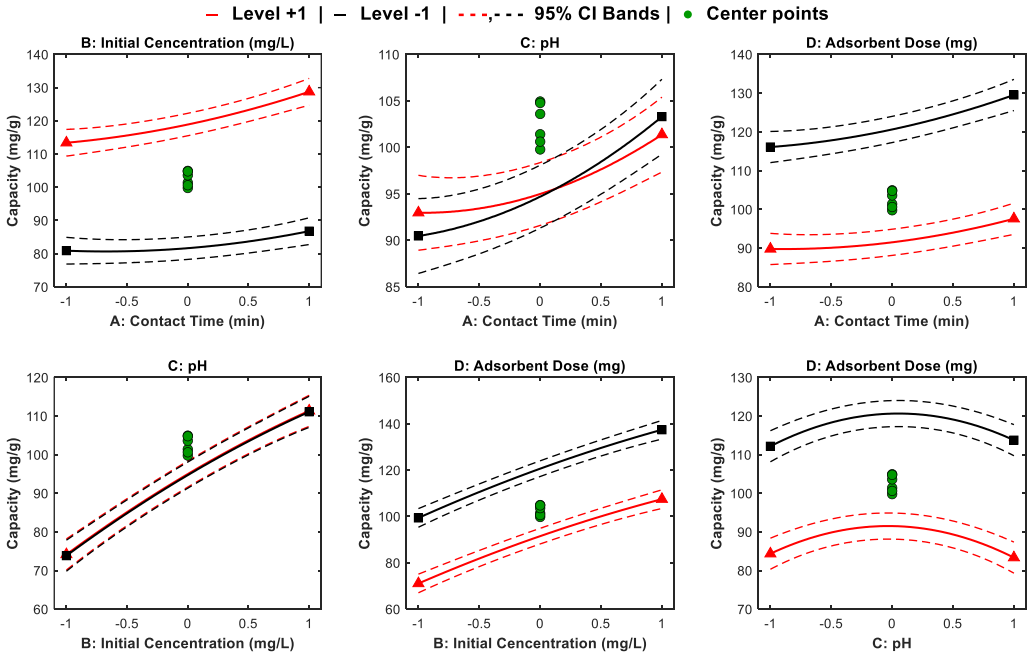

Figure VI.5 Two-dimensional interaction plots derived from the RSM-CCD model demonstrating the effects of paired operational variables on CAT adsorption capacity

The remaining binary interactions were confirmed to be statistically non–significant (*p–value* > 0.05), as indicated by near–parallel response trajectories in the two–dimensional plots. Specifically, the consistent vertical separation observed between the low–dosage and high–dosage response curves across all respective plots confirms that the adsorbent mass functions as an entirely independent physical scaling factor. The negative linear effect of dosage identified in the earlier

ANOVA strictly indicates that higher applied solid masses reduce q_e due to the localized aggregation or unsaturation of available binding sites. Crucially, this independent scaling effect does not alter the fundamental kinetic or thermodynamic trajectories of the other system variables.

Similarly, the interaction plots incorporating *pH* display extensive geometric overlapping or strictly parallel slopes. This confirms that the initial solution *pH* does not fundamentally alter the underlying concentration–driven mass transfer rates. Because the *pH* range evaluated primarily lies below CAT's pKa_1, the adsorbate remains predominantly in its neutral molecular state, thereby reducing the system's sensitivity to transient electrostatic fluctuations.

Finally, the broad graphical maxima observed in the *pH*–related interaction plots (e.g., *CD*) suggest a high degree of operational robustness. While the absolute optimal uptake strictly occurs near neutral *pH* (simultaneously avoiding hydronium competition at low *pH* and electrostatic repulsion at high *pH*), the system successfully maintains 90 to 95% of its theoretical maximum capacity across a notably wide operational window (*pH* 5 to 7). This inherent resilience to minor *pH* deviations mathematically demonstrates that the adsorption process will require less stringent continuous *pH* control during eventual industrial–scale implementation.

VI.8.5.2 Interactive effects on removal percentage

The interaction plots (**Figure VI.6**) and the ANOVA results (**Table VI.8**) comprehensively illustrate how the operational parameters jointly govern the overall *R*. In stark contrast to the q_e analysis, the ANOVA for the *R* reveals that the interaction between initial concentration and adsorbent dosage *(BD)* is highly significant *(F–value* = 30.83, *p–value* < 0.0001). This establishes it as a critical limiting factor for overall process efficiency. All other binary interactions (*AB*, *AC*, *AD*, *BC*, *CD*) were determined to be statistically non–significant (*p–value* > 0.05), confirming that these factor pairs operate entirely independently.

The graphical divergence between the high–dosage (red line) and low–dosage (black line) profiles is highly pronounced. When applying a high adsorbent dose, the extreme abundance of active sites relative to the sparse number of pollutant molecules yields near–complete macroscopic removal (approximately 98-100%). Conversely, at a low dose, limited site availability physically restricts the *R* to roughly 60%. This substantial performance gap (roughly 40%) demonstrates that under dilute conditions, the process is strictly dosage–controlled. As the initial concentration increases,

the *R* inherently declines for both dosage levels due to the rapid saturation of available binding sites. However, the respective slopes of decline differ; the high–dosage condition maintains a significantly superior *R*, although the performance gap between the two trajectories narrows slightly in the high–concentration region.

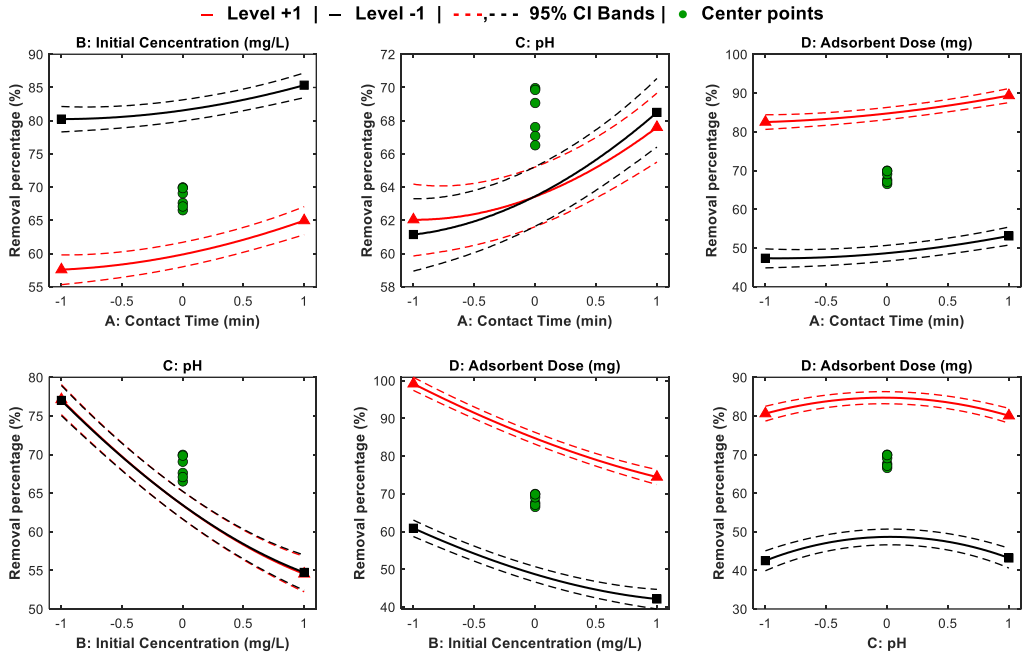

Figure VI.6 Two-dimensional interaction plots derived from the RSM-CCD model demonstrating the effects of paired operational variables on CAT removal percentage

This profound interaction confirms that the *R* does not scale linearly with dosage or concentration individually, but rather relies directly on the stoichiometric excess of active sites. The strict statistical significance (*p–value* < 0.0001) indicates that increasing the adsorbent dose is highly effective for maximizing *R* when the pollutant concentration remains low to moderate, ensuring nearly complete cleanup. At severely elevated concentrations, even the maximum applied dosage struggles to achieve 100% removal due to the overwhelming mass of pollutant rapidly saturating the solid surface. This physical limitation necessitates a strategic shift toward multi–stage adsorption system designs for highly concentrated effluents.

The remaining two–dimensional interaction plots (*AB*, *AC*, *AD*, *BC*, *CD*) display trajectories that are strictly parallel or nearly parallel, visually confirming the statistical non–significance identified in the ANOVA (*p–value* > 0.05). This parallelism indicates a pure additivity of effects.

Specifically, the contact-time interactions (*AB*, *AC*, *AD*) yield completely parallel response lines, indicating that the fundamental removal kinetics remain consistent across applied concentration, *pH*, and dosage. For example, extending the contact time provides a fixed percentage increase in total removal, regardless of the initial solution *pH* (4 or 8).

Furthermore, while the quadratic term for *pH* (C^2) is extremely significant (*F–value* = 155.00), generating a strong bell–shaped optimization curve, the binary interaction terms involving *pH* remain completely insignificant. Consequently, the optimal *pH* condition (centered near neutral, as evident from the peak of the response curves) remains physically fixed regardless of variations in adsorbent dosage or initial pollutant concentration. The vertically parallel bell curves observed in the *CD* plot clearly show that, while increasing the adsorbent dose scales the entire response curve upward (achieving higher total removal), it does not shift the optimal *pH* to the left or right. This is a critical finding for eventual engineering–scale–up, as it mathematically guarantees that the optimal *pH* established during laboratory–scale experiments remains valid even if the influent pollutant load or operational dosage fluctuates within a full–scale reactor.

VI.8.6 Three–Dimensional response surfaces for adsorption capacity

The 3D response surface plots (**Figure VI.7**) provide a comprehensive spatial representation of the empirical regression equation, visualizing the simultaneous interactive effects of two operational variables on q_e while holding all other factors at their central levels. The response surface relating contact time and initial concentration exhibits a distinct rising ridge. At a low initial concentration (100 mg/L), the surface remains relatively flat over time, as graphically confirmed, indicating that thermodynamic equilibrium is rapidly achieved. However, at a highly concentrated state (200 mg/L), the surface develops a steep ascending slope towards the upper boundaries of the design space. This topological plane visually corroborates the significant positive two–factor interaction (*AB*) established during the ANOVA, demonstrating that prolonged contact time is highly beneficial only when the concentration gradient (C_0) is sufficiently robust to sustain internal mass transfer into the micropores.

All generated surface plots incorporating solution *pH* display a characteristic convex curvature, visually validating the high statistical significance of the quadratic term (C^2). The geometric apex of these surfaces consistently centers around the near–neutral region (*pH* ≈6.0), regardless of

fluctuations in contact time, initial concentration, or adsorbent mass. Ultimately, the absolute maximum adsorption capacity coordinates are localized at high contact times, elevated initial concentrations, and a low applied adsorbent mass.

The spatial plots involving adsorbent mass consistently reveal a linear, descending slope as the applied dosage increases from 30 to 70 mg. This negative gradient is clearly evident in the transition from the high–capacity red zone at low mass to the low–capacity blue zone at high mass. This distinct topological trend visually reinforces the physical phenomenon of site unsaturation; applying greater adsorbent mass partitions the fixed influent pollutant load across a vast stoichiometric excess of binding sites, thereby fundamentally reducing the specific pollutant uptake per unit weight (q_e) without altering the underlying adsorption mechanism.

VI.8.7 Three–dimensional response surfaces for removal percentage

The corresponding three–dimensional response surface plots (**Figure VI.8**) illustrate the simultaneous effects of paired independent variables on the total R (%) while holding remaining factors strictly constant. Unlike q_e surfaces, which mathematically favor high solute concentrations, the R topologies are distinctly driven by active site availability and surface stoichiometry.

Evaluating the initial concentration versus adsorbent mass spatial surface, the R drops precipitously (from approximately 80% to below 50%) as the concentration increases under low–dosage conditions (30 mg), marked by a steep topological descent into the low–performing blue region. This visual confirms that high pollutant loads rapidly saturate the strictly limited binding sites. Conversely, at an elevated adsorbent mass (70 mg), the spatial surface remains suspended in the high–efficiency red zone (exceeding 90%) across a substantially broader concentration range. The visibly flatter contour slope at high dosage indicates that providing a strict stoichiometric excess of active sites effectively buffers the macroscopic system against influent concentration spikes, consistently maintaining near–complete pollutant removal.

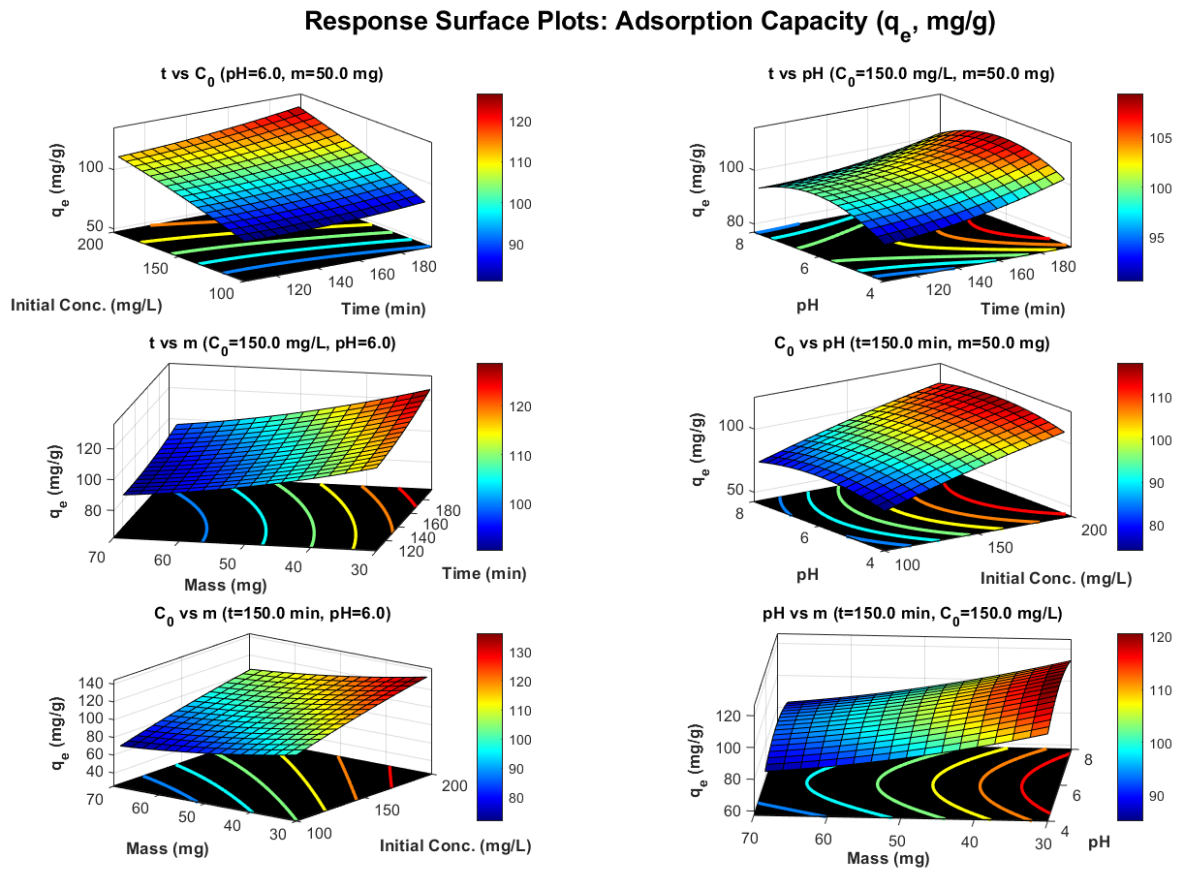

Figure VI.7 Three-dimensional response surface plots illustrating the interactive effects of operational parameters on the CAT adsorption capacity of the ZnO@DPS-AC composite

The curvature analysis of all response surfaces involving *pH* reveals a highly consistent topological pattern across every evaluated dimension. In each instance, the spatial surface displays a characteristic parabolic-cylinder or ridge geometry, characterized by pronounced convex curvature and a sharply defined maximum crest near *pH* 6.0. The precipitous decline in overall *R* observed as operating conditions diverge towards *pH* 4.0 or *pH* 8.0 provides powerful visual corroboration of the significant quadratic effect (C^2) identified computationally. Furthermore, the striking uniformity of this central ridge structure across various parametric combinations physically demonstrates that the optimal operational *pH* functions as an intrinsic property of the specific adsorbent–adsorbate interface. This profound stability suggests that the optimal condition is governed fundamentally by the chemical interplay between the specific dissociation constant of the adsorbate (*pKa*) and the point of zero charge of the adsorbent (pH_{pzc}), remaining largely invariant

despite deliberate fluctuations in total dosage or extended contact time.

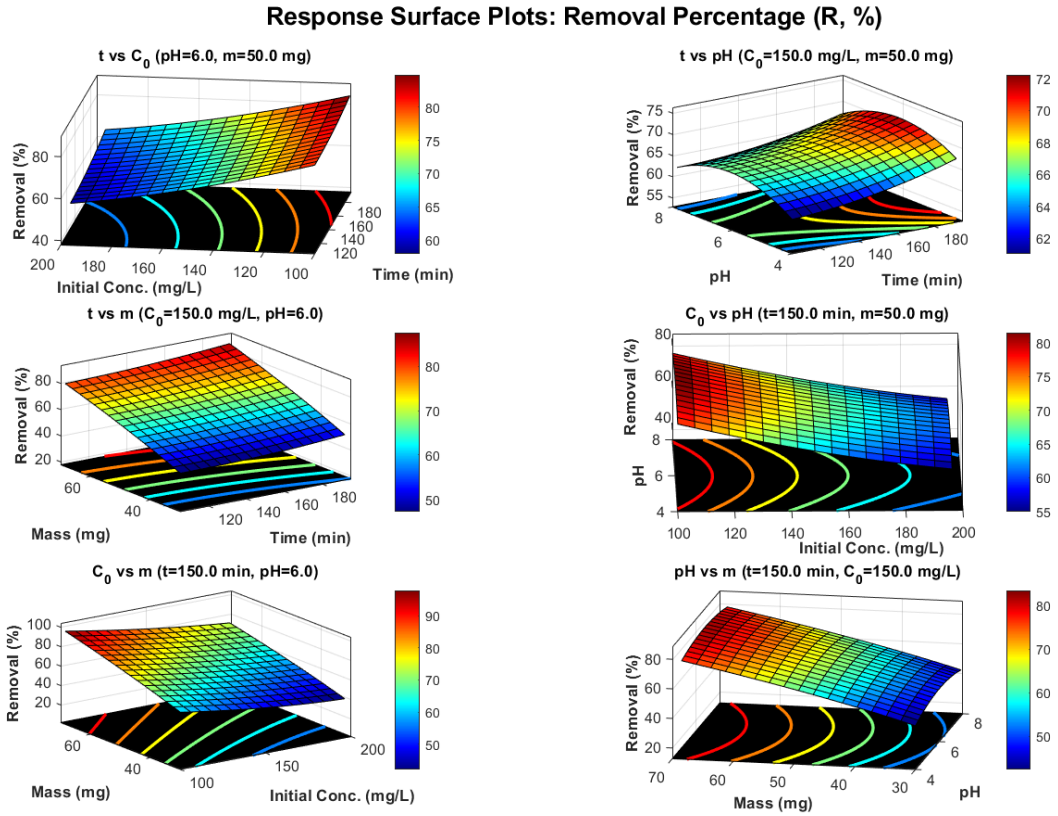

Figure VI.8 Three-dimensional response surface plots illustrating the interactive effects of operational parameters on the CAT removal percentage of the ZnO@DPS-AC composite

Finally, the response surface plots incorporating adsorbent mass consistently exhibit the steepest linear spatial gradients. As explicitly illustrated in the contact time-mass interaction space, scaling the dosage from 30 to 70 mg physically drives the response directly from the lower–performing blue region (approximately 50%) to the optimal red region (approximately 90%). Unlike the strict convex curvature associated with pH, the spatial slope associated with solid mass is notably linear. This geometric linearity mathematically indicates that dosage functions as a highly direct process scaling factor. Consequently, systematically increasing the adsorbent mass applied serves as the single most effective operational method to maximize the absolute macroscopic *R*, provided the system pH is strictly maintained within the established optimal range.

VI.8.8 Multi-objective optimization of process parameters

To mathematically determine the optimal operational conditions for CAT adsorption, numerical optimization was performed using the DFA. Based on the fundamental economic and environmental objectives of the treatment process, three distinct scenarios were evaluated: maximizing q_e (prioritizing resource efficiency), maximizing R (prioritizing effluent quality), and a multi–objective operational trade–off. The optimization results are summarized in **Table VI.9**.

Table VI.9 RSM desirability optimization scenarios for CAT adsorption onto ZnO@DPS-AC

Optimization Criterion	*t* (min)	C_0 (mg/L)	*pH*	*m* (mg)	*Pred-*q_e (mg/g)	*Pred-R* (%)	Desirability
Maximum Capacity	194.963	199.849	5.642	30.422	147.970	47.559	1.000
Maximum Removal	194.287	100.380	5.419	67.508	75.783	100	1.000
Multi–Objective	195.000	200.000	5.806	70.000	116.022	79.730	0.686

Scenario 1: maximizing adsorption capacity

This optimization scenario targets maximum resource efficiency, explicitly aiming to utilize the adsorbent material to its absolute physical limit. The empirical model predicted a maximum capacity of 147.97 mg/g with a perfect desirability score of 1.000. These results are achievable under conditions of an elevated initial concentration (200 mg/L) and a minimal adsorbent dosage (30.4 mg). This specific configuration maximizes the concentration gradient driving force while strictly limiting the overall availability of active sites, thereby forcing each unit mass of the solid adsorbent to capture the maximum possible mass of pollutant. Although this approach is highly efficient regarding material utilization, the resulting overall R is relatively low (47.6%). This physical constraint indicates that this parameter set is best suited for initial, high–strength recovery stages rather than final effluent polishing.

Scenario 2: maximizing removal percentage

This scenario emphasizes strict environmental compliance by targeting the highest possible effluent quality. The model predicted a theoretical R of 100%. The optimal conditions to achieve this benchmark are a moderate initial concentration (100.4 mg/L) and a high adsorbent dosage (67.5 mg). Under these operational parameters, complete pollutant removal is achieved by

maintaining a manageable influent contaminant load while simultaneously providing a vast stoichiometric excess of adsorption sites. Any slight mathematical prediction exceeding 100% is a minor statistical artifact, indicating that the system's physical performance comfortably exceeds the strict threshold required for total removal within the evaluated design space.

Scenario 3: multi–objective optimization (industrial balance)

For practical industrial applications, achieving a sustainable operational balance between treating high–strength wastewater and maintaining strict effluent quality is essential. Therefore, the multi–objective optimization aimed to maximize both q_e and R simultaneously. The software predicted optimal balanced conditions at a high initial concentration (200 mg/L) and the maximum tested adsorbent dosage (70 mg). Under these parameters, the system exhibited highly balanced performance, yielding a substantial adsorption capacity of 116.0 mg/g alongside a strong R of 79.7%. The corresponding composite desirability score (0.686) was inherently lower than those obtained in the single–objective scenarios. This statistical reduction accurately reflects the unavoidable physical trade–off between maximizing site saturation and ensuring abundant site availability; these two distinct thermodynamic states cannot be perfectly maximized simultaneously within a single batch operational unit.

Operational Consistency

Across all three optimized scenarios, the ideal t consistently converged to approximately 195 min, and the optimal pH settled strictly within the narrow band of 5.4 to 5.8. This high degree of consistency rigorously validates the earlier three–dimensional response surface analysis (**sections VI.8.6** and **VI.8.7**). It mathematically confirms that a mildly acidic environment ($pH \approx 5.6$) serves as the robust operational sweet spot for CAT adsorption, remaining entirely valid regardless of the specific pollutant load or dosage strategy employed.

VI.8.9 Experimental validation

To definitively validate the predictive accuracy of the developed RSM model, confirmatory physical experiments were conducted under the exact optimized conditions determined for the multi–objective scenario ($C_0 = 200$ mg/L, $m = 70$ mg, $pH = 5.8$, $t = 195$ min). The laboratory results yielded a q_e of 108.52 mg/g and a final R of 75.97 %. The relative error between the model–predicted values and the experimental observations was 4.95 % for R, which falls well within the

acceptable statistical threshold. This close agreement in physical measurements rigorously confirms the validity, precision, and reproducibility of the developed quadratic model for predicting CAT adsorption performance under variable operating conditions.

VI.9 Modeling of CAT adsorption via an artificial neural network

VI.9.1 Model development and hyperparameter optimization

A systematic grid search was conducted to evaluate various ANN configurations for modeling the batch adsorption of CAT onto ZnO@DPS-AC. This evaluation encompassed multiple network architectures, training algorithms, transfer functions, and hidden layer hyperparameter settings. The optimal predictive model was identified based on two primary performance criteria, evaluated via 3-fold cross-validation and ensemble averaging, as detailed in **section III.15**.

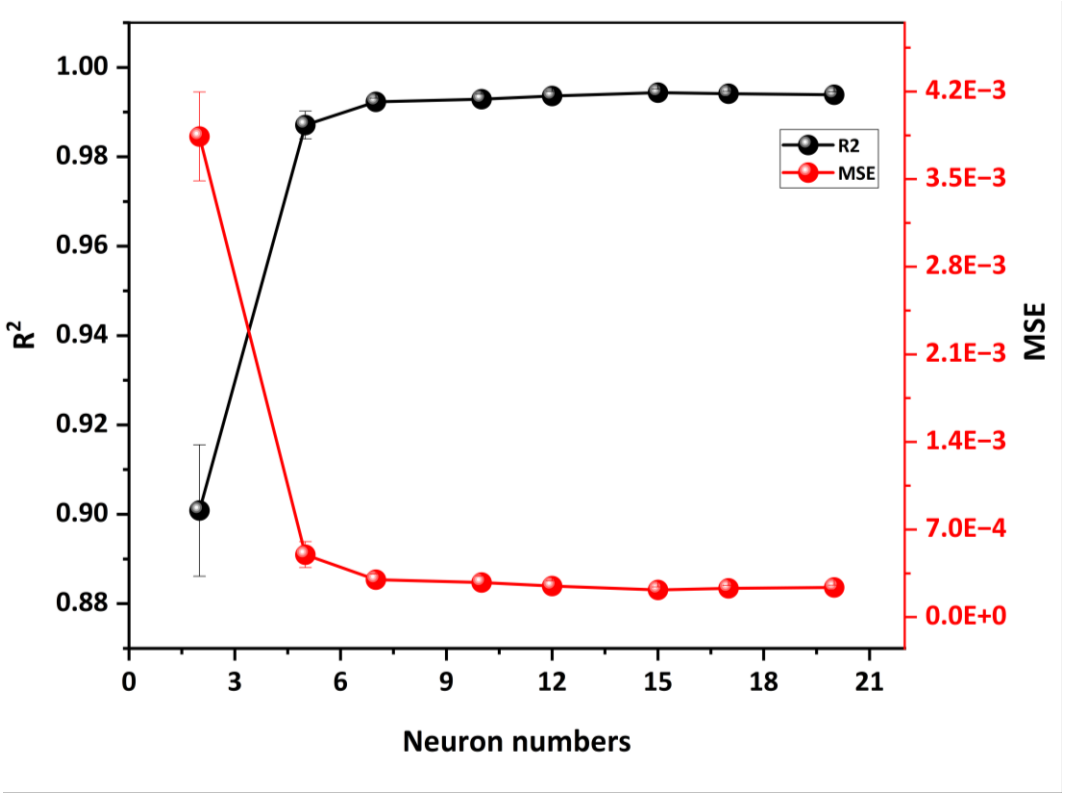

Figure VI.9 Effect of the number of hidden layer neurons on the mean squared error (MSE) and coefficient of determination (R^2) during hyperparameter optimization for the CAT adsorption model

During the optimization of the hidden layer, the number of neurons was systematically varied to balance computational efficiency with predictive power. Increasing the neuron count initially led

to a sharp decrease in the mean squared error (*MSE*) and a corresponding improvement in the R^2 coefficient, as shown in **Figure V.11**. Beyond 15 neurons, the performance metrics plateaued and showed minor fluctuations. This stabilization indicates that a 15-neuron configuration provides optimal network complexity while mitigating the risk of overfitting. Based on the quantitative metrics summarized in **Table V.10**, the most effective configuration utilized the Scaled Conjugate Gradient (trainscg) algorithm. Furthermore, the optimal activation functions were established as the sigmoidal (Logsig) transfer function for the hidden layer and a linear (Purelin) transfer function for the output layer.

VI.9.2 Best model architecture and training convergence

The optimized ANN architecture, illustrated schematically in **Figure VI.10(a)**, consists of an input layer with four nodes corresponding to the independent experimental parameters, a single hidden layer comprising 15 neurons, and an output layer with two nodes predicting the adsorption capacity and removal efficiency.

The training performance metrics for this selected ensemble configuration demonstrate high predictive accuracy. The model achieved a low mean *MSE* of 2.19E-04 and a standard deviation of 2.4E-05, along with a mean R^2 of 0.9944 and a standard deviation of 8E-04. These narrow standard deviations relative to the overall mean values indicate highly stable training performance and robust generalization, confirming that the model is well-equipped to process unseen data without significant mathematical variance.

The learning curve (**Figure VI.10(b)**), which plots MSE versus epoch, illustrates the training convergence behavior across the cross-validation folds. The network exhibits a rapid, steep decline in *MSE* during the initial epochs, followed by stabilization at a minimum threshold. This behavior reflects efficient learning convergence without prolonged oscillation or instability.

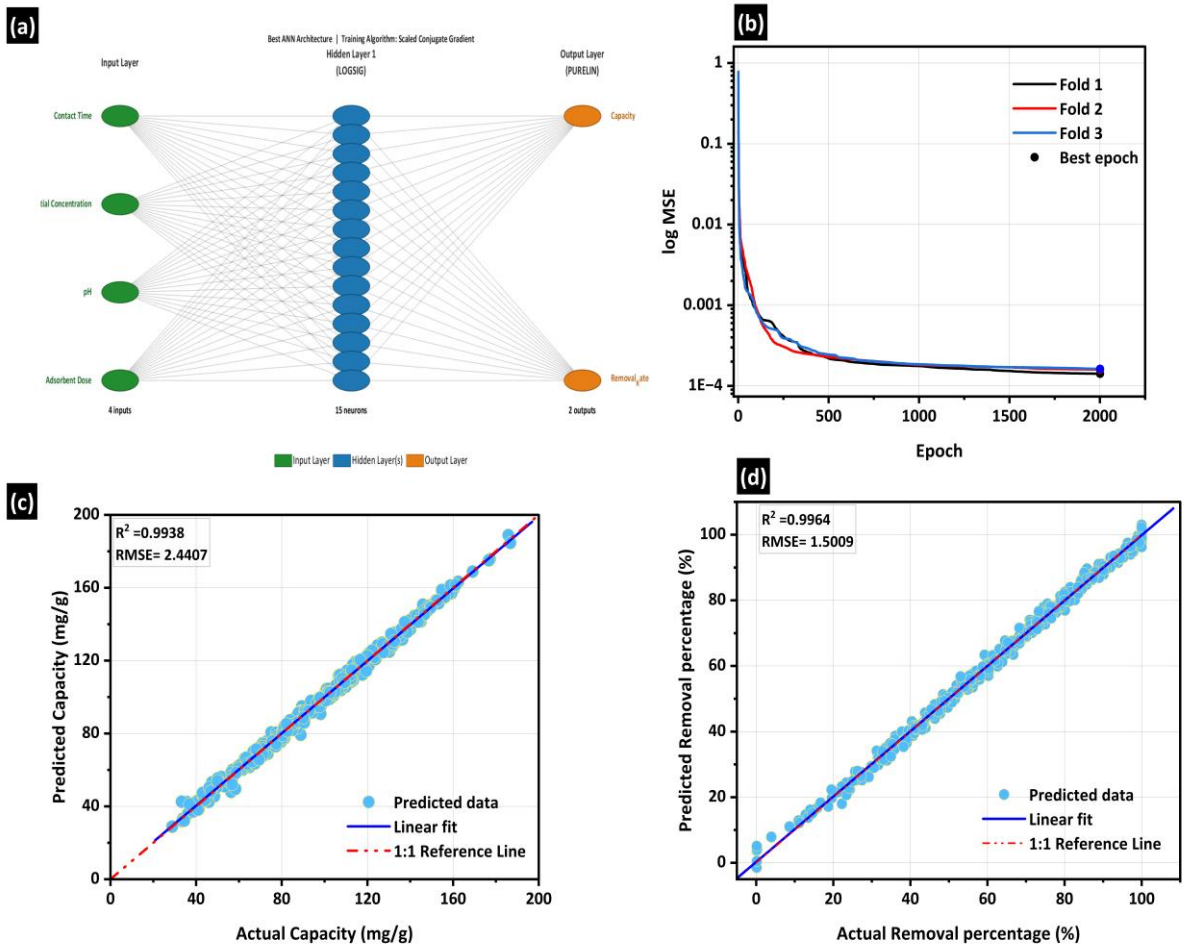

Figure VI.10 Evaluation of the optimized ANN architecture for CAT adsorption: (**a**) schematic representation of the network topology; (**b**) learning curve demonstrating training convergence across cross-validation folds; and scatter plots comparing ANN-predicted values against actual experimental data for (**c**) equilibrium adsorption capacity and (**d**) removal percentage

Table VI.10 Summary of the top 10 ANN configurations evaluated during the systematic grid search for CAT adsorption

N	Algorithm	Code	Neurons	Hidden TF.	Output TF.	Mean MSE	SD MSE	Mean R^2	SD R^2
1	Scaled Conjugate Gradient	trainscg	15	Logsig	Purelin	2.19E-04	2.4E-05	0.99435	8.0E-04
2	BFGS Quasi-Newton	trainbfg	15	Logsig	Purelin	2.24E-04	4.4E-05	0.99419	1.5E-03
3	BFGS Quasi-Newton	trainbfg	17	Tansig	Purelin	2.24E-04	3.5E-05	0.99428	5.4E-04
4	Conjugate Gradient Polak-Ribiere	traincgp	15	Tansig	Purelin	2.25E-04	6.9E-06	0.99424	4.0E-04
5	BFGS Quasi-Newton	trainbfg	17	Logsig	Purelin	2.27E-04	2.6E-06	0.99417	4.2E-04
6	Levenberg-Marquardt	trainlm	10	Tansig	Purelin	2.28E-04	2.2E-05	0.99416	6.9E-04
7	BFGS Quasi-Newton	trainbfg	20	Tansig	Purelin	2.28E-04	4.2E-05	0.99415	9.3E-04
8	Levenberg-Marquardt	trainlm	15	Logsig	Purelin	2.28E-04	2.6E-05	0.99415	6.7E-04
9	Scaled Conjugate Gradient	trainscg	20	Tansig	Purelin	2.29E-04	2.6E-06	0.99408	8.4E-04
10	BFGS Quasi-Newton	trainbfg	12	Tansig	Purelin	2.30E-04	1.7E-05	0.99413	2.9E-04

Note: TF = Transfer Function; SD = Standard Deviation; Code = MATLAB training algorithm function name.

VI.9.3 Predictive accuracy and residual analysis

To further evaluate predictive accuracy, scatter plots were generated comparing the ANN-predicted values against the actual experimental data for each output variable (**Figure VI.10**(**c**,**d**)). The data points cluster tightly along the 1:1 reference line for both outputs, indicating strong quantitative agreement between the experimental results and the network predictions.

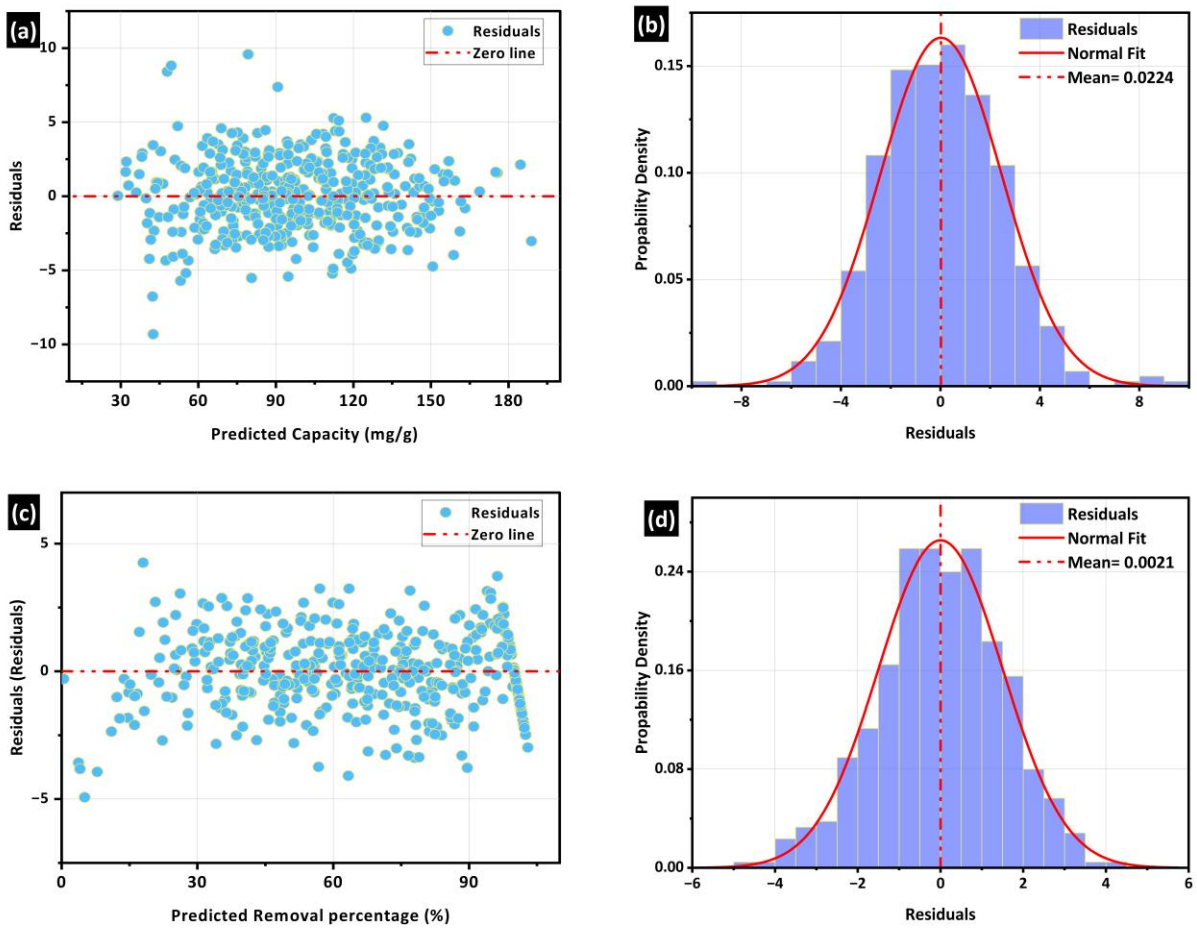

Figure VI.11 Residual analysis of the optimized ensemble model for CAT adsorption: (**a**) residuals versus predicted values and (**b**) residual probability distribution for adsorption capacity; (**c**) residuals versus predicted values and (**d**) residual probability distribution for removal percentage

Residual analysis was subsequently conducted to identify potential systematic errors and verify the model's physical reliability (**Figure VI.11**). The residuals are randomly distributed around the zero line, without discernible geometric patterns. Furthermore, their probability distribution closely approximates a normal distribution centered near zero. This stochastic residual behavior confirms the absence of systematic bias in the network predictions for both the CAT equilibrium adsorption

capacity and removal percentage.

VI.9.4 Cross-validation and model robustness

The robustness of the selected architecture was rigorously validated using a 3-fold cross-validation. **Figure VI.12** presents fold-by-fold performance charts showing R^2 and MSE for both q_e and R across individual folds. The model demonstrated consistent performance across all cross-validation subsets, maintaining high R^2 values and low *MSE*s, with values tightly clustered around the overall ensemble mean. This uniform consistency across independent data segments provides strong statistical evidence against overfitting. It establishes that the trained neural network successfully captured the underlying physical mechanisms of the CAT adsorption process rather than merely memorizing the training dataset.

A distinct two-tier validation strategy was employed. While 3-fold cross-validation was used to tune hyperparameters and select the optimal network architecture, a traditional data partitioning approach divided the dataset into discrete training, validation, and test subsets to train and evaluate the final model. **Figure VI.13(a)** displays the training convergence, revealing that the minimum validation *MSE* (3.8E-4) occurred at epoch 163. The test and validation curves track closely together without diverging at higher epochs, further indicating that the model did not overfit. Regression plots for this specific data split (**Figure VI.13(b)**) confirm robust correlation, yielding correlation coefficients (R) of 0.9942, 0.9956, and 0.9924 for the training, validation, and testing phases, respectively. Finally, the error histogram (**Figure VI.13(c)**) maps the distribution of errors across all three data subsets. The tight clustering of instances around the zero-error line in a standard normal distribution reaffirms the high precision and minimal bias of the optimized neural network.

VI.9.5 Mechanistic insights via sensitivity analysis

To extract mechanistic insights from the computational model, sensitivity analysis was performed using the Garson algorithm to quantify the relative importance of each input parameter on the final predictions (**Figure VI.13(d)**). The analysis revealed that initial *pH* is the most influential variable governing the adsorption process, accounting for 32.8% of the relative importance for adsorption capacity and 36.4% for the removal rate. This high statistical weight directly aligns with the electrostatic interaction mechanisms discussed previously, dictating the speciation of CAT and the surface charge of the ZnO@DPs-AC composite.

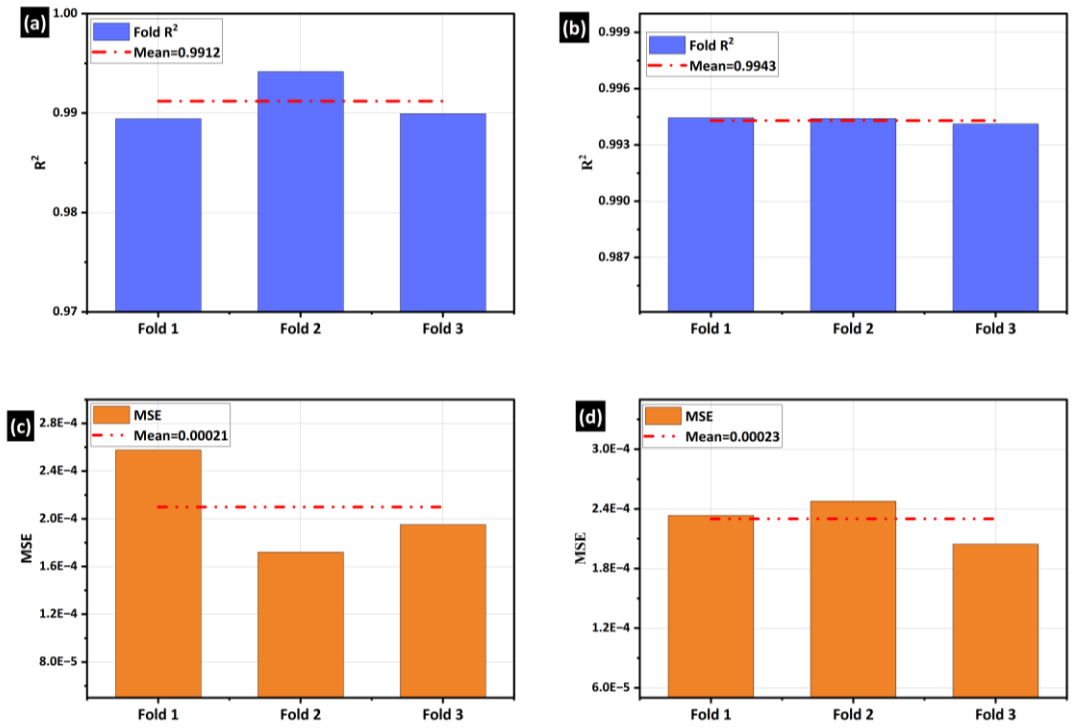

Figure VI.12 Cross-validation performance charts detailing the fold-by-fold validation metrics for CAT adsorption: (**a**) R^2 for adsorption capacity, (**b**) R^2 for removal percentage, (**c**) mean squared error (MSE) for adsorption capacity, and (**d**) MSE for removal percentage

Initial CAT concentration and adsorbent dose were of similar importance, driving the mass transfer gradient and the available active site density, respectively. Conversely, contact time demonstrated the lowest relative significance in determining the final outputs, suggesting rapid equilibrium kinetics.

With its predictive capabilities and physical reliability thoroughly validated, the optimized ANN model is robustly prepared for integration with genetic algorithms, where it will serve as the rigorous evaluation mechanism for the fitness function.

VI.10 Optimization of catechol batch adsorption via genetic algorithm

VI.10.1 Optimization framework and parameter selection for CAT

To establish optimal operational parameters for batch adsorption of CAT onto the ZnO@DPS-AC composite, a multi-objective optimization was performed using the Non-dominated Sorting Genetic Algorithm II (NSGA-II) with an island model architecture. The primary objective of this computational framework was to maximize adsorption capacity and removal efficiency simultaneously.

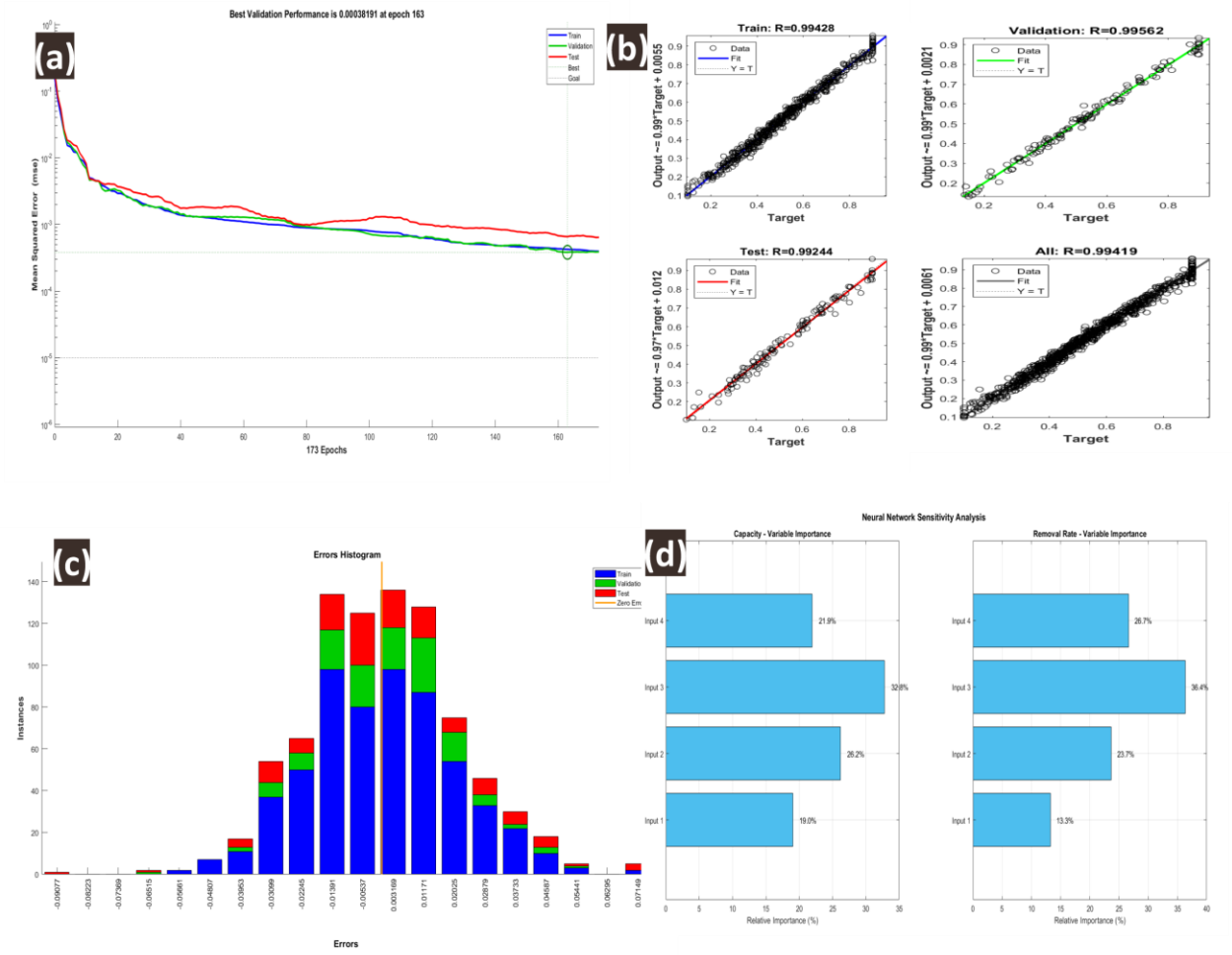

Figure VI.13 Comprehensive performance evaluation of the optimized ANN configuration: (**a**) MSE convergence versus epoch during the training, validation, and testing phases; (**b**) regression plots for data subsets; (**c**) error histogram across all data partitions; and (**d**) mechanistic sensitivity analysis via the Garson algorithm evaluating the relative importance of independent input variables

The efficacy of evolutionary algorithms depends heavily on precise hyperparameter tuning. Accordingly, a systematic grid search was executed to evaluate three fundamental variables: mutation rate, crossover rate, and population size. Evaluating three distinct levels for each parameter yielded 27 unique algorithmic configurations. To rigorously isolate the most effective setup, a multi-criteria composite scoring system was implemented. This system assessed each configuration across five weighted statistical metrics: hypervolume (35%), Pareto front size (20%), spacing uniformity (20%), spread (15%), and convergence speed (10%).

Figure VI.14 details the outcomes of this evaluation. **Figure VI.14**(**a**) presents hypervolume heatmaps illustrating the variance across the tested hyperparameters, whereas **Figure VI.14**(**b**) ranks

all 27 configurations based on their composite scores. The configuration achieving the highest composite score was strictly designated as the baseline framework for all subsequent optimization runs.

The highly non-linear interaction between CAT molecules and the heterogeneous surface of the ZnO@DPS-AC composite requires an algorithm capable of escaping local optima. Thus, this systematic hyperparameter selection protocol ensures a sufficiently diverse computational search space while maintaining underlying mathematical stability.

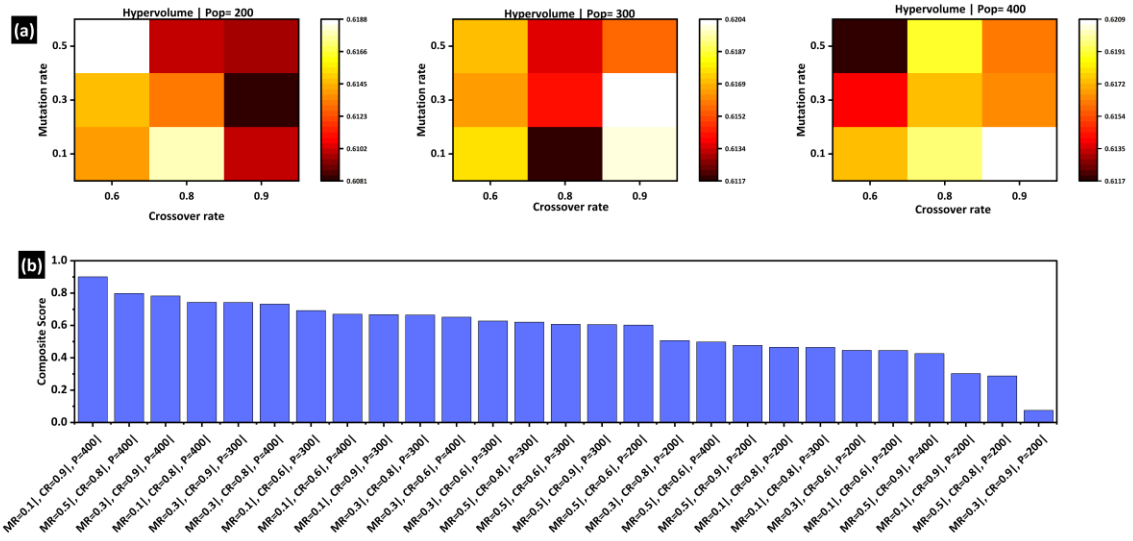

Figure VI.14 Comprehensive evaluation of Genetic Algorithm grid search parameters for CAT adsorption: (**a**) hypervolume heatmaps across varying population sizes, crossover rates, and mutation rates, and (**b**) ranking of the 27 evaluated configurations based on their overall composite scores

VI.10.2 Convergence and optimization dynamics of the CAT system

The evolutionary dynamics of the optimized GA configuration exhibited highly stable convergence toward the true Pareto-optimal front. As illustrated in **Figure VI.15**(**a**), the progression of the best and average values for both adsorption capacity and removal efficiency stabilized predictably across successive computational generations. Furthermore, the hypervolume metric displayed rapid initial growth prior to reaching a definitive plateau (**Figure VI.15**(**b**)), mathematically confirming successful algorithmic convergence.

The integrated island-model topology effectively maintained genetic variance throughout the entire optimization sequence (**Figure VI.15(d)**). This specific structural feature prevented premature convergence, ensuring an exhaustive exploration of the physical boundary conditions governing the adsorption system. Secondary statistical indicators—such as the generational expansion of the Pareto front size (**Figure VI.16(a)**), periodic generation-to-generation improvements (**Figure VI.16(b)**), spacing uniformity (**Figure VI.16(c)**), and solution spread (**Figure VI.16(d)**)—further substantiate the mathematical robustness of the algorithm. Together, these metrics verify the attainment of global optimization without the need for forced restart mechanisms.

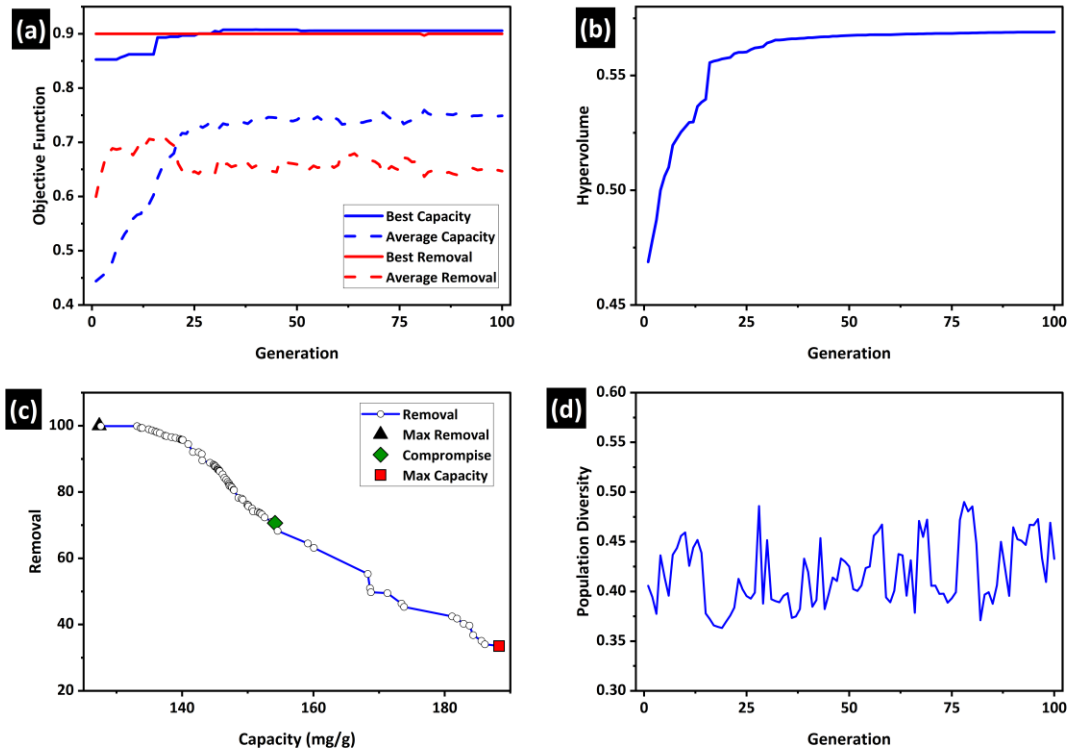

Figure VI.15 Evolutionary dynamics of the multi-objective optimization for CAT adsorption: (**a**) progression of the best and average values for adsorption capacity and removal efficiency, (**b**) hypervolume progression, (**c**) final Pareto front highlighting representative optimal solutions, and (**d**) population diversity across generations

VI.10.3 Pareto front analysis for the CAT adsorption

Building on the previously established convergence dynamics, the genetic algorithm successfully identified the true Pareto-optimal front for the CAT adsorption system. As detailed in the preceding analysis of convergence metrics and genetic variance (see **section VI.10.2**), the prevention of premature convergence ensured an exhaustive exploration of the operational boundary conditions. The resulting frontier, depicted in **Figure VI.15(c)**, maps the continuum of non-dominated solutions and explicitly defines the fundamental trade-off between maximizing specific adsorption capacity and overall removal efficiency. This comprehensive mathematical solution space serves as the requisite foundation for extracting targeted operational parameters.

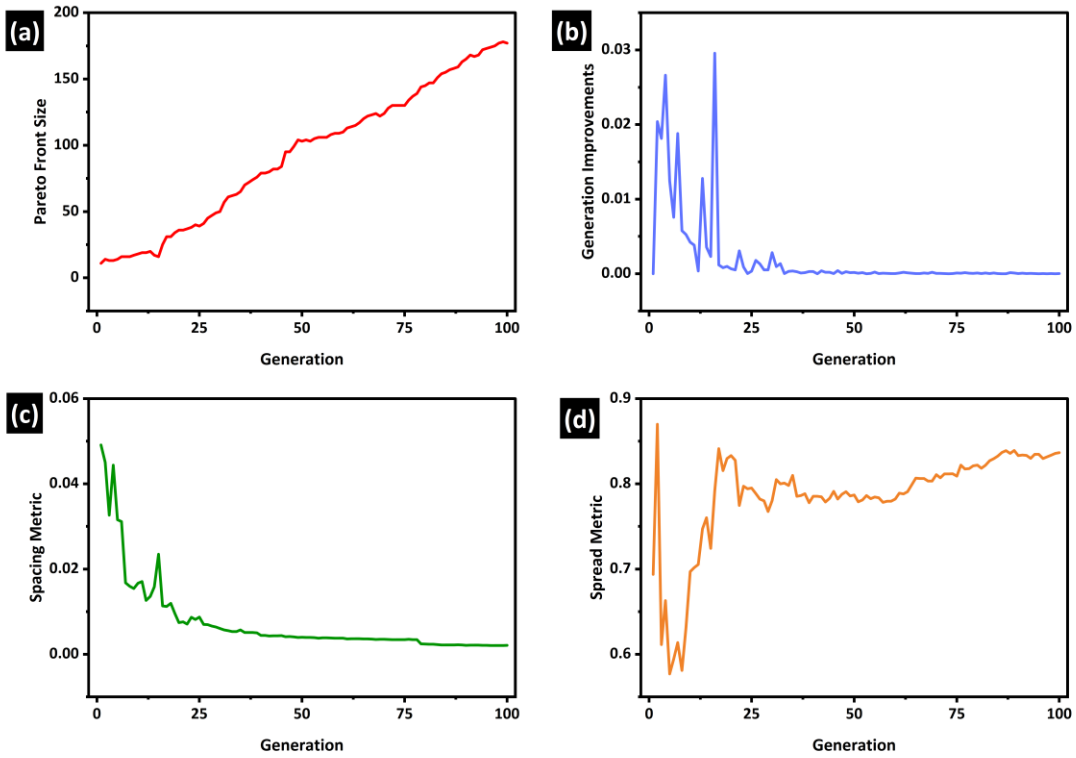

Figure VI.16 Progression of key multi-objective optimization metrics over generations during catechol adsorption: (**a**) Pareto front size, (**b**) generation-to-generation improvements, (**c**) spacing metric, and (**d**) spread metric

VI.10.4 Optimal adsorption conditions for CAT adsorption

To translate the theoretical computational findings into actionable engineering parameters, three representative solutions were extracted from the final Pareto front: maximum capacity, maximum removal, and a balanced compromise. **Table VI.11** delineates the specific operational configurations—contact time, initial concentration, pH, and adsorbent mass—that dictate these outcomes.

Table VI.11 Optimal batch adsorption conditions derived from the Genetic Algorithm for three representative Pareto solutions for CAT: maximum capacity, maximum removal rate, and the compromise solution

Solution Type	q_e (mg/g)	R (%)	t (min)	C_0 (mg/L)	pH	m (mg)
Max q_e	188.31	33.48	239.93	250.00	5.92	10.00
Max R	127.38	100.00	240.00	229.28	5.61	90.00
Compromise	154.14	70.61	240.00	250.00	6.19	50.01

Maximum Capacity: Driven by fundamental mass-transfer principles, the peak capacity solution (188.31 mg/g) requires an elevated initial CAT concentration (250.00 mg/L) and a strictly limited adsorbent mass (10.00 mg). The rapid exhaustion of available active sites under these conditions inherently constrains the overall removal efficiency to 33.48%.

Maximum Removal: Conversely, complete pollutant elimination (100.00%) necessitates a significant expansion of the available active surface area, requiring an adsorbent dosage of 90.00 mg. This stoichiometric surplus fundamentally reduces the localized specific capacity to 127.38 mg/g.

Compromise Solution: To balance material resource efficiency with practical environmental compliance, the compromise solution establishes an optimal operational state. This configuration achieves an adsorption capacity of 154.14 mg/g and a 70.61% removal efficiency by utilizing an intermediate adsorbent dosage of 50.01 mg.

Notably, across all three operational scenarios, the algorithm consistently converged upon a moderately acidic environment ($pH \approx 6.0$) and extended contact times (approaching 240 min). This computational alignment directly corresponds to the kinetic equilibrium thresholds and point of zero charge dependencies established during the preliminary batch evaluations. Consequently, these results

validate the algorithm's mathematical capacity to identify the exact physicochemical parameters required to maximize electrostatic attraction while preventing competitive hydronium interference.

VI.10.5 Experimental validation

To definitively validate the predictive accuracy and practical applicability of the developed NSGA-II computational framework, a confirmatory physical experiment was conducted under the exact operational parameters determined for the compromise solution. The laboratory evaluation yielded an equilibrium adsorption capacity of 158.77 mg/g and a final removal percentage of 63.52%. Compared with the algorithmically predicted values (q_e = 154.14 mg/g and R = 70.61%), the experimental observations show strong agreement. The relative errors between the actual and predicted values were 3.00% for the adsorption capacity and approximately 10.04% for the overall removal efficiency. This empirical correlation rigorously validates the mathematical robustness and precision of the integrated ANN-GA model, confirming its capability to reliably translate complex, multi-objective computational predictions into viable engineering parameters for phenolic wastewater treatment.

VI.11 Mechanistic insights into catechol adsorption

The adsorption of CAT by the ZnO–modified DPS-activated carbon proceeds via a complex, multi-pathway process. The structural hierarchy, surface chemistry, and engineered active sites of the composite strictly dictate this mechanism. Comprehensive physicochemical characterizations and batch equilibrium evaluations (**section VI.4**) validate that adsorption proceeds through a synergistic combination of pore-filling, hydrogen bonding, π–π interactions, and inner-sphere surface complexation as outlined below and comprehensively illustrated in **Figure VI.17**.

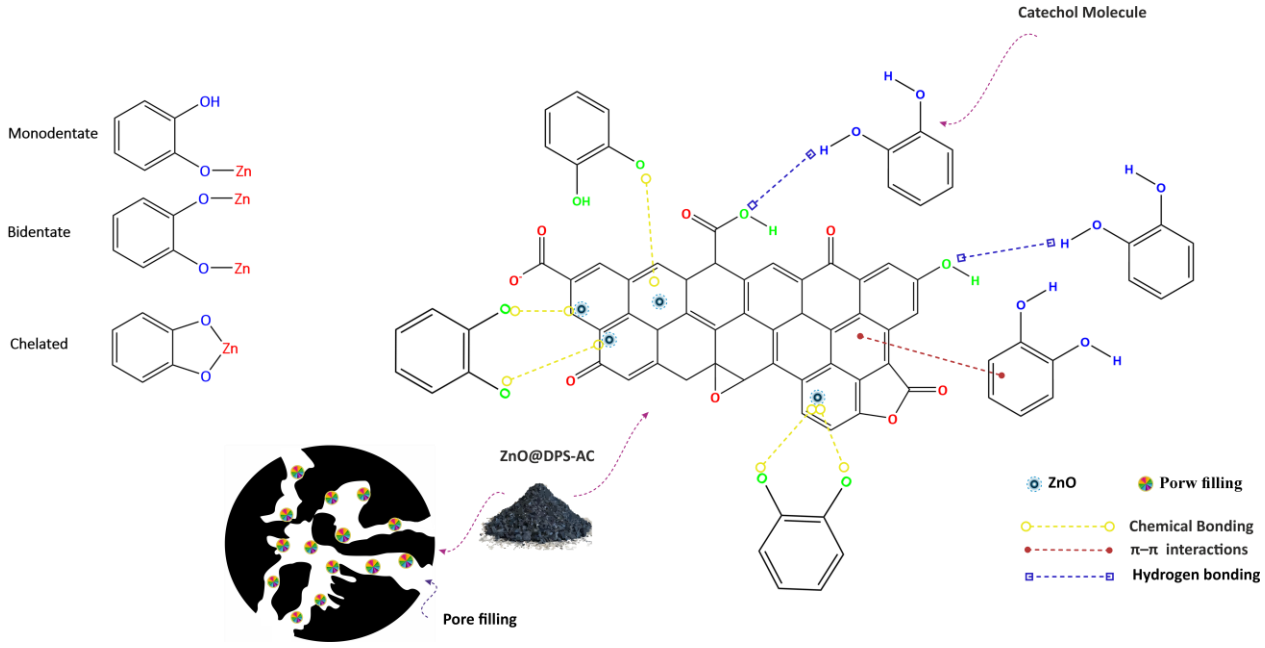

Figure VI.17 Schematic illustration of the proposed physicochemical mechanisms for the adsorption of catechol onto the hierarchical ZnO@DPS-AC composite

VI.11.1 Pore-filling mechanism

Textural analysis yields direct physical evidence that pore-filling operates as a primary physical adsorption mechanism. Upon reaching equilibrium, the specific surface area of the composite declined significantly from 1028.63 m^2/g to 589.13 m^2/g. This reduction coincides with a near-total depletion of the measurable micropore volume, which decreased from 0.159 cm^3/g to 0.050 cm^3/g. Because CAT possesses relatively small molecular dimensions and low steric hindrance, the adsorbate diffuses effectively into the carbonaceous skeleton. It packs densely within the internal micro- and mesoporous cavities without causing complete pore-mouth occlusion (as detailed in **section IV.9**). This physical behavior aligns with the findings of Suresh et al. (2011b), who utilized scanning electron microscopy and textural analysis to confirm the progressive filling of internal voids by CAT molecules within GAC networks. The diffusion and subsequent physical entrapment of CAT molecules within the hierarchical mesoporous and microporous cavities are geometrically represented in **Figure VI.17**.

VI.11.2 Hydrogen bonding

FTIR spectroscopy provides definitive confirmation of extensive hydrogen bonding between the adsorbate and the carbon interface. Following adsorption, the most pronounced spectral transformation is the near-total attenuation of the broad –OH stretching band between 3000 and 3500

cm–1 (Figure IV.4). This severe signal reduction indicates that the surface hydroxyl groups of the ZnO@DPS–AC composite are fully occupied. These groups act as primary binding loci, forming hydrogen bonds with the adjacent phenolic hydroxyl groups of the target CAT molecules.

This spectral shift is rigorously supported by contemporary literature. Suresh et al. (2011b) similarly attributed the complete disappearance of surface –OH bands in FTIR spectra to hydrogen-bonding interactions between the CAT and GAC surfaces. Additionally, cooperative hydrogen-bonding mechanisms between the neighboring hydroxyl groups of CAT and surface hydroxyls have been reported by Bayram et al. (2009) for activated carbon cloth and by Yeh et al. (2015) for pristine alumina substrates. This hydrogen-bonding network—specifically involving the adjacent hydroxyl (-OH) groups of the catechol molecule, acting as donors/acceptors, with the oxygen-containing functionalities of the composite—is visually summarized in **Figure VI.17**.

VI.11.3 Inner-sphere surface complexation

Spectroscopic and thermodynamic data confirm direct chemical interactions between CAT molecules and the embedded ZnO active sites. Post-adsorption FTIR spectra show distinct intensity shifts in the 500-400 cm^{-1} frequency range, corresponding directly to Zn–O lattice vibrations. Raman spectroscopy further indicates a transition from broad amorphous carbon bands to highly resolved vibrational modes. This spectral sharpening verifies the chemical anchoring of CAT to the active sites in a rigid coordination geometry, forming stable catecholate-zinc complexes. Crystallographic analysis corroborates this complexation, evidenced by the enhanced diffraction intensity of the (010) plane in the hexagonal wurtzite ZnO crystal system (**Figure IV.5**).

Macroscopic performance metrics support the formation of these stable chemisorptive bonds. Specifically, the limited regeneration efficiencies documented during cyclic desorption studies (**section VI.7**) indicate strong chemical affinities. The highly positive enthalpy values (ΔH°) calculated from the Langmuir, Redlich-Peterson, and Khan models provide thermodynamic validation (**Table VI.4**). This adsorption mechanism aligns with established interactions for metal oxides. The observed behavior mirrors the findings of Gulley-Stahl et al. (2010), Finkelstein-Shapiro et al. (2016), and Yang et al. (2012), who demonstrated the formation of highly stable binuclear bidentate surface complexes between CAT and specific metal oxides, including TiO_2 and goethite.

The specific transition between monodentate, bidentate, and chelated surface complexes depends on the adsorbent's structural properties and the adsorbate's steric geometry. Mononuclear monodentate binding is kinetically rapid on well-ordered stoichiometric mineral surfaces, often serving as the initial adsorption state (Terranova & Bowler, 2010; Yang et al., 2012). However, surface defects (such as oxygen vacancies or undercoordinated metal sites) supply a thermodynamic driving force that stabilizes dissociative bidentate and chelated geometries (Finkelstein-Shapiro et al., 2016; Terranova & Bowler, 2010). The molecular structure of the adsorbate dictates these allowable configurations. The adjacent ortho-hydroxyl groups of catechol offer the flexibility required to form stable binuclear bidentate or chelating complexes on the ZnO sites. In contrast, para-substituted phenolics are sterically restricted to monodentate interactions (Abugazleh et al., 2020).

Extrinsic physicochemical conditions (notably solution pH, adsorbate concentration, and contact time) dynamically drive the transition between these binding modes. Monodentate complexes typically predominate at acidic to neutral *pH* and at low surface coverages. As established previously in **section VI.2.2**, increasing the solution *pH* initiates the deprotonation of the phenolic hydroxyl groups. This deprotonation enables the second oxygen atom to bind to the metal surface, converting the initial monodentate complex into a bidentate structure. Elevated initial adsorbate concentrations further enhance surface coverage. This dense coverage promotes bidentate complexation through stabilizing substrate-mediated intermolecular attractions. Because adsorption remains a dynamic process, initially formed monodentate structures progressively transition into bidentate configurations over extended contact times when the localized *pH* and concentration gradients are favorable (Yang et al., 2012). The direct coordination between the oxygen atoms of the catechol molecule and the embedded ZnO active centers is explicitly highlighted in the schematic **Figure VI.17**.

VI.11.4 π–π electron-donor-acceptor interactions

As illustrated by the molecular alignments in **Figure VI.17**, strong non-covalent π–π attractions arise between the electron-rich aromatic ring of the catechol molecule and the localized graphitic planes of the activated carbon matrix. This attractive force occurs solely between the delocalized π-electrons of the aromatic rings in the ZnO@DPS–AC basal planes and the aromatic phenylene ring of the approaching CAT molecules.

The graphitic framework of the activated carbon matrix functions as a primary platform for electron-donor-acceptor interactions. This attractive force occurs between the delocalized π–electrons of the ZnO@DPS–AC basal planes and the aromatic phenylene rings of the approaching CAT molecules.

Controlled H_2O_2 oxidation isolated and validated this specific mechanism by introducing excess oxygen functional groups onto the composite surface. This targeted oxidation reduces the π–electron density across individual graphene layers, subsequently weakening the π–π dispersion forces. As theoretically anticipated, the equilibrium adsorption capacity of CAT onto the oxidized ZnO@DPS–AC composite declined significantly relative to that of the pristine material (**Figure VI.18**). This capacity reduction unequivocally underscores the physical significance of π–π interactions in the overall pollutant capture mechanism. These findings are highly consistent with Bayram et al. (2009), who established that dispersive interactions between surface carbon charges and the π–electrons of aromatic adsorbates heavily govern the uptake of phenolics.

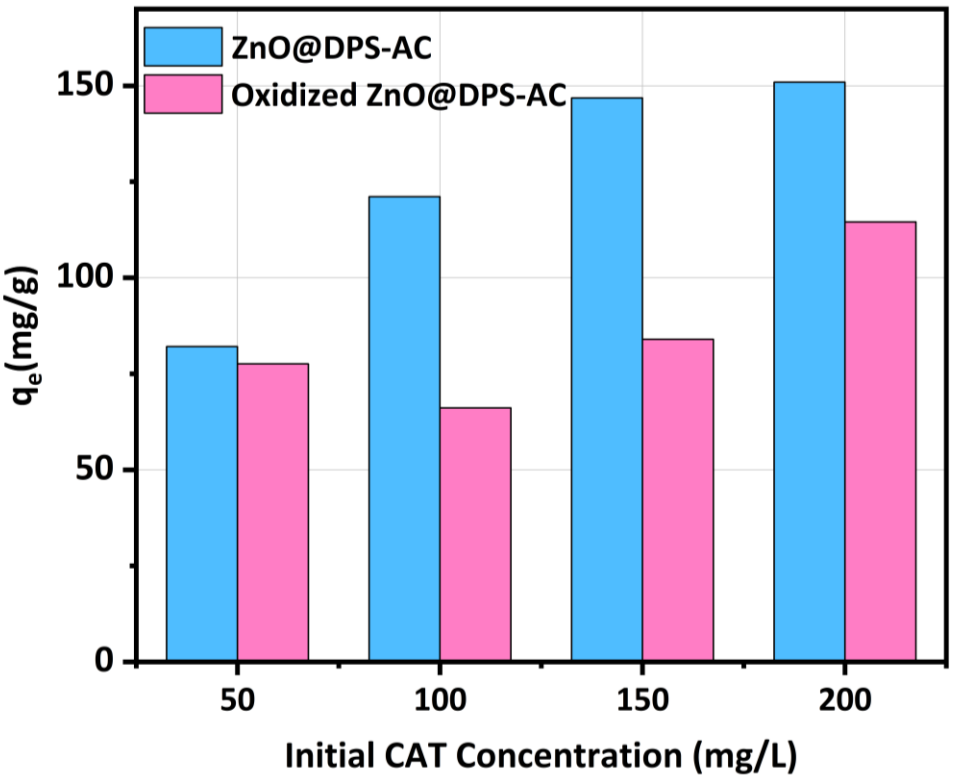

Figure VI.18 Comparison of equilibrium adsorption capacity between pristine ZnO@DPS-AC and oxidized ZnO@DPS-AC

VI.11.5 Role of electrostatic interactions

Although electrostatic forces frequently govern the adsorption of charged species, they exert a negligible influence on the initial capture of CAT by the ZnO@DPS–AC composite. Because the operational *pH* remains strictly below the pKa_1 of catechol (as detailed in **section VI.2.2** and **Figure VI.1(b)**, the adsorbate exists entirely in its non-ionized, neutral state. Consequently, classical electrostatic attraction does not occur between the bulk CAT molecules and the functionalized carbon matrix below the pKa_1.Ionic-strength evaluations (**section VI.2.3** and **Figure VI.1**(a)) empirically confirm the theoretical absence of electrostatic governance. While elevated background salinity slightly decreased the equilibrium adsorption capacity, this minor reduction is solely due to physical active-site competition and localized salting-out effects. It does not indicate the severe electrical double-layer compression typically associated with the repulsion of ionized pollutants.

VI.1 Conclusion

This chapter evaluated the adsorptive performance of the engineered ZnO@DPS-AC composite for CAT adsorption. CAT is a low-molecular-weight, hydroxyl-rich phenolic intermediate structurally distinct from the anionic dye investigated in **Chapter V**. Empirical evidence confirms that the hierarchical carbon matrix and embedded ZnO active sites readily adapt their binding chemistry to remediate fundamentally different classes of organic contaminants.

The composite demonstrates robust CAT adsorption, maximized under near-neutral to mildly acidic conditions (*pH* 6-8), consistent with its pH_{pzc} of 6.67. High uptake capacities, reaching a Langmuir-derived maximum of 140-170 mg/g, position this material competitively against most existing activated carbon adsorbents. Kinetic and equilibrium analyses characterize a highly favorable, endothermic process exhibiting an H-type isotherm profile. Uptake follows FSO kinetics ($Adj\text{-}R^2$ = 0.993), and the Vermeulen model validates intraparticle diffusion as a dominant mass transfer mechanism. Thermodynamic data yield consistently negative $\Delta G°$ values and $\Delta H°$ values ranging from 42.27 to 110.16 kJ/mol, depending on the specific isotherm framework used. These energetics denote a hybrid interaction combining strong physisorption and chemisorption, a profile typical of metal oxide-carbon composites.

A synthesized mechanistic evaluation confirms four concurrent adsorption pathways: pore-filling within the hierarchical network, extensive hydrogen bonding, π-π electron-donor-acceptor

interactions, and inner-sphere surface complexation. This complexation occurs via the direct coordination of catecholate oxygen atoms with embedded ZnO metallic centers. Notably, the composite maintains its performance across ionic strengths up to 0.2 M NaCl. This insensitivity to low-salinity conditions validates inner-sphere complexation, and the other mechanisms are the primary initial binding modes. As a result, the material proves highly viable for treating saline or brackish industrial effluents where electrostatically driven adsorbents typically fail.

Advanced computational models transcended standard univariate batch analysis to map the non-linear interaction space. Robust RSM-CCD quadratic models (R^2 = 0.9863 for capacity; R^2 = 0.9949 for removal) identified initial concentration, adsorbent dosage, and *pH* as primary system drivers. An optimized Artificial Neural Network architecture (4-15-2 topology, traincgda algorithm, R^2 = 0.9944, MSE = 2.19×10^-4) provided a continuous surrogate fitness function for NSGA-II GA optimization. This ANN-GA framework isolated a stable operational state (*pH* 6.19, 50.01 mg dosage, 250 mg/L initial concentration, 240 min contact time), predicting a capacity of 154.14 mg/g and a 70.61% removal efficiency. Experimental validation confirmed these predictions within a 10% relative error. Furthermore, utilizing RSM-augmented data to ensure adequate topological density establishes an effective modeling strategy for adsorption systems constrained by limited experimental data.

While strong chemical coordination bonds confer exceptional binding affinity, they pose distinct operational challenges. Ambient chemical regeneration proved only marginally effective, recovering substantially less capacity than the initial cycle. This performance deficit highlights the necessity for high-energy thermal regeneration protocols to establish an economically viable, closed-loop treatment cycle.

Ultimately, the empirical and computational findings of this chapter establish the structural and chemical versatility of the ZnO@DPS-AC composite. The material effectively sequesters both large anionic dyes and small, neutral phenolic intermediates through entirely distinct interaction paradigms. Building upon these foundations, **Chapter VII** introduces a third, fundamentally different pollutant class. The subsequent phase evaluates the batch adsorption of acetamiprid, a cyanoimine-based neonicotinoid pesticide. This investigation will characterize how the composite's active sites interact with a recalcitrant, nitrogen-rich agrochemical, introducing new competitive binding chemistry and unique environmental remediation challenges.

Chapter VII: Batch Adsorption of Acetamiprid onto ZnO@DPS-AC: Modeling, Optimization, and Mechanisms

* * * * *

VII.1 Introduction

The structural versatility of the engineered ZnO@DPS-AC composite has been validated against large anionic dyes (**Chapter V**) and reactive phenolic intermediates (**Chapter VI**). However, a comprehensive evaluation of an agricultural waste-derived adsorbent remains incomplete without addressing contaminants directly associated with agricultural runoff. Consequently, this chapter transitions to the remediation of ACE, a cyanoimine-based neonicotinoid pesticide recognized for its severe environmental persistence and high aqueous solubility. Evaluating ACE at this specific stage of the thesis is strictly necessary to ascertain how the hierarchical porosity and metallic active sites of the composite interact with complex, nitrogen-rich agrochemicals that exhibit fundamentally distinct steric and electronic profiles compared to industrial pollutants.

To rigorously assess the adsorptive efficacy for ACE, this chapter systematically investigates the impact of primary operational variables, including initial solution pH, adsorbent dosage, ionic strength, contact time, and initial pesticide concentration. The progression follows the standardized analytical framework established in preceding chapters. The dynamics of the solid-liquid interface are initially evaluated using kinetic modeling and equilibrium isotherm analysis, followed by a detailed thermodynamic assessment to determine the energetic nature of the ACE adsorption process. The practical viability and structural robustness of the composite are subsequently tested through cyclic desorption and regeneration protocols. Advancing beyond conventional univariate analysis, the multivariable adsorption process is optimized by comparing the response surface topologies generated via RSM with the high-fidelity predictive modeling capabilities of an ANN coupled with GA. Ultimately, by integrating empirical and statistical data, this chapter elucidates the specific physicochemical mechanisms governing the sequestration of ACE at the composite interface.

VII.2 Effect of operational parameters

VII.2.1 Effect of adsorbent mass

The influence of the ZnO@DPS-AC composite dosage on ACE removal was investigated by

varying the adsorbent mass from 15 to 200 mg, as illustrated in **Figure VII.1(a)**. The experimental data revealed a clear inverse relationship between R (%) and q_e (mg/g). Specifically, the removal efficiency increased substantially from 49.75% at 15 mg to 98.0% at 100 mg. Upon further increasing the dosage beyond 100 mg, the removal efficiency plateaued at 100%, indicating the complete elimination of the pollutant from the aqueous phase. Conversely, the specific q_e declined progressively as the adsorbent mass increased.

The observed trend (enhanced removal efficiency accompanied by reduced specific uptake at higher dosages) is consistent with the behavior reported for various carbon-based adsorbents in the literature. For instance, Dolatabadi et al. (2021) observed that increasing the dosage of pistachio shell-based modified activated carbon (MAC) from 100 to 300 mg/L improved ACE removal from 65.5% to 91.6%. Similarly, Kumar et al. (2025) reported that for a zinc peroxide-activated carbon (ZnO_2-AC) composite, the removal efficiency rose rapidly with dosage until reaching a plateau at 55 mg, after which no significant improvement was observed. This pattern was further corroborated by Mohammad and Ahmed (2019) using orange peel- and almond-shell-activated carbons, where increased dosage led to greater availability of exchangeable sites. Ali et al. (2026) also noted that removal efficiencies for neonicotinoids plateaued once the adsorbent dose provided sufficient sites for near-complete adsorption.

The initial increase in removal percentage is attributed to the expansion of available surface area and the proliferation of active binding sites associated with the composite's higher mass (Srikhaow et al., 2022). At higher dosages, the ratio of surface-active sites to ACE molecules is elevated, thereby facilitating rapid adsorbate uptake. However, the concurrent decrease in specific q_e can be explained by a split in the mass flux and a reduced concentration gradient driving force. As the adsorbent mass increases while the initial ACE concentration remains constant, the amount of adsorbate captured per unit weight of adsorbent decreases because a significant portion of the active sites remains unsaturated. Furthermore, at high solid-to-liquid ratios, particle aggregation may occur. This aggregation reduces the total effective surface area and increases the diffusion path length, thereby diminishing the specific uptake per unit mass (AlNeyadi et al., 2026; Dolatabadi et al., 2021).

Notably, the ZnO@DPS-AC composite synthesized in this study achieved a 100% removal efficiency, demonstrating superior performance compared to several alternative adsorbents

reported in the literature. For example, Srikhaow et al. (2022) reported a maximum ACE removal efficiency of only 16.0% for eucalyptus woodchip-derived biochar, even at high adsorbent loadings (5 g/L). Furthermore, while the ZnO_2-AC composite reported by Kumar et al. (2025) achieved a comparable 99.3% removal, the current system realizes complete elimination (100%) at dosages exceeding 100 mg. This superior performance suggests that integrating ZnO into the DPS-AC matrix minimizes steric hindrance and enhances the accessibility of active binding sites when compared to pristine agricultural waste-derived chars.

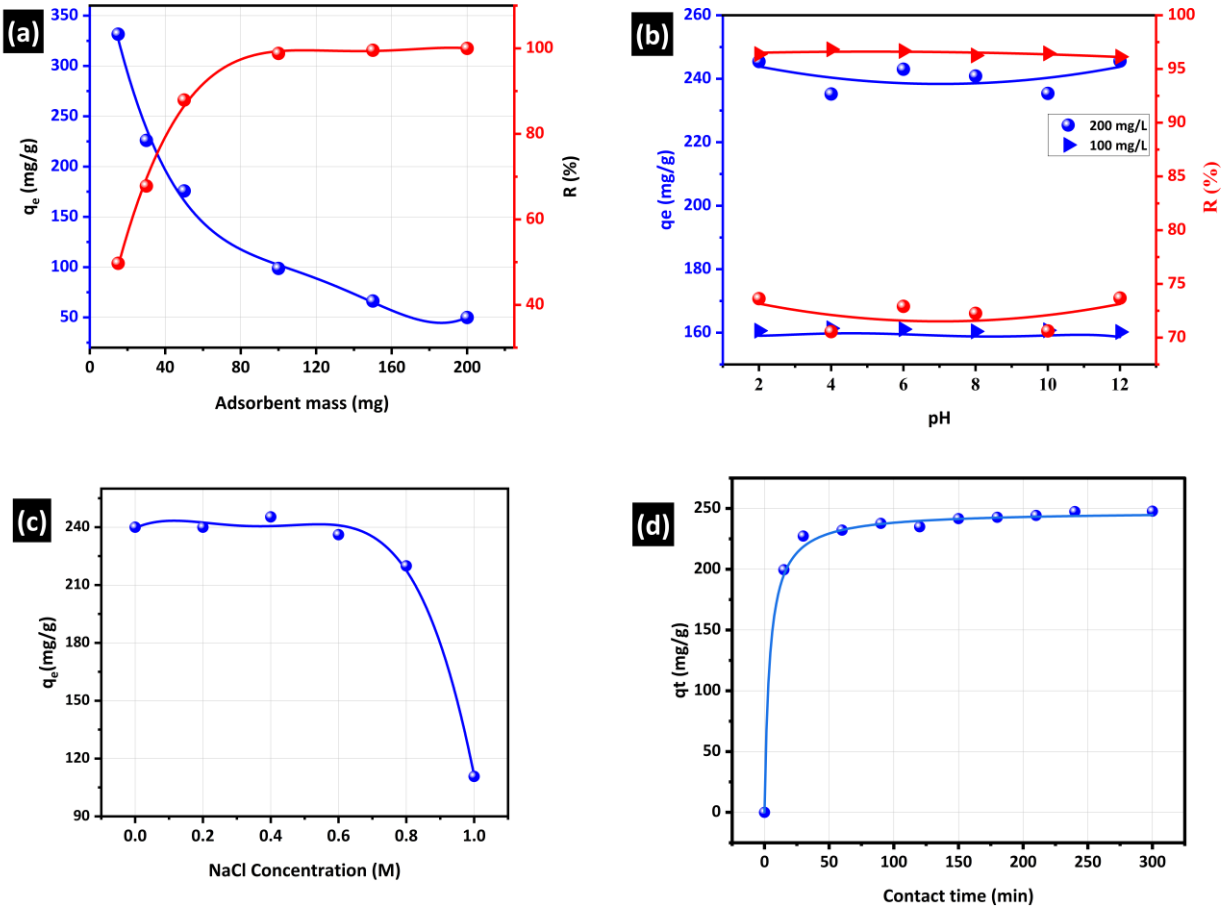

Figure VII.1 Influence of operating parameters on ACE adsorption onto ZnO@DPS-AC: (**a**) effect of adsorbent mass, (**b**) effect of initial solution pH, (**c**) effect of ionic strength, and (**d**) effect of contact time

VII.2.2 Effect of initial solution *pH*

The influence of initial solution *pH* on the adsorption of ACE onto the ZnO@DPS-AC composite

was evaluated over a broad *pH* range (2-12) at two initial concentrations (100 and 200 mg/L). As depicted in **Figure VII.1(b)**, the removal efficiency and equilibrium q_e exhibited negligible variation across the entire *pH* interval studied. Specifically, the capacity stabilized at approximately 160 mg/g for C_0 = 100 mg/L and remained near 240 mg/g for C_0 = 200 mg/L, regardless of bulk acidity or alkalinity. This trend indicates that the adsorption performance of the ZnO@DPS-AC composite toward ACE is fundamentally independent of the solution *pH*.

The *pH*-independent behavior observed in this system is primarily attributed to the specific ionization characteristics of the ACE molecule and the dominant binding mechanisms. ACE has a very low *pKa*≈of 0.7 (Dolatabadi et al., 2021; Srikhaow et al., 2022). Consequently, within the experimental range of *pH* 2 to 12, the pesticide exists predominantly in its molecular (non-protonated) form rather than as a cationic or anionic species (Wang et al., 2016). Because the adsorbate remains electronically neutral, electrostatic forces (whether attractive or repulsive) between the ACE molecules and the functional groups on the adsorbent surface are minimized.

This neutrality suggests that the removal mechanism is governed principally by non-electrostatic interactions. These interactions include physical pore filling and π–π electron donor-acceptor interactions between the aromatic pyridine ring of ACE and the graphitic structure of the activated carbon matrix (Srikhaow et al., 2022; Yao et al., 2024). Additionally, the structural stability of the ZnO@DPS-AC composite ensures that its surface-active sites (which are likely rich in delocalized π−electrons) remain accessible and unaltered by the concentration of hydronium or hydroxide ions in the bulk solution.

This finding of *pH* independence aligns with specific studies on carbonaceous adsorbents but contrasts with others, thereby highlighting the unique stability of the ZnO@DPS-AC composite. These results are corroborated by Razavi et al. (2022), who reported that the adsorption efficiency of ACE onto graphene oxide and multi-walled carbon nanotubes was independent of *pH*, attributing this behavior to the stability of the carbon nanostructures and the neutral state of the pesticide. Similarly, Yao et al. (2024) observed that while the pH_{pzc} of KOH-modified biochar was 9.2, it had no significant effect on ACE adsorption; the pesticide remained nonionic, sustaining high removal efficiencies (>90%) from *pH* 2 to 10.

In contrast, Dolatabadi et al. (2021) reported a significant decline in ACE removal by pistachio

shell-based activated carbon at alkaline *pH* (>7.3), attributing the loss in efficiency to electrostatic repulsion between the negatively charged carbon surface and anionic species. Furthermore, Ali et al. (2026) observed that amide-functionalized silica exhibited optimal removal strictly at *pH* 6. This discrepancy is logical given the material differences; functionalized silica experiences significant efficiency losses in acidic and alkaline conditions due to the protonation of surface amides and hydroxide competition, respectively.

The fact that ZnO@DPS-AC maintains a high q_e even at extreme *pH* values (*pH* 2 and 12) distinguishes it from many conventional adsorbents that require rigorous *pH* control. This stability implies that the integration of ZnO may buffer the surface charge, or that the adsorption process is driven almost exclusively by robust physical forces (such as π–π stacking and hydrogen bonding) rather than sensitive electrostatic exchanges. Consequently, this characteristic makes the composite highly suitable for treating real industrial wastewater, where *pH* levels often fluctuate significantly.

VII.2.3 Effect of ionic strength

The influence of ionic strength on the adsorption of ACE onto the ZnO@DPS-AC composite was investigated by varying NaCl concentration from 0 to 1.0 M, as depicted in **Figure VII.1(c)**. The experimental data indicate that the adsorption process exhibits two distinct behaviors depending on the electrolyte concentration. In the lower range of ionic strength (0 to 0.6 M), the equilibrium q_e remained statistically constant at approximately 240 mg/g. This stability suggests that the system is relatively insensitive to variations in salt concentration within this regime. However, as the NaCl concentration exceeded 0.6 M, a progressive decline in capacity was observed, ultimately reaching a minimum of 219 mg/g at 1.0 M NaCl.

The observed insensitivity to low-to-moderate ionic strength is consistent with recent findings regarding ACE adsorption on carbonaceous materials. For instance, AlNeyadi et al. (2026) reported that the adsorption capacities of ACE onto magnetic covalent organic frameworks (COFs) decreased only slightly with increasing ionic strength, suggesting that electrostatic interactions do not govern the adsorption mechanism. Similarly, Li et al. (2026) observed that background ions caused only minor interference in ACE adsorption onto H_3PO_4-modified biochar, attributing the primary uptake mechanism to non-electrostatic forces. The trend of decreased efficiency at very high salt concentrations also aligns with Yao et al. (2024), who noted that elevated anion

concentrations reduced the removal efficiencies of ACE and triadimefon by crayfish shell biochar due to competitive inhibition.

The stability of the q_e between 0 and 0.6 M NaCl directly supports the mechanistic hypotheses derived from the initial *pH* studies (discussed previously in **section VII.2.3**). Because the ACE molecule exists predominantly as a neutral species under these conditions, the shielding of surface charges by Na^+ and Cl^- ions in dilute solutions does not significantly alter the adsorbate-adsorbent attraction. This confirms that the removal is driven primarily by robust non-electrostatic forces (such as π–π electron donor-acceptor interactions and hydrogen bonding) rather than sensitive ion-exchange processes.

However, the reduction in specific uptake observed at higher ionic strengths (>0.6 M) can be attributed to two concurrent physical phenomena. At elevated salt concentrations, hydrated sodium and chloride ions may aggregate at the adsorbent interface or within the mesoporous network. As suggested by Yao et al. (2024) and Li et al. (2026), these clustered ions can competitively occupy or physically block access to the high-energy binding sites required for hydrogen bonding with the ACE molecule. Furthermore, elevated electrolyte concentrations inherently increase the kinematic viscosity of the aqueous solution. This increased viscosity impedes the mass transfer and intraparticle diffusion of the bulky ACE molecules into the internal microporous structure of the activated carbon composite.

VII.2.4 Effect of contact time

The kinetic behavior of ACE adsorption onto the ZnO@DPS-AC composite was investigated over a contact time range of 15-300 min, as depicted in **Figure VII.1(d)**. The adsorption profile exhibits a distinct biphasic characteristic. A rapid initial uptake occurred within the first 15 min, yielding a q_e of 200 mg/g and a corresponding removal efficiency of 60%. Following this rapid phase, the adsorption rate attenuated. The process progressed gradually until a dynamic equilibrium was established at approximately 180 min, achieving a maximum q_e of 242 mg/g (R = 77%). Extending the contact time beyond 300 min did not yield a significant change in uptake; therefore, an equilibrium time of 240 min was selected for all subsequent optimization experiments to ensure complete saturation.

The rapid initial adsorption is attributed to the abundance of vacant active sites on the composite's

external surface and to a high solute concentration gradient at the solid-liquid interface. This gradient provides a strong driving force for external mass transfer (Mohammad & Ahmed, 2019). As the process continues, the adsorption rate becomes controlled by the diffusion of ACE molecules into the internal mesopores and micropores.

The deceleration observed between 15 and 180 min. First, as the external sites reach saturation, the adsorbate must penetrate deeper into the porous network, making intraparticle diffusion the rate-limiting step. Second, as adsorbed ACE molecules populate the surface, they generate steric hindrance and repulsive forces that impede the attachment of subsequent molecules to the remaining active sites (Benhalima et al., 2024).

The equilibration time of 180 min is consistent with, or slightly longer than, trends reported for other carbon-based adsorbents. Dolatabadi et al. (2021) reported a rapid equilibrium time of 23 min for pistachio shell-based activated carbon. Similarly, Ali et al. (2026) observed equilibrium within 60 min for amide-functionalized silica, attributing this speed to readily accessible surface functional groups. The longer equilibrium time observed in the current study suggests that the ZnO@DPS-AC composite possesses a more intricate internal pore structure, thereby necessitating a longer intraparticle diffusion time than for purely surface-functionalized materials. This finding aligns with Mohammad and Ahmed (2019), who reported an equilibrium time of 120 min for orange peel and almond shell activated carbons, while Srikhaow et al. (2022) reported a significantly slower equilibrium time of approximately 360 min for eucalyptus woodchip biochar.

VII.2.5 Effect of initial ACE concentration

The adsorption behavior of ACE onto the ZnO@DPS-AC composite was evaluated by varying the initial concentration (C_0) from 50 to 400 mg/L across three distinct temperatures, as illustrated in **Figure VII.2(a)**. The experimental data indicate a direct positive correlation between the initial concentration and the equilibrium q_e. At lower concentrations (50 to 100 mg/L), the composite demonstrated exceptional efficacy, achieving removal rates of 96.2% to 99.0%. As the initial concentration increased further, specific uptake (q_e) continued to increase. Naturally, the overall removal efficiency declined as the finite number of active sites approached saturation.

As in the CAT system (**section VI.2.5**), the ACE adsorption isotherms exhibited H-type behavior according to the Giles classification (Giles et al., 1974), indicating exceptionally high adsorbent-

adsorbate affinity. The phenomenon where capacity increases with rising initial concentration is well documented in the ACE adsorption literature. For instance, Mohammad and Ahmed (2019) reported that the equilibrium q_e of ACE on KOH-activated biochar increased significantly from 9.9 to 79.5 mg/g as the initial concentration rose from 100 to 800 mg/L. Similarly, Ali et al. (2026) observed that neonicotinoid removal efficiencies increased with concentration until saturation was reached. The high removal efficiency (>96%) observed in this study at dilute concentrations aligns with the findings of Dolatabadi et al. (2021), who noted near-complete removal of ACE using modified pistachio shell carbon, attributing this performance to the abundance of unoccupied active sites relative to the solute molecules.

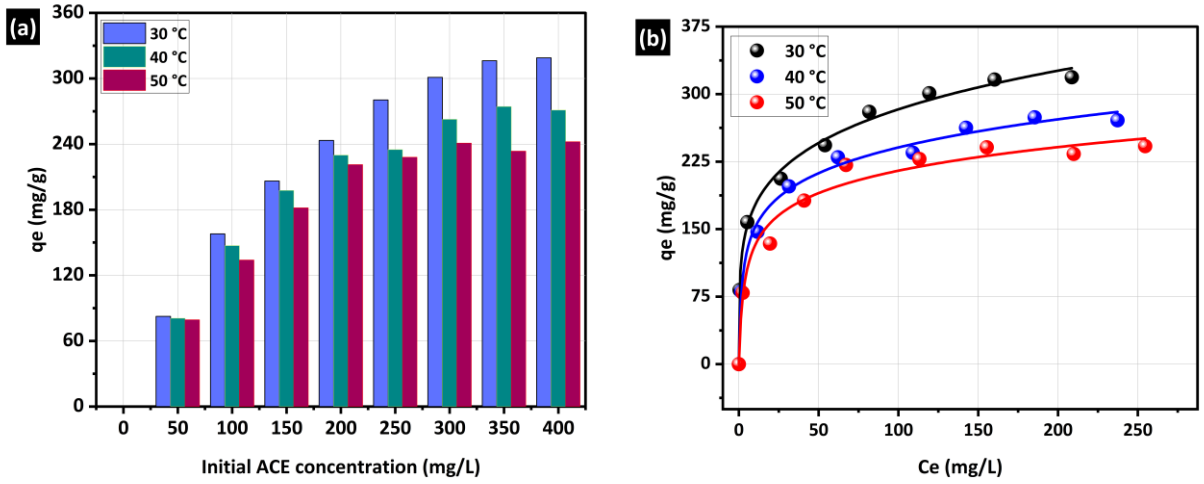

Figure VII.2 (**a**) Effect of initial concentration on the specific uptake of ACE at different temperatures, and (**b**) equilibrium adsorption isotherms for ACE onto ZnO@DPS-AC.

Regarding the specific isotherm shape, the H-type curve provides critical mechanistic insights. According to the classification by Giles et al. (1974), and subsequently reviewed by Al-Ghouti and Da'ana (2020), an H-type isotherm implies an exceptionally high affinity between the adsorbate and the adsorbent. This often suggests that chemisorption is a dominant binding mechanism. Consequently, the binding sites on the ZnO@DPS-AC surface (likely the ZnO-modified functionalities) interact so strongly with the ACE molecules that negligible solute remains in the bulk solution during the initial stages of adsorption.

While the general trend of increasing capacity with concentration is expected, the observation of an H-type isotherm distinguishes this composite from many others reported in the literature. Most

carbonaceous adsorbents for ACE, such as the eucalyptus woodchip biochar studied by Srikhaow et al. (2022), exhibit standard L-type isotherms. L-type isotherms indicate a progressive saturation of sites for monolayer coverage but lack the extreme initial verticality characteristic of the H-type profile.

VII.3 Kinetic modeling and mass transfer mechanisms

To elucidate the adsorption mechanism and identify the rate-controlling steps for ACE removal by the ZnO@DPS-AC composite, the experimental kinetic data were analyzed. Nonlinear regression was performed using five models: PFO, PSO, Avrami, Elovich, and Vermeulen. The corresponding kinetic parameters and error functions are summarized in **Table VII.1**.

Statistical analysis, evaluated via the highest adjusted coefficient of determination ($Adj\text{-}R^2$) and the lowest reduced chi-square ($Red\text{-}\chi^2$), indicates that the PSO model provides the most accurate mathematical description of the adsorption process ($Adj\text{-}R^2 = 0.998$; $Red\text{-}\chi^2 = 0.041$). Furthermore, the equilibrium q_e calculated by the PSO model ($q_{e,cal}$ = 247.84 mg/g) demonstrates excellent agreement with the experimental value ($q_{e,exp}$ = 247.73 mg/g). In contrast, while the PFO model showed a reasonable mathematical fit ($Adj\text{-}R^2 = 0.994$), it underestimated the equilibrium capacity ($q_{e,cal}$ = 240.84 mg/g) and exhibited a larger error ($Red\text{-}\chi^2 = 0.120$). As cautioned in **section VI.3** following (Kumar, 2006; Lima et al., 2016; Tran, You, Hosseini-Bandegharaei, et al., 2017), the PSO fit does not independently confirm chemisorption; the mechanistic classification is supported separately by FTIR, thermodynamics, and regeneration data (**section VII.11**).

The conformity of ACE adsorption to PSO kinetics is a prevalent trend in the literature for carbonaceous and composite adsorbents. Srikhaow et al. (2022) reported that the adsorption of ACE onto eucalyptus woodchip biochar was best described by the PSO model ($R^2 > 0.97$). Dolatabadi et al. (2021) observed a similar adherence to PSO kinetics for ACE removal using a pistachio shell-based modified activated carbon (R^2=0.998). However, they calculated an experimental capacity of 73.85 mg/g, which is significantly lower than the 247.73 mg/g achieved in this study.

Beyond standard kinetics, the Elovich model showed a high correlation ($Adj\text{-}R^2$ = 0.995), with physical significance. According to Wang and Guo (2020), the Elovich equation characterizes adsorption on energetically heterogeneous solid surfaces where the activation energy increases

with surface coverage. This heterogeneity is expected in a composite material such as ZnO@DPS-AC, where both graphitic carbon zones and zinc oxide particles provide distinct binding sites.

Additionally, the Vermeulen model was applied to investigate the diffusion mechanism. The experimental data demonstrated a strong fit to the Vermeulen model, which approximates the exact solution for intraparticle diffusion. This statistical fit corroborates the mechanistic hypothesis discussed previously in **section VII.2.4**: intraparticle diffusion dictates the transport of ACE molecules through the mesopores to the internal active sites. The relatively high q_e (≈248 mg/g) implies a deep pore network; therefore, the adsorbate must overcome substantial diffusive resistance within the particle to reach equilibrium.

Table VII.1 Kinetic model parameters and statistical error functions for the adsorption of ACE onto ZnO@DPS-AC

Model	Unit	Value	Model	Unit	Value
Experimental			**Avrami**		
q_e	mg/g	247.73	q_e	mg/g	247.73
$t_{0.5}$	min	<15	k_{AV}	min^{-1}	0.308
PFO			n_{AV}	–	0.352
q_e	mg/g	240.84	$t_{0.5}$	min	1.15
k_1	L/min	0.114	R^2	–	0.998
$t_{0.5}$	min	6.06	*Adj-*R^2	–	0.997
R^2	–	0.994	*Red-*χ^2	–	0.054
Adj-R^2	–	0.994	**Elovich**		
Red-χ^2	–	0.120	α_e	mg/(g.min)	1.00E+06
PSO			β_e	g/mg	0.067
q_e	mg/g	247.84	R^2	–	0.996
k_2	g/mg.min	0.001	*Adj-*R^2	–	0.995
$t_{0.5}$	min	3.48	*Red-*χ^2	–	0.113
R^2	–	0.998	**Vermeulen**		
Adj-R^2	–	0.998	Slope	min^{-1}	0.0214
Red-χ^2	–	0.041	R^2	–	0.989
			Adj-R^2	–	0.989
			Red-χ^2	–	8.69E-04

VII.4 Isotherm modeling and equilibrium studies

The equilibrium adsorption data of ACE onto the ZnO@DPS-AC composite were analyzed using five isotherm models: Langmuir, Freundlich, Sips, Redlich-Peterson (R-P), and Khan. The specific fitting parameters and error functions (R^2, *Adj-*R^2, and *Red-*χ^2) are summarized in **Table VII.2**. The

statistical analysis indicates that the three-parameter models consistently outperformed the two-parameter models in describing the equilibrium state. The goodness-of-fit followed the order: Khan > Redlich-Peterson > Sips > Freundlich > Langmuir. The Khan model provided the highest correlation (R^2 = 0.996 at 30 °C) and the lowest error magnitude *Red*-χ^2= 0.256), identifying it as the most suitable empirical model for this system.

The superiority of three-parameter models (Khan, Sips, R-P) over the classical Langmuir model is consistent with findings in complex composite systems governed by surface heterogeneity. Srikhaow, Srikhaow et al. (2022) similarly reported that the adsorption of neonicotinoids on eucalyptus biochar was best described by the Sips and R-P models, attributing this to a combination of homogeneous and heterogeneous binding sites. In contrast, Ali et al. (2026) found that ACE adsorption onto amide-functionalized silica was best fitted by the Langmuir model (R^2 = 0.981), implying monolayer coverage on a chemically uniform surface. The statistical reality that the present data fit the Khan and Freundlich (R^2≈ 0.99) models better than the Langmuir model (R^2≈ 0.92) confirms that the ZnO@DPS-AC surface is energetically heterogeneous, directly corroborating the kinetic findings from the Elovich model.

The success of the Khan model, a generalized isotherm capable of describing both Langmuir and Freundlich behaviors, indicates a highly complex adsorption mechanism. The Khan model parameter b_K (which relates to adsorption energy) decreased significantly from 9.024 L/mg at 30 °C to 0.498 L/mg at 50 °C. This reduction suggests that the adsorbent's affinity for the pesticide decreases with increasing temperature. Regarding the Freundlich model, the exponent (1/n) was approximately 4.6 (**Table VII.2**). Because $1/n > 1$, the adsorption process is highly favorable. This aligns with Yao et al. (2024), who reported favorable adsorption of ACE onto KOH-activated biochar with $1/n$ values well below 1.

A critical observation in the equilibrium data is the inverse relationship between temperature and q_e. Specifically, the experimental q_{max} decreased by approximately 24% (from 318.89 mg/g to 242.25 mg/g) as the temperature rose from 30 °C to 50 °C (**Figure VII.2(b)**). This trend strongly suggests that the adsorption of ACE onto ZnO@DPS-AC is exothermic. In exothermic adsorption, elevating the system temperature imparts thermal energy to the adsorbate molecules. This added thermal energy increases their vibrational states and desorption probability, effectively weakening the physical forces that anchor them to the carbon surface.

This thermal behavior parallels the findings of Yao et al. (2024), who observed a decrease in ACE q_e on biochar from 40.41 mg/g to 38.27 mg/g as temperature increased, concluding the process was exothermic. However, it contradicts the findings of Li et al. (2026) and AlNeyadi et al. (2026), who reported endothermic adsorption for ACE on H_3PO_4-modified biochar and magnetic COFs, respectively. In their studies, higher temperatures facilitated pore diffusion and the activation of chemical sites. The exothermic nature observed in the current study implies that, for ZnO@DPS-AC, uptake is primarily governed by physical forces (physisorption) that are destabilized by heat, rather than by an energy-barrier-driven chemisorption that requires thermal input to proceed.

Table VII.2 Adsorption isotherm model parameters for ACE removal using the ZnO@DPS-AC composite

		T=30 °C	T=35 °C	T=45 °
Model	**Unit**	**Value**	**Value**	**Value**
Experimental				
q_m	mg/g	318.89	271.17	242.25
Langmuir				
q_m	mg/g	303.468	270.486	250.908
K_L	L/mg	0.175	0.116	0.082
R^2	–	0.925	0.921	0.963
$Adj–R^2$	–	0.900	0.889	0.950
$Red–\chi^2$	–	21.305	6.975	5.676
Freundlich				
K_F	(mg/g)/(mg/L)^n	104.764	87.956	77.994
n	–	4.640	4.633	4.625
R^2	–	0.995	0.970	0.968
Adj R^2	–	0.993	0.957	0.957
$Red–\chi^2$	–	0.346	0.973	1.528
Sips				
q_{ms}	mg/g	1001.025	377.260	309.259
K_s	(mg/L)$^{-ns}$	0.111	0.216	0.186
n_s	–	0.276	0.464	0.557
R^2	–	0.996	0.990	0.985
$Adj–R^2$	–	0.993	0.983	0.975
$Red–\chi^2$	–	0.295	0.273	0.906
R–P				
K_{RP}	L/g	1056.102	132.380	68.150
a_{RP}	(mg/L)$^{-g}$	9.379	1.129	0.588
g	–	0.799	0.839	0.858
R^2	–	0.996	0.987	0.979

Adj–R^2	–	0.994	0.977	0.966
Red–χ^2	–	0.261	0.395	1.176
Khan				
q_{mK}	mg/g	71.206	111.691	119.760
b_K	L/mg	9.024	0.965	0.498
a_K	–	0.797	0.830	0.846
R^2	–	0.996	0.986	0.978
Adj–R^2	–	0.994	0.976	0.965
Red–χ^2	–	0.256	0.420	1.212

VII.5 Comparative assessment of adsorbent performance

To evaluate the practical efficacy of the synthesized composite, the q_m of ZnO@DPS-AC for ACE was benchmarked against those of various adsorbents reported in the recent literature. The comparative data are summarized in **Table VII.3**.

Table VII.3 Comparison of the maximum adsorption capacity of ZnO@DPS-AC for ACE with other reported adsorbents in the literature

Adsorbent	Adsorption Conditions					q_m(mg/g)	Ref.
	t (min)	C_0 (mg/L)	*m*/*V* (g/L)	*T*(°C)	*pH*		
Fe_3O_4-modified magnetic covalent organic frameworks Fe_3O_4@HMN-COF	1440	5-50	1	-	-	460	(AlNeyadi et al., 2026)
Pear Branches H_3PO_4-Modified Biochar	1440	10	0.2	25	6.8	181.9	(Li et al., 2026)
ZnO-AC	40	50-250	2.2	25	6.5	166.7	(Kumar et al., 2025)
Pistachio Shell-Based Modified-AC	23	2-25	0.3	22	6.5	86.1	(Dolatabadi et al., 2021)
Date Palm Spikelets-Derived Composite (ZnO@DPS-AC)	240	50-400	1	30	7	291.38	**This work**

The ZnO@DPS-AC composite synthesized in this work exhibited a maximum experimental q_e of 291.38 mg/g. As shown in **Table VII.3**, this value places the composite in the upper tier of performance among waste-derived adsorbents. It significantly outperforms conventional

agricultural waste-based activated carbons, such as pistachio shell-derived carbon (86.1 mg/g). Furthermore, it surpasses other zinc-based composites, including ZnO-AC (166.7 mg/g). However, the q_e remains lower than that of highly engineered synthetic materials, such as amide-functionalized silica (705.5 mg/g) (Ali et al., 2026).

The superior performance of ZnO@DPS-AC relative to unmodified biochars and standard activated carbons is attributed to the synergistic effect of the graphitic carbon matrix and the zinc oxide nanoparticles. Standard biochars rely primarily on physical pore filling. In contrast, the integration of ZnO likely introduces specific active sites that interact strongly with the nitrogen-bearing functional groups (cyano and pyridine-like moieties) of the ACE molecule. The ZnO@DPS-AC composite developed in the current study appears to achieve a more optimal dispersion or surface area utilization, resulting in nearly double the q_e of the ZnO-AC reported in their study.

Advanced synthetic materials, such as Fe_3O_4@HMN-COF (AlNeyadi et al., 2026), exhibit exceptionally high capacities. Nevertheless, these materials frequently require expensive precursors and complex, multi-step synthesis routes. In contrast, the ZnO@DPS-AC composite is derived from date palm spikelets, which constitute an abundant agricultural waste product. A q_e of 291.38 mg/g is remarkably high for a waste-derived material, surpassing even chemically activated pear branch biochars (181.9 mg/g). Consequently, ZnO@DPS-AC presents a more sustainable and economically viable alternative for large-scale wastewater treatment, offering a strategic balance between advanced adsorption performance and low production costs.

VII.6 Thermodynamic analysis

The thermodynamic feasibility and thermal nature of ACE adsorption onto the ZnO@DPS-AC composite were evaluated by determining the standard Gibbs free energy change (ΔG°), enthalpy change (ΔH°), and entropy change (ΔS°) across a temperature range of 303 to 323 K. The thermodynamic equilibrium constants (K_{eq}°) were derived from the Langmuir, Sips, Khan, and Redlich-Peterson (R-P) isotherm models. As presented in **Table VII.4** and **Figure VII.3**, the Keq° values derived from the Langmuir, Khan, and R-P models exhibited a consistent decrease as temperature increased. This inverse relationship indicates that the q_e naturally diminishes at elevated temperatures.

The thermodynamic parameters calculated using the non-linear van't Hoff equation showed negative ΔG° values, confirming that the adsorption process is thermodynamically favorable and spontaneous. Furthermore, the enthalpy change (ΔH°) was negative across the Langmuir, Khan, and R-P models, definitively indicating that the adsorption process is exothermic. This exothermic behavior aligns with several recent reports on carbonaceous adsorbents. Yao et al. (2024) reported a negative enthalpy (ΔH° = -22.74 kJ/mol) for ACE adsorption onto KOH-activated biochar, and observed a similar decrease in q_e with increasing temperature. Mosavi et al. (2024) also found that the adsorption of ACE onto lignin-based activated carbon was exothermic (ΔH° = -16.6 kJ/mol), attributing this behavior to strong physical binding forces.

Consistent with the methodological framework established in **sections II.2.6.3** and **III.12**, both linear and non-linear van't Hoff regression were applied. As previously justified, non-linear fitting provides more accurate parameter estimates Lima et al. (2020) and Tran et al. (2021). This mathematical discrepancy is evident in the current data, where the Khan model yielded significantly different enthalpy values between the linear (-118 kJ/mol) and non-linear (-169 kJ/mol) fittings.

The negative enthalpy indicates that the system releases heat upon adsorption. Physically, this occurs because the energy released during the formation of weak intermolecular bonds (such as van der Waals forces and dipole-dipole interactions) between the ACE molecules and the ZnO@DPS-AC surface exceeds the energy required to break the pesticide's hydration shell in the bulk solution. As discussed previously in **section VII.4**, the general decrease in q_e at higher temperatures is a direct consequence of Le Chatelier's principle. Adding thermal energy to an exothermic system shifts the equilibrium toward desorption, increasing the solubility of the pesticide and weakening the physical forces anchoring it to the surface (Al-Ghouti & Da'ana, 2020).

Regarding system entropy, the data in **Table VII.4** reveal negative ΔS° values. A negative ΔS° reflects a decrease in randomness at the solid-solution interface. This implies that the adsorbed ACE molecules form a structured, highly ordered layer on the composite surface, effectively losing their translational and rotational degrees of freedom compared to their highly mobile state in the aqueous phase. K_{eq}°.

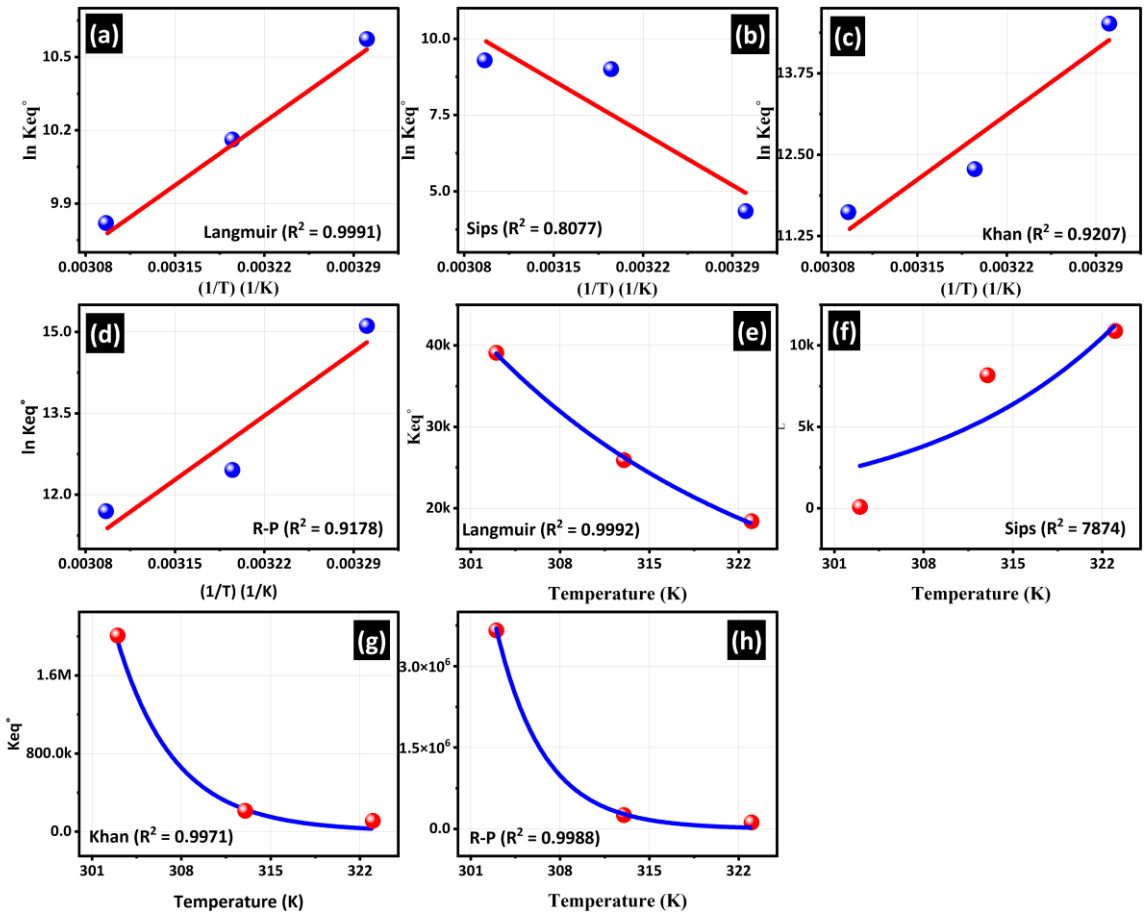

Figure VII.3 Linear (**a-d**) and non-linear (**e-h**) van 't Hoff plots for the thermodynamic evaluation of ACE adsorption onto ZnO@DPS-AC.

While the Langmuir, Khan, and R-P models consistently point to an exothermic process, two notable anomalies distinguish this dataset. First, the Sips model yielded a positive ΔH° (+59.6 kJ/mol) and erratic K_{eq}° behavior (initially decreasing, then increasing), which contradicts the fundamental trends established by the other three models. This discrepancy is likely a mathematical artifact resulting from the over-parameterization of the Sips equation within these specific concentration ranges, rather than a genuine physical phenomenon. As noted by Tran et al. (2021), thermodynamic parameters must be extracted from the model that best captures the physical reality of the isotherm; therefore, the Langmuir-derived parameters are considered the most reliable representation of the baseline thermodynamics here. Second, the general exothermic nature of this system contradicts findings by AlNeyadi et al. (2026) and Kumar et al. (2025), who reported

endothermic adsorption ($\Delta H^{\circ} > 0$) for ACE on magnetic COFs and zinc peroxide-carbon composites, respectively. In those specific studies, higher temperatures were necessary to facilitate pore diffusion or activate chemical bonding sites. The exothermic results in the current work suggest that ZnO@DPS-AC does not require thermal activation for ACE uptake, making the material highly energy-efficient for practical operation at ambient temperatures. ΔG°

Table VII.4 Thermodynamic parameters of ACE adsorption onto ZnO@DPS-AC

				Linear Fitting			Non–Linear Fitting		
Model	***T* (K)**	K_{Model}	K_{eq}°	ΔG°	ΔH°	ΔS°	ΔG°	ΔH°	ΔS°
Langmuir									
	303	0.175	3.91E+04	-26.648	-30.773	-0.014	-26.648	-31.177	-0.015
	313	0.116	2.59E+04	-26.460			-26.460		
	323	0.082	1.84E+04	-26.377			-26.377		
Sips									
	303	3.49E-04	7.77E+01	-10.972	202.96	0.711	-10.972	59.575	0.262
	313	0.037	8.17E+03	-23.453			-23.453		
	323	0.049	1.09E+04	-24.965			-24.965		
Khan									
	303	9.024	2.01E+06	-36.579	-118.65	-0.273	-36.579	-169.209	-0.438
	313	0.965	2.15E+05	-31.965			-31.965		
	323	0.498	1.11E+05	-31.207			-31.207		
R–P									
	303	16.458	3.66E+06	-38.094	-140.02	-0.339	-38.094	-204.747	-0.550
	313	1.156	2.57E+05	-32.436			-32.436		
	323	0.539	1.20E+05	-31.421			-31.421		

VII.7 Desorption, regeneration, and cyclic reusability

The economic viability and operational sustainability of the ZnO@DPS-AC composite were evaluated through cyclic adsorption-desorption experiments using initial concentrations of 100 and 200 mg/L. As presented in **Figure VII.4**, the adsorbent exhibited progressive saturation when used consecutively without intermediate regeneration. For the 100 mg/L solution, the removal efficiency declined sharply from 99.14% in the first cycle to 58.88% in the second, and then to 16.27% in the third. A similar exhaustion trend was observed for the 200 mg/L concentration, where efficiency dropped from an initial 72.04% to just 1.12% after three cycles. However, following chemical regeneration with pure ethanol, the composite demonstrated a significant recovery of its active adsorption sites. In the subsequent regenerated cycle, the removal efficiency was restored to 81.39% for the 100 mg/L solution and reached 87.57% for the 200 mg/L solution.

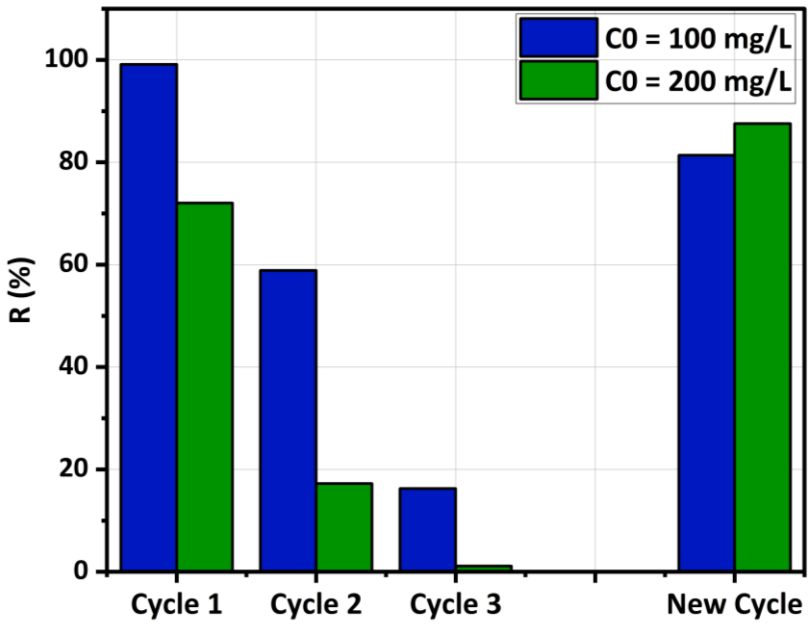

Figure VII.4 Cyclic reusability and ethanol regeneration of the ZnO@DPS-AC composite

The successful regeneration of the spent adsorbent using ethanol aligns with recent findings involving carbonaceous and composite materials for neonicotinoid removal. The effectiveness of ethanol as a desorbing agent corroborates the work of Yao et al. (2024), who reported that ethanol successfully regenerated KOH-activated biochar loaded with ACE and triadimefon, maintaining high removal efficiencies (>88%) over four cycles. Similarly, Ali et al. (2026) utilized methanol elution to regenerate amide-functionalized silica, retaining over 80% of the initial q_e for ACE after multiple cycles. They attributed this recovery to the solvent's ability to disrupt surface interactions. The cyclic behavior of the ZnO@DPS-AC composite directly parallels that of the zinc peroxide-activated carbon (ZnO-AC) composite studied by Kumar et al. (2025). In their investigation, ethanol sonication regenerated the Zn-based adsorbent, yielding exceptional stability with less than a 1% capacity loss over five cycles. Although the current study shows a slightly higher capacity loss (approximately 18% for the 100 mg/L solution) than Kumar et al. (2025), it confirms that zinc-integrated carbon frameworks are sufficiently robust to withstand repeated solvent regeneration.

The rapid decline in removal efficiency during the initial consecutive cycles is a direct consequence of the physical saturation of high-affinity binding sites. Once ACE molecules occupy these active pores and functional groups, they remain unavailable for further uptake until the adsorbate is actively desorbed. Two primary mechanisms underlie ethanol's efficacy in regenerating the

ZnO@DPS-AC composite. First, ACE has high solubility in polar organic solvents, such as ethanol. This solubility allows the solvent to penetrate the porous network, dissolve the sequestered ACE molecules, and create a strong concentration gradient that drives outward desorption. Second, as suggested by Ali et al. (2026), solvent molecules compete for hydrogen-bonding sites. This competitive action disrupts the weaker physical forces that anchor the pesticide to the carbon surface and the ZnO particles.

VII.8 Optimization via response surface methodology

VII.8.1 Model development and selection

The interactive effects of contact time, initial ACE concentration, temperature, and adsorbent dosage on the adsorption performance of the ZnO@DPS-AC composite were investigated using a CCD design. A sequential model-sum-of-squares analysis (**Table VII.5** and **Table VII.6**) was used to select the most statistically robust polynomial model. For both response variables, q_e and R, the quadratic model was identified as the most suitable.

For q_e, the quadratic terms provided a statistically significant contribution, as the calculated *F-value* of 7.69 exceeded the critical *F-Table* limit of 3.06 (*p-value* = 0.0014). This represented a marked improvement over the linear and two-factor interaction (2FI) models, whereas the cubic model was aliased and consequently rejected. Furthermore, for R, the quadratic model exhibited an even more pronounced statistical significance. The calculated *F-value* of 77.58 vastly surpassed the 3.06 *F-Table* threshold (*p-value* < 0.0001), indicating that second-order effects are fundamentally essential for accurately describing the removal percentage.

The need for a quadratic model for ACE adsorption aligns with the findings of Dolatabadi et al. (2021), who employed a CCD framework to optimize ACE removal using a modified pistachio shell-activated carbon. In their study, a quadratic polynomial was also required to accurately capture the physical curvature of the response surface (R^2 = 0.9952), confirming that the relationship between operational parameters (specifically *pH* and *m*) and ACE uptake is inherently non-linear. Similarly, Duran et al. (2024) utilized statistical optimization (Taguchi design) for pesticide removal. They emphasized that interaction effects between operational variables significantly influence the total q_e, strictly necessitating higher-order statistical modeling to interpret the system dynamics.

Table VII.5 Fit statistics and adequacy evaluation of the mathematical models for ACE adsorption capacity

Sequential model sum of squares							
Source	***SS***	***DF***	***MS***	***F−value***	***F−Table***	***p−value***	**Remarks**
Mean vs Total	1.032E+06	1	1.032E+06				
Linear vs Mean	1.015E+05	4	25374.86	470.91	2.76	< 0.0001	
2FI vs Linear	643.05	6	107.18	2.89	2.63	0.0356	
Quadratic vs 2FI	**473.26**	**4**	**118.31**	**7.69**	**3.06**	**0.0014**	**Suggested**
Cubic vs Quadratic	140.86	8	17.61	1.37	3.73	0.3455	**Aliased**
Residual	89.95	7	12.85				
Total	1.135E+06	30	37826.37				
Lack of Fit Test							
Source	***SS***	***DF***	***MS***	***F−value***		***p−value***	**Remarks**
Linear	1320.84	20	66.04	12.56	4.56	0.0053	
2FI	677.79	14	48.41	9.21	4.64	0.0114	
Quadratic	**204.53**	**10**	**20.45**	**3.89**	**4.74**	**0.0734**	**Suggested**
Cubic	63.67	2	31.83	6.06	5.79	0.0462	**Aliased**
Pure Error	26.28	5	5.26				
Model summary statistics							
Source	**SD**	R^2	$Adj-R^2$	$Pre-R^2$	**PRESS**		
Linear	7.34	0.9869	0.9848	0.9790	2163.19		
2FI	6.09	0.9932	0.9896	0.9754	2525.62		
Quadratic	**3.92**	**0.9978**	**0.9957**	**0.9896**	**1071.10**	**Suggested**	
Cubic	3.58	0.9991	0.9964	0.9213	8095.55	**Aliased**	

VII.8.2 Statistical validation and goodness-of-fit observation

The adequacy of the developed quadratic models was rigorously evaluated using standard fit statistics. Specifically, for the q_e model, the LoF *F-value* was calculated at 3.89. Crucially, this value is strictly less than the critical *F-Table* value of 4.74. Similarly, for the removal efficiency model, the LoF *F-value* was 4.15, which also falls comfortably below the 4.74 theoretical threshold. Because the calculated *F-values* for both responses do not exceed their respective *F-Table* limits, their associated *p-values* remain greater than the 0.05 confidence threshold (0.0734 and 0.0650, respectively). Therefore, the LoF is statistically considered insignificant relative to the pure error. Similarly, the model for *R* yielded an R^2 of 0.9940 and an adjusted R^2 of 0.9885,

alongside a high predicted R^2 of 0.9724. The high R^2 values obtained in this study (>0.99) generally exceed those reported in comparable literature. **Appendix. C** presents the full experimental matrix, including both predicted values and residuals. For instance, Dolatabadi et al. (2021) reported a predicted R^2 of 0.9914 for ACE removal, which is highly comparable to the current work. This robust statistical fit confirms the high precision and reliability of the experimental data generated for the ZnO@DPS-AC composite. Furthermore, the adequate precision values (which measure the signal-to-noise ratio) were well above the requisite threshold of 4 for both models, validating that the developed equations can effectively navigate the chosen design space.

Table VII.6 Fit statistics and adequacy evaluation of the mathematical models for ACE removal percentage

Sequential model sum of squares							
Source	***SS***	***DF***	***MS***	***F−value***	***F-value***	***p−value***	**Remarks**
Mean vs Total	1.980E+05	1	1.980E+05				
Linear vs Mean	6926.48	4	1731.62	19.54	2.76	< 0.0001	
2FI vs Linear	1032.09	6	172.01	2.76	2.63	0.0421	
Quadratic vs 2FI	**1129.23**	**4**	**282.31**	**77.58**	**3.06**	**< 0.0001**	**Suggested**
Cubic vs Quadratic	43.87	8	5.48	3.58	3.73	0.0550	Aliased
Residual	10.72	7	1.53				
Total	2.072E+05	30	6905.71				
Lack of Fit Test							
Source	***SS***	***DF***	***MS***	***F−value***		***p−value***	**Remarks**
Linear	2210.03	20	110.50	94.06	4.56	< 0.0001	
2FI	1177.94	14	84.14	71.62	4.64	< 0.0001	
Quadratic	**48.71**	**10**	**4.87**	**4.15**	**4.74**	**0.0650**	**Suggested**
Cubic	4.85	2	2.42	2.06	5.79	0.2223	**Aliased**
Pure Error	5.87	5	1.17				
Model summary statistics							
Source	**SD**	***R²***	***Adj−R²***	***Pre−R²***		**PRESS**	
Linear	9.41	0.7576	0.7188	0.6181		3491.14	
2FI	7.89	0.8705	0.8024	0.5670		3959.02	
Quadratic	**1.91**	**0.9940**	**0.9885**	**0.9724**		**252.34**	**Suggested**
Cubic	1.24	0.9988	0.9951	0.8771		1123.97	**Aliased**

The models were further validated using an LoF analysis, which compares residual errors with pure

errors to identify model deficiencies. Specifically, for the q_e model, the LoF *F−value* was 3.89, corresponding to a *p−value* of 0.0734. For the removal efficiency model, the LoF *F−value* was 4.15 with a *p−value* of 0.0650. Because the *p−value*s for the LoF test are greater than the 0.05 confidence threshold for both responses, the LoF is statistically considered insignificant relative to the pure error. This non-significant LoF is a highly desirable statistical outcome. It confirms that the quadratic models adequately fit the experimental data and that any localized deviations are attributable to random experimental noise rather than a fundamental failure of the mathematical model to describe the physical system. Moreover, this outcome validates the omission of aliased cubic terms as statistically justified, ensuring that the quadratic surfaces provide a robust and accurate predictor of batch adsorption of ACE onto the composite.

VII.8.3 ANOVA analysis and significance of model terms

The statistical significance of the quadratic models developed for q_e and *R* was rigorously assessed using ANOVA, as detailed in **Table VII.7** and **Table VII.8**. The statistical significance of the quadratic models developed for q_e and R was rigorously assessed using ANOVA, as detailed in Table VII.7 and Table VII.8. For q_e, the model exhibited an exceptionally high *F-value* of 476.34 with a *p-value* of < 0.0001. This calculated variance ratio vastly exceeds the theoretical *F-Table* limits, confirming profound statistical significance. Similarly, the *R* model yielded a highly significant *F-value* of 178.38 (*p-value* < 0.0001), further confirming that the regression models reliably capture the experimental data.

The magnitude of these *F−values* and the overall significance of the models are consistent with high-quality optimization studies in the literature. For instance, Dolatabadi et al. (2021) reported an *F−value* of 797.5 for the optimization of ACE removal using pistachio shell carbon. This confirms that quadratic models are well-suited for capturing the behavior of adsorption systems with dynamic variables such as dosage and concentration. Furthermore, the dominance of dosage and concentration as primary variables aligns with the Pareto analysis reported by Dolatabadi et al. (2021), in which these two factors accounted for over 60% of the total process variation.

The statistical dominance of adsorbent dosage (factor C) and initial concentration (factor B) across both models fundamentally reflects the governing mass transfer principles of the system. Specifically, for the q_e (q_e), the massive *F−value* for concentration (*F−value* = 2784.73) indicates

that the concentration gradient provides the critical driving force required to maximize specific uptake per unit mass. Conversely, for the *R*, the overwhelming *F−value* for dosage (*F−value* = 1369.91) confirms that expanding the available surface area is the most direct method to ensure high overall pollutant elimination, even if it inherently reduces the efficiency per unit mass. Regarding temperature (factor D), although the variable is statistically significant (*p−value* < 0.05), it exhibited the lowest *F−value* in both models. This relatively weak influence corroborates the thermodynamic analysis established earlier in **section VII.6**; the moderate enthalpy change indicates that the physical adsorption process relies less on thermal activation energy and more on mass-transfer driving forces.

Table VII.7 ANOVA analysis for the quadratic model describing ACE adsorption capacity

Source	SS	DF	MS	*F−value*	*p−value*	
Model	1.026E+05	14	7329.70	476.34	< 0.0001	**Significant**
A-Time	310.36	1	310.36	20.17	0.0004	Significant
B-Concentration	42849.98	1	42849.98	2784.73	< 0.0001	Significant
C-Dose	58136.90	1	58136.90	3778.20	< 0.0001	Significant
D-Temperature	202.19	1	202.19	13.14	0.0025	Significant
AB	24.09	1	24.09	1.57	0.2300	
AC	9.73	1	9.73	0.6326	0.4388	
AD	40.97	1	40.97	2.66	0.1235	
BC	519.88	1	519.88	33.79	< 0.0001	Significant
BD	47.06	1	47.06	3.06	0.1008	
CD	1.32	1	1.32	0.0857	0.7737	
A^2	28.30	1	28.30	1.84	0.1951	
B^2	35.27	1	35.27	2.29	0.1508	
C^2	25.08	1	25.08	1.63	0.2211	
D^2	52.22	1	52.22	3.39	0.0853	
Residual	230.81	15	15.39			
Lack of Fit	204.53	10	20.45	3.89	0.0734	**Not significant**
Pure Error	26.28	5	5.26			
Cor Total	1.028E+05	29				

A critical finding is the statistical significance of the *BC* in both models (*F−value* = 33.79 for q_e; *F−value* = 271.36 for removal). Physically, this interaction indicates that the effect of adsorbent mass depends strongly on the pollutant load. At elevated initial concentrations, increasing the dosage significantly improves removal efficiency because the system is saturation-limited. Conversely, at dilute concentrations, increasing the mass yields diminishing returns due to the split in mass flux phenomenon (as detailed in **section VII.2.1**), as supported by the review by Al-Ghouti

and Da'ana (2020). Additionally, the removal model exhibited a significant concentration-temperature interaction (*BD*, $p-value$= 0.0114). This suggests that thermal variations alter the aqueous solubility and molecular mobility of ACE, consequently influencing how effectively the pesticide molecules compete for binding sites across different concentration regimes.

Table VII.8 ANOVA analysis for the quadratic model describing ACE removal percentage

Source	SS	DF	MS	$F-value$	$p-value$	
Model	9087.80	14	649.13	178.38	< 0.0001	**Significant**
A-Time	59.77	1	59.77	16.42	0.0010	Significant
B-Concentration	1804.14	1	1804.14	495.78	< 0.0001	Significant
C-Dose	4985.12	1	4985.12	1369.91	< 0.0001	Significant
D-Temperature	77.45	1	77.45	21.28	0.0003	Significant
AB	0.1269	1	0.1269	0.0349	0.8544	
AC	4.24	1	4.24	1.16	0.2975	
AD	2.49	1	2.49	0.6838	0.4212	
BC	987.48	1	987.48	271.36	< 0.0001	Significant
BD	30.19	1	30.19	8.30	0.0114	
CD	7.56	1	7.56	2.08	0.1699	
A^2	1.65	1	1.65	0.4531	0.5111	
B^2	9.21	1	9.21	2.53	0.1326	
C^2	364.13	1	364.13	100.06	< 0.0001	Significant
D^2	0.1431	1	0.1431	0.0393	0.8455	
Residual	54.59	15	3.64			
Lack of Fit	48.71	10	4.87	4.15	0.0650	**Not significant**
Pure Error	5.87	5	1.17			
Cor Total	9142.38	29				

Evaluating the system's nonlinearity through quadratic terms reveals a clear divergence between the two response variables. For q_e, the quadratic terms (A^2, B^2, C^2, D^2) were statistically insignificant ($p-value > 0.05$), as shown in **Table VII.7**. This lack of significance suggests that within the selected experimental domain, the relationship between the operational factors and the specific uptake is predominantly linear or interactive (forming a planar or twisted response surface) rather than parabolic. In sharp contrast, the removal model (**Table VII.8**) exhibited a highly significant quadratic term for adsorbent dosage (C^2, $F-value$ = 100.06). This mathematical term captures the asymptotic behavior of R as it approaches the theoretical maximum of 100%. As the adsorbent mass increases, the incremental gain in pollutant removal decreases, necessitating a quadratic (curvilinear) term to accurately model physical saturation.

Finally, as detailed previously in **section VII.8.2**, the lack-of-fit (LOF) tests yielded non-significant

p−values for both models. Adhering to standard statistical protocols for response surface methodology (Montgomery, 2017; Montgomery et al., 2012; Montgomery & Runger, 2018; Montgomery et al., 2009), a non-significant LOF is the requisite outcome. It definitely confirms that the quadratic models effectively fit the experimental data and that residual variations stem from random system noise rather than underlying mathematical deficiencies.

VII.8.4 Development of regression equations

To mathematically describe the adsorption performance of the ZnO@DPS-AC composite, multiple regression analysis was applied to the experimental data obtained from the CCD design. The relationships between the independent variables and the system responses were expressed using second-order polynomial equations. These equations were derived in terms of coded factors to allow direct comparison of the relative impact of each factor and in terms of actual factors to facilitate precise response prediction in real-world units.

The final empirical models in terms of coded factors are presented in **Eq. VII.1** and **Eq. VII.2**:

$$q_e(mg/g) = 190.49 + 4.15A + 48.79B - 56.83C - 3.35D + 1.23(AB) - 0.78(AC) - 1.60(AD) + 5.70(BC) + 1.71(BD) + 0.29(CD) - 3.30(A^2) - 3.69(B^2) + 3.11(C^2) - 4.49(D^2) \quad \textbf{Eq. VII.1}$$

$$\mathrm{R}(\%) = 88.87 + 1.82A - 10.01B + 16.64C - 2.07D - 0.09(AB) + 0.51(AC) - 0.39(AD) + 7.86(BC) + 1.37(BD) - 0.69(CD) + 0.80(A^2) - 1.88(B^2) - 11.85(C^2) + 0.24(D^2) \quad \textbf{Eq. VII.2}$$

The corresponding equations in terms of actual factors are provided in **Eq. VII.3** and **Eq. VII.4**:

$$q_e(mg/g) = 144.16 + 0.25(\mathrm{Time}) + 0.37(\mathrm{Concentration}) - 2.31(\mathrm{Dose}) + 3.05(\mathrm{Temperature}) + 0.00013(\mathrm{Time} \times \mathrm{Concentration}) - 0.0003(\mathrm{Time} \times \mathrm{Dose}) - 0.0021(\mathrm{Time} \times \mathrm{Temperature}) + 0.0013(\mathrm{Concentration} \times \mathrm{Dose}) + 0.0014(\mathrm{Concentration} \times \mathrm{Temperature}) + 0.0008(\mathrm{Dose} \times \mathrm{Temperature}) - 0.0006(\mathrm{Time}^2) - 0.0002(\mathrm{Concentration}^2) + 0.0025(\mathrm{Dose}^2) - 0.0449(\mathrm{Temperature}^2) \quad \textbf{Eq. VII.3}$$

$$\begin{aligned} R(\%) = {} & 78.98 + 0.0054(\text{Time}) - 0.17(\text{Concentration}) + 1.30(\text{Dose}) \\ & - 0.51(\text{Temperature}) - 9.5 \times 10^{-6}(\text{Time} \times \text{Concentration}) \\ & + 0.0002(\text{Time} \times \text{Dose}) - 0.0005(\text{Time} \times \text{Temperature}) \\ & + 0.0018(\text{Concentration} \times \text{Dose}) \\ & + 0.0011(\text{Concentration} \times \text{Temperature}) \\ & - 0.0020(\text{Dose} \times \text{Temperature}) + 0.0001(\text{Time}^2) \\ & - 0.0001(\text{Concentration}^2) - 0.0097(\text{Dose}^2) \\ & + 0.0024(\text{Temperature}^2) \end{aligned} \quad \textbf{Eq. VII.4}$$

The magnitude and sign of the coefficients in the coded equations provide critical insights into the relative influence of each operational factor, a methodology strongly advocated by Myers (2016) for process optimization. Specifically concerning the q_e, the coefficient for initial concentration (*B*) is +48.79, while the coefficient for adsorbent mass (*C*) is -56.83. The large positive coefficient for factor *B* indicates that increasing the initial ACE concentration significantly enhances specific uptake. This enhancement is attributed to the increased mass transfer driving force resulting from the higher concentration gradient, which overcomes the external mass transfer resistance at the aqueous-ZnO@DPS-AC interface. Conversely, the negative coefficient for factor *C* implies that increasing the adsorbent mass fundamentally reduces the specific uptake (q_e). This directly corresponds to the split in mass flux phenomenon detailed previously in **section VII.2.1**, where a surplus of adsorbent distributes the available solute across a larger number of active sites, leaving many binding sites unsaturated.

Evaluating the *R*, the adsorbent dose shows the largest positive coefficient (+16.64), while concentration (*B*) shows a negative coefficient (-10.01). This mathematically confirms that while a high initial concentration favors q_e, it is detrimental to the overall *R* due to the rapid saturation of available binding sites. Furthermore, increasing the dosage provides the necessary surface area to achieve near-complete removal. This aligns with the highly negative quadratic term (-11.85 C^2) in **Eq. VII.2**, indicating a distinct region of diminishing returns where adding excess adsorbent yields minimal additional pollutant removal once system equilibrium is established.

The mathematical structure of these regression equations is highly consistent with findings in the broader literature for pesticide adsorption. For instance, Dolatabadi et al. (2021) optimized ACE removal using a pistachio shell-based carbon and similarly reported a negative coefficient for concentration (-5.15) and a positive coefficient for dosage (+6.52) in their *R* model. The results obtained in this work exhibit identical directional trends but feature significantly larger coefficients

(+16.64 for dosage). This deviation suggests that the ZnO@DPS-AC system is considerably more sensitive to dosage variations than the material studied by Dolatabadi et al. (2021). Furthermore, the significant positive interaction term (+7.86 *BC*) in the *R* equation (**Eq. VII.2**) is particularly noteworthy. It indicates a powerful synergistic effect, in which increasing the adsorbent dosage is most effective when the pollutant concentration is concurrently high.

A distinguishing feature of the derived models is the relatively low impact of temperature (factor D) compared to concentration and dosage, as evidenced by the small coefficients (-3.35 for q_e and -2.07 for *R*). In many adsorption studies governed by strong chemisorption, temperature strictly dictates the reaction rate and overall uptake. However, the statistical dominance of mass transfer variables over temperature in this system suggests that the process remains highly robust across the entire studied thermal range (30-50 °C). Consequently, the ZnO@DPS-AC composite represents a highly practical candidate for full-scale wastewater treatment, particularly in scenarios where thermal regulation is economically or logistically unfeasible.

VII.8.5 Two-Dimensional interaction analysis

To visualize the synergistic and antagonistic effects of the operational parameters on the adsorption of ACE, two-dimensional interaction plots were generated (**Figure VII.5** and **Figure VII.6**). These plots graphically depict the regression of the response variable on two selected factors, while holding the remaining parameters at their central levels.

VII.8.5.1 Interactive effects on adsorption capacity

As indicated by the ANOVA analysis (**Table VII.7**), the interaction between *BC* term was statistically significant for the q_e. The corresponding interaction plot for the *BC* term reveals distinct non-parallel lines, which is a mathematical hallmark of a significant factor interaction. Specifically, at low adsorbent dosages, the specific q_e increases sharply with escalating initial ACE concentration. However, at higher adsorbent dosages, the slope of this increase becomes noticeably less pronounced.

This physical behavior characterizes the saturation dynamics of the active sites. At low dosages, the ratio of ACE molecules to available binding sites is very high; consequently, increasing the initial concentration maximizes utilization per unit mass of adsorbent. Conversely, at high dosages,

the split in mass flux phenomenon (discussed previously in **section VII.2.1**) occurs. The adsorbate is distributed across a wide surplus of sites, preventing the full saturation of the ZnO@DPS-AC surface and thereby dampening the q_e gains normally expected from an increased concentration gradient.

Regarding the remaining variables, the plots of interactions involving contact time (terms *AB*, *AC*, and *AD*) show nearly parallel lines with constant vertical separation. This geometric parallelism visually confirms the ANOVA finding that contact time acts strictly as an additive factor rather than an interactive one within this specific design space. Unlike the findings of Dolatabadi et al. (2021), who observed significant *pH* × time interactions for pistachio shell carbon, the ZnO@DPS-AC system shows that kinetic equilibrium is reached relatively independently of concentration or dosage extremes over the tested temporal range (15 to 300 min).

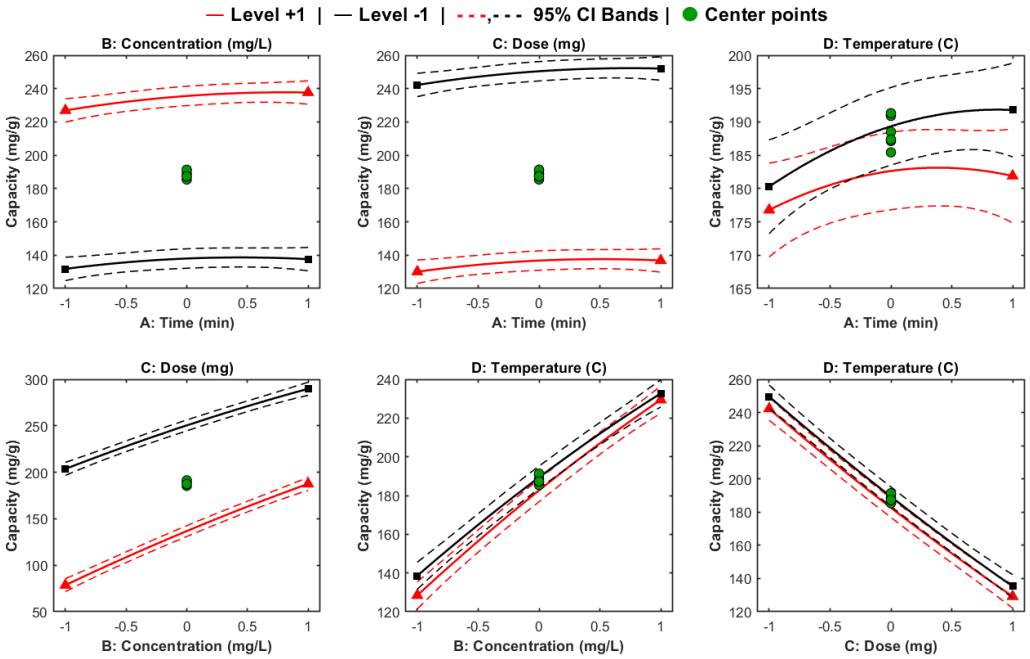

Figure VII.5 Two-dimensional interaction plots illustrating the combined effects of operating parameters on the ACE adsorption capacity

VII.8.5.2 Interactive effects on removal percentage

The interaction plots for *R* (**Table VII.6**) elucidate the significant contributions of *BC* and *BD* terms. Regarding the *BC* interaction, the plot shows distinct convergence of the response lines at high dosages. When the adsorbent mass is set to its upper limit, the *R* remains near 100% regardless

of the initial pollutant concentration. However, at the lowest dosage level, a dramatic divergence occurs; the *R* drops precipitously from approximately 80% to 40% as the concentration increases. This physical trend strongly aligns with the mass transfer principles described by Srikhaow et al. (2022) for biochar systems. It validates that at high solid-to-liquid ratios, the composite provides sufficient surface area to accommodate the entire pollutant load, effectively rendering the system insensitive to concentration spikes. Conversely, at low dosages, the finite number of available active sites becomes rapidly saturated. This rapid saturation naturally leads to early breakthrough and a drastically reduced overall *R*.

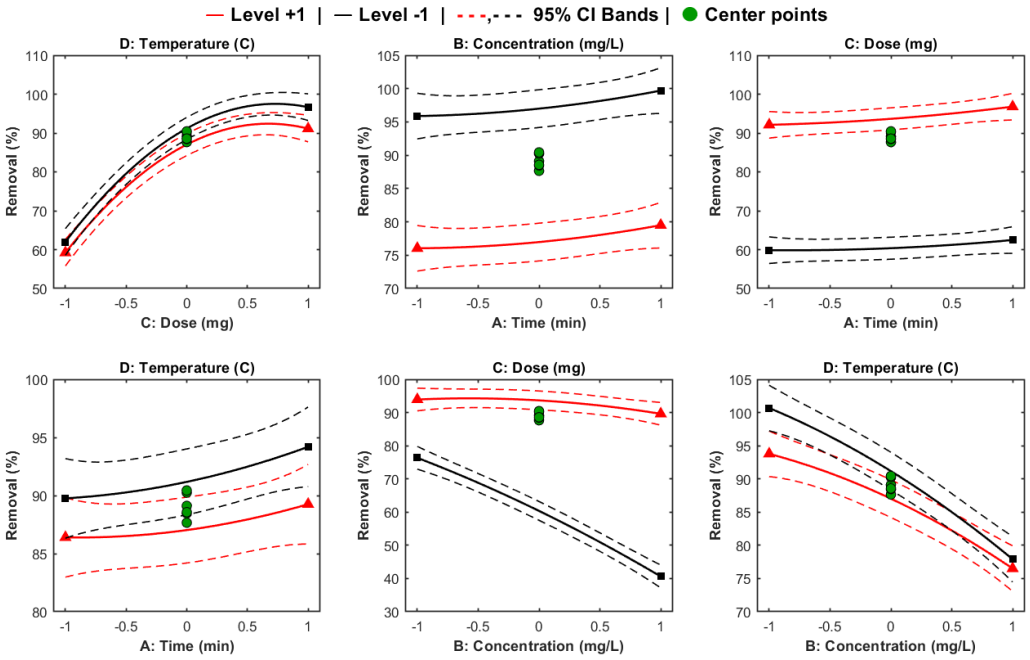

Figure VII.6 Two-dimensional interaction plots illustrating the combined effects of operating parameters on the ACE removal

Evaluating *BD* interaction, the corresponding plot reveals that the negative impact of increasing the initial concentration on *R* becomes significantly more severe at elevated temperatures. This statistical interaction directly corroborates the thermodynamic findings established in **section VII.6**, which characterized the adsorption process as strictly exothermic ($\Delta H^{\circ} < 0$). Elevated temperatures increase the aqueous solubility of the ACE molecules, thereby decreasing their thermodynamic drive to partition out of the bulk liquid phase. Furthermore, as thermal energy increases, the specific physical bonds anchoring the pesticide to the adsorbent surface (such as π–π

stacking and hydrogen bonding) are progressively weakened. Consequently, when high thermal energy is combined with a high pollutant load, the desorption probability increases, resulting in a compounded decline in overall removal efficiency.

VII.8.6 Three-dimensional response surface topologies

To visualize the global maxima and the nature of the interactive effects between independent variables, 3D response surface plots were generated for both q_e and R. Derived directly from the quadratic regression models (**Eq. VII.1** and **Eq. VII.2**), these plots graphically represent the simultaneous variation of two operational parameters while maintaining the others fixed at their central levels.

VII.8.6.1 Three-Dimensional response surfaces for adsorption capacity

The 3D response surfaces for q_e reveal that the system is kinetically driven by the concentration gradient but constrained by the adsorbent mass distribution. The surface plot of initial concentration and adsorbent mass exhibits a distinct twisted-plane topology, highly characteristic of a mathematically significant interaction. The highest specific q_e is observed in the geometric region of high C_0 and m. The steep ascent along the concentration axis confirms that the process is heavily diffusion-controlled; a high C_0 provides the necessary driving force to overcome the intraparticle diffusion resistance identified previously in the kinetic modeling (**section VII.3**). Conversely, the precipitous drop in q_e as mass increases (at a fixed C_0) visually demonstrates the split in mass flux phenomenon (detailed in **section VII.2.1**). This distinct topography confirms that to maximize the specific uptake of the ZnO@DPS-AC composite, the ratio of adsorbate to adsorbent must remain high to ensure the complete saturation of available active sites.

The response surface mapping of temperature versus concentration shows a linear increase in qe with concentration, along with a noticeable depression as temperature rises. The maximum q_e is located exactly at the spatial coordinate with the lowest temperature and the highest concentration. This negative slope along the temperature axis provides visual confirmation of the thermodynamic parameters calculated in **section VII.6** ($\Delta H^\circ < 0$). It confirms that adsorption is exothermic, whereby increased thermal energy disrupts the physical binding forces (such as π–π stacking and hydrogen bonding) between the ACE molecules and the composite surface, an effect similarly described by Li et al. (2026).

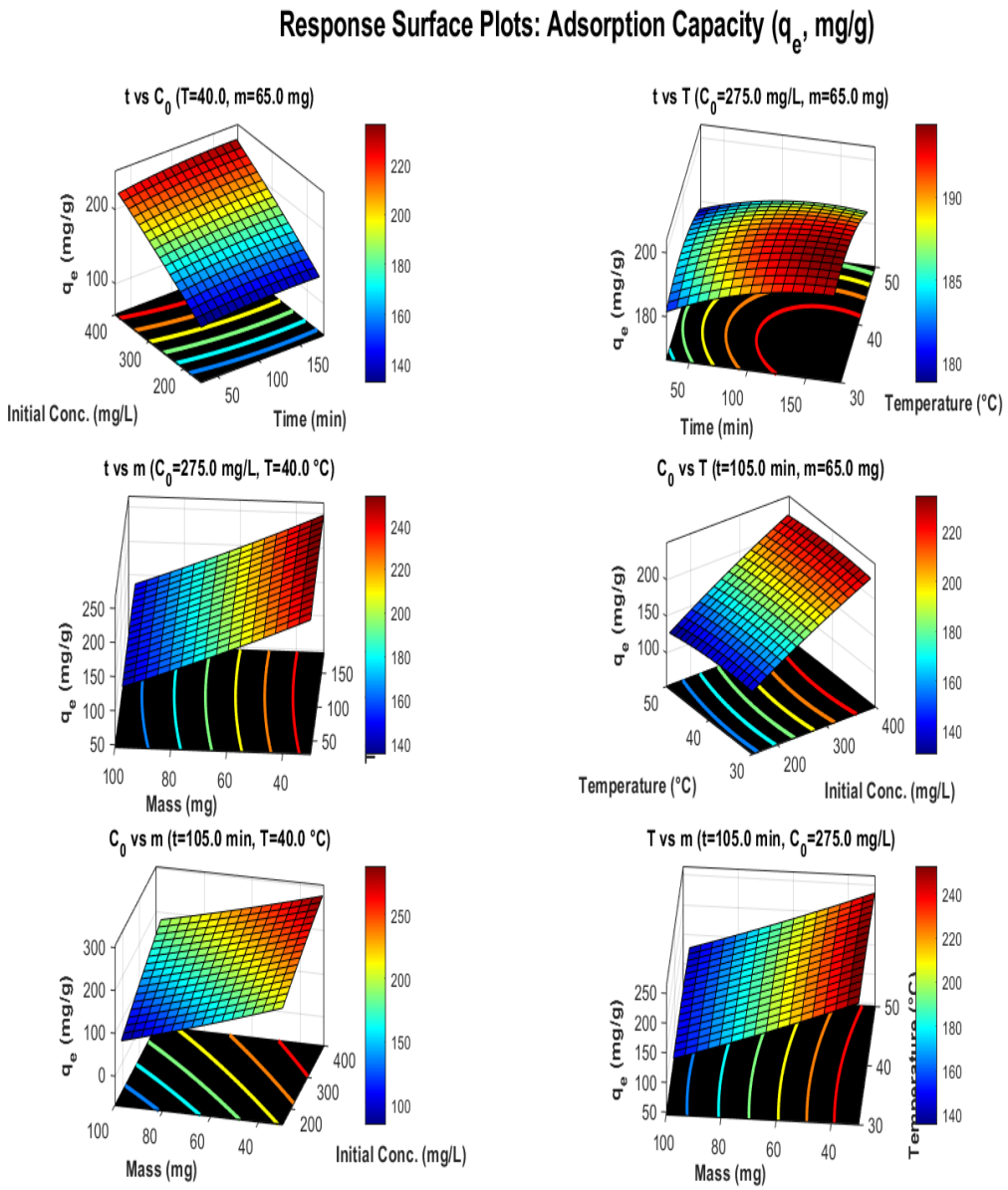

Figure VII.7 Three-dimensional response surface plots demonstrating the interactive effects of operating parameters on the ACE adsorption capacity

Finally, the response surfaces involving contact time display a rapid initial rise followed by a distinctly flattened plateau. This terminal flatness at higher temporal values precisely corresponds to the equilibrium state predicted by the pseudo-second-order kinetic model. It clearly indicates that once surface saturation is achieved, extending the operational duration yields negligible

additional gains in q_e.

VII.8.6.2 Three-Dimensional response surfaces for removal percentage

The 3D response surfaces for *R* display topological trends that are fundamentally inverse to those observed for specific q_e, with prominent curvature indicating highly significant quadratic effects. The surface plot of C_0 versus *m* shows a rising ridge that peaks at high adsorbent dosages (e.g., 100 mg) and at low initial concentrations. Crucially, this surface exhibits distinct geometric curvature along the mass axis, which directly corresponds to the highly significant quadratic term (C^2; *F-value* = 100.06) identified in the previous ANOVA (**Table VII.8**).

This structural curvature visually represents a distinct region of diminishing returns. As the composite dosage increases from 30 to approximately 70 mg, the *R* rises sharply (from 49% to 98%). However, beyond 80 mg, the response surface visibly plateaus. This plateau implies that adding excess adsorbent does not yield a linear increase in pollutant removal once the available ACE in the aqueous phase is largely exhausted. Furthermore, this topological saturation fully validates the empirical H-type isotherm behavior discussed previously in **section VII.2.5**. At low concentrations, the adsorbent exhibits an exceptionally high affinity that strips the solute from the solution, rendering further mass additions redundant.

The remaining response surfaces involving adsorbent mass exhibit only minor curvature relative to the other operational axes. While this persistent curvature visually confirms the global significance of the C^2 mathematical term, the absolute change in *R* along these specific interactive vectors is minimal. This observation directly corroborates the ANOVA findings regarding the statistical non-significance of the time-mass and temperature-mass interactions. Globally, the spatial analysis confirms that low temperatures, dilute initial concentrations, high adsorbent dosages, and extended contact times thermodynamically and kinetically favor the overall *R*.

VII.8.7 Multi-objective optimization of process parameters

To ascertain the precise operational conditions that satisfy the conflicting goals of high economic efficiency (maximum q_e) and environmental compliance (maximum *R*), a numerical optimization was performed using the desirability function approach. As summarized in **Table VII.9**, three specific scenarios were simulated: (1) maximizing q_e, (2) maximizing *R*, and (3) a multi-objective

trade-off designed to balance both responses.

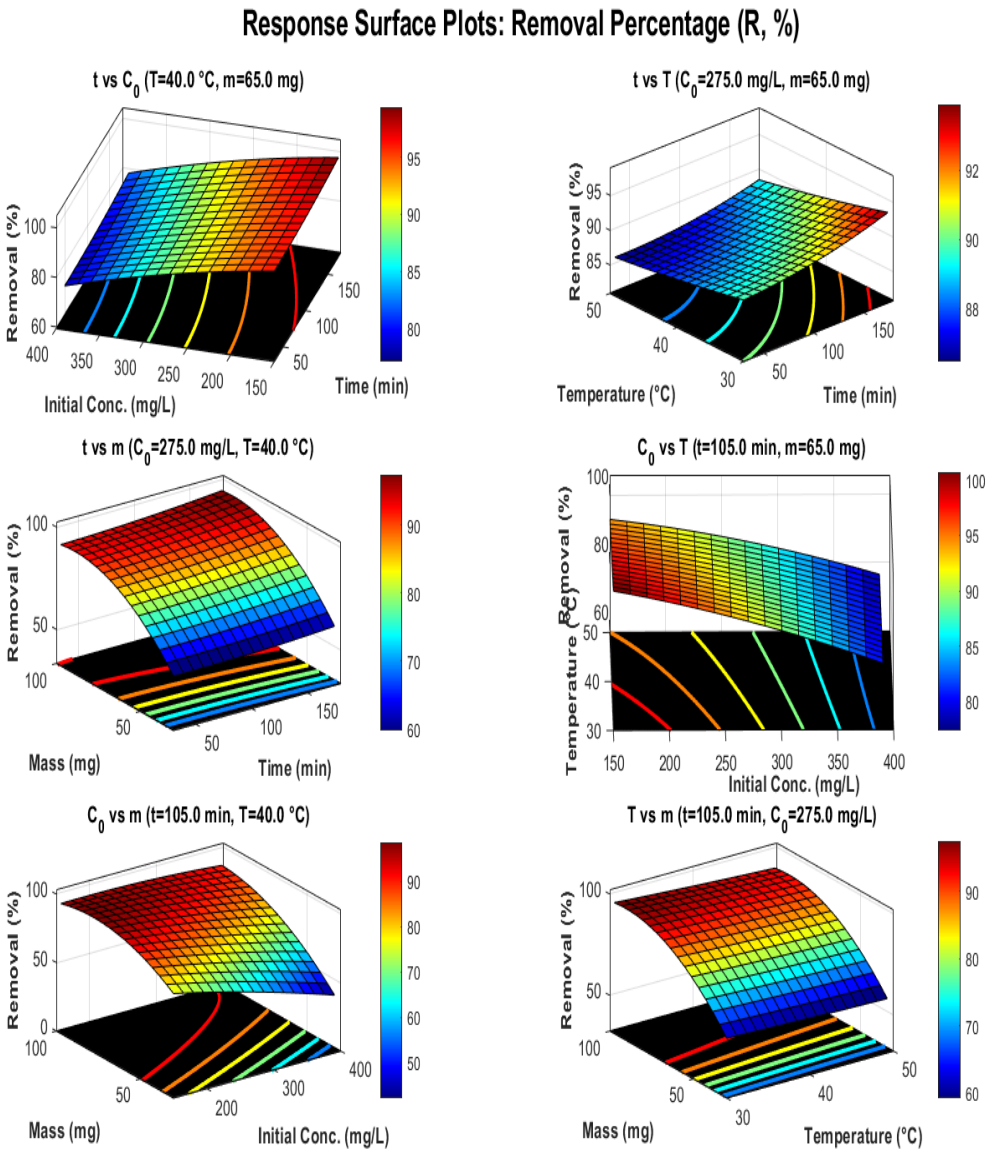

Figure VII.8 Three-dimensional response surface plots demonstrating the interactive effects of operating parameters on the ACE removal percentage

Scenario 1: Resource Efficiency

When the numerical goal was set solely to maximize q_e, the software predicted an optimum at a high initial concentration (396.3 mg/L) and a low adsorbent dosage (30.1 mg). Under these

conditions, the predicted capacity reached 290.8 mg/g, but the *R* was only 42.1%.

Table VII.9 Desirability function optimization scenarios for ACE adsorption

Optimization Criterion	*t* (min)	C_0 (mg/L)	*m* (mg)	*T* (°C)	*Pred-*q_e (mg/g)	*Pred-R* (%)	Desirability
Maximum Capacity	135.4	396.3	30.1	38.5	290.8	42.1	1.0
Maximum Removal	76.658	157.194	76.658	30.289	119.261	101.293	1
Multi-Objective	179.998	399.996	79.473	30.138	215.439	89.411	0.778

Scenario 2: Effluent Quality

Conversely, prioritizing maximum *R* shifted the optimal conditions to a moderate concentration (157.2 mg/L) and a significantly higher dosage (76.7 mg). This configuration yielded a predicted *R* of 101.3% (physically capped at 100%) alongside a reduced specific capacity of 119.3 mg/g.

Scenario 3: Industrial Balance

The multi-objective optimization, which assigned equal weight to both physical responses, identified a viable compromise solution: a contact time of 180 min, an initial concentration of 400.0 mg/L, an adsorbent dosage of 79.5 mg, and a temperature of 30.1 °C. This scenario yielded a desirability score of 0.778, with a predicted capacity of 215.4 mg/g and an *R* of 89.4%.

The divergence in optimal conditions between Scenarios 1 and 2 reinforces the split in mass flux mechanism discussed previously in **section VII.2.1**. Maximizing specific capacity strictly requires a high solute-to-sorbent ratio to establish the strong driving force described in the kinetic modeling (**section VII.3**). These gradient forces drive the ACE molecules deep into the ZnO@DPS-AC micropores. In contrast, maximizing overall *R* requires a surplus of active binding sites (high dosage) to ensure that nearly every solute molecule is captured. This condition inevitably leaves many binding sites unsaturated, thereby lowering the specific q_e.

Crucially, the optimal temperature identified in the multi-objective scenario (30.1 °C) provides robust validation of the thermodynamic analysis. As determined in **section VII.6**, the adsorption of ACE onto ZnO@DPS-AC is exothermic ($\Delta H^\circ < 0$). The optimization algorithm correctly identified that maintaining a lower temperature is essential to prevent thermal desorption and

maximize the stability of the hydrogen bonds and π–π interactions governing the uptake. This contrasts with the findings of Dolatabadi et al. (2021), who optimized ACE removal on pistachio shell carbon at ambient conditions and observed high removal rates, but only at highly dilute initial concentrations of 1-25 mg/L.

The predicted *R* of >100% in Scenario 2 is a statistical artifact common in polynomial regression when approaching asymptotic limits, as noted in RSM studies by Myers (2016). Physically, however, it signifies complete remediation of the aqueous phase. Additionally, the optimal contact time of 180 min aligns perfectly with the equilibration time established in the pseudo-second-order kinetic study. This alignment confirms that the statistical model accurately captures the underlying physicochemical reality of the system's mass transfer limitations.

The desirability function analysis demonstrates that the ZnO@DPS-AC composite can be mathematically tuned for different industrial needs. For applications requiring strict discharge limits (such as drinking water treatment), the conditions modeled in Scenario 2 are preferable. However, for industrial wastewater pre-treatment where resource recovery and material efficiency are highly prioritized, Scenario 3 offers a strategic advantage. It delivers high uptake capacity with acceptable *R* at energy-efficient ambient temperatures.

VII.8.8 Experimental validation

To validate the mathematical accuracy of the RSM models, confirmatory experiments were conducted under the exact optimized conditions derived from the multi-objective scenario (C_0 = 400.0 mg/L, adsorbent dosage = 79.5 mg, temperature = 30.1 °C, and contact time = 180 min). The laboratory results yielded a q_e of 222.97 mg/g and an overall *R* of 85.47%. The relative error between the model-predicted values and the experimental data was 6.72%, which falls well within an acceptable range. This close agreement definitively confirms the physical validity and reproducibility of the developed polynomial equations for predicting the composite's ACE adsorption performance.

VII.9 Modeling of ACE adsorption via an artificial neural network

VII.9.1 Model development and hyperparameter optimization

Developing a highly predictive ANN requires stringent hyperparameter optimization. To identify

the optimal network architecture for the acetamiprid batch adsorption process, a systematic grid search was executed. **Figure VII.9** depicts the impact of the hidden layer neuron count on model performance, assessed via MSE and the R^2 coefficient. **Table VII.10** outlines the top 10 ANN configurations identified in this evaluation.

The optimal configuration used the Resilient Backpropagation algorithm (trainrp), with four hidden neurons, a Logsig transfer function in the hidden layer, and a Purelin transfer function in the output layer. This specific architecture achieved a mean *MSE* of 1.08E-03 and a mean R^2 of 0.9635. Alternate algorithms, including BFGS Quasi-Newton (trainbfg) and Conjugate Gradient with Fletcher-Reeves (traincgf), generated higher R^2 values (0.9756 and 0.9769, respectively); however, they produced marginally higher mean MSE values than the optimized trainrp model.

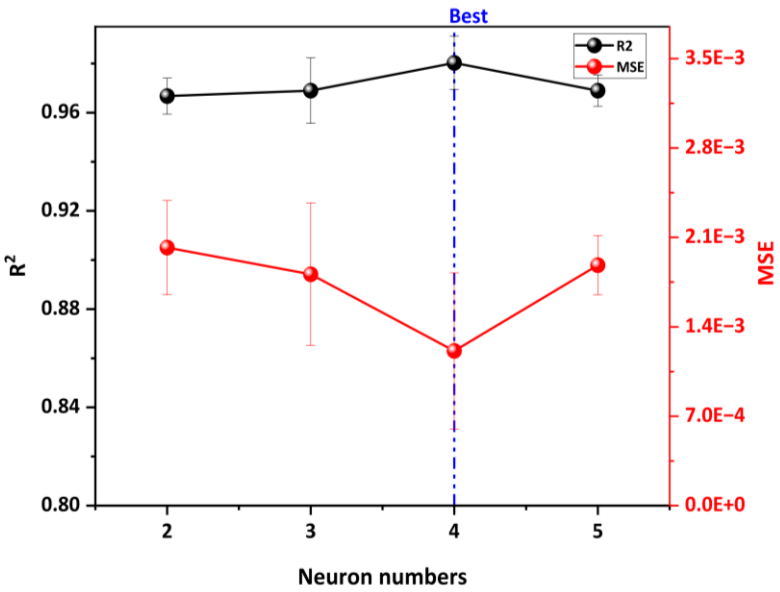

Figure VII.9 Effect of the number of hidden layer neurons on the mean squared error (MSE) and coefficient of determination (R^2) during hyperparameter optimization for the ACE adsorption model

VII.9.2 Best model architecture and training convergence

Based on the hyperparameter optimization, the definitive ANN architecture was established as a multi-layer perceptron comprising four inputs, four hidden neurons, and two outputs. **Figure VII.10(a)** provides a structural schematic of this network topology. The learning convergence across the cross-validation folds, shown in **Figure VII.10(b)**, indicates rapid stabilization of the MSE and efficient training.

Model predictive accuracy was quantified by plotting ANN-simulated values against experimental data. The resulting scatter plots demonstrate excellent agreement between the predicted and actual results. For the equilibrium adsorption capacity (**Figure VII.10**(**c**)), the model returned an R^2 of 0.9945 and an *RMSE* of 4.796. Similarly, for the removal percentage (**Figure VII.10**(**d**)), the network achieved an R^2 of 0.9891 and an *RMSE* of 1.949.

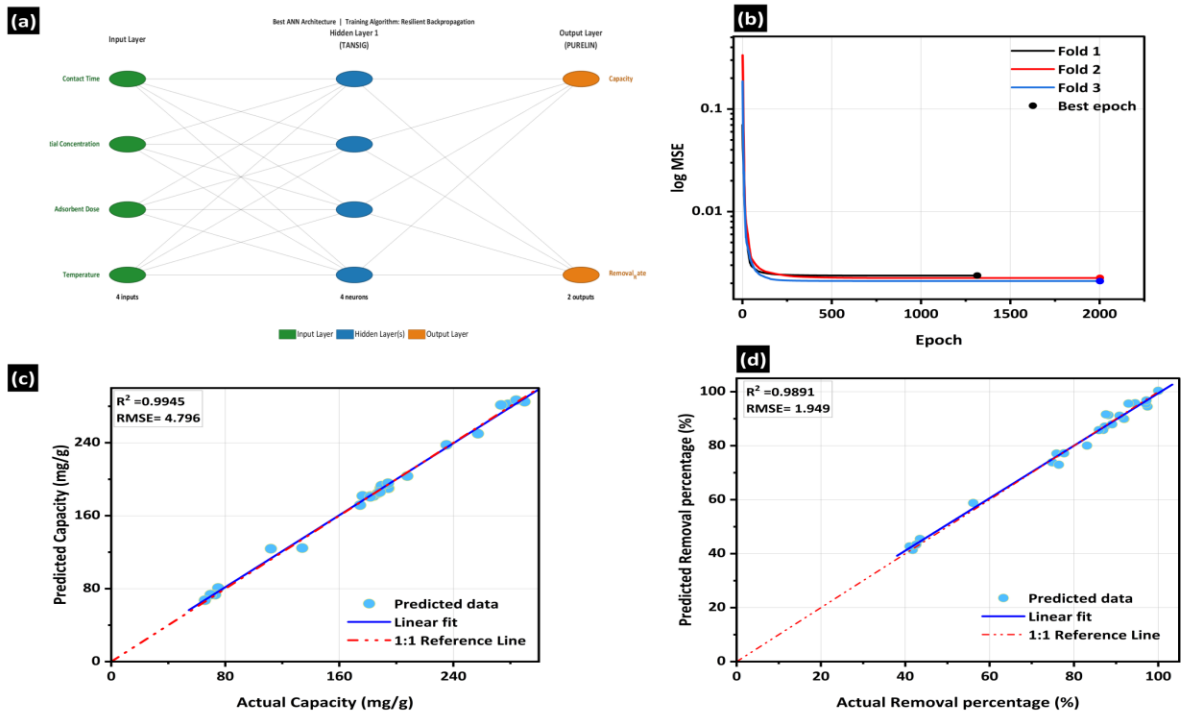

Figure VII.10 Evaluation of the optimized ANN architecture for ACE adsorption: (**a**) schematic representation of the network topology; (**b**) learning curve demonstrating training convergence across cross-validation folds; and scatter plots comparing ANN-predicted values against actual experimental data for (**c**) equilibrium adsorption capacity and (**d**) removal percentage

VII.9.3 Predictive accuracy and residual analysis

To rigorously validate precision and detect potential systematic errors, a comprehensive residual analysis was performed. **Figure VII.11** displays the residuals plotted against the predicted values, along with their corresponding probability distributions. The residual profiles for both adsorption capacity (**Figure VII.11**(**a**,**b**)) and removal percentage (**Figure VII.11**(**c**,**d**)) show narrow error margins, randomly distributed around zero. This confirms the optimized ensemble model accurately captures the experimental variance without introducing significant bias.

Table VII.10 Summary of the top 10 ANN configurations evaluated during the systematic grid search for ACE adsorption

N	Algorithm	Code	Neurons	Hidden TF.	Output TF.	Mean MSE	SD MSE	Mean R^2	SD R^2
1	Resilient Backpropagation	trainrp	4	Logsig	Purelin	1.08E-03	5.0E-04	0.9635	4.5E-02
2	Resilient Backpropagation	trainrp	4	Tansig	Purelin	1.21E-03	6.1E-04	0.9803	1.1E-02
3	BFGS Quasi-Newton	trainbfg	5	Tansig	Purelin	1.34E-03	1.9E-04	0.9756	9.9E-03
4	One-Step Secant	trainoss	5	Tansig	Purelin	1.38E-03	3.4E-04	0.9779	2.9E-03
5	Conjugate Gradient with Fletcher-Reeves	traincgf	3	Logsig	Purelin	1.39E-03	5.6E-04	0.9769	9.5E-03
6	Resilient Backpropagation	trainrp	5	Logsig	Purelin	1.42E-03	2.6E-04	0.9751	1.1E-02
7	Resilient Backpropagation	trainrp	5	Elliotsig	Purelin	1.45E-03	1.7E-04	0.9717	1.7E-02
8	Bayesian Regularization	trainbr	4	Tansig	Purelin	1.47E-03	7.9E-04	0.9748	1.6E-02
9	Resilient Backpropagation	trainrp	5	Poslin	Purelin	1.48E-03	4.6E-04	0.9752	4.4E-03
10	Conjugate Gradient with Fletcher-Reeves	traincgf	4	Tansig	Purelin	1.48E-03	2.9E-04	0.9751	4.8E-03

Note: TF = Transfer Function; SD = Standard Deviation; Code = MATLAB training algorithm function name.

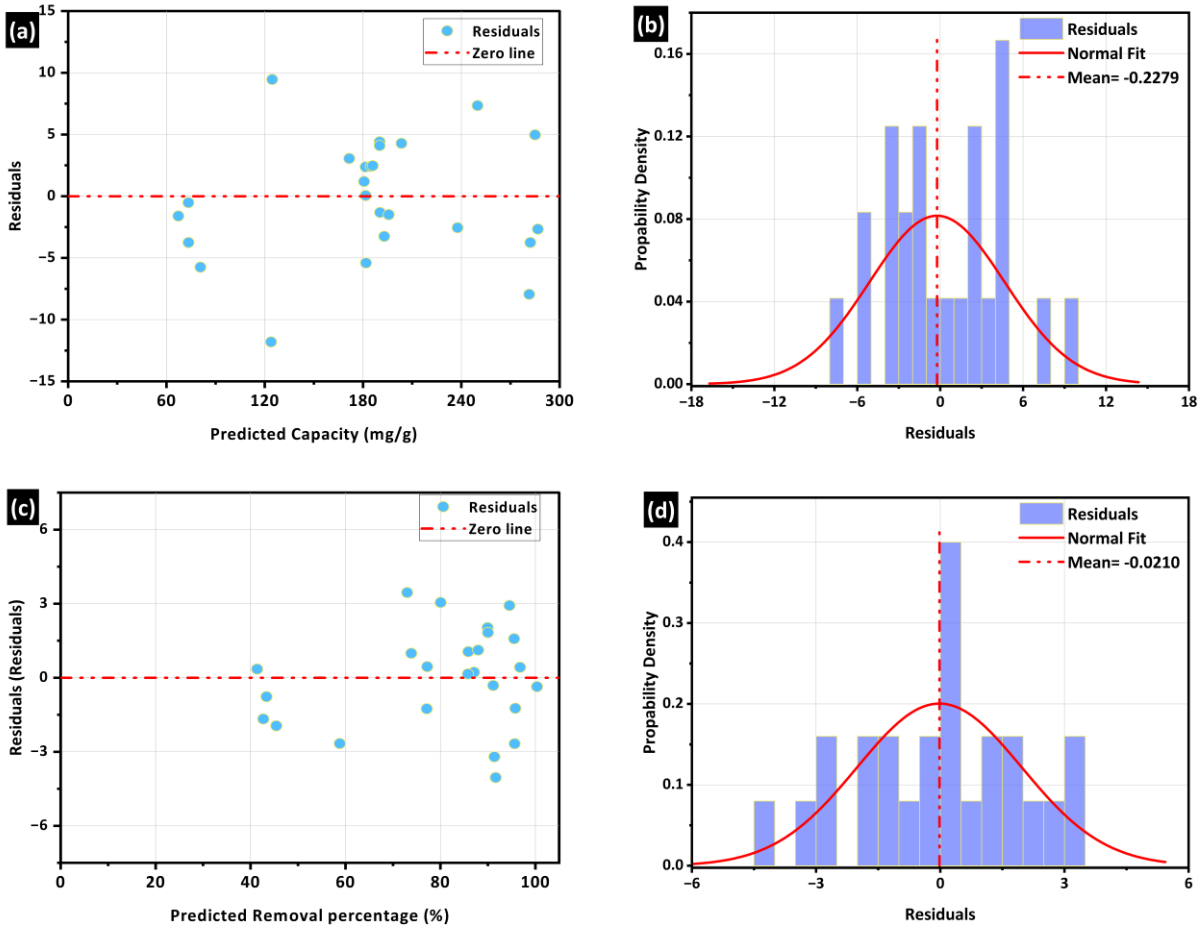

Figure VII.11 Residual analysis of the optimized ensemble model for ACE adsorption: (**a**) residuals versus predicted values and (**b**) residual probability distribution for adsorption capacity; (**c**) residuals versus predicted values and (**d**) residual probability distribution for removal percentage

VII.9.4 Cross-validation and model robustness

Network robustness and generalizability were verified through fold-by-fold cross-validation, with detailed metrics presented in **Figure VII.12**. The model demonstrated consistent predictive capability, recording a mean validation R^2 of 0.9871 for adsorption capacity (Figure V.4(a)) and 0.9701 for removal percentage (**Figure VII.12**(**b**)). Furthermore, the mean squared errors remained remarkably low across all folds (averaging 0.0006 for capacity (**Figure VII.12**(**c**)) and 0.0018 for removal (**Figure VII.12**(**d**))), which verifies excellent model stability against unseen data.

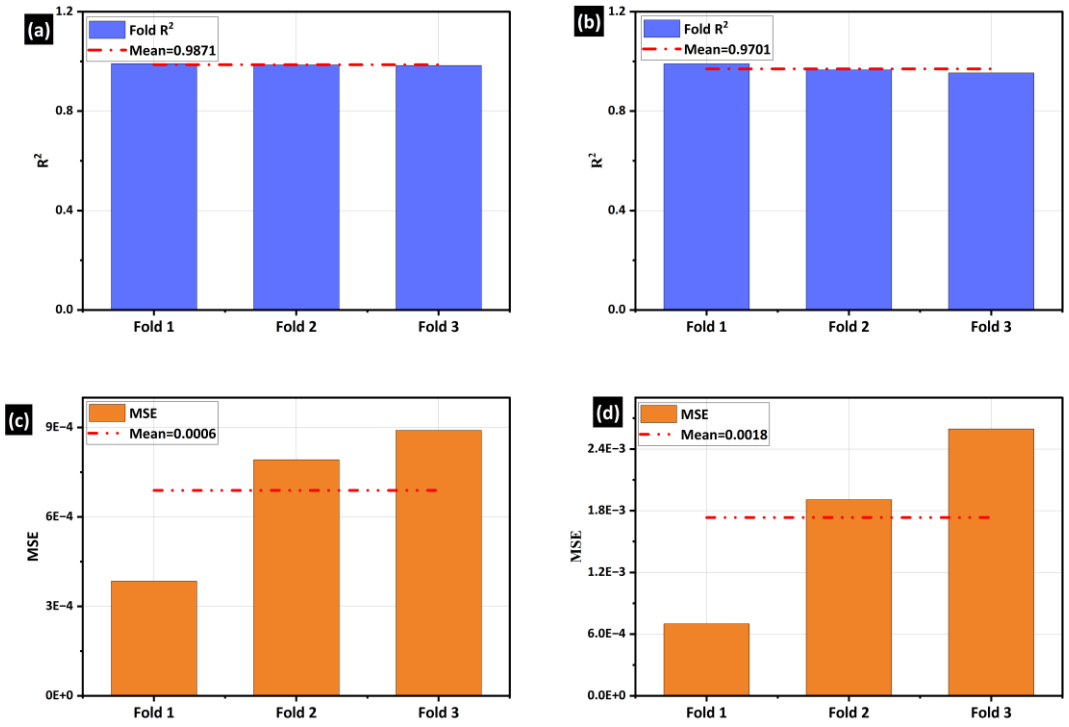

Figure VII.12 Cross-validation performance charts detailing the fold-by-fold validation metrics for ACE adsorption: (**a**) R^2 for adsorption capacity, (**b**) R^2 for removal percentage, (**c**) mean squared error (MSE) for adsorption capacity, and (**d**) MSE for removal percentage

VII.9.5 Mechanistic insights via sensitivity analysis

A holistic performance evaluation of the optimized ANN is summarized in **Figure VII.13**. The MSE convergence profiles for the training, validation, and test partitions (**Figure VII.13** (a)) indicate optimal validation performance at epoch 120, successfully avoiding overfitting. This high degree of correlation is reinforced by the subset regression plots (**Figure VII.13**(**b**)) and the error histogram spanning all data partitions (**Figure VII.13**(**c**)).

Finally, to translate the ANN's mathematical abstraction into a physical, mechanistic understanding, a sensitivity analysis was conducted using the Garson algorithm. **Figure VII.13**(**d**) quantifies the relative importance of the independent input variables. This provides a direct assessment of how strongly each operational parameter dictates the equilibrium adsorption capacity and the final removal efficiency.

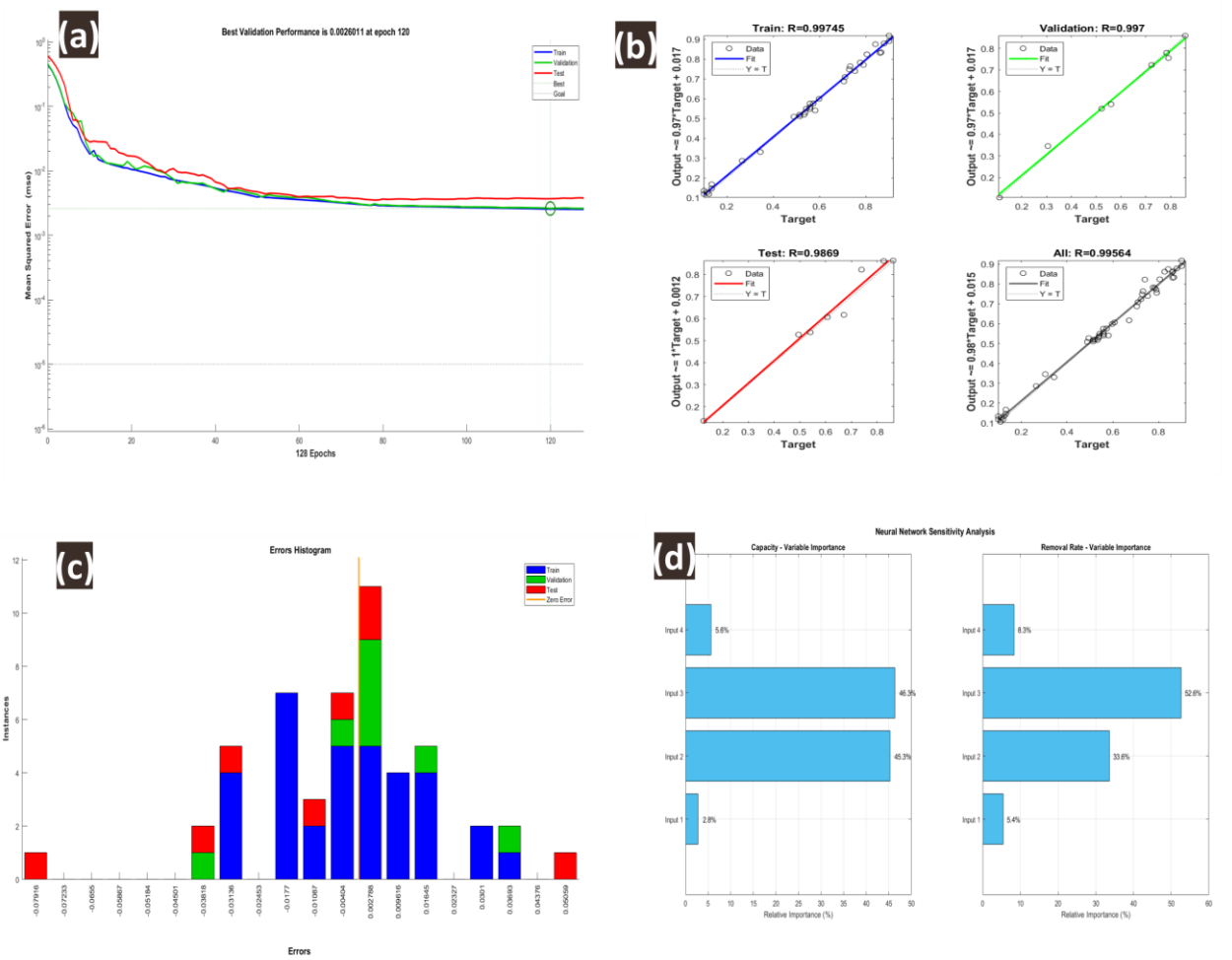

Figure VII.13 Comprehensive performance evaluation of the optimized ANN configuration: (**a**) MSE convergence versus epoch during the training, validation, and testing phases; (**b**) regression plots for data subsets; (**c**) error histogram across all data partitions; and (**d**) mechanistic sensitivity analysis via the Garson algorithm evaluating the relative importance of independent input variables

VII.10 Optimization of acetamiprid adsorption via genetic algorithm

The simultaneous maximization of adsorption capacity and removal efficiency presents a classic multi-objective optimization (MOO) dilemma in wastewater treatment processes. During the adsorption of ACE onto the ZnO@DPS-AC composite, these two objectives are inherently conflicting. Maximizing q_e typically requires a higher initial adsorbate concentration and a lower adsorbent dosage, which invariably reduces the overall percentage of ACE removed from the effluent. To resolve this trade-off, a non-dominated sorting genetic algorithm was employed to identify the optimal operating conditions that satisfy both criteria.

VII.10.1 Optimization framework and parameter selection for ACE

The efficacy of a genetic algorithm relies heavily on precise hyperparameter tuning, which establishes the critical balance between exploring the global parameter space and exploiting local optima. Accordingly, a comprehensive grid search was conducted to evaluate fundamental algorithmic configurations systematically. The hypervolume (a defining metric for convergence and diversity in multi-objective optimization) was mapped across multiple combinations of population sizes, crossover rates, and mutation rates, yielding 27 distinct setups.

Figure VII.14 details the outcomes of this evaluation. **Figure VII.14**(**a**) presents hypervolume heatmaps that illustrate the algorithm's sensitivity to variations in these genetic operators. Concurrently, **Figure VII.14**(**b**) ranks all 27 configurations based on their composite scores. The configuration that achieved the highest rank was designated as the final ACE adsorption optimization model, ensuring maximum algorithmic efficiency while preventing premature convergence.

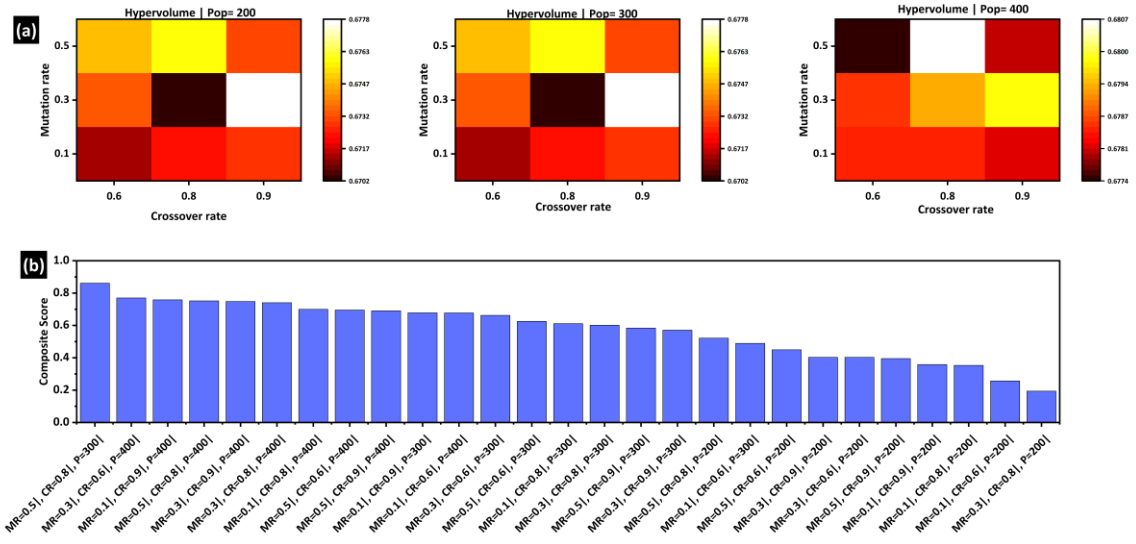

Figure VII.14 Comprehensive evaluation of Genetic Algorithm (GA) grid search parameters for ACE adsorption: (**a**) hypervolume heatmaps across varying population sizes, crossover rates, and mutation rates, and (**b**) ranking of the 27 evaluated configurations based on their overall composite scores

VII.10.2 Convergence and optimization dynamics of the ACE system

The evolutionary dynamics of the optimized genetic algorithm demonstrated highly stable convergence toward the true Pareto-optimal front. As illustrated in **Figure VII.15**(**a**), the best and average values for both adsorption capacity and removal efficiency exhibited a rapid initial improvement, followed by asymptotic stabilization across successive computational generations. Furthermore, the hypervolume metric displayed a steady, monotonic increase before reaching a definitive plateau **Figure VII.15**(**b**)). This behavior mathematically confirms that the non-dominated solution set achieved its maximum potential.

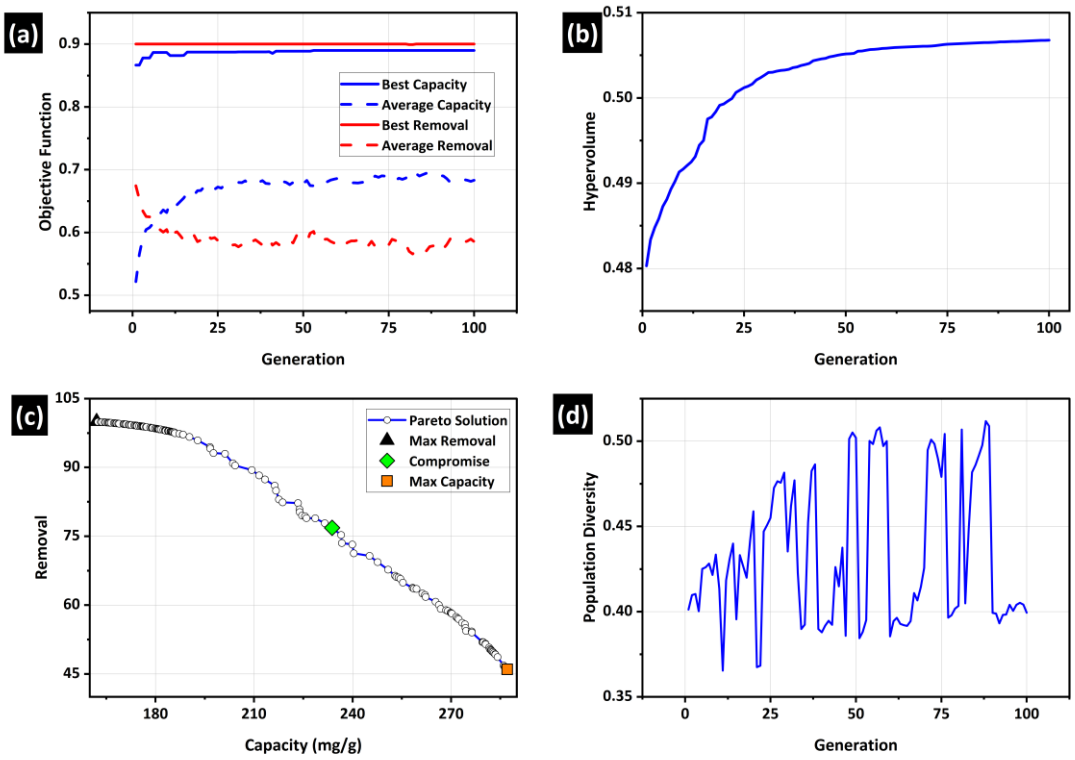

Figure VII.15 Evolutionary dynamics of the multi-objective optimization for ACE adsorption: (**a**) progression of the best and average values for adsorption capacity and removal efficiency, (**b**) hypervolume progression, (**c**) final Pareto front highlighting representative optimal solutions, and (**d**) population diversity across generations

Maintaining high population diversity throughout the optimization sequence (**Figure VII.15**(**d**)) was essential to prevent premature convergence and yield a well-distributed optimal front.

Secondary statistical indicators further substantiate this mathematical robustness. The continuous expansion of the Pareto front size (**Figure VII.16(a)**) demonstrates the algorithm's capacity to discover an increasing number of viable trade-off configurations. Periodic generation-to-generation improvements decayed logarithmically (**Figure VII.16(b)**), a characteristic behavior of mature optimization runs approaching true convergence. Additionally, the spacing metric exhibited a sharp, consistent decline (**Figure VII.16(c)**), ensuring the uniform distribution of optimal solutions without restrictive clustering. Finally, the solution spread (**Figure VII.16(d)**) confirms that the algorithm successfully captured the extreme ends of the objective space, securing comprehensive bounds for both maximum capacity and maximum removal scenarios.

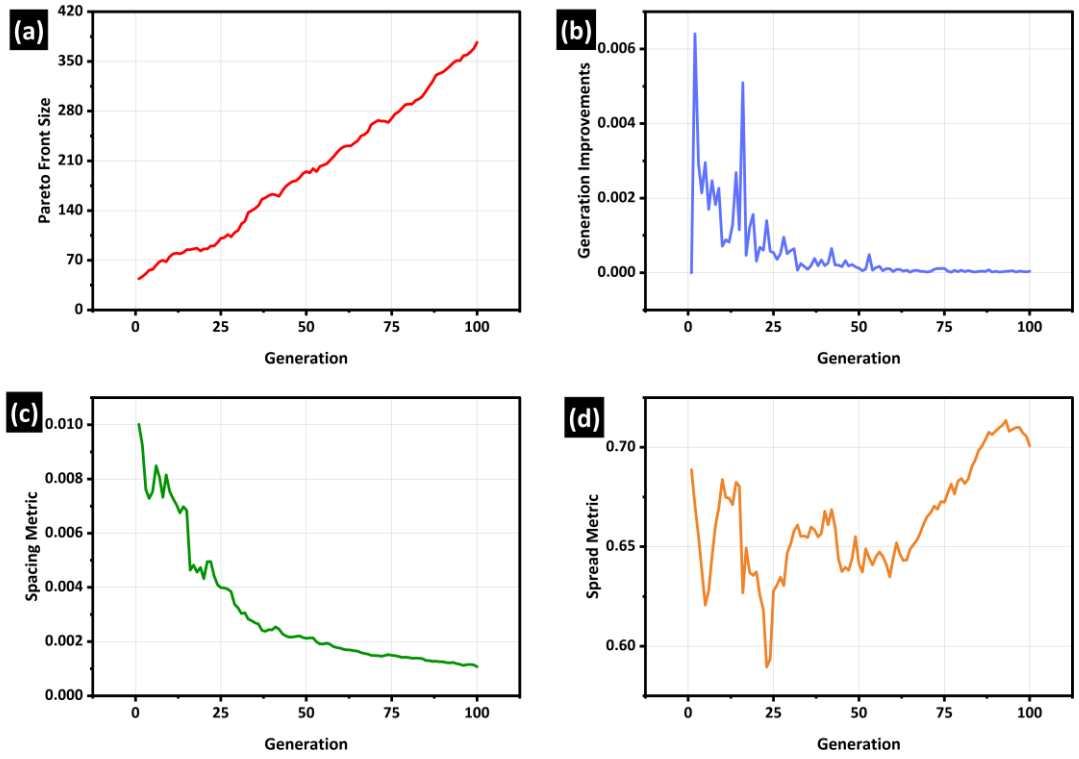

Figure VII.16 Progression of key multi-objective optimization metrics over generations during ACE adsorption: (**a**) Pareto front size, (**b**) generation-to-generation improvements, (**c**) spacing metric, and (**d**) spread metric

VII.10.3 Pareto front analysis for the ACE adsorption

Building on established convergence dynamics and statistical indicators, the genetic algorithm

successfully identified the true Pareto-optimal boundary for the ACE adsorption system. The resulting frontier (**Figure VII.15(c)**) maps the continuum of non-dominated solutions, explicitly defining the trade-off between maximizing specific adsorption capacity and overall removal efficiency. This comprehensive solution space serves as the mathematical foundation for extracting targeted, actionable operational parameters.

VII.10.4 Optimal adsorption conditions for ACE adsorption

To translate the theoretical computational findings into actionable engineering parameters, three critical, representative solutions were extracted from the final Pareto front: maximum capacity, maximum removal, and a strategically balanced compromise. **Table VII.11** delineates the specific operational configurations (adsorbent mass, initial concentration, contact time, and temperature) that dictate these optimal outcomes.

Maximum Capacity: Driven by fundamental mass-transfer principles, achieving the absolute maximum capacity (287.12 mg/g) requires an elevated initial ACE concentration (400.00 mg/L) and a strictly limited adsorbent dosage (30.00 mg). The rapid exhaustion of available active sites under these conditions inherently constrains the overall removal efficiency to 45.99%.

Table VII.11 Optimal batch adsorption conditions derived from the Genetic Algorithm for three representative Pareto solutions for ACE: maximum capacity, maximum removal rate, and the compromise solution

Solution Type	q_e (mg/g)	R (%)	t (min)	C_0 (mg/L)	m (mg)	T(°C)
Max q_e	287.12	45.99	180.00	400.00	30.00	30.00
Max R	162.07	100.00	180.00	324.15	100.00	30.00
Compromise	233.79	76.83	180.00	362.75	61.01	30.00

Maximum Removal: Conversely, complete pollutant elimination (100.00%) requires a significant expansion of the available active surface area, necessitating an adsorbent dosage of 100.00 mg. Lowering the initial concentration to 324.15 mg/L alongside this stoichiometric surplus fundamentally reduces the localized specific capacity to 162.07 mg/g.

Compromise Solution: For practical industrial application, the compromise solution balances material resource efficiency with environmental compliance. This optimal configuration achieves an adsorption capacity of 233.79 mg/g and a 76.83% removal efficiency by utilizing an intermediate adsorbent dosage of 61.01 mg at an initial concentration of 362.75 mg/L.

Notably, across all three operational scenarios, the algorithm consistently converged upon an equilibrium contact time of 180.00 min and an ambient operating temperature of 30.00°C.

VII.10.5 Experimental validation

To verify the predictive fidelity of the optimization framework, the theoretically derived parameters require empirical validation. Subsequent batch adsorption experiments will utilize the precise conditions dictated by the compromise solution (C_0 = 362.75 mg/L, m = 61.01 mg, t = 180.00 min, T = 30.00°C). The alignment between the experimentally observed adsorption metrics (q_e ≈ 227.54 mg/g; R ≈ 77.17%) and the algorithm-predicted values provides definitive confirmation of the model's reliability for full-scale process design.

VII.11 Mechanistic insights into acetamiprid adsorption

Structural analyses confirm the successful embedding of nanometric ZnO particles (averaging 33.07 nm in crystallite size, **section IV.7**) within a partially graphitized carbon framework. This specific configuration provides a highly reactive surface chemistry populated by oxygen-containing functional groups and Zn-O bonds (**Figure IV.4**). The material exhibits a point of zero charge of 6.67 (**Figure IV.2**). It achieves highly efficient, pH-independent ACE removal with a maximum experimental equilibrium adsorption capacity of 291.38 mg/g. Furthermore, thermodynamic evaluations confirm that the adsorption process is strictly exothermic. By synthesizing these physicochemical properties with the batch adsorption model, the distinct mechanistic pathways governing ACE uptake are detailed below.

VII.11.1 Pore-filling mechanism

Textural characterization provides direct physical evidence that pore filling is the primary adsorption mechanism (**Figure VII.18**). As previously detailed in section IV.2.8, BET analysis of the post-adsorption samples revealed the complete obliteration of measurable microporosity. Specifically, the micropore volume decreased precipitously from 0.159 cm^3/g to 0.000 cm^3/g. This reduction was accompanied by an approximate 50% attenuation of the specific surface area, dropping from 1028.63 m^2/g to 513.11 m^2/g (**Table IV.3**). Furthermore, morphological evaluations via SEM (**Figure IV.3(e)**) illustrate the deposition of bulky molecular aggregates. These adsorbate clusters partially mask the underlying honeycomb architecture of the carbon matrix. This structural

evidence confirms that bulky ACE molecules actively diffuse into and become permanently wedged within the internal void spaces. This pore-filling phenomenon aligns with findings reported by Wang et al. (2016) for biochar-amended sand, Yao et al. (2024) for KOH-activated crayfish shell biochar, and Li et al. (2026) for H_3PO_4-modified pear branch biochar.

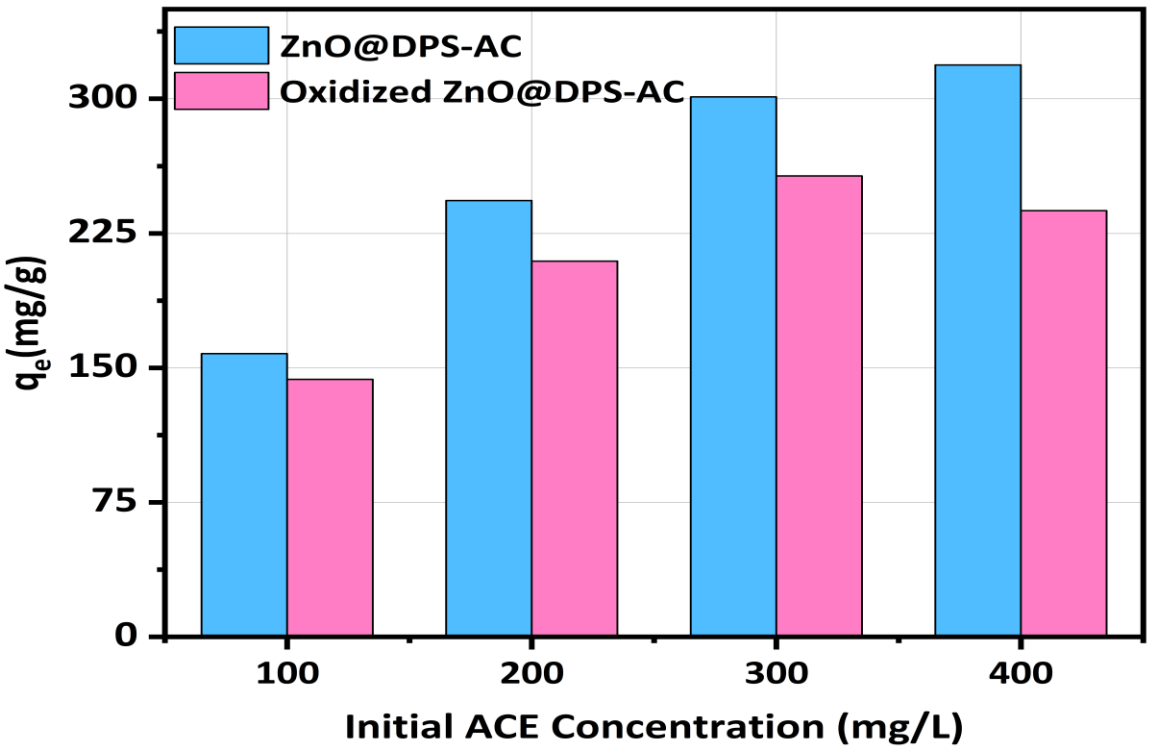

Figure VII.17 Performance comparison between the pristine ZnO@DPS-AC and oxidized ZnO@DPS-AC composites

VII.11.2 Hydrogen bonding

The surface chemistry of the pristine ZnO@DPS–AC composite is exceptionally rich in oxygen-containing functional groups. Spectral evidence derived from FTIR analysis (**Figure IV.4**) demonstrates that the most pronounced change following ACE adsorption is the near-total disappearance of the broad hydroxyl stretching band located between 3000 and 3500 cm^{-1}. This severe spectral attenuation provides definitive evidence that surface hydroxyl groups serve as primary anchoring sites. These specific functional groups engage in strong hydrogen bonding and dipole-dipole interactions with the electronegative nitrogen and chlorine heteroatoms present in the

ACE molecule. Similar hydrogen bonding mechanisms for ACE removal have been validated by Srikhaow et al. (2022), Yao et al. (2024), and Li et al. (2026).

VII.11.3 π–π electron donor-acceptor interactions

Batch experiments demonstrated that the equilibrium adsorption capacity of ACE onto the ZnO@DPS–AC composite remains essentially independent of the initial solution pH over a broad pH range of 2 to 12 (**Figure VII.1(b)**). As established in section **VII.2.2**, ACE's very low *pKa* (≈0.7) maintains the molecule in a predominantly neutral form across the entire pH range evaluated, eliminating electrostatic interactions as a primary binding mechanism.

Specifically, π–π electron donor-acceptor interactions occur between the electron-deficient aromatic pyridine ring of the ACE molecule and the π–electron-rich, partially graphitized structure of the activated carbon matrix. This phenomenon is corroborated by FTIR analysis, which reveals distinct shifts and signal masking within the aromatic C=C stretching domain following adsorption (**Figure IV.4**).

To further validate this mechanism, the composite was subjected to H_2O_2 oxidation to introduce excess oxygen functional groups. As depicted in the performance comparison in **Figure VII.17**, this oxidation procedure systematically reduces the π–electron density of the individual graphene layers. This corresponding reduction in electron density weakens the π–π interactions, thereby diminishing the overall adsorption capacity. This specific π–π mechanistic pathway is widely supported in the literature by Wang et al. (2016), Yao et al. (2024), and Srikhaow et al. (2022).

VII.11.4 Thermodynamic exclusion of surface complexation

While Lewis acid-base interactions frequently drive adsorption on metal oxide-modified materials, thermodynamic data indicate that strong chemical surface complexation is not the dominant pathway for ACE removal in this system. Specifically, the adsorption process is demonstrably exothermic. This thermal behavior is explicitly evidenced by the inverse relationship between temperature and maximum uptake capacity observed in the equilibrium isotherms (**Figure VII.2(b)**, **Table VII.2**).

Furthermore, the ΔH° calculated using the non-linear van't Hoff equation via the Langmuir constant is -31.177 kJ/mol. This magnitude falls well below the standard energetic threshold for

chemisorption (> 40 kJ/mol). As previously detailed in **section VII.7**, ΔH° values derived from the Redlich-Peterson and Khan models were excluded from this specific mechanistic deduction due to severe mathematical discrepancies between their linear and non-linear forms.

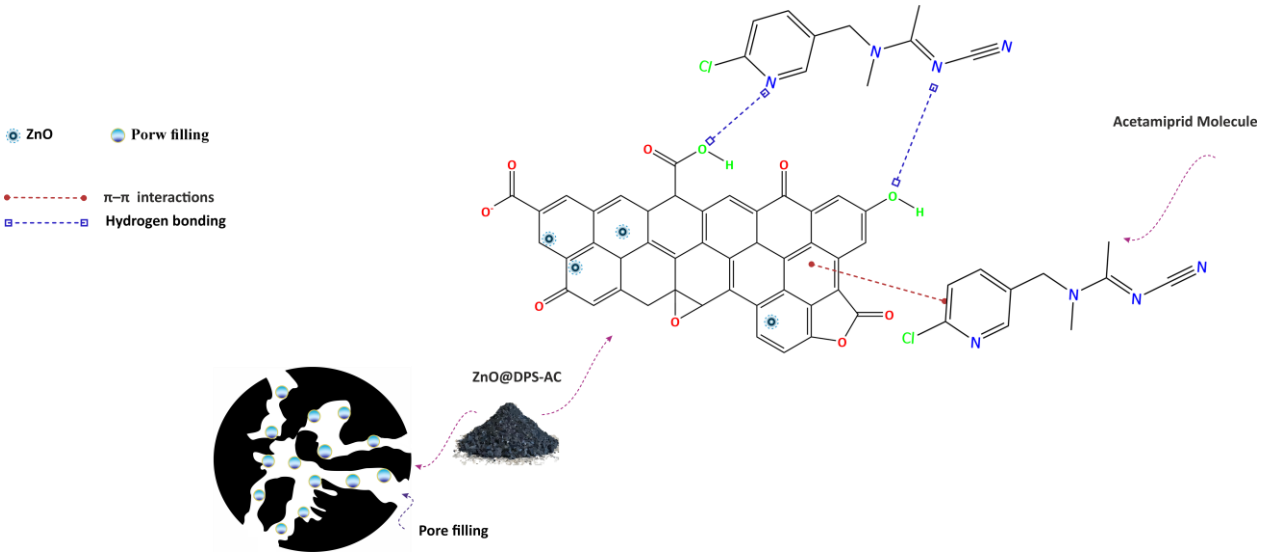

Figure VII.18 Schematic illustration of the proposed physicochemical mechanisms for the adsorption of ACE onto the ZnO@DPS-AC composite

The absence of irreversible chemical bonding is also corroborated by the cyclic regeneration studies discussed in **section VII.7**. The high desorption and recovery efficiency achieved using a simple polar solvent, such as ethanol, demonstrates that the adsorbate is not permanently anchored to the solid matrix (**Figure VII.4**). Consequently, irreversible surface complexation is either completely absent or exerts a negligible influence on the overall adsorption process. The uptake mechanism is instead governed almost exclusively by the physical driving forces established earlier, namely pore filling, hydrogen bonding, and π–π electron donor-acceptor interactions.

VII.12 Conclusion

The investigations detailed in this chapter establish a comprehensive physicochemical profile of ACE adsorption by the ZnO@DPS-AC composite. This adsorption system exhibits distinct behavioral characteristics compared to the dye and phenolic systems analyzed in preceding chapters. Most notably, empirical batch studies confirm that ACE removal is entirely *pH*-independent between *pH* 2.0 and 12.0. The system also maintains stability at ionic strengths up to

0.6 M NaCl. This exceptional operational robustness is driven by the ACE molecule's predominantly neutral state ($pKa \approx 0.7$) and the dominance of non-electrostatic binding forces. Consequently, ZnO@DPS-AC eliminates the need for strict *pH* management. This finding holds significant practical value. It proves the composite can function effectively under the highly variable conditions typical of agricultural runoff, directly addressing the core application scenario of this chapter.

Kinetic and equilibrium modeling further underscore the material's high efficiency. The adsorption profile follows a biphasic PSO model ($R^2_{adj} = 0.998$), reaching dynamic equilibrium at 180 min. Concurrent Elovich and Vermeulen fits verify the energetic heterogeneity of the surface and highlight intraparticle diffusion as a rate-controlling step. This aligns seamlessly with the complex hierarchical pore architecture established in **Chapter IV**. The composite achieves an outstanding maximum experimental capacity of 291.38 mg/g. This value firmly positions the material in the upper tier of agricultural by-product-based carbons in terms of performance.

Equilibrium data are best described by the three-parameter Khan model ($R^2 = 0.996$ at 30 °C), corroborating the kinetic evidence of surface heterogeneity. Furthermore, thermodynamic analysis marks a fundamental departure from the endothermic profiles of Methyl Orange and Catechol observed earlier. A 24% reduction in q_m as temperatures rise from 30 °C to 50 °C confirms an unambiguously exothermic process ($\Delta H^\circ = -31.177$ kJ/mol). From an engineering perspective, this means ACE remediation operates at peak efficiency at ambient temperatures. Full-scale deployment would therefore require no thermal energy input, significantly enhancing the system's economic viability.

Advanced computational modeling reinforced these empirical findings through multivariable optimization. The RSM-CCD produced highly accurate quadratic models ($R^2 > 0.99$). This statistical analysis identified adsorbent dosage and initial concentration as the primary governing parameters. An ANN-GA validated this outcome. Trained strictly on a non-augmented experimental matrix, the ANN-GA framework yielded an optimized compromise solution (q_e = 215.4 mg/g, R = 89.4%) with a relative error of only 6.72%. This architecture proves the predictive power of the machine learning strategy even under data-sparse conditions. Garson sensitivity analysis confirmed the primary operational determinants, ensuring strict mechanistic consistency between the statistical and machine-learning approaches.

Mechanistically, spectroscopic, textural, and thermodynamic evidence indicate that the system is exclusively governed by physical forces, not electrostatic forces. Complete obliteration of microporosity following adsorption (micropore volume reduced from 0.159 to 0.000 cm^3/g) identifies physical pore-filling as the primary capture pathway. This mechanism is supplemented by hydrogen bonding between the composite's surface hydroxyl groups and the electronegative heteroatoms of ACE. Additionally, π-π electron donor-acceptor interactions occur between the aromatic pyridine ring of ACE and the graphitized carbon matrix. Systematic reductions in capacity following controlled H_2O_2 surface oxidation empirically confirmed these interactions. Irreversible inner-sphere surface complexation is definitively excluded by the low enthalpy magnitude (ΔH° < 40 kJ/mol) and a high ethanol regeneration efficiency exceeding 80%.

While these findings conclusively demonstrate the structural versatility of the ZnO@DPS-AC composite, the current thermodynamic and kinetic parameters are restricted to static batch conditions (50–400 mg/L and 30–50 °C). Extrapolation beyond these boundaries requires further validation. The preceding chapters have now fully characterized the fundamental equilibrium behavior, kinetic profiles, and mechanistic drivers for three distinct pollutant classes in static systems. The next logical step is to evaluate the composite's performance under dynamic, continuous-flow conditions—consequently, **Chapter VIII** transitions to fixed-bed column adsorption systems. By modeling breakthrough curves and analyzing mass transfer zones, the subsequent chapter will translate these static parameters into the dynamic engineering metrics required for real-world industrial wastewater treatment design.

Chapter VIII: Column Adsorption Studies of Methyl Orange, Catechol, and Acetamiprid onto ZnO@DPS-AC

* * * * *

VIII.1 Introduction

The batch adsorption investigations detailed in preceding chapters established the fundamental thermodynamic and kinetic baselines for pollutant uptake by the ZnO@DPS-AC composite. These characterizations yielded maximum equilibrium capacities and intrinsic rate constants under well-controlled, static conditions. However, batch methodologies inherently fail to replicate the complex concentration gradients, non-ideal mass-transfer dynamics, and variable empty bed contact times (EBCT) that strictly govern large-scale wastewater treatment operations. Industrial and pilot-scale facilities operate almost exclusively utilizing continuous-flow, fixed-bed configurations. In these continuous systems, localized adsorbate concentration is simultaneously dependent on spatial position within the bed and elapsed operational time. This establishes a non-steady-state hydrodynamic environment characterized by the progressive propagation of an MTZ from the column inlet toward the effluent boundary (as comprehensively detailed in **section II.7.1**).

Transitioning from batch-scale feasibility to continuous-flow process design constitutes a mandatory step for validating the practical utility of ZnO@DPS-AC for remediating the three target micropollutants: MO, CAT, and ACE. Consequently, this chapter details a series of fixed-bed column experiments executed across a systematic parameter matrix (described conceptually in **section III.16.3**). Three primary operational variables were sequentially manipulated: adsorbent bed mass (125, 250, and 500 mg), volumetric flow rate (3, 6, and 9 mL/min), and initial influent concentration. The baseline influent concentration was established at 100 mg/L for both MO and CAT (with subsequent experimental elevations to 200 and 300 mg/L). Conversely, the ACE matrix used an elevated baseline of 200 mg/L (with extensions to 300 and 400 mg/L) to appropriately challenge the significantly higher solid-phase affinity observed for this agrochemical in prior batch studies. For rigorous comparative analysis, Experiment 3 of each series (500 mg, 3 mL/min, at the respective baseline concentration) functions as the universally shared reference condition.

Structurally, **section VIII.2** initiates the chapter with a critical evaluation of the mathematical frameworks applied to model the empirical breakthrough trajectories. This theoretical analysis

specifically demonstrates the mathematical equivalence of classical symmetric logistic models, explores the flexibility of logarithmic boundary modifications, and establishes the mechanistic superiority of the dual-rate Chu-Hashim (C-H XE "C-H" \t ": Chu-Hashim Model") model. **Sections VIII.3**, **VIII.4**, and **VIII.5** systematically present the dynamic breakthrough behavior and optimized predictive modeling results for MO, CAT, and ACE, respectively. These sections employ a rigidly parallel organizational structure to facilitate direct inter-pollutant benchmarking. Finally, **section VIII.6** synthesizes the macroscopic fixed-bed performance and mathematical modeling outcomes across the three target contaminants, explicitly contextualizing mass-transfer limitations and q_e within the physicochemical parameters of the composite matrix.

VIII.2 Mathematical models for breakthrough curve analysis

The quantitative description of fixed-bed adsorption behavior fundamentally relies on mathematical models that relate the ratio of effluent to influent pollutant concentration (C_t/C_0) to elapsed operation time (t). These models serve a dual engineering purpose. First, they distill complex experimental breakthrough data into a concise set of physically interpretable parameters. Second, they facilitate the prediction of essential design metrics, including breakthrough time (t_b), exhaustion time (t_e), and dynamic adsorption capacity, under conditions extending beyond direct empirical measurement. Consequently, selecting an appropriate model transcends pure statistical fitting. It demands a rigorous evaluation of the model's mathematical framework alongside the physical validity of its boundary conditions and resulting predictions.

This study evaluates three distinct families of mathematical models. The first category comprises the classical symmetric logistic models (namely the Yoon-Nelson (Y-N), Thomas (Th), and Adams-Bohart (A-B) equations). The strict mathematical equivalence of these formulations is demonstrated in **section VIII.2.1**. The second family includes logarithmic modifications of these classical equations. These variants are designed to relax the rigid symmetry constraints of their precursors and are detailed in **section VIII.2.2**. The third approach utilizes the C-H model. This mechanistically motivated, two-rate-constant formulation is explicitly engineered to capture asymmetric tailing behavior. It is outlined in **section VIII.2.3**. For the dynamic analysis of each pollutant (**sections VIII.3** to **VIII.5**), one representative classical logistic model is evaluated alongside its logarithmic counterpart and the C-H model.

VIII.2.1 Classical logistic models and their mathematical equivalence

The Th (**Eq. II.24**), Y-N (**Eq. II.25**), and A-B (**Eq. II.26**) models, detailed in **section II.7.3**, share a unified general logistic form (**Eq. VIII.1**) despite originating from distinct physical premises. Busmundrud (1991) first noted this equivalence for the A-B and Y-N models (Chu, 2020c). Chu (2010) and Yan et al. (2001) subsequently extended the framework to encompass the Th model, a finding further discussed and validated by Lee et al. (2015) and Chatterjee and Schiewer (2011), among others. The unified general logistic expression is formulated as follows:

$$\frac{C_t}{C_0} = \frac{1}{1 + exp(a - b \times t)} \qquad \textbf{Eq. VIII.1}$$

The variables a and b serve as generalized parameters that encode the specific constants of all three models:

$$a = \frac{k_{Th} \times q_0 \times m}{Q} = \frac{k_{BA} \times N_0 \times L}{u} = k_{YN}\tau$$
$$b = k_{Th}C_0 = k_{BA}C_0 = k_{YN}$$

A direct consequence of this shared mathematical architecture is that the three models yield strictly identical R^2, *RMSE*, and *AW* values for any given breakthrough dataset. While the models may appear to differ in goodness-of-fit during statistical comparisons, these differences are merely artifacts of linearization procedures. Each equation utilizes a different subset of interconvertible system parameters (such as bed length, superficial velocity, adsorbent mass, and volumetric flow rate) during linear regression (Chu, 2020a, 2020b; Chu & Zhao, 2020). Therefore, treating the A-B, Th, and Y-N models as independent equations and selecting one based on statistical performance constitutes a fundamental methodological error, as explicitly recognized in the recent literature (Chatterjee & Schiewer, 2011; Chu, 2020a, 2020b; Juela, 2021); Kumar et al. (2025)Kumar et al. (2025).

Table VIII.1 conclusively demonstrates this equivalence by applying all three models to the primary MO breakthrough dataset (C_0 = 100 mg/L, Q_v = 3 mL/min, m = 125 mg). Although the models generate numerically distinct rate constants and capacity parameters derived from their unique physical definitions, they produce identical statistical fits (R^2= 0.796, *RMSE* = 0.121, *AW*

= 33.333%). This confirms the absence of any statistical justification for preferring one model over another. Consequently, subsequent analyses use a representative classical model for each pollutant to reflect specific disciplinary conventions, acknowledging that this selection is not statistically significant. The Y-N model is applied to MO, the Th model to CAT, and the A-B model to ACE.

Table VIII.1 Mathematical equivalence of the Y-N, Th, and A-B models demonstrated on the MO Experiment 1 dataset (C_0 = 100 mg/L, Q_v = 3 mL/min, m = 125 mg)

Parameter	Value	Model	$K_{(Y\text{-}N/Th/A\text{-}B)}$	$\tau/q_0/N_0$	R^2	*RMSE*	*AW*(%)
C_0 (mg/L)	100	Y-N	0.063 (min^{-1})	19.690	0.796	0.121	33.333
Q_v (ml/min)	3	Th	0.0006 (L/mg.min)	51.078	0.796	0.121	33.333
m (mg)	125	A-B	0.0006 (L/mg.min)	5294.059	0.796	0.121	33.333

Beyond the issue of mathematical equivalence, classical logistic models have a structural limitation that severely limits their application to breakthrough experimental data. Because they originate from the symmetric logistic function, their inflection point remains mathematically fixed at C_t/C_0= 0.5 (Chu, 2021a). Experimental breakthrough curves, however, frequently exhibit asymmetric profiles. They may demonstrate fronting (an early rise in effluent concentration due to axial dispersion, preferential flow paths, or heterogeneous binding site energies) or tailing (a slow, protracted approach to bed saturation driven by intra-particle diffusion resistance) (Apiratikul & Chu, 2021; Chu, 2021a, 2021b). Both phenomena violate the rigid symmetry constraint, leading classical logistic models to systematically misrepresent early-time concentrations and exhaustion times.

Furthermore, these models predict a non-zero C_t/C_0 at t=0, which is physically inconsistent for a freshly packed, uncontaminated column. The magnitude of this spurious initial concentration scales with the ratio a/b and can be substantial in experiments with short breakthrough times, as demonstrated in **section VIII.3.2**, **VIII.4.2**, and **VIII.5.2**.

VIII.2.2 Logarithmic modified models

To overcome the rigid symmetry constraints of the classical logistic models, C-H (Apiratikul & Chu, 2021; Chu & Hashim, 2023a, 2024a) developed a family of logarithmic modifications by

substituting the linear time variable t with its natural logarithm, $\ln(t)$. This substitution fundamentally alters the predicted breakthrough trajectory by shifting the linear time scale into a logarithmic domain. The critical mechanical consequence of this transformation is that the inflection point is no longer statically fixed at 0.5 but becomes a freely floating parameter optimized by the experimental data during nonlinear regression (Chu, 2021a).

Applying this temporal transformation to the standard Th, Y-N, and A-B frameworks generates the log-Th (**Eq. VIII.2**), log Y-N (**Eq. VIII.3**), and log A-B (**Eq. VIII.4**) models, respectively:

$$\frac{C_t}{C_0} = \frac{1}{1 + \exp\left(K_{Th} \cdot \ln\left(\frac{q_0 \cdot m}{Q_v}\right) - K_{Th} \cdot \ln(C_0 \cdot t)\right)} \quad \textbf{Eq. VIII.2}$$

$$\frac{C_t}{C_0} = \frac{1}{1 + \exp\left(k \cdot (\ln(\tau) - \ln(t))\right)} \quad \textbf{Eq. VIII.3}$$

$$\frac{C_t}{C_0} = \frac{1}{1 + \exp\left(K_{AB} \cdot \ln\left(\frac{N_0 \cdot L}{U_0}\right) - K_{AB} \cdot \ln(C_0 \cdot t)\right)} \quad \textbf{Eq. VIII.4}$$

In sharp contrast to the absolute mathematical equivalence that governs their classical counterparts (established in **section VIII.2.1**), these three logarithmic models are not mutually interchangeable. The distinct exponentiation of t, implicitly embedded in each formulation, dictates that the numerical values of the fitted parameters and the calculated positions of the inflection points will generally differ when applied to the same dataset (Apiratikul & Chu, 2021). In practice, however, the three variants tend to demonstrate comparable goodness-of-fit. Consequently, this analysis uses a single representative logarithmic model for each pollutant, paired with its selected classical counterpart.

By allowing the inflection point to float freely, logarithmic models resolve the spurious boundary errors associated with symmetric functions. They naturally predict a physical initial condition in which $C_t/C_0 \approx 0$ approaches zero at $t \approx 0$, satisfying the boundary condition for an uncontaminated, freshly packed column. This mathematical flexibility produces highly realistic estimations of early breakthrough thresholds and exhaustion times. Extrapolating exhaustion times from these models requires strict critical assessment, however. If the experimental dataset lacks sufficient data points

in the protracted tailing region (a condition present in several experimental runs within this chapter), the logarithmically extrapolated saturation time may substantially overestimate the true physical exhaustion point of the adsorbent bed.

VIII.2.3 Chu-Hashim model

The C-H model (Chu & Hashim, 2023b) represents a physically motivated extension of the Th model framework, specifically engineered to describe breakthrough trajectories characterized by pronounced tailing. Unlike purely empirical modifications, this model integrates the concept of steric hindrance directly into the adsorption rate expression. As the adsorbent surface undergoes progressive loading, previously adsorbed molecules physically obstruct access to remaining vacant binding sites, thereby progressively attenuating the effective adsorption rate (Chu & Hashim, 2023b, 2024b).

To accurately capture these biphasic kinetics, the C-H model utilizes two distinct rate coefficients, formulated as follows:

$$\frac{C_t}{C_0} = \frac{1}{1 + exp(k_{CH1}(\tau_{CH} - t) + exp(-k_{CH2}.t)} \quad \textbf{Eq. VIII.5}$$

Here, k_{CH1} (min^{-1}) denotes the primary rate constant governing the rapid initial surface uptake phase, while k_{CH2} (min^{-1}) represents the secondary rate constant controlling the slow, intra-particle diffusion-limited tailing. The parameter τ_{CH} (min) serves as a characteristic time constant analogous to the Y-N 50% breakthrough parameter.

By definition, $k_{CH1} \gg k_{CH2}$. The large magnitude of k_{CH1} drives a steep initial breakthrough front, whereas the comparatively small k_{CH2} effectively tracks the gradual tailing phase that classical and logarithmic models frequently underestimate (Chu & Hashim, 2023b, 2024b). Consequently, the ratio k_{CH1}/k_{CH2} functions as a quantitative tailing index. A large ratio indicates a sharp initial breakthrough succeeded by a highly protracted saturation phase, whereas a ratio approaching unity denotes nearly symmetric hydrodynamic behavior.

The C-H model offers three distinct mathematical and physical advantages that render it highly suitable for the experimental conditions evaluated in this chapter. First, it generates an initial

predicted concentration (C_t/C_0 at t = 0) that is effectively zero (typically ranging from 0.001 to 0.063, as detailed subsequently in **Table VIII.4**, **Table VIII.7**, and **Table VIII.10**). This aligns perfectly with the physical boundary condition of an uncontaminated column. Second, the formulation successfully relaxes the rigid symmetry constraint. Its inflection point shifts to lower values (typically 0.27-0.45), accurately mirroring the leftward asymmetry typical of continuous-flow systems experiencing rapid preferential uptake. Finally, the dual rate constants provide transparent, mechanistic interpretations of the biphasic adsorption kinetics for each target pollutant interacting with the ZnO@DPS-AC matrix.

Parameter optimization for all three evaluated model families was executed via nonlinear least-squares regression, utilizing the methodology established in s**ection III.16.5**. Key operational metrics, including inflection points, breakthrough times, and absolute exhaustion times, were subsequently derived from the optimized curves utilizing established analytical procedures (Apiratikul & Chu, 2021; Chu, 2020a, 2021a; Chu & Hashim, 2023a).

VIII.3 Dynamic adsorption of Methyl Orange

VIII.3.1 Breakthrough curve behavior and column performance metrics

The experimental breakthrough curves for MO adsorption onto ZnO@DPS-AC across all seven evaluated conditions are shown in **Figure VIII.1**. These curves consistently exhibit a characteristic sigmoidal profile, reflecting the progressive migration of the MTZ from the column inlet to the outlet during continuous bed loading. The experimental parameters and corresponding column performance metrics (including integrated breakthrough area, q_{total}, q_e, M_{total}, and R) are comprehensively detailed in **Table VIII.2**. These metrics were calculated using **Eq. III.27-Eq. III.30** (**section III.16.4**) Experiment 3 (C_0 = 100 mg/L, Q_v = 3 mL/min, m = 500 mg) functions as the central reference condition to enable direct comparative analysis across the three process variables.

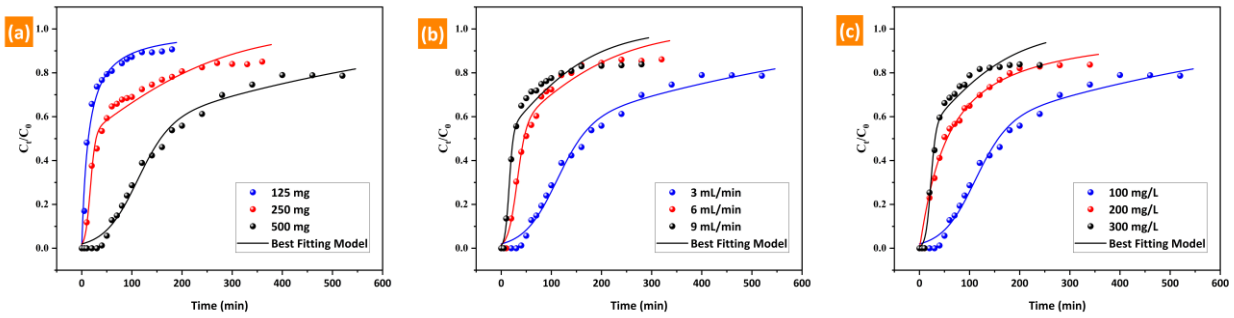

Figure VIII.1 Experimental breakthrough curves for MO adsorption onto ZnO@DPS-AC, illustrating the effects of (**a**) adsorbent bed mass, (**b**) volumetric flow rate, and (**c**) initial concentration

VIII.3.1.1 Effect of adsorbent mass

Expanding the adsorbent bed mass from 125 mg (Exp. 1) to 500 mg (Exp. 3) at a constant influent concentration (C_0 = 100 mg/L) and flow rate (Q_v = 3 mL/min) generated a substantial, progressive enhancement across all breakthrough metrics. This behavior aligns closely with established fixed-bed adsorption theory, which states that an expanded active-site inventory inherently improves column performance (Abdolali et al., 2017; Sazali et al., 2020). Quantitatively, the integrated breakthrough area increased from 36.70 to 232.30 min, reflecting a significantly extended operational period prior to threshold breakthrough. Correspondingly, q_{total} escalated from 11.90 to 68.14 mg, driving the equilibrium capacity (q_e) from 95.20 to 136.27 mg/g, while the overall removal efficiency (R) improved from 20.93% to 44.67%.

Mechanistically, augmenting the bed mass expands the total accessible surface area and increases the inventory of functional binding sites, specifically the surface hydroxyl groups of the ZnO nanoparticles and the π-electron-rich domains of the activated carbon matrix. This expanded site availability prolongs the hydraulic contact time, broadens the MTZ, and systematically delays its propagation toward the column effluent (Abdolali et al., 2017; Olgun et al., 2013). However, the capacity enhancement exhibits a distinct non-linear saturation profile. Doubling the mass from 125 to 250 mg yielded a significant increase in q_e (from 95.20 to 134.27 mg/g), whereas a subsequent doubling to 500 mg produced only a marginal increase (to 136.27 mg/g). This attenuation confirms that, while absolute mass removal scales directly with bed height, the q_e does not. At elevated bed depths, increased intra-particle mass transfer resistance restricts solute diffusion into deep-bed interior sites (Dovi et al., 2022; Guo et al., 2024). Consequently, the q_e of ZnO@DPS-AC for MO

approaches a functional thermodynamic plateau near 136 mg/g under these specific hydraulic conditions.

VIII.3.1.2 Effect of volumetric flow rate

The dynamic influence of volumetric flow rate was assessed by increasing Q_v from 3 to 9 mL/min while keeping C_0 (100 mg/L) and bed mass (500 mg) constant. Accelerating the superficial velocity from 3 to 6 mL/min induced a severe contraction of the breakthrough area (from 232.30 to 93.04 min), alongside reductions in q_{total} (from 68.14 to 55.54 mg) and overall removal efficiency (from 44.67% to 29.08%). This degradation in performance strongly corroborates the inverse proportional relationship between flow rate and fixed-bed utilization efficiency (Abdolali et al., 2017; Sazali et al., 2020). Mechanistically, elevated superficial velocities drastically truncate the EBCT within the column (Chowdhury et al., 2014; Khan et al., 2017). This abbreviated residence time restricts the diffusion kinetics of adsorbate molecules from the bulk fluid across the external boundary layer and into the intra-particle pore network, thereby physically compressing the MTZ, bypassing available binding sites, and inducing premature breakthrough (Abdolali et al., 2017; Du et al., 2018).

An unexpected deviation occurred at Q_v = 9 mL/min (Exp. 5), where absolute mass metrics recovered. The q_{total} rose to 73.44 mg, and q_e climbed to 146.87 mg/g, marginally exceeding the 3 mL/min baseline. This apparent paradox is fully resolved by fundamental mass-balance principles: higher volumetric flow rates deliver a vastly greater absolute mass of target solute over identical experimental durations (Mon et al., 2024). The M_{total} delivered at 9 mL/min was 276.24 mg, compared to 191.00 mg at 6 mL/min. This intensified mass loading establishes a steeper local concentration gradient across the liquid-solid boundary layer, forcing a greater absolute mass of dye into the solid phase before total column exhaustion. Crucially, despite this elevated absolute uptake, the R at 9 mL/min remained severely depressed (26.58%). This distinction rigorously confirms that, while q_e may be artificially inflated by extreme kinetic loading, the column's practical operational efficiency inherently deteriorates at high velocities.

VIII.3.1.3 Effect of initial dye concentration

Elevating the influent concentration from 100 to 300 mg/L resulted in minimal increases in qtotal, which increased from 68.14 to 68.38 mg, and in q_e, which shifted from 136.27 to 136.77 mg/g.

From a thermodynamic perspective, higher bulk concentrations generate a steeper concentration gradient across the solid-liquid interface (Abdolali et al., 2017; Nazari et al., 2016). This intensified gradient serves as a potent driving force, capable of overcoming external fluid-film and internal intra-particle mass transfer resistances, thereby facilitating intra-particle diffusion and accelerating bed-loading kinetics.

Conversely, this elevated kinetic loading exerts a severe negative impact on the dynamic breakthrough profile. The integrated breakthrough area contracted sharply from 232.30 to 71.92 min, and *R* declined from 44.67% to 29.97%. This behavior aligns precisely with standard fixed-bed transport models, which show that high-concentration influents rapidly overwhelm the finite inventory of active surface sites, leading to steep, left-shifted breakthrough curves (Abdolali et al., 2017; Omitola et al., 2022; Sazali et al., 2020). Because the absolute dye load delivered to the column (M_{total}) increased from 152.52 to 228.18 mg, the MTZ was forced to propagate rapidly through the bed. These empirical observations indicate that continuous-flow systems handling high-concentration effluents will experience premature exhaustion, necessitating either significantly expanded bed volumes or highly frequent regeneration cycles to maintain strict environmental discharge limits.

Table VIII.2 Summary of experimental conditions and breakthrough performance metrics for dynamic adsorption of MO. Experiment 3 (shaded) serves as the shared reference condition across all three variable groups

N	C_0 (mg/L)	Q_v (mL/min)	m (mg)	Area (min)	q_{total} (mg)	q_e (mg/g)	M_{total} (mg)	R (%)	Variable
1	100	3	125	36.699	11.900	95.202	58.369	20.93	**Mass**
2	100	3	250	100.480	33.568	134.273	120.269	27.911	**Mass**
3	100	3	500	232.297	68.135	136.270	152.521	44.672	**Shared**
4	100	6	500	93.044	55.536	111.072	191.002	29.076	**Flow rate**
5	100	9	500	74.435	73.436	146.87	276.242	26.584	**Flow rate**
6	200	3	500	107.619	60.116	120.232	189.924	31.653	**Conc.**
7	300	3	500	71.924	68.383	136.765	228.182	29.968	**Conc.**

VIII.3.2 Breakthrough curve modeling and model comparison

The experimental breakthrough trajectories for MO were evaluated against three distinct mathematical formulations: the Y-N model (representing the classical symmetric logistic family), the logarithmic log Y-N model (incorporating a temporal scale transformation), and the dual-rate

C-H model. The optimized kinetic parameters, goodness-of-fit statistics, and predictive boundary analyses are detailed in **Table VIII.3** and **Table VIII.4**.

VIII.3.2.1 Evaluation of the classical Y-N model

The standard Y-N model generated moderate R^2 values ranging from 0.731 (Exp. 2) to 0.895 (Exp. 3), with corresponding *RMSE* values between 0.095 and 0.138. However, these baseline statistics mask a fundamental physical inconsistency inherent to the model's mathematical architecture. As established in **section VIII.2.1**, the Y-N formulation is strictly bound to a symmetric logistic distribution with an invariant inflection point locked at C_t/C_0=0.5 (Chu, 2020a, 2023). Because empirical breakthrough curves frequently demonstrate asymmetry driven by heterogeneous binding energies or intra-particle diffusion resistance, this rigid symmetry forces the model to fit poorly at the boundary conditions (Chu, 2023; Hu & Zhang, 2020).

Consequently, the Y-N model systematically predicts a physically impossible non-zero effluent concentration at t=0 (C_t/C_0 values ranging from 0.085 to 0.257). This structural failure severely contradicts the physical reality of a freshly packed column. It effectively neutralizes the model's predictive utility for early-stage leakage, leading to undefined (NaN) or negative breakthrough time predictions when the spurious initial concentration exceeds the standard 5% threshold (a phenomenon particularly exacerbated in the low-mass Exps. 1 and 2). Despite these boundary failures, the Y-N inflection time parameter (τ), representing the 50% breakthrough milestone, accurately mirrored physical expectations. The parameter increased proportionally with bed mass and contracted at elevated flow rates, mechanistically reflecting the truncation of empty bed contact time that accelerates premature saturation (Ansari et al., 2021; Chowdhury et al., 2014).

VIII.3.2.2 Evaluation of the logarithmic Y-N model

The application of the log Y-N model substantially elevated the regression quality across the entire dataset, achieving exceptional R^2 values (0.932–0.990) and highly minimized *RMSE* values (0.018–0.048). *AW* analysis definitively confirmed a statistical preference for the log Y-N model over the standard formulation in six of the seven experiments, validating that the mathematical modification improves accuracy without overfitting. Mechanistically, the logarithmic temporal transformation introduces a floating inflection point, effectively relaxing the symmetry constraints of the classical logistic function (Apiratikul & Chu, 2021; Chu & Hashim, 2024a). This flexibility

successfully resolved the boundary initialization error, producing physically realistic early-time concentrations characteristic of an uncontaminated column (Chu & Hashim, 2023a). By accurately tracking this early leakage phase, the log Y-N model generated highly reliable breakthrough time predictions that aligned with empirical observations.

However, the model systematically overpredicted exhaustion times relative to the classical Y-N formulation (e.g., 666.27 versus 385.24 min for Exp. 3). This discrepancy arises from the heavy, extended tail of the logarithmic distribution, which models the slow intra-particle diffusion phase as the bed approaches complete saturation. Because absolute experimental column saturation (C_t/C_0= 1) was not achieved during these runs, extrapolating definitive exhaustion times from log-linear models requires stringent validation and caution.

Table VIII.3 Fitted kinetic parameters of Y-N, log Y-N, and C-H models for all seven MO breakthrough experiments

Parameter	Unit	Exp. 1	Exp. 2	Exp. 3	Exp. 4	Exp. 5	Exp. 6	Exp. 7
Y-N Model								
$k_{Y\text{-}N}$	min^{-1}	0.063	0.018	0.0119	0.033	0.034	0.020	0.038
τ	min	19.690	59.619	200.128	61.487	41.607	74.875	47.427
R^2	—	0.796	0.731	0.895	0.880	0.755	0.831	0.813
RMSE	—	0.121	0.135	0.095	0.107	0.138	0.116	0.130
AW	%	8.03E-05	1.43E-10	2.37E-09	1.09E-06	4.93E-06	1.56E-09	1.24E-07
Log Y-N Model								
$k_{Y\text{-}Nl}$	—	1.018	0.889	1.665	1.392	1.004	1.086	1.1409
τ_l	min	13.113	38.303	177.980	51.122	28.482	54.998	34.411
R^2	—	0.962	0.966	0.985	0.972	0.932	0.990	0.934
RMSE	—	0.0386	0.033	0.032	0.036	0.048	0.018	0.041
AW	%	79.089	3.275	3.54E-06	0.047	1.760	95.944	0.007
C-H Model								
k_{CH1}	min^{-1}	0.556	0.201	0.031	0.116	0.247	0.105	0.204
k_{CH2}	min^{-1}	0.022	0.007	0.003	0.009	0.011	0.006	0.011
τ_{CH}	min	7.546	19.963	123.823	35.516	18.016	34.022	24.940
R^2	—	0.970	0.980	0.989	0.985	0.969	0.983	0.984
RMSE	—	0.046	0.036	0.030	0.037	0.049	0.036	0.038
AW	%	20.911	96.725	100.000	99.953	98.240	4.056	99.993

VIII.3.2.3 Evaluation of the Chu-Hashim model

The C-H model delivered a clearly superior mathematical description of the MO breakthrough

dynamics, achieving the lowest *RMSE* (0.030–0.049) and the highest R^2 (0.969–0.989) metrics across six of the seven experiments. In five experiments, *AW* analysis assigned decisive statistical dominance (*AW* ≥ 96.7%) to the C-H model. This robust performance is explicitly linked to the formulation's capability to capture asymmetric tailing behavior where classical frameworks systematically fail (Chu & Hashim, 2023b). By abandoning rigid symmetric constraints, the C-H model established highly realistic initial boundary conditions (C_t/C_0= 0.006–0.027 at t=0), resulting in predicted breakthrough times that closely mirrored empirical observations (e.g., predicting tb2 = 66.92 min versus an observed 60 min for Exp. 3).

Mechanistically, the dual-rate architecture directly accounts for the physical phenomenon of progressive steric hindrance (Chu & Hashim, 2023b). The model partitions the overall kinetics into a primary rate constant (k_{CH1}) governing rapid initial surface uptake and a secondary rate constant (k_{CH2}) controlling the protracted, diffusion-limited tailing phase. The derived ratio k_{CH1}/k_{CH2} decreased from 25.3 to 10.3 as the bed mass was expanded from 125 to 500 mg. This reduction quantifiably indicates that deeper beds broaden the mass transfer zone, rendering the transition to the sterically hindered tailing phase significantly more gradual.

Furthermore, accelerating the superficial flow velocity drastically elevated the primary surface uptake rate (k_{CH1} increased from 0.031 to 0.247 min^{-1}). This mathematical behavior mechanistically corroborates that higher superficial velocities physically compress the external fluid film thickness, thereby diminishing external mass transfer resistance and accelerating initial localized uptake (de Franco et al., 2017). In stark contrast, k_{CH2} remained remarkably stable across flow variations. This stability provides robust mathematical confirmation that the protracted tailing phase is governed strictly by intra-particle diffusion and the internal solid-phase properties of the adsorbent, rendering it completely independent of external fluid hydrodynamics.

Table VIII.4 Comparison of experimental and model-predicted breakthrough and exhaustion parameters for MO

Parameter	Unit	Exp. 1	Exp. 2	Exp. 3	Exp. 4	Exp. 5	Exp. 6	Exp. 7
Experimental Data								
$(C_t/C_0)_b$ (threshold) †	—	0.05	0.05	0.05	0.05	0.05	0.05	0.05
t_b	min	<5	<5	<50	<20	<10	<20	<20
$(C_t/C_0)_b$ (adj.) ‡	—	0.485	0.377	0.1286	0.136	0.406	0.230	0.254

t_{b2}§	min	10	20	60	20	20	20	20
t_e	min	N/D	N/D	N/D	N/D	N/D	N/D	N/D
Y-N Model Predictions								
C_t/C_0 **at** $t = 0$	—	0.223	0.257	0.085	0.118	0.196	0.181	0.143
$(C_t/C_0)_{0.5}$	—	0.5	0.5	0.5	0.5	0.5	0.5	0.5
$t_{0.5}$	min	19.690	59.619	200.128	61.487	41.607	74.875	47.427
t_b	min	NaN	NaN	NaN	NaN	NaN	NaN	NaN
t_{b2}	min	18.555	31.480	38.928	4.937	30.347	18.083	18.941
t_e	min	54.296	182.706	385.240	128.599	106.340	183.661	105.606
Logarithmic Y-N Model Predictions								
C_t/C_0 **at** $t = 0$*	—	—	—	—	—	—	—	—
$(C_t/C_0)_{0.5}$	—	0.009	NaN	0.199	0.141	0.002	0.040	0.062
$t_{0.5}$	min	0.131	NaN	77.276	13.933	0.0618	2.930	3.169
t_b	min	0.728	1.395	30.348	6.163	1.5178	3.657	2.605
t_{b2}	min	12.217	21.767	56.383	13.516	19.467	15.051	13.402
t_e	min	113.400	453.808	666.268	247.892	253.973	415.702	236.104
C-H Model Predictions								
C_t/C_0 **at** $t = 0$	—	0.015	0.017	0.019	0.0160	0.012	0.027	0.006
$(C_t/C_0)_{0.5}$	—	0.279	0.273	0.3103	0.302	0.282	0.289	0.294
$t_{0.5}$	min	6.572	17.130	111.170	31.741	15.844	29.338	22.584
t_b	min	2.343	5.626	31.408	10.460	6.284	6.335	10.733
t_{b2}	min	9.887	21.155	66.924	20.713	19.721	25.261	21.218
t_e	min	98.815	323.831	798.913	257.328	204.171	341.949	204.992

Notes: *† Standard breakthrough threshold $C_t/C_0 = 0.05$. ‡ Adjusted breakthrough C_t/C_0: first experimental point exceeding the Y-N-predicted C_t/C_0 =5%. § t_{b2}: time corresponding to the adjusted breakthrough point. N/D: not detected because the standard column saturation ($C_t/C_0 \geq 1.00$) was not observed within the experimental run. *: Mathematically undefined at exactly $t = 0$ due to the ln(t) term; however, the limit approaches zero ($C_t/C_0 \rightarrow 0$ as $t \rightarrow 0$).*

VIII.4 Dynamic adsorption of Catechol

VIII.4.1 Breakthrough curve behavior and column performance metrics

The experimental breakthrough trajectories for CAT adsorption onto ZnO@DPS-AC are illustrated in **Figure VIII.2**, with the corresponding mass-transfer performance metrics systematically detailed in **Table VIII.5**. The experimental matrix precisely mirrors the parameter space previously evaluated for MO. Experiment 3 (C_0 = 100 mg/L, Q_v = 3 mL/min, m = 500 mg) serves as the shared baseline condition to facilitate direct inter-pollutant comparison.

A comparative analysis of the CAT and MO reference experiments (**Table VIII.2** and **Table VIII.5**) reveals a striking quantitative convergence. The equilibrium adsorption capacity for CAT

(q_e = 131.18 mg/g) closely matches the MO baseline (136.27 mg/g), with nearly identical overall fractional removal efficiencies (44.60% and 44.67%, respectively). This quantitative parity indicates that the accessible binding sites on the ZnO@DPS-AC composite achieve comparable thermodynamic saturation limits under equivalent fixed-bed hydrodynamic conditions. Remarkably, this macroscopic utilization remains consistent despite the profound chemical and spatial disparities between a sterically demanding, highly conjugated azo dye and a low-molecular-weight dihydric phenol.

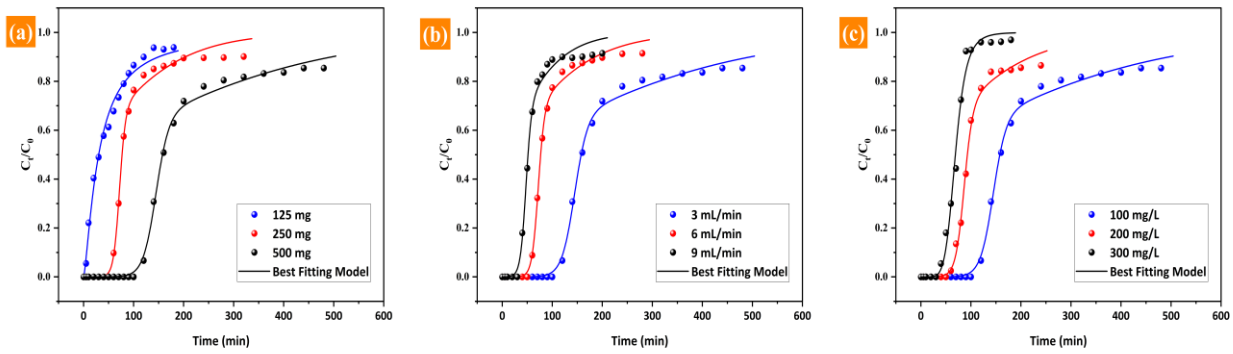

Figure VIII.2 Experimental breakthrough curves for CAT adsorption onto ZnO@DPS-AC, illustrating the effects of (**a**) adsorbent bed mass, (**b**) volumetric flow rate, and (**c**) initial concentration

VIII.4.1.1 Effect of adsorbent mass

Consistent with observations for MO, increasing the CAT adsorbent bed mass from 125 to 500 mg (C_0 = 100 mg/L, Q_v = 3 mL/min) progressively extended the integrated breakthrough area from 49.13 to 214.10 min and elevated q_{total} from 14.89 to 65.59 mg. Simultaneously, the q_e increased from 119.13 to 131.18 mg/g, driving fractional R from 27.29% to 44.60%. These systematic improvements are mechanistically driven by the expanded active-site inventory, which collectively extends the usable bed lifetime and delays the progression of the MTZ toward the column outlet (Khan et al., 2017; Sazali et al., 2020), as established for MO in **section VIII.3.1.1**.

Crucially, the per-gram capacity enhancement exhibited the same diminishing returns detailed previously. The incremental q_e improvement between 250 and 500 mg was restricted to 1.56 mg/g, compared to a 10.49 mg/g surge between 125 and 250 mg. This distinct saturation profile confirms that the specific surface capacity of ZnO@DPS-AC for phenolic compounds approaches a practical

thermodynamic limit of 130-135 mg/g at this influent concentration. This plateau dictates that the progressive expansion of the MTZ in deeper beds cannot overcome the finite availability of specific hydrogen-bond-donor hydroxyl sites and π-stacking domains within the intra-particle micropores, regardless of total bulk surface area.

VIII.4.1.2 Effect of volumetric flow rate

Elevating the Q_v from 3 to 9 mL/min (Exps. 3 to 5) yielded a dynamic behavioral pattern broadly analogous to MO, albeit with critical quantitative deviations. The breakthrough area contracted sharply from 214.10 min (at 3 mL/min) to 100.68 min (at 6 mL/min) and 67.46 min (at 9 mL/min). Concurrently, overall removal efficiency deteriorated monotonically from 44.60% to 33.73%. This is reflected physically in consistently worsening column performance, driven by higher superficial velocities that reduce hydraulic residence time and truncate EBCT, thereby restricting the diffusion of adsorbate molecules from the bulk solution into the solid matrix (as comprehensively detailed in **section VIII.3.1.2**) (Khan et al., 2017).

However, the impact of elevated flow rates on absolute uptake metrics was notably attenuated for CAT. The q_{total} declined moderately from 65.59 to 59.27 mg at 6 mL/min, then recovered to 61.11 mg at 9 mL/min, while qe remained relatively stable across the varying velocities (131.18, 118.55, and 122.21 mg/g, respectively). This structural deviation from the highly variable MO response is strictly dictated by molecular geometry. Because CAT has a significantly smaller molecular footprint than the sterically bulky MO dye (see **Table VIII.2** and **Table VIII.5**), it encounters drastically reduced steric hindrance during intra-particle pore diffusion. This accelerated internal mass transfer partially compensates for the truncated external fluid-film contact time at elevated velocities. Furthermore, the monotonic efficiency decline confirms that CAT adsorption is exempt from the artificial mass-loading artifact that complicated the MO interpretation at 9 mL/min, largely because the absolute influent load delivered (M_{total} = 181.15 mg) was substantially lower.

VIII.4.1.3 Effect of initial pollutant concentration

Elevating the C_0 from 100 to 300 mg/L (Exps. 3, 6, and 7; Q_v = 3 mL/min, m = 500 mg) yielded a markedly different mass-transfer response for CAT compared to the strictly negative impact observed for MO. Unlike the monotonic degradation detailed for MO in **section VIII.3.1.3**, CAT exhibited a distinct non-monotonic efficiency response. As C_0 increased to an intermediate loading

of 200 mg/L, the q_e rose from 131.18 to 138.74 mg/g, accompanied by an improvement in R from 44.60% to 47.24%. However, further concentration elevation to 300 mg/L reversed this trend, causing q_e to decline to 127.82 mg/g and the removal efficiency to fall to 40.26%.

Mechanistically, at intermediate loadings (200 mg/L), the steeper concentration gradient drives faster adsorption kinetics by intensifying the mass transfer driving force across the liquid-solid interface (Ansari et al., 2021). This intensified thermodynamic driving force effectively overcomes external fluid-film resistances, facilitating more complete utilization of the deep-bed capacity and maximizing active site engagement within the MTZ before it reaches the column outlet.

Conversely, at the elevated 300 mg/L threshold, the accelerated kinetic loading fundamentally overwhelms the finite bed capacity. The rate of bed saturation exceeds the rate of deep-bed intra-particle diffusion, causing the MTZ to propagate rapidly and prematurely truncating the integrated breakthrough area from 113.38 to 72.47 min. This non-monotonic behavior confirms that the continuous-flow system is operating near the linear-to-nonlinear transition region of the CAT adsorption isotherm. In this specific hydrodynamic regime, the mass-transfer advantage provided by a higher concentration driving force is ultimately counteracted by the rapid, competitive saturation of the available specific binding sites.

Table VIII.5 Summary of experimental conditions and breakthrough performance metrics for dynamic adsorption of CAT

N	C_0 (mg/L)	Q_v (mL/min)	m (mg)	Area (min)	q_{total} (mg)	q_e (mg/g)	M_{total} (mg)	R (%)	Variable
1	100	3	125	49.127	14.891	119.131	54.562	27.293	**Mass**
2	100	3	250	107.1626	32.406	129.624	96.768	33.488	**Mass**
3	100	3	500	214.098	65.591	131.182	147.053	44.604	**Shared**
4	100	6	500	100.683	59.274	118.548	164.842	35.958	**Flow rate**
5	100	9	500	67.462	61.105	122.209	181.152	33.731	**Flow rate**
6	200	3	500	113.381	69.369	138.738	146.837	47.242	**Conc.**
7	300	3	500	72.466	63.908	127.816	158.744	40.259	**Conc.**

VIII.4.2 Breakthrough curve modeling and model comparison

The empirical breakthrough trajectories for CAT were evaluated using the Th model (representing the classical symmetric logistic family), the log-Th formulation, and the dual-rate C-H model. The Th framework was specifically selected for CAT to directly derive the maximum dynamic

adsorption capacity (q_0, mg/g), a parameter of high practical relevance for the process design of phenolic compound treatment. However, as rigorously established in **sections VIII.2.1** and **VIII.3.2**, this selection lacks statistical significance due to the fundamental mathematical equivalence among all classical logistic models. The optimized kinetic parameters and corresponding predictive performance metrics are detailed in **Table VIII.6** and **Table VIII.7**.

VIII.4.2.1 Evaluation of the classical Th model

The standard Th model achieved satisfactory statistical correlations, producing R^2 values ranging from 0.937 to 0.995. The derived q_0 ranged from 95.24 to 104.72 mg/g across the mass- and flow-rate experiments, rising to 119.39–123.34 mg/g under elevated influent concentrations. Notably, these theoretical q_0 values systematically underestimate the previously established experimental qe capacities in **Table VIII.5**. This discrepancy is a direct mathematical artifact of the rigid symmetric inflection constraint, which forces the model to truncate the integrated area under highly asymmetric, tailing breakthrough curves. Furthermore, the model predicted a severe non-zero initial concentration (C_t/C_0 = 0.167 at t=0) for the low-mass Experiment 1, reaffirming the structural failure of symmetric logistic functions when confronted with rapid early-stage leakage dynamics.

VIII.4.2.2 Evaluation of the log-Th model

Applying the logarithmic transformation (log-Th) substantially rectified the boundary failures observed in Experiment 1, yielding an excellent fit (R^2 = 0.986, *RMSE* = 0.031) and capturing 86.30% of the *AW*. Conversely, the log-Th model demonstrated substantial statistical instability in Experiments 2 and 3, producing highly inflated *RMSE* values (0.082 and 0.847, respectively) and near-zero *AWs*. The anomalous *RMSE* of 0.847 observed for Experiment 3 is characteristic of numerical instability inherent to the logarithmic transformation at extended operational times as C_t/C_0 approaches unity. This mathematical breakdown constitutes a well-documented limitation of log-linear models when experimental datasets extend deeply into the prolonged saturation phase.

VIII.4.2.3 Evaluation of the C-H model

The C-H model emerged as the statistically dominant and physically superior framework, achieving R^2 values of 0.983-0.998 and minimizing *RMSE* to an exceptionally low range of 0.018–0.039. *AW* analysis assigned near-exclusive support (*AW* = 100.00%) to the C-H formulation for

Experiments 2-6. By seamlessly accommodating asymmetric trajectories without triggering numerical instability, the model generated precise finite breakthrough time predictions that closely matched experimental observations.

Table VIII.6 Fitted parameters of the Th, log-Th, and C-H models for all seven CAT breakthrough experiments

Parameter	Unit	Exp.1	Exp. 2	Exp. 3	Exp. 4	Exp. 5	Exp. 6	Exp. 7
Th Model								
k_{TH}	L/(min.mg)	4E-04	0.001	0.0003	0.0008	0.001	0.0003	0.0003
q_0	mg/g	98.712	98.546	104.717	95.239	99.363	119.385	123.337
R^2	—	0.937	0.957	0.937	0.965	0.967	0.957	0.995
RMSE	—	0.076	0.083	0.094	0.075	0.072	0.0779	0.030
AW	%	0.002	3.19E-08	1.55E-15	3.33E-09	1.57E-04	5.80E-08	86.034
Logarithmic -Th Model (log-TH)								
k_{Thl}	—	1.370	4.131	2.962	4.650	3.802	4.597	6.279
q_{0l}	mg/g	73.171	98.010	105.224	94.489	95.974	119.468	121.482
R^2	—	0.986	0.890	0.861	0.915	0.926	0.938	0.984
RMSE	—	0.031	0.082	0.847	0.074	0.060	0.077	0.043
AW	%	86.303	5.49E-16	4.77E-28	2.45E-17	1.44E-09	4.55E-16	2.03E-08
C-H Model								
k_{CH1}	min^{-1}	0.127	0.169	0.079	0.162	0.181	0.119	0.093
k_{CH2}	min^{-1}	0.016	0.011	0.004	0.012	0.018	0.010	0.200
τ_{CH}	min	20.731	73.526	148.949	73.589	48.715	88.605	69.926
R^2	—	0.983	0.996	0.998	0.998	0.994	0.997	0.995
RMSE	—	0.039	0.026	0.018	0.019	0.030	0.022	0.030
AW	%	13.696	100.000	100.000	100.000	100.000	100.000	13.966

The derived k_{CH1}/k_{CH2} ratio quantitatively illustrates the mechanistic value of the C-H model. For CAT, this tailing index ranged from 7.9 to 19.8, a significantly higher baseline than that observed for MO (~10.3). These elevated ratios indicate a severe kinetic disparity during adsorption. Initial localized surface uptake (k_{CH1}) proceeds exceptionally fast, driven by the strong π-electron stacking and hydrogen-bonding affinities between the CAT ring system and the active carbon matrix. However, this rapid monolayer formation induces severe structural and chemical blockages at the pore entrances. This bottleneck drastically retards the k_{CH2}, exacerbating steric hindrance at high surface coverages and generating a highly extended, asymmetric tailing trajectory (Chu & Hashim, 2024a).

Table VIII.7 Comparison of experimental and model-predicted breakthrough and exhaustion parameters for CAT

Parameter	Unit	Exp. 1	Exp. 2	Exp. 3	Exp. 4	Exp. 5	Exp. 6	Exp. 7
Experimental Data								
$(C_t/C_0)_b$ (threshold)	—	0.050	0.050	0.050	0.050	0.050	0.050	0.050
t_b	min	<5	<60	<120	<60	<40	<70	<40
$(C_t/C_0)_b$ (adj.)	—	10	—	—	—	—	—	—
t_{b2}	min	0.2211	—	—	—	—	—	—
t_e	min	120	N/D	N/D	N/D	N/D	N/D	<90
Th Model Predictions								
C_t/C_0 at $t = 0$	—	0.167	0.002	0.004	0.002	0.007	0.003	0.002
$(C_t/C_0)_{0.5}$	—	0.500	0.500	0.500	0.500	0.500	0.500	0.500
$t_{0.5}$	min	40.707	81.470	170.905	80.887	54.851	97.565	69.926
t_b	min	NaN	42.813	81.513	43.774	22.046	48.776	38.265
t_{b2}	min	8.769	—	—	—	—	—	—
t_e	min	96.433	110.318	237.612	108.582	79.331	133.973	93.553
Logarithmic-Th Model Predictions								
C_t/C_0 at $t = 0$	—	—	—	—	—	—	—	—
$(C_t/C_0)_{0.5}$	—	0.135	0.379	0.331	0.393	0.369	0.391	0.420
$t_{0.5}$	min	7.772	71.894	135.455	73.052	45.982	88.678	65.438
t_b	min	3.516	39.725	63.548	42.602	24.424	51.451	43.091
t_{b2}	min	12.032	—	—	—	—	—	—
t_s	min	150.082	137.923	360.611	128.726	94.420	157.471	97.733
C-H Model Predictions								
C_t/C_0 at $t = 0$	—	0.0627	4.024e-06	7.777e-06	6.756e-06	0.0002	2.609e-05	0.002
$(C_t/C_0)_{0.5}$	—	0.3183	0.357	0.340	0.367	0.373	0.370	0.500
$t_{0.5}$	min	18.128	71.776	144.527	71.962	47.444	86.525	69.919
t_b	min	5.96e-11	56.271	112.081	55.560	32.611	64.121	38.265
t_{b2}	min	12.894	—	—	—	—	—	—
t_e	min	138.022	203.225	496.227	186.048	121.363	220.634	93.553

VIII.5 Dynamic adsorption of Acetamiprid

VIII.5.1 Breakthrough curve behavior and column performance metrics

The experimental breakthrough trajectories for the dynamic adsorption of the agrochemical ACE onto ZnO@DPS-AC are illustrated in **Figure VIII.3**, with the corresponding quantitative performance metrics summarized in **Table VIII.8**. Unlike the prior protocols established for MO and CAT, the ACE matrix utilized a higher baseline reference concentration (C_0 = 200 mg/L). This

elevated baseline was selected based on prior batch equilibrium studies that demonstrated a substantially higher solid-phase adsorption capacity for ACE. Consequently, higher influent loadings were required to drive the fixed-bed system toward macroscopic exhaustion within a practically viable operational timeframe. Furthermore, this parameter adjustment accurately reflects the elevated concentration profiles typical of actual agricultural runoff and industrial pesticide manufacturing effluents.

The central reference condition (Experiment 3: C_0 = 200 mg/L, Q_v = 3 mL/min, m = 500 mg) yielded a q_e of 261.49 mg/g and an overall fractional R of 52.13%. These metrics substantially exceed the baseline performance established for both MO and CAT under equivalent hydrodynamic conditions.

This markedly superior q_e indicates an exceptionally strong thermodynamic affinity between the ACE molecule and the ZnO@DPS-AC composite. Mechanistically, this robust uptake is driven by highly specific, simultaneous multi-site interactions. These encompass π-π donor-acceptor interactions between the electron-deficient chloropyridyl ring of ACE and the graphitic carbon planes, as well as hydrogen bonding between the cyanoimine group and the functional surface hydroxyls. Additionally, the inherent hydrophobic exclusion of the ACE molecule from the bulk aqueous phase accelerates its partitioning into the solid matrix.

Consequently, the fixed-bed columns experimentally approached absolute macroscopic saturation for ACE, with absolute exhaustion times recorded as definitive finite limits or close upper bounds (**Table VIII.8**). This represents a distinct dynamic deviation from the MO and CAT systems, where definitive saturation was not achieved under equivalent temporal constraints. This rapid progression to saturation, coupled with high absolute capacity, rigorously confirms that ACE undergoes highly efficient, rapid multi-mechanism kinetic adsorption.

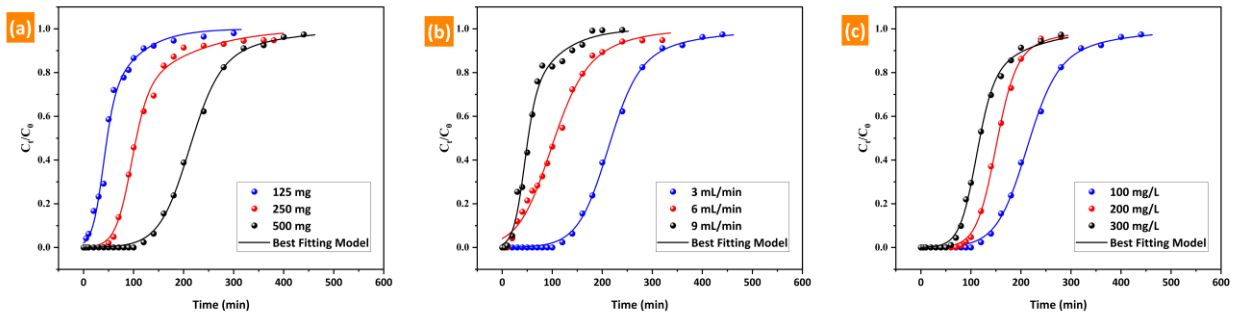

Figure VIII.3 Experimental breakthrough curves for the agrochemical ACE adsorption onto ZnO@DPS-AC, illustrating the effects of (**a**) adsorbent bed mass, (**b**) volumetric flow rate, and (**c**) initial concentration

VIII.5.1.1 Effect of adsorbent mass

Increasing the adsorbent mass from 125 to 500 mg (C_0 = 200 mg/L, Q_v = 3 mL/min) led to progressively better breakthrough performance. The integrated breakthrough area expanded from 62.48 to 229.39 min, q_{total} increased from 37.17 to 130.74 mg, and overall R improved from 20.83% to 52.13%. As previously established in **section VIII.3.1.1**, these improvements are fundamentally driven by the expansion of the available active site inventory, thereby delaying the propagation of the MTZ toward the column outlet.

However, the q_e followed an inverse trajectory, declining from 297.38 mg/g (at 125 mg) to 261.49 mg/g (at 500 mg). This apparent reduction constitutes an operational artifact driven by the exceptionally high adsorbate-to-adsorbent ratio at the lowest bed mass. At 125 mg, the elevated influent load generates an extreme, localized concentration gradient that forces near-complete saturation of the available binding sites before the abbreviated EBCT expires. Conversely, the extended bed lifetime provided by a 500 mg mass leads to a significant broadening of the MTZ. This distribution leaves a larger fraction of deep-bed interior sites underutilized at the macroscopic breakthrough threshold, a well-documented phenomenon reflecting lower sorbent use at extended EBCTs (Chatterjee & Schiewer, 2011). This mass-dependent capacity artifact underscores the need to evaluate qe alongside fractional removal (R) rather than using either metric in isolation.

VIII.5.1.2 Effect of volumetric flow rate

Modulating the Q_v from 3 to 9 mL/min (Exps. 3-5) produced the most severe hydrodynamic degradation among the three investigated pollutants. The breakthrough area contracted sharply

from 229.39 to 63.90 min, while R deteriorated from 52.13% to 26.63%. As established in **section VIII.3.1.2**, this decline is inherently linked to the truncation of hydraulic residence time.

Unlike the MO system (where intense influent mass loading at 9 mL/min artificially inflated q_e), the absolute mass transfer metrics for ACE failed to recover at the highest velocity. While q_{total} initially rose from 130.74 to 143.17 mg at 6 mL/min due to elevated bulk mass delivery (M_{total} = 398.63 mg), it collapsed to 114.89 mg at 9 mL/min despite an even greater total influent load (431.53 mg). Consequently, q_e followed an identical non-monotonic trajectory (261.49 → 286.34 → 229.79 mg/g).

Mechanistically, the adsorption of the bulky ACE molecule onto ZnO@DPS-AC is strictly governed by slow intra-particle diffusion into the micro- and mesoporous network. At 9 mL/min, the severely truncated external fluid-film contact time completely outpaces the internal diffusion rate. This kinetic mismatch physically prevents ACE molecules from accessing the deep intra-particle active sites, resulting in substantial column bypass (Chatterjee & Schiewer, 2011; Khan et al., 2017). For agrochemicals exhibiting stringent environmental discharge limits, this extreme sensitivity to external fluid velocity represents a critical process design constraint.

Table VIII.8 Summary of experimental conditions and breakthrough performance metrics for dynamic adsorption of ACE

N	C_0 (mg/L)	Q_v (mL/min)	m (mg)	Area (min)	q_{total} (mg)	q_e (mg/g)	M_{total} (mg)	R (%)	Variable
1	200	3	125	62.481	37.172	297.376	178.479	20.827	**Mass**
2	200	3	250	127.598	77.091	308.364	229.585	33.579	**Mass**
3	200	3	500	229.388	130.744	261.489	250.787	52.1337	**Shared**
4	200	6	500	114.929	143.169	286.338	398.63	35.915	**Flow rate**
5	200	9	500	63.9001	114.894	229.787	431.525	26.625	**Flow rate**
6	300	3	500	158.870	146.062	292.123	257.426	56.7392	**Conc.**
7	400	3	500	129.873	174.277	348.554	375.732	46.383	**Conc.**

VIII.5.1.3 Effect of initial pollutant concentration

Elevating C_0 from 200 to 400 mg/L yielded a monotonic increase in total adsorbed mass (130.74 → 146.06 → 174.28 mg) and specific dynamic capacity (261.49 → 292.12 → 348.55 mg/g). The peak value of 348.55 mg/g constitutes the highest dynamic capacity recorded in this study, confirming the exceptional chemical affinity of the ZnO@DPS-AC composite for treating highly

concentrated pesticide effluents. Concurrently, the integrated breakthrough area contracted strictly from 229.39 to 129.87 min, reflecting the expected acceleration of bed saturation under elevated kinetic loading.

Notably, the *R* exhibited a non-monotonic profile, peaking at 56.74% at 300 mg/L before declining to 46.38% at 400 mg/L. This precisely mirrors the transition behavior documented for CAT in **section VIII.4.1.3**. At optimal intermediate loadings (300 mg/L), the elevated influent concentration provides a superior thermodynamic driving force that effectively overcomes both external fluid-film resistance and internal steric hindrance (Chu & Hashim, 2024a; Nazari et al., 2016). This intensified mass-transfer gradient fully exploits the π-electron-rich affinities of the composite surface for the cyanoimine group of ACE. However, at extreme concentrations (400 mg/L), the accelerated dye loading rapidly compresses the MTZ and advances macroscopic breakthrough, overwhelming the finite bed residence time.

VIII.5.2 Breakthrough curve modeling and model comparison

The empirical breakthrough trajectories for ACE were evaluated utilizing the A-B model as the representative classical symmetric formulation, alongside the log-AB and the dual-rate C-H models. The A-B framework was specifically selected for this evaluation because its fundamental capacity parameter, N_0 (mg/L), provides a direct volumetric measure of bed saturation. This metric is highly intuitive for assessing pesticide removal efficiency in continuous-flow process design. The A-B framework was selected by convention, as its mathematical equivalence to Y-N and Th was demonstrated in section **VIII.2.1.** The optimized kinetic parameters and boundary predictions are detailed in **Table VIII.9** and **Table VIII.10**.

VIII.5.2.1 Evaluation of the classical A-B model

The classical A-B formulation generated R^2 values ranging from 0.973 to 0.997. This constitutes a notably higher statistical baseline than the corresponding classical fits for MO and CAT. This improved performance logically reflects the shallower, more gradual breakthrough profiles characteristic of ACE. Wider, more symmetric curves align better with the symmetric logistic function because a smaller fraction of the trajectory lies in the asymmetric tailing region. The derived volumetric saturation capacity (N_0) increased substantially with both expanded adsorbent mass (from 25,102 to 75,619 mg/L) and elevated influent concentration (from 75,619 to 98,450

mg/L), accurately reflecting the heightened mass retention per unit bed volume.

Despite this adequate baseline fit, the A-B model predicted undefined (NaN) breakthrough times for Experiments 1 and 4. In these instances, the large spurious initial predicted concentrations (C_t/C_0 = 0.063 and 0.054, respectively) inherently exceeded the standard 5% operational threshold. This explicitly reproduces the fundamental structural boundary failure previously demonstrated for the entire classical logistic family in **section VIII.3.2**.

VIII.5.2.2 Evaluation of the logarithmic A-B(log-AB) model

Implementing the logarithmic temporal modification improved the R^2 metric to an exceptional range of 0.979–0.999 while systematically reducing the *RMSE*. Its floating inflection point (ranging from 0.295 to 0.424) successfully captured the left-asymmetric character of the early leakage phase. However, despite these improved descriptive statistics, the *AW* completely rejected the log-AB formulation. The assigned *AW* was effectively zero (*AW* < 1%) across nearly all experiments, with Experiment 1 retaining only marginal support (*AW* = 0.74%). This near-absolute statistical rejection indicates that the minor incremental improvement in R^2 does not mathematically justify the added parameter complexity relative to the C-H model.

VIII.5.2.3 Evaluation of the C-H model

The C-H model overwhelmingly dominated the ACE analytical matrix, achieving the highest R^2 (0.991–0.999) and the lowest *RMSE* (0.012–0.036) metrics across all pollutants and experiments in this study. *AW* analysis assigned definitive, near-exclusive support (≥ 99.16%) to the C-H model for six of the seven runs. Furthermore, the model precisely reproduced both the early breakthrough thresholds and terminal exhaustion times (e.g., predicting t_b = 10.12 min versus an experimental < 10 min for Exp. 1), validating its strict predictive utility for industrial process scale-up.

The derived kinetic parameters provide critical mechanistic clarity. The k_{CH1}/k_{CH2} tailing ratios for ACE ranged from a uniquely low 2.8 to 7.8, starkly contrasting the highly elevated ratios observed for MO (~10) and CAT (~8–20). In sharp contrast to the sterically hindered, heavily tailing CAT system detailed in **section VIII.4.2**, these suppressed ratios signify a remarkably symmetric breakthrough profile. Mechanistically, this indicates a highly balanced dynamic regime. The k_{CH1} does not outpace the k_{CH2} by a large margin. This equilibrium minimizes pore-mouth blockages

and facilitates a smooth, progressive saturation of the deep micro- and mesoporous network within the activated carbon matrix.

Table VIII.9 Fitted parameters of the A-B, log A-B, and C-H models for all seven ACE breakthrough experiments

Parameter	Unit	Exp. 1	Exp. 2	Exp. 3	Exp. 4	Exp. 5	Exp. 6	Exp. 7
A-B Model								
k_{AB}	L/(min.g)	3.0E-04	2.0E-04	2.0E-04	2.0E-04	3.0E-04	0.0	1.0E-04
N_0	mg/L	2.51E+04	5.41E+04	7.56E+04	4.00E+04	1.95E+04	8.52E+04	9.85E+04
R^2	—	0.973	0.985	0.997	0.990	0.975	0.997	0.990
RMSE	—	0.060	0.0499	0.0218	0.035	0.060	0.019	0.038
AW	%	0.105	2.36E-05	2.24E-04	20.619	0.088	0.058	9.11E-05
Logarithmic-A-B Model								
k_{ABl}	—	2.439	3.838	5.7616	2.493	2.724	6.545	4.792
N_{0l}	mg/L	23151.509	52131.915	74165.352	36888.1519	18423.213	84007.775	95763.451
R^2	—	0.984	0.993	0.999	0.979	0.985	0.999	0.997
RMSE	—	0.043	0.031	0.012	0.0462	0.041	0.010	0.020
AW	%	0.738	1.34E-08	5.63E-22	7.91E-06	0.064	6.28E-13	1.09E-11
C-H Model								
k_{CH1}	min^{-1}	0.094	0.064	0.0340	0.033	0.093	0.053	0.061
k_{CH2}	min^{-1}	0.018	0.010	0.008	0.012	0.018	0.012	0.011
τ_{CH}	min	41.116	98.484	212.101	94.314	46.221	150.162	112.434
R^2	—	0.991	0.997	0.999	0.992	0.991	0.999	0.998
RMSE	—	0.035	0.022	0.012	0.03	0.036	0.012	0.017
AW	%	99.157	100.000	100.000	79.381	99.848	99.942	100.000

VIII.6 Comparative analysis across pollutants

The results from **sections VIII.3** through **VIII.5** collectively establish a coherent, multi-faceted understanding of the dynamic adsorption behavior of ZnO@DPS-AC toward three chemically distinct micropollutants. A summary of the key comparative metrics derived from the shared baseline reference condition is presented in **Table VIII.11**.

Table VIII.10 Comparison of experimental and model-predicted breakthrough and exhaustion parameters for ACE

Parameter	Unit	Exp. 1	Exp. 2	Exp. 3	Exp. 4	Exp. 5	Exp. 6	Exp. 7
Experimental Data								
$(C_t/C_0)_b$ (threshold)	—	0.05	0.05	0.05	0.05	0.05	0.05	0.05
t_b	min	<10	60	<140	<30	<20	<120	<80
$(C_t/C_0)_b$ (adj.)	—	0167	—	—	0.120	—	—	—
t_{b2}	min	20	—	—	30	—	—	—
t_e	min	<120	200	<320	200	140	<240	<200
A-BModel Predictions								
C_t/C_0 at $t = 0$	—	0.0627	0.013	0.002	0.054	0.036	0.001	0.005
$(C_t/C_0)_{0.5}$	—	0.5	0.5	0.5	0.5	0.500	0.500	0.500
$t_{0.5}$	min	50.887	112.565	222.278	107.650	54.404	155.299	122.917
t_b	min	NaN	36.733	116.578	NaN	5.755	89.512	53.957
t_{b2}	min	20.706						
t_e	min	92.226	169.153	301.154	190.161	90.707	204.390	174.378
Logarithmic-A-BModel Predictions								
C_t/C_0 at $t = 0$	—	—	—	—	—	—	—	—
$(C_t/C_0)_{0.5}$	—	0.295	0.370	0.413	0.300	0.316	0.424	0.396
$t_{0.5}$	min	32.839	94.356	205.132	70.563	38.813	146.051	109.450
t_b	min	14.037	50.345	130.774	30.460	17.470	97.625	64.680
t_{b2}	min	24.315	—	—	—	—	—	—
t_e	min	115.518	192.196	319.2168	239.520	115.393	214.160	189.108
C-H Model Predictions								
C_t/C_0 at $t = 0$	—	0.0205	0.002	0.0007	0.041	0.013	0.0004	0.001
$(C_t/C_0)_{0.5}$	—	0.382	0.391	0.448	0.444	0.388	0.455	0.416
$t_{0.5}$	min	39.749	96.0638	211.032	96.451	44.906	149.585	110.858
t_b	min	10.121	52.974	125.986	6.321	15.031	94.452	64.766
t_{b2}	min	25.412	—	—	—	—	—	—
t_e	min	120.314	225.698	319.234	207.204	123.516	214.760	205.790

In terms of absolute dynamic adsorption capacity at the reference state, ACE substantially outperforms the other two species. It achieved q_e = 261.49 mg/g at C_0 = 200 mg/L, compared to 136.27 mg/g for MO and 131.18 mg/g for CAT at their respective C_0 = 100 mg/L baselines. When normalized to the influent concentration, the q_e remains highly comparable across the three

pollutants (ranging from 1.31 to 1.36 mg/g per mg/L of influent). However, the q_e for ACE increased dramatically with higher influent concentrations, peaking at 348.55 mg/g at 400 mg/L. In contrast, MO and CAT capacities were far less sensitive to concentration variations, reflecting a significantly steeper isotherm slope for ACE within this concentration range (as mechanistically detailed in sections **VIII.3.1.3** and **VIII.5.1.3**, respectively).

Unlike MO and CAT, which rapidly approach a steric saturation plateau governed by the finite physical surface area of the intra-particle pores, the adsorption of ACE is driven by highly specific, concentration-dependent complexation. The intensified thermodynamic driving force at elevated concentrations fully exploits the Lewis basic sites, overcoming both external and internal mass-transfer resistances (Ahmed & Hameed, 2018; Mon et al., 2024).

The fractional removal efficiencies (R) at the reference condition exhibit striking parity across the three targets (44.67% for MO, 44.60% for CAT, and 52.13% for ACE). This quantitative convergence suggests that overall column performance is governed primarily by fixed-bed hydrodynamics, particularly the EBCT dictated by the ratio of bed mass to volumetric flow rate (see **sections VIII.3.1.2** and **VIII.4.1.2**). This establishes a fundamental fixed-bed principle: regardless of the adsorbate's specific chemical affinity or maximal theoretical capacity, the R in a continuous-flow regime is ultimately constrained by the external fluid-film resistance and the hydraulic residence time (Chu, 2023; Zarcheva & Chu, 2025). If the MTZ is not fully contained within the bed due to excessive superficial velocity, premature breakthrough is unavoidable. The elevated R observed for ACE reflects the combination of its higher baseline concentration (providing a stronger driving force for deep-bed utilization) and rapid adsorption kinetics, which collectively ensure the MTZ remains highly contained within the 500 mg bed.

The analytical model comparison reveals a consistent descriptive hierarchy. The C-H formulation universally outperforms both the classical logistic and logarithmic models across all three pollutants, avoiding the fundamental boundary condition failures demonstrated in **section VIII.3.2** and **Table VIII.1**. Its statistical dominance was absolute for ACE (AW > 99% in six of seven experiments) and MO (AW > 96% in five of seven experiments), with slightly more variable support in the heavily tailing CAT system.

This differential modeling performance is strictly governed by varying degrees of breakthrough curve asymmetry, effectively quantified by the k_{CH1}/k_{CH2} parameter ratio. By utilizing this ratio as a quantitative tailing index, the C-H model seamlessly links macroscopic breakthrough asymmetry to microscopic mass-transfer phenomena (Chu & Hashim, 2023b). The severe tailing of CAT (ratio ~19.8) highlights extreme kinetic disparity where rapid initial π-stacking induces severe steric hindrance. MO exhibits an intermediate tailing index (~10.3). Conversely, the highly symmetric profile of ACE (ratio ~4.3) indicates a highly balanced progression between surface uptake and intra-particle diffusion.

For practical scale-up and industrial process design, the C-H model provides a mathematically robust framework that accurately predicts premature breakthrough caused by asymmetric tailing. This represents a critical requirement for maintaining strict environmental discharge limits where classical symmetric models systematically fail (Apiratikul & Chu, 2021; Zarcheva & Chu, 2025). Under the conditions evaluated, a minimum bed mass of 500 mg and an EBCT of 3 mL/min are strictly necessary to ensure baseline removal efficiencies above 44%. Finally, a clear priority for future investigation involves extending experimental timelines to reach absolute column saturation across all operational matrices. This will enable direct empirical validation of the C-H model's theoretical exhaustion time predictions, which presently rely on mathematical extrapolation beyond experimentally accessible temporal domains (as detailed in **Table VIII.4**, **Table VIII.7**, and **Table VIII.10**).

Table VIII.11 Comparative summary of dynamic adsorption performance and model results for MO, CAT, and ACE at the shared reference condition

Pollutant	C_0 (mg/L)	q_e (mg/g)	R (%)	Best model	Best R^2 range	Best *RMSE* range	k_{CH1}/k_{CH2} ratio
MO	100	136.27	44.67	C-H	0.969–0.989	0.030–0.049	~10.3
CAT	100	131.18	44.60	C-H	0.983–0.998	0.018–0.039	~19.8
ACE	200	261.49	52.13	C-H	0.991–0.999	0.012–0.036	~4.3

Note: Best model R^2 and RMSE ranges are reported across all seven experiments of each pollutant series. The k_{CH1}/k_{CH2} ratio, C_0, q_e, and R are reported for the reference experiment (Exp. 3) of each

series.

VIII.7 Conclusion

This chapter established a comprehensive quantitative and mechanistic framework for the continuous-flow fixed-bed adsorption of MO, CAT, and ACE onto the ZnO@DPS-AC composite. The investigation systematically evaluated the hydrodynamic and thermodynamic impacts of adsorbent bed mass, volumetric flow rate, and initial influent concentration. Furthermore, it provided a rigorous, mathematically grounded critique of three distinct families of breakthrough curve models. The principal findings are summarized below.

(i) **High-performance dynamic capacity**: The q_e at the shared reference condition was determined to be 136.27 mg/g for MO, 131.18 mg/g for CAT, and an exceptional 261.49 mg/g for ACE. The dynamic capacity for ACE, which escalated to 348.55 mg/g at elevated influent loadings (400 mg/L), ranks among the highest q_e documented for continuous pesticide removal. This superior uptake is fundamentally driven by simultaneous multi-mechanism interactions (hydrophobic and π-electron exchange) occurring at the functionalized composite surface.

(ii) **Hydrodynamic and thermodynamic sensitivities**: Expanding the adsorbent bed mass predictably delayed MTZ propagation, extending overall column service life. However, diminishing q_e returns indicated a distinct approach toward steric site saturation at higher bed depths. Elevated volumetric flow rates systematically degraded R by severely truncating the EBCT. Conversely, elevated influent concentrations intensified the thermodynamic mass-transfer driving force, maximizing localized q_e while inherently accelerating total bed exhaustion. Notably, both CAT and ACE exhibited distinct non-monotonic operational efficiency responses near their respective isotherm transition zones.

(iii) **Methodological correction in classical modeling**: The absolute mathematical equivalence of the classical Y-N, Th, and A-B formulations was rigorously empirically proven across all three pollutant matrices. Because these models share a unified, symmetric logistic architecture, they yield identical statistical metrics when applied to a single dataset. Consequently, selecting among them based on comparative statistical goodness-of-fit is definitively exposed as a fundamental methodological error in adsorption engineering.

(iv) **Dominance of the dual-rate C-H framework**: The C-H model universally delivered the most precise mathematical description of the experimental breakthrough trajectories, achieving R^2 values approaching 0.999 and monopolizing *AW* support. By establishing physically accurate boundary conditions (specifically, near-zero initial effluent concentrations and a floating left-asymmetric inflection point), the C-H formulation successfully resolved the structural failures of classical symmetric models. The derived k_{CH1}/k_{CH2} tailing index accurately quantified breakthrough asymmetry, confirming that CAT experiences the most severe kinetic blockages and steric hindrance, followed by MO and the highly symmetric ACE system. Consequently, the C-H model is unequivocally recommended for the industrial-scale-up and process-predictive design of ZnO@DPS-AC fixed-bed adsorbers.

General Conclusion

* * * * *

Water contamination by synthetic dyes, phenolic compounds, and neonicotinoid pesticides constitutes an escalating environmental crisis. This reality demands the urgent development of sustainable, high-performance remediation materials. This doctoral thesis addressed the challenge by valorizing DPS, an abundant agricultural residue from the Biskra region, into a novel zinc oxide-modified activated carbon composite designated as ZnO@DPS-AC. The research pursued six integrated objectives. These included the synthesis and functionalization of the composite, physicochemical characterization, and batch adsorption studies against three distinct pollutant classes. The study also encompassed advanced computational optimization, continuous fixed-bed column evaluation, and cyclic reusability assessments.

The synthesis protocol employed simultaneous chemical activation with $ZnCl_2$ and thermal pyrolysis at 600°C. This approach successfully transformed the dense fibrous structure of raw date palm spikelets into a hierarchically porous composite. The resulting material exhibited a specific surface area of 1028.63 m^2/g, nearly three times that of the unmodified biochar. Comprehensive characterization via TGA-DTG, SEM-EDX, FTIR, XRD, Raman spectroscopy, and BET analysis confirmed the successful embedding of nanometric ZnO particles. These particles, averaging 33.07 nm in crystallite size, resided within a partially graphitized carbon matrix adopting a hexagonal wurtzite crystal structure. The surface chemistry of the composite proved rich in oxygenate functional groups and Zn-O coordination centers. Consequently, this configuration established the physicochemical preconditions required for versatile pollutant binding across chemically diverse contaminant classes.

Batch adsorption studies evaluated the performance of ZnO@DPS-AC against MO, CAT, and ACE. The composite achieved remarkable maximum equilibrium capacities of 274 mg/g, 170 mg/g, and 291.38 mg/g, respectively. These metrics position the material competitively among the highest-performing agricultural waste-derived adsorbents reported in current literature. Beyond absolute capacity values, the most scientifically significant finding was the demonstration of genuine thermodynamic and mechanistic adaptability within a single material. The adsorption of MO and CAT was endothermic, with standard enthalpy changes of +77.45 to +83.47 kJ/mol and +42.27 to +110.16 kJ/mol, respectively. Cooperative mechanisms, including electrostatic attraction, hydrogen bonding,

π-π stacking, physical pore filling, and inner-sphere surface complexation at the embedded ZnO active centers, drove these processes.

In striking contrast, ACE adsorption was unambiguously exothermic with a ΔH° of -31.177 kJ/mol. This interaction operated exclusively through physical forces, specifically pore filling, hydrogen bonding, and π-π electron donor-acceptor interactions. Surface complexation was thermodynamically excluded. This exclusion was further confirmed by the process's complete *pH* independence across pH 2 to 12 and by a high ethanol regeneration efficiency exceeding 80%. This endothermic-exothermic thermodynamic divergence across three pollutants on a single adsorbent platform represents a unique contribution not previously documented for agricultural waste-derived composite materials. Cyclic reusability studies confirmed structural stability across regeneration cycles. Sodium hydroxide regeneration recovered 71% to 77% of the MO capacity, while ethanol regeneration restored over 80% of the ACE capacity. However, the limited chemical regeneration efficiency observed for CAT led to the identification of thermal desorption as the necessary future strategy for strongly chemisorbed phenolic compounds.

The advanced computational framework deployed in this thesis demonstrated that ANN coupled with GA optimization consistently and quantifiably surpasses RSM for multi-variable adsorption systems. The ANN models were developed through a systematic grid search utilizing ensemble learning and k-fold cross-validation. These models achieved R^2 values of 0.9944 or higher across all response variables. When integrated as fitness functions within the NSGA-II framework, these models resolved Pareto-optimal operational fronts. These fronts exceeded RSM-identified optima by 8.5% to 32.8% in predicted adsorption capacity. Subsequent experimental validation confirmed these predictions within acceptable engineering margins. A methodologically novel contribution emerged from the systematic comparison of RSM-augmented data training for MO and CAT against purely experimental matrix training for ACE. This comparison demonstrated that data augmentation significantly improves the predictive accuracy of ANNs. Nevertheless, both architectures retained sufficient robustness to support reliable GA optimization, thereby establishing a generalizable template applicable to resource-constrained experimental programs.

Continuous fixed-bed column investigations validated the industrial scalability of the composite. The material achieved dynamic adsorption capacities of 136.27 mg/g for MO, 131.18 mg/g for CAT, and 261.49 mg/g for ACE under reference operating conditions. Notably, ACE reached a maximum dynamic capacity of 348.55 mg/g at elevated influent concentrations. Mathematical modeling of the

breakthrough curves yielded an important methodological correction. Rigorous statistical analysis showed that the Yoon-Nelson, Thomas, and Adams-Bohart models are mathematically equivalent and yield identical goodness-of-fit statistics. Therefore, selecting among them based on statistical grounds constitutes a methodological error. Alternatively, the dual-rate Chu-Hashim model uniquely captures asymmetric breakthrough tailing through two physically interpretable rate constants. This model achieved R^2 values approaching 0.999 across all experimental conditions. It is thus recommended as the standard framework for designing ZnO@DPS-AC fixed-bed adsorbers at an industrial scale.

In conclusion, the valorization of DPS into ZnO@DPS-AC yields a structurally sophisticated, chemically versatile, and operationally robust adsorbent. This material is well-suited to advanced remediation of chemically diverse aquatic pollutants within a unified circular bioeconomy framework. The principal scientific contributions of this research are multifold. First, it details the synthesis of a novel hierarchically porous ZnO-carbon composite from an underutilized agricultural waste. Second, it provides a documented demonstration of endothermic-exothermic thermodynamic duality across multiple pollutant classes on a single agricultural waste-derived composite. Third, it quantitatively validates the superiority of ANN-GA over RSM for complex adsorption optimization. Fourth, it offers a distinct methodological correction regarding the mathematical equivalence of classical breakthrough models. Finally, it provides a proof-of-concept translation of batch findings into continuous-flow industrial performance.

Recommendations and Perspective

* * * * *

While this doctoral research has successfully demonstrated the high efficiency and feasibility of the synthesized ZnO@DPS-AC composite for the advanced remediation of aqueous pollutants, the transition from fundamental laboratory-scale investigations to full-scale industrial application presents new challenges and opportunities. Based on the findings and conclusions of this study, the following recommendations and perspectives are proposed for future scientific investigations:

1. Application to real industrial wastewater and multi-component systems

- **Real effluent matrices:** The present study evaluated the adsorptive performance of the ZnO@DPS-AC composite using synthetic, single-pollutant aqueous solutions. Future research must prioritize testing the adsorbent in real, complex industrial effluents (e.g., textile dye baths, agricultural runoff, or pharmaceutical wastewater). Real matrices contain natural organic matter (NOM), varying ionic strengths, and competing ions that can significantly alter adsorption capacities and mechanisms.
- **Competitive adsorption:** Environments rarely contain a single contaminant. It is highly recommended to conduct multi-component adsorption studies (binary and ternary systems) to understand the competitive binding dynamics among dyes, phenolic compounds, and pesticides for the composite's available active sites.

2. Process scale-up and pilot-plant engineering

- **Pilot-scale implementation:** To bridge the gap between bench-scale column studies and industrial reality, future work should focus on pilot-scale fixed-bed or fluidized-bed continuous reactors. This will provide critical engineering data regarding pressure drop, bed exhaustion rates, and hydrodynamic channeling under high-throughput conditions.
- **Dynamic modeling:** Expanding the ANN and GA models to simulate dynamic, multi-column configurations (e.g., series or parallel bed arrangements) would provide a powerful predictive tool for industrial plant operators.

3. Advanced material engineering and mechanistic studies

- **Magnetic functionalization:** To overcome operational challenges in separating and recovering powdered activated carbon from treated water, future synthesis protocols could explore ternary composites. Incorporating magnetic nanoparticles (e.g., Fe_3O_4) alongside ZnO would enable rapid, energy-efficient post-adsorption separation using an external magnetic field.
- **Broadening the pollutant spectrum:** Given the versatile porous structure and active binding sites of the ZnO@DPS-AC composite, its applicability should be tested against emerging contaminants of concern (CECs), such as pharmaceutical residues, endocrine-disrupting chemicals (EDCs), microplastics, and heavy metals (e.g., Pb(II), Cd(II), Hg(II)).

Appendix

* * * * *

Appendix. A

Table Append. A.1 Remediation technologies for MO (Cheng et al., 2016; Dai et al., 2025; Z. Liu et al., 2021; Nazir et al., 2023; Ouazene et al., 2025; Souhıla, 2024; Tang et al., 2024; Van Thang et al., 2025; Yajie Wang et al., 2024)

Feature	Adsorption (MOFs/Nanocomposites)	Photocatalysis (TiO_2/ZnO)	Membrane Filtration (PVC/Bentonite)	Fenton Oxidation
Principle	Physisorption & Chemisorption (Electrostatic, π–π stacking)	Advanced Oxidation (AOP); Generation of •OH radicals via light irradiation	Physical sieving combined with specific adsorption in membrane pores	Generation of •OH radicals via Fe^{2+} + H_2O_2 reaction
Removal Efficiency	High (~99.6% for UiO–66–NH_2)	High (>98% degradation)	High (>97% rejection)	High (~99% COD removal)
Advantages	Simple design; No sludge generation; High capacity at acidic pH	Complete mineralization potential; Rapid decolorization	High-quality permeate; Continuous operation; Reusable water	Fast reaction rates; Non-selective degradation
Disadvantages/ Limitations	pH sensitive (efficiency drops at alkaline pH); Spent adsorbent disposal	Light penetration issues in dark effluents; Catalyst recovery	Membrane fouling; High-pressure requirements; Concentrated brine disposal	Generation of iron sludge; Strict pH requirement (pH 3–3.5)
Cost	Moderate/High (Material dependent)	Moderate (Energy for UV lamps)	High (Pumping energy & membrane replacement)	Moderate (Chemical reagents)
Energy Consumption	Low (Mixing only)	High (UV source) / Medium (Solar)	High (High-pressure pumps)	Low (Ambient T/P)
Env. Impact	Secondary solid waste (spent adsorbent)	Potential toxicity of nanoparticles if released	Disposal of concentrated retentate stream	Iron sludge disposal; Chemical handling
Scalability	High (Packed columns)	Moderate (Reactor geometry limits)	High (Modular units)	High (Existing tank infrastructure)
Practical Feasibility	High for polishing steps	Medium (Turbidity limits light)	High for water reuse applications	High for pre-treatment
Operational Complexity	Low	Moderate	Moderate (Cleaning cycles)	Moderate (pH adjustment)
Typical Applications	Textile polishing; Laboratory waste	Final effluent decolorization	Industrial water recycling (Zero Liquid Discharge)	Bulk textile effluent treatment

By-products	None (Phase transfer only)	Sulfanilic acid, Aromatic amines (potentially toxic)	Concentrated brine (requires further treatment)	Short-chain organic acids, CO_2, H_2O

Table Append. A.2 Remediation technologies for CAT (Afsharnia et al., 2016; Al-Onazi et al., 2021; Hecini et al., 2022; Mofrad et al., 2025; Parisheva & Demirev, 2001; Pillar-Little et al., 2015; Saleh et al., 2025)

Feature	Enzymatic Degradation (Peroxidase)	Adsorption (Biomass/AC)	AOPs	Electrocoagulation
Principle	Biocatalytic oxidation/polymerization using enzymes (e.g., Arugula Peroxidase)	Surface accumulation via Hydrogen bonding and pore filling	Direct electrophilic attack or radical oxidation (•OH) at high pH	In situ generation of coagulants (Al^{3+}/Fe^{2+}) via electrolysis
Removal Efficiency	High	High	Moderate	High
Advantages	Specificity; Mild conditions (40°C); Green chemistry	Cost-effective (agri-waste); Simple operation; Solvent recovery potential	No solid sludge; Effective at alkaline pH (>11)	Removal of colloidal particles; Compact reactor
Disadvantages/ Limitations	Enzyme stability/cost; Slow kinetics vs. chemical AOPs	Desorption/Regeneration costs; Efficiency drops at low concentration	High operational cost (Ozone generation); Low mineralization	Electrode passivation; Sludge generation; Electricity cost
Cost	High (Pure enzyme)/Low (Crude)	Low (Using bio-waste/agri-peels)	High (Ozone generation)	Moderate
Energy Consumption	Low (Ambient conditions)	Low	High (Ozonator)	Moderate (Electrolysis)
Env. Impact	Positive (Biodegradable)	Spent adsorbent waste	Potential toxic intermediates	Metal sludge disposal
Scalability	Low/Moderate (Enzyme supply)	High	High	Moderate
Practical Feasibility	Medium (Requires specific conditions)	High	High (if cost permits)	High
Operational Complexity	Moderate (pH/Temp control)	Low	Moderate (Gas transfer)	Low
Typical Applications	Pharmaceutical/Fine chemical waste	Petrochemical/Agrochemical effluents	Post-treatment polishing	Oily/Phenolic wastewater
By-products	Poly(CAT) precipitates (insoluble)	None (Phase transfer)	*cis,cis*-muconic acid, Quinones, Glyoxylic acid	Metal-organic sludge

Table Append. A.3 Remediation technologies for ACE (Abualnaja et al., 2021; Guzsvány et al., 2009; Kaludjerović et al., 2025; Kashid, 2025; Kobkeatthawin et al., 2022; Nunes de Morais et al., 2023; Pham et al., 2021; Sanz-Santos et al., 2021; Srikhaow et al., 2022)

Feature	Electrochemical Oxidation (BDD Anode)	Photocatalysis (g–C_3N_4/TiO_2)	Adsorption (Activated Carbon)	Biochar Adsorption
Principle	Anodic electron transfer & •OH generation on diamond surface	Heterojunction charge separation generating O_2^- and •OH	Micropore filling and π–π interactions	Surface interaction (limited by steric hindrance)
Removal Efficiency	Very High	High	High	Low
Advantages	High mineralization; No chemical addition; Breaks the pyridine ring	Solar potential; Stable catalyst; Ambient temp/pressure	Simple technology; Proven industrial track record	Extremely low cost; Carbon sequestration
Disadvantages/ Limitations	High capital/energy cost; Electrode cost	Slower kinetics than electro-oxidation; Light scattering	Non-destructive (transfers pollution); Regeneration cost	Low capacity for complex molecules like ACE
Cost	High	Moderate	Moderate	Very Low
Energy Consumption	Very High	Moderate (Solar/UV)	Low	Low
Env. Impact	Low (if mineralized); Risk of perchlorates	Nanocatalyst recovery: Potential leaching	Spent carbon disposal/regeneration	Spent char disposal
Scalability	Moderate (Mass transfer limits)	Low/Moderate	High	High
Practical Feasibility	Medium (Cost barrier)	Medium (Solar dependence)	High	Low (Performance barrier)
Operational Complexity	Moderate (Current density control)	Moderate	Low	Low
Typical Applications	Pesticide manufacturing; Concentrated waste	Agricultural runoff (low conc.)	Drinking water treatment; Polishing	Soil amendment/Runoff filtration
By-products	6-chloronicotinic acid, CO_2, NO_3^-	6-chloronicotinic acid, Acetic acid	None (Phase transfer)	None (Phase transfer)

Appendix. B

Table Append. B.1 Summary of common adsorption isotherm models

Model	Assumptions/Features	Equation	Parameters	Ref.
Langmuir	Monolayer, homogeneous surface, no lateral interactions.	$q_e = \frac{q_m K_L C_e}{1 + K_L C_e}$	$\mathbf{q_m}$ (mg/g): maximum saturated monolayer adsorption capacity; $\mathbf{K_L}$: a constant related to the affinity between an adsorbent and adsorbate.	(Langmuir, 1918)
Freundlich	Multilayer, heterogeneous surface, exponential energy distribution.	$q_e = K_F C_e^n$	$\mathbf{K_F}$ (mg/g)(L/mg)$^{1/n}$: Adsorption strength; **n** (dimensionless): **Freundlich** exponent related to the energetic heterogeneity of the adsorbent.	(Freundlich, 1907)
Dubinin-Radushkevich	Pore-filling mechanism: Gaussian energy distribution.	$q_e = q_{mD-R} exp^{-K_{D-R}\varepsilon^2}$	$\mathbf{q_{mD\text{-}R}}$ (mg/g): Saturation capacity; $\mathbf{K_{D\text{-}R}}$ (mol/kJ)^2: Mean free energy constant; **ε**: Polanyi potential.	(Dubinin M, 1947)
Redlich-Peterson	Hybrid Langmuir-Freundlich; versatile over wide concentration ranges.	$q_e = \frac{K_{RP} C_e}{1 + a_{RP} {C_e}^g}$	$\mathbf{K_{RP}}$ (L/g) and $\mathbf{a_{RP}}$ (L/mg)^g: RP constants; **g**: Exponent (0 to 1).	(Redlich & Peterson, 1959)
Sips	Corrects Freundlich at high concentrations (saturation limit).	$q_e = \frac{q_{ms} K_s {C_e}^{n_s}}{1 + K_s {C_e}^{n_s}}$	$\mathbf{q_{ms}}$ (mg/g): Max Sips capacity; $\mathbf{K_S}$(L/mg)^{ns}: Affinity constant; $\mathbf{n_S}$: Heterogeneity factor.	(Sips, 1948)
Khan	Specifically designed for multi-component systems but used for single pollutants.	$q_e = \frac{q_{mK} b_K C_e}{(1 + b_K C_e)^{a_K}}$	$\mathbf{q_{mK}}$ (mg/g): Max capacity; $\mathbf{b_K}$ (L/mg): Khan constant; $\mathbf{a_K}$ (dimensionless): Khan exponent.	(Khan et al., 1997)
LF	Combines features of Langmuir and Freundlich; assumes saturation at high C_e.	$q_e = \frac{q_{LF}(K_{LF} C_e)^{n_{LF}}}{1 + (K_{LF} C_e)^{n_{LF}}}$	$\mathbf{q_{LF}}$ (mg/g): Max capacity; $\mathbf{K_{LF}}$ (L/mg): Affinity constant; $\mathbf{n_{LF}}$: Heterogeneity parameter.	(Liu et al., 2003)
Liu		$q_e = \frac{q_{mL}(C_e)^{n_{Liu}}}{{K_{Liu}}^{n_L} + (C_e)^{n_{Liu}}}$		

Toth	Effective for describing heterogeneous systems at both low and high C_e.	$q_e = \frac{q_{mT} C_e}{(a_T + C_e^t)^{1/t}}$	$\mathbf{q_{mT}}$ (mg/g): Max capacity; $\mathbf{a_T}$: Toth constant; $\mathbf{n_T}$: System heterogeneity factor.	(Tóth, 1971)

Table Append. B.2 Relationship between isotherm constants and equilibrium thermodynamic constant (Tran et al., 2021)

Equilibrium Model	K_{Model}	Unit of K_{Model}	Equation of K_{eq}°
Langmuir	K_L	(L/mg)	$K_{eq}^{\circ} = K_L \times \frac{C_{Adsorbate}^{\circ}}{\gamma_{Adsorbate}}$
Redlich-Peterson	a_{RP}	$(L/mg)^g$	$K_{eq}^{\circ} = \sqrt[g]{a_{RP}} \times \frac{C_{Adsorbate}^{\circ}}{\gamma_{Adsorbate}}$
Sips	K_S	$(L/mg)^{ns}$	$K_{eq}^{\circ} = \sqrt[n_s]{K_s} \times \frac{C_{Adsorbate}^{\circ}}{\gamma_{Adsorbate}}$
Khan	b_K	(L/mg)	$K_{eq}^{\circ} = b_K \times \frac{C_{Adsorbate}^{\circ}}{\gamma_{Adsorbate}}$
LF	K_{LF}	(L/mg)	$K_{eq}^{\circ} = K_{LF} \times \frac{C_{Adsorbate}^{\circ}}{\gamma_{Adsorbate}}$
Liu	K_{Liu}	(mg/L)	$K_{eq}^{\circ} = \frac{1}{K_{Liu}} \times \frac{C_{Adsorbate}^{\circ}}{\gamma_{Adsorbate}}$

Appendix. C

Appendix. C.1 Analysis of variance framework

The ANOVA table tests the overall significance of the regression model—specifically, whether at least one independent variable (X) is a significant predictor of the dependent variable (Y).

Table Append. C.1 ANOVA table for multiple linear regression

Source of Variation	DF	SS	MS	F-Statistic
Regression (Model)	k	SSR	$MSR = \frac{SSR}{k}$	$F = \frac{MSR}{MSE}$
Error (Residual)	n - k - 1	SSE	$MSE = \frac{SSE}{n-k-1}$	
Total	n - 1	SST		

Breakdown of components

- n: The total number of observations (sample size).
- k: The number of independent variables (predictors) in your model.
- y_i: The actual observed value for the i-th observation.
- $\hat{y}_i$: The predicted value for the i-th observation.

$\bar{y}$: The overall mean of the observed values.

Appendix. C.2 Model selection and adequacy

Selecting the most appropriate polynomial model (Linear, 2FI, Quadratic, or Cubic) in Response Surface Methodology relies on two primary critical evaluations: the sequential model sum of squares test and the lack of fit test. The statistical metrics like R^2, Adj-R^2, pred-R^2, and PRESS are also taking in consideration for the selection. Together, these determine the highest-order model that significantly improves prediction without overfitting the data.

1. **Sequential model sum of squares test**

This test evaluates whether adding higher-order terms (e.g., moving from a Linear to a Quadratic model) significantly improves the model's ability to explain the variance in the data.

- **Formulation of the Hypothesis:**

Null hypothesis (H_0): The model adequately fits the data (i.e., there is no significant lack of fit).

Alternative hypothesis (H_1): The model does not adequately fit the data.

- **Calculation of F-values:**

$$F_{\text{seq}} = \frac{MS_{\text{Source}}}{MS_{\text{Stage } Residual}}$$

To calculate this, the mean squares (*MS*) are derived from the sum of squares (*SS*) and degrees of freedom (*DF*) as follows:

$\boldsymbol{MS_{\text{Source}}}$: Calculated as $\text{SS}_{\text{Source}}/\text{DF}_{\text{Source}}$ for the specific polynomial terms being tested.

$\boldsymbol{MS_{\text{Stage Residua}}}$: The stage residual is dynamic. It is calculated by pooling the variance of all remaining unmodeled terms. This is found by adding the *SS* of all subsequent terms (including the final residual) and dividing by the sum of their respective *DF*.

Example for calculating the sequential *F-value* (F_{seq}) for the Linear vs Mean for MO case see **Table V.5** for more details:

$$F_{\text{seq(Linear)}} = \frac{MS_{\text{Linear}}}{MS_{\text{Stage } Residual}}$$

$$MS_{\text{Linear}} = \frac{\text{SS}_{\text{Linear}}}{\text{DF}_{\text{Linear}}}$$

$$\text{SS}_{\text{Stage Residual}} = \text{SS}_{\text{2FI}} + \text{SS}_{\text{Quadratic}} + \text{SS}_{\text{Cubic}} + \text{SS}_{\text{Final Residual}} (= 75.91)$$

$$\text{DF}_{\text{Stage Residual}} = \text{DF}_{\text{2FI}} + \text{DF}_{\text{Quadratic}} + \text{DF}_{\text{Cubic}} + \text{DF}_{\text{Final Residual}} (= 10)$$

$$MS_{\text{Stage } Residual} = \frac{\text{SS}_{\text{Stage Residual}}}{\text{DF}_{\text{Stage Residual}}}$$

- Critical table value (F_{table}): Obtained from standard F-distribution tables using the significance level ($\alpha = 0.05$), the numerator degrees of freedom (DF_1), and the denominator degrees of freedom (DF_2), or using the function *=F.INV.RT(0.05; DF_1; DF_2)* in excel.

$$F_{table} = F_{\alpha, DF_1, DF_2}$$

- **Comparison and decision rule**

If $F_{\text{seq}} > F_{\text{table}}$ ($\alpha = 0.05$), the null hypothesis is rejected. This indicates that adding the complexity of the higher-order terms is statistically justified. In RSM, the highest-order polynomial model where the sequential addition is significant—and not aliased—is generally selected.

2. **Lack of Fit test**

While the sequential test looks at what the model explains, the Lack of Fit test assesses what the model misses. It tests whether the residual error is purely due to natural experimental noise (Pure Error) or if the model itself is failing to capture the true shape of the data.

- **Formulation of the Hypothesis:**

Null hypothesis (H_0): The model adequately fits the data (i.e., there is no significant lack of fit).

Alternative hypothesis (H_1): The model does not adequately fit the data.

- **Calculation of F-values:**

The calculated F-statistic (F_{LoF}) compares the mean square of the lack of fit to the mean square of the pure error:

$$F_{\text{LoF}} = \frac{MS_{\text{LoF}}}{MS_{\text{Pure Error}}}$$

Comparison and Decision Rule:

Unlike the overall and sequential F-tests, a non-significant result is desired here.

If $F_{\text{LoF}} < F_{\text{table}}$ ($\alpha = 0.05$), the null hypothesis (H_0) is accepted. The lack of fit is insignificant, meaning the model adequately represents the experimental data.

If $F_{\text{LoF}} > F_{\text{table}}$ ($\alpha = 0.05$), the null hypothesis is rejected, indicating that the model does not fit the data well and higher-order terms or data transformations may be required.

3. **Final selection criteria**

The best model is typically the highest-order polynomial that satisfies two conditions simultaneously: a significant sequential model test ($F_{\text{seq}} > F_{\text{table}}$, $p < 0.05$) and an insignificant lack of fit test ($F_{\text{LoF}} < F_{\text{table}}$, $p > 0.05$).

Appendix. C.3 F-Test: overall model significance

The Fisher's F-test is a fundamental statistical method used in multiple regression and RSM to assess the overall significance of the fitted model. It determines whether the set of independent variables (and their interactions) taken together reliably predicts the dependent variable better than the dependent variable's mean alone.

1. Formulation of the Hypothesis

- Null hypothesis (H_0): All regression coefficients (excluding the intercept) are equal to zero ($\beta_1 = \beta_2 = \ldots = \beta_k = 0$). This implies that the independent variables have no effect on the response and that the model has no predictive power.
- Alternative hypothesis (H_1): At least one regression coefficient is non-zero ($\beta_j \neq 0$ for at least one j). This implies that the model explains a significant proportion of the variance in the experimental data.

2. Calculation and extraction of F-values

- Calculated F-Statistic (F_{calc}): Calculated directly from the ANOVA table as the ratio of the Model Mean Square to the Residual Mean Square:

$$F_{calc} = \frac{MS_{Model}}{MS_{Residual}}$$

3. Comparison and Decision Rule

- **If $F_{calc} > F_{table}$:** The null hypothesis (H_0) is rejected. The variance explained by the model is significantly greater than the experimental error, indicating that the overall regression equation is statistically significant.
- **If $F_{calc} < F_{table}$:** The null hypothesis (H_0) is accepted. The model does not adequately explain the variation in the target response.

Appendix. C.4 Mathematical formulas for statistical validation

The adequacy and significance of the generated response surface models were evaluated using the following standard statistical equations. (Notation: n = number of runs, p = number of regression parameters, SE = standard error).

1. Sum of squares and mean squares

- **Total sum of squares:**

$$SS_{Total} = \sum_{i=1}^{n} (y_i - \bar{y})^2$$

- **Model/Regression sum of squares:**

$$SSR = \sum_{i=1}^{n} (\hat{y}_i - \bar{y})^2$$

- **Residual/Error sum of squares:**

$$SSE = \sum_{i=1}^{n} (y_i - \hat{y}_i)^2$$

- **Mean square:**

$$MS = \frac{SS}{DF}$$

2. Additional hypothesis testing

- Lack of fit (LoF) F-test:

$$F_{LoF} = \frac{MS_{LoF}}{MS_{Pure_Error}}$$

3. Goodness-of-fit and predictive capabilities

- Coefficient of determination (R^2):

$$R^2 = 1 - \frac{SS_{Residual}}{SS_{Total}}$$

- Adjusted R^2:

$$R^2_{adj} = 1 - \left[\left(\frac{SS_{Residual}}{SS_{Total}}\right) \times \left(\frac{n-1}{n-p}\right)\right]$$

- Predicted residual error sum of squares (PRESS):

$$PRESS = \sum_{i=1}^{n} \left(y_i - \widehat{y_{i,-i}}\right)^2$$

- **Predicted R^2:**

$$R^2_{pred} = 1 - \frac{PRESS}{SS_{Total}}$$

4. Error and precision metrics

- Standard deviation:

$$SD = \sqrt{MS_{Residual}}$$

- Coefficient of variation:

$$CV = \left(\frac{SD}{\bar{y}}\right) \times 100$$

- Adequate precision:

$$AP = \frac{\max(\hat{y}_i) - \min(\hat{y}_i)}{\sqrt{\frac{p \cdot MS_{Residual}}{n}}}$$

Appendix. D

The following tables summarize the experimental runs, comparing the actual capacity (q_e) with the predicted values to determine the model accuracy.

Table Append. D.1 Complete experimental design matrix with predicted values and residuals for adsorption capacity and removal percentage for MO

Run	Time	C_0	Dose	pH	T	Capacity	Predicted Capacity	Residual	Removal	Predicted Removal	Residual
	min	mg/L	mg		˚C	mg/g	(mg/g)	(mg/g)	%	(%)	(%)
1	240	250	100	6	35	124.86	120.30	4.55	99.88	100.28	-0.40
2	80	250	65	4	35	156.40	148.41	7.99	81.33	79.42	1.91
3	160	100	65	8	35	76.92	78.26	-1.33	100.00	98.86	1.14
4	160	400	30	6	35	234.60	232.76	1.84	35.19	28.45	6.74
5	160	400	100	6	35	197.75	200.34	-2.59	98.87	96.67	2.20
6	160	250	100	6	25	125.00	127.74	-2.74	100.00	99.22	0.78
7	240	100	65	6	35	76.34	75.19	1.15	99.24	98.43	0.81
8	240	250	65	8	35	191.09	192.48	-1.40	99.36	97.38	1.98
9	160	250	100	4	35	124.71	131.63	-6.93	99.76	102.89	-3.13
10	240	250	65	6	25	181.30	177.68	3.62	94.28	92.46	1.82
11	160	100	30	6	35	134.17	129.02	5.14	80.50	79.60	0.90
12	160	250	30	6	25	174.03	181.27	-7.24	41.77	43.23	-1.46
13	240	250	65	6	45	187.02	183.09	3.93	97.25	94.67	2.58
14	160	250	65	4	25	164.31	157.59	6.72	85.44	82.53	2.91
15	80	250	30	6	35	157.27	164.02	-6.75	37.74	37.37	0.37
16	160	250	65	6	35	184.39	184.93	-0.55	95.88	96.00	-0.12
17	80	250	65	6	45	154.62	160.77	-6.16	80.40	84.62	-4.22
18	160	250	100	6	45	124.63	120.30	4.33	99.70	98.30	1.40
19	240	250	30	6	35	268.57	278.66	-10.10	64.46	68.98	-4.52
20	160	250	65	4	45	191.21	186.79	4.42	99.43	95.18	4.25
21	160	250	30	8	35	241.77	232.76	9.01	58.02	57.93	0.09

22	160	100	65	6	25	76.92	75.94	0.98	100.00	98.13	1.87
23	80	250	100	6	35	123.47	120.30	3.17	98.78	94.26	4.52
24	160	250	30	6	45	271.88	267.74	4.15	65.25	66.10	-0.85
25	160	400	65	6	45	249.39	247.15	2.23	81.05	82.08	-1.03
26	80	400	65	6	35	154.79	159.17	-4.39	50.31	52.58	-2.28
27	80	250	65	8	35	147.68	142.59	5.08	76.79	75.63	1.16
28	160	250	65	8	25	155.22	157.59	-2.38	80.71	83.34	-2.63
29	160	250	100	8	35	123.05	127.74	-4.69	98.44	100.20	-1.76
30	160	250	65	8	45	175.72	183.09	-7.38	91.37	92.65	-1.28
31	80	100	65	6	35	76.28	73.70	2.58	99.17	95.63	3.54
32	160	100	65	6	45	75.42	77.48	-2.06	98.05	98.91	-0.86
33	160	100	100	6	35	47.98	46.99	0.98	95.95	99.58	-3.63
34	160	400	65	8	35	237.35	228.15	9.20	77.14	75.85	1.29
35	160	250	65	6	35	188.01	184.93	3.07	97.76	96.00	1.76
36	240	250	65	4	35	188.55	186.79	1.76	98.05	95.31	2.74
37	160	400	65	6	25	192.68	183.09	9.58	62.62	60.91	1.71
38	160	250	65	6	35	189.62	184.93	4.68	98.60	96.00	2.60
39	160	250	65	6	35	186.40	184.93	1.47	96.93	96.00	0.93
40	160	250	65	6	35	180.48	184.93	-4.46	93.85	96.00	-2.15
41	80	250	65	6	25	115.15	120.30	-5.15	59.88	64.87	-4.99
42	160	400	65	4	35	212.50	217.02	-4.52	69.06	72.69	-3.63
43	160	250	65	6	35	178.85	184.93	-6.09	93.00	96.00	-3.00
44	240	400	65	6	35	253.59	267.74	-14.15	82.42	87.42	-5.01
45	160	250	30	4	35	232.02	228.15	3.87	55.68	56.96	-1.28
46	160	100	65	4	35	76.89	83.10	-6.20	99.96	103.74	-3.78

Table Append. D.2 Complete experimental design matrix with predicted values and residuals for adsorption capacity and removal percentage for CAT

Run	Time (min)	Concentration (mg/L)	pH	Dose (mg)	Capacity (mg/g)	Predicted Capacity (mg/g)	Residual (mg/g)	Removal (%)	Predicted Removal (%)	Residual (%)

1	105	100	8	100	67.49	64.69	2.80	94.48	93.50	0.98
2	195	200	8	30	137.45	140.71	-3.26	41.24	41.11	0.13
3	105	200	8	100	96.43	96.32	0.11	67.50	67.05	0.45
4	150	150	2	65	71.00	71.57	-0.57	47.33	47.56	-0.22
5	150	150	6	65	103.60	102.52	1.08	69.07	68.36	0.71
6	150	50	6	65	50.00	56.35	-6.35	100.00	98.58	1.42
7	195	200	4	100	108.31	109.90	-1.59	75.82	75.94	-0.12
8	150	150	6	65	104.78	102.52	2.26	69.85	68.36	1.50
9	150	150	6	65	101.42	102.52	-1.10	67.61	68.36	-0.74
10	240	150	6	65	120.00	121.87	-1.87	80.00	79.72	0.28
11	105	200	4	100	97.60	95.15	2.45	68.32	66.92	1.40
12	195	100	4	30	97.98	98.55	-0.57	58.79	59.59	-0.80
13	195	100	8	30	100.56	97.94	2.62	60.34	59.42	0.92
14	150	150	6	65	100.62	102.52	-1.90	67.08	68.36	-1.28
15	150	150	10	65	68.10	72.14	-4.04	45.40	47.51	-2.11
16	150	150	6	135	82.21	87.63	-5.42	98.65	98.92	-0.26
17	150	150	6	10	146.69	145.88	0.81	19.56	22.40	-2.85
18	105	100	8	30	92.58	91.46	1.12	55.55	55.74	-0.19
19	105	100	4	30	90.00	87.64	2.36	54.00	53.99	0.01
20	150	150	6	65	104.94	102.52	2.42	69.96	68.36	1.60
21	150	250	6	65	132.55	130.81	1.74	53.02	57.05	-4.03
22	105	100	4	100	66.26	63.46	2.80	92.77	93.12	-0.35
23	150	150	6	65	99.78	102.52	-2.74	66.52	68.36	-1.84
24	105	200	4	30	116.67	120.98	-4.31	35.00	32.98	2.02
25	195	100	4	100	71.04	68.72	2.32	99.45	99.74	-0.29
26	195	200	8	100	109.35	106.65	2.70	76.55	74.40	2.15
27	60	150	6	65	97.90	100.64	-2.74	65.27	67.55	-2.28
28	195	100	8	100	69.39	65.53	3.86	97.15	98.64	-1.49
29	195	200	4	30	143.65	141.38	2.27	43.10	41.70	1.39
30	105	200	8	30	127.50	124.74	2.76	38.25	34.75	3.50

Table Append. D.3 Complete experimental design matrix with predicted values and residuals for adsorption capacity and removal percentage for ACE

Run	Time	Concentration	Dose	pH	Capacity	Predicted Capacity	Residual	Removal	Predicted Removal	Residual
	min	mg/L	mg		mg/g	(mg/g)	(mg/g)	%	(%)	(%)
1	30	400	100	50	174.635	175.43	-0.80	87.3175	87.41	-0.09
2	180	400	100	30	189.065	187.33	1.73	94.5325	94.68	-0.15
3	30	275	65	40	183.923	183.03	0.89	86.9455	87.85	-0.90
4	180	150	100	30	75	79.32	-4.32	100	101.92	-1.92
5	105	275	65	40	188.508	190.49	-1.98	89.11	88.87	0.24
6	180	275	65	40	194.546	191.34	3.21	91.97	91.49	0.48
7	105	275	100	40	134.035	136.77	-2.74	97.48	93.66	3.82
8	105	275	65	30	194.277	189.35	4.93	91.84	91.18	0.66
9	180	150	30	50	189.683	192.61	-2.93	75.8733	75.63	0.24
10	180	400	100	50	181.64	181.43	0.21	90.82	91.12	-0.30
11	105	275	65	40	190.915	190.49	0.42	90.2509	88.87	1.38
12	180	150	30	30	207.783	206.52	1.26	83.11	81.94	1.17
13	105	275	65	40	191.308	190.49	0.82	90.4364	88.87	1.57
14	30	400	30	50	278.383	275.56	2.82	41.76	40.82	0.94
15	105	275	65	40	187.138	190.49	-3.35	88.4655	88.87	-0.40
16	105	275	65	40	187.354	190.49	-3.14	88.5673	88.87	-0.30
17	105	150	65	40	142.5	138.01	4.49	97.11	97	0.11
18	105	275	65	40	185.431	190.49	-5.06	87.6582	88.87	-1.21
19	30	150	30	30	194.2	195.91	-1.71	77.68	78.36	-0.68
20	30	400	30	30	273.517	276.2	-2.68	41.03	40.05	0.98
21	30	400	100	30	176.36	174.93	1.43	88.18	89.4	-1.22
22	105	275	30	40	257.267	250.43	6.84	56.13	60.37	-4.24
23	30	150	30	50	187.133	188.4	-1.27	74.8533	73.63	1.22
24	30	150	100	30	72.91	71.83	1.08	97.21	96.28	0.93
25	180	400	30	30	290	291.72	-1.72	43.5	43.28	0.22

26	180	150		100	50		69.72	66.56	3.16	92.96	92.86	0.10
27	105	400		65	40		235.2	235.59	-0.39	76.44	76.97	-0.53
28	105	275		65	50		181.823	182.65	-0.83	85.95	87.03	-1.08
29	180	400		30	50		284.067	284.68	-0.61	42.61	42.47	0.14
30	30	150		100	50		65.7	65.47	0.23	87.6	88.79	-1.19

References

* * * * *

Abbou, B., Lebkiri, I., Ouaddari, H., El Amri, A., Achibat, F. E., Kadiri, L., Ouass, A., Lebkiri, A., & Rifi, E. H. (2023). Improved removal of methyl orange dye by adsorption using modified clay: Combined experimental study using surface response methodology. *Inorganic Chemistry Communications*, *155*, 111127. https://doi.org/10.1016/j.inoche.2023.111127

Abdolali, A., Ngo, H. H., Guo, W., Zhou, J. L., Zhang, J., Liang, S., Chang, S. W., Nguyen, D. D., & Liu, Y. (2017). Application of a breakthrough biosorbent for removing heavy metals from synthetic and real wastewaters in a lab-scale continuous fixed-bed column. *Bioresource Technology*, *229*, 78-87. https://doi.org/10.1016/j.biortech.2017.01.016

Abualnaja, K. M., Alprol, A. E., Ashour, M., & Mansour, A. T. (2021). Influencing Multi-Walled Carbon Nanotubes for the Removal of Ismate Violet 2R Dye from Wastewater: Isotherm, Kinetics, and Thermodynamic Studies. *Applied Sciences*, *11*(11), 4786. https://doi.org/10.3390/app11114786

Abugazleh, M. K., Rougeau, B., & Ali, H. (2020). Adsorption of catechol and hydroquinone on titanium oxide and iron (III) oxide. *Journal of Environmental Chemical Engineering*, *8*(5), 104180. https://doi.org/10.1016/j.jece.2020.104180

Afsharnia, M., Saeidi, M., Zarei, A., Narooie, M. R., & Biglari, H. (2016). Phenol Removal from Aqueous Environment by Adsorption onto Pomegranate Peel Carbon. *Electron Physician*, *8*(11), 3248-3256. https://doi.org/10.19082/3248

Agency, U. S. E. P. (2020). *Acetamiprid Proposed Interim Registration Review Decision: Case Number 7617*. https://www.regulations.gov/document/EPA-HQ-OPP-2012-0329-0043

Agency, U. S. E. P. (2023). *Acetamiprid Biological Evaluation and Associated Effects Determinations for Federally Listed Endangered and Threatened Species and Their Designated Critical Habitats*. https://www.regulations.gov/docket/EPA-HQ-OPP-2023-0506

Ahlawat, W., Dilbaghi, N., Kumar, R., Singhal, N. K., Kaushik, A., & Kumar, S. (2023). Adsorption of harmful dyes and antimicrobial studies utilizing recyclable ZnO, its composites with conventionally used activated carbon, and waste orange peel as a greener approach. *Journal of Environmental Chemical Engineering*, *11*(3), 110268. https://doi.org/10.1016/j.jece.2023.110268

Ahmed, M. J., & Dhedan, S. K. (2012). Equilibrium isotherms and kinetics modeling of methylene blue adsorption on agricultural wastes-based activated carbons. *Fluid Phase Equilibria*, *317*, 9-14. https://doi.org/10.1016/j.fluid.2011.12.026

Ahmed, M. J., & Hameed, B. H. (2018). Removal of emerging pharmaceutical contaminants by adsorption in a fixed-bed column: A review. *Ecotoxicology and Environmental Safety*, *149*, 257-266. https://doi.org/10.1016/j.ecoenv.2017.12.012

Aichour, A., Zaghouane-Boudiaf, H., & Djafer Khodja, H. (2022). Highly removal of anionic dye from aqueous medium using a promising biochar derived from date palm petioles: Characterization, adsorption properties and reuse studies. *Arabian Journal of Chemistry*,

15(1), 103542. https://doi.org/10.1016/j.arabjc.2021.103542

Aichour, A., Zaghouane-Boudiaf, H., Mohamed Zuki, F. B., Kheireddine Aroua, M., & Ibbora, C. V. (2019). Low-cost, biodegradable and highly effective adsorbents for batch and column fixed bed adsorption processes of methylene blue. *Journal of Environmental Chemical Engineering*, *7*(5), 103409. https://doi.org/10.1016/j.jece.2019.103409

Al-Degs, Y. S., El-Barghouthi, M. I., El-Sheikh, A. H., & Walker, G. M. (2008). Effect of solution pH, ionic strength, and temperature on adsorption behavior of reactive dyes on activated carbon. *Dyes and Pigments*, *77*(1), 16-23. https://doi.org/10.1016/j.dyepig.2007.03.001

Al-Ghouti, M. A., & Da'ana, D. A. (2020). Guidelines for the use and interpretation of adsorption isotherm models: A review. *Journal of Hazardous Materials*, *393*, 122383. https://doi.org/10.1016/j.jhazmat.2020.122383

Al-Hazeef, M. S. F., Aidi, A., Hecini, L., Osman, A. I., Hasan, G. G., Althamthami, M., Ziad, S., Otmane, T., & Rooney, D. W. (2024). Valorizing date palm spikelets into activated carbon-derived composite for methyl orange adsorption: advancing circular bioeconomy in wastewater treatment—a comprehensive study on its equilibrium, kinetics, thermodynamics, and mechanisms. *Environmental Science and Pollution Research*, *31*, 50493–50512. https://doi.org/10.1007/s11356-024-34581-3

Al-Maliky, E. A., Gzar, H. A., & Al-Azawy, M. G. (2021). Determination of Point of Zero Charge (PZC) of Concrete Particles Adsorbents. *IOP Conference Series: Materials Science and Engineering*, *1184*(1), 012004. https://doi.org/10.1088/1757-899X/1184/1/012004

Al-Onazi, W. A., Ali, M. H. H., & Al-Garni, T. (2021). Using Pomegranate Peel and Date Pit Activated Carbon for the Removal of Cadmium and Lead Ions from Aqueous Solution. *Journal of Chemistry*, *2021*(1), 5514118. https://doi.org/10.1155/2021/5514118

Alam, G., Ihsanullah, I., Naushad, M., & Sillanpää, M. (2022). Applications of artificial intelligence in water treatment for optimization and automation of adsorption processes: Recent advances and prospects. *Chemical Engineering Journal*, *427*, 130011. https://doi.org/10.1016/j.cej.2021.130011

Albo Hay Allah, M. A., & Alshamsi, H. A. (2023). Green synthesis of AC/ZnO nanocomposites for adsorptive removal of organic dyes from aqueous solution. *Inorganic Chemistry Communications*, *157*, 111415. https://doi.org/10.1016/j.inoche.2023.111415

Alharbi, H. A., Hameed, B. H., Alotaibi, K. D., Al-Oud, S. S., & Al-Modaihsh, A. S. (2022). Recent methods in the production of activated carbon from date palm residues for the adsorption of textile dyes: A review [Review]. *Frontiers in Environmental Science*, *10*. https://doi.org/10.3389/fenvs.2022.996953

Ali, A., Kanwal, N., Alharthi, S., Santali, E. Y., & Zhao, W. (2026). Facile synthesis of amide-functionalized mesoporous silica for efficient removal of acetamiprid, imidacloprid and lambda-cyhalothrin from water. *Separation and Purification Technology*, *381*, 135598. https://doi.org/10.1016/j.seppur.2025.135598

Ali, W., Bilal, M., Alharbi, A., Jaffar, A., Miyajan, A., & Hassnain Mohsan, S. A. (2024). Intelligent Bayesian regularization backpropagation neuro computing paradigm for state features estimation of underwater passive object [Original Research]. *Frontiers in Physics*, *Volume 12 - 2024*. https://doi.org/10.3389/fphy.2024.1374138

Allalou, O., Miroud, D., Belmedani, M., & Sadaoui, Z. (2019). Performance of surfactant-modified activated carbon prepared from dates wastes for nitrate removal from aqueous solutions. *Environmental Progress & Sustainable Energy*, *38*(s1), S403-S411. https://doi.org/10.1002/ep.13090

AlNeyadi, S. S., Alblooshi, H. K., & Mukhtar, M. R. (2026). High-performance magnetic COFs for synergistic adsorption–photocatalysis of thiamethoxam and acetamiprid in water. *Case Studies in Chemical and Environmental Engineering*, *13*, 101325. https://doi.org/10.1016/j.cscee.2026.101325

Alomar, T., Qiblawey, H., Almomani, F., Al-Raoush, R. I., Han, D. S., & Ahmad, N. M. (2023). Recent advances on humic acid removal from wastewater using adsorption process. *Journal of Water Process Engineering*, *53*, 103679. https://doi.org/10.1016/j.jwpe.2023.103679

Andrew, D., & Samuels, S. (2024). Cholinergic Neurotransmission and Toxicity – Neonicotinoids and Spinosad. In K. N. Woodward & T. Marrs (Eds.), *Neurotransmitters and Toxicology* (Vol. 48, pp. 0). Royal Society of Chemistry. https://doi.org/https://doi.org/10.1039/9781839165795-00049

Ansari, A., Nadres, E. T., Đỗ, M., & Rodrigues, D. F. (2021). Investigation of the removal and recovery of nitrate by an amine-enriched composite under different fixed-bed column conditions. *Process Safety and Environmental Protection*, *150*, 365-372. https://doi.org/10.1016/j.psep.2021.04.027

Apiratikul, R., & Chu, K. H. (2021). Improved fixed bed models for correlating asymmetric adsorption breakthrough curves. *Journal of Water Process Engineering*, *40*, 101810. https://doi.org/10.1016/j.jwpe.2020.101810

Arif, M. (2025). Catalytic reduction/degradation of methyl orange by metal nanoparticle containing systems: a critical review [10.1039/D5RA04059K]. *RSC Advances*, *15*(34), 27668-27684. https://doi.org/10.1039/D5RA04059K

Arreola-Najera, L. G., Ramírez-Márquez, C., Sánchez-Ramírez, E., Contreras-Zarazúa, G., & Segovia-Hernández, J. G. (2025). Optimized Sustainable Production of Catechol from Lignin-Rich Agricultural Waste. *Process Integration and Optimization for Sustainability*, *9*, 651-666. https://doi.org/10.1007/s41660-024-00481-9

Astolfi, D. L., & Mayville, F. C. (2003). Synthesis of methyl orange using ionic liquids. *Tetrahedron Letters*, *44*(51), 9223-9224. https://doi.org/10.1016/j.tetlet.2003.10.036

Authority, E. F. S. (2016). Peer review of the pesticide risk assessment of the active substance acetamiprid. *EFSA Journal*, *14*(11), e04610. https://doi.org/10.2903/j.efsa.2016.4610

Azami, M., Bahram, M., Nouri, S., & Naseri, A. (2012). Central composite design for the optimization of removal of the azo dye, methyl orange, from waste water using fenton reaction. *Journal of the Serbian Chemical Society*, *77*(2), 235-246. https://doi.org/10.2298/JSC110315165A

Azoulay, K., Bencheikh, I., Moufti, A., Dahchour, A., Mabrouki, J., & El Hajjaji, S. (2020). Comparative study between static and dynamic adsorption efficiency of dyes by the mixture of palm waste using the central composite design. *Chemical Data Collections*, *27*, 100385. https://doi.org/10.1016/j.cdc.2020.100385

Babić, S., Čižmek, L., Maršavelski, A., Malev, O., Pflieger, M., Strunjak-Perović, I., Popović, N. T., Čož-Rakovac, R., & Trebše, P. (2021). Utilization of the zebrafish model to unravel the harmful effects of biomass burning during Amazonian wildfires. *Scientific Reports*, *11*(1), 2527. https://doi.org/10.1038/s41598-021-81789-1

Bagheri, M., Mirbagheri, S. A., Bagheri, Z., & Kamarkhani, A. M. (2015). Modeling and optimization of activated sludge bulking for a real wastewater treatment plant using hybrid artificial neural networks-genetic algorithm approach. *Process Safety and Environmental Protection*, *95*, 12-25. https://doi.org/10.1016/j.psep.2015.02.008

Balderas-Hernández, V. E., Treviño-Quintanilla, L. G., Hernández-Chávez, G., Martinez, A., Bolívar, F., & Gosset, G. (2014). Catechol biosynthesis from glucose in Escherichia coli anthranilate-overproducer strains by heterologous expression of anthranilate 1,2-dioxygenase from Pseudomonas aeruginosa PAO1. *Microbial Cell Factories*, *13*(1), 136. https://doi.org/10.1186/s12934-014-0136-x

Bandosz, T. J. (2006). *Activated Carbon Surfaces in Environmental Remediation* (T. J. Bandosz, Ed.). Elsevier Ltd.

Bansal, R. C., & Goyal, M. (2005). *Activated carbon adsorption*. CRC press.

Barrett, E. P., Joyner, L. G., & Halenda, P. P. (1951). The Determination of Pore Volume and Area Distributions in Porous Substances. I. Computations from Nitrogen Isotherms. *Journal of the American Chemical Society*, *73*(1), 373-380. https://doi.org/10.1021/ja01145a126

Basheer, I. A., & Hajmeer, M. (2000). Artificial neural networks: fundamentals, computing, design, and application. *Journal of Microbiological Methods*, *43*(1), 3-31. https://doi.org/10.1016/S0167-7012(00)00201-3

Bass, C., Denholm, I., Williamson, M. S., & Nauen, R. (2015). The global status of insect resistance to neonicotinoid insecticides. *Pesticide Biochemistry and Physiology*, *121*, 78-87. https://doi.org/10.1016/j.pestbp.2015.04.004

Bassam, A., Bassam, R., El Alouani, M., Rachdi, Y., Saufi, H., & Belaaouad, S. (2024). Synthesis of geopolymer powder and beads based on red clay waste for the adsorption of methyl orange dye from aqueous solutions: Characterization, application of response surface methodology, and cost analysis. *Sustainable Chemistry and Pharmacy*, *39*, 101575. https://doi.org/10.1016/j.scp.2024.101575

Bayram, E., Hoda, N., & Ayranci, E. (2009). Adsorption/electrosorption of catechol and resorcinol onto high area activated carbon cloth. *Journal of Hazardous Materials*, *168*(2), 1459-1466. https://doi.org/10.1016/j.jhazmat.2009.03.039

Benhalima, T., Mokhtari, M., & Ferfera-Harrar, H. (2024). Synergistic adsorption/photodegradation effect for effective removal of crystal violet dye and acetamiprid pesticide using Fe3+ cross-linked ternary carboxymethyl cellulose/polyaniline/TiO2 photocomposites. *Journal of Water Process Engineering*, *57*, 104670. https://doi.org/10.1016/j.jwpe.2023.104670

Berillo, D., & Ermukhambetova, A. (2024). The review of oral adsorbents and their properties. *Adsorption*, *30*(6), 1505-1527. https://doi.org/10.1007/s10450-024-00515-1

Bessaha, F., Bessaha, G., Ziane, S., & Khelifa, A. (2023). Adsorption of Methyl Orange on

Bentonite: Design, Modeling, and Analysis of Experiments. *Iranian Journal of Chemistry and Chemical Engineering*, *42*(10), 3306-3323. https://doi.org/10.30492/ijcce.2023.1971110.5663

Bhowmik, M., Deb, K., Debnath, A., & Saha, B. (2018). Mixed phase Fe2O3/Mn3O4 magnetic nanocomposite for enhanced adsorption of methyl orange dye: Neural network modeling and response surface methodology optimization. *Applied Organometallic Chemistry*, *32*(3), e4186. https://doi.org/10.1002/aoc.4186

Bhuyan, A., & Ahmaruzzaman, M. (2023). Recent advances in new generation nanocomposite materials for adsorption of pharmaceuticals from aqueous environment. *Environmental Science and Pollution Research*, *30*(14), 39377-39417. https://doi.org/10.1007/s11356-023-25707-0

Blaisi, N. I., Zubair, M., Ihsanullah, Ali, S., Kazeem, T. S., Manzar, M. S., Al-Kutti, W., & Al Harthi, M. A. (2018). Date palm ash-MgAl-layered double hydroxide composite: sustainable adsorbent for effective removal of methyl orange and eriochrome black-T from aqueous phase. *Environmental Science and Pollution Research*, *25*(34), 34319-34331. https://doi.org/10.1007/s11356-018-3367-2

Blanchard, G., Maunaye, M., & Martin, G. (1984). Removal of heavy metals from waters by means of natural zeolites. *Water Research*, *18*(12), 1501-1507. https://doi.org/10.1016/0043-1354(84)90124-6

Bohart, G. S., & Adams, E. Q. (1920). SOME ASPECTS OF THE BEHAVIOR OF CHARCOAL WITH RESPECT TO CHLORINE.1. *Journal of the American Chemical Society*, *42*(3), 523-544. https://doi.org/10.1021/ja01448a018

Bolton, J. L., Trush, M. A., Penning, T. M., Dryhurst, G., & Monks, T. J. (2000). Role of Quinones in Toxicology. *Chemical Research in Toxicology*, *13*(3), 135-160. https://doi.org/10.1021/tx9902082

Borah, A. (2020). Review Of the Emerging Use Of Activated Carbon Or Biochar Media as Stormwater Source Controls [Online]. Canada: The University of British Columbia & UBC Sustainability. In.

Brunauer, S., Emmett, P. H., & Teller, E. (1938). Adsorption of Gases in Multimolecular Layers. *Journal of the American Chemical Society*, *60*(2), 309-319. https://doi.org/10.1021/ja01269a023

Bumajdad, A., & Hasila, P. (2023). Surface modification of date palm activated carbonaceous materials for heavy metal removal and CO2 adsorption. *Arabian Journal of Chemistry*, *16*(1), 104403. https://doi.org/10.1016/j.arabjc.2022.104403

Busmundrud, O. (1991). Derivation of the Yoon-Nelson equation for breakthrough in carbon beds from the Bohart-Adams equation. *American Industrial Hygiene Association Journal*, *52*(4), A216-A217.

Cancer, I. A. f. R. o. (1999). IARC monographs on the evaluation of carcinogenic risk to humans: re-evaluation of some organic chemicals, hydrazine and hydrogen peroxide. In *IARC monographs on the evaluation of carcinogenic risk to humans: re-evaluation of some organic chemicals, hydrazine and hydrogen peroxide* (pp. 315-315).

Cartereau, A., Martin, C., & Thany, S. H. (2018). Neonicotinoid insecticides differently modulate acetycholine-induced currents on mammalian α7 nicotinic acetylcholine receptors. *Br J Pharmacol*, *175*(11), 1987-1998. https://doi.org/10.1111/bph.14018

Çeçen, F., & Aktas, Ö. (2012). *Activated carbon for water and wastewater treatment: integration of adsorption and biological treatment*. Wiley-VCH Verlag & Co.

Chang, J.-H., Sivasubramanian, P., Dong, C.-D., & Kumar, M. (2023). Study on adsorption of ammonium and nitrate in wastewater by modified biochar. *Bioresource Technology Reports*, *21*, 101346. https://doi.org/10.1016/j.biteb.2023.101346

Chang, R., & Thoman Jr, J. (2014). Chapter 17-Intermolecular forces. In *Physical Chemistry for Chemical Sciences* (pp. 779-808). University Science Books.

Chatterjee, A., & Schiewer, S. (2011). Biosorption of Cadmium(II) Ions by Citrus Peels in a Packed Bed Column: Effect of Process Parameters and Comparison of Different Breakthrough Curve Models. *CLEAN – Soil, Air, Water*, *39*(9), 874-881. https://doi.org/10.1002/clen.201000482

Chen, X. (2015). Modeling of Experimental Adsorption Isotherm Data. *Information*, *6*(1), 14-22. https://doi.org/10.3390/info6010014

Cheng, Z., Zhao, S., Han, Z., Zhang, Y., Zhao, X., & Kang, L. (2016). A novel preparation of Ag@TiO2 tubes and their potent photocatalytic degradation efficiency [10.1039/C6CE02063A]. *CrystEngComm*, *18*(45), 8756-8761. https://doi.org/10.1039/C6CE02063A

Chowdhury, Z., Abd Hamid, S. B., & Zain, S. (2014). Evaluating Design Parameters for Breakthrough Curve Analysis and Kinetics of Fixed Bed Columns for Cu(II) Cations Using Lignocellulosic Wastes. *BioResources*, *10*. https://doi.org/10.15376/biores.10.1.732-749

Chowdhury, Z. Z., Hamid, S. B. A., Das, R., Hasan, M. R., Zain, S. M., Khalid, K., & Uddin, M. N. (2013). Preparation of carbonaceous adsorbents from lignocellulosic biomass and their use in removal of contaminants from aqueous solution. *BioResources*, *8*(4), 6523-6555.

Christl, I., Ruiz, M., Schmidt, J. R., & Pedersen, J. A. (2016). Clarithromycin and Tetracycline Binding to Soil Humic Acid in the Absence and Presence of Calcium [Article]. *Environmental Science and Technology*, *50*(18), 9933-9942. https://doi.org/10.1021/acs.est.5b04693

Chu, K. H. (2010). Fixed bed sorption: Setting the record straight on the Bohart–Adams and Thomas models. *Journal of Hazardous Materials*, *177*(1), 1006-1012. https://doi.org/10.1016/j.jhazmat.2010.01.019

Chu, K. H. (2020a). Breakthrough curve analysis by simplistic models of fixed bed adsorption: In defense of the century-old Bohart-Adams model. *Chemical Engineering Journal*, *380*, 122513. https://doi.org/10.1016/j.cej.2019.122513

Chu, K. H. (2020b). Comments on "Breakthrough analysis of continuous fixed-bed adsorption of sevoflurane using activated carbons". *Chemosphere*, *247*, 125841. https://doi.org/10.1016/j.chemosphere.2020.125841

Chu, K. H. (2020c). Rebuttal to comment on "Breakthrough curve analysis by simplistic models of fixed bed adsorption: in defense of the century-old Bohart-Adams model". *Chemical*

Engineering Journal, *398*, 125546. https://doi.org/10.1016/j.cej.2020.125546

Chu, K. H. (2021a). Fixed bed adsorption of chromium and the Weibull function. *Journal of Hazardous Materials Letters*, *2*, 100022. https://doi.org/10.1016/j.hazl.2021.100022

Chu, K. H. (2021b). A Modified Belter Model for Correlating Asymmetric Breakthrough Curves of Water Pollutants. *Water, Air, & Soil Pollution*, *232*(11), 451. https://doi.org/10.1007/s11270-021-05399-3

Chu, K. H. (2023). Fixed Bed Adsorption of Water Contaminants: A Cautionary Guide to Simple Analytical Models and Modeling Misconceptions. *Separation & Purification Reviews*, *52*(2), 75-97. https://doi.org/10.1080/15422119.2022.2039196

Chu, K. H., & Hashim, M. A. (2023a). Fixed bed adsorption of water and air contaminants: analysis of breakthrough curves using probability distribution functions. *Chemical Engineering Communications*, *210*(9), 1528-1537. https://doi.org/10.1080/00986445.2022.2116325

Chu, K. H., & Hashim, M. A. (2023b). Removal of antibiotics through fixed bed adsorption: Comparison of different breakthrough curve models. *Journal of Water Process Engineering*, *56*, 104512. https://doi.org/10.1016/j.jwpe.2023.104512

Chu, K. H., & Hashim, M. A. (2024a). Can the Bass innovation diffusion model describe adsorption breakthrough curves of pharmaceutical contaminants? *Green Chemical Engineering*, *5*(2), 145-149. https://doi.org/10.1016/j.gce.2023.07.001

Chu, K. H., & Hashim, M. A. (2024b). Comparing different versions of the Yoon–Nelson model in describing organic micropollutant adsorption within fixed bed adsorbers. *Environmental Science and Pollution Research*, *31*(14), 21136-21143. https://doi.org/10.1007/s11356-024-32450-7

Chu, K. H., Hashim, M. A., Zawawi, M. H., & Bollinger, J.-C. (2025). The Weber–Morris model in water contaminant adsorption: Shattering long-standing misconceptions. *Journal of Environmental Chemical Engineering*, *13*(4), 117266. https://doi.org/10.1016/j.jece.2025.117266

Chu, K. H., & Zhao, B. (2020). Comment on "Easily Regenerative Carbon/Boehmite Composites with Enhanced Cyclic Adsorption Performance towards Methylene Blue in Batch and Continuous Aqueous Systems" and "Highly Enhanced Adsorption of Dimethyl Disulfide from Model Oil on MOF-199/Attapulgite Composites". *Industrial & Engineering Chemistry Research*, *59*(1), 497-498. https://doi.org/10.1021/acs.iecr.9b04767

Cojocaru, C., Humelnicu, A. C., Pascariu, P., & Samoila, P. (2021). Artificial neural network and molecular modeling for assessing the adsorption performance of a hybrid alginate-based magsorbent. *Journal of Molecular Liquids*, *337*, 116406. https://doi.org/10.1016/j.molliq.2021.116406

Costas-Ferreira, C., & Faro, L. R. F. (2021). Neurotoxic Effects of Neonicotinoids on Mammals: What Is There beyond the Activation of Nicotinic Acetylcholine Receptors?-A Systematic Review. *Int J Mol Sci*, *22*(16). https://doi.org/10.3390/ijms22168413

Dai, J., Wu, Y., Yao, Y., & Zhang, B. (2025). ZnO/TiO2 photocatalysts for degradation of methyl orange by low-power irradiation. *Science Progress*, *108*(1), 00368504251322606. https://doi.org/10.1177/00368504251322606

(https://pubchem.ncbi.nlm.nih.gov/compound/Catechol)

de Andrade, R. C., de Almeida, C. F., Suegama, P. H., de Arruda, E. J., Arroyo, P. A., & de Carvalho, C. T. (2015). Buriti palm stem as a potential renewable source for activated carbon production. *Environmental Technology & Innovation*, *3*, 28-34. https://doi.org/10.1016/j.eti.2015.02.002

De Boer, J. H., Lippens, B. C., Linsen, B. G., Broekhoff, J. C. P., van den Heuvel, A., & Osinga, T. J. (1966). The t-curve of multimolecular N_2-adsorption. *Journal of Colloid and Interface Science*, *21*(4), 405-414. https://doi.org/10.1016/0095-8522(66)90006-7

de Franco, M. A. E., de Carvalho, C. B., Bonetto, M. M., Soares, R. d. P., & Féris, L. A. (2017). Removal of amoxicillin from water by adsorption onto activated carbon in batch process and fixed bed column: Kinetics, isotherms, experimental design and breakthrough curves modelling. *Journal of Cleaner Production*, *161*, 947-956. https://doi.org/10.1016/j.jclepro.2017.05.197

De Smedt, J., Heynderickx, P. M., Arauzo, P. J., & Ronsse, F. (2024). Adsorption mechanism of different dyes on chemical activated carbon as quantitative assessment for wastewater treatment: Comparative study between ZnCl2 and its eutectic. *Separation and Purification Technology*, *334*, 126002. https://doi.org/10.1016/j.seppur.2023.126002

De Vargas Brião, G., Hashim, M. A., & Chu, K. H. (2023). The Sips isotherm equation: Often used and sometimes misused. *Separation Science and Technology*, *58*(5), 884-892. https://doi.org/10.1080/01496395.2023.2167662

Dean, A. M., Morris, M., Stufken, J., & Bingham, D. (2015). *Handbook of design and analysis of experiments* (Vol. 7). CRC Press Boca Raton, FL, USA:.

Desalegn, Y. M., Bekele, E. A., Dagnaw, G. H., Marye, S. A., & Reta, Y. D. (2024). RSM versus ANN for modeling and optimization of magnetic adsorbent based on montmorillonite and CoFe2O4. *Applied Water Science*, *14*(6), 129. https://doi.org/10.1007/s13201-024-02187-2

Djaber, S., Reffas, A., & El-Shafey, E.-S. I. (2025). Activated carbons produced by thermochemical means from date palm spathes impregnated with H3PO4 for Congo red removal. *Biomass Conversion and Biorefinery*, *15*(8), 12873-12890. https://doi.org/10.1007/s13399-024-06135-7

Djezzar, Z., Aidi, A., Rehali, H., Ziad, S., & Othmane, T. (2024). Characterization of activated carbon produced from the green algae Spirogyra used as a cost-effective adsorbent for enhanced removal of copper(ii): application in industrial wastewater treatment [10.1039/D3RA08678J]. *RSC Advances*, *14*(8), 5276-5289. http://dx.doi.org/10.1039/D3RA08678J

Dolatabadi, M., Naidu, H., & Ahmadzadeh, S. (2021). A green approach to remove acetamiprid insecticide using pistachio shell-based modified activated carbon; economical groundwater treatment. *Journal of Cleaner Production*, *316*, 128226. https://doi.org/10.1016/j.jclepro.2021.128226

Dovi, E., Aryee, A. A., Kani, A. N., Mpatani, F. M., Li, J., Qu, L., & Han, R. (2022). High-capacity amino-functionalized walnut shell for efficient removal of toxic hexavalent chromium ions in batch and column mode. *Journal of Environmental Chemical Engineering*, *10*(2),

107292. https://doi.org/10.1016/j.jece.2022.107292

Draths, K. M., & Frost, J. W. (1993). *Biocatalytic synthesis of catechol from glucose* (United States Patent No. https://patents.google.com/patent/US5272073A/en

Du, Z., Zheng, T., & Wang, P. (2018). Experimental and modelling studies on fixed bed adsorption for Cu(II) removal from aqueous solution by carboxyl modified jute fiber. *Powder Technology*, *338*, 952-959. https://doi.org/10.1016/j.powtec.2018.06.015

Dubey, P., Shrivastav, V., Maheshwari, P. H., & Sundriyal, S. (2020). Recent advances in biomass derived activated carbon electrodes for hybrid electrochemical capacitor applications: Challenges and opportunities. *Carbon*, *170*, 1-29. https://doi.org/10.1016/j.carbon.2020.07.056

Dubinin M, M. (1947). The Equation of the Characteristic Curve of Activated Charcoal. *Dokl. Akad. Nauk. SSSR.*, *55*, 327-329. Available: https://cir.nii.ac.jp/crid/1573950400604554624

Duran, J. E., Bayarri, B., & Sans, C. (2024). Taguchi optimisation of the synthesis of vine-pruning-waste hydrochar as potential adsorbent for pesticides in water. *Bioresource Technology*, *399*, 130552. https://doi.org/10.1016/j.biortech.2024.130552

Dvoynenko, O., Lo, S.-L., Chen, Y.-J., Chen, G. W., Tsai, H.-M., Wang, Y.-L., & Wang, J.-K. (2021). Speciation Analysis of Cr(VI) and Cr(III) in Water with Surface-Enhanced Raman Spectroscopy. *ACS Omega*, *6*(3), 2052-2059. https://doi.org/10.1021/acsomega.0c05020

El-Azazy, M., Almeer, S., Al-Saad, K., S. El-Shafie, A., Issa, A., & El-Gendy, A. (2020). Carbon-Based Materials (CBMs) for Determination and Remediation of Antimicrobials in Different Substrates: Wastewater and Infant Foods as Examples. In M. Bartoli, M. Frediani, & L. Rosi (Eds.), *Carbon-Based Material for Environmental Protection and Remediation*. IntechOpen. https://doi.org/https://doi.org/10.5772/intechopen.91750

El Hamdouni, Y., El Hajjaji, S., Szabó, T., Trif, L., Felhősi, I., Abbi, K., Labjar, N., Harmouche, L., & Shaban, A. (2022). Biomass valorization of walnut shell into biochar as a resource for electrochemical simultaneous detection of heavy metal ions in water and soil samples: Preparation, characterization, and applications. *Arabian Journal of Chemistry*, *15*(11), 104252. https://doi.org/10.1016/j.arabjc.2022.104252

El Ouadrhiri, F., Elyemni, M., Lahkimi, A., Lhassani, A., Chaouch, M., & Taleb, M. (2021). Mesoporous Carbon from Optimized Date Stone Hydrochar by Catalytic Hydrothermal Carbonization Using Response Surface Methodology: Application to Dyes Adsorption. *International Journal of Chemical Engineering*, *2021*, 5555406. https://doi.org/10.1155/2021/5555406

Emami, Z., & Azizian, S. (2014). Preparation of activated carbon from date sphate using microwave irradiation and investigation of its capability for removal of dye pollutant from aqueous media. *Journal of Analytical and Applied Pyrolysis*, *108*, 176-184. https://doi.org/10.1016/j.jaap.2014.05.002

Eren, B., & Gurkan, Y. Y. (2018). Possible reaction pathways of the acetamiprid molecule according to the DFT calculation method [Article]. *Bulgarian Chemical Communications*, *50*, 45-52. https://www.scopus.com/inward/record.uri?eid=2-s2.0-85058147970&partnerID=40&md5=e8ddcb86d15ec1b8dae8d0b1a68b2910

Factors Affecting the Adsorption of Some Ionic Dyes on the Surface of Modify CaO from Eggshell. (2019). *Asian Journal of Applied Sciences*, *7*(1). https://doi.org/10.24203/ajas.v7i1.5690

Faizal, A. N. M., Putra, N. R., & Zaini, M. A. A. (2023). Insight into the adsorptive mechanisms of methyl violet and reactive orange from water—a short review. *Particulate Science and Technology*, *41*(5), 730-739. https://doi.org/10.1080/02726351.2022.2140462

Fastuca, N. (2018, January 2). *Synthesis of and Fabric Test for Methyl Orange, and an Investigation of Acid-Base Properties of Textile Dyes*. https://www.odinity.com/fabric-test-for-methyl-orange-investigation-textile-dyes/

Faust, S. D., & Aly, O. M. (2013). *Adsorption processes for water treatment*. Elsevier.

Feng, J., Cerniglia, C. E., & Chen, H. (2012). Toxicological significance of azo dye metabolism by human intestinal microbiota. *Front. Biosci. (Elite Ed)*, *4*(2), 568-586. https://doi.org/10.2741/e400

Finkelstein-Shapiro, D., Davidowski, S. K., Lee, P. B., Guo, C., Holland, G. P., Rajh, T., Gray, K. A., Yarger, J. L., & Calatayud, M. (2016). Direct Evidence of Chelated Geometry of Catechol on TiO2 by a Combined Solid-State NMR and DFT Study. *The Journal of Physical Chemistry C*, *120*(41), 23625-23630. https://doi.org/10.1021/acs.jpcc.6b08041

Freundlich, H. (1907). Über die adsorption in lösungen. *Zeitschrift für physikalische Chemie*, *57*(1), 385-470. https://doi.org/10.1515/zpch-1907-5723

Fu, P., Hu, S., Sun, L., Xiang, J., Yang, T., Zhang, A., & Zhang, J. (2009). Structural evolution of maize stalk/char particles during pyrolysis. *Bioresource Technology*, *100*(20), 4877-4883. https://doi.org/10.1016/j.biortech.2009.05.009

Gabelman, A. (2017). Adsorption basics: Part 1 [Article]. *Chemical Engineering Progress*, *113*(7). https://www.scopus.com/inward/record.uri?eid=2-s2.0-85027026905&partnerID=40&md5=2217a1bcfce38852e0ce4308dfa2009d

Gałązka, A., Jankiewicz, U., & Szczepkowski, A. (2023). Biochemical Characteristics of Laccases and Their Practical Application in the Removal of Xenobiotics from Water. *Applied Sciences*, *13*(7), 4394. https://doi.org/10.3390/app13074394

Ghaedi, A. M., & Vafaei, A. (2017). Applications of artificial neural networks for adsorption removal of dyes from aqueous solution: A review. *Advances in Colloid and Interface Science*, *245*, 20-39. https://doi.org/10.1016/j.cis.2017.04.015

Gierak, A., & Łazarska, I. (2017). Adsorption of nitrate, nitrite, and ammonium ions on carbon adsorbents. *Adsorption Science & Technology*, *35*(7-8), 721-727. https://doi.org/10.1177/0263617417708085

Giles, C. H., Smith, D., & Huitson, A. (1974). A general treatment and classification of the solute adsorption isotherm. I. Theoretical. *Journal of Colloid and Interface Science*, *47*(3), 755-765. https://doi.org/10.1016/0021-9797(74)90252-5

Gong, R., Ye, J., Dai, W., Yan, X., Hu, J., Hu, X., Li, S., & Huang, H. (2013). Adsorptive Removal of Methyl Orange and Methylene Blue from Aqueous Solution with Finger-Citron-Residue-Based Activated Carbon. *Industrial & Engineering Chemistry Research*, *52*(39), 14297-14303. https://doi.org/10.1021/ie402138w

Greenstein, B. L., Elsey, D. C., & Hutchison, G. R. (2023). Determining best practices for using

genetic algorithms in molecular discovery. *The Journal of Chemical Physics*, *159*(9). https://doi.org/10.1063/5.0158053

Grover, A., Mohiuddin, I., Malik, A. K., Aulakh, J. S., & Kim, K.-H. (2019). Zn-Al layered double hydroxides intercalated with surfactant: Synthesis and applications for efficient removal of organic dyes. *Journal of Cleaner Production*, *240*, 118090. https://doi.org/10.1016/j.jclepro.2019.118090

Gulley-Stahl, H., Hogan, P. A., II, Schmidt, W. L., Wall, S. J., Buhrlage, A., & Bullen, H. A. (2010). Surface Complexation of Catechol to Metal Oxides: An ATR-FTIR, Adsorption, and Dissolution Study. *Environmental Science & Technology*, *44*(11), 4116-4121. https://doi.org/10.1021/es902040u

Guo, G., Muhammad, T., Dolkun, A., & Gao, J. (2024). Fixed-bed adsorption kinetics study of plant total flavonoids based on a flow-injection online spectrophotometric method. *Separation and Purification Technology*, *339*, 126554. https://doi.org/10.1016/j.seppur.2024.126554

Gurvich, L. (1915). Cited in SJ Gregg, KSW sing, adsorption, surface area and porosity. *J. Phys. Chem. Soc. Russ*, *47*, 49-56.

Guzsvány, V. J., Csanádi, J. J., Lazić, S. D., & Gaál, F. F. (2009). Photocatalytic degradation of the insecticide acetamiprid on TiO2 catalyst. *Journal of the Brazilian Chemical Society*, *20*.

Haghbin, M. R., & Niknam Shahrak, M. (2021). Process conditions optimization for the fabrication of highly porous activated carbon from date palm bark wastes for removing pollutants from water. *Powder Technology*, *377*, 890-899. https://doi.org/10.1016/j.powtec.2020.09.051

Hai, T. N. (2017). Comments on "Effect of Temperature on the Adsorption of Methylene Blue Dye onto Sulfuric Acid–Treated Orange Peel". *Chemical Engineering Communications*, *204*(1), 134-139. https://doi.org/10.1080/00986445.2016.1245185

Haque, M. M., Hossen, M. N., Rahman, A., Roy, J., Talukder, M. R., Ahmed, M., Ahiduzzaman, M., & Haque, M. A. (2024). Decolorization, degradation and detoxification of mutagenic dye Methyl orange by novel biofilm producing plant growth-promoting rhizobacteria. *Chemosphere*, *346*, 140568. https://doi.org/10.1016/j.chemosphere.2023.140568

He, H., Huang, Y., Yan, M., Xie, Y., & Li, Y. (2020). Synergistic effect of electrostatic adsorption and ion exchange for efficient removal of nitrate. *Colloids and Surfaces A: Physicochemical and Engineering Aspects*, *584*, 123973. https://doi.org/10.1016/j.colsurfa.2019.123973

He, Y., Grieser, F., & Ashokkumar, M. (2011). The mechanism of sonophotocatalytic degradation of methyl orange and its products in aqueous solutions. *Ultrasonics Sonochemistry*, *18*(5), 974-980. https://doi.org/10.1016/j.ultsonch.2011.03.017

Hecini, L., Boukerker, H., Kherifi, W., Mellah, A., & Achour, S. (2022). The removal efficiency and reaction mechanism of the aluminum coagulant on phenolic compounds in the presence of hardness salts. *Journal of Water and Land Development*, 225-233-225-233.

Heffner, H., Marchetti, J. M., Faccio, R., & López-Corral, I. (2022). Density Functional Evaluation of Catechol Adsorption on Pristine and Reduced TiO2(B)(100) Ultrathin Sheets for Dye-Sensitized Solar Cell Applications. *Inorganic Chemistry*, *61*(48), 19248-19260.

https://doi.org/10.1021/acs.inorgchem.2c02933

Ho, Y. S., Wase, D. A. J., & Forster, C. F. (1996). Kinetic Studies of Competitive Heavy Metal Adsorption by Sphagnum Moss Peat. *Environmental Technology*, *17*(1), 71-77. https://doi.org/10.1080/09593331708616362

Hsu, C.-Y., Saleh, E. A. M., Moharam, M. M., Alshahrani, M. Y., Singh, S., Kashyap, A., Krithiga, T., Chaudhary, P., Mengelizadeh, N., & Balarak, D. (2025). Optimization of Pyrocatechol and p-Cresol adsorption onto a composite of Chitosan and polyacrylamide incorporated with zeolitic imidazolate Framework-8. *Scientific Reports*, *15*(1), 22298. https://doi.org/10.1038/s41598-025-07613-2

Hu, Q., Xie, Y., Feng, C., & Zhang, Z. (2019). Fractal-like kinetics of adsorption on heterogeneous surfaces in the fixed-bed column. *Chemical Engineering Journal*, *358*, 1471-1478. https://doi.org/10.1016/j.cej.2018.10.165

Hu, Q., & Zhang, Z. (2020). Comment on ″Exponential and logistic functions: The two faces of the Bohart–Adams model″. *Journal of Hazardous Materials*, *394*, 122508. https://doi.org/10.1016/j.jhazmat.2020.122508

Hu, Y., Guo, T., Ye, X., Li, Q., Guo, M., Liu, H., & Wu, Z. (2013). Dye adsorption by resins: Effect of ionic strength on hydrophobic and electrostatic interactions. *Chemical Engineering Journal*, *228*, 392-397. https://doi.org/10.1016/j.cej.2013.04.116

Huang, C., Ghavtadze, N., Chattopadhyay, B., & Gevorgyan, V. (2011). Synthesis of Catechols from Phenols via Pd-Catalyzed Silanol-Directed C–H Oxygenation. *Journal of the American Chemical Society*, *133*(44), 17630-17633. https://doi.org/10.1021/ja208572v

Huang, J., Shi, B., Han, W., Qiu, S., Li, H., Hou, P., Wu, W., & Tang, J. (2021). Effect of pH on hexavalent chromium removal driven by henna (Lawsonia inermis) fermentation. *Biochemical Engineering Journal*, *167*, 107919. https://doi.org/10.1016/j.bej.2020.107919

Huang, X., Cao, H., & Jia, B. (2023). Optimization of Levenberg Marquardt Algorithm Applied to Nonlinear Systems. *Processes*, *11*(6), 1794. https://doi.org/10.3390/pr11061794

Im, K. M., & Jeon, J.-R. (2016). *Synthesis of Plant Phenol-derived Polymeric Dyes for Direct or Mordant-based Hair Dyeing* (Vol. 118). 1940-087X. https://doi.org/https://doi.org/10.3791/54772

Information, N. C. f. B. (2004). *PubChem Compound Summary for CID 23673835: Methyl Orange*. National Library of Medicine (US). https://pubchem.ncbi.nlm.nih.gov/compound/C.I.-Acid-Orange-52

Information, N. C. f. B. (2025a, December 24). *PubChem Compound Summary for CID 289: Catechol*. National Library of Medicine (US).

Information, N. C. f. B. (2025b, December 25). *PubChem Compound Summary for CID 213021: Acetamiprid*. National Library of Medicine (US). https://pubchem.ncbi.nlm.nih.gov/compound/213021

International Agency for Research on, C. (1999). Re-evaluation of some organic chemicals, hydrazine and hydrogen peroxide. *JARC Monographs on the Evaluation on the Carcinogenic Risks to Humans*, *71*, 319-335. https://cir.nii.ac.jp/crid/1571698599602762752

Isoda, N., Rodrigues, R., Silva, A., Gonçalves, M., Mandelli, D., Figueiredo, F. C. A., & Carvalho, W. A. (2014). Optimization of preparation conditions of activated carbon from agriculture waste utilizing factorial design. *Powder Technology*, *256*, 175-181. https://doi.org/10.1016/j.powtec.2014.02.029

Iwuozor, K. O., Ighalo, J. O., Emenike, E. C., Ogunfowora, L. A., & Igwegbe, C. A. (2021). Adsorption of methyl orange: A review on adsorbent performance. *Current Research in Green and Sustainable Chemistry*, *4*, 100179. https://doi.org/10.1016/j.crgsc.2021.100179

James, T. H. (1946). The Site of Reaction in Direct Photographic Development. *The Journal of Chemical Physics*, *14*(9), 536-539. https://doi.org/10.1063/1.1724190

Jarabak, R., Harvey, R. G., & Jarabak, J. (1998). Redox cycling of polycyclic aromatic hydrocarbon o-quinones: metal ion-catalyzed oxidation of catechols bypasses inhibition by superoxide dismutase. *Chemico-Biological Interactions*, *115*(3), 201-213. https://doi.org/10.1016/S0009-2797(98)00070-2

Joyner, L. G., Barrett, E. P., & Skold, R. (1951). The Determination of Pore Volume and Area Distributions in Porous Substances. II. Comparison between Nitrogen Isotherm and Mercury Porosimeter Methods. *Journal of the American Chemical Society*, *73*(7), 3155-3158. https://cir.nii.ac.jp/crid/1571135649638605440

Juela, D. M. (2021). Comments on "Dynamic Adsorption of Sulfamethoxazole from Aqueous Solution by Lignite Activated Coke". *Materials*, *14*(4), 848. https://doi.org/10.3390/ma14040848

Kaludjerović, M., Savić, S., Bajuk-Bogdanović, D., Jovanović, A., Rakočević, L., Roglić, G., Milikić, J., & Stanković, D. (2025). Holmium Metal Nanoparticle PbO2 Anode Formed by Electrodeposition for Efficient Removal of Insecticide Acetamiprid and Improved Oxygen Evolution Reaction. *Micromachines*, *16*(8), 960. https://doi.org/10.3390/mi16080960

Kamarehie, B., Jafari, A., Azimi, F., Rashidipour, M., & Sepahvand, A. (2024). Removal of Pyrocatechol from Aqueous Solution Using Activated Carbon Coated with Aluminum Nanoparticles by a Green Method. *Health Scope*, *In Press*. https://doi.org/10.5812/healthscope-144472

Kamdod, A. S., & Kumar, M. V. P. (2022). Adsorption of Methylene Blue, Methyl Orange, and Crystal Violet on Microporous Coconut Shell Activated Carbon and Its Composite with Chitosan: Isotherms and Kinetics. *Journal of Polymers and the Environment*, *30*(12), 5274-5289. https://doi.org/10.1007/s10924-022-02597-w

Karri, R. R., Tanzifi, M., Tavakkoli Yaraki, M., & Sahu, J. N. (2018). Optimization and modeling of methyl orange adsorption onto polyaniline nano-adsorbent through response surface methodology and differential evolution embedded neural network. *Journal of Environmental Management*, *223*, 517-529. https://doi.org/10.1016/j.jenvman.2018.06.027

Kashid, L. M. (2025). Monitoring the Electrochemical Breakdown of Acetamiprid by Differential Pulse Polarography. *Journal of Advanced Scientific Research*, *16*(06), 49-55. https://doi.org/10.55218/JASR.2025160605

Kasozi, G. N., Zimmerman, A. R., Nkedi-Kizza, P., & Gao, B. (2010). Catechol and Humic Acid Sorption onto a Range of Laboratory-Produced Black Carbons (Biochars). *Environmental Science & Technology*, *44*(16), 6189-6195. https://doi.org/10.1021/es1014423

Katoch, S., Chauhan, S. S., & Kumar, V. (2021). A review on genetic algorithm: past, present, and future. *Multimedia Tools and Applications*, *80*(5), 8091-8126. https://doi.org/10.1007/s11042-020-10139-6

Kaya, N., & Uzun, Z. Y. (2021). Investigation of effectiveness of pine cone biochar activated with KOH for methyl orange adsorption and CO2 capture. *Biomass Conversion and Biorefinery*, *11*(3), 1067-1083. https://doi.org/10.1007/s13399-020-01063-8

Khan, A. R., Ataullah, R., & Al-Haddad, A. (1997). Equilibrium Adsorption Studies of Some Aromatic Pollutants from Dilute Aqueous Solutions on Activated Carbon at Different Temperatures. *Journal of Colloid and Interface Science*, *194*(1), 154-165. https://doi.org/10.1006/jcis.1997.5041

Khan, A. U., Zahoor, M., Rehman, M. U., Shah, A. B., Zekker, I., Khan, F. A., Ullah, R., Albadrani, G. M., Bayram, R., & Mohamed, H. R. H. (2022). Biological Mineralization of Methyl Orange by Pseudomonas aeruginosa. *Water*, *14*(10), 1551. https://doi.org/10.3390/w14101551

Khan, T. A., Rahman, R., & Khan, E. A. (2017). Adsorption of malachite green and methyl orange onto waste tyre activated carbon using batch and fixed-bed techniques: isotherm and kinetics modeling. *Modeling Earth Systems and Environment*, *3*(1), 38. https://doi.org/10.1007/s40808-017-0284-1

Khiam, G. K., Karri, R. R., Mubarak, N. M., Khalid, M., Walvekar, R., Abdullah, E. C., & Rahman, M. E. (2022). Modelling and optimization for methylene blue adsorption using graphene oxide/chitosan composites via artificial neural network-particle swarm optimization. *Materials Today Chemistry*, *24*, 100946. https://doi.org/10.1016/j.mtchem.2022.100946

Kobkeatthawin, T., Trakulmututa, J., Amornsakchai, T., Kajitvichyanukul, P., & Smith, S. M. (2022). Identification of Active Species in Photodegradation of Aqueous Imidacloprid over g-C3N4/TiO2 Nanocomposites. *Catalysts*, *12*(2), 120. https://doi.org/10.3390/catal12020120

Kostoglou, M., & Karapantsios, T. D. (2022). Why Is the Linearized Form of Pseudo-Second Order Adsorption Kinetic Model So Successful in Fitting Batch Adsorption Experimental Data? *Colloids and Interfaces*, *6*(4), 55. https://doi.org/10.3390/colloids6040055

Krishnani, K. K., Srinives, S., Mohapatra, B. C., Boddu, V. M., Hao, J., Meng, X., & Mulchandani, A. (2013). Hexavalent chromium removal mechanism using conducting polymers. *Journal of Hazardous Materials*, *252-253*, 99-106. https://doi.org/10.1016/j.jhazmat.2013.01.079

Kumar, A., Jash, A., Priyadarshinee, R., Sengupta, B., Dasguptamandal, D., Halder, G., & Mandal, T. (2017). Removal of catechol from aqueous solutions by adsorption using low cost activated carbon prepared from Eichhornia crassipes. *Desalination and Water Treatment*, *73*, 389-398. https://doi.org/10.5004/dwt.2017.20434

Kumar, K. V. (2006). Comments on "Adsorption of acid dye onto organobentonite". *Journal of Hazardous Materials*, *137*(1), 638-639. https://doi.org/10.1016/j.jhazmat.2006.03.056

Kumar, S., Gupta, H., Gautam, A., & Singh, N. (2025). Zinc Peroxide-based Carbon Composite for the Removal of Highly Toxic Insecticide Acetamiprid from Water. *Water, Air, & Soil Pollution*, *237*(4), 201. https://doi.org/10.1007/s11270-025-08792-4

Kwiatkowski, J. F. (2011). *Activated carbon: classifications, properties and applications*. Nova Science Publishers, Incorporated.

Ladadok, C., Yamaki, T., Matsuda, K., Matsumoto, H., & Na-Ranong, D. (2018). Kinetics, isotherm, and thermodynamics of adsorption of sterol on strong acid ion exchange resin [Article]. *Chemical Engineering Transactions*, *70*, 1075-1080. https://doi.org/10.3303/CET1870180

Lagergren, S. (1898). About the theory of so-called adsorption of soluble substances. Available: https://sid.ir/paper/563615/en

Langmuir, I. (1918). The Adsorption of Gases on Plane Surfaces of Glass, Mica and Platinum. *Journal of the American Chemical Society*, *40*(9), 1361-1403. https://doi.org/10.1021/ja02242a004

Lee, C.-G., Kim, J.-H., Kang, J.-K., Kim, S.-B., Park, S.-J., Lee, S.-H., & Choi, J.-W. (2015). Comparative analysis of fixed-bed sorption models using phosphate breakthrough curves in slag filter media. *Desalination and Water Treatment*, *55*(7), 1795-1805. https://doi.org/10.1080/19443994.2014.930698

Levenberg, K. (1944). A method for the solution of certain problems in least squares. Quart. Appl Math.

Lewis, K. A., Tzilivakis, J., Warner, D. J., & Green, A. (2016). An international database for pesticide risk assessments and management. *Human and Ecological Risk Assessment: An International Journal*, *22*(4), 1050-1064. https://doi.org/10.1080/10807039.2015.1133242

Li, A., Ge, W., Liu, L., Zhang, Y., & Qiu, G. (2022). Synthesis and application of amine-functionalized MgFe2O4-biochar for the adsorption and immobilization of Cd(II) and Pb(II). *Chemical Engineering Journal*, *439*, 135785. https://doi.org/10.1016/j.cej.2022.135785

Li, B., Wang, Q., Guo, J.-Z., Huan, W.-W., & Liu, L. (2018). Sorption of methyl orange from aqueous solution by protonated amine modified hydrochar. *Bioresource Technology*, *268*, 454-459. https://doi.org/10.1016/j.biortech.2018.08.023

Li, J., Han, P., Zhang, R., Tao, Y., Zhang, J., Yu, P., Zhao, E., Jing, J., Wang, K., & Wu, J. (2026). H_3PO_4-modified biochar derived from pear branches for efficient neonicotinoid removal. *Environmental Technology & Innovation*, *41*, 104747. https://doi.org/10.1016/j.eti.2026.104747

Lima, E. C., Cestari, A. R., & Adebayo, M. A. (2016). Comments on the paper: a critical review of the applicability of Avrami fractional kinetic equation in adsorption-based water treatment studies. *Desalination and Water Treatment*, *57*(41), 19566-19571. https://doi.org/10.1080/19443994.2015.1095129

Lima, E. C., Gomes, A. A., & Tran, H. N. (2020). Comparison of the nonlinear and linear forms of the van't Hoff equation for calculation of adsorption thermodynamic parameters (ΔS° and ΔH°). *Journal of Molecular Liquids*, *311*, 113315. https://doi.org/10.1016/j.molliq.2020.113315

Lima, E. C., Hosseini-Bandegharaei, A., Moreno-Piraján, J. C., & Anastopoulos, I. (2019). A critical review of the estimation of the thermodynamic parameters on adsorption equilibria.

Wrong use of equilibrium constant in the Van't Hoof equation for calculation of thermodynamic parameters of adsorption. *Journal of Molecular Liquids*, *273*, 425-434. https://doi.org/10.1016/j.molliq.2018.10.048

Lin, P., Xia, Y., & Liu, Z. (2022). Influence of Different Activators on the Structure and Properties of Activated Carbon Based on Bamboo Fiber. *Polymers*, *14*(24), 5500. https://doi.org/10.3390/polym14245500

Liu, Q., Yang, J., Li, H., Ye, J., Fei, Z., Chen, X., Zhang, Z., Tang, J., Cui, M., & Qiao, X. (2021). Activated carbon prepared from catechol distillation residue for efficient adsorption of aromatic organic compounds from aqueous solution. *Chemosphere*, *269*, 128750. https://doi.org/10.1016/j.chemosphere.2020.128750

Liu, Y., Xiang, Y., Xu, H., & Li, H. (2022). The reuse of nano-TiO2 under different concentration of CO32– using coagulation process and its photocatalytic ability in treatment of methyl orange. *Separation and Purification Technology*, *282*, 120152. https://doi.org/10.1016/j.seppur.2021.120152

Liu, Y., Xu, H., Yang, S.-F., & Tay, J.-H. (2003). A general model for biosorption of Cd2+, Cu2+ and Zn2+ by aerobic granules. *Journal of biotechnology*, *102*(3), 233-239. https://doi.org/10.1016/s0168-1656(03)00030-0

Liu, Z., He, W., Zhang, Q., Shapour, H., & Bakhtari, M. F. (2021). Preparation of a GO/MIL-101(Fe) Composite for the Removal of Methyl Orange from Aqueous Solution. *ACS Omega*, *6*(7), 4597-4608. https://doi.org/10.1021/acsomega.0c05091

Lopez-Ramon, M. V., Stoeckli, F., Moreno-Castilla, C., & Carrasco-Marin, F. (1999). On the characterization of acidic and basic surface sites on carbons by various techniques. *Carbon*, *37*(8), 1215-1221. https://doi.org/10.1016/S0008-6223(98)00317-0

Luo, J., Zhou, X., Ma, L., Xu, X., Wu, J., & Liang, H. (2016). Enhanced photodegradation activity of methyl orange over Ag2CrO4/SnS2 composites under visible light irradiation. *Materials Research Bulletin*, *77*, 291-299. https://doi.org/10.1016/j.materresbull.2016.02.005

Ma, Y. (2017). Comparison of Activated Carbons Prepared from Wheat Straw via ZnCl2 and KOH Activation. *Waste and Biomass Valorization*, *8*(3), 549-559. https://doi.org/10.1007/s12649-016-9640-z

Machado, C. P. B. F. M. (2015). *Carbon Nanomaterials as Adsorbents for Environmental and Biological Applications* (C. P. B. F. M. Machado, Ed.). Springer International Publishing. https://doi.org/https://doi.org/10.1007/978-3-319-18875-1

Machrouhi, A., Khnifira, M., Boumya, W., Sadiq, M., Abdennouri, M., Elhalil, A., Mahjoubi, F. Z., & Barka, N. (2023). Experimental and density functional theory studies of methyl orange adsorption on Ni-Al/LDH intercalated sodium dodecyl sulfate. *Chemical Physics Impact*, *6*, 100214. https://doi.org/10.1016/j.chphi.2023.100214

MacKay, D. J. C. (1992). Bayesian Interpolation. *Neural Computation*, *4*(3), 415-447. https://doi.org/10.1162/neco.1992.4.3.415

Marinković, V. (2021). Some Applications of a Novel Desirability Function in Simultaneous Optimization of Multiple Responses. *FME Transactions*, *49*(3). https://doi.org/10.5937/fme2103534m

Marquardt, D. W. (1963). An algorithm for least-squares estimation of nonlinear parameters. *Journal of the society for Industrial and Applied Mathematics*, *11*(2), 431-441. https://doi.org/10.1137/0111030

Marrot, B., Barrios-Martinez, A., Moulin, P., & Roche, N. (2006). Biodegradation of high phenol concentration by activated sludge in an immersed membrane bioreactor. *Biochemical Engineering Journal*, *30*(2), 174-183. https://doi.org/10.1016/j.bej.2006.03.006

Marsh, H., & Rodriguez-Reinonso, F. (2006). *Activated carbon Elsevier Science & Technology Books*.

Martínez, M. L., Torres, M. M., Guzmán, C. A., & Maestri, D. M. (2006). Preparation and characteristics of activated carbon from olive stones and walnut shells. *Industrial Crops and Products*, *23*(1), 23-28. https://doi.org/10.1016/j.indcrop.2005.03.001

Martínez, R. J., Vela-Carrillo, A. Z., Godínez, L. A., Pérez-Bueno, J. d. J., & Robles, I. (2023). Competitive adsorption of anionic and cationic molecules on three activated carbons derived from agroindustrial waste. *Biomass and Bioenergy*, *168*, 106660. https://doi.org/10.1016/j.biombioe.2022.106660

Mason, J. A., Veenstra, M., & Long, J. R. (2014). Evaluating metal–organic frameworks for natural gas storage [10.1039/C3SC52633J]. *Chemical Science*, *5*(1), 32-51. https://doi.org/10.1039/C3SC52633J

Masoumi, S., & Dalai, A. K. (2020). Optimized production and characterization of highly porous activated carbon from algal-derived hydrochar. *Journal of Cleaner Production*, *263*, 121427. https://doi.org/10.1016/j.jclepro.2020.121427

Matsuura, T., Oinuma, H., Komatsu, M., Asano, K., & Itoh, H. (1974). *Process for preparing catechol and hydroquinone* (United States Patent No. https://patents.google.com/patent/US3825604A/en

Mergbi, M., Galloni, M. G., Aboagye, D., Elimian, E., Su, P., Ikram, B. M., Nabgan, W., Bedia, J., Amor, H. B., Contreras, S., Medina, F., & Djellabi, R. (2023). Valorization of lignocellulosic biomass into sustainable materials for adsorption and photocatalytic applications in water and air remediation. *Environmental Science and Pollution Research*, *30*(30), 74544-74574. https://doi.org/10.1007/s11356-023-27484-2

Miller, S. C. (2010). Profiling sulfonate ester stability: Identification of complementary protecting groups for sulfonates [Article]. *Journal of Organic Chemistry*, *75*(13), 4632-4635. https://doi.org/10.1021/jo1007338

Mofrad, M. M. G., Mahdavi, M., & Azari, M. (2025). Treatment of synthetic catechol solution by electrocoagulation-magnetic granular activated pomegranate peel carbon: A cost-effective approach. *Water Environment Research*, *97*(3), e70045. https://doi.org/10.1002/wer.70045

Mohammad, S. G., & Ahmed, S. M. (2019). Adsorptive removal of acetamiprid pesticide from aqueous solution using environmentally friendly natural and agricultural wastes. *Desalination and Water Treatment*, *145*, 280-290. https://doi.org/10.5004/dwt.2019.23644

Mon, P. P., Cho, P. P., Rangappa, H. S., Dobhal, S., Duvvuri, S., Madras, G., Chang-Chien, G.-P., Masimukku, S., & Subrahmanyam, C. (2024). Multiwalled Carbon Nanotube-Foam Composites for Fixed-Bed Continuous Flow Column Adsorption of Dyes. *ACS Applied*

Nano Materials, *7*(22), 25931-25943. https://doi.org/10.1021/acsanm.4c05010

Montgomery, D. C. (2017). *Design and analysis of experiments*. John wiley & sons.

Montgomery, D. C., Peck, E. A., & Vining, G. G. (2012). *Introduction to linear regression analysis* (Fifth ed.). John Wiley & Sons.

Montgomery, D. C., & Runger, G. C. (2018). *Applied statistics and probability for engineers* (Seventh ed.). Hoboken, NJ : Wiley.

Montgomery, D. C., Runger, G. C., & Hubele, N. F. (2009). *Engineering statistics*. John Wiley & Sons.

Moradmand, Z., Dehdashti, B., Mohammadi, F., Zahedi, N., Razaghi, M., & Amin, M. M. (2023). Artificial Neural Networks and Genetic Algorithms: An Efficient Modeling and Optimization Methodology for Degradation of Atenolol Using Activated Persulfate with Ultrasound. *Journal of Environmental and Public Health*, *2023*(1), 9763022. https://doi.org/10.1155/2023/9763022

Morash, M. G., Soanes, K. H., Achenbach, J. C., & Ellis, L. D. (2022). Assessing the Morphological and Behavioral Toxicity of Catechol Using Larval Zebrafish. *International Journal of Molecular Sciences*, *23*(14), 7985. https://doi.org/10.3390/ijms23147985

Moreno-Piraján, J. C., Blanco, D., & Giraldo, L. (2012). Relation Between the Adsorbed Quantity and the Immersion Enthalpy in Catechol Aqueous Solutions on Activated Carbons. *International Journal of Molecular Sciences*, *13*(1), 44-55. https://doi.org/10.3390/ijms13010044

Mosavi, S. S., Zare, E. N., Behniafar, H., Nezhad, S. M., & Neisiany, R. E. (2024). Remediation of acetamiprid pesticide from contaminated water by antibacterial biosorbent based on carboxymethyl tragacanth-grafted-poly(3-aminophenol) decorated with ZnO@Fe3O4. *Environmental Research*, *252*, 118893. https://doi.org/10.1016/j.envres.2024.118893

Mourabet, M. (2014). Comparative Study of Artificial Neural Network and Response Surface Methodology for Modelling and Optimization the Adsorption Capacity of Fluoride onto Apatitic Tricalcium Phosphate. *Universal Journal of Applied Mathematics*, *2*, 84-91. https://doi.org/10.13189/ujam.2014.020202

Murphy, O. P., Vashishtha, M., Palanisamy, P., & Kumar, K. V. (2023). A Review on the Adsorption Isotherms and Design Calculations for the Optimization of Adsorbent Mass and Contact Time. *ACS Omega*, *8*(20), 17407-17430. https://doi.org/10.1021/acsomega.2c08155

Myers, R. H. (2016). *Response surface methodology : process and product optimization using designed experiments* (Fourth ed.).

Najibikhah, P., & Rahbar-Kelishami, A. (2024). Preparation of cationic surfactant modified two-dimensional (2D) multi-layered Ti3C2Tx MXene for methyl orange removal from aqueous solution: Kinetic, equilibrium, and adsorption mechanisms. *Chemosphere*, *350*, 141058. https://doi.org/10.1016/j.chemosphere.2023.141058

Nasser, R. A., Salem, M. Z. M., Hiziroglu, S., Al-Mefarrej, H. A., Mohareb, A. S., Alam, M., & Aref, I. M. (2016). Chemical Analysis of Different Parts of Date Palm (Phoenix dactylifera L.) Using Ultimate, Proximate and Thermo-Gravimetric Techniques for Energy

Production. *Energies*, *9*(5), 374. https://doi.org/10.3390/en9050374

Nazari, G., Abolghasemi, H., Esmaieli, M., & Sadeghi Pouya, E. (2016). Aqueous phase adsorption of cephalexin by walnut shell-based activated carbon: A fixed-bed column study. *Applied Surface Science*, *375*, 144-153. https://doi.org/10.1016/j.apsusc.2016.03.096

Nazir, M. A., Najam, T., Zarin, K., Shahzad, K., Javed, M. S., Jamshaid, M., Bashir, M. A., Shah, S. S. A., & Rehman, A. U. (2023). Enhanced adsorption removal of methyl orange from water by porous bimetallic Ni/Co MOF composite: a systematic study of adsorption kinetics. *International Journal of Environmental Analytical Chemistry*, *103*(16), 4841-4856. https://doi.org/10.1080/03067319.2021.1931855

Ngouallat, N. M., Malanda, N., Malanda, C., Maniongui, K. B., Madila, E., & Louzolo-Kimbembe, P. (2024). Comparative analysis of statistical thickness models for the determination of the external specific surface and the surface of the micropores of materials: the case of a clay concrete stabilized using sugar cane molasses. *Geomaterials*, *14*(02), 13-28. https://doi.org/10.4236/gm.2024.142002

Ngwabebhoh, F. A., & Yildiz, U. (2019). Pyrocatechol Recovery from Aqueous Phase by Nanocellulose-Based Platelet-Shaped Gels: Response Surface Methodology and Artificial Neural Network Design Study. *Journal of environmental engineering*, *145*(2), 04018140. https://doi.org/10.1061/(ASCE)EE.1943-7870.0001491

Nighojkar, A., Zimmermann, K., Ateia, M., Barbeau, B., Mohseni, M., Krishnamurthy, S., Dixit, F., & Kandasubramanian, B. (2023). Application of neural network in metal adsorption using biomaterials (BMs): a review [10.1039/D2VA00200K]. *Environmental Science: Advances*, *2*(1), 11-38. https://doi.org/10.1039/D2VA00200K

Nunes de Morais, A. M., Medeiros Araújo, D., Barbosa Segundo, I. D., Vieira dos Santos, E., Leal de Castro, S. S., Martínez-Huitle, C. A., & Fernandes Alves, J. J. (2023). A Sustainable Electrochemical-Based Solution for Removing Acetamiprid from Water. *Applied Sciences*, *13*(19), 10963. https://doi.org/10.3390/app131910963

Olgun, A., Atar, N., & Wang, S. (2013). Batch and column studies of phosphate and nitrate adsorption on waste solids containing boron impurity. *Chemical Engineering Journal*, *222*, 108-119. https://doi.org/10.1016/j.cej.2013.02.029

Omitola, O. B., Abonyi, M. N., Akpomie, K. G., & Dawodu, F. A. (2022). Adams-Bohart, Yoon-Nelson, and Thomas modeling of the fix-bed continuous column adsorption of amoxicillin onto silver nanoparticle-maize leaf composite. *Applied Water Science*, *12*(5), 94. https://doi.org/10.1007/s13201-022-01624-4

Ouazene, N., Harrar, K., Gharbi, A., Zahi, S. E., Mokrane, S., & Mokrane, H. (2025). Machine learning algorithms prediction of methyl orange removal by Fenton oxidation process. *Chemical Papers*, *79*(7), 4671-4685. https://doi.org/10.1007/s11696-025-04089-2

Ouedrhiri, A., Ait Himi, M., Youbi, B., Lghazi, Y., Bahar, J., El Haimer, C., Aynaou, A., & Bimaghra, I. (2022). Biochar material derived from natural waste with superior dye adsorption performance. *Materials Today: Proceedings*, *66*, 259-267. https://doi.org/10.1016/j.matpr.2022.04.928

Parisheva, Z., & Demirev, A. (2001). Ozonation of aqueous solutions of resorcinol and catechol. *Environment Protection Engineering*, *27*(2), 17-25.

Patel, H. (2019). Fixed-bed column adsorption study: a comprehensive review. *Applied Water Science*, *9*(3), 45. https://doi.org/10.1007/s13201-019-0927-7

Patra, C., & Narayanasamy, S. (2022). Polypyrrole complexation on biomass-derived powdered carbon for adsorptive elimination of emerging pharmaceutical contaminant Sulfamethoxazole: A comprehensive insight. *Journal of Cleaner Production*, *370*, 133565. https://doi.org/10.1016/j.jclepro.2022.133565

Pham, M.-T., Luu, H. Q., Nguyen, T.-M. T., Tran, H.-H., You, S.-J., & Wang, Y.-F. (2021). Rapid and Scalable Fabrication of TiO2@g-C3N4 Heterojunction for Highly Efficient Photocatalytic NO Removal under Visible Light. *Aerosol and Air Quality Research*, *21*(12), 210276. https://doi.org/10.4209/aaqr.210276

Pillar-Little, E. A., & Guzman, M. I. (2017). Oxidation of Substituted Catechols at the Air–Water Interface: Production of Carboxylic Acids, Quinones, and Polyphenols. *Environmental Science & Technology*, *51*(9), 4951-4959. https://doi.org/10.1021/acs.est.7b00232

Pillar-Little, E. A., Zhou, R., & Guzman, M. I. (2015). Heterogeneous Oxidation of Catechol. *The Journal of Physical Chemistry A*, *119*(41), 10349-10359. https://doi.org/10.1021/acs.jpca.5b07914

Pires, M. J. R. G. R., Ferra, M. I. A., & Marques, A. M. M. (2012). Ionization of methyl orange in aqueous sodium chloride solutions. *The Journal of Chemical Thermodynamics*, *53*, 93-99. https://doi.org/10.1016/j.jct.2012.04.023

Pirilä, M. (2015). Adsorption and photocatalysis in water treatment: active, abundant and inexpensive materials and methods.

Ponnusamy, R., Venkatesan, R., Gangan, A., Samal, R., Chakraborty, B., Late, D. J., & Rout, C. S. (2019). Experimental and density functional theory investigations of catechol sensing properties of ZnO/RGO nanocomposites. *Applied Surface Science*, *495*, 143588. https://doi.org/10.1016/j.apsusc.2019.143588

Pradhan, S., Anuraag, N. S., Jatav, N., Sinha, I., & Prasad, N. K. (2023). Magnetic Ni@C nanoadsorbents for methyl orange removal from water. *Environmental Science and Pollution Research*, *30*(56), 118634-118646. https://doi.org/10.1007/s11356-023-30588-4

Prakash, D., Pandey, J., Tiwary, B. N., & Jain, R. K. (2010). A process optimization for bio-catalytic production of substituted catechols (3-nitrocatechol and 3-methylcatechol. *BMC Biotechnology*, *10*(1), 49. https://doi.org/10.1186/1472-6750-10-49

Praveen Kumar, D. G., Hebbar, H. U., & Ramesh, M. N. (2006). Suitability of thin layer models for infrared–hot air-drying of onion slices. *LWT - Food Science and Technology*, *39*(6), 700-705. https://doi.org/10.1016/j.lwt.2005.03.021

Pravina, R., Uthayakumar, H., & Sivasamy, A. (2023). Hybrid approach based on response surface methodology and artificial neural networks coupled with genetic algorithm (RSM-GA-ANN) for the Prediction and optimization for the Photodegradation of dye using nano ZnO anchored glass fiber under solar light irradiation. *Journal of the Taiwan Institute of Chemical Engineers*, *153*, 105248. https://doi.org/10.1016/j.jtice.2023.105248

Products, E. P. o. P. P., & Residues, t. (2013). Scientific Opinion on the developmental neurotoxicity potential of acetamiprid and imidacloprid. *EFSA Journal*, *11*(12), 3471.

https://doi.org/10.2903/j.efsa.2013.3471

Ramath, R., Sukumaran, A. M., Ramachandran, A., & Basheer, S. B. (2023). Methyl orange dye adsorption and degradation at low temperature using iron oxide-incorporated biochar derived from industrial by-products. *Bioresource Technology Reports*, *22*, 101470. https://doi.org/10.1016/j.biteb.2023.101470

Ramutshatsha-Makhwedzha, D., Mavhungu, A., Moropeng, M. L., & Mbaya, R. (2022). Activated carbon derived from waste orange and lemon peels for the adsorption of methyl orange and methylene blue dyes from wastewater. *Heliyon*, *8*(8), e09930. https://doi.org/10.1016/j.heliyon.2022.e09930

Rápó, E., & Tonk, S. (2021). Factors Affecting Synthetic Dye Adsorption; Desorption Studies: A Review of Results from the Last Five Years (2017–2021). *Molecules*, *26*(17), 5419. https://doi.org/10.3390/molecules26175419

Rashed, M. N., Eltaher, M. A., & Abdou, A. N. A. (2017). Adsorption and photocatalysis for methyl orange and Cd removal from wastewater using TiO2/sewage sludge-based activated carbon nanocomposites. *Royal Society Open Science*, *4*(12). https://doi.org/10.1098/rsos.170834

Rattanapan, S., Srikram, J., & Kongsune, P. (2017). Adsorption of Methyl Orange on Coffee grounds Activated Carbon. *Energy Procedia*, *138*, 949-954. https://doi.org/10.1016/j.egypro.2017.10.064

Razavi, R., Basij, M., Beitollahi, H., & Panahandeh, S. (2022). Experimental and theoretical investigation of acetamiprid adsorption on nano carbons and novel PVC membrane electrode for acetamiprid measurement. *Scientific Reports*, *12*(1), 12145. https://doi.org/10.1038/s41598-022-16459-x

Redfern, P. C., Zapol, P., Curtiss, L. A., Rajh, T., & Thurnauer, M. C. (2003). Computational Studies of Catechol and Water Interactions with Titanium Oxide Nanoparticles. *The Journal of Physical Chemistry B*, *107*(41), 11419-11427. https://doi.org/10.1021/jp0303669

Redlich, O., & Peterson, D. L. (1959). A Useful Adsorption Isotherm. *The Journal of Physical Chemistry*, *63*(6), 1024-1024. https://doi.org/10.1021/j150576a611

Ren, B. (2011). Kinetics and thermodynamics of the phosphine adsorption on the modified activated carbon [Article]. *Frontiers of Chemical Engineering in China*, *5*(2), 203-208. https://doi.org/10.1007/s11705-010-0571-0

Revellame, E. D., Fortela, D. L., Sharp, W., Hernandez, R., & Zappi, M. E. (2020). Adsorption kinetic modeling using pseudo-first order and pseudo-second order rate laws: A review. *Cleaner Engineering and Technology*, *1*, 100032. https://doi.org/10.1016/j.clet.2020.100032

Richard, D., Delgado Núñez, M. d. L., & Schweich, D. (2009). Adsorption of complex phenolic compounds on active charcoal: Adsorption capacity and isotherms. *Chemical Engineering Journal*, *148*(1), 1-7. https://doi.org/10.1016/j.cej.2008.07.023

Rodríguez-Reinoso, F., Molina-Sabio, M., & González, M. T. (1995). The use of steam and CO2 as activating agents in the preparation of activated carbons. *Carbon*, *33*(1), 15-23.

https://doi.org/10.1016/0008-6223(94)00100-E

Roginsky, S., & Zeldovich, Y. B. (1934). The catalytic oxidation of carbon monoxide on manganese dioxide. *Acta Phys. Chem. USSR*, *1*(554), 2019. https://doi.org/10.1021/ja01417a002

Rouquerol, J., Rouquerol, F., Llewellyn, P., Maurin, G., & Sing, K. S. (2013). *Adsorption by powders and porous solids: principles, methodology and applications*. Academic press.

Rumelhart, D. E., Hinton, G. E., & Williams, R. J. (1986). Learning representations by back-propagating errors. *Nature*, *323*(6088), 533-536. https://doi.org/10.1038/323533a0

Rungsawang, T., Krobthong, S., Paengpan, K., Kaewtrakulchai, N., Manatura, K., Eiad-Ua, A., Boonruang, C., & Wongrerkdee, S. (2024). Synergy of functionalized activated carbon and ZnO nanoparticles for enhancing photocatalytic degradation of methylene blue and carbaryl. *Radiation Physics and Chemistry*, *223*, 111924. https://doi.org/10.1016/j.radphyschem.2024.111924

Rzig, B., Guesmi, F., Sillanpää, M., & Hamrouni, B. (2021). Modelling and optimization of hexavalent chromium removal from aqueous solution by adsorption on low-cost agricultural waste biomass using response surface methodological approach. *Water Science and Technology*, *84*(3), 552-575. https://doi.org/10.2166/wst.2021.233

Saha, S., Mistri, R., & Ray, B. C. (2013). A rapid and selective method for simultaneous determination of six toxic phenolic compounds in mainstream cigarette smoke using single-drop microextraction followed by liquid chromatography–tandem mass spectrometry. *Analytical and Bioanalytical Chemistry*, *405*(28), 9265-9272. https://doi.org/10.1007/s00216-013-7351-x

Saleh, H. S., Mahdii, B. A., & Altahir, B. M. (2025). Wastewater Benzenediol Removal Catalyzed by Crude Arugula Peroxidase. *Nature Environment & Pollution Technology*, *24*(4). https://doi.org/10.46488/NEPT.2025.v24i04.D1789

Samiey, B., & Toosi, A. R. (2010). Adsorption of malachite green on silica gel: Effects of NaCl, pH and 2-propanol. *Journal of Hazardous Materials*, *184*(1-3), 739-745.

Sangoremi, A. A. (2025). Adsorption kinetic models and their applications: A critical review. *Int. J. Res. Sci. Innov*, *12*, 245-258. https://doi.org/10.51244/IJRSI.2025.120500019

Santana, J. C., Souza Abud, A. K., Wisniewski, A., Navickiene, S., & Romão, L. P. C. (2020). Optimization of an organosolv method using glycerol with iron catalysts for the pretreatment of water hyacinth. *Biomass and Bioenergy*, *133*, 105454. https://doi.org/10.1016/j.biombioe.2019.105454

Sanz-Santos, E., Álvarez-Torrellas, S., Ceballos, L., Larriba, M., Águeda, V. I., & García, J. (2021). Application of Sludge-Based Activated Carbons for the Effective Adsorption of Neonicotinoid Pesticides. *Applied Sciences*, *11*(7), 3087. https://doi.org/10.3390/app11073087

Sayed, F., Parmar, M., & Auti, S. (2019). A Review on Graphene. In H. Vasudevan, V. K. N. Kottur, & A. A. Raina, *Proceedings of International Conference on Intelligent Manufacturing and Automation* Singapore.

Sayed, N. S. M., Ahmed, A. S. A., Abdallah, M. H., & Gouda, G. A. (2024). ZnO@ activated

carbon derived from wood sawdust as adsorbent for removal of methyl red and methyl orange from aqueous solutions. *Scientific Reports*, *14*(1), 5384. https://doi.org/10.1038/s41598-024-55158-7

Sazali, N., Harun, Z., & Sazali, N. (2020). A review on batch and column adsorption of various adsorbent towards the removal of heavy metal. *Journal of Advanced Research in Fluid Mechanics and Thermal Sciences*, *67*(2), 66-88.

Scherrer, P. (1918). Nachr Ges Wiss Goettingen. *Math. Phys.*, *2*, 98-100. https://cir.nii.ac.jp/crid/1571417126345362048

Schweigert, N., Zehnder, A. J. B., & Eggen, R. I. L. (2001). Chemical properties of catechols and their molecular modes of toxic action in cells, from microorganisms to mammals. *Environmental Microbiology*, *3*(2), 81-91. https://doi.org/10.1046/j.1462-2920.2001.00176.x

Sen, T. K. (2017). *Air, gas, and water pollution control using industrial and agricultural solid wastes adsorbents*. CRC Press.

Seow, Y. X., Tan, Y. H., Mubarak, N. M., Kansedo, J., Khalid, M., Ibrahim, M. L., & Ghasemi, M. (2022). A review on biochar production from different biomass wastes by recent carbonization technologies and its sustainable applications. *Journal of Environmental Chemical Engineering*, *10*(1), 107017. https://doi.org/10.1016/j.jece.2021.107017

Serafin, J., Dziejarski, B., Cruz Junior, O. F., & Sreńscek-Nazzal, J. (2023). Design of highly microporous activated carbons based on walnut shell biomass for H2 and CO2 storage. *Carbon*, *201*, 633-647. https://doi.org/10.1016/j.carbon.2022.09.013

Serban, G. V., Iancu, V. I., Dinu, C., Tenea, A., Vasilache, N., Cristea, I., Niculescu, M., Ionescu, I., & Chiriac, F. L. (2023). Removal efficiency and adsorption kinetics of methyl orange from wastewater by commercial activated carbon. *Sustainability*, *15*(17), 12939. https://doi.org/10.3390/su151712939

Shah, S. S., Sharma, T., Dar, B. A., & Bamezai, R. K. (2021). Adsorptive removal of methyl orange dye from aqueous solution using populous leaves: Insights from kinetics, thermodynamics and computational studies. *Environmental Chemistry and Ecotoxicology*, *3*, 172-181. https://doi.org/10.1016/j.enceco.2021.05.002

Shahwan, T. (2021). Critical insights into the limitations and interpretations of the determination of ΔGo, ΔHo, and ΔSo of sorption of aqueous pollutants on different sorbents. *Colloid and Interface Science Communications*, *41*, 100369. https://doi.org/10.1016/j.colcom.2021.100369

Shakir, K., Ghoneimy, H. F., Elkafrawy, A. F., Beheir, S. G., & Refaat, M. (2008). Removal of catechol from aqueous solutions by adsorption onto organophilic-bentonite. *Journal of Hazardous Materials*, *150*(3), 765-773. https://doi.org/10.1016/j.jhazmat.2007.05.037

Shanmugaprakash, M., & Sivakumar, V. (2013). Development of experimental design approach and ANN-based models for determination of Cr(VI) ions uptake rate from aqueous solution onto the solid biodiesel waste residue. *Bioresource Technology*, *148*, 550-559. https://doi.org/10.1016/j.biortech.2013.08.149

Sharifpour, E., Alipanahpour Dil, E., Asfaram, A., Ghaedi, M., & Goudarzi, A. (2019). Optimizing

adsorptive removal of malachite green and methyl orange dyes from simulated wastewater by Mn-doped CuO-Nanoparticles loaded on activated carbon using CCD-RSM: Mechanism, regeneration, isotherm, kinetic, and thermodynamic studies. *Applied Organometallic Chemistry*, *33*(3), e4768. https://doi.org/10.1002/aoc.4768

Shen, M., Zhu, M., Sun, J., Zhang, Y., Li, R., Niu, F., Li, S., Mi, X., & Li, G. (2019). Comparison for the adsorption of catechol and hydroquinone on activated carbon fibre: kinetic analysis. *Nature Environment and Pollution Technology*, *18*(4), 1369-1374.

Shin, J., Lee, S.-H., Kim, S., Ochir, D., Park, Y., Kim, J., Lee, Y.-G., & Chon, K. (2021). Effects of physicochemical properties of biochar derived from spent coffee grounds and commercial activated carbon on adsorption behavior and mechanisms of strontium ions (Sr2+). *Environmental Science and Pollution Research*, *28*(30), 40623-40632. https://doi.org/10.1007/s11356-020-10095-6

Simão, D., & Cerdeira, A. C. (2016). 5.1.1. Synthesis of Methyl Orange. In C. A. M. Afonso, N. R. Candeias, D. P. Simão, A. F. Trindade, J. A. S. Coelho, B. Tan, & R. Franzén (Eds.), *Comprehensive Organic Chemistry Experiments for the Laboratory Classroom* (pp. 0). The Royal Society of Chemistry. https://doi.org/https://doi.org/10.1039/9781849739634-00448

Sing, K. S. W. (1985). Reporting physisorption data for gas/solid systems with special reference to the determination of surface area and porosity (Recommendations 1984). *Pure and Applied Chemistry*, *57*(4), 603-619. https://doi.org/10.1351/pac198557040603

Sips, R. (1948). On the Structure of a Catalyst Surface. *The Journal of Chemical Physics*, *16*(5), 490-495. https://doi.org/10.1063/1.1746922

Sorayyaei, S., Raji, F., Rahbar-Kelishami, A., & Ashrafizadeh, S. N. (2021). Combination of electrocoagulation and adsorption processes to remove methyl orange from aqueous solution. *Environmental Technology & Innovation*, *24*, 102018. https://doi.org/10.1016/j.eti.2021.102018

Souhıla, K. (2024). Efficient Removal of Methyl Orange from Water onto PVC/Bentonite Membranes: Experimental Validation and COMSOL Multiphysics. *International Journal of Intelligent Systems and Applications in Engineering*, *12*(4), 4094 – 4102. https://ijisae.org/index.php/IJISAE/article/view/6988

Srikhaow, A., Chaengsawang, W., Kiatsiriroat, T., Kajitvichyanukul, P., & Smith, S. M. (2022). Adsorption Kinetics of Imidacloprid, Acetamiprid and Methomyl Pesticides in Aqueous Solution onto Eucalyptus Woodchip Derived Biochar. *Minerals*, *12*(5), 528. https://doi.org/10.3390/min12050528

Stoeckli, F., Centeno, T. A., Donnet, J.-B., Pusset, N., & Papirer, E. (1995). Characterization of industrial activated carbons by adsorption and immersion techniques and by STM. *Fuel*, *74*(11), 1582-1588. https://doi.org/10.1016/0016-2361(95)00168-5

Stoeckli, F., Guillot, A., Slasli, A. M., & Hugi-Cleary, D. (2002). Microporosity in carbon blacks. *Carbon*, *40*(2), 211-215. https://doi.org/10.1016/S0008-6223(01)00176-2

Su, J., Noro, J., Fu, J., Wang, Q., Silva, C., & Cavaco-Paulo, A. (2018). Enzymatic polymerization of catechol under high-pressure homogenization for the green coloration of textiles. *Journal of Cleaner Production*, *202*, 792-798. https://doi.org/10.1016/j.jclepro.2018.08.205

Sultana, M., Rownok, M. H., Sabrin, M., Rahaman, M. H., & Alam, S. M. N. (2022). A review on experimental chemically modified activated carbon to enhance dye and heavy metals adsorption. *Cleaner Engineering and Technology*, *6*, 100382. https://doi.org/10.1016/j.clet.2021.100382

Sun, S., Guo, J., Zhu, Z., & Zhou, J. (2024). Microbial degradation mechanisms of the neonicotinoids acetamiprid and flonicamid and the associated toxicity assessments [Mini Review]. *Frontiers in Microbiology*, *Volume 15 - 2024*. https://doi.org/10.3389/fmicb.2024.1500401

Sunthar, L., Asharp, T., & Nadarajah, K. (2023). Insights into Mechanisms of Novel Engineered Biochar Derived from Neem Chips via Iron Catalyst for the Removal of Methyl Orange from Aqueous Phase *Water, Air, & Soil Pollution*, *234*(3), 178. https://doi.org/10.1007/s11270-023-06187-x

Suresh, S., Srivastava, V. C., & Mishra, I. M. (2011a). Isotherm, Thermodynamics, Desorption, and Disposal Study for the Adsorption of Catechol and Resorcinol onto Granular Activated Carbon. *Journal of Chemical & Engineering Data*, *56*(4), 811-818. https://doi.org/10.1021/je100303x

Suresh, S., Srivastava, V. C., & Mishra, I. M. (2011b). Study of Catechol and Resorcinol Adsorption Mechanism through Granular Activated Carbon Characterization, pH and Kinetic Study. *Separation Science and Technology*, *46*(11), 1750-1766. https://doi.org/10.1080/01496395.2011.570284

Suresh, S., Srivastava, V. C., & Mishra, I. M. (2012a). Adsorption of catechol, resorcinol, hydroquinone, and their derivatives: a review. *International Journal of Energy and Environmental Engineering*, *3*(1), 32. https://doi.org/10.1186/2251-6832-3-32

Suresh, S., Srivastava, V. C., & Mishra, I. M. (2012b). Adsorption of catechol, resorcinol, hydroquinone, and their derivatives: a review. *International Journal of Energy and Environmental Engineering*, *3*(1 (December 2012)). https://doi.org/10.1186/2251-6832-3-32

Taillebois, E., Cartereau, A., & Thany, S. H. (2024). Effect of Acetamiprid, a Neonicotinoid Insecticide, on Locomotor Activity of the American Cockroach. *Insects*, *15*(1). https://doi.org/10.3390/insects15010054

Tamaš, N., Špirović Trifunović, B., Brkić, D., Miletić, N., & Sretenović, M. (2025). Possibilities for Controlling the Most Important Diseases and Pests of Sour Cherries and an Analysis of Pesticide Residues in Fruits. *Horticulturae*, *11*(2), 191. https://doi.org/10.3390/horticulturae11020191

Tang, Z., Yang, Y., & Wei, W. (2024). Efficient Catalytic Degradation of Methyl Orange by Various ZnO-Doped Lignin-Based Carbons. *Molecules*, *29*(8), 1817. https://doi.org/10.3390/molecules29081817

Tcheka, C., Conradie, M. M., Assinale, V. A., & Conradie, J. (2024). Mesoporous biochar derived from Egyptian doum palm (Hyphaene thebaica) shells as low-cost and biodegradable adsorbent for the removal of methyl orange dye: Characterization, kinetic and adsorption mechanism. *Chemical Physics Impact*, *8*, 100446. https://doi.org/10.1016/j.chphi.2023.100446

Terranova, U., & Bowler, D. R. (2010). Adsorption of Catechol on TiO2 Rutile (100): A Density Functional Theory Investigation. *The Journal of Physical Chemistry C*, *114*(14), 6491-6495. https://doi.org/10.1021/jp911214w

Testing, A. S. f., & Materials. (2009). Standard Test Method for Moisture in Activated Carbon In (Vol. D2867–09): ASTM International West Conshohocken.

Testing, A. S. f., & Materials. (2011). Standard Test Methods for Total Ash Content of activated carbon. In (Vol. D2866–11): ASTM International West Conshohocken.

Tewari, P. H. (1981). *Adsorption from aqueous solutions*. Springer.

Thao, T. P., Kao, H.-C., Juang, R.-S., & Lan, J. C.-W. (2013). Kinetic characteristics of biodegradation of methyl orange by Pseudomonas putida mt2 in suspended and immobilized cell systems. *Journal of the Taiwan Institute of Chemical Engineers*, *44*(5), 780-785. https://doi.org/10.1016/j.jtice.2013.01.015

Thomas, H. C. (1944). Heterogeneous Ion Exchange in a Flowing System. *Journal of the American Chemical Society*, *66*(10), 1664-1666. https://doi.org/10.1021/ja01238a017

Thommes, M., Kaneko, K., Neimark, A. V., Olivier, J. P., Rodriguez-Reinoso, F., Rouquerol, J., & Sing, K. S. W. (2015). Physisorption of gases, with special reference to the evaluation of surface area and pore size distribution (IUPAC Technical Report). *Pure and Applied Chemistry*, *87*(9-10), 1051-1069. https://doi.org/10.1515/pac-2014-1117

Tien, C. (1994). *Adsorption calculations and modeling*. Butterworth-Heinemann.

Tomul, F., Arslan, Y., Kabak, B., Trak, D., & Tran, H. N. (2021). Adsorption process of naproxen onto peanut shell-derived biosorbent: important role of n–π interaction and van der Waals force. *Journal of Chemical Technology & Biotechnology*, *96*(4), 869-880. https://doi.org/10.1002/jctb.6613

Tóth, J. (1971). State Equation of the Solid-Gas Interface Layers.

Tran, H. N. (2022). Improper Estimation of Thermodynamic Parameters in Adsorption Studies with Distribution Coefficient KD (qe/Ce) or Freundlich Constant (KF): Considerations from the Derivation of Dimensionless Thermodynamic Equilibrium Constant and Suggestions. *Adsorption Science & Technology*, *2022*, 5553212. https://doi.org/10.1155/2022/5553212

Tran, H. N., Lee, C.-K., Nguyen, T. V., & Chao, H.-P. (2018). Saccharide-derived microporous spherical biochar prepared from hydrothermal carbonization and different pyrolysis temperatures: synthesis, characterization, and application in water treatment. *Environmental Technology*, *39*(21), 2747-2760. https://doi.org/10.1080/09593330.2017.1365941

Tran, H. N., Lima, E. C., Juang, R.-S., Bollinger, J.-C., & Chao, H.-P. (2021). Thermodynamic parameters of liquid–phase adsorption process calculated from different equilibrium constants related to adsorption isotherms: A comparison study. *Journal of Environmental Chemical Engineering*, *9*(6), 106674. https://doi.org/10.1016/j.jece.2021.106674

Tran, H. N., Nguyen, H. C., Woo, S. H., Nguyen, T. V., Vigneswaran, S., Hosseini-Bandegharaei, A., Rinklebe, J., Kumar Sarmah, A., Ivanets, A., Dotto, G. L., Bui, T. T., Juang, R.-S., & Chao, H.-P. (2019). Removal of various contaminants from water by renewable

lignocellulose-derived biosorbents: a comprehensive and critical review. *Critical Reviews in Environmental Science and Technology*, *49*(23), 2155-2219. https://doi.org/10.1080/10643389.2019.1607442

Tran, H. N., Tomul, F., Thi Hoang Ha, N., Nguyen, D. T., Lima, E. C., Le, G. T., Chang, C.-T., Masindi, V., & Woo, S. H. (2020). Innovative spherical biochar for pharmaceutical removal from water: Insight into adsorption mechanism. *Journal of Hazardous Materials*, *394*, 122255. https://doi.org/10.1016/j.jhazmat.2020.122255

Tran, H. N., You, S.-J., & Chao, H.-P. (2016). Thermodynamic parameters of cadmium adsorption onto orange peel calculated from various methods: A comparison study. *Journal of Environmental Chemical Engineering*, *4*(3), 2671-2682. https://doi.org/10.1016/j.jece.2016.05.009

Tran, H. N., You, S.-J., & Chao, H.-P. (2017). Insight into adsorption mechanism of cationic dye onto agricultural residues-derived hydrochars: Negligible role of π-π interaction. *Korean Journal of Chemical Engineering*, *34*(6), 1708-1720. https://doi.org/10.1007/s11814-017-0056-7

Tran, H. N., You, S.-J., Hosseini-Bandegharaei, A., & Chao, H.-P. (2017). Mistakes and inconsistencies regarding adsorption of contaminants from aqueous solutions: A critical review. *Water Research*, *120*, 88-116. https://doi.org/10.1016/j.watres.2017.04.014

Trifi, B., Bouallegue, M. C., & Marzouk Trifi, I. (2019). Application of response surface methodology for optimization of methyl red adsorption by orange peels. *Desalination and Water Treatment*, *154*, 369-375. https://doi.org/10.5004/dwt.2019.24086

Uddin, M. K., & Baig, U. (2019). Synthesis of Co_3O_4 nanoparticles and their performance towards methyl orange dye removal: Characterisation, adsorption and response surface methodology. *Journal of Cleaner Production*, *211*, 1141-1153. https://doi.org/10.1016/j.jclepro.2018.11.232

Van Thang, V., Nguyen, N. T. D., Nguyen, P. L., & Phung, T. V. B. (2025). Effective Adsorption of Methyl Orange from Aqueous Solution Using MOFs Nanocomposites UiO-66-NH2/GO@PVA. *ACS Omega*, *10*(35), 40162-40173. https://doi.org/10.1021/acsomega.5c04958

Vunain, E., Houndedjihou, D., Monjerezi, M., Muleja, A. A., & Kodom, B. (2018). Adsorption, Kinetics and Equilibrium Studies on Removal of Catechol and Resorcinol from Aqueous Solution Using Low-Cost Activated Carbon Prepared from Sunflower (Helianthus annuus) Seed Hull Residues. *Water, Air, & Soil Pollution*, *229*(11), 366. https://doi.org/10.1007/s11270-018-3993-9

Wallace, D. R. (2014). Acetamiprid. In P. Wexler (Ed.), *Encyclopedia of Toxicology (Third Edition)* (pp. 30-32). Academic Press. https://doi.org/https://doi.org/10.1016/B978-0-12-386454-3.00091-9

Wang, H., Huang, Y., Shen, C., Wu, J., Yan, A., & Zhang, H. (2016). Co-transport of Pesticide Acetamiprid and Silica Nanoparticles in Biochar-Amended Sand Porous Media. *Journal of Environmental Quality*, *45*(5), 1749-1759. https://doi.org/10.2134/jeq2016.02.0073

Wang, J., & Guo, X. (2020). Adsorption kinetic models: Physical meanings, applications, and solving methods. *Journal of Hazardous Materials*, *390*, 122156.

https://doi.org/10.1016/j.jhazmat.2020.122156

Wang, L., Shi, C., Wang, L., Pan, L., Zhang, X., & Zou, J.-J. (2020). Rational design, synthesis, adsorption principles and applications of metal oxide adsorbents: a review [10.1039/C9NR09274A]. *Nanoscale*, *12*(8), 4790-4815. https://doi.org/10.1039/C9NR09274A

Wang, Q., Jia, X., Jin, M., Guo, R., Niu, B., Yan, H., & Wang, H. (2023). A magnetically recyclable carboxyl-functionalized chitosan composite for efficiently removing methyl orange from wastewater: Isotherm, kinetics, thermodynamic, and adsorption mechanism. *International Journal of Biological Macromolecules*, *253*, 126631. https://doi.org/10.1016/j.ijbiomac.2023.126631

Wang, S., Huang, Y., Wu, Y., Zhang, X., Wan, L., Liu, X., & Zhang, W. (2021). Re-utilization of Chinese medicinal herbal residue: waste wormwood rod-derived porous carbon as a low-cost adsorbent for methyl orange removal. *Water Science and Technology*, *84*(9), 2601-2614. https://doi.org/10.2166/wst.2021.453

Wang, W., Le, T., Wang, W.-W., Yin, J.-F., & Jiang, H.-Y. (2023). The Effects of Structure and Oxidative Polymerization on Antioxidant Activity of Catechins and Polymers. *Foods*, *12*(23), 4207. https://doi.org/10.3390/foods12234207

Wang, Y., Qiu, C., Cheng, P., Li, Y., Ma, Y., Tao, X., Weng, B., & Mailhot, G. (2024). Enhanced Orange II Removal Using Fe/Mn/Mg2-LDH Activated Peroxymonosulfate: Synergistic Radical Oxidation and Adsorption. *Catalysts*, *14*(6), 380. https://doi.org/10.3390/catal14060380

Wang, Y., Wang, C., Huang, X., Zhang, Q., Wang, T., & Guo, X. (2024). Guideline for modeling solid-liquid adsorption: Kinetics, isotherm, fixed bed, and thermodynamics. *Chemosphere*, *349*, 140736. https://doi.org/10.1016/j.chemosphere.2023.140736

Weber Jr, W. J. (1984). Evolution of a technology. *Journal of environmental engineering*, *110*(5), 899-917. https://doi.org/10.1061/(ASCE)0733-9372(1984)110:5(899

Weber Jr, W. J., & Morris, J. C. (1963). Kinetics of adsorption on carbon from solution. *Journal of the sanitary engineering division*, *89*(2), 31-59. https://doi.org/10.1061/JSEDAI.0000430

Wei, K., Lv, T., Wang, T., Zhou, H., Jiang, Y., Qin, X., & Liu, Z. (2023). High adsorption of methyl orange by nitrogen-doped activated carbon derived from kraft lignin via self-activation. *Surfaces and Interfaces*, *42*, 103484. https://doi.org/10.1016/j.surfin.2023.103484

Werbos, P. (1974). Beyond regression: new tools for prediction and analysis in the behavioral sciences. *PhD thesis, Committee on Applied Mathematics, Harvard University, Cambridge, MA*. https://cir.nii.ac.jp/crid/1571135649638605440

Worch, E. (2012). *Adsorption Technology in Water Treatment*. Walter de Gruyter GmbH & Co.

Wu, Y., Zhang, X., Liu, C., Tian, L., Zhang, Y., Zhu, M., Qiao, W., Wu, J., Yan, S., Zhang, H., & Bai, H. (2024). Adsorption Behaviors and Mechanism of Phenol and Catechol in Wastewater by Magnetic Graphene Oxides: A Comprehensive Study Based on Adsorption Experiments, Mathematical Models, and Molecular Simulations. *ACS Omega*, *9*(13),

15101-15113. https://doi.org/10.1021/acsomega.3c09346

Yadav, D., Ranjan, B., McHunu, N., Le Roes-Hill, M., & Kudanga, T. (2021). Enzymatic treatment of phenolic pollutants by a small laccase immobilized on APTES-functionalised magnetic nanoparticles. *3 Biotech*, *11*(6), 302. https://doi.org/10.1007/s13205-021-02854-0

Yahia, I. S., Abd El-sadek, M. S., & Yakuphanoglu, F. (2012). Methyl orange (C.I. acid orange 52) as a new organic semiconductor: Conduction mechanism and dielectrical relaxation. *Dyes and Pigments*, *93*(1), 1434-1440. https://doi.org/10.1016/j.dyepig.2011.10.002

Yahya, M. A., Al-Qodah, Z., & Ngah, C. W. Z. (2015). Agricultural bio-waste materials as potential sustainable precursors used for activated carbon production: A review. *Renewable and Sustainable Energy Reviews*, *46*, 218-235. https://doi.org/10.1016/j.rser.2015.02.051

Yahya, S. A., Iqbal, T., Omar, M. M., & Ahmad, M. (2021). Techno-Economic Analysis of Fast Pyrolysis of Date Palm Waste for Adoption in Saudi Arabia. *Energies*, *14*(19), 6048. https://doi.org/10.3390/en14196048

Yan, G., Viraraghavan, T., & Chen, M. (2001). A New Model for Heavy Metal Removal in a Biosorption Column. *Adsorption Science & Technology*, *19*(1), 25-43. https://doi.org/10.1260/0263617011493953

Yang, Y., Yan, W., & Jing, C. (2012). Dynamic Adsorption of Catechol at the Goethite/Aqueous Solution Interface: A Molecular-Scale Study. *Langmuir*, *28*(41), 14588-14597. https://doi.org/10.1021/la303413j

Yao, X.-W., Chen, X., Chen, M.-L., Feng, N.-J., Tong, L.-Y., Yi, Y.-Q., Qian, W., & Diao, Z.-H. (2024). Removal of pesticide acetamiprid using KOH activated biochar derived from crayfish shell: Behavior and mechanism. *Process Safety and Environmental Protection*, *186*, 808-818. https://doi.org/10.1016/j.psep.2024.04.076

Yap, Y. W., Mahmed, N., Norizan, M. N., Abd Rahim, S. Z., Ahmad Salimi, M. N., Abdul Razak, K., Mohamad, I. S., Abdullah, M. M. A.-B., & Mohamad Yunus, M. Y. (2023). Recent Advances in Synthesis of Graphite from Agricultural Bio-Waste Material: A Review. *Materials*, *16*(9), 3601. https://doi.org/10.3390/ma16093601

Yeh, I.-C., Lenhart, J. L., & Rinderspacher, B. C. (2015). Molecular Dynamics Simulations of Adsorption of Catechol and Related Phenolic Compounds to Alumina Surfaces. *The Journal of Physical Chemistry C*, *119*(14), 7721-7731. https://doi.org/10.1021/jp512780s

Yoon, Y. H., & Nelson, J. H. (1984). Application of Gas Adsorption Kinetics I. A Theoretical Model for Respirator Cartridge Service Life. *American Industrial Hygiene Association Journal*, *45*(8), 509-516. https://doi.org/10.1080/15298668491400197

Yu, L., Cao, M.-y., Wang, P.-t., Wang, S., Yue, Y.-r., Yuan, W.-d., Qiao, W.-c., Wang, F., & Song, X. (2017). Simultaneous Decolorization and Biohydrogen Production from Xylose by Klebsiella oxytoca GS-4-08 in the Presence of Azo Dyes with Sulfonate and Carboxyl Groups. *Applied and Environmental Microbiology*, *83*(10), e00508-00517. https://doi.org/10.1128/AEM.00508-17

Zarcheva, M. N., & Chu, K. H. (2025). Predictive modeling of micropollutant removal in fixed-bed adsorbers. *Environmental Chemistry and Safety*, *1*(3), 9600026. https://doi.org/10.1016/10.26599/ECS.2025.9600026

Zbair, M., Anfar, Z., Ait Ahsaine, H., El Alem, N., & Ezahri, M. (2018). Acridine orange adsorption by zinc oxide/almond shell activated carbon composite: Operational factors, mechanism and performance optimization using central composite design and surface modeling. *Journal of Environmental Management*, *206*, 383-397. https://doi.org/10.1016/j.jenvman.2017.10.058

Zhang, J. (2019). Physical insights into kinetic models of adsorption. *Separation and Purification Technology*, *229*, 115832. https://doi.org/10.1016/j.seppur.2019.115832

Zhang, J., Wang, X., Yue, W., Bao, J., Yao, M., & Ge, L. (2024). Toxicological Analysis of Acetamiprid Degradation by the Dominant Strain Md2 and Its Effect on the Soil Microbial Community. *Toxics*, *12*(8). https://doi.org/10.3390/toxics12080572

Zhang, T., Wojtal, P., Rubel, O., & Zhitomirsky, I. (2015). Density functional theory and experimental studies of caffeic acid adsorption on zinc oxide and titanium dioxide nanoparticles [10.1039/C5RA21511K]. *RSC Advances*, *5*(129), 106877-106885. https://doi.org/10.1039/C5RA21511K

Zhang, X., Saravanakumar, K., Sathiyaseelan, A., Lu, Y., & Wang, M.-H. (2023). Adsorption of methyl orange dye by SiO2 mesoporous nanoparticles: adsorption kinetics and eco-toxicity assessment in Zea mays sprout and Artemia salina. *Environmental Science and Pollution Research*, *30*(55), 117000-117010. https://doi.org/10.1007/s11356-023-26173-4

Zhang, X., Tran, H. N., Liu, Y., Yang, C., Zhang, T., Guo, J., Zhu, W., Ahmad, M., Xiao, H., & Song, J. (2023). Nitrogen-doped magnetic biochar made with K3[Fe(C2O4)3] to adsorb dyes: Experimental approach and density functional theory modeling. *Journal of Cleaner Production*, *383*, 135527. https://doi.org/10.1016/j.jclepro.2022.135527

Zhang, Y., Boyd, S. A., Teppen, B. J., Tiedje, J. M., & Li, H. (2014). Role of tetracycline speciation in the bioavailability to escherichia coli for uptake and expression of antibiotic resistance [Article]. *Environmental Science and Technology*, *48*(9), 4893-4900. https://doi.org/10.1021/es5003428

Zhao, L., Xue, H., Elumalai, P., Zhu, X., Wang, L., Zhang, K., Li, D., Ji, J., Luo, J., Cui, J., & Gao, X. (2024). Sublethal acetamiprid affects reproduction, development and disrupts gene expression in Binodoxys communis. *Environmental Science and Pollution Research*. https://doi.org/10.1007/s11356-024-33415-6

Zollinger, H. (2003). *Color chemistry: syntheses, properties, and applications of organic dyes and pigments*. John Wiley & Sons.

Zubair, M., Mu'azu, N. D., Jarrah, N., Blaisi, N. I., Aziz, H. A., & A. Al-Harthi, M. (2020). Adsorption Behavior and Mechanism of Methylene Blue, Crystal Violet, Eriochrome Black T, and Methyl Orange Dyes onto Biochar-Derived Date Palm Fronds Waste Produced at Different Pyrolysis Conditions. *Water, Air, & Soil Pollution*, *231*(5), 240. https://doi.org/10.1007/s11270-020-04595-x

Zuščíková, L., Bažány, D., Greifová, H., Knížatová, N., Kováčik, A., Lukáč, N., & Jambor, T. (2023). Screening of Toxic Effects of Neonicotinoid Insecticides with a Focus on Acetamiprid: A Review. *Toxics*, *11*(7), 598. https://doi.org/10.3390/toxics11070598

List of Publications and Communications

* * * * *

- **Peer-Reviewed Publications**

1. Hazmoune, A., Boukaous, C., **Al-Hazeef, M. S. F.**, Aida, M. S., Fadhillah, F., Assadi, A. A., Amrane, A., Ali, F. A., Zhang, J., & Tahraoui, H. (2026). *Eco-Friendly Synthesis of Zn-Doped CuO Nanoparticles Using Aloysia citrodora Extract for Highly Efficient Fenton-like Dye Degradation*. Catalysts, *16*(4), 352. https://doi.org/https://doi.org/10.3390/catal16040352
2. Mebarka, K., Aidi, A., **Al-Hazeef, M. S. F**., Rehali, H., Hameurlaine, S., Djezzar, Z., Hamida, K., & Ziad, S. (2025). *Date palm leaf-derived activated carbon for enhanced copper (II) removal from aqueous solutions: A sustainable adsorbent for water treatment applications*. Desalination and Water Treatment, *324*, 101522. https://doi.org/https://doi.org/10.1016/j.dwt.2025.101522
3. Hasan, G. G., Laouini, S. E., Osman, A. I., Bouafia, A., Althamthami, M., Meneceur, S., **Al-Hazeef, M. S. F.**, Al-Fatesh, A. S., & Rooney, D. W. (2024). *Green synthesis of Mn_3O_4@CoO nanocomposites using Rosmarinus officinalis L. extract for enhanced photocatalytic hydrogen production and CO_2 conversion*. Journal of Environmental Chemical Engineering, *12*(5), 113911. https://doi.org/https://doi.org/10.1016/j.jece.2024.113911
4. **Al-Hazeef, M. S. F**., Aidi, A., Hecini, L., Osman, A. I., Hasan, G. G., Althamthami, M., Ziad, S., Otmane, T., & Rooney, D. W. (2024). *Valorizing date palm spikelets into activated carbon-derived composite for methyl orange adsorption: advancing circular bioeconomy in wastewater treatment—a comprehensive study on its equilibrium, kinetics, thermodynamics, and mechanisms*. Environmental Science and Pollution Research, *31*, 50493–50512. https://doi.org/https://doi.org/10.1007/s11356-024-34581-3
5. **Al-Hazeef, M. S. F.**, Aidi, A., Hecini, L., Hasan, G. G., Hu, J., & Althamthami, M. (2024). *Unveiling the efficiency of peanut shell-derived porous composite for water denitrification: Characterization, kinetic, isotherm and thermodynamic studies*. Journal of Molecular Liquids, *410*, 125668. https://doi.org/https://doi.org/10.1016/j.molliq.2024.125668

- **International Communications**

1. **M.S.F Al-Hazeef**, A. Aidi, L. Hecini; *Bioremediation of Dyes in Wastewater: A Sustainable Approach Using Date Palm Waste-Derived Activated Carbon***,** The First International Seminar on Agri-Food and Industrial Biotechnology (ISABI), 26-27 June 2024, Khemis Miliana University, Algeria.
2. **M.S.F Al-Hazeef**, A. Aidi, L. Hecini; *Production of activated carbons from agriculture wastes for nitrates removal*, The First International Seminar on Chemical Process & Environment, 14-15 March, 2023, University of Biskra, Biskra, Algeria.

- **National Communications**

1. **M.S.F Al-Hazeef**, L. Hecini; A. Aidi,S. Senouci, *Comparative Characterization of Biochar and ZnO-Modified Activated Carbon Composites Using XRD and SEM Techniques*, The Second National Symposium on Analysis Techniques in Different Fields, 30 Nov and 01 Dec, 2025, Biskra University, Biskra, Algeria.
2. **M.S.F Al-Hazeef**, A. Aidi, L. Hecini; *Valorization of Date Palm Waste in the Production of Activated Carbon for Dye Removal*, The First National Seminar on Valorization of Natural and Residual Biomass (SNVBNR), 20, 21 April, 2024, Biskra University, Biskra, Algeria.
3. **M.S.F Al-Hazeef**, A. Aidi, L. Hecini; Date Palm Waste-Derived Activated Carbon for Organic Dye Removal: Thermodynamic study, The Second National Conference on Materials, Energy & Environment (NCMEE), 13, 14 February, 2024, Biskra University, Biskra, Algeria.
4. **M.S.F Al-Hazeef**, A. Aidi, *Preparation of a new adsorbent from agricultural residue: Application to water treatment*, The Second Study Day on Materials: Synthesis and Energy Applications, 03 December, 2023, Biskra University, Biskra, Algeria.
5. **M.S.F Al-Hazeef**, A. Aidi, *Dépollution des eaux usées par un biochar: Activation, Caractérisation et Application*, The First Study Day on Characterization Methods of Materials and Biomaterials, 19 November, 2023, Biskra University, Biskra, Algeria.